Experimental and numerical study of the mechanical behavior of metal/polymer multilayer composite for ballistic protection

Charles Francart

UNIVERSITÉ DE STRASBOURG

ÉCOLE DOCTORALE ED269

ICUBE – Equipe MMB

THÈSE présentée par :

Charles FRANCART

soutenue le : **13th Octobre 2017**

pour obtenir le grade de : **Docteur de l'université de Strasbourg**

Discipline/ Spécialité : Mécanique des Matériaux

Experimental and numerical study of the mechanical behavior of metal/polymer multilayer composite for ballistic protection

THÈSE dirigée par :

Mr AHZI Said	Pr., ICUBE – Université de Strasbourg
Mme BAHLOULI Nadia	Pr., ICUBE – Université de Strasbourg

RAPPORTEURS :

Mr LAURO Franck	Pr., LAMIH – Université de Valenciennes
Mr RUSINEK Alexis	Pr., LEM3 – Université de Lorraine

AUTRES MEMBRES DU JURY :

Mme DEMARTY Yaël	Dr., French-German Institute of Saint-Louis (ISL)
Mr RITTEL Daniel	Pr., Technion (Israël)
Mme VERLEYSEN Patricia	Pr., University of Ghent

Symbol	Signification	Unit
a	Fitting parameter of kinetic of microstructure change	-
α	Empirical coefficient for Taylor equation	-
A_E	Preexponential parameter for damage evolution	MPa
b	Burger's vector (metals) Temperature sensitivity of locking parameter N (polymers)	nm K^{-1}
B	Plastic modulus	MPa
B_E	Exponential parameter for damage evolution	-
C_p	Specific heat	$J.kg^{-1}.K^{-1}$
C_0	Sound velocity	$m.s^{-1}$
C_R	Rubber modulus	MPa
c_1^g	First parameter of William-Lundon-Ferry relation	-
c_2^g	Second parameter of William-Lundon-Ferry relation	K
D	Damage variable Diameter of the projectile	- mm
d	Interdislocation distance	nm
d_1, d_2, d_3, d_4	Triaxiality sensitivity parameters of the plastic strain at initiation of failure (d_4 for epoxy resin only)	-
D_g	Grain size	µm
E	Young's modulus	GPa
$\langle E \rangle$	Average Young's modulus (in case of viscoelasticity)	GPa
E_M	Damage energy	MPa
ε_e	True elastic strain	-
ε_p	True plastic strain	-
ε_n	Nominal strain	-
ε_p^f	Plastic strain at initiation of failure	-
ε_p^u	Plastic strain at ultimate failure	-
ε_C^{plug}	Plastic strain at initiation of failure at low strain rate in shear-compression state of stress	-
ε_{lim}^f	Minimum limit value of plastic strain at initiation of failure at high strain rates for polymers materials	-
$\dot{\varepsilon}_e$	Elastic strain rate	s^{-1}
$\dot{\varepsilon}_p$	Plastic strain rate	s^{-1}

$\dot{\varepsilon}_0$	Reference strain rate of the calorific model (metals) Reference strain rate of the cooperative model (polymers)	s^{-1}
$\dot{\varepsilon}_{e0}$	Reference strain rate of the elastic modulus model	s^{-1}
$\dot{\varepsilon}_r$	Reference strain rate of the stress model	s^{-1}
$\dot{\varepsilon}_m$	Athermal transition strain rate	s^{-1}
$\dot{\varepsilon}_{0f}$	Reference strain rate for the failure model	s^{-1}
E_A	Stress loss during per Kelvin adiabatic heating	$Pa.K^{-nT}$
f_H	Strain hardening function	MPa
f_{SR}	Strain rate sensitivity function of internal stress	-
f_{σ^*}	State of stress sensitivity function of plastic strain at initiation of failure	-
f_{vf}	Strain rate sensitivity function of plastic strain at initiation of failure	-
f_{T_f}	Temperature sensitivity function of plastic strain at initiation of failure	-
f_A	Adiabatic heating sensitivity function	-
g_0	Adimensional energy of thermo-activation of overcoming of Peierls barriers	-
G_0	Total energy required to overcome the obstacles through thermal activation for one atom	eV
γ	Shear strain	-
H	Target thickness	mm
h	Depth of penetration of the projectile in the target	mm
h_{lim}	Limit value of h for plug detachment	mm
ΔH	Enthalpy of activation of β relaxation phenomenon of polymers	$kJ.mol^{-1}$
J_3	Third invariant of stress deviator	MPa^3
k	Average coefficient of annihilation of dislocations	-
κ	Kocks formula parameter	-
k_B	Boltzmann's constant $k_B = 1.381e-23$	$m^2.kg.s^{-2}.K^{-1}$
κ	Kocks formula parameter	-
l_v	Phenomenological parameter of internal stress strain rate sensitivity	-
l_{vf}	Phenomenological parameter of strain rate sensitivity of plastic strain at initiation of failure	-
L_{eff}	Effective projectile length	mm
λ	Stretch parameter	-
μ	Shear modulus	GPa
M	Number of phenomena leading to the effective stress	-

m	Temperature sensitivity for Johnson-Cook model (metals) Temperature sensitivity for cooperative model (polymers) Temperature sensitivity for strain at initiation of failure (polymers)	-
ν	Elastic Poisson's ratio	-
ν_p	Plastic Poisson's ratio	-
N	Number of change of microstructure for calorific ratio (metals) Locking parameter (polymers)	-
n	Value of parameter for the type of microstructure change in calorific ratio (0 or 1) Parameter of cooperative model (polymers)	-
n_p	Isotropic hardening coefficient	-
n_T	Adiabatic heating sensitivity	-
n_v	Phenomenological parameter of internal stress strain rate sensitivity	-
n_{vf}	Phenomenological parameter of strain rate sensitivity of plastic strain at initiation of failure	-
Ω	Calorific ratio (stress modeling)	-
$\mho = \Omega^{-1}$	Inverse calorific ratio (failure modeling)	-
ω	Kocks' formula parameter	-
ω_0	Attempt frequency (Debye frequency)	s^{-1}
ϖ	Temperature of microstructural change strain rate sensitivity	K
ψ	Normalized energetic balance function (polymers)	-
φ	$\frac{k_B}{g_0 \mu b^3}$	K^{-1}
R	Kinematic hardening coefficient Perfect gas constant $R = 8.314$	MPa $J.mol^{-1}.K^{-1}$
ρ	Volumetric mass of the material	$kg.m^{-3}$
ρ_t	Equivalent volumetric mass of the target	$kg.m^{-3}$
ρ_p	Equivalent volumetric mass of the projectile	$kg.m^{-3}$
ρ_m	Density of mobile dislocations	m^{-2}
σ	True plastic stress	MPa
σ_{eq}	True equivalent stress	MPa
σ_{exp}	Experimental stress	MPa
σ_n	Nominal stress	MPa
σ_e	True elastic stress	MPa
σ_{int}	Internal stress (metals)	MPa

σ_{eff}	Effective stress (metals)	MPa
σ_{ath}	Athermal stress (metals)	MPa
σ_{th}	Thermal stress (metals)	MPa
σ_{VS}	Viscous drag stress (metals)	MPa
σ_B	Back stress from hyperelasticity phenomenon (polymers)	MPa
σ_y	Yield stress (polymers)	MPa
σ_r	Effective resistive stress of the target	MPa
T	Absolute temperature	K
t	Time	s
T_C	Critical temperature (metals)	K
T_m	Melting temperature (metals)	K
T_p	Temperature of microstructural change (metals) – calorific model	K
T_r	Reference temperature of the considered model	K
T_t	Range of temperature of microstructural change – calorific ratio and cooperative model)	K
T_g	Glass transition temperature (polymers)	K or °C
T_β	Temperature of β relaxation phenomenon (polymers)	K or °C
T_γ	Temperature of γ relaxation phenomenon (polymers)	K or °C
T_d	Temperature of degradation (polymers)	K or °C
T_0	Initial temperature	K
τ	True shear stress	MPa
θ^*	Homologous temperature of the elastic modulus model	-
θ^p	Homologous temperature of the calorific model	-
V	Activation volume for chains crawling (polymers)	m^3
v	Phenomenological parameter of internal stress strain rate sensitivity	-
v_f	Phenomenological parameter of strain rate sensitivity of plastic strain at initiation of failure	-
V_0	Impact velocity of the projectile	$m.s^{-1}$
V_r	Residual velocity of the projectile	$m.s^{-1}$
V_p	Plug velocity	$m.s^{-1}$
V_{bl}	Theoretical ballistic limit velocity	$m.s^{-1}$
χ	Taylor-Quinney coefficient	-
Y	Yield stress (metals)	MPa
Y_a	Athermal yield stress	MPa

Y_r	Reference yield stress at $\dot{\varepsilon}_r$ and T_r	MPa
ξ	Normalized third stress invariant	-
ζ	Strain rate sensitivity of homologous temperature θ^*	-

INTRODUCTION

Nowadays, one of the main issues addressed to the industry of transportation consists into the development of lightweight materials aiming to reduce fuel consumption and increase the autonomy of the vehicles. This problematic is also pertinent in the military industry for strategic purposes. Indeed, the higher the autonomy of the vehicles is, the larger their area of action will become. Therefore, the development of lightweight protective materials are currently under investigation. This work concerns more precisely light structures submitted to extreme conditions undergone during an impact loading.

This study aims to develop a numerical model (using ABAQUS®/Explicit) allowing the evaluation of the dynamic mechanical response of a sintered polymer/metal multilayer composite due to high velocity impact. Both materials have been sintered using Spark Plasma Sintering process (SPS) and are developed at the French-German Institute of Saint-Louis (ISL). This work has for objective to evaluate their protective potential. The metallic material is a sintered 7020 aluminum alloy [1] which can be compared to the commercial AA7020-T651 aluminum alloy, well-known for its efficiency as a ballistic protection. The polymer is a thermoplastic amorphous sintered polyimide [2]. The polyimide presents very high mechanical properties (for a polymer) and thermal stability with a temperature of glass transition around 310 °C. The density of the sintered polyimide is around half of the one of the aluminum alloy; leading to high potential improvement to mass reduction. The sintered aluminum alloy and thermoplastic polyimide layers are assembled together using an epoxy resin. Besides, the multilayer composite has to be designed in order to keep a high level of mechanical performances for diverse kind of solicitations encountered during an impact loading [3]. For this purpose, the stacking sequence of the layers, their number and their respective thicknesses have to be numerically investigated to optimize the efficiency and the cost of the study by keeping the experimental impact tests for the validation of the numerical model. The mechanical behavior of the epoxy resin interface is addressed by considering the presence of this material as an interlayer possessing its own material properties.

Such an approach has already been followed in the literature (with spaced layers [4, 5], with stacked metallic plates [5-8] or with stacked polymer plates [9]) but the use of SPS sintered materials and more particularly the involvement of such polymer in a protective architecture can be considered as innovative ideas. As a first step, the different materials have been separately studied and then a numerical model has been built from the consideration of the mechanical properties of each layer.

This work aims to present a methodology to develop such predictive numerical model which might be adapted for other kinds of materials. The numerical tool would then offer the possibility to optimize multilayer composite structures to reach the targeted specifications (weight, volume and performances) but which is not the purpose of this work. The first chapter of this manuscript aims to explain the main strain and failure mechanisms occurring in metals and amorphous polymers. The modeling of metallic materials is also discussed and is generally performed using analytical expressions such as the Johnson-Cook [10] or the Mechanical Threshold [11] models. Concerning the mechanical modeling of the

polymers, models such as Ree-Eyring [12] or cooperative [13] models (for the yield stress) coupled with a hyperelastic expression (e.g. 8-chains model [14], Gent model [15] …) can be employed. The choice of the constitutive expressions has to be done with the consideration of the different mechanism behavior leading to the strain of the material. This can only be carried out through experimental mechanical characterization tests.

Therefore, the second chapter of this work concerns the experimental characterization of the mechanical behavior of each material (sintered 7020 aluminum alloy, thermoplastic polyimide and epoxy resin). Such sintered materials can be studied over three different scales which are the macroscopic scale (sample size), the mesoscopic scale (powder grains scale) and microscopic-nanoscopic scale (crystal for metals and chains for the polymers). The mechanical responses of the stress and failure behaviors (including damage evolution) have to be investigated in order to understand the phenomena leading to the strain, strain rate and temperature sensitivities of each material (including epoxy resin). Indeed, the phenomena leading to the deformation of metallic materials and polymers are very different due to their respective microstructures: crystalline lattices with propagation/multiplication of dislocations [16] and entanglement of cross-linked long molecules (chains) which crawl and slip between each other [17]. The identification of these different phenomena allows a better and more efficient development of constitutive modeling of the mechanical behavior of the materials.

In the third chapter, a new approach to develop constitutive models describing the level of stress of FCC metals according to the temperature, strain and strain rate is suggested. The resulting model allows an accurate modeling of the mechanical behavior of the 7020 aluminum alloy from quasi-static up to ballistic conditions and takes into account microstructural phenomena such as the dissolution of the precipitates [18]. The constitutive modeling of the sintered polyimide is based on the expression of the cooperative model [19] coupled with the hyperelastic Gent model [20]. The failure behavior is modeled with two coupled phenomena: the evaluation of the plastic strain at initiation of failure (with the state of stress, temperature and strain rate) and the damage energy evolution. Specific analytical expressions are suggested to take into account the observed failure behavior with an improved accuracy.

The last chapter of the manuscript consists in the implementation of the identified constitutive models in a Finite Element Software ABAQUS®/Explicit by the development of VUMAT subroutines in FORTRAN. The simulations are performed by modeling the experimental setup used for impact tests in order to keep the same boundary conditions for constitutive model validation. Comparison between the simulated and experimental data, acquired during steel ball impact tests, is performed in order to validate the development of the numerical models.

References

1. Queudet, H., et al., *One-step consolidation and precipitation hardening of an ultrafine-grained Al-Zn-Mg alloy powder by Spark Plasma Sintering.* Materials Science and Engineering: A, 2017. **685**: p. 227-234.
2. Schwertz, M., *Technologie Spark Plasma Sintering (SPS) appliquée aux composites polymère/métal pour allègement de structure*, 2014.
3. Rosenberg, Z. and E. Dekel, *Terminal ballistics*2016: Springer.
4. Wielewski, E., A. Birkbeck, and R. Thomson, *Ballistic resistance of spaced multi-layer plate structures: Experiments on Fibre Reinforced Plastic targets and an analytical framework for calculating the ballistic limit.* Materials & Design, 2013. **50**: p. 737-741.
5. Jankowiak, T., A. Rusinek, and P. Wood, *A numerical analysis of the dynamic behaviour of sheet steel perforated by a conical projectile under ballistic conditions.* Finite Elements in Analysis and Design, 2013. **65**: p. 39-49.
6. Børvik, T., M. Forrestal, and T. Warren, *Perforation of 5083-H116 aluminum armor plates with ogive-nose rods and 7.62 mm APM2 bullets.* Experimental mechanics, 2010. **50**(7): p. 969-978.
7. Woodward, R. and S. Cimpoeru, *A study of the perforation of aluminium laminate targets.* International Journal of Impact Engineering, 1998. **21**(3): p. 117-131.
8. Børvik, T., S. Dey, and A. Clausen, *Perforation resistance of five different high-strength steel plates subjected to small-arms projectiles.* International Journal of Impact Engineering, 2009. **36**(7): p. 948-964.
9. Hsieh, A.J., et al., *The effects of PMMA on ballistic impact performance of hybrid hard/ductile all-plastic-and glass-plastic-based composites*, 2004, DTIC Document.
10. Wright, S., N. Fleck, and W. Stronge, *Ballistic impact of polycarbonate—an experimental investigation.* International Journal of Impact Engineering, 1993. **13**(1): p. 1-20.
11. Mohagheghian, I., G. McShane, and W. Stronge, *Impact perforation of monolithic polyethylene plates: Projectile nose shape dependence.* International Journal of Impact Engineering, 2015. **80**: p. 162-176.
12. Ree, T. and H. Eyring, *Theory of Non-Newtonian Flow. I. Solid Plastic System.* Journal of Applied Physics, 1955. **26**(7): p. 793-800.
13. Richeton, J., et al., *Influence of temperature and strain rate on the mechanical behavior of three amorphous polymers: Characterization and modeling of the compressive yield stress.* International Journal of Solids and Structures, 2006. **43**(7–8): p. 2318-2335.
14. Klepaczko, J. and C. Chiem, *On rate sensitivity of fcc metals, instantaneous rate sensitivity and rate sensitivity of strain hardening.* Journal of the Mechanics and Physics of Solids, 1986. **34**(1): p. 29-54.
15. Drucker, D.C. and W. Prager, *Soil mechanics and plastic analysis or limit design.* Quarterly of applied mathematics, 1952. **10**(2): p. 157-165.
16. Hull, D. and D.J. Bacon, *Introduction to dislocations*. Vol. 257. 1984: Pergamon Press Oxford.
17. Bergstrom, J.S., *Mechanics of solid polymers: theory and computational modeling*2015: William Andrew.
18. Francart, C., et al., *Application of the Crystallo-Calorific Hardening approach to the constitutive modeling of the dynamic yield behavior of various metals with different crystalline structures.* International Journal of Impact Engineering, 2017.
19. Richeton, J., et al., *Modeling and validation of the large deformation inelastic response of amorphous polymers over a wide range of temperatures and strain rates.* International Journal of Solids and Structures, 2007. **44**(24): p. 7938-7954.
20. Horgan, C.O., *The remarkable Gent constitutive model for hyperelastic materials.* International Journal of Non-Linear Mechanics, 2015. **68**(0): p. 9-16.

Chapter 1

CONSTITUTIVE BEHAVIOR OF METALLIC AND POLYMER MATERIALS

The present study aims to develop a numerical model of high velocity impacts on a metal/polymer (sintered 7020 aluminum alloy and sintered thermoplastic polyimide (amorphous)) multilayer composite assembled using a thermoset epoxy resin (amorphous). To address the problematic of this work, the mechanical behavior of each material has to be investigated in order to obtain the experimental data required for the simulations. However, before starting the experiments, it is important to have an overview of the mechanical phenomena of each material concerning the strain mechanisms leading to their mechanical resistance and the failure mechanisms leading to their limits under different loadings. This first part of the report aims to provide some explanations about the mechanical behavior of metallic and polymer materials by describing the different phenomena, which are responsible of their mechanical response. Some models from the open literature are as well discussed to understand their range of application and their limits.

A. Description of strain mechanisms

1. Elasticity and plasticity strain domains

The understanding of mechanisms linked to the strain are mandatory for any constitutive modeling of the mechanical behavior of the material. Indeed, the resistance of all materials is always a response to the strain imposed by a loading.

The first part of this chapter focuses on the description of the different mechanical phenomena observed in metallic and polymer materials under thermomechanical loading.

a. Elastic behavior

Elasticity is a reversible strain mechanism and is present for all materials as a first step of strain. Therefore the evolution of the internal thermodynamic variables V_k is neglected. Concerning metallic materials, at low strain, the mechanical resistance $\overline{\overline{\sigma_e}}$ is directly function of the elastic strain tensor $\overline{\overline{\varepsilon_e}}$ following a linear relation called the Hook law (Eq 1.1) [1].

$$\overline{\overline{\sigma_e}} = \overline{\overline{C_{ijkl}}}\,\overline{\overline{\varepsilon_e}} \qquad (1.1)$$

With $\overline{\overline{C_{ijkl}}}$ the stiffness matrix of the material.

The generalized Hook law can be considered for higher strain ranges and is described by the Eq 1.2 [1]:

$$\overline{\overline{\sigma_e}} = \frac{E}{1-\nu}\left(\overline{\overline{\varepsilon_e}} + \frac{\nu}{1-2\nu} Tr(\overline{\overline{\varepsilon_e}})\overline{\overline{I}}\right) \qquad (1.2)$$

With ν the Poisson's ratio of the material.

Another type of elasticity behavior can be encountered: the viscoelasticity. It concerns generally soft materials such as polymers.

Viscoelasticity is, as linear elasticity, a reversible mechanism. It is based on the Boltzmann's superposition principle which states that the overall viscoelastic behavior is the superposition of many independent linear elasticity mechanisms. Therefore, the modeling of the elastic strain $\overline{\overline{\varepsilon_e}}$ is performed through an integral equation (for small strain) which uses the Heaviside step time function $H(t)$ defined by Eq 1.3 [2]:

$$H(t) = \begin{cases} 0, & if\ t < 0 \\ \frac{1}{2}, & if\ t = 0 \\ 1, & if\ t > 0 \end{cases} \quad (1.3)$$

The function $H(t)$ is then used as follows (Eq 1.4) to compute the strain in function of the time:

$$\varepsilon_e(t) = \varepsilon_0 H(t) \quad (1.4)$$

With $\varepsilon_0 = \frac{\sigma(t)}{E_r(t)}$ the applied strain jump and $E_r(t)$ the stress relaxation modulus.

The model can be then generalized for an infinite number of steps to get an arbitrary strain history, by decomposing it into a sum an infinitesimal strain steps (see Eq 1.5):

$$\varepsilon_e(t) = \sum_{i=1}^{\infty} \Delta\varepsilon_i H(t - \tau_i) \quad (1.5)$$

With $\Delta\varepsilon_i$ the strain increment applied at the time τ_i. The stress is computed as follow (Eq 1.6):

$$\sigma(t) = \sum_{i=1}^{\infty} \Delta\varepsilon_i E_r(t - \tau_i) \quad (1.6)$$

The integral form of the viscoelastic law (Eq 1.7) can be written from the previous equation:

$$\sigma(t) = \int_{-\infty}^{t} E_r(t - \tau) d\varepsilon(t) = \int_{-\infty}^{t} E_r(t - \tau) \frac{d\varepsilon(\tau)}{d\tau} d\tau \quad (1.7)$$

With $E_r(t) = E_0 e^{-\frac{t}{\tau_0}}$ (for $t \geq 0$), E_0 being the instantaneous Young's modulus and τ_0 the characteristic relaxation time.

In the case of a monotonic loading response, the applied strain increases linearly with the time and can therefore be written as follow (Eq 1.8):

$$\varepsilon(t) = \begin{cases} 0, & if\ t \leq 0 \\ \dot{\varepsilon}_0 t, & if\ t \geq 0 \end{cases} \quad (1.8)$$

And the stress becomes Eq 1.9:

$$\sigma(t) = E_0 \dot{\varepsilon}_0 \tau_0 \left[1 - e^{-\frac{\varepsilon(t)}{\dot{\varepsilon}\tau_0}}\right] \quad (1.9)$$

b. Plasticity criteria

i. **Construction of yield surfaces**

In case of plastic deformation, the variation of internal thermodynamic variables V_k can be neglected. Indeed, phenomena such as dislocation motion, the formation of voids or thermoactivated microstructural changes lead to the evolution of thermodynamic variables such as the entropy S or the plastic stress $\overline{\overline{\sigma_p}}$. For simplification, $\overline{\overline{\sigma_p}}$ will be written as $\bar{\bar{\sigma}}$ for the rest of the manuscript.

The threshold level value f of a thermodynamic criterion is most commonly used to mathematically model the transition of an elastic behavior to a plastic behavior for a particular microstructural mechanism (as kinematic hardening) [3, 4].

The consideration of a f_k criterion associated with thermodynamic variables V_k allows to apply the following mathematical modeling:

- $f_k(\bar{\bar{\sigma}}, A_k) < 0$, elastic behavior
- $f_k(\bar{\bar{\sigma}}, A_k) = 0$, possible evolution of thermodynamic variables V_k
- $f_k(\bar{\bar{\sigma}}, A_k) > 0$, impossible for a non-time dependent behavior

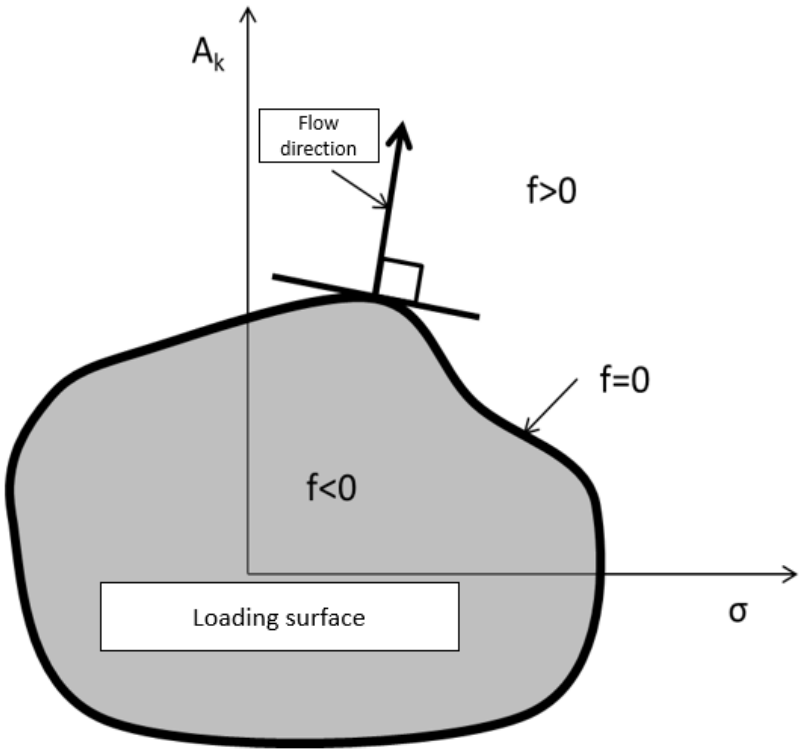

Figure 1 - Exemple of loading surface

The Hill's principle (or principle of maximum dissipation) imposes two conditions on the criterion f:

- The loading surface is convex (Figure 1).
- The flow of normality rule over the loading surface is verified (Figure 1, only for metallic materials) and corresponds to the following mathematical expression (Eq 1.10):

$$\dot{V}_k = \dot{\lambda}_k \frac{\partial f}{\partial A_k} \text{ if } f_k \dot{\lambda}_k = 0 \text{ and } \dot{\lambda}_k \geq 0 \qquad (1.10)$$

With $\dot{\lambda}_k$ a multiplicative coefficient of plasticity, damage (corresponding to the V_k thermodynamic variables) and $A_k = -\rho \frac{\partial \psi}{\partial V_k}$ with $\psi = e - Ts$ the specific free energy (e the mass density of internal energy, s the mass density of entropy and T the temperature).

This normality corresponds to a physical reality for metals for which the surface of the flowing material is normal to the sliding speed which is collinear to the force applied. However, for polymeric materials (and more generally, materials for which internal entropy tends to change greatly), the normality of the flow with respect to the load surface is no longer valid. Another function called dissipation potential is then introduced and is denoted by φ (Eq 1.11):

$$\varphi = \varphi(\bar{\bar{\sigma}}, A_k, grad\ T) \qquad (1.11)$$

The law of evolution of thermodynamic variables for polymer materials is then (Eq 1.12):

$$\dot{V}_k = \frac{\partial \varphi}{\partial A_k} \text{ if } f_k = 0 \text{ and } \dot{f}_k = 0 \qquad (1.12)$$

The thermodynamic system can therefore be defined for a plastic regime from the following functions [4]:

- The thermodynamic potential: $\rho\dot{e} = \rho T\dot{s} + \bar{\bar{\sigma}}:\dot{\bar{\bar{\varepsilon}}} - A_k\dot{V}_k \quad or \quad \rho\Psi = -\rho s\dot{T} + \bar{\bar{\sigma}}:\dot{\bar{\bar{\varepsilon}}} - A_k\dot{V}_k$
- The dissipation potential (for polymers): $\varphi = \varphi(\bar{\bar{\sigma}}, A_k, grad\ T)$
- Loads criteria: $f_k = f_k(\bar{\bar{\sigma}}, A_k)$

The construction of the potentials is performed through experimental observations by conducting well-chosen experiments to uncouple each contribution.

ii. **Von Mises yield criterion for isotropic materials**

In the isotropic case, only the stress tensor is involved in the expression of the load test. The boundary field of flow stress is then written in the general case with Eq 1.13 [3]:

$$f(\sigma_I, \sigma_{II}, \sigma_{III}, \sigma_S) = 0 \qquad (1.13)$$

Using these criteria provides a good approximation for most mechanical problems involving materials with low anisotropy. These expressions are also used in finite element softwares. It is therefore essential to choose and define the proper charge criterion for the concerned materials if a predictable numerical calculation is desired.

For materials insensitive to hydrostatic stresses and for moderate strain rates, the expression can be simplified in this manner (Eq 1.14):

$$f(\sigma_{II}, \sigma_{III}, \sigma_S) = 0 \qquad (1.14)$$

The Von Mises criterion is suitable for metallic materials in the sense that it is based on the consideration of shear energy as the slides of crystal planes governed by the shear stresses. The yield stress is related to the shear energy. This latter is given by Eq 1.15:

$$w_e = \int_0^{\varepsilon} \bar{\bar{\sigma}}:\bar{\bar{\varepsilon}} \qquad (1.15)$$

By separating the magnitudes in terms of spherical and deviatoric parts, the following equation is obtained (Eq 1.16):

$$w_e = \int_0^{\varepsilon} \left(\overline{\overline{\sigma_D}} + \frac{1}{3}Tr(\bar{\bar{\sigma}})\bar{\bar{I}}\right):\left(\overline{\overline{\dot{\varepsilon}_D}} + \frac{1}{3}Tr(\dot{\bar{\bar{\varepsilon}}})\bar{\bar{I}}\right) \qquad (1.16)$$

The shear strain energy (or distortion) is (with μ the Lamé coefficient) describes by Eq 1.17:

$$w_D = \frac{1}{4\mu}\overline{\overline{\sigma_D}}:\overline{\overline{\sigma_D}} \qquad (1.17)$$

The Von Mises criterion expresses the fact that when the distortion energy w_D reaches a threshold value in the material, dislocation movements are initiated and the flow begins. The criterion can then be written (Eq 1.18):

$$f(w_D, \sigma_S) = 0 \quad (1.18)$$

For a simple case of tension or compression, one can write Eq 1.19 (with σ_S the yield strength of the material for the corresponding level of strain hardening):

$$\overline{\overline{\sigma_D}}:\overline{\overline{\sigma_D}} = \frac{2}{3}{\sigma_S}^2 \quad (1.19)$$

Then by using the equivalent stress flow threshold (Eq 1.20):

$$\sigma_{eq} = \sqrt{\frac{3}{2}\overline{\overline{\sigma_D}}:\overline{\overline{\sigma_D}}} \quad (1.20)$$

The following yield criterion is considered (Eq 1.21 and 1.22):

$$f = \sigma_{eq} - \sigma_S \quad (1.21)$$

$$(\sigma_{11} - \sigma_{22})^2 + (\sigma_{22} - \sigma_{33})^2 + (\sigma_{33} - \sigma_{11})^2 = 2{\sigma_S}^2 \quad (1.22)$$

This is the equation of a circular cylinder which its axis is the trisector of the orthonormal coordinate system $(\sigma_I, \sigma_{II}, \sigma_{III})$ and of radius $R = \sqrt{\frac{2}{3}\sigma_S}$

2. Strain mechanisms in metallic materials

The current section aims to describe the different phenomena which are encountered in metallic materials and impact the deformation of the metal (e.g. structural strain hardening, temperature and strain rate sensitivities …).

a. Internal stress and structural strain hardening

Generally, metallic materials harden with the strain. This strain hardening is caused by the elevation of the density of dislocations in the metal. The stress resulting from the evolution of the density of dislocations is called the internal stress. Indeed, the internal stress σ_{int} and the plastic strain ε_p are linked by two relations referring to a single variable which is the density of dislocations (Eq 1.23 and 1.24) [5-7].

$$\sigma_{int} = \alpha E b \sqrt{\rho_d} \quad (1.23)$$

$$\varepsilon_p = b d \rho_m \zeta \quad (1.24)$$

With α an empirical parameter, E the Young's modulus, b the Burgers' vector, d the dislocations spacing, ζ the average distance crossed by the dislocations, ρ_m the density of mobile dislocations and ρ_d the density of stored dislocations.

The evolution of ρ_d is specific for each lattice structure (FCC, BCC, HCP …) and leads to specific hardening behaviors [8, 9] and is directly linked to the value of density of mobile dislocations ρ_m and their associate propagation velocity [6, 10]. An example of evolution of ρ with the strain is given for the FCC metals in the Figure 2. For instance, BCC materials generate nearly no forests of dislocations and a homogeneous germination of dislocations [11] (homogeneous hardening) contrary to the FCC metals for which the propagation of forests of dislocations takes generally the major part of the total density of dislocations [11] (heterogeneous hardening). Some sources of mobile dislocations can be enounced such as the Franck & Read sources [6, 12] or the grain boundaries [6, 13].

The meeting of two mobile dislocations leads to their annihilation. Therefore, the greater their density is, the higher the probability of annihilation will be and the density will grow slower and slower. This phenomenon can be seen as an asymptotic behavior of the stress at high strain. However, since forest dislocations are not mobile, this last phenomenon is greatly delayed for metallic materials presenting lattice structures such as FCC and HCP.

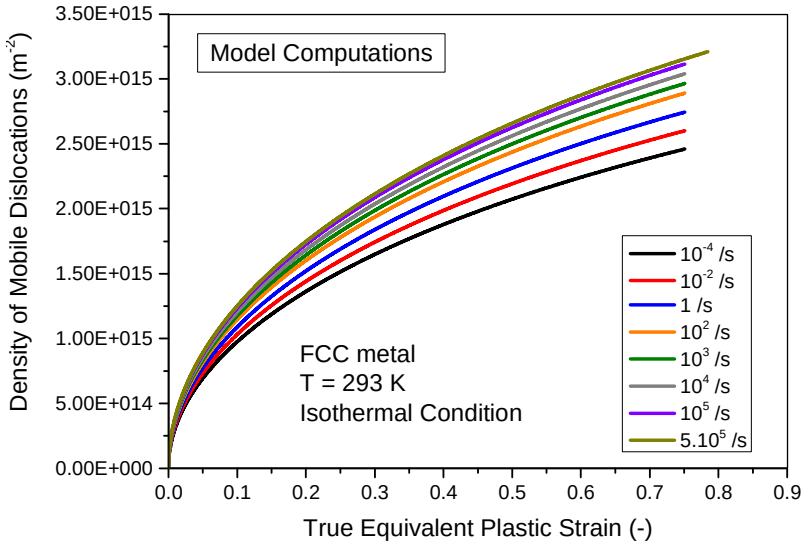

Figure 2 - Evolution of the density of mobile dislocations with the strain plastic strain computed for a random monocrystalline FCC metal with Matlab®

The velocity of mobile dislocations increases with the temperature [6, 10, 14] (thermo-activated phenomenon) causing an augmentation of the probability of annihilation of mobile dislocations. This can be observed directly on the internal stress of FCC metals for phenomena such as adiabatic heating leading to the softening of the material at high strain or at elevated temperatures where the stress is generally decreasing (in the absence of other structural hardening phenomenon such as precipitation).

The strain hardening is macroscopically divided in four stages when increasing plastic strain (Figure 3) [5, 6]. Stage I corresponds to the “easy glide” process at the beginning of the stress. No multiplication happens and the dislocations are only gliding along the lowest energy paths until reaching a “dead-end” requiring higher energy and therefore multiplication. It essentially depends on the lattice orientation and is not observable anymore as long as different slips systems are involved (polycrystalline metal). At this point, stage II starts, the multiplication of the dislocations is very quick in all directions, (there is no saturation) leading to the steepest part of the hardening. Stages I and II correspond generally to small ranges of plastic strain and are only dependent on the slip system orientation and on the shear modulus. However, stages III and IV show an important material dependency. During stage III, the saturation in dislocations of the lattice starts to appear and the hardening is slower with the strain than for stage II. Stage IV shows an asymptotic behavior: it continuously increases until its gradient becomes zero at infinite plastic strain. During stage IV, the saturation in dislocations is nearly maximal and the rate multiplication is very low due to the high rate of annihilation.

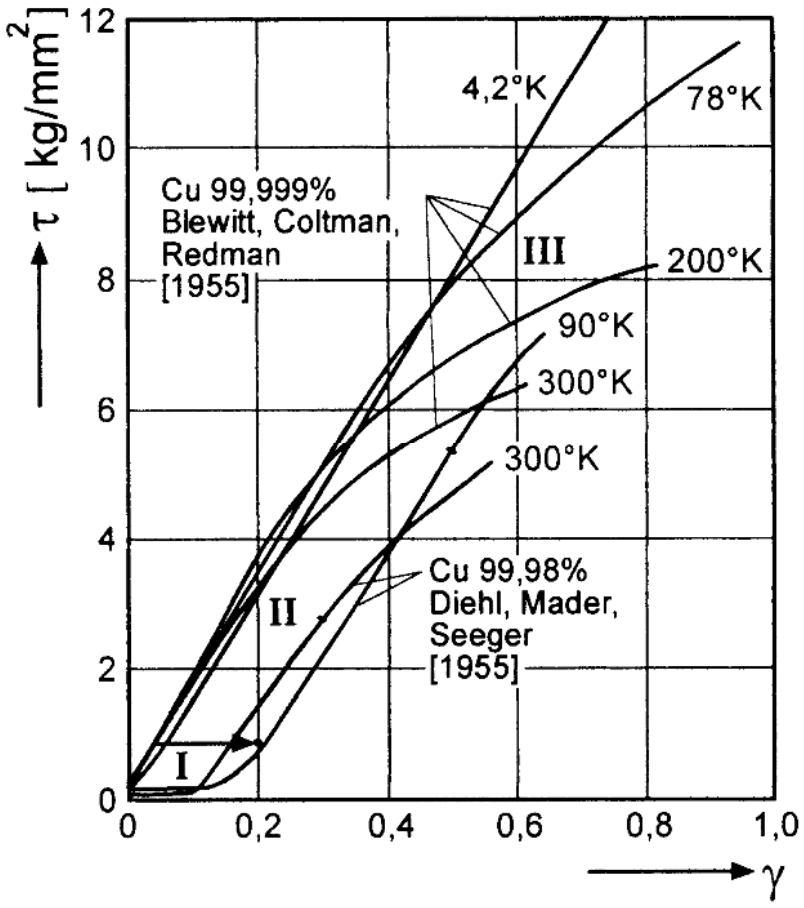

Figure 3 – Illustration of the different hardening stages which might be observed during yielding of a 99,999% pure single crystal copper (the asymptotic stage IV is not present) [5]

b. Effective stress and overcoming of Peierls' barriers

The Peierls' barriers are considered as the linear short-range obstacle (thermo-activated phenomenon) with the biggest impact on the effective stress σ_{eff} [11, 15]. The effective stress corresponds to the part of the stress which is not dependent on the level of plastic strain ε_p. A Peierls' barrier consists in the energy required for a dislocation to move between two positions of equilibrium. This energy is generally low for FCC metals and high for BCC metals. The highest the Peierls' energy [16] is, the stronger the resistance of the metal to the strain will be important and this will result in a high effective stress.

Besides, strain rate and temperature sensitivities of the effective stress exist. The strain rate sensitivity of such thermo-activated phenomenon (Figure 4) is caused by an increase of the Peierls' energy (which is quasi nonexistent for FCC metals). The effective stress follows an exponential relation with the strain rate and can be modeled by an expression such as Eq 1.25 [17]:

$$\sigma_{eff} = Y_r \left(1 - \left(\frac{k_B T}{g_0 \mu b^3} \ln \left(\frac{\dot{\varepsilon}_r}{\dot{\varepsilon}_p} \right) \right)^{\frac{1}{p}} \right)^{\frac{1}{q}} \qquad (1.25)$$

With Y_r a reference value of the effective stress at $\dot{\varepsilon}_r$ and $0\ K$, p and q empirical parameters, μ the shear modulus and g_0 a dimensionless energy inversely proportional to the Peierls' energy.

Furthermore, the elevation of the temperature brings more energy to the system, consequently, the amount of energy required to move the dislocations is reduced. This decrease of the Peierls' energy leads to the thermal softening of the effective stress (Figure 4).

Other linear short-range mechanisms can be found in metallic materials such as cross-slip or Cottrel-Lomer [10, 18] or localized obstacles such as solute atoms creating stress fields [10, 19-21] or repulsive dislocation trees [10, 22]. However, this manuscript will exclusively assimilate the contribution of the Peierls' barriers as all short-range obstacles for simplification.

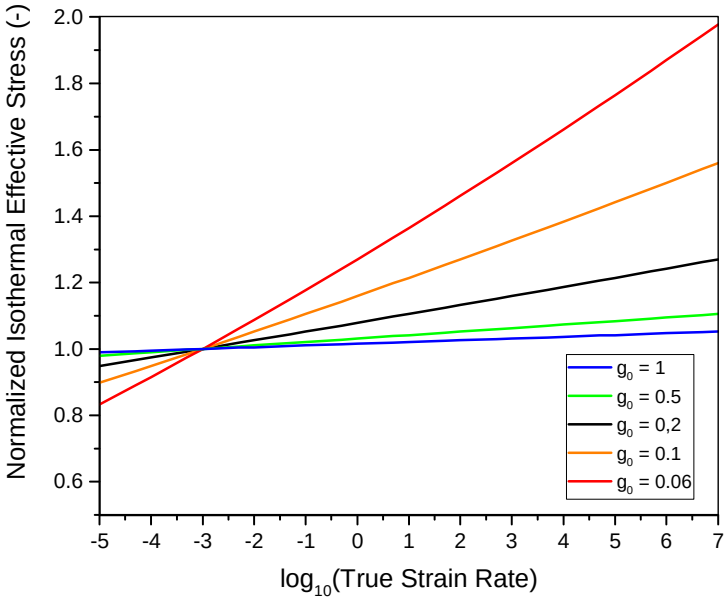

Figure 4 - Evolution of the normalized effective stress with the strain rate

c. Athermal stress

As stated by its name, the athermal stress σ_{ath} corresponds to the part of the overall stress which is considered independent to the temperature. It is generally generated by the presence of inherent and conditional long range-obstacles [10]. The inherent obstacles (Fisher's SRO [10, 23] or cutting APBs [10, 24]) are directly linked to the chemical composition of the metal and the conditional obstacles to the level of density of dislocations (cutting attractive junctions or long-range stresses). These last obstacles lead technically to thermo-activated mechanisms but the energies involved along such long ranges (grains size) are very important. Therefore the thermal sensitivities are so small that the mechanisms generated by the conditional long-range obstacles are supposed athermal.

As for the thermal stress, σ_{ath} is composed of an initial effective stress Y_a and of a hardening internal part corresponding respectively to the inherent and conditional contribution of the long range-obstacles [10]. The conditional part of the athermal stress is generally neglected in FCC and BCC metals (the internal thermal stress of this last being considered temperature independent) but is present in other lattice structure such as HCP. An AZ31B-O magnesium alloy is taken as an example (Figure 5).

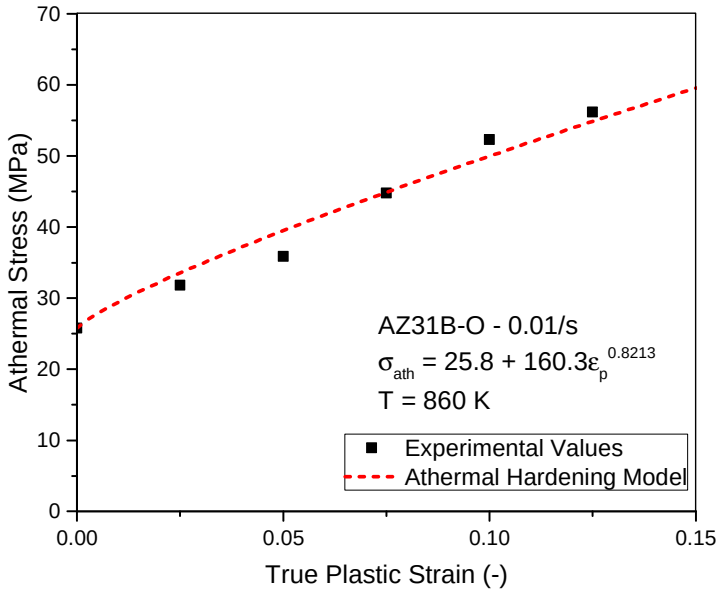

Figure 5 - Example of athermal stress presenting a hardening phenomenon due to long range interaction (Mg alloy AZ31B-O)

d. Strain rate sensitivity of internal stress and viscous drag effect

The evolution of the density of dislocations represents the strain history of the metal. If only the density of mobile dislocations is considered, the history will be identical whatever the strain rate because the statistical mean path of propagation of mobile dislocations stays the same for any value of strain. However, if the density of stored dislocations is taken into consideration, the impact of the strain rate on the internal stress can be important [25] (depending on the density of initial dislocations and amplitude of slip plane activation stress).

Consequently, FCC metallic materials present generally a positive strain rate sensitivity of the strain hardening [26, 27] (Figure 6) (contrary to the BCC metals for which it is null). However, this sensitivity is not always monotonous. Indeed, phenomenon such as dynamical strain ageing (DSA) can be encountered in metallic alloys. DSA effect causes a negative strain rate sensitivity due to the presence of specific precipitates preventing a smooth motion of the dislocations in their neighborhood [28, 29]. Many dislocations are therefore stacked in a small space causing a high rate of annihilation which increases with the strain rate.

At high strain rates, viscous drag mechanisms (see Appendix D for detailed information) start to be preponderant on the thermo-activated phenomena. The strain rate sensitivity of the stress becomes exponentially important with the rate of deformation [10].

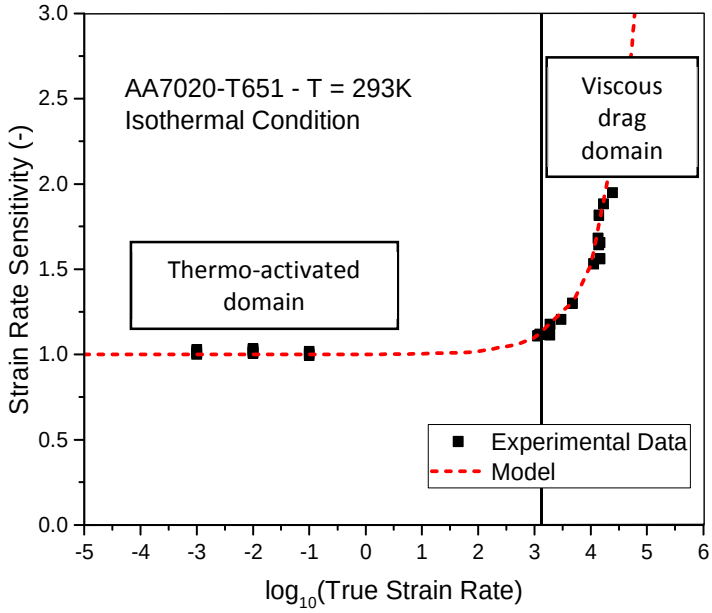

Figure 6 - Normalized strain rate sensitivity of the internal stress of a AA7020-T651 aluminum alloy

e. Temperature and strain rate coupling

It has been reported many times in the literature that the thermo-mechanical behavior of metallic materials is greatly dependent on the strain rate. Indeed, the mechanical response of the metals increases with the rate of deformation for a given temperature.

This behavior is mainly caused by the fact that metallic materials do not follow a thermal softening based on a fix reference temperature (generally taken as the melting point). Indeed, the reference temperature, called critical temperature T_C, can be lower or higher than the melting point and is function of the strain rate as shown (Eq 1.26 and 1.27) [11, 30, 31]:

$$T_C = \left(\frac{-k_B}{G_0}\ln\left(\frac{\dot{\varepsilon}_p}{\dot{\varepsilon}_m}\right)\right)^{-1} \quad (1.26)$$

$$\dot{\varepsilon}_m = b\, d\rho_m\omega_0 \quad (1.27)$$

With k_B the Boltzman constant, G_0 the total energy which is required to overcome the obstacles through thermal activation, $\dot{\varepsilon}_m$ the athermal transition strain rate, b the Burgers' vector, d the dislocation spacing, ρ_m the density of mobile dislocation and $\omega_0 \sim 10^{12}\ /s$ the attempt frequency. The evolution of the critical temperature for different metallic material is shown in Figure 7.

Furthermore, in the case of metallic alloys, a conflict may appear between rates of deformation and kinetics of microstructural changes at very high strain rates (high speed impact …) and a modeling of such phenomena might be needed in some cases.

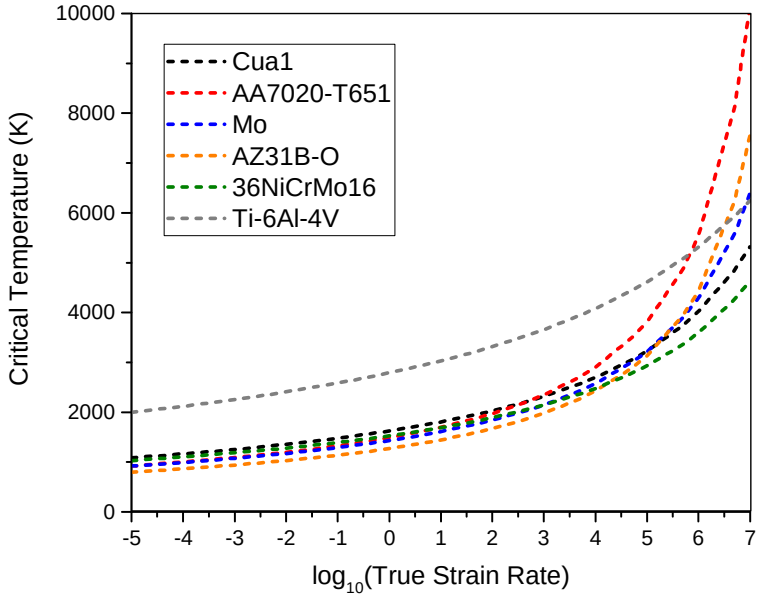

Figure 7 - Theoretical evolution of the critical temperature with the strain rate for several metals

f. Microstructural changes

Most of metals and metallic alloys presents microstructural changes with the temperature. The only possible change for pure metals is the variation of the grain size but it is much more complex in the cases of multiphasic alloys. Indeed, the thermodynamic equilibrium of the different phases is temperature dependent and these lasts interact between each other. This lead to phenomena such as dissolution or precipitation of phases in a dominant matrix (for instance, the $MgZn_2$ precipitates in the AA7020 aluminum alloys follow a dissolution process in the aluminum matrix around 490 K [32, 33] (Figure 8)). Besides, the specificities and amount of the phases present in the matrix, condition the mechanical behavior because of their huge impact on the generation and motion of dislocations. Furthermore, for each metallic alloy, many phases can exist outside of the thermodynamic equilibrium: the metastable phases and can be computed using different dedicated software. The Figure 8, shows the evolution of the calorific ratio [34, 35] which consists into the normalized isothermal thermal stress at a given temperature and strain rate (here at room temperature).

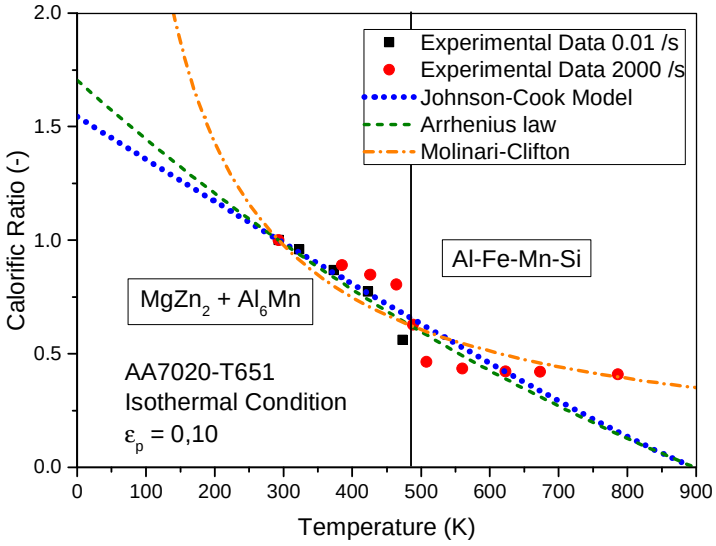

Figure 8 - Normalized evolution of the thermal stress (isothermal condition) with the temperature in quasi-static and dynamic conditions of the AA7020-T651 aluminum alloy

The two main phenomena which can lead to a significant change in the mechanical behavior are the dissolution of a phase or the precipitation of a phase. The dissolution causes a sudden drop of the stress due to the annihilation of the dislocations around these phases. The precipitation phenomenon leads to a sudden jump of the stress due to the appearing of phases with hardening potential (such as some high strength steels or nickel-based alloys [36-38]).

To fully understand the thermo-mechanic behavior of a metallic alloy over a wide range of temperature, its phase composition has to be investigated and eventually modeled.

3. Strain mechanisms in amorphous polymers

Polymer materials can be sorted in two categories: amorphous or semi-crystalline. Amorphous polymers are assumed composed of a unique phase of randomly assembled molecule chains. The semi-crystalline polymers are bi-phasic structures, one is amorphous (as for the previous category) and the other is crystalline (the molecule are sorted in a lattice structure in which slips and strain hardening occurs).

In this work, only assumed amorphous polymers are studied (Polyimide and epoxy resin). Therefore, only strain mechanisms related to amorphous polymers are explained in this section of the manuscript.

a. Structure of amorphous polymers

i. **Molecular chains**

The amorphous polymers do not have an ordered structure as other types of materials possessing a crystalline microstructure [4, 39].

The main concept to be retained concerning the structure of an amorphous polymer is the molecular chain (see Figure 9). An elementary segment [AB] is an element of the macromolecular skeleton containing a single rotatable link and is characterized by its length l as well as by the angle Θ which it makes with the adjacent elementary segments [BC]; these two quantities being considered as constant.

A polymer molecular chain is a succession of elementary segments (which may be different) and have branches. This chain is characterized by various properties such as the molar mass *M* or its tortuosity.

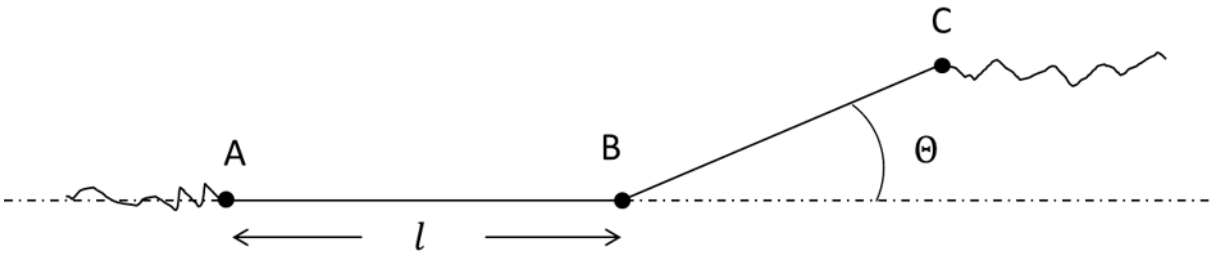

Figure 9 - Schematic representation of a polymer chain

ii. **Random coil**

The tortuosity of a molecular chain arises from the probability that an elementary segment is in a trans-left + or - conformation. At each node of elementary segments, the main skeleton of the chain takes the direction imposed by the configuration defined by the following segment (trans = locally straight chain). The end result is a string in the form of a random coil.

The average distance between the ends can easily be calculated by calculating the modulus of the vector OM (Figure 10) (Eq 1.28) [2, 4, 39, 40]:

$$r^2 = (OM)^2 = \left(\sum_i^N a_i\right)^2 \qquad (1.28)$$

With a_i the length of the i^{th} elementary segment and N the number of elementary segments in the molecular chain. If one considers a molecule at rest (isotropic), for a sufficiently long chain, the sum of scalar products $a_i.a_j$ vanishes and one can then write Eq 1.29:

$$r^2 = (OM)^2 = \sum_i^N {a_i}^2 \qquad (1.29)$$

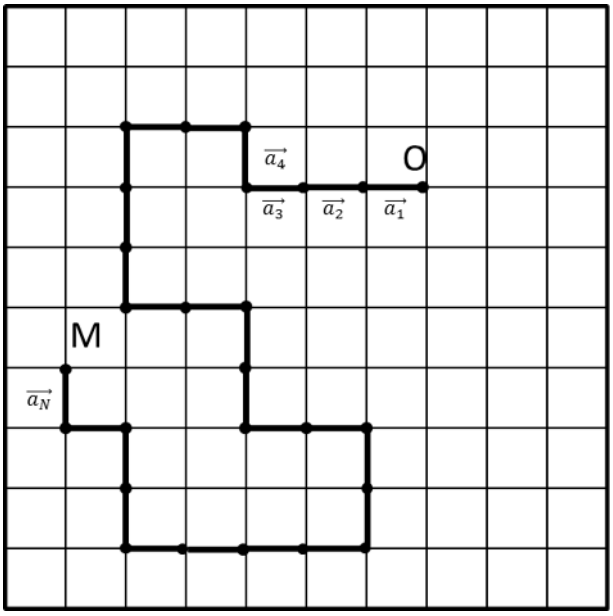

Figure 10 - Schematic representation of the random coil in an amorphous polymer.

If l characterizes the average length of an elementary segment, one can write Eq 1.30:

$$r^2 = Nl^2 \qquad (1.30)$$

Note that the average distance of the two ends is proportional to the square root of the "deployed" length of the chain.

It is then possible to define the characteristic ratio C_∞ of the chain defining a quantity closer to reality (Eq 1.31):

$$C_\infty = \lim_{N\to\infty}\left(\frac{r^2}{Nl^2}\right) \qquad (1.31)$$

The lower the C_∞, the more compact the statistic ball will be, indicating a great tortuosity of the chain (generally between 1 and 20).

iii. **Chain entanglement**

When the chains become too long (usually corresponding to a critical molar mass M_C of several kg / mol), the macromolecules are assembled into a structure which has a very important influence on the thermomechanical behavior of the material [4, 41, 42]. This critical molar mass defines the beginning of a critical entanglement of the polymer molecules [43, 44].

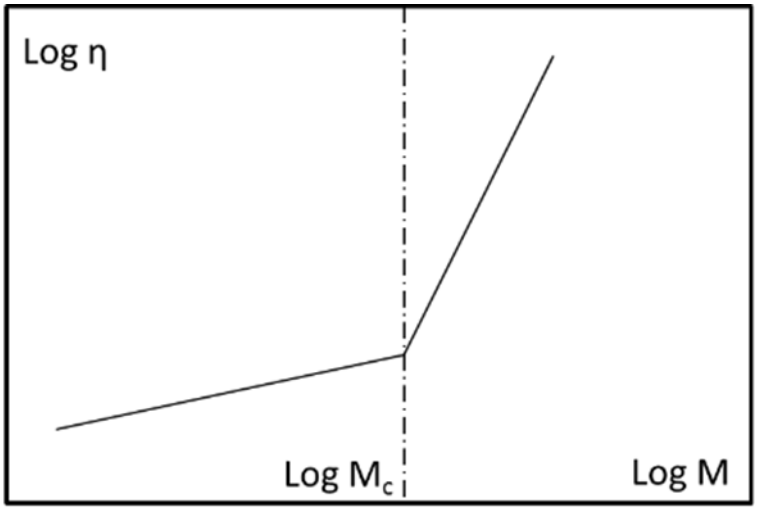

(a)

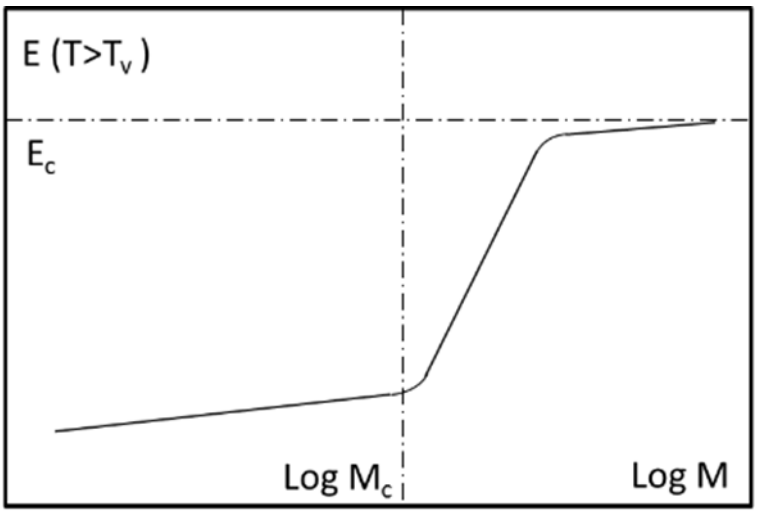

(b)

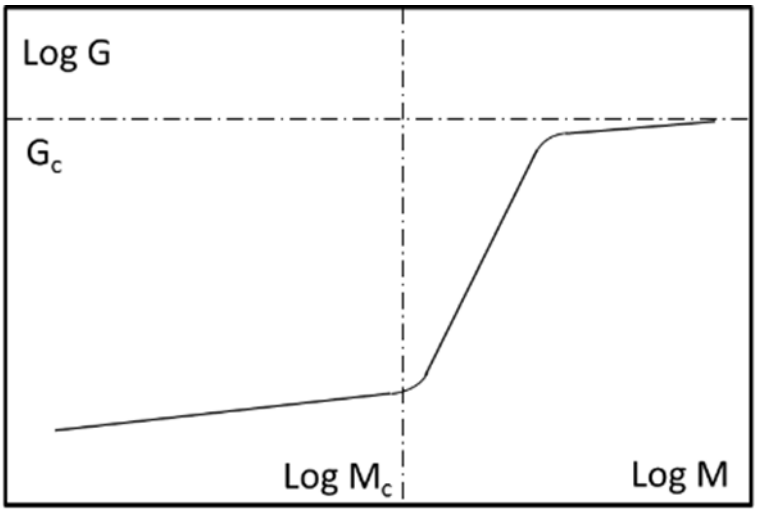

(c)

Figure 11 - Evolution with the molecular mass of (a) the viscosity, (b) the rigidity and (c) the energy of propagation of the chains [4]

It is noted that beyond this critical molar mass, several mechanical quantities change suddenly in regime:

- The viscosity for the melted state η increases much more rapidly with the molar mass beyond this critical molar mass (Figure 11.a).
- The modulus of elasticity (at a temperature above T_v) also increases much more rapidly beyond the critical molar mass and tends towards a finite E_C value (Figure 11.b).
- The propagation energy G (critical rate of restitution of the elastic energy) exhibits the same tendency as the modulus of elasticity and tends towards a finite G_C value (Figure 11.c).

These large increases in mechanical magnitudes are mainly due to the multiplication of intermolecular interactions (increase in cohesion energy) caused by the entanglement of molecules (Debye interactions, London, Hydrogen bonds, etc.). Indeed, the longer the molecules, the more they create links with other molecules, so that they can all become linked to one another (extreme case causing infinite viscosity). In an intermediate case, it is easy to see that the molecules thus entangled have more difficulty to move by crawling than weakly bound molecules leading to a higher viscosity. In the end, this leads to a greater cohesion of the molecules between them, leading to an increase in the modulus of elasticity and toughness of the material (through the increase of the propagation energy G).

iv. **Temperature of glass transition**

The glass transition temperature T_g marks the transition from a thermodynamic state of equilibrium to an unbalanced state (transition from glassy state to rubber state). This is the vitrification state of the polymer [4, 40, 45].

This condition occurs when the cooling of a polymer material is too fast in response to the rate of conformational changes imposed by thermodynamics. The chains thus remain in the configuration which they had just before the cooling. This phenomenon can be compared with the quenching of metals which pass to a metastable state outside the thermodynamic equilibrium by retaining the crystallographic structure which they had at high temperature. The slower the polymer was cooled, the closer its structure was to thermodynamic equilibrium [46].

One can define four temperature domains defining the evolution of the molecular structure without thermodynamic equilibrium [4, 46]:

- If $T > T_g$, the polymer reaches very quickly thermodynamic equilibrium.
- If $T_g > T > T_g - \Delta T$, (ΔT corresponds to a few tens of degrees) this domain is called "annealing". The polymer may reach thermodynamic equilibrium after a specific duration.
- If $T_g - \Delta T > T > T_\beta$, this domain is called "physical aging". The structure of the polymer evolves but will never reach the thermodynamic equilibrium (even over very long durations).
- If $T < T_\beta$, the polymer material does not see any evolution in its structure.

It is important to know that the glass transition temperature is a very difficult quantity to evaluate experimentally because it depends on many parameters such as cooling rate and measurement frequency (to not miss the transition of thermodynamic behavior). This is why the values found in literature are those measured under industrial conditions so that they are relevant (in most cases) under the conditions of use of engineers and researchers.

The value of T_g strongly depends on the strength of cohesion between the chains (intermolecular interactions), the static rigidity of the material and on the density of patella (particularly in presence of aromatic cycles). However, the influence of these quantities may also greatly varies with the level of entanglement of the chains, therefore, the molecular mass plays also a major role in the value of T_g.

b. Physical signification of the yield stress in amorphous polymers

i. **Chain motion**

The movement of the molecular chains is induced by a phenomenon of crawling of the latter. The intensity of this phenomenon increases with the rise in temperature. To understand its origin, we must consider the different conformations of the secondary groups around the axis of the main skeleton of the macromolecule (representation of Newman). These conformations are defined as a function of the steric hindrance of the secondary groups [4, 40].

In general, the conformation trans (0°) is the most thermodynamically stable contrary to the left conformations (± 120°). Indeed, the energy is then the most important. The energy necessary to stabilize this conformation is therefore the lowest. Consequently, the energy necessary to achieve a conformational jump increases with the gap of this activation energy (Figure 12). However, raising the temperature makes it possible to increase the probability of a conformation jump and is defined by the relation (Eq 1.32) [39, 42]:

$$p = e^{-\frac{U}{RT}} \qquad (1.32)$$

With U the energy to be crossed to accomplish the conformation jump, R the perfect gas constant and T the absolute temperature (K).

It is noted that if $E > RT$, the jumps are rare events characterizing a rigid chain. However, if $E < RT$, the jumps have a high probability and the conformational changes are numerous then producing significant motions in the molecular chain and then causing its breakdown.

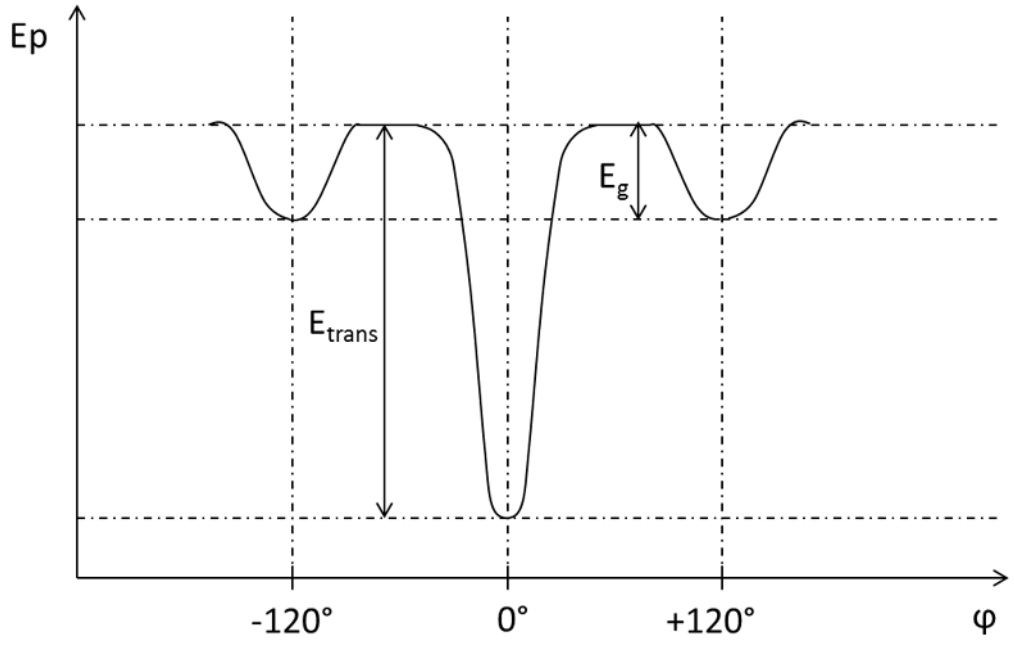

Figure 12 - Potential energy E_p of secondary groups according to their spatial conformation [4]

There are several critical temperatures for each type of polymer molecules defining the transition from a low probability of conformation jump to a high probability because not all conformation sites necessarily have the same secondary group configuration.

These temperatures are called the transition temperatures T_β, T_γ, … and correspond in general to the secondary relaxation mechanisms of the following groups (A, B and C) (see Figure 13):

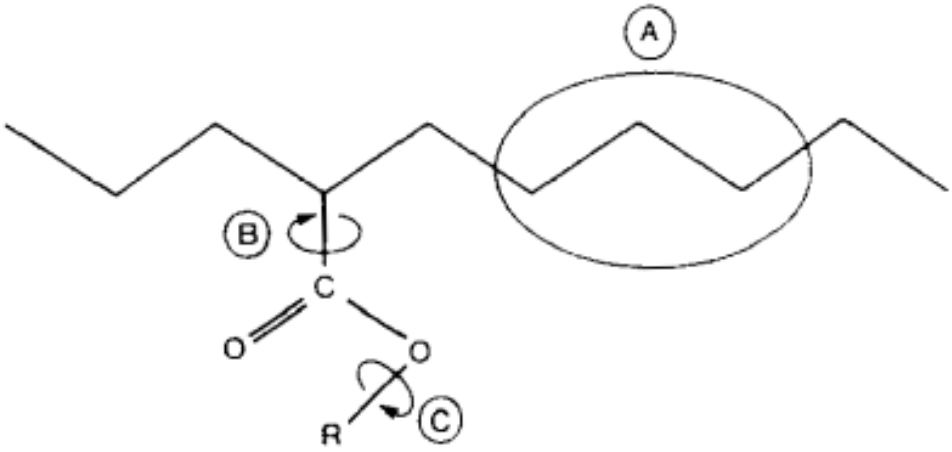

Figure 13 - Illustration of the different mechanisms leading to the crawling of the chains [4]

Another phenomenon may be responsible for the movement of the polymer chains, it is the slipping of these chains induced by an external stress (see Eyring theory in the next section about the yield stress).

Another characteristic aspect of amorphous polymer can be enounced: the free volume V_f [47-49]. It corresponds to the volume of the polymer which is not occupied by the chain segments (occupied volume V_0) and is consequently composed of voids. The free volume increases linearly with the temperature up to the glass transition temperature T_g (temperature of activation for jumps of full chain segments) above which its sensitivity is much stronger (Figure 14). The higher the free volume is, the easier the flow will be. Therefore, at high temperature (above T_g), the yield stress is much smaller than at lower temperature. At a given temperature T, the fraction of free volume $f(T)$ can be written by Eq 1.33.

$$f(T) = \frac{V_f}{V_f + V_0} \qquad (1.33)$$

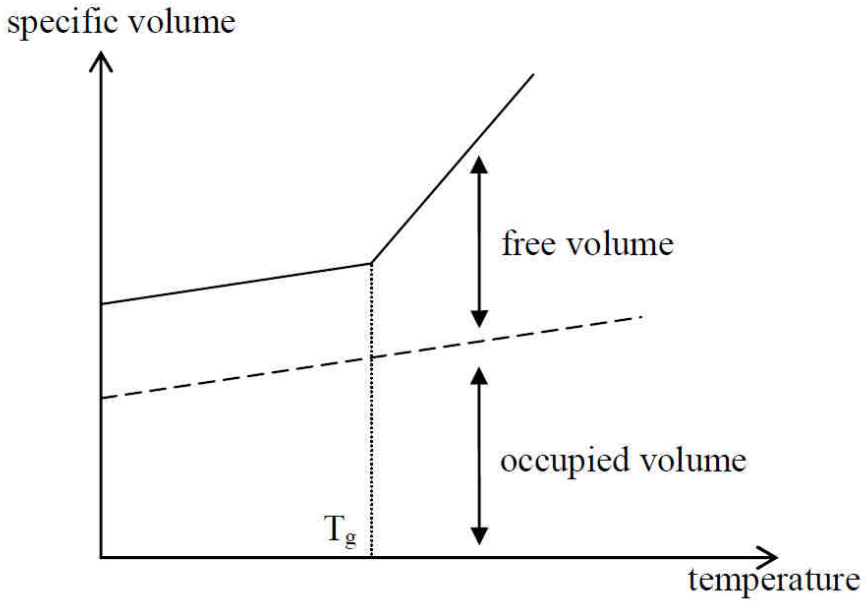

Figure 14 - Evolution of the free and occupied volume with the temperature

ii. **Yield stress**

The theory developed by Eyring aims to model yield stress [50, 51] . This one is based on the state transition theory. This theory makes possible to model all the thermo-activated phenomena in amorphous polymers. The primary concept consists in the jumps of the segments of the macromolecules from one configuration to another (causing the macromolecule to break). The energy provided by a constraint will allow such jumps. It is assumed that such phenomena start when the stress reaches the

flow constraint (even if it is a simplification because other phenomena exist such as adiabatic heating, expansion effects, etc.). Eyring posed three hypotheses:

- In the absence of stress, the ends of the chains of the macromolecules are in a state of thermodynamic equilibrium.
- The deformation of the polymer materials involves the displacement of the chain segments from one thermodynamic state of equilibrium to another.
- The displacement of the polymer chain segments follows a stochastic process. The existence of energy barriers is due to the presence of neighboring polymer chains.

The basic deformation process can be either intermolecular (chain slippage) or intramolecular (chain conformation change). In the absence of stress, the system is in thermodynamic equilibrium and the chain segments move with an oscillation frequency ν between the equilibrium positions (Eq 1.34):

$$\nu = \nu_0 e^{-\frac{\Delta H}{k_b T}} \quad (1.34)$$

With ν_0 the fundamental vibration frequency of the chains, ΔH the activation energy required for molecular displacement, T the temperature and k_b the Boltzmann constant. It is assumed that the applied stress σ is responsible for the variation of a symmetrical offset of the activation energy ΔH. Indeed, under constraint, the frequency of conformal jumps increases in the direction of application of the latter. The activation energy thus tends to decrease in this direction by an amount corresponding to the work performed by the displacement of the chains by sliding. This work is expressed by the following expression (Eq 1.35):

$$W = \frac{\sigma V}{2} \quad (1.35)$$

With V an activation volume (or Eyring volume) representing the volume in which a polymer chain must be able to move to activate the flow. The factor 1/2 is explained by the presence of two chains for each equilibrium position. Whenever an equilibrium position changes, two polymer chains will move. The frequency of the flow ν_f is given by the following expression (Eq 1.36):

$$\nu_f = \nu_0 e^{-\frac{\Delta H}{k_b T} + \frac{\sigma V}{2 k_b T}} \quad (1.36)$$

Symmetrically, the probability of molecular change in the opposite direction to the direction of stress application decreases. The flow frequency ν_b in this backward direction is expressed by the following expression (Eq 1.37):

$$\nu_b = \nu_0 e^{-\frac{\Delta H}{k_b T} - \frac{\sigma V}{2 k_b T}} \quad (1.37)$$

The rate of deformation of a polymer chain being proportional to the difference of the two frequencies ν_f and ν_b, one has in the direction of application of the constraint (see Eqs 1.38 and 1.39):

$$\dot{\varepsilon} \propto \nu_f - \nu_b = \nu_0 e^{-\frac{\Delta H}{k_b T}} \left(e^{\frac{\sigma V}{2k_b T}} - e^{-\frac{\sigma V}{2k_b T}} \right) \quad (1.38)$$

$$\dot{\varepsilon} = \dot{\varepsilon}_0 e^{-\frac{\Delta H}{k_b T}} \sinh\left(\frac{\sigma V}{2k_b T}\right) \quad (1.39)$$

With the consideration of the limited expansion of the first order, one can write the flow constraint (Eqs 1.40 and 1.41) with the following expression corresponding to the linear Ree-Eyring model [50, 51]:

$$\sinh^{-1} x = \ln 2x \quad (1.40)$$

$$\sigma_y = \frac{2\Delta H}{V} + \frac{2k_b T}{V} \ln\left(\frac{2\dot{\varepsilon}}{\dot{\varepsilon}_0}\right) \quad (1.41)$$

The effect of the hydrostatic pressure on the amorphous polymer can be implemented in the Ree-Eyring model by simply writing (Eq 1.42):

$$\dot{\varepsilon} = \dot{\varepsilon}_0 e^{-\frac{\Delta H - \sigma V + P\Omega}{k_b T}} \quad (1.42)$$

With P the hydrostatic pressure and $\Omega = \alpha_p V$ the activation volume under pressure (α_p is a coefficient modeling the sensitivity of the polymer to pressure).

c. Strain softening and relaxation of the chains

After yielding, the polymer presents irreversible microstructural changes which can be interpreted as an increase of the internal entropy of the material. Indeed, once the molecules start to slip, the complexity of the chain network can be observed. On one hand, a strong friction, influenced by the local state of stress between the chains, increases the strength of the material with the strain. On the other hand, the chains are not yet in tension and an important freedom of motion of the chain segments is present, leading to a decrease of the resistance of the polymer [52, 53] (depending on the entanglement, the length and the tortuosity of the chains [54]). The strain softening can be seen as the slow extension of the chain fragments (Figure 15) [2]. This relative free motion of the chains lasts until a majority of those chains starts to be locally strained due to excessive tension, causing the hyperelasticity phenomenon.

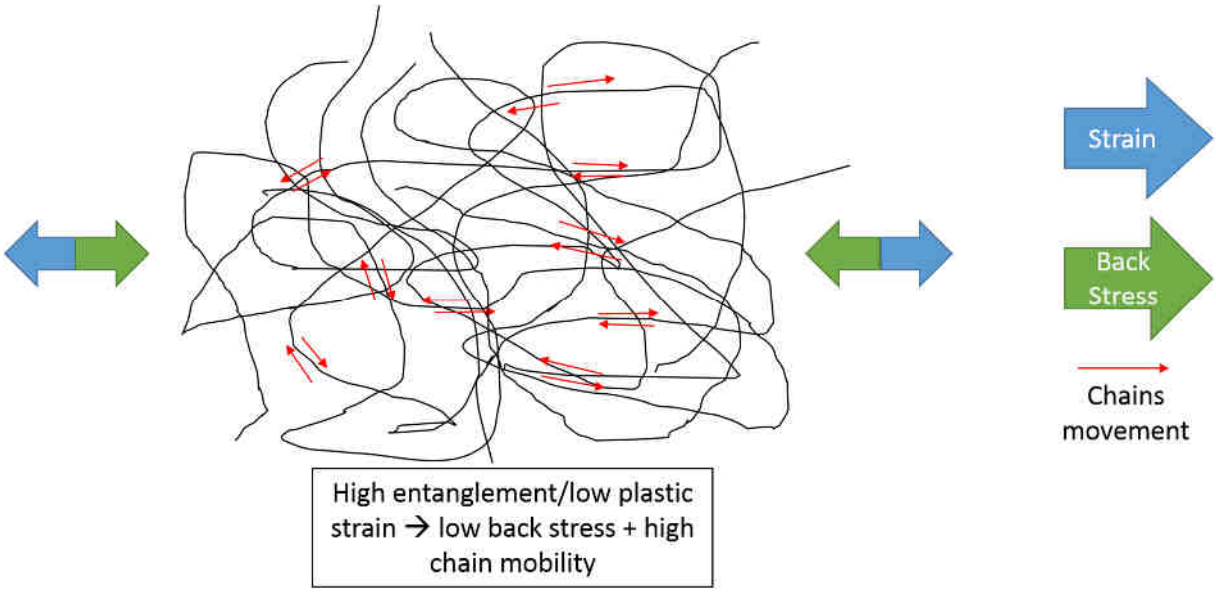

Figure 15 - Illustration of mechanisms and resultant stress of strain softening phenomenon

The relaxation of chains is a phenomenon which can be observed when the tension on a chain segment is locally released. The hyperelasticity being a reversible phenomenon, the chain segment springs back to an energetically optimal position in the chain network depending on the available local free volume [52]. The corresponding time of this phenomenon is called the characteristic relaxation time of the polymer [2].

d. Hyperelasticity phenomenon

The hyperelasticity phenomenon is caused by the overall resistance to the applied strain of the polymer chains network and results in a back stress [2, 55]. The higher the strain is, the higher the back stress will become. This increase of the hyperelastic stress can be microscopically explained by the alignment of all the chains, which can be considered as strings, in the direction of the highest local equivalent strain. Therefore, at macroscopic level, the back stress will be highly dependent on the state of stress which will condition the alignment behavior of the chains. Thermodynamically speaking, hyperelasticity is associated with a decrease in the entropy of chain configuration during the extension of the material and an increase during the compression (Figure 16).

The back stress is generally computed from an energy density of deformation function W. Two hypotheses are made [56]:

- The strain energy density is a function of the strain gradient.
- The intrinsic dissipation during the deformation is zero.

The energy density of deformation can be written (by considering the two first principles of thermodynamics) with the following expression (Eq 1.43):

$$W(\overline{\overline{E_{GL}}}) = \frac{\mu}{2}\left(Tr(\overline{\overline{E_{GL}}})\right)^2 + 2\kappa Tr\left(\overline{\overline{E_{GL}}}^2\right) \quad (1.43)$$

With $\overline{\overline{E_{GL}}}$ the strain tensor of Green-Lagrange and κ and μ are elastic constants of the hyperelastic material.

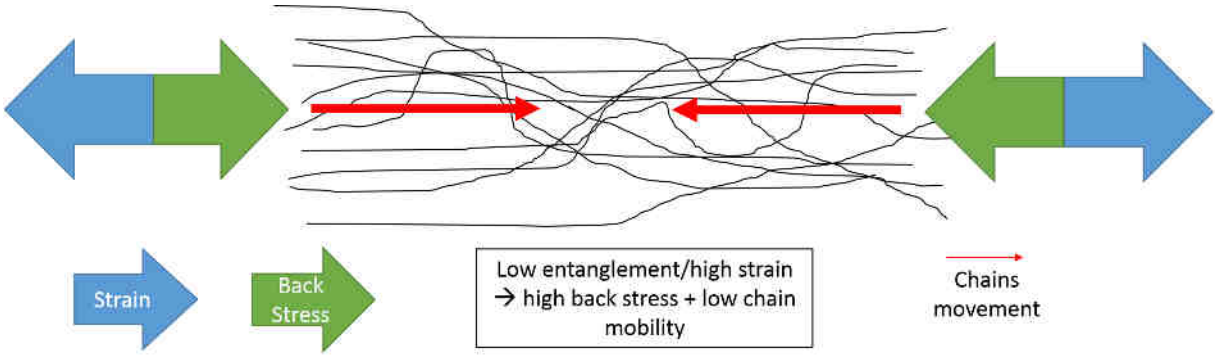

Figure 16 - Illustration of hyperelasticity phenomenon and resultant stress

B. Constitutive modeling of mechanical behavior

1. Constitutive of mechanical behavior

The necessity of using constitutive mechanical law is of the upmost importance. There are several analytical methods to address the problems of mechanics. The first historically uses the concept of force while newer methods use the energy or power concepts. This last is the most practical to use (since the force can be directly measured through force cell) for modeling of complex mechanical systems and is becoming one on which is based the finite element method widely used by simulation softwares.

The virtual power is expressed (Eq 1.44) in terms of the velocity field v and force ϕ which may correspond to any type of action (internal or external). For a system Σ [4, 57]:

$$P = \int_{\Sigma} \phi . v \, dm \quad (1.44)$$

With dm an infinitesimal fraction of the system Σ.

The action which may be encountered:

- External P_e if there is an exchange of energy with the outer part of Σ (contact or remote)
- Interior P_i if the action concerns interactions between particles within the system. The power of deformation is opposed to the power of internal actions and is expressed as follow (Eq 1.45):

$$P_{def} = -P_i \quad (1.45)$$

- The acceleration actions P_a corresponds to the volumetric field $-\rho\gamma$ with ρ the density and γ the acceleration.

Assuming that there are at any time and for any movement a Galilean space in which the sum of the virtual power related to Σ vanishes (especially when considering eulerian tensor systems):

$$P_e + P_i + P_a = 0 \quad (1.46)$$

The principle of virtual power is stated entirely on equation (Eq 1.46).

If we consider the eulerian Cauchy strain tensor $\overline{\overline{D}}$ is considered (Eq 1.47), the tensor of the associated constraints, also eulerian, is called Cauchy stress tensor $\overline{\overline{\sigma}}$.

$$\overline{\overline{D}} = \frac{1}{2}\left(\overline{\overline{{}^{T}\nabla}}v + \overline{\overline{\nabla}}v\right) \quad (1.47)$$

Assuming that the system Σ is subjected to forces only on a part of $\partial\Sigma_F$ and the displacements on the complementary part $\partial\Sigma_V$ to be zero. The motion is considered kinetically admissible to zero. We then find (Eq 1.48):

$$P_{def} = \int_{\Sigma} \overline{\overline{\sigma}}.\overline{\overline{D}}\, dV \quad (1.48)$$

With dV an infinitesimal volume fraction of the system Σ.

By considering the strength of external actions, the forces of volume actions f (always related to the density ρ) have to be taken into account separately from the surface forces F exerted on $\partial\Sigma_F$. If coupled masses are neglected, we get Eqs 1.49 and 1.50:

$$P_e = \int_{\Sigma} \rho f.v\, dV + \int_{\partial\Sigma_F} F.v\, dS \quad (1.49)$$

With:

$$P_a = -\int_{\Sigma} \rho\gamma.v\, dV \quad (1.50)$$

We can then write the full form of the virtual power principle (Eq 1.51) [58, 59]:

$$\int_{\Sigma} \overline{\overline{\sigma}}.\overline{\overline{D}}\, dV - \left(\int_{\Sigma} \rho f.v\, dV + \int_{\partial\Sigma_F} F.v\, dS\right) + \int_{\Sigma} \rho\gamma.v\, dV = 0 \quad (1.51)$$

Considering the expression of the Cauchy strain tensor $\overline{\overline{D}}$ and the symmetry of $\overline{\overline{\sigma}}$, the formulation becomes Eq 1.52:

$$\int_{\Sigma} \bar{\bar{\sigma}} : \bar{\bar{\nabla}} v \, dV - \int_{\Sigma} \rho(f - \gamma) . v \, dV - \int_{\partial\Sigma_F} F . v \, dS = 0, \forall v \qquad (1.52)$$

By integration by part of the first integral and using the Ostrogradski relationship, we get Eq 1.53:

$$\int_{\Sigma} \left(\frac{\partial \sigma_{ij}}{\partial x_i} + \rho(f_i - \gamma_i) \right) v_j \, dV - \int_{\partial\Sigma_F} \sigma_{ij} n_i v_j \, dS + \int_{\partial\Sigma_F} F_i v_j \, dS = 0 \qquad (1.53)$$

Virtual movements are random, if any v are taken in Σ and if v is considered null on $\partial\Sigma_F$, then the first integral should be zero regardless of v (Eq 1.54):

$$\frac{\partial \sigma_{ij}}{\partial x_i} + \rho(f_i - \gamma_i) = 0 \qquad (1.54)$$

Eq 1.38 is also called the indefinite equations of motion (3 in number) or of equilibrium if γ is zero. A more practical expression (Eq 1.55) [59]:

$$div \bar{\bar{\sigma}} + \rho(f - \gamma) = 0 \qquad (1.55)$$

The virtual movement being always random, a second equality comes from both remaining surface integrals on $\partial\Sigma_F$ (Eq 1.56):

$$\sigma_{ij} n_i = F_i \qquad \text{or} \qquad \bar{\bar{\sigma}} n = F \qquad (1.56)$$

These three equations (given by Eq 1.39) from the latter formulation give the boundary conditions of the principle of virtual power and raise the unknowns of the problem.

These formulations allow the determination of the value of the Cauchy stress tensor $\bar{\bar{\sigma}}$ for all the system according to the deformation and also to be able to know the power levels and thus the energy of the system.

The discretization in small elements is easy to do and allows very precise computations across complex systems. However, the calculation time is very long. For this reason, the finite element method and diverse algorithms have been created (size and shape of the surface elements or discretization volume for example). Conversely, the finite element method can be used to solve other problems from thermal to magnetic ones (with integral formulations from other principles than the one of virtual power).

A summary of all the equations available after processing the principle of virtual power can be found in Table 1 [4].

Table 1 - Bilan of the virtual power system of equations [4]

Unknown	Scalar unknowns number	Equations	Scalar equations number
Displacement u	3	-	0
Strain $\bar{\bar{\varepsilon}}$	6 (symmetry)	$\bar{\bar{\varepsilon}} = \frac{1}{2}\left(\overline{\overline{{}^{T}\nabla}}v + \overline{\overline{\nabla}}v\right)$	6
Stress $\overline{\overline{\sigma}}$	6 (symmetry)	$div\bar{\bar{\sigma}} + \rho(f - \gamma) = 0$	3
Density ρ	1	Equation of continuity	1

There is a gap of six equations to fully determine the mechanical problem. These missing equations come from the study of the behavior of the material and requires the establishment of behavior laws. These are well known in the regime of elastic deformation of materials but these laws become more complex and difficult to establish for plastic or viscoplastic domains of deformation (excluding specific regimes for certain types of material or under certain stress conditions).

2. Constitutive modeling of metallic materials

Metallic materials being purely crystalline, the deformation mechanisms of the material are governed, in addition to the elastic behavior, by two main mechanisms: the evolution of the dislocations density regarding the configuration of the lattice system (internal stress σ_{int}) and the crossing of Peierls barriers (effective stress σ_{eff}). Furthermore, separation of athermal (σ_a) and thermal (σ_{th}) [7, 17, 60] stresses has to be taken into account for both σ_{int} and σ_{eff} [7, 17, 60, 61] in order to model efficiently the mechanical behavior of the material. Many other phenomena are responsible for variations in the mechanical behavior such as dissolution or precipitation caused by temperature changes, micro-inertial effects leading to a very high sensitivity in the high strain rate domain. The overall stress σ of the plastic regime can therefore be written as (Eq 1.57):

$$\sigma = \sigma_{eff}{}_{a}\left(\dot{\varepsilon}_p\right) + \sigma_{eff}{}_{th}\left(\dot{\varepsilon}_p, T\right) + \sigma_{int}{}_{a}\left(\varepsilon_p, \dot{\varepsilon}_p\right) + \sigma_{int}{}_{th}\left(\varepsilon_p, \dot{\varepsilon}_p, T\right) \quad (1.57)$$

The athermal stress is generally considered as strain rate independent in most models.

a. Phenomenological constitutive models

Constitutive models for metallic materials can be considered as phenomenological if no elementary physical considerations are taken into account such as the lattice structure or the decomposition of the stress in athermal-thermal parts and the thermal stress in effective-internal parts. Therefore, those models generally shows a lack of predictability over a wide range of temperatures and strain rates and are considered as descriptive models. In this section, several well-known models are presented and discussed.

i. **Johnson-Cook model**

The Johnson-Cook model [62-64] is probably the most used due to its simplicity and implementation in most of finite element softwares. This model is composed of three multiplicative parts:

- The strain hardening defined by the parameters: A the reference yield stress, B the plastic modulus and n the hardening coefficient
- The strain rate sensitivity defined by the parameter C
- The temperature sensitivity defined by the parameter m

The strain hardening parameters have be determined at the reference strain rate $\dot{\varepsilon}_0$ and reference temperature T_r. The expression (Eq 1.58) of the plastic stress described by the Johnson-Cook model is shown below.

$$\sigma = (A + B{\varepsilon_p}^n)\left(1 + C\log\frac{\dot{\varepsilon}_p}{\dot{\varepsilon}_0}\right)\left(1 - \left(\frac{T - T_r}{T_m - T_r}\right)\right)^m \quad (1.58)$$

The strain rate sensitivity suggested by the Johnson-Cook model consists in a linear relationship with the logarithm of the strain rate and can therefore only model thermo-activated phenomena. The viscous drag phenomenon cannot be taken into account without the computation of two values of C (one for quasi-static and one for dynamic domains). Besides, the temperature and rate sensitivities are applied on the effective stress A and on the internal stress ${B\varepsilon_p}^n$ which have generally very different responses to these experimental variables. Indeed, FCC and BCC metals have opposite strain rate sensitivities (negligible for the effective stress of FCC and for the internal stress of BCC metals and important for internal stress of FCC and effective of BCC metals) causing the Johnson-Cook model to be not suited for a large panel of materials. It can be noted that the Eq 1.58 is slightly different than the one suggested by the authors. Indeed, the parameter m is out of the parenthesis and allows the model to be able to compute values of stress below T_r.

ii. **Molinari-Clifton model**

The Molinari-Clifton model [65] shows a similar multiplicative structure as the Johnson-Cook model, with simpler expressions, corresponding to:

- The strain hardening defined by the parameters: σ_0 the plastic modulus and n the hardening coefficient.
- The strain rate sensitivity defined by the parameter m
- The temperature sensitivity defined by the parameter ν

The strain hardening parameters have to be determined at the reference strain rate $\dot{\varepsilon}_0$ and reference temperature T_0. The expression (Eq 1.59) of the plastic stress described by the Molinari-Clifton model is shown below.

$$\sigma = \sigma_0 {\varepsilon_p}^n \left(\frac{\dot{\varepsilon}_p}{\dot{\varepsilon}_0}\right)^m \left(\frac{T}{T_0}\right)^\nu \quad (1.59)$$

The main advantage of the Molinari-Clifton model is its high simplicity of use due to very few parameters. However, the simplicity of the expressions used for the different sensitivities is meanwhile an important drawback. Indeed, the lack of yield stress modeling leads to a null initial value of the plastic stress and therefore to a huge physical inaccuracy. Furthermore, the model is valid for a narrower range of temperature than for the Johnson-Cook model (see Figure 8).

b. Physically-based constitutive models

Contrary to phenomenological models, physically-based models take into consideration the decomposition of the stress into thermal and athermal stresses and also generally in internal and effectives stresses. The differences between these models come from the mechanisms considered in for the modeling of each stress contribution. The physically-based models present generally different expressions according to the lattice structure or can be easily modified to take this latter into account.

i. **Zerilli-Armstrong model**

The Zerilli-Armstrong model [64, 66] is based on the Orowan relation for the dislocation motion [67]. Different relations have been developed for the different lattice structure systems (BCC, FCC [9, 66] or HCP [68]) due to the fact that the multiplication of mobile dislocations and the creation of forests of dislocations are largely dependent on the lattice configuration [69]. This model is implemented in few finite element softwares. Only the expression for FCC metals (aluminum alloys) is presented here (Eq 1.60).

$$\sigma = \sigma_a + B_0\sqrt{\varepsilon^p}e^{-(\alpha_0 - \alpha_1 \ln \dot{\varepsilon}^p)T} \quad (1.60)$$

With B_0 the plastic modulus and α_0 and α_1 material parameters.

The athermal stress is modeled by Eq 1.61 (Hall-Petch expression):

$$\sigma_a = \sigma_0 + \frac{k}{\sqrt{d}} \quad (1.61)$$

With σ_0 a stress representing the overall resistance of the crystal lattice to dislocation movement, k the locking parameter and d the average grain diameter.

In this model, the effective stress is considered athermal, rate independent and equal to σ_a for the FCC metals. The thermal stress only consists in the internal stress (Eq 1.62):

$$\sigma_{th} = \sigma_{int} = B_0\sqrt{\varepsilon^p}e^{-(\alpha_0 - \alpha_1 \ln \dot{\varepsilon}^p)T} \quad (1.62)$$

The Zerilli-Armstrong model presents a temperature/rate coupled expression but a few drawbacks can be enounced. Firstly, the hardening coefficient is considered equal to 0.5 (square root) for all FCC metals and this expression does not model the kinematic hardening specific to FCC materials. This modeling

problem can easily be corrected by using a hardening coefficient n instead of the square root of the original expression (Eq 1.44). Secondly, the exponential term shows mathematical inconsistency at extreme temperatures and strain rates. Finally, the original Zerilli-Armstrong model follows the thermo-activation of dislocations motion and no viscous drag effect modeling is present, leading to a lack of predictability at high strain rates. Finally, the model does not allow the stress to go down the value of σ_a. Therefore, the model becomes more and more inaccurate with the temperature softening of the materials.

ii. **Modified Rusinek-Klepaczko model**

The modified Rusinek-Klepaczko model (MRK) [70] has been developed from the original RK model [60, 71] for the characterization of FCC metals. This model aims to model the overall stress of the materials through the evaluation of the internal stress σ^* and the effective stress σ_μ (Eqs 1.63 to 1.65). An additional study as also provided to the model a simplified expression of the viscous drag stress σ_{VS} [28].

$$\sigma = \frac{E(T)}{E_0}\left(\sigma_\mu + \sigma^*\right) + \sigma_{VS} \tag{1.63}$$

With:

$$\begin{cases} \sigma_\mu = Y \\ \sigma^*\left(\varepsilon_p, \dot{\varepsilon}_p, T\right) = B\left(\dot{\varepsilon}_p, T\right){\varepsilon_p}^{n\left(\dot{\varepsilon}_p, T\right)}\left[1 - D_1\frac{T}{T_m}\ln\left(\frac{\dot{\varepsilon}_{max}}{\dot{\varepsilon}_p}\right)\right]^{\frac{1}{m}} \\ \sigma_{VS}\left(\dot{\varepsilon}_p\right) = \chi\left(1 - e^{-\alpha\dot{\varepsilon}_p}\right) \end{cases} \tag{1.64}$$

And:

$$\begin{cases} E(T) = E_0\left[1 - \frac{T}{T_m}e^{\theta^*\left(1-\frac{T_m}{T}\right)}\right] \\ B\left(\dot{\varepsilon}_p, T\right) = B_0\left(\frac{T}{T_m}\ln\frac{\dot{\varepsilon}_{max}}{\dot{\varepsilon}_p}\right)^{-\nu} \\ n\left(\dot{\varepsilon}_p, T\right) = n_0\left(1 - D_2\frac{T}{T_m}\ln\left(\frac{\dot{\varepsilon}_p}{\dot{\varepsilon}_{min}}\right)\right) \end{cases} \tag{1.65}$$

The parameter Y corresponds to the yield stress of the metal. D_1, D_2, m, ν, α and χ are material constants. B is the plastic modulus and E_0 the elastic modulus at 0K. $\dot{\varepsilon}_{max}$ is the upper limit of the strain rate level of the material is generally taken as $\dot{\varepsilon}_{max} = 10^7\ /s$. $\dot{\varepsilon}_{min} = 10^{-5}\ /s$ is the lower limit [60].

The decomposition of the overall stress in internal and effective stress is a very important aspect in mechanical modeling. It allows to separate sensitivities of each stress component to the temperature and strain rate which are inherent material properties. The suggestion of an expression of the viscous drag stress is interesting and allows here a potential validity of the model over a wide range of strain rate. However, this last expression does not depend on the temperature. Another limitation of the MRK model

could be the expression describing the structural hardening trough an isotropic homogeneous hardening coefficient n which might not be suited for heterogeneous hardening as exhibited by FCC metals.

iii. **Mechanical Threshold Stress model**

The Mechanical Threshold Stress model (MTS) [17, 61, 64, 72] has been developed for FCC and BCC metals from the physical assumption of the separation of the thermal stress into internal (σ_ε) and effective (σ_i) parts corresponding respectively to the evolution of the density of dislocations with the strain (structural hardening) and to the overcoming of short-range obstacles such as Peierls' barriers (independent from the strain). The global expression of the model is the following (Eq 1.66):

$$\sigma\left(\varepsilon_p, \dot{\varepsilon}_p, T\right) = \sigma_a + \left(\sigma_\varepsilon\left(\varepsilon_p, \dot{\varepsilon}_p, T\right) S_\varepsilon\left(\varepsilon_p, \dot{\varepsilon}_p, T\right) + \sigma_i S_i\left(\varepsilon_p, \dot{\varepsilon}_p, T\right)\right) \frac{E(T)}{E_0} \qquad (1.66)$$

The parameter σ_a refers to the athermal stress. S_ε and S_i are dimensionless factors modeling the evolution of the internal and effective stresses respectively with the thermal activation of the respective phenomena (coupled with the strain rate). The factors S_j are generally computed using the Kocks expression (Eq 1.67):

$$S_j = \left[1 - \left(\frac{k_b T}{g_{0_j} \mu b^3} \ln\left(\frac{\dot{\varepsilon}_{0_j}}{\dot{\varepsilon}_p}\right)\right)^{\frac{1}{q_j}}\right]^{\frac{1}{p_j}} \qquad (1.67)$$

With k_b the Boltzmann constant, μ the shear modulus, b the Burger vector, g_0 a normalized characteristic energy of the phenomenon, $\dot{\varepsilon}_{0_j}$ a reference strain rate and q_j and p_j parameters corresponding to the shape of the obstacles.

The structural hardening is modeled through the computation of a hardening rate $\theta\left(\varepsilon_p, \dot{\varepsilon}_p, T\right)$ (see Eq 1.68).

$$\theta\left(\varepsilon_p, \dot{\varepsilon}_p, T\right) = \frac{d\sigma_\varepsilon\left(\varepsilon_p, \dot{\varepsilon}_p, T\right)}{d\varepsilon_p} = \theta\left[1 - F(X)\right] \qquad (1.68)$$

With θ_0 the initial hardening rate.

A lot of expressions for θ depending on the strain rate and sometimes on the temperature can be found in the literature.

Many $F(X)$ functions exists in the literature for FCC metals such as the Voce expression $F(X) = \left(\frac{\sigma_\varepsilon}{\sigma_{\varepsilon s}}\right)^2$ or the expression $F(X) = \frac{\sigma - \sigma_a}{\sigma_{\varepsilon s} - \sigma_a}$

With α an empirical parameter and $\sigma_{\varepsilon s}$ the thermal saturation stress modeling the evolution of microstructural texture state of the metal and given by Eq 1.69:

$$\ln\left(\frac{\dot{\varepsilon}_{\varepsilon s0}}{\dot{\varepsilon}_p}\right) = \frac{\mu b^3 g_{\varepsilon s0}}{k_b T} \ln\left(\frac{\sigma_{\varepsilon s}}{\sigma_{\varepsilon s0}}\right) \quad (1.69)$$

With $g_{\varepsilon s0}$ a normalized characteristic overall energy of the phenomena responsible of the texture evolution, $\dot{\varepsilon}_{\varepsilon s0}$ a reference strain rate and $\sigma_{\varepsilon s0}$ the value of $\sigma_{\varepsilon s}$ at $0K$ corresponding to a non-existent hardening rate.

The MTS model is widely used in many advanced industrial cases. Indeed, its physical approach allows a validity of the modeling over a wide range of temperatures and strain rates for most FCC and BCC metals. However, the "as proposed" model does not take into account viscous drag effect (only thermal activation at low and medium strain rates) and the viscous stress needs to be additionally computed. Another drawback of the MTS model is its non-linearity leading to a complex implementation in Finite Element Software and to a longer computation time than linear models.

c. Models comparison

A comparison of the constitutive models for metallic materials is presented in this section (Figure 11). The Mechanical Threshold Stress (MTS) [17], Johnson-Cook (JC) [62], Molinari-Clifton (MC) [65], Zerilli-Armstrong FCC (ZA) [66] and Rusinek-Klepaczko (MRK) [60] (without viscous drag extension) models are compared over wide ranges of temperatures (from 293 K to 786 K) and strain rates (from 0.001 /s to 17500 /s) (see Figure 17). The tested material is the AA7020-T651 aluminum alloy (the model parameters can be found in the APPENDIX E).

In quasi-static and room temperature conditions (Figure 17.a), all the models are in good agreement with the experimental data (except the ZA model which underestimate of 20% the stress). However, when the temperature increases (Figure 17.b), all the models have high difficulties to correlate with the experimental data. The ZA model cannot get a value lower than $\sigma_a = 400\ MPa$ due to its mathematical construction, and needs modification to be valid at higher temperatures. At 473K, the other models greatly overestimates the stress: 25% for the MTS and MRK models, 20% for JC model and 10% for MC. This mismatch is mainly due to the fact that the AA7020-T651 aluminum alloy is subjected to a change of microstructure around this temperature which leads to a drop of the stress. The models do not take into account this phenomenon (see Figure 8). At room temperature and high strain rates (Figure 17.c and 17.d), the models are all in good agreement with the experimental data. However, it can be seen that the MRK expression needs the viscous drag extension expression to be able to fit with the experimental data for the higher strain rates (Figure 17.d).

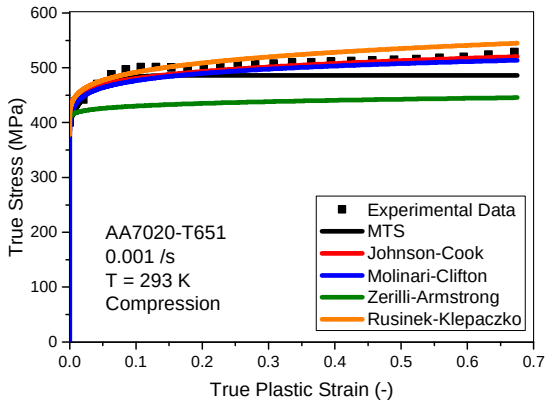

(a)

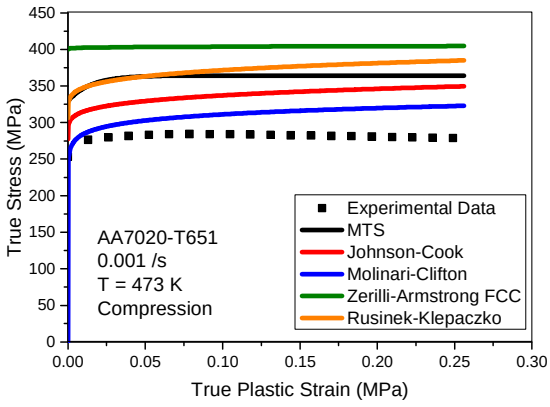

(b)

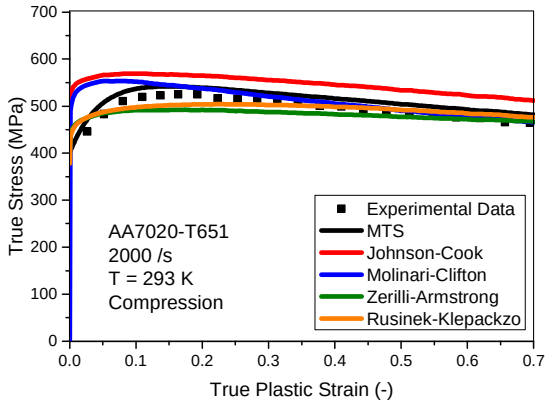

(c)

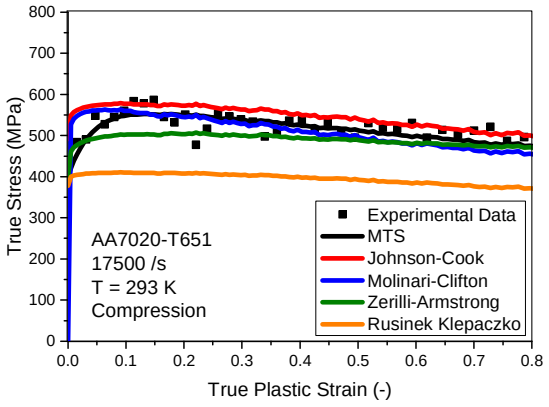

(e)

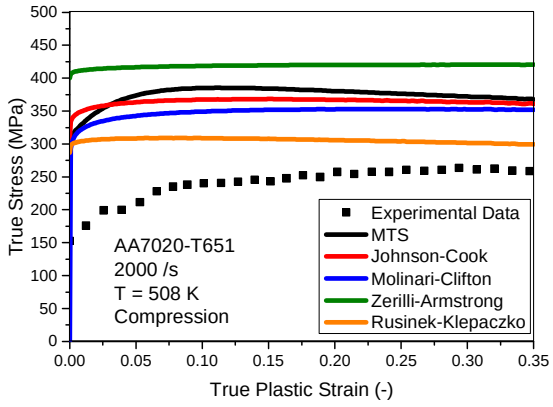

(f)

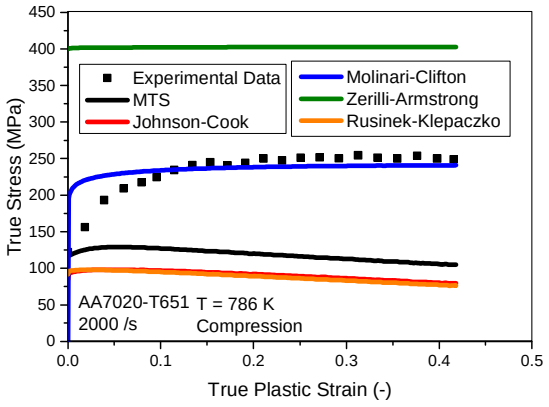

(g)

Figure 17 – Comparison of the different constitutive models at (a) room temperature and quasi-static conditions, (b) 473 K and quasi-static conditions, (c) room temperature and high strain rate conditions, (d) room temperature and very high strain rate conditions, (e) 508 K (change of microstructure) and high strain rate conditions and (f) 786 K (athermal plateau) and high strain rate conditions

The main drawback of the presented models consists into their inability to model the thermal behavior at high temperature due to phenomena which are not taken into account (e.g. change of microstructure, athermal plateau).

At higher temperature and high strain rates, (Figure 17.e and 17.f), the correlation of the models with the experimental data is highly variable. Indeed, due to the absence of modeling of phenomena such as the dissolution of the precipitates (around 490 K, see Figure 17.e) which is followed by the athermal plateau (Figure 17.d), the accuracy of the models from the literature is, in most cases, insufficient. The ZA model cannot go down below $\sigma_a = 400\ MPa$ and is therefore not suited for these applications. The MTS, JC and MRK models overestimate the stress just after the temperature of change of microstructure (Figure 17.e) and then underestimates it at higher temperatures (Figure 17.f). Concerning the MC model, the same observation can be done even if the modeling at 786 K (Figure 17.f) is satisficing. However, this accuracy is caused by the mathematical function of this model for the temperature sensitivity which is much slower with increasing temperatures (it does not become zero even above the melting temperature) and the good correlation can be observed only for this temperature.

3. Constitutive modeling of amorphous polymers

Polymers being composed of macromolecules and not of crystals, the mechanisms of deformation of the materials are, in addition to the elastic behavior, governed by laws of hardening H completely different from metals (for semi-crystalline polymers [73]). Indeed, the equivalent of the hardening mechanism for amorphous polymers is a rearrangement of macromolecules by decreasing the radius of crawling tubes of these latter. Then the molecules lose freedom of movement and the viscosity of the material increases. The yield stress σ_y is also directly linked to the initial free volume of the macromolecules. The higher it is, the smaller σ_y will be. The relaxation of the chains after yielding is due to the increase of the free volume caused by the augmentation of the crawling activity of the lateral sub-molecules of the macromolecules (β transition). A decrease of the stress is therefore observed and is qualified as the strain softening S [47]. Another specific mechanism to polymers is the hyperelasticity. It ensures the overall cohesion of the material and has to be taken into account (especially for large deformations) as the Langevin spring B acting in parallel to the other mechanisms [2, 55]. All polymer materials presenting a relatively low viscosity η, all the mechanisms are greatly temperature and strain rate sensitive. The overall stress σ of the viscoplastic regime can therefore be written as (see Eq 1.70) [73-75]:

$$\sigma = \sigma_y(\dot{\varepsilon}_p, T) + H(\varepsilon_p, \dot{\varepsilon}_p, T) + S(\varepsilon_p, \dot{\varepsilon}_p, T) + B(\varepsilon_p, \dot{\varepsilon}_p, T) \quad (1.70)$$

The polymer materials, studied in this work, are assumed amorphous. Therefore, only models dedicated to amorphous polymer are presented in this section and the model extensions for the semi-crystalline

polymers are not treated ($H = 0$). In this manuscript, only the expressions modeling the yield part are presented.

The constitutive modeling of polymers can be performed with two different methods:

- A phenomenological method aiming to evaluate the level stress in the material by using a unique expression which takes into account all the different phenomena occurring during the deformation.
- A physically-based method which models separately the different phenomena and the contribution are summed after.

The second method gives generally more predictable results over a wider range of temperatures and strain rates than the first method.

a. Phenomenological constitutive models for complete mechanical behavior

The phenomenological approach does not aim to follow any physical consideration but to provide expressions allowing a good fitting of the stress-strain curves. Many models even propose a modeling of both elastic and plastic parts in one expression.

i. G'Sell-Jonas model

The G'Sell-Jonas model [76] is a phenomenological constitutive law for the mechanical behavior specifically developed for glassy polymers. It consists in four multiplicative terms corresponding to:

- The yield stress defined by the parameter K
- The thermal sensitivity defined by the parameter a
- The strain rate sensitivity defined by the parameters c_1, c_2 and c_3 (modification of the original model for a larger range of validity)
- The hyperelasticity phenomenon defined by the parameters h and n

All the parameters (except c) have to be determined at the reference strain rate $\dot{\varepsilon}_0$. The full expression of the plastic stress is the following (Eq 1.71):

$$\sigma = K e^{h{\varepsilon_p}^n} e^{\frac{a}{T}} \left(1 + c_1 \left(\frac{\dot{\varepsilon}_p}{\dot{\varepsilon}_0}\right)^{c_2} + c_3 \ln\left(\frac{\dot{\varepsilon}_p}{\dot{\varepsilon}_0}\right)\right) \qquad (1.71)$$

The G'Sell-Jonas model uses an exponential form for the hyperelasticity behavior which is therefore not physically modeled and can lead to high inaccuracies at high strain rates and temperatures. Another drawback of this expression is that the strain softening caused by the relaxation of the polymer chains is not modeled at all due to the exponential form of the hardening.

ii. **Mastuoka's model**

The Mastuoka's model [77] has been developed to allow the evaluation of the stress response of glassy polymers. The expression is the following (Eq 1.72):

$$\sigma = E_0 e^{-C\varepsilon}\, \varepsilon\, e^{-\left(\frac{\varepsilon}{\dot{\varepsilon}\tau}\right)^{\beta}} \qquad (1.72)$$

With τ an effective relaxation time linked to the temperature. E_0, β and C are materials parameters.

The Matsuoka's model takes into account of the viscoelasticity, yielding and strain softening phenomena in the same expression.

b. Constitutive modeling of the yield stress

The physically-based approach of constitutive modeling of polymer materials aims to take into account each contribution to the stress separately through micromechanical considerations such as crawling tube or free volume. Therefore, this kind of modeling provides expressions for the yield stress, the hyperelasticity, the strain softening and eventually for the structural hardening (semi-crystalline polymer) have to be modelled separately.

i. **Argon model**

The Argon model [78-80] takes into account the intermolecular resistance during the shearing of the polymer material. Argon proposes a representation of the shear deformation involving the rotation of the chain segments of length z in a cylinder of radius a. The rotation of the chain segments is achieved by the generation of two structural anomalies separated by the distance of the chain segment z forming an angle ω with it. The Argon model is only valid for low temperature (below the glass temperature transition T_g).

The free energy variation ΔG_f^* required to produce such a phenomenon is given by the following expression (Eq 1.73) (calculated from the theory of disclinations [81]):

$$\Delta G_f^* \approx \frac{3\pi G \omega^2 a^3}{16(1-\nu)}\left(1 - 8.53(1-\nu)^{\frac{5}{6}}\left(\frac{\tau}{\mu}\right)^{\frac{5}{6}}\right) \qquad (1.73)$$

With μ the shear modulus, ν the Poisson coefficient and τ the shear stress.
If we consider a thermally activated mechanism, we then have a relation of the type (Eq 1.74):

$$\dot{\gamma} = \dot{\gamma}_0 e^{-\frac{\Delta G_f^*}{RT}} \qquad (1.74)$$

With $\dot{\gamma}$ the rate of deformation in shear, T the temperature and R the constant of the perfect gases. Finally, the limit of elasticity in shear τ_y is set (Eq 1.75):

$$\frac{\tau_y}{G} \approx \frac{0.076}{1-\nu}\left(1 - \frac{16(1-\nu)RT}{3\pi G\omega^2 a^3}\ln\left(\frac{\dot{\gamma}_0}{\dot{\gamma}}\right)\right)^{\frac{6}{5}} \quad (1.75)$$

The shear stress is more often taken as t_0 ($\lim_{T\to 0K} \tau_y = t_0$) so that it leads to Eq 1.76:

$$\tau_y = t_0\left(1 - \frac{RT}{t_0 A}\ln\left(\frac{\dot{\gamma}_0}{\dot{\gamma}}\right)\right)^{\frac{6}{5}} \quad (1.76)$$

With Eq 1.77:

$$\dot{\gamma} = \dot{\gamma}_0 e^{-\frac{t_0 A}{RT}\left(1-\left(\frac{\tau_y}{t_0}\right)^{\frac{5}{6}}\right)} \quad (1.77)$$

And Eqs 1.78 and 1.79:

$$A = \frac{6^{\frac{7}{5}}\pi\omega^2 a^3}{5} \approx \frac{39\pi\omega^2 a^3}{16} \quad (1.78)$$

$$t_0 = \left(\frac{2}{17}\right)^{\frac{6}{5}}\frac{G}{1-\nu} \approx \frac{0.077G}{1-\nu} \quad (1.79)$$

The coefficient A has the dimension of a volume. The approximation $G = constant$ is often used for this model.

However, this model is only effective at low temperatures because the intermolecular energy barriers are predominant compared to the intramolecular forces which the most important at higher temperatures (around the glass transition temperature T_g).

With the following relations (Eqs 1.80 and 1.81), it is possible to get the values of the equivalent strain and stress [3]:

$$\sigma_y = \tau_y\sqrt{3} \quad (1.80)$$

$$\dot{\varepsilon} = \frac{\dot{\gamma}}{\sqrt{3}} \quad (1.81)$$

ii. **Ree-Eyring theory**

The Ree-Eyring theory [51] takes into account only one thermally activated phenomenon. In order to model the behavior of the amorphous polymer over wide ranges of strain rate and temperature, we must consider all the phenomena and construct a more global model. The validity of the Ree-Eyring model [50] is assumed correct for low and medium ranges of temperatures and strain rates. Concerning the temperature above T_g and at high strain rates the accuracy of the model is assumed less predictable (see Figure 18). The general expression (Eq 1.82) is of the following form (for N thermoactivated phenomena):

$$\frac{\sigma_y}{T} = \sum_i^N A_i \sinh^{-1}\left(\frac{C_i \dot{\varepsilon}}{T} e^{\frac{\Delta H_i}{k_b T}}\right) \quad (1.82)$$

With A_i, C_i and ΔH_i constant. In general, two phenomena are sufficient to model the behavior of the flow stress over a wide range of strain rate and temperature. The phenomena generally modeled are the relaxations α and β of the groups of the macromolecules. The form of the model then becomes (Eq 1.83):

$$\frac{\sigma_y}{T} = A_\alpha \left(\ln(2C_\alpha \dot{\gamma}) + \frac{Q_\alpha}{k_b T}\right) + A_\beta \sinh^{-1}\left(C_\beta \dot{\gamma} e^{\frac{Q_\beta}{k_b T}}\right) \quad (1.83)$$

With Q_α and Q_β the activation energies for the relaxation phenomena α and β respectively. C_i are the activation parameters. The phenomenon of relaxation α generally refers to low strain rates and high temperatures. The phenomenon of β relaxation generally refers to high strain rates and low temperatures. However, this model only makes it possible to determine the limit of flow of the material and does not make it possible to obtain directly a stress/strain curve. The relaxation phenomenon β is often attributed to the secondary relaxation mechanism of the peripheral groups along the main chain. The phenomenon of relaxation α is linked to the concept of increasing the free volume (William-London-Ferry equation [48]) and is in no way linked to a rheological mechanism.

iii. **Cooperative model**

The cooperative model [74, 75] is a derived form of the Ree-Eyring theory [50] which takes into account the existence of an internal stress σ_i in the amorphous polymer. So that the effective stress σ^* is described by the following expression (Eq 1.84):

$$\sigma^* = \sigma_y - \sigma_i \quad (1.84)$$

The phenomenon of relation β is the only one considered (the one responsible for the majority of motions of the molecules of the amorphous polymer). The calculations show that the flow stress can be written (Eq 1.85):

$$\begin{cases} \sigma_y = \sigma_i(0) - mT + \dfrac{2k_b T}{V} \sinh^{-1}\left(\dfrac{\dot{\varepsilon}}{\dot{\varepsilon}_0 e^{-\frac{\Delta H_\beta}{RT}}}\right)^{\frac{1}{n}} & for\ T \le T_g \\ \sigma_y = \dfrac{2k_b T}{V} \sinh^{-1}\left(\dfrac{\dot{\varepsilon}}{\dot{\varepsilon}_0 e^{-\frac{\Delta H_\beta}{RT}} e^{\frac{\ln(10) c_1^g (T - T_g)}{c_2^g + T - T_g}}}\right)^{\frac{1}{n}} & for\ T > T_g \end{cases} \quad (1.85)$$

With Eqs 1.86 to 1.89:

$$\sigma_i(T) = \sigma_i(0) - mT \qquad avec \qquad \begin{cases} \sigma_i(0) = -B \\ m = \dfrac{1}{T_{ref}}\left(\sigma_i(0) - \sigma_i\left(T_{ref}\right)\right) \end{cases} \tag{1.86}$$

$$\dot{\varepsilon}^*(T) = \dot{\varepsilon}_0 e^{-\frac{\Delta H_\beta}{RT}} \qquad avec \qquad \begin{cases} \Delta H_\beta = AR\ln 10 \\ \dot{\varepsilon}_0 = \dot{\varepsilon}^*\left(T_{ref}\right) e^{\frac{\Delta H_\beta}{RT_{ref}}} \end{cases} \tag{1.87}$$

$$\begin{cases} A = \dfrac{Q_\beta}{R\ln 10} \\ B = -\dfrac{A_\alpha\left(Q_\alpha - Q_\beta\right)}{R} \end{cases} \tag{1.88}$$

$$\begin{cases} \Delta H_\beta = Q_\beta \\ \sigma_i(0) = \dfrac{A_\alpha\left(Q_\alpha - Q_\beta\right)}{R} \end{cases} \tag{1.89}$$

With Q_β, Q_α, A_α the parameters identified for the Ree-Eyring model, V the activation volume, n a parameter of the material designating the cooperative degree of the strain-hardening of the polymer, $\sigma_i(0)$ is the internal stress at 0K, m is a parameter of the material, $\dot{\varepsilon}_0$ is a reference strain rate, R is the perfect gas constant, k_b the Boltzmann constant and c_1^g and c_2^g the WLF parameters of the materials (determined by DMA but the "universal" parameters: c_1^g = 17.44 and c_2^g= 51.6 K can be used). We can note that the internal stress $\sigma_i(T)$ is zero for all temperatures higher than the glass transition temperature T_g.

iv. **Models comparison**

The Figure 12 shows a comparison of the presented models for the yield stress of amorphous polymers [47], it can be clearly seen that the cooperative model has a range of validity wider than the Argon and Rie-Eyring models and particularly at high temperatures (Figure 18.a) and strain rates (Figure 18.b). Indeed, the cooperative model is the only one which takes into account the changes of activation volume due to the transition from glassy state to rubber state, and provides better accuracy for both materials (PMMA and PC) than any other model.

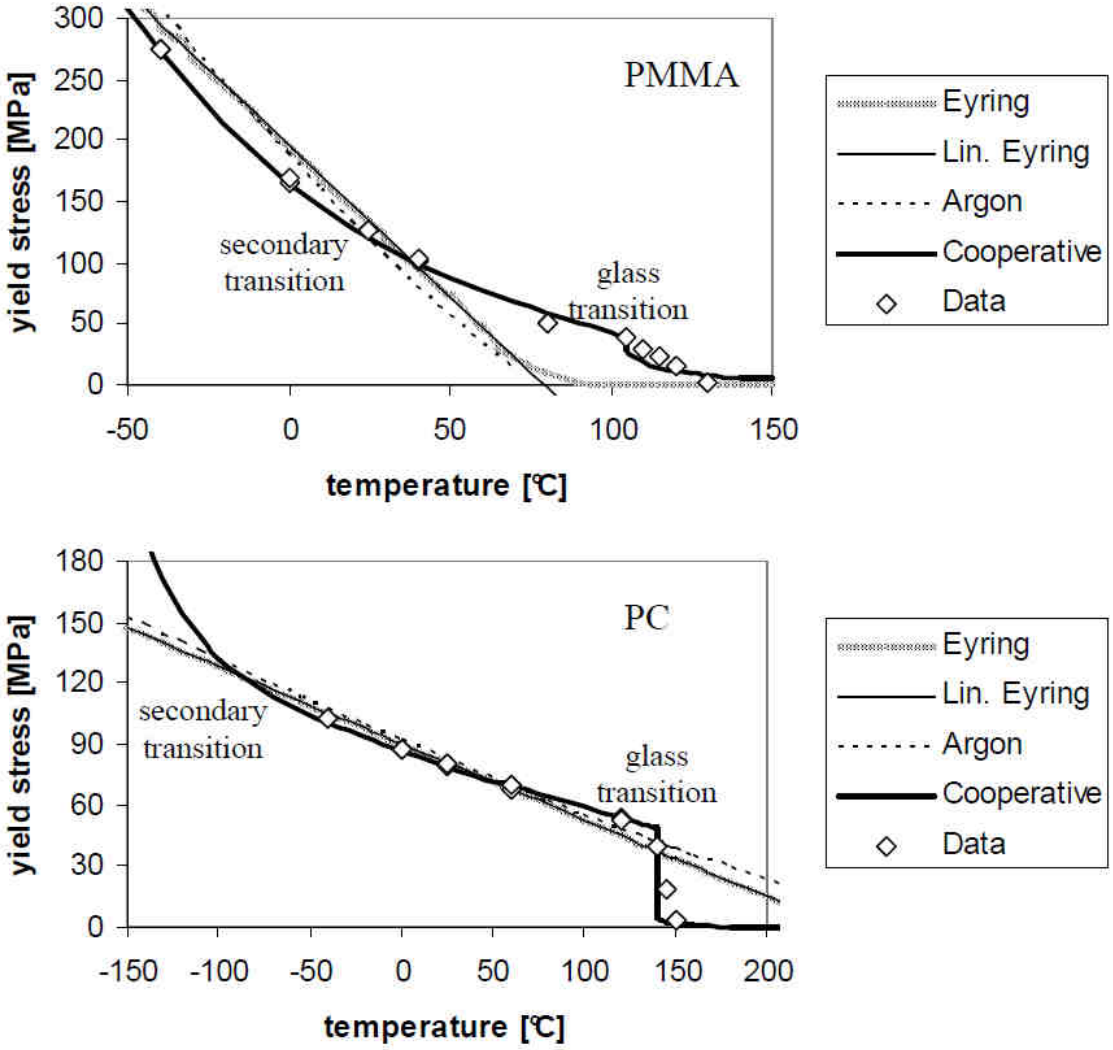
PMMA
yield stress [MPa]
temperature [℃]
secondary transition
glass transition
Eyring
Lin. Eyring
Argon
Cooperative
Data
PC
yield stress [MPa]
temperature [℃]
secondary transition
glass transition
Eyring
Lin. Eyring
Argon
Cooperative
Data

(a)

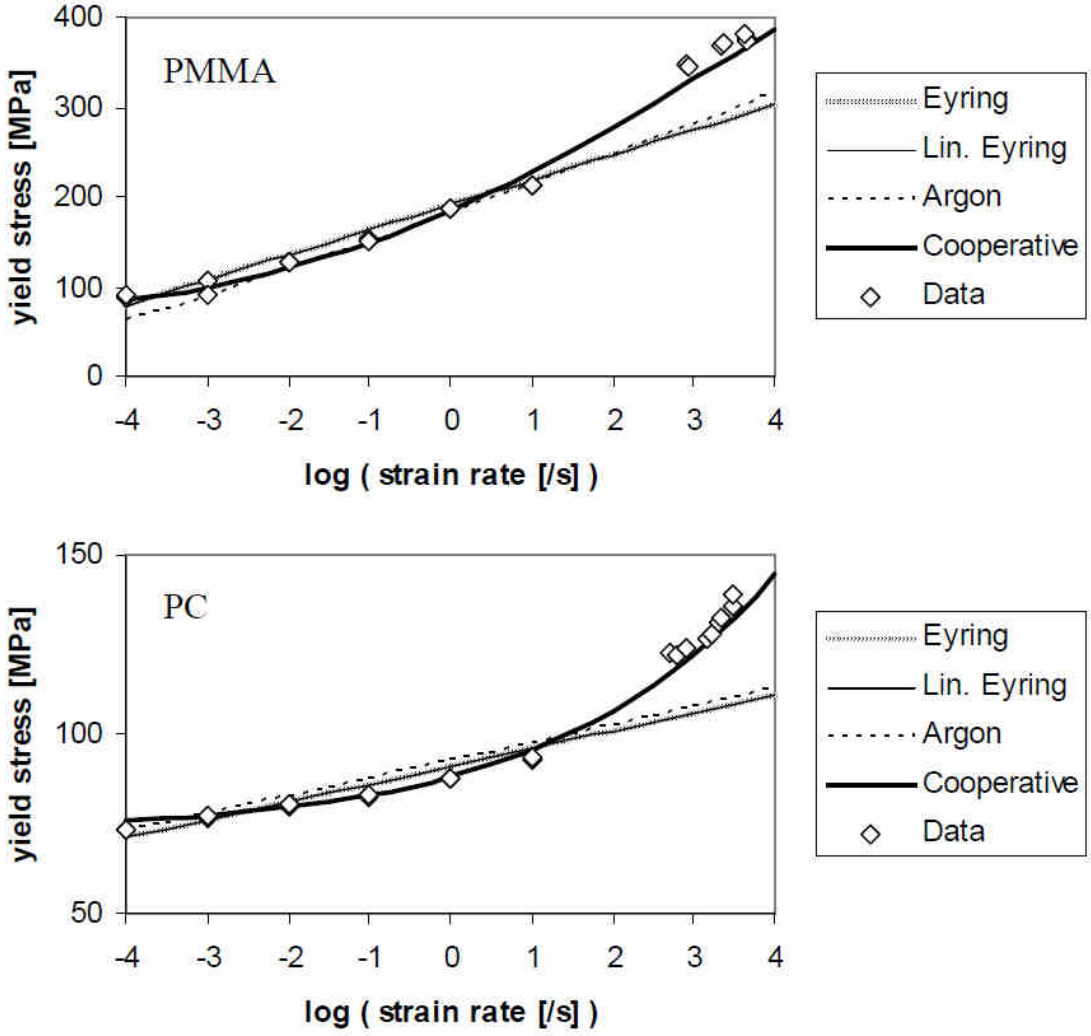

(b)

Figure 18 – Comparison between Argon, Rie-Eyring and Cooperative models allowing to check the domain of validity of each one for the PMMA and PC amorphous polymers for (a) the temperature and (b) the strain rate

c. Constitutive modeling of hyperelasticity phenomenon

Network models are used to represent the entropy resistance to chain alignment during deformation. They are essential for the modeling of the mechanical behavior of polymeric materials, especially for high deformations. There are many models based on physical and empirical considerations [55]. Physical models are based on the theory of materials hyperelasticity which assumes that the material is considered incompressible (although some models allow to take into account the effects of compressibility).

The statistical approach describes chain networks as long chains randomly oriented and interconnected by chemical or physical bonds [55, 56].

The quantitative expression of the entropy for a single molecular chain comes from the energy of the chain network W derived by the distance between the extremities λ_i of the latter. The resulting Cauchy constraint σ_i is then written (Eq 1.90):

$$\sigma_i = -p + \lambda_i \frac{\partial W}{\partial \lambda_i} \quad (1.90)$$

With p an additional hydrostatic pressure coming from the incompressibility hypothesis ($\lambda_1\lambda_2\lambda_3 = 1$). In isothermal conditions, the variation of the strain network energy W can be written as follows (Eq 1.91):

$$\dot{W} = \sigma_i \dot{\varepsilon}_i \quad (1.91)$$

With: $\dot{\varepsilon}_i = \frac{\dot{\lambda}_i}{\lambda_i} \rightarrow \lambda_i = e^{\varepsilon_p}$ (ε_p is the true strain)

There are two different statistical approaches:

- The classic Gaussian approach of the effective chain model for weak deformations, whose chain energy function is defined by the following relation (Eq 1.92):

  $$W = \frac{nk_bT}{2}(\lambda_1^2 + \lambda_2^2 + \lambda_3^2 - 3) \quad (1.92)$$

  With n the number of chains per unit volume, k_b the Boltzmann constant and T the temperature.

- The non-Gaussian approach of the chain model (Kuhn and Grün model [82]), valid for all strain values, whose chain energy function is based on the random displacement of an ideal phantom chain, is defined by the following relationship (Eq 1.93):

  $$W = NkT\left(\frac{\lambda}{\sqrt{N}}\beta + \ln\left(\frac{\beta}{\sinh\beta}\right)\right) \quad (1.93)$$

  With $\beta = \mathcal{L}^{-1}\left(\frac{\lambda}{\sqrt{N}}\right)$, $\mathcal{L}^{-1}$ the inverse Langevin function defined by $\mathcal{L}(x) = \coth x - \frac{1}{x}$. The resulting constraint for a single chain then becomes (N being the number of rigid chains in the entanglements) (Eq 1.94):

  $$\sigma = \lambda\frac{\partial W}{\partial \lambda} = \lambda kT\sqrt{N}\mathcal{L}^{-1}\left(\frac{\lambda}{\sqrt{N}}\right) \quad (1.94)$$

  The macroscopic behavior of the material is directly related to the three - dimensional behavior of the chain network. The entropy of the network is calculated by summing the entropy of each chain. We then find many models based on the physical approach such as the 8-chains model.

i. **Neo-Hookean model**

The Neo-Hookean model [83-85] is the simplest mechanical model of hyperelasticity. It is a physical model describing the energy of the network by the following expression (Eq 1.95) in a case of one-dimensional solicitation (incompressible case):

$$W = C_1(I_1 - 3) \quad (1.95)$$

With C_1 a material constant $I_1 = \lambda_1^2 + \lambda_2^2 + \lambda_3^2$

In the case of tri-dimensional solicitation, the network strain energy becomes (Eq 1.96):

$$W = C_1(\bar{I}_1 - 3) + D_1(J-1)^2 \quad (1.96)$$

With D_1 a constant of the material, $\bar{I}_1 = J^{-2/3} I_1$ and $\bar{I}_2 = J^{-4/3} I_2$ (Eq 1.97):

$$\begin{cases} I_1 = \lambda_1^2 + \lambda_2^2 + \lambda_3^2 \\ I_2 = \lambda_1^2\lambda_2^2 + \lambda_2^2\lambda_3^2 + \lambda_3^2\lambda_1^2 \\ J = \det(F) \end{cases} \quad (1.97)$$

F is the strain gradient tensor. In the compressive case, the model becomes Eq 1.98:

$$W = C_1(I_1 - 3 - 2\ln J) + D_1(J-1)^2 \quad (1.98)$$

The back stress can therefore be computed by using the following expression (Eq 1.99):

$$\sigma = 4C_1\left(\varepsilon - \frac{1}{3}Tr(\varepsilon)\right) + 2D_1 Tr(\varepsilon) \quad (1.99)$$

The incompressible case can easily be used by considering $\det(F) = 1$

ii. **Gent model**

The Gent model [55, 86] is a semi-empirical model proposing a simple expression of the network strain energy W (for a material considered compressible) (Eq 1.100):

$$W_{Gent} = -\frac{\mu}{2} J_m \ln\left(1 - \frac{I_1 - 3}{J_m}\right) + \frac{\kappa}{2}(J-1)^2 \quad (1.100)$$

With μ the shear modulus, J_m the value of I_1 at the limit of extensibility ($I_1 = \lambda_1^2 + \lambda_2^2 + \lambda_3^2$), κ the bulk modulus and $J = \det(F)$ with F as previously mentioned.

The back stress can then be computed using the following expressions (Eq 1.101) for uniaxial, planar and biaxial loadings:

$$\begin{cases} \sigma_{uniax} = \mu\left(\lambda^2 - \frac{1}{\lambda}\right)\frac{J_m}{J_m - \left(\lambda^2 + \frac{2}{\lambda} - 3\right)} \\ \sigma_{planar} = \mu\left(\lambda^2 - \frac{1}{\lambda^2}\right)\frac{J_m}{J_m - \left(\lambda^2 + \frac{2}{\lambda} - 3\right)} \\ \sigma_{biax} = \mu\left(\lambda^2 - \frac{1}{\lambda^4}\right)\frac{J_m}{J_m - \left(\lambda^2 + \frac{2}{\lambda} - 3\right)} \end{cases} \quad (1.101)$$

iii. **8-chains model**

The 8-chains model [87-89] uses a representation of the chain network composed of eight chains of equal length (9). This model has the property that in the case of a uniform deformation rate of the material, the 8 chains undergo an identical relative deformation. Preferred directions are defined here by the half diagonals of the cube.

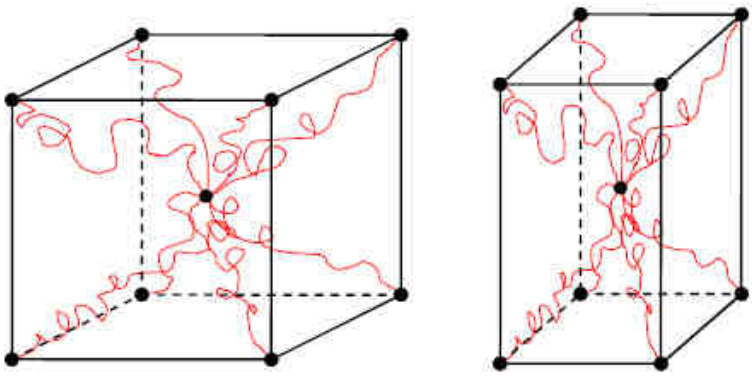

Figure 19 - Schematic representation of the 8-chains model

The back stress B for the 8-chains model is modeled by the following relationship (Eq 1.102):

$$B_i^{8-ch} = -p + \frac{C_R\sqrt{N}}{3}\mathcal{L}^{-1}\left(\frac{\lambda_{chain}}{\sqrt{N}}\right)\frac{\lambda_i^2}{\lambda_{chain}} \qquad (1.102)$$

With λ_{chain} the equivalent locking strain of the 8-chains network and expressed by (in the case of a uniform deformation) (Eq 1.103):

$$\lambda_{chain} = \sqrt{\frac{\lambda_1^2 + \lambda_2^2 + \lambda_3^2}{3}} \qquad (1.103)$$

If the hypothesis of incompressibility has been done (Eq 1.104):

$$Tr(B) = 0 \qquad (1.104)$$

An expression of B independent of the hydrostatic pressure p can then be applied (p is still taken into account in the expression) (Eq 1.105):

$$B_i^{8-ch} = \frac{C_R\sqrt{N}}{3}\mathcal{L}^{-1}\left(\frac{\lambda_{chain}}{\sqrt{N}}\right)\frac{\lambda_i^2 - \lambda_{chain}^2}{\lambda_{chain}} \qquad (1.105)$$

With $\mathcal{L}^{-1}(X)$ the inverse Langevin function [2, 89].

This model underestimates the real value of constraint B.

C. Description of failure mechanisms

The failure of materials is of the upmost importance in mechanical modeling. Indeed, these mechanisms depict the limitation of the materials and allows efficient designs of functional parts in mechanical systems. For this purpose, the failure behavior has to be investigated in addition of the stress behavior explained previously to complete the study toward a complete numerical model. The failure behavior of materials can be generally decomposed in two steps: the initiation of failure at which starts the damage evolution leading to the final fracture of the material.

1. Threshold failure criteria in yielding materials

In yielding materials, the mechanisms leading to the ultimate failure of the materials can be sorted in two categories:

- The initiation of failure (initiation of damage)
- The damage mechanisms

The initiation of failure corresponds to the Consider criterion mathematically represented by the following expression (for nominal stress vs nominal strain curves) (Eq 1.106) [2]:

$$\frac{d\sigma_n}{d\varepsilon_p} = 0 \qquad (1.106)$$

The damage mechanisms starts at the value of true strain ε_p^f for which the Consider criterion is fulfilled. These mechanisms can be of two different natures:

- Apparition and expansion of adiabatic shear bands leading to localized crack segments (for state of stress below tensile condition) [90-94]
- Germination, growth and coalescence of voids (Figure 20) leading to creation of cupules (for positive state of stress) [95-100]

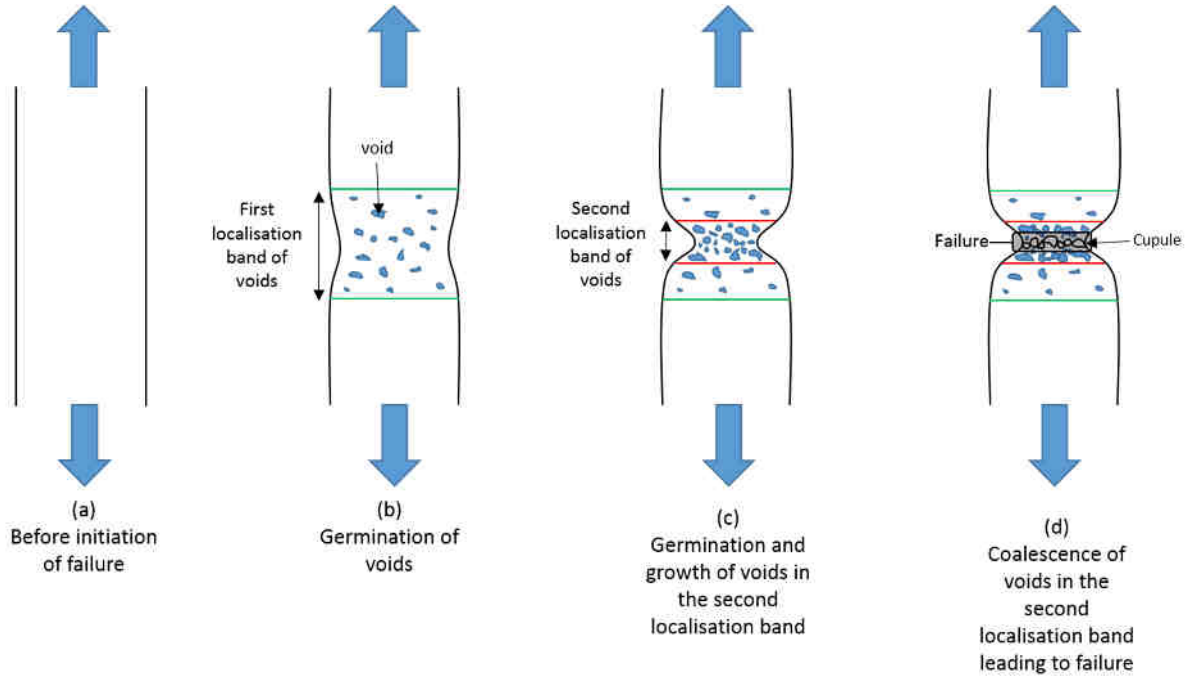

Figure 20 - Illustration of the different steps leading to the ultimate failure

2. Sensitivities of threshold failure criteria

a. Effect of triaxiality

i. **Definition**

The triaxiality σ^* is a dimensionless figure representing the local state of stress. It is defined as a ratio of the hydrostatic stress σ_H applied on the representative volume and the equivalent stress σ_{eq} (see Eq 1.107).

$$\sigma^* = \frac{\sigma_H}{\sigma_{eq}} \qquad (1.107)$$

In the case of Von Mises hypothesis, the triaxiality can be computed as follows (Eq 1.108):

$$\sigma^* = \frac{\sqrt{2}}{3} \frac{(\sigma_I + \sigma_{II} + \sigma_{III})}{\sqrt{(\sigma_I - \sigma_{II})^2 + (\sigma_{II} - \sigma_{III})^2 + (\sigma_{III} - \sigma_I)^2}} \qquad (1.108)$$

A few particular values of triaxiality can be enounced: 0 for pure shear, $\frac{1}{3}$ for pure tension, $-\frac{1}{3}$ for pure compression. Another figure can be defined to represent the deviatoric state of stress in addition to the triaxiality: the normalized third stress invariant ξ (Eq 1.109).

$$\xi = \frac{27}{2} \frac{J_3}{{\sigma_{eq}}^3} \qquad (1.109)$$

With J_3 the third invariant of the stress tensor.

The Lode angle is computed from ξ as follows (Eq 1.109):

$$\theta = 1 - \frac{2}{\pi}\cos^{-1}\xi \qquad (1.109)$$

ii. Effect of triaxiality in cohesive materials

Cohesive materials correspond to materials exhibiting a homogeneous yielding phenomenon for positive state of stress (presenting germination, growth and coalescence of voids). The cohesiveness of metals mainly depends on the shaping process of the part. Materials processed using lamination or casting methods present generally a good cohesiveness. A global tendency of the sensitivity of the strain at initiation of failure ε_p^f with the triaxiality can be observed:

- The value of ε_p^f increases exponentially with decreasing triaxiality up to a cutting value for the state of stress of pure compression $\sigma^* = -\frac{1}{3}$ below which the value of ε_p^f is considered infinite [101] (domain 1 in Figure 21).
- The value of ε_p^f converges asymptotically to a specific material dependent value at high triaxiality (domain 2 in Figure 21) [102, 103].

However, the triaxiality sensitivity of such materials is much more complex in the domain of positive state of stress (Figure 21). A peak value of ε_p^f in pure tension condition ($\sigma^* = \frac{1}{3}$) can be observed.

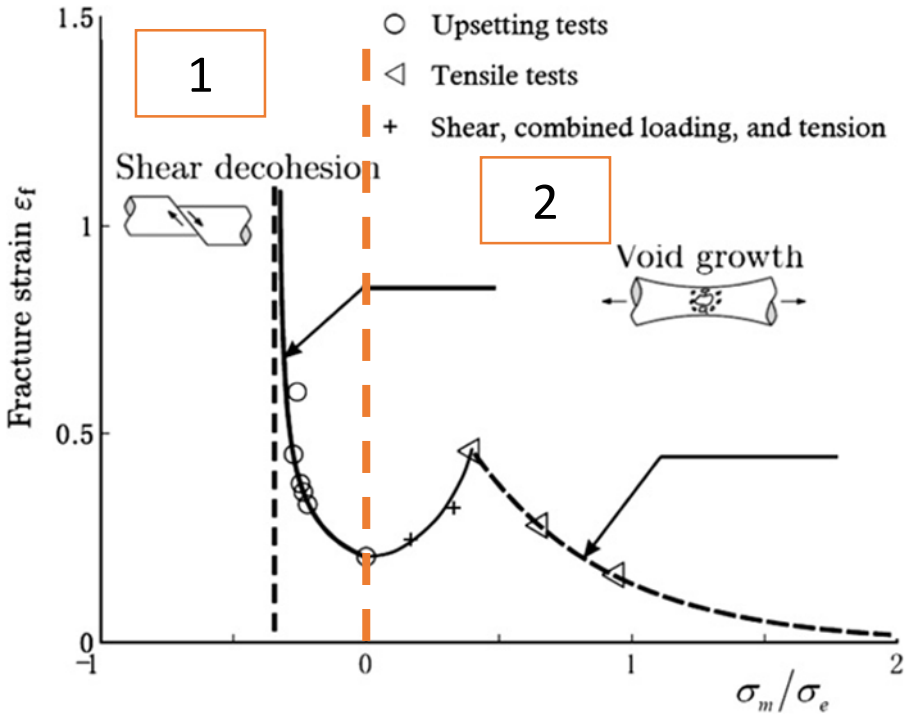

Figure 21 - Focus on the triaxiality sensitivity of a fully coherent material [102]

iii. **Effect of triaxiality in low-cohesive materials**

Some shaping processes such as sintering can produce materials with low-cohesive behavior. In those conditions, the material can be associated to a complex structure made of aggregates at the mesoscopic level (Figure 22). The low cohesiveness of this kind of materials is caused by a much lower tensile strength required to separate the aggregates than for the yielding of those lasts. Therefore, in positive state of stress, this is the mechanical behavior of the structure which is observed and not the one of a cohesive yielding material. This is mainly due to stress concentration at pores which leads to brittle failure caused by particle decohesion (intergranular failure) [104-106]. This phenomenon of local stress concentration is dependent to the grain size and shape [105] and is present under all state of stress [107]. Furthermore, the failure of such structures presents a very brittle behavior (hardly no damage) and a very low plastic strain.

Another particularity of low-cohesive materials can be observed at low triaxiality. Indeed, failure below the cut-off value of pure compression ($\sigma^* = -\frac{1}{3}$) can be observed due to the high sensitivity to pressure of structure-like materials.

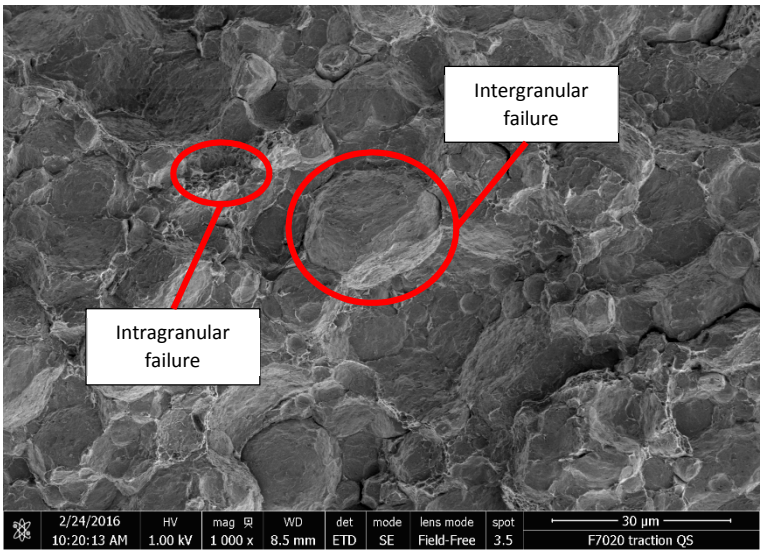

Figure 22 - SEM picture of a profile failure of a sintered 7020 aluminum alloy

b. Effect of temperature

The evolution of the strain at initiation of failure and of the material strength are closely linked. Indeed, the potential mechanical energy absorbed by the material stays the same for any temperature (in the case of ductile failure involving yielding phenomenon).

Consequently, the strain at initiation of failure increases with the thermal softening of the material [108, 109]. However, the behavior can be much more complex because many different microstructural phenomena can occur. For example, precipitation or dissolution in metallic materials lead respectively

to a hardening and to a sudden drop of the stress. Therefore, a precipitation phenomenon causes a decrease of the strain at initiation of failure, and a dissolution to a sudden increase [36, 37].

At higher temperatures, the stress shows nearly no temperature dependency (athermal behavior due to a monophasic matrix). Finally, near the melting point, a sudden drop of the stress down to zero. The impact on the strain at initiation of failure is an exponential asymptotic increase when approaching the melting point just after a stagnation of its value in the range of the athermal behavior.

Concerning the amorphous polymer, the failure is generally performed through the propagation of cracks which are slowed by fibrils of polymer which prevent the Crack Opening Displacement (COD) (Figure 23) [4, 40, 110, 111]. The stress behavior of the material impact significantly the propagation of the craze by the mean of the fibrils. Indeed, the softer the resistance of the fibrils is (low strain rate and/or high temperature), the higher the COD will be allowed to be and the crack propagation will be slower. The main microstructural change consists in the transition from glassy state to rubber state at the glass transition temperature T_g. The mechanical behavior of the material drop significantly during this transition leading to an increase of the strain at initiation of failure up to the T_g where its value remains nearly unchanged at higher temperature [112].

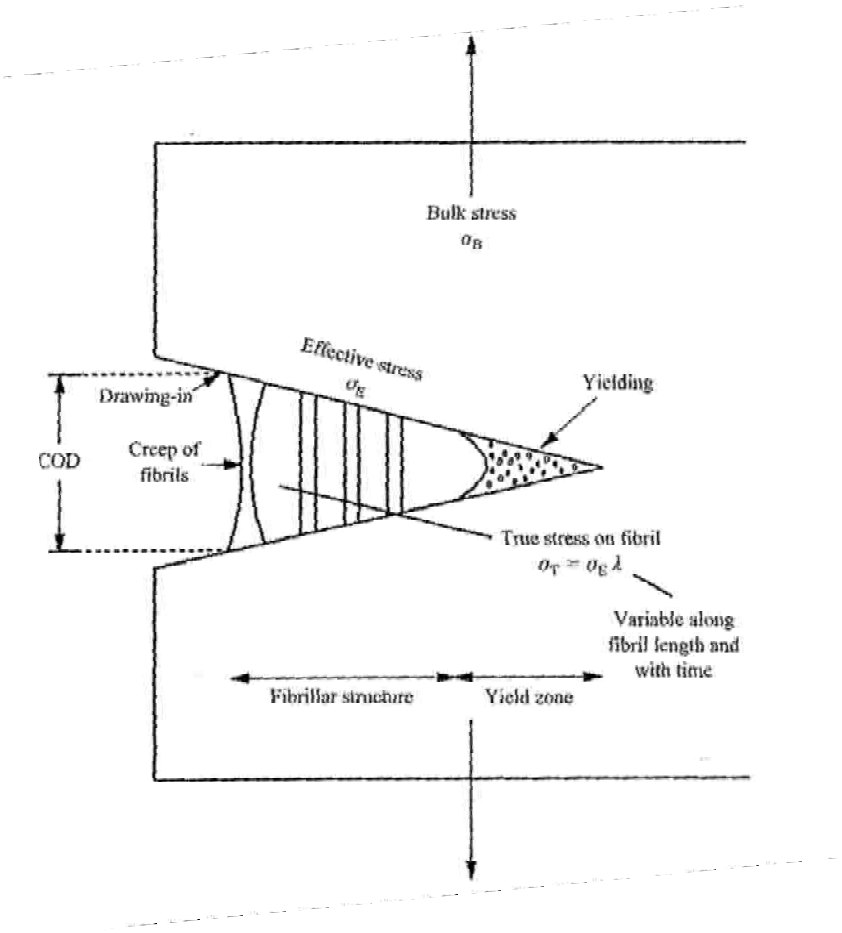

Figure 23 - Schematic diagram showing model for craze growth and processes involved [40]

It can be noted that in the case of low-cohesive failure for positive state of stress, due to the structure-like characteristic of the involved materials, hardly no temperature dependency of failure mechanisms can be observed.

c. Effect of strain rate on isothermal strain at initiation of failure

For metallic materials, the positive sensitivity to the strain rate of the isothermal strain at initiation of failure can be divided in two domains separated by a transition strain rate $\dot{\varepsilon}_{trans}$ ($\sim$1000 /s) above which viscous drag effect cannot be neglected (for the metals) [36, 108, 109]:

- Below $\dot{\varepsilon}_{trans}$, the strain at initiation of failure shows hardly no sensitivity to the strain rate and the experimental results may show a higher dispersion than in dynamic conditions.
- Above $\dot{\varepsilon}_{trans}$, the normalized strain rate sensitivity follows an exponential positive sensitivity which is mainly caused by the micro-inertia effects encountered in viscous drag phenomena.

Concerning the polymer materials, the evolution of the strain rate of the isothermal strain at initiation of failure with the strain rate can also be divided in two domains [40, 111, 113]. However, the transition strain rate $\dot{\varepsilon}_{trans}$ separating these two different behavior can be very different according to the considered polymer. Indeed, the higher the chain entanglement is, the lower $\dot{\varepsilon}_{trans}$ will be: the increase of the strain rate will lower the time during the chain structure can accommodate to the strain which can be assimilated to the relaxation time. At low strain rate, the stress transfer is efficiently redistributed on the full length of the entangled chains [114] (Figure 24). If the chain structure does not have enough time to accommodate itself to the deformation, damage will start to appear in the material more and more earlier with increasing strain rate due to constrained stress transfer via segments of entangled chains [114, 115]. This effect is called the locking phenomenon. Therefore, the trends is the opposite than the one observed for the metals: the strain at initiation of failure decreases with the strain rate.

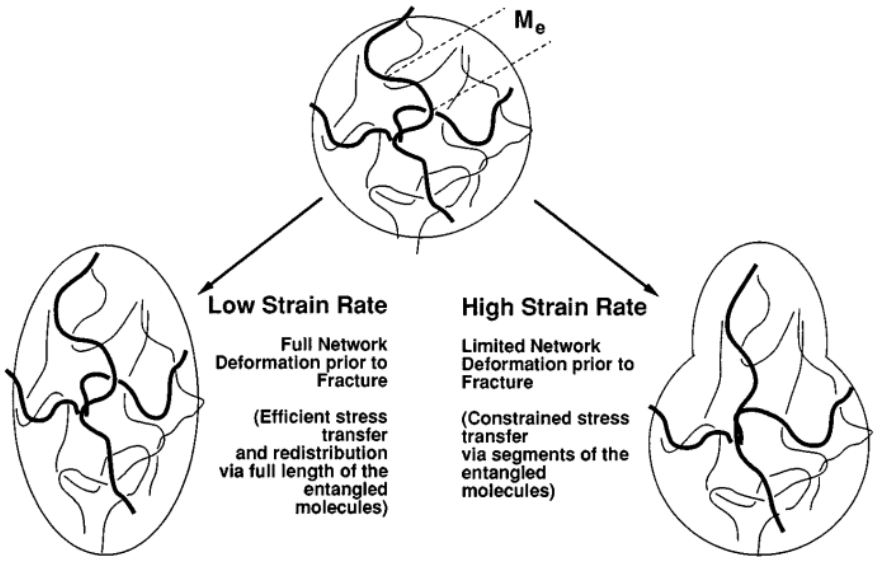

Figure 24 – Effect of strain rate on the deformability of the entanglement network structure [114]

D. Constitutive modeling of failure behavior

1. Constitutive modeling of the strain at initiation of failure

As explained in the previous parts, the initiation of the strain at failure is sensitive to the triaxiality σ^*, the strain rate $\dot{\varepsilon}_p$ and the temperature T and shows a coupled effect between those two last parameters. The construction of a typical model which takes into account all the effects can lead to the following expression (Eq 1.110) [116, 117]:

$$\varepsilon_p^f\left(\sigma^*, \xi, \theta, \dot{\varepsilon}_p, T\right) = f_\sigma(\sigma^*, \xi, \theta) f_{SR}\left(\dot{\varepsilon}_p\right) f_T\left(\dot{\varepsilon}_p, T\right) \quad (1.110)$$

The function f_σ models the sensitivity to the state of stress and modeling the value of ε_p^f at the reference strain rate $\dot{\varepsilon}_0$ and temperature T_r. The function f_{SR} aims to model the evolution of isothermal strain at initiation of failure with the strain rate and f_T describes the temperature sensitivity of ε_p^f with strain rate coupling.

The expressions shown in the Table 2, 3 and 4 are not presented in the full model in which they might be found (e.g. the Johnson-Cook model for failure [116]). The current presentation approach aims to show that a model can be built from a choice of the most adequate expression regarding the tests performed over the ranges of states of stress, temperatures and strain rates. This is why the following tables presents decomposed expressions for each sensitivity and can be assembled regarding the needs.

Different expressions for each function can be found in the literature, leading to different degrees of accuracy and complexity to describe the different phenomena. Those different expressions can be found in the Table 2.

Table 2 - Triaxiality sensitivity of strain at initiation of failure models

$f_\sigma(\sigma^*, \xi, \theta)$	Commentaries	+/-	References
ε_0^f	Easiest model possible: constant fracture strain. Not suited for conditions other than the one used for its determination. Independent from triaxiality and normalized third stress invariant.	Accuracy --- Usage +++	[117, 118]
$d_0 e^{-3c\sigma^*} + d_1 e^{3c\sigma^*}$ With c and d_i material parameters	Similar to Johnson-Cook expression (used in PAM-CRASH®). Does not represent the complex behavior of the materials. Independent from the	Accuracy + Usage ++	[117]

	normalized third stress invariant. Over-estimation at high triaxiality.		
$d_1 + d_2 e^{d_3 \sigma^*}$ With d_i material parameters	Johnson-Cook expression Easy to use and require few experimental tests, model the global sensitivity to the state of stress. However, does not represent the complex behavior of the materials. Independent from the normalized third stress invariant.	Accuracy + Usage +++	[116]
$C_1 e^{-C_2 \sigma^*} - \left(C_1 e^{-C_2 \sigma^*} - C_3 e^{-C_4 \sigma^*}\right)\left(1 - \xi^{\frac{1}{n}}\right)^n$ With C_i and n material parameters	Triaxiality and normalized third stress invariant dependent. Takes into account the complex behavior of the materials for triaxiality above compression state.	Accuracy ++ Usage -	[119, 120]
$\left\{c_2\left[c_3 + \frac{\sqrt{3}}{2-\sqrt{3}}(c^{ax}(\theta) - c_3)\left(\sec\left(\frac{\pi\theta}{6}\right) - 1\right)\right]\left[\sqrt{\frac{1+{c_1}^2}{3}}\cos\left(\frac{\pi\theta}{6}\right) + c_1\left(\sigma^* + \frac{1}{3}\sin\left(\frac{\pi\theta}{6}\right)\right)\right]\right\}^{-\frac{1}{n}}$ With c_i and n material parameters	Triaxiality and normalized third stress invariant. Very few parameters. Takes into account the complex behavior of the materials with better accuracy than the previous ones for triaxiality above compression state.	Accuracy +++ Usage --	[100, 121]

As explained before, the material presenting a low-cohesive behavior have a specific triaxiality sensitivity above the compression state which is biased by the structure-like behavior of the material. Therefore, the expressions describing its behavior over this range of triaxiality are more suited for fully cohesive materials presenting ductile failure.

Different expressions modeling the strain rate sensitivity (Table 3) and the temperature sensitivity (Table 4) can also be found in the open literature.

Table 3 – Strain rate sensitivity of strain at initiation of failure models

$f_{SR}(\dot{\varepsilon}_p)$	Commentaries	+/-	References
$1 + d_4 \ln\left(\frac{\dot{\varepsilon}_p}{\dot{\varepsilon}_0}\right)$ With d_4 material parameter	Easy to use but not very accurate over a wide range of strain rates. Models only linear sensitivity to the strain rate such as	Accuracy - Usage	[116]

	caused by thermo-activated phenomena and not by viscous drag effect.	++	
$\left(1+\frac{\dot{\varepsilon}_p}{\dot{\varepsilon}_0}\right)^{d_4}$ With d_4 material parameter	Easy to use with a slightly wider range of validity than the expression above. No viscous drag effect.	Accuracy - Usage ++	[108]
$1+l_v \ln\left(\frac{\dot{\varepsilon}_p}{\dot{\varepsilon}_0}\right)+v\left(\frac{\dot{\varepsilon}_p}{\dot{\varepsilon}_0}\right)^{n_v}$ With v, l_v and n_v material parameters	Valid over a wide range of strain rate. Modeling of thermo-activated phenomena and viscous drag effect.	Accuracy ++ Usage +	[17]

Table 4 - Temperature sensitivity of strain at initiation of failure models

$f_T(\dot{\varepsilon}_p, T)$	Commentaries	+/-	References
$\left(\frac{T_r}{T}\right)^a$ With a material parameter	Very simple modeling but valid over a very limited range of temperatures.	Accuracy -- Usage +++	[65]
$1+d_5\left(\frac{T-T_r}{T_m-T_r}\right)$ With d_5 material parameter	Easy to use but valid over a limited range of temperatures due to the linear sensitivity to the temperature. No coupling between temperature and strain rate.	Accuracy - Usage ++	[116]
Inverse Calorific Ratio $\mho(\dot{\varepsilon}_p, T)$	Coupling between temperature and strain rate. Modeling of microstructure changes (dissolutions and precipitations). Modeling of the asymptotic behavior near the melting point.	Accuracy +++ Usage --	

2. Constitutive modeling of the damage evolution

The damage evolution consists into the variation of a measurable phenomenon which will leads to the final failure of the material (e.g. void growth, adiabatic shear bands genesis, the absorbed energy).

Concerning the modeling of the damage evolution $\dot{D}$, different approaches have been developed:

- The energetic approach which evaluates the energy absorbed by the material from the initiation of failure to the ultimate failure (can be sensitive to the state of stress, temperature and strain rate) (Eq 1.111) [122].

$$D = \int_{\varepsilon_p^f}^{\varepsilon_p^u} \frac{\sigma}{A\left(\sigma^*, \theta, \dot{\varepsilon}_p, T\right)} d\varepsilon_p \qquad (1.111)$$

  With A the damage energy, function of the state of stress, the temperature and the strain rate and ε_p^u the plastic strain at ultimate failure.

- The evaluation of the porosity ratio $f_v = D$ and its evolution in the material up to a critical value defining the coalescence of the voids (of total radius R) and the ultimate failure. This approach generally requires specific microscopic characterization methods which can lead to a complex model investigation for validation. The relation between the void ratio f_v and its evolution $\dot{f}_v$ can be computed using the hypothesis of mass conservation for plastic incompressibility (Table 5).

Table 5 - Porosity evolution models

$f_v\left(\varepsilon_p, \sigma_e, \sigma_H\right)$	Model	References
$\dot{f}_v = (1 - f_v)\dot{\varepsilon}_p$	Mass conservation principle	[2]
$\dot{f}_v = \frac{dR}{R} = 0.8e^{\sqrt{3}\sigma^*} d\varepsilon_p$	Mc Clintock model	[123]
$\frac{\dot{f}_v}{f_v \dot{\varepsilon}_p} = \frac{3}{2}(1 - f_v)\sinh\left(\frac{3}{2}\sigma_H\right)\left[1 + {f_v}^2 - 2f_v \cosh\left(\frac{3\sigma_H}{2\sigma_y}\right)\right]^{-\frac{1}{2}}$	Gurson model	[124]
$\left(\frac{\sigma_e}{\sigma_y}\right)^2 + 2q_1 f_v \cosh\left(\frac{3q_2\sigma_H}{2\sigma_y}\right) - 1 - q_3 {f_v}^3 = 0$ With q_i material parameters	Tvergaard model	[125, 126]

- The stochastic approach using the Boltzmann's statistic at the microscopic level and considering a damage distribution law (eg. a distribution law giving the damage characterized by the number of cavities N having a radius R). This approach can be applied on different mechanisms such as the growth and coalescence of cavities (total volume of void V_v) or the stacking of dislocations which can lead to the brittle failure (eg. Curran model [127], Stroh model [128], NAG model [95]). The stochastic approach has been mainly developed for metallic materials (Table 6).

Table 6 - Stochastic damage models

$D(\dot{N}, \sigma_H)$	Model	References
$D = V_v = \frac{4\pi}{3}\int_0^\infty R^3 \frac{dN}{dR} dR$ $N = N_0 e^{-\frac{R}{R_0}}$ $\dot{N} = \dot{N}_0 e^{\frac{P_S - P_{N0}}{P_1}}$ With $\dot{N}_0$ the threshold speed of germination, P_S the tension pressure, P_{N0} the threshold pressure of germination and P_1 a characteristic pressure of the material defining its sensitivity to germination	Curran model	[127]
$V_T = V_I + V_N + V_G$ With V_I the initial void volume, V_N the nucleation void volume and V_G the growth void volume $\begin{cases} V_I = 8\pi N_I {R_0}^3 \\ V_N = \sum_t (\Delta V_{N\varepsilon} + \Delta V_{N\sigma}) \\ V_G = 8\pi R_0^3 \left[e^{\frac{3h(1-\nu)}{16 g^2 \mu^2 t^*} \int_0^t \left(\langle \sigma_H - \sigma_{g0} \rangle^+\right)^2} - 1 \right] \end{cases}$ With N_I the initial void number and R_0 their average radius, $\Delta V_{N\varepsilon}$ the relative volume of voids controlled by the strain rate during a time step Δt and $\Delta V_{N\sigma}$ the relative volume of voids controlled by the pressure during a time step Δt, μ is the shear modulus, ν the Poisson ratio, g the ductile/brittle parameter of the material and $h \approx 3$, σ_{g0} the threshold stress of nucleation	NAG model	[95]

$\begin{cases} \Delta V_{N\varepsilon} = 8\pi {R_0}^3 \dot{N}_{\varepsilon 0} \left(1 - e^{-\omega t\left(\frac{\dot{\varepsilon}_p}{\dot{\varepsilon}_0}\right)}\right) \Delta t \\ \Delta V_{N\sigma} = 8\pi {R_{\sigma 0}}^3 \dot{N}_0 e^{\frac{P_S - P_{N0}}{P_1}} \Delta t \end{cases}$		

The damage has an important influence on the stress of the material. Indeed, the real stress σ_e, corresponding to the stress taking into account the evolution of the damage is computed as follows (Eq 1.112):

$$\sigma_e = \sigma(1 - D) \qquad (1.112)$$

References

1. Mura, T., *Micromechanics of defects in solids*. Vol. 3. 2012: Springer Science & Business Media.
2. Bergstrom, J.S., *Mechanics of solid polymers: theory and computational modeling*2015: William Andrew.
3. Hill, R., *The mathematical theory of plasticity*. Vol. 11. 1998: Oxford university press.
4. Christian G'SELL, J.-M.H., *Introduction à la mécanique des polymères*1995.
5. Kocks, U.F. and H. Mecking, *Physics and phenomenology of strain hardening: the FCC case.* Progress in materials science, 2003. **48**(3): p. 171-273.
6. Hull, D. and D.J. Bacon, *Introduction to dislocations*2001: Butterworth-Heinemann.
7. Mecking, H. and U. Kocks, *Kinetics of flow and strain-hardening.* Acta Metallurgica, 1981. **29**(11): p. 1865-1875.
8. Voyiadjis, G.Z. and F.H. Abed, *Microstructural based models for bcc and fcc metals with temperature and strain rate dependency.* Mechanics of Materials, 2005. **37**(2): p. 355-378.
9. Abed, F.H. and G. Voyiadjis, *A consistent modified Zerilli-Armstrong flow stress model for BCC and FCC metals for elevated temperatures.* Acta mechanica, 2005. **175**(1-4): p. 1-18.
10. Klahn, D., A. Mukherjee, and J. Dorn, *STRAIN-RATE EFFECTS*, 1970, California Univ., Berkeley. Lawrence Radiation Lab.
11. Abed, F.H., *Physically based multiscale-viscoplastic model for metals and steel alloys: theory and computation*, 2005, Jordan University of Science and Technology.
12. Nabarro, F.R. and M.S. Duesbery, *Dislocations in solids*. Vol. 11. 2002: Elsevier.
13. Van Swygenhoven, H., *Grain boundaries and dislocations.* Science, 2002. **296**(5565): p. 66-67.
14. Regazzoni, G., U. Kocks, and P.S. Follansbee, *Dislocation kinetics at high strain rates.* Acta Metallurgica, 1987. **35**(12): p. 2865-2875.
15. Abed, F.H. and G.Z. Voyiadjis, *Plastic deformation modeling of AL-6XN stainless steel at low and high strain rates and temperatures using a combination of bcc and fcc mechanisms of metals.* International Journal of Plasticity, 2005. **21**(8): p. 1618-1639.
16. Wang, G., et al., *Calculating the Peierls energy and Peierls stress from atomistic simulations of screw dislocation dynamics: application to bcc tantalum.* Modelling and Simulation in Materials Science and Engineering, 2004. **12**(4): p. S371.
17. Follansbee, P. and U. Kocks, *A constitutive description of the deformation of copper based on the use of the mechanical threshold stress as an internal state variable.* Acta Metallurgica, 1988. **36**(1): p. 81-93.
18. Cottrell, A., *LX. The formation of immobile dislocations during slip.* The London, Edinburgh, and Dublin Philosophical Magazine and Journal of Science, 1952. **43**(341): p. 645-647.
19. Cottrell, A.H. and B. Bilby, *Dislocation theory of yielding and strain ageing of iron.* Proceedings of the Physical Society. Section A, 1949. **62**(1): p. 49.
20. Cottrell, A. and M. Jaswon. *Distribution of solute atoms round a slow dislocation*. in *Proceedings of the Royal Society of London A: Mathematical, Physical and Engineering Sciences*. 1949. The Royal Society.
21. Mott, N. and F.N. Nabarro, *An attempt to estimate the degree of precipitation hardening, with a simple model.* Proceedings of the Physical Society, 1940. **52**(1): p. 86.
22. Weertman, J., *Steady-State Creep of Crystals.* Journal of Applied Physics, 1957. **28**(10): p. 1185-1189.
23. Fisher, J., *On the strength of solid solution alloys.* Acta Metallurgica, 1954. **2**(1): p. 9-10.
24. Cottrell, A., *Relation of properties to microstructure.* ASM Monograph, 1954. **131**: p. 1954.
25. Klepaczko, J., *Constitutive modeling in dynamic plasticity based on physical state variables-A review.* Le Journal de Physique Colloques, 1988. **49**(C3): p. C3-553-C3-560.
26. Klepaczko, J. and C. Chiem, *On rate sensitivity of fcc metals, instantaneous rate sensitivity and rate sensitivity of strain hardening.* Journal of the Mechanics and Physics of Solids, 1986. **34**(1): p. 29-54.

27. Klepaczko, J., *Thermally activated flow and strain rate history effects for some polycrystalline FCC metals.* Materials Science and Engineering, 1975. **18**(1): p. 121-135.
28. Rusinek, A. and J.A. Rodríguez-Martínez, *Thermo-viscoplastic constitutive relation for aluminium alloys, modeling of negative strain rate sensitivity and viscous drag effects.* Materials & Design, 2009. **30**(10): p. 4377-4390.
29. McCormick, P., *Theory of flow localisation due to dynamic strain ageing.* Acta Metallurgica, 1988. **36**(12): p. 3061-3067.
30. Nemat-Nasser, S. and M. Hori, *Micromechanics: overall properties of heterogeneous solids.* Applied Mathematics and Mechanics. Elsevier, Amsterdam, 1993.
31. Nemat-Nasser, S., W.-G. Guo, and D.P. Kihl, *Thermomechanical response of AL-6XN stainless steel over a wide range of strain rates and temperatures.* Journal of the Mechanics and Physics of Solids, 2001. **49**(8): p. 1823-1846.
32. Dmitry, E., et al., *Multicomponent Phase Diagrams: Applications for Commercial Aluminum Publisher*, 2005, Elsevier Science.
33. Chinella, J.F. and Z. Guo, *Computational Thermodynamics Characterization of 7075, 7039, and 7020 Aluminum Alloys Using JMatPro*, 2011, DTIC Document.
34. FRANCART, C., et al., *Constitutive modelling of high thermal softening phenomenon in metallic materials*, in *ICILSM*2016: Torino.
35. Francart, C., et al., *Application of the Crystallo-Calorific Hardening approach to the constitutive modeling of the dynamic yield behavior of various metals with different crystalline structures.* International Journal of Impact Engineering, 2017.
36. Wang, J., et al., *Dynamic tensile properties of a single crystal Nickel-base superalloy at high temperatures measured with an improved SHTB technique.* Materials Science and Engineering: A, 2016. **670**: p. 1-8.
37. Wang, J., et al., *Anomalous behaviors of a single-crystal Nickel-base superalloy over a wide range of temperatures and strain rates.* Mechanics of Materials, 2016. **94**: p. 79-90.
38. Rodríguez-Martínez, J., et al., *Extension of R–K constitutive relation to phase transformation phenomena.* Materials & Design, 2009. **30**(7): p. 2513-2520.
39. Van Krevelen, D.W. and K. Te Nijenhuis, *Properties of polymers: their correlation with chemical structure; their numerical estimation and prediction from additive group contributions*2009: Elsevier.
40. Ward, I. and J. Sweeney, *An Introduction to the Mechanical Properties of Solid Polymers 2004.* England: John Wiley & Sons, Ltd.
41. Wu, S., *Chain structure and entanglement.* Journal of Polymer Science Part B: Polymer Physics, 1989. **27**(4): p. 723-741.
42. Bellenger, V., J. Verdu, and E. Morel, *Structure-properties relationships for densely cross-linked epoxide-amine systems based on epoxide or amine mixtures.* Journal of Materials Science, 1989. **24**(1): p. 63-68.
43. Fox, T. and S. Loshaek, *Influence of molecular weight and degree of crosslinking on the specific volume and glass temperature of polymers.* Journal of Polymer Science, 1955. **15**(80): p. 371-390.
44. Fox Jr, T.G. and P.J. Flory, *Second-order transition temperatures and related properties of polystyrene. I. Influence of molecular weight.* Journal of Applied Physics, 1950. **21**(6): p. 581-591.
45. Barton, J. and J. Critchley, *Effect of structure on the glass transition temperatures of some perfluoroalkylene-linked aromatic polyimides.* Polymer, 1970. **11**(4): p. 212-221.
46. Struik, L.C.E., *Physical aging in amorphous polymers and other materials*. Vol. 106. 1978: Elsevier Amsterdam.
47. RICHETON, J., *Modeling and validation of the finite strain response of amorphous polymers for a wide range of temperature and strain rate*, 2005, Université de Strasbourg.
48. Williams, M.L., R.F. Landel, and J.D. Ferry, *The temperature dependence of relaxation mechanisms in amorphous polymers and other glass-forming liquids.* Journal of the American Chemical society, 1955. **77**(14): p. 3701-3707.

49. Vrentas, J. and J. Duda, *A free-volume interpretation of the influence of the glass transition on diffusion in amorphous polymers.* Journal of applied polymer science, 1978. **22**(8): p. 2325-2339.
50. Ree, T. and H. Eyring, *Theory of Non-Newtonian Flow. I. Solid Plastic System.* Journal of Applied Physics, 1955. **26**(7): p. 793-800.
51. Eyring, H., *Viscosity, plasticity, and diffusion as examples of absolute reaction rates.* The Journal of Chemical Physics, 1936. **4**(4): p. 283-291.
52. Struik, L.C.E., *Dependence of relaxation times of glassy polymers on their specific volume.* Polymer, 1988. **29**(8): p. 1347-1353.
53. Struik, L.C.E., *Effect of thermal history on secondary relaxation processes in amorphous polymers.* Polymer, 1987. **28**(1): p. 57-68.
54. Chen, L.P., A.F. Yee, and E.J. Moskala, *The molecular basis for the relationship between the secondary relaxation and mechanical properties of a series of polyester copolymer glasses.* Macromolecules, 1999. **32**(18): p. 5944-5955.
55. Boyce, M.C. and E.M. Arruda, *Constitutive models of rubber elasticity: a review.* Rubber chemistry and technology, 2000. **73**(3): p. 504-523.
56. Manuel J. Garcia R., O.E.R.S., Carlos Lopez, *Hyperelastic Material Modeling*, 2005, Departamento de Ingenieria Mecanica: Medellin.
57. Germain, P. and P. Muller, *Introduction à la mécanique des milieux continus*1980: Masson.
58. Grediac, M., et al., *The virtual fields method for extracting constitutive parameters from full-field measurements: a review.* Strain, 2006. **42**(4): p. 233-253.
59. Pierron, F. and M. Grédiac, *The virtual fields method: extracting constitutive mechanical parameters from full-field deformation measurements*2012: Springer Science & Business Media.
60. Rusinek, A. and J.R. Klepaczko, *Shear testing of a sheet steel at wide range of strain rates and a constitutive relation with strain-rate and temperature dependence of the flow stress.* International Journal of Plasticity, 2001. **17**(1): p. 87-115.
61. Banerjee, B., *The Mechanical Threshold Stress model for various tempers of AISI 4340 steel.* International Journal of Solids and Structures, 2007. **44**(3–4): p. 834-859.
62. Johnson, G.R. and W.H. Cook. *A constitutive model and data for metals subjected to large strains, high strain rates and high temperatures*. in *Proceedings of the 7th International Symposium on Ballistics*. 1983. The Netherlands.
63. Rule, W.K. and S.E. Jones, *A REVISED FORM FOR THE JOHNSON–COOK STRENGTH MODEL.* International Journal of Impact Engineering, 1998. **21**(8): p. 609-624.
64. Banerjee, B., *An evaluation of plastic flow stress models for the simulation of high-temperature and high-strainrate deforamtion metals.* 2008.
65. Molinari, A. and R. Clifton, *Localisation de la déformation viscoplastique en cisaillement simple: résultats exacts en théorie non linéaire.* Comptes Rendus Academie des Sciences, II, 1983. **296**: p. 1-4.
66. Zerilli, F.J. and R.W. Armstrong, *Dislocation-mechanics-based constitutive relations for material dynamics calculations.* Journal of Applied Physics, 1987. **61**(5): p. 1816-1825.
67. Hull, D. and D.J. Bacon, *Introduction to dislocations*. Vol. 257. 1984: Pergamon Press Oxford.
68. Meyer Jr, H.W., *A Modified Zerilli-Armstrong Constitutive Model Describing the Strength and Localizing Behavior of Ti-6A1-4V*, 2006, DTIC Document.
69. Zerilli, F.J. and R.W. Armstrong. *Constitutive relations for the plastic deformation of metals*. in *High-pressure science and technology—1993*. 1994. AIP Publishing.
70. Frąś, T., *Modélisation de la surface d'écoulement des matériaux incluant l'anisotropie initiale et l'effet différentiel des contraintes: approche expérimentale et numérique*, 2013, Université de Lorraine.
71. Rodríguez-Martínez, J.A., A. Rusinek, and A. Arias, *Thermo-viscoplastic behaviour of 2024-T3 aluminium sheets subjected to low velocity perforation at different temperatures.* Thin-Walled Structures, 2011. **49**(7): p. 819-832.

72. Biswajit Banerjee, A.S.B., *An extended mechanical threshold stress plasticity model: modeling 6061-T6 aluminum alloy.* Journal of Mechanics of Materials and Structures, 2008. **3**(3).
73. Gueguen, O., et al., *Micromechanically based formulation of the cooperative model for the yield behavior of semi-crystalline polymers.* Acta Materialia, 2008. **56**(7): p. 1650-1655.
74. Richeton, J., et al., *Modeling and validation of the large deformation inelastic response of amorphous polymers over a wide range of temperatures and strain rates.* International Journal of Solids and Structures, 2007. **44**(24): p. 7938-7954.
75. Richeton, J., et al., *Influence of temperature and strain rate on the mechanical behavior of three amorphous polymers: Characterization and modeling of the compressive yield stress.* International Journal of Solids and Structures, 2006. **43**(7–8): p. 2318-2335.
76. G'sell, C. and J. Jonas, *Determination of the plastic behaviour of solid polymers at constant true strain rate.* Journal of Materials Science, 1979. **14**(3): p. 583-591.
77. Matsuoka, S., *Nonlinear Viscoelastic Stress--Strain Relationships in Polymeric Solids.* Carl Hanser Verlag, Failure of Plastics, 1986: p. 24-59.
78. Argon, A.S. and M. Bessonov, *Plastic flow in glassy polymers.* Polymer Engineering & Science, 1977. **17**(3): p. 174-182.
79. Argon, A., *Physical basis of distortional and dilational plastic flow in glassy polymers.* Journal of Macromolecular Science, Part B: Physics, 1973. **8**(3-4): p. 573-596.
80. Argon, A., *A theory for the low-temperature plastic deformation of glassy polymers.* Philosophical Magazine, 1973. **28**(4): p. 839-865.
81. Li, J. and J. Gilman, *Disclination loops in polymers.* Journal of Applied Physics, 1970. **41**(11): p. 4248-4256.
82. Kuhn, W. and F. Grün, *Beziehungen zwischen elastischen Konstanten und Dehnungsdoppelbrechung hochelastischer Stoffe.* Kolloid-Zeitschrift, 1942. **101**(3): p. 248-271.
83. Rivlin, R., *Large elastic deformations of isotropic materials. I. Fundamental concepts.* Philosophical Transactions of the Royal Society of London. Series A, Mathematical and Physical Sciences, 1948. **240**(822): p. 459-490.
84. Kerner, E., *The elastic and thermo-elastic properties of composite media.* Proceedings of the physical society. Section B, 1956. **69**(8): p. 808.
85. Staverman, A. and F. Schwarzl, *Non Linear Deformation Behaviour of High Polymers*, in *Theorie und molekulare Deutung technologischer Eigenschaften von hochpolymeren Werkstoffen*1956, Springer. p. 126-164.
86. Horgan, C.O., *The remarkable Gent constitutive model for hyperelastic materials.* International Journal of Non-Linear Mechanics, 2015. **68**(0): p. 9-16.
87. Arruda, E.M., M.C. Boyce, and H. Quintus-Bosz, *Effects of initial anisotropy on the finite strain deformation behavior of glassy polymers.* International Journal of Plasticity, 1993. **9**(7): p. 783-811.
88. Arruda, E.M. and M.C. Boyce, *Evolution of plastic anisotropy in amorphous polymers during finite straining.* International Journal of Plasticity, 1993. **9**(6): p. 697-720.
89. Arruda, E.M. and M.C. Boyce, *A three-dimensional constitutive model for the large stretch behavior of rubber elastic materials.* Journal of the Mechanics and Physics of Solids, 1993. **41**(2): p. 389-412.
90. Osovski, S., et al., *Microstructural effects on adiabatic shear band formation.* Scripta Materialia, 2012. **66**(1): p. 9-12.
91. Rittel, D., Z. Wang, and M. Merzer, *Adiabatic shear failure and dynamic stored energy of cold work.* Physical review letters, 2006. **96**(7): p. 075502.
92. Rittel, D. and S. Osovski, *Dynamic failure by adiabatic shear banding.* International Journal of Fracture, 2010. **162**(1): p. 177-185.
93. Mason, J.J., A.J. Rosakis, and G. Ravichandran, *Full field measurements of the dynamic deformation field around a growing adiabatic shear band at the tip of a dynamically loaded crack or notch.* Journal of the Mechanics and Physics of Solids, 1994. **42**(11): p. 1679-1697.
94. Rittel, D., *A different viewpoint on adiabatic shear localization.* Journal of Physics D: Applied Physics, 2009. **42**(21): p. 214009.

95. CAMPAGNE, L., *Modélisation et simulation de la viscoplasticité et de l'endommagement en grandes vitesses de déformation*, 2003.
96. Lemaitre, J., *A continuous damage mechanics model for ductile fracture.* Transactions of the ASME. Journal of Engineering Materials and Technology, 1985. **107**(1): p. 83-89.
97. Needleman, A., V. Tvergaard, and J. Hutchinson, *Void growth in plastic solids*, in *Topics in Fracture and Fatigue*1992, Springer. p. 145-178.
98. Potirniche, G., et al., *A molecular dynamics study of void growth and coalescence in single crystal nickel.* International Journal of Plasticity, 2006. **22**(2): p. 257-278.
99. Hammi, Y. and M. Horstemeyer, *A physically motivated anisotropic tensorial representation of damage with separate functions for void nucleation, growth, and coalescence.* International Journal of Plasticity, 2007. **23**(10): p. 1641-1678.
100. Mohr, D. and S.J. Marcadet, *Micromechanically-motivated phenomenological Hosford–Coulomb model for predicting ductile fracture initiation at low stress triaxialities.* International Journal of Solids and Structures, 2015. **67**: p. 40-55.
101. Bao, Y. and T. Wierzbicki, *On the cut-off value of negative triaxiality for fracture.* Engineering fracture mechanics, 2005. **72**(7): p. 1049-1069.
102. Bao, Y. and T. Wierzbicki, *On fracture locus in the equivalent strain and stress triaxiality space.* International Journal of Mechanical Sciences, 2004. **46**(1): p. 81-98.
103. Bao, Y. and T. Wierzbicki, *A comparative study on various ductile crack formation criteria.* TRANSACTIONS-AMERICAN SOCIETY OF MECHANICAL ENGINEERS JOURNAL OF ENGINEERING MATERIALS AND TECHNOLOGY, 2004. **126**: p. 314-324.
104. Skiba, T., et al., *Mechanical properties of spark plasma sintered FeAl intermetallics.* Intermetallics, 2010. **18**(7): p. 1410-1414.
105. Kubicki, B., *Stress concentration at pores in sintered materials.* Powder metallurgy, 1995. **38**(4): p. 295-298.
106. Dudrová, E. and M. Kabátová, *Fractography of sintered iron and steels.* Powder Metallurgy Progress, 2008. **8**(2): p. 59-75.
107. Elkadi, A., J. Van Mier, and L. Sluys, *Multiaxial failure of low-cohesive frictional materials: fracture behaviour and size dependency.* Philosophical Magazine, 2006. **86**(21-22): p. 3137-3159.
108. Clausen, A.H., et al., *Flow and fracture characteristics of aluminium alloy AA5083–H116 as function of strain rate, temperature and triaxiality.* Materials Science and Engineering: A, 2004. **364**(1): p. 260-272.
109. Klepaczko, J.R., et al., *Modelling of thermo-viscoplastic behaviour of DH-36 and Weldox 460-E structural steels at wide ranges of strain rates and temperatures, comparison of constitutive relations for impact problems.* Mechanics of Materials, 2009. **41**(5): p. 599-621.
110. Rottler, J. and M.O. Robbins, *Growth, microstructure, and failure of crazes in glassy polymers.* Physical Review E, 2003. **68**(1): p. 011801.
111. Kinloch, A.J., *Fracture behaviour of polymers*2013: Springer Science & Business Media.
112. Fleck, N., W. Stronge, and J. Liu. *High strain-rate shear response of polycarbonate and polymethyl methacrylate*. in *Proceedings of the Royal Society of London A: Mathematical, Physical and Engineering Sciences*. 1990. The Royal Society.
113. Arruda, E.M., M.C. Boyce, and R. Jayachandran, *Effects of strain rate, temperature and thermomechanical coupling on the finite strain deformation of glassy polymers.* Mechanics of Materials, 1995. **19**(2-3): p. 193-212.
114. Karger-Kocsis, J. and T. Czigány, *Strain rate dependence of the work of fracture response of an amorphous poly (ethylene-naphthalate)(PEN) film.* Polymer Engineering & Science, 2000. **40**(8): p. 1809-1815.
115. Segreti, M., A. Rusinek, and J. Klepaczko, *Experimental study on puncture of PMMA at low and high velocities, effect on the failure mode.* Polymer Testing, 2004. **23**(6): p. 703-718.
116. Johnson, G.R. and W.H. Cook, *Fracture characteristics of three metals subjected to various strains, strain rates, temperatures and pressures.* Engineering fracture mechanics, 1985. **21**(1): p. 31-48.
117. Wierzbicki, T., et al., *Calibration and evaluation of seven fracture models.* International Journal of Mechanical Sciences, 2005. **47**(4): p. 719-743.

118. Huber, M., *Contribution to the Foundation of the Strength of the Material.* Czas. Tech, 1904. **22**: p. 81.
119. Wierzbicki, T. and L. Xue, *On the effect of the third invariant of the stress deviator on ductile fracture.* Impact and Crashworthiness Laboratory, Technical Report, 2005(136).
120. Xue, L., *Damage accumulation and fracture initiation in uncracked ductile solids subject to triaxial loading.* International Journal of Solids and Structures, 2007. **44**(16): p. 5163-5181.
121. Dunand, M. and D. Mohr, *On the predictive capabilities of the shear modified Gurson and the modified Mohr–Coulomb fracture models over a wide range of stress triaxialities and Lode angles.* Journal of the Mechanics and Physics of Solids, 2011. **59**(7): p. 1374-1394.
122. Abaqus, *Damage evolution and element removal for ductile metals.* Abaqus Documentation, 2014.
123. McClintock, F.A. *A criterion for ductile fracture by the growth of holes*. 1968. ASME.
124. Gurson, A.L., *Continuum theory of ductile rupture by void nucleation and growth: Part I—Yield criteria and flow rules for porous ductile media.* Journal of engineering materials and technology, 1977. **99**(1): p. 2-15.
125. Tvergaard, V. and A. Needleman, *Analysis of the cup-cone fracture in a round tensile bar.* Acta Metallurgica, 1984. **32**(1): p. 157-169.
126. Tvergaard, V., *Material failure by void growth to coalescence.* Advances in applied Mechanics, 1989. **27**: p. 83-151.
127. Curran, D., L. Seaman, and D. Shockey, *Dynamic failure of solids.* Physics reports, 1987. **147**(5-6): p. 253-388.
128. Stroh, A.N., *A theory of the fracture of metals.* Advances in Physics, 1957. **6**(24): p. 418-465.

Chapter 2

MECHANICAL CHARACTERIZATION OF METALLIC AND POLYMER MATERIALS

The present chapter aims to provide the experimental work performed during the investigation of the mechanical behavior of the different materials studied. The acquisition of experimental data is the first step toward the development of a material constitutive numerical model. Indeed, these data are mandatory to understand the mechanical behavior of the materials in order to choose the most pertinent models and to calibrate them.

The first part of this chapter has for objective to present the different materials studied in this work (7020 aluminum alloy, polyimide and epoxy resin) by explaining their different intrinsic properties (density, specific heat …).

A second part is dedicated to the description of the different experimental tests which have been used for the mechanical characterization of the three materials.

Once the different materials and the experimental procedures have been introduced, the mechanical behavior of each material is detailed in a third part. The different physical phenomena responsible of the level of stress and failure with the strain, the temperature and the strain rate are cautiously commented and explained.

A. Descriptions of the materials

1. F7020 aluminum alloy

The denomination F7020 corresponds to a specific aluminum alloy processed using Spark Plasma Sintering (SPS). The powder used for the sintering process is a commercial atomized powder. The density of the F7020 is $\rho = 2880\ \mathrm{kg.m^{-3}}$ (determined through Archimedes procedure) and its specific heat (at room temperature) is $C_p = 875\ \mathrm{J.kg^{-1}.K^{-1}}$ (values given at room temperature). The elastic modulus is $E = 72\ \mathrm{GPa}$ and the Poisson's ratio $\nu = 0.3$. The chemical composition of the F7020 aluminum alloy can be found in Table 7.

Table 7 - Chemical composition of the F7020 aluminum alloy

	Element	Al	Zn	Mg	Cu	Fe	Si
F7020	Wt. %	Bal.	4.80	1.20	<0.20	<0.35	<0.35

The aluminum alloys are considered as Face Centered Cubic metals (FCC) which exhibit kinematic structural hardening due to the germination and propagation of forests of dislocations. The 7020 based alloys have a stable microstructure which can be computed through thermodynamic software allowing the evaluation of the equilibrium phases in presence [1], in function of the temperature (such as JMatPro TS [2]). The Figure 25 shows that, at room temperature, the main phases in presence are:

- Around 6% of $MgZn_2$ precipitates which consist in the biggest equilibrium phase. These HCP (Hexagonal Close-Packed) precipitates have a strong hardening potential and cause a high generation of dislocations. The amount of $MgZn_2$ precipitates decreases quickly with the temperature leading to a softening of the internal stress (stress caused by the structural hardening). In the case of the F7020 (see Figure 26.a), the $MgZn_2$ precipitates are much bigger than for the commercial AA7020-T651 (see Figure 26.b).
- Around 1.5% of Al_6Mn orthorhombic precipitates. In the case of the F7020, these precipitates are much smaller than the precipitates of $MgZn_2$ (see Figure 26.a).
- The aluminum matrix making the balance ratio with the other phases.

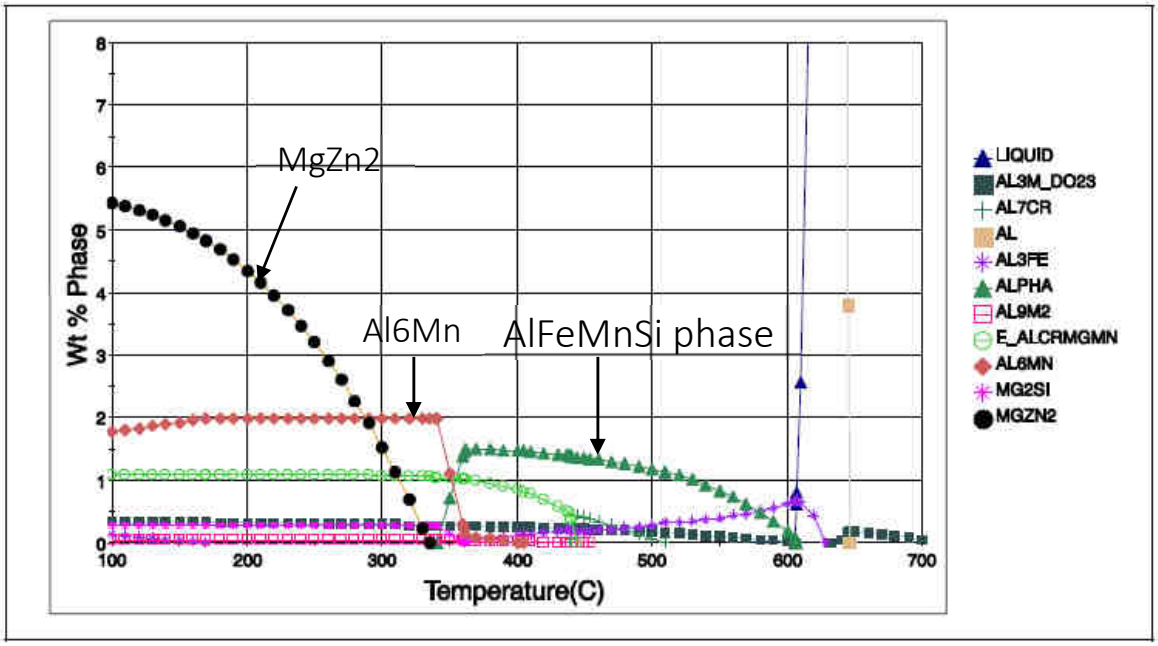

Figure 25 – Equilibrium phases of 7020 aluminum alloy computed by JMatPro TS [2]

At higher temperatures, the microstructure changes completely. Indeed, above a transition temperature (around 600 K according to JMatPro TS [2] and around 500 K for the F7020), the $MgZn_2$ and Al_6Mn phases have been completely dissolved in the Al matrix and a AlFeMnSi phase has appeared.

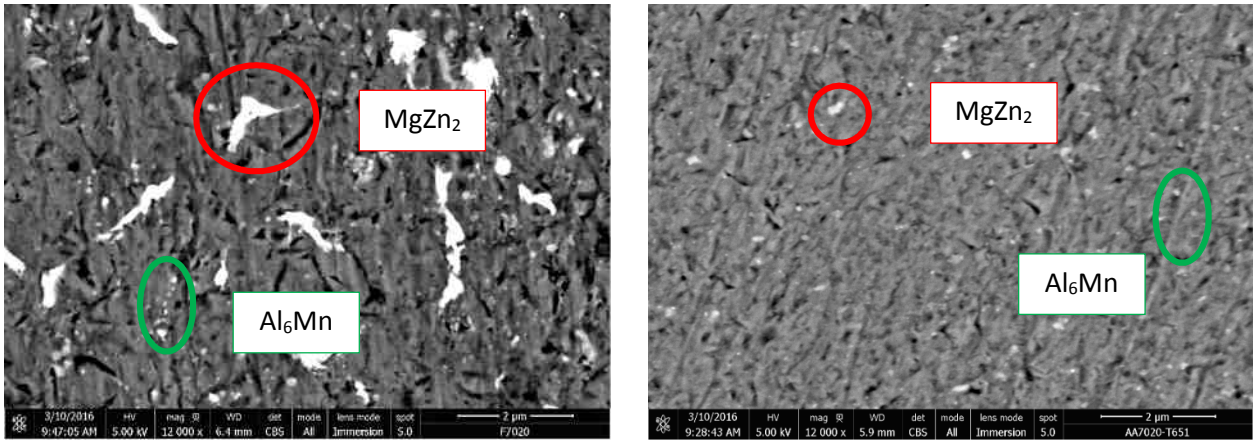

(a) (b)

Figure 26 - SEM picture of (a) F7020 (x12000) and (b) AA7020-T651 at 293K

The optic microscopy study of the F7020 aluminum alloy (Figure 27.a) provides other information such as the grain size ($\langle D_g \rangle \approx 14$ µm) and the ratio shape factor of the grains $R_s = 1.148$ (Figure 27.b). The value of R_s is close to 1 which allows us to make the assumption of spherical grains. The grain size has been measured by averaging the minimum and maximum diameter of more than 20 grains and the mean value is then taken as $\langle D_g \rangle$ (see Figure 27.b).

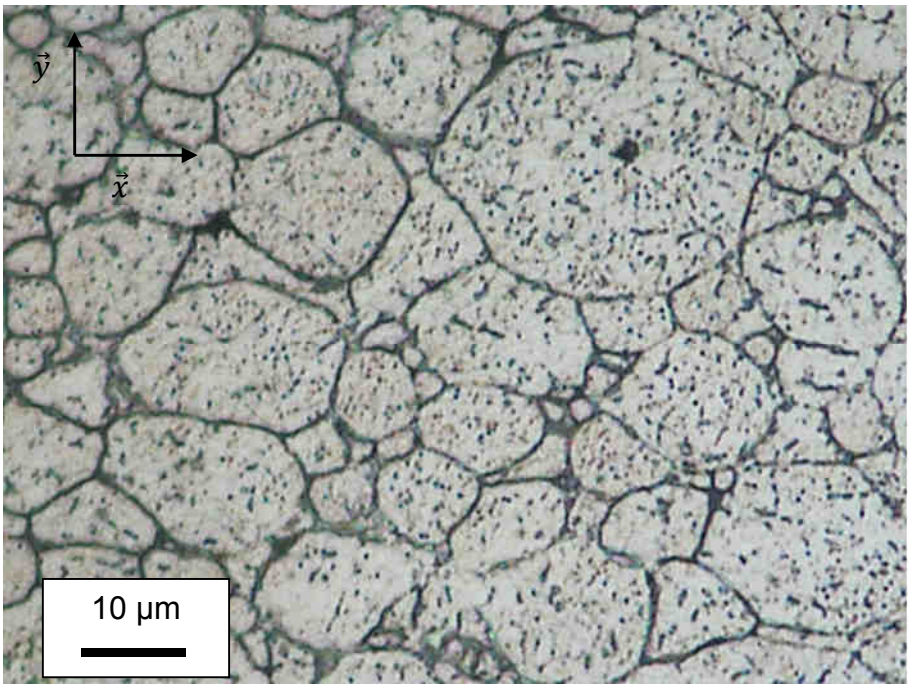

(a)

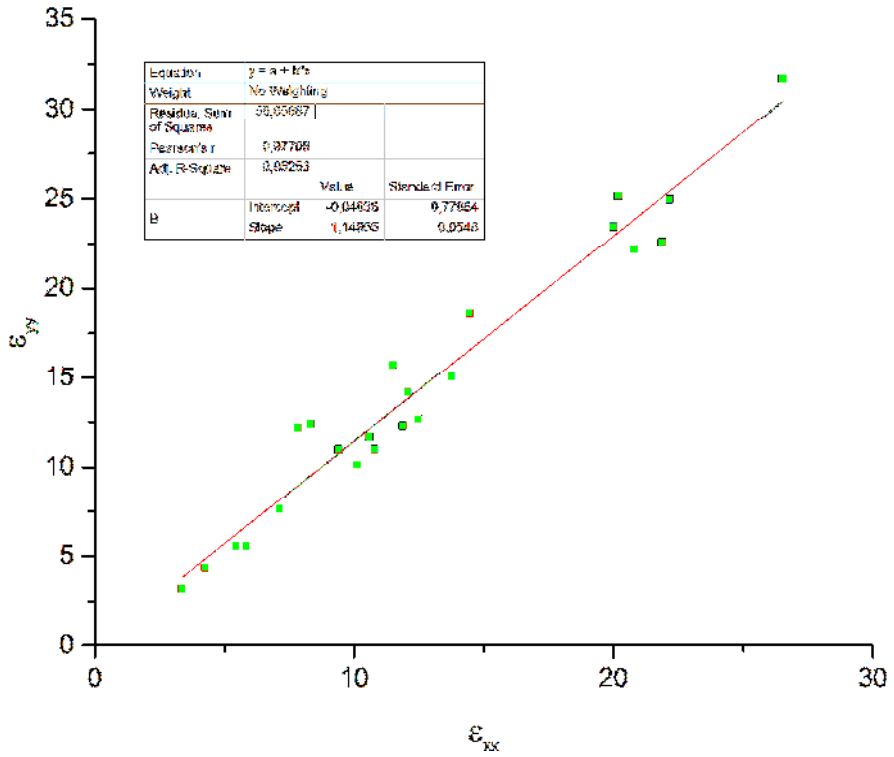

(b)

Figure 27 - (a) Optic microscopic picture of F7020 and (b) Study of the grains size ratio for shape determination

2. Sintered polyimide

The polyimide (PI) studied in this work has been sintered using Spark Plasma sintering (SPS) (Figure 28). The polyimide is an amorphous thermoplastic polymer with very high mechanical properties (limited entanglement). Such mechanical performances are mainly due to the very high temperature of glass transition of the sintered polyimide ($T_g = 583$ K – see Figure 29) which allows a strong resistance to strain at room temperature. At even higher temperature ($T_d \approx 683$ K), the polymer reaches its degradation state leading to the global failure of the material. The density (at room temperature) of the PI is $\rho = 1380\ \mathrm{kg.m^{-3}}$ (determined using Archimedes procedure) and its specific heat (at room temperature) is $C_p = 1170\ \mathrm{J.kg^{-1}.K^{-1}}$. The Poisson's ratio is taken as $\nu = 0.4$.

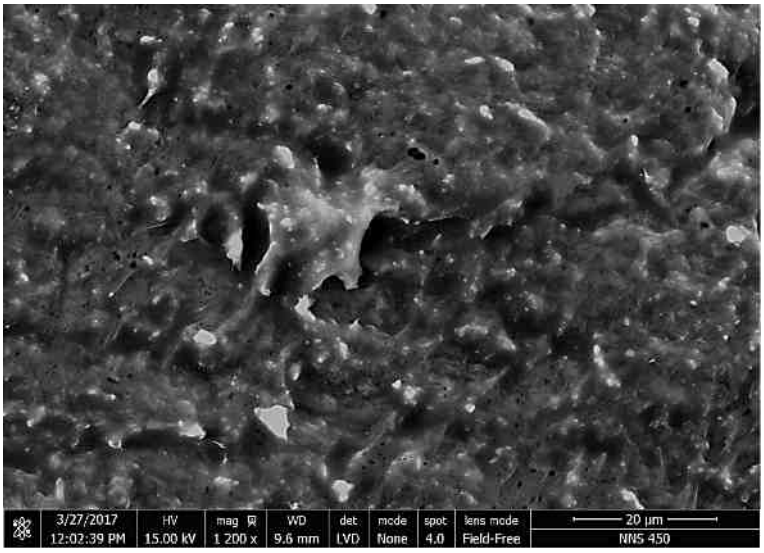

Figure 28 - Topologic SEM focus picture of sintered polyimide surface fracture profile

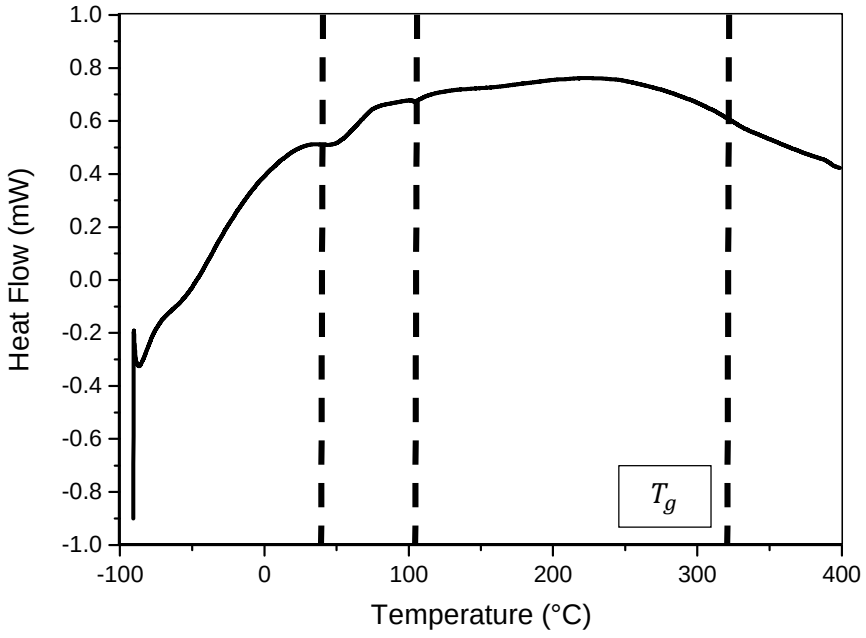

Figure 29 - Heat flow vs temperature during DSC test for the sintered polyimide

Differential Scanning Calorimetry test has been carried out from -90°C to 400°C (maximum reachable of the testing device) at 5° per min under nitrogen gas (50 mL per min). The heat flow of the medium exchanged with the sample is shown on Figure 29. The temperature of glass transition T_g can be identified by using the result as the temperature at the mean endothermic measured process. Other characteristic temperatures can be seen around 45°C and 100°C. They might correspond to the transition temperatures T_β and T_γ of the secondary relaxation mechanisms of peripheral groups. The temperature of degradation of the polymer is higher than the maximum range allowed by the used DSC.

3. Epoxy resin

The epoxy resin is a well-known thermoset polymer which is processed by mixing two different components: a resin and a hardener for the polymerization (Figure 30). This epoxy resin has a very low pot time of 8 minutes (time during which the epoxy resin can be manipulated before the sudden hardening) but reaches its optimum mechanical properties after around 3 days. The different tests have revealed several important properties of this particular epoxy resin such as its temperature of glass transition $T_g = 333\ K$ (see Figure 31), its density (at room temperature) of $\rho = 1200\ kg.m^{-3}$. Its specific heat (at room temperature) of $C_p = 1000\ J.kg^{-1}.K^{-1}$ was provided by the manufacturer. The relatively low value of the temperature of glass transition leads to a quick change of mechanical behavior of the epoxy resin in dynamic conditions from glassy state to rubber state due to the adiabatic heating. The Poisson's ratio is taken as $\nu = 0.4$.

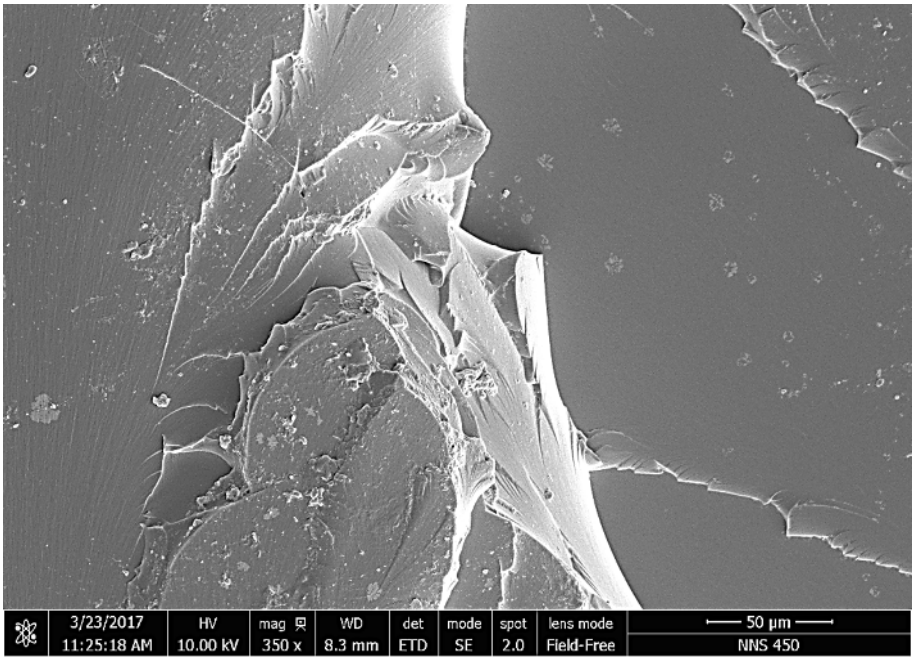

Figure 30 - Topologic SEM focus picture of epoxy resin surface fracture profile

Differential Scanning Calorimetry test has been carried out from -90°C to 300°C at 5° per min under nitrogen gas (50 mL per min). The heat flow of the medium exchanged with the sample is shown on Figure 31. The temperature of glass transition T_g can be identified by using the result as the temperature at the middle of the first endothermic measured process. Around -50°C a phenomenon of secondary relaxation of peripheral groups might be identified. The temperature of relaxation seems to be around 275°C.

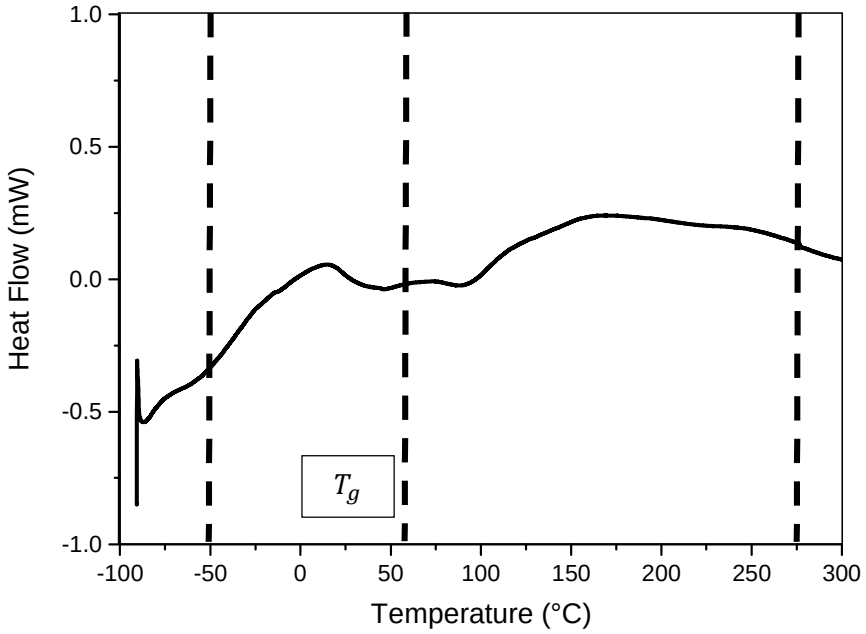

Figure 31 - Heat flow vs temperature during DSC test for the sintered polyimide

B. Descriptions of the experimental tests

1. Uniaxial quasi-static experiments

The mechanical tests in quasi-static conditions ($10^{-5}/s$ to $1\ /s$) are generally carried out with an uniaxial testing machine which allows classic tests such as tension and compression. The force F transmitted through the sample is measured by the means of a cell force unit which is characterized by its force limit. The recording of the extension Δl is performed by a calibrated LVDT allowing a very accurate measure of the length variation of the sample. The use of a camera to record the stretching of the sample can also provide a strain map (with Digital Image Correlation) and provides important local information on the mechanical behavior of the sample (e.g. the recording of the necking in tension tests). The true strain ε_t and the nominal strain ε_n are computed from the extension and the effective length l of the sample (Eqs 2.1 and 2.2). The true stress σ_t and the nominal stress σ_n are calculated from the force F, ε_n and the effective surface S of the sample (Eqs 2.3 and 2.4) [3, 4].

$$\varepsilon_e = \frac{\Delta l}{l_0} \quad (2.1)$$

$$\varepsilon_t = \frac{\Delta l}{l} = \ln(1 + \varepsilon_n) \quad (2.2)$$

$$\sigma_n = \frac{F}{S_0} \quad (2.3)$$

$$\sigma_t = \frac{F}{S} = \sigma_n\left(1\text{-}2\nu_p\varepsilon_n\right) \quad (2.4)$$

With ν_p the coefficient of plastic expansion ($\nu_p = 0.5$ for incompressible flow).

In this manuscript, the stress will always define the true stress and the strain, the true strain.

The size ratio of the sample generally used for cylindrical compression tests is 1:1 in quasi-static condition. If the ratio is too high, the sample might bulk and invalidates the test (see technical drawing Appendice B). The geometry of the samples for tension samples [4] are much more complex and has to be designed for each different material to avoid unwanted stress concentration outside of the effective zone. Many other kinds of tests, requiring specific geometry of the sample, can be done with such testing machine such as shear-compression tests [5], shear tests [4], bi-tension tests [6] … An electromechanical K9400 INSTRON uniaxial quasi-static machine has been used in this work with a 100kN force cell.

The compressive tests at high temperature have been carried out using a custom resistive oven which can heat up to 300°C. The temperature was monitored through a thermocouple set on the sample coupled with an infrared measurement (Figure 32.a and 32.b).

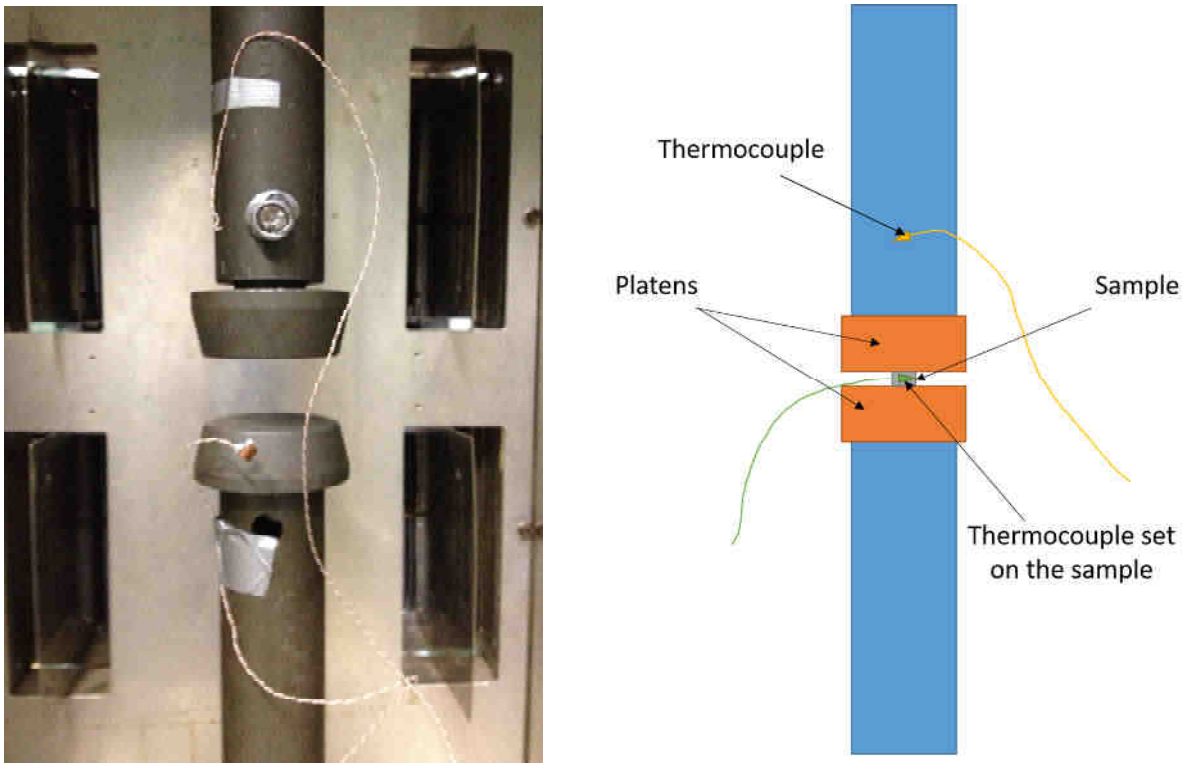

(a) (b)

Figure 32 – (a) Quasi-static heating setup and (b) its schematic representation

2. Dynamic experiments using Split Hopkinson Pressure Bar setup

Dynamic experiments have been conducted using Split Hopkinson Pressure Bars (SHPB) [7-10] is an experimental setup developed in order to test materials (mainly metals and polymers) in compression state of stress at high strain rate ($500\ /s$ to $10.000\ /s$). The sample of radius r is placed between two bars (input and output bars) of wave velocity $C_0 = \sqrt{\frac{E}{\rho}}$ and of radius R (Figure 33).

A striker of length L_0 hits the input bar of length L_I at a known velocity. Two mechanical wave fronts are generated at the surfaces of impact. One of the wave fronts propagates along the input bar up to the sample (rising time), the second wave front goes along the striker up to its free end and goes back up to the impacted end and next along the input bar (drop time). The mechanical wave between the two fronts is a called the incident pulse of length $2L_0$. At the input face end of the sample, the incident wave encounters a break of mechanical impedance depending on the diameter, the elastic properties and the density of the bars and sample. When a wave reaches an important mismatch of impedance, a transmitted wave continues along the sample and next along the output bar, a reflected wave goes back along the

input bar. The amplitude of the waves is measured through strain gages placed onto the surfaces of the input bar (incident and reflected waves) and of the output bar (transmitted wave) to obtain the elastic strain of these lasts (ε_I for incident wave, ε_R for reflected wave and ε_T for transmitted wave). The experimental results are next processed with the assumption of force equilibrium (Eq 2.5) which states that the input force applied to the sample is equal to the output force. However, this equilibrium is not present during the first steps of the loading due to the inhomogeneous state of stress in the sample. The force equilibrium is also broken in case of failure of the material.

$$\varepsilon_I + \varepsilon_R = \varepsilon_T \qquad (2.5)$$

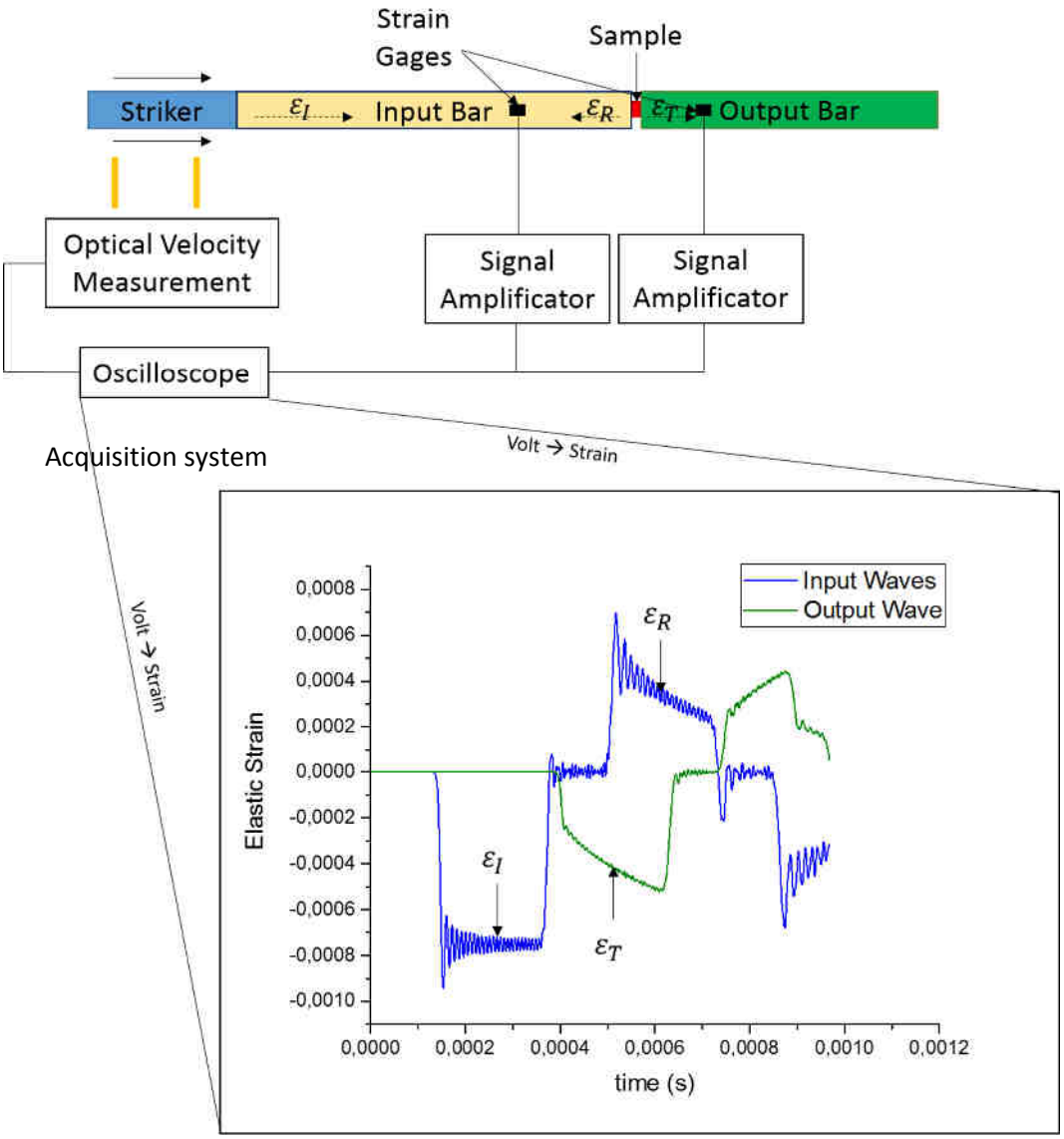

Figure 33 - Schematic representation of SHPB setup

The shortening of the specimen is computed by evaluating the velocities of the sample interfaces (Eqs 2.6 and 2.7):

$$V_{input} = -C_0(\varepsilon_I - \varepsilon_R) \quad (2.6)$$

$$V_{output} = -C_0\varepsilon_T \quad (2.7)$$

Therefore the evolution of the specimen length l can be obtained with Eq 2.8:

$$l = (V_{input} - V_{output})\Delta t \quad (2.8)$$

With Δt the time increment between two measurements.

The value of the forces applied on the sample and transmitted by it are computed as follows (Eqs 2.9 and 2.10):

$$F_{input} = \pi R^2 E(\varepsilon_I + \varepsilon_R) \quad (2.9)$$

$$F_{output} = \pi R^2 E\varepsilon_T \quad (2.10)$$

The value of the output force is generally taken for the computation of the stresses (assumption of the force equilibrium).

The nominal strain rate $\dot{\varepsilon}_n$ and strain ε_n are computed with a classic method (Eqs 2.11 and 2.12):

$$\dot{\varepsilon}_n = \frac{V_{input} - V_{output}}{l_0} \quad (2.11)$$

$$\varepsilon_n = \int_0^t \dot{\varepsilon}_n d\tau \quad (2.12)$$

The nominal stress is obtained using Eq 13:

$$\sigma_n = \frac{F_{output}}{\pi r^2} \quad (2.13)$$

The true values of the strain, strain rate and stress can be calculated with (Eqs 2.14 to 2.16):

$$\varepsilon_t = -\ln(1-\varepsilon_n) \quad (2.14)$$

$$\dot{\varepsilon}_t = \frac{\dot{\varepsilon}_n}{1-\varepsilon_n} \quad (2.15)$$

$$\sigma_t = \sigma_n(1-2\nu_p\varepsilon_n) \quad (2.16)$$

Some further post-processing of the results may be needed to correct the influence of some phenomena occurring during the test such as friction [11, 12], inertia effect [7, 12] or the punching of the bar by the sample [7, 13].

The size ratio of the compression samples is generally 1:2 to allow an optimal force equilibrium [12]. In order to control and reach different values of strain rates, two sizes of samples have been used (Ø=8mm/t=4mm and Ø=6mm/t=3mm, see technical drawing Appendix B).

Other kind of tests can be performed using a SHPB setup such as shear-compression [5], shear [14], bending [15] … by slightly changing the setup and the sample geometry. Different Hopkinson bar setups have been developed to allow other kind of mechanical solicitations such tensile [16, 17] or torsion [18, 19].

Dynamic tests at high temperatures have been carried using a pulsated air flux system (schematic representation in Figure 34.b). The sample was heated alone (the bars were put in contact with it just before the test) and its temperature was monitored using a thermocouple set on its surface (Figure 34.a).

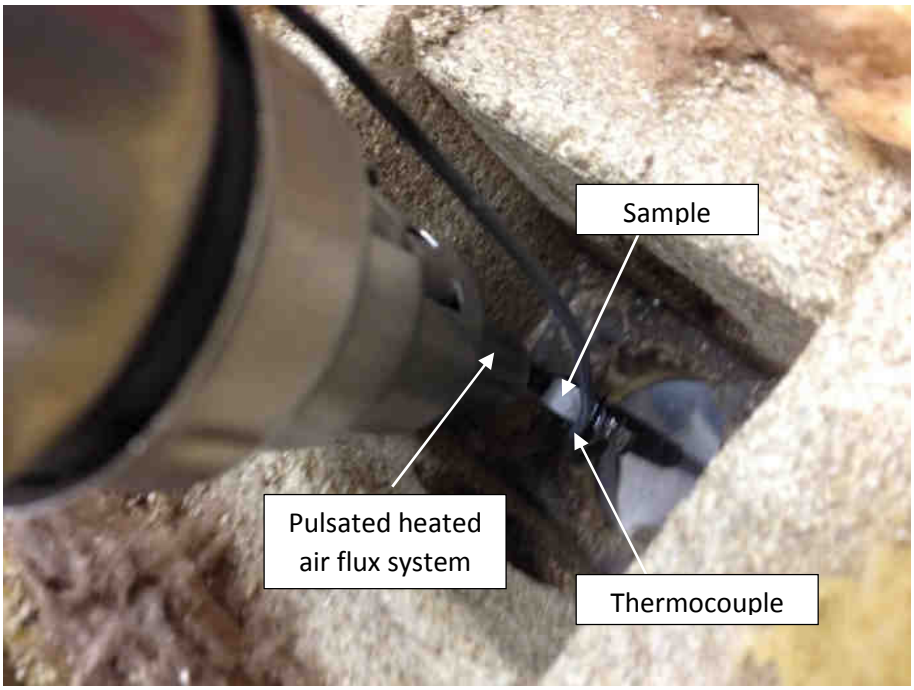

(a)

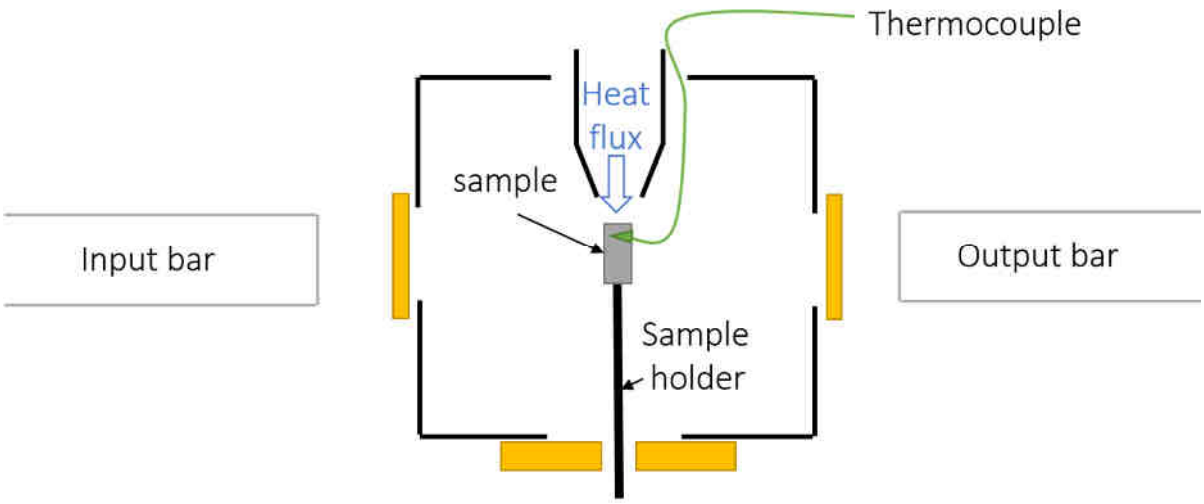

(b)

Figure 34 - Pulsated heated air flux system for SHPB setup (a) focus on the sample and (b) schematic representation of the setup

Other dynamic tests at cryogenic temperature have also been performed using liquid nitrogen and ethanol to adjust to the desired temperatures (Figure 35.a). The temperature of the sample was monitored using an infrared measuring device (Figure 35.b).

(a) (b)

Figure 35 – Cryogenic system for SHPB setup (a) whole setup and (b) focus on the sample

3. Dynamic experiments using Direct Impact setup

The direct impact (DI) test allows to reach an even higher decade of strain rates (10^4 /s to 10^5 /s) [20, 21]. The concept is similar to the SHPB setup but uses only the striker and a bar. The sample is fixed on the free end of the bar and the striker impacts it directly (see Figure 36). To obtain the displacement of the ends of the sample, two different methods are used:

- For the output end of the sample, a strain gage is set onto the bar and, as for the SHPB setup, its recorded deformation allows the determination of velocity of the output end of the sample and of the output force.
- The velocity of the input end is the same as the striker. This lasts can be directly measured using a high speed camera or computed through Finite Element Method (FEM). A strong initial velocity dependency can be observed and the deceleration profile has to be computed for each different impact velocity and is also sensitive to the mechanical characteristics of the tested material.

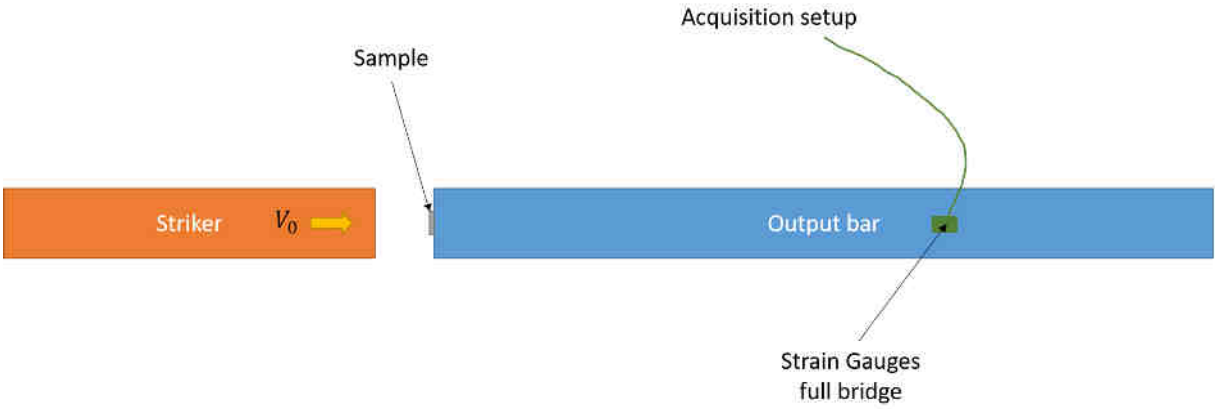

Figure 36 - Schematic representation of Direct Impact experiment (using simulation data to compute the deceleration of the striker)

Once the velocities of the two interfaces are known, the processing of the experimental data is the same as for the SHPB setup (also with friction, inertia and punching corrections). The size ratio of the samples are generally very small to reach the highest possible strain rate. The thickness is therefore around 1 mm (or even less) for a radius designed to allow a measurable strength output. In this work, the F7020 sample sizes are Ø=5mm/h=1mm and the PI sample sizes are Ø=6mm/h=1mm (see technical drawing Appendix B).

4. Shear-compression tests

The shear-compression tests allow the study of the mechanical behavior (stress and failure) in a different state of stress than classical compression, tension or shear states. The state of stress under which the material is loaded in such experiments has the particularity of being lower than the state of compression $\left(\sigma^* < -\frac{1}{3}\right)$. These specific tests are needed in this work for two reasons. Firstly, it provides values of strain at initiation of failure in the negative domain of triaxiality and will then enhanced the modeling of the failure behavior. Secondly, the sintered materials (F7020 aluminum alloy and polyimide) present a low-cohesive behavior in positive state of stress which leads to the decohesion of the sintered powder grains. Regarding this particular behavior, the study of the sensitivities of the failure mechanisms to the temperature and strain rate have to be performed in negative state of stress such as encountered in compression or shear-compression tests.

Different geometries of samples have been developed over the years (from parallelepiped shape with square groove [22, 23] to cylindrical shape with round groove [5]). The advantage of the cylindrical shape of the specimen consists in a better wave propagation in dynamical conditions in SHPB experiments [5, 24] leading to a better force equilibrium. However, the advantage of using a round groove over a square groove is much more important regarding the study of the failure behavior and the stress homogeneity across the effective area of the sample. Indeed, the failure profile of the sample using the square groove is not optimal and the crack does not propagate along the groove [23, 24] contrary to the sample with round groove [5]. Furthermore, the angle of the groove with the perpendicular of the axis of the cylinder φ, can be changed to get different states of stress (see Figure 37). The presented geometry has been used in quasi-static and dynamic conditions (SHPB and direct impact).

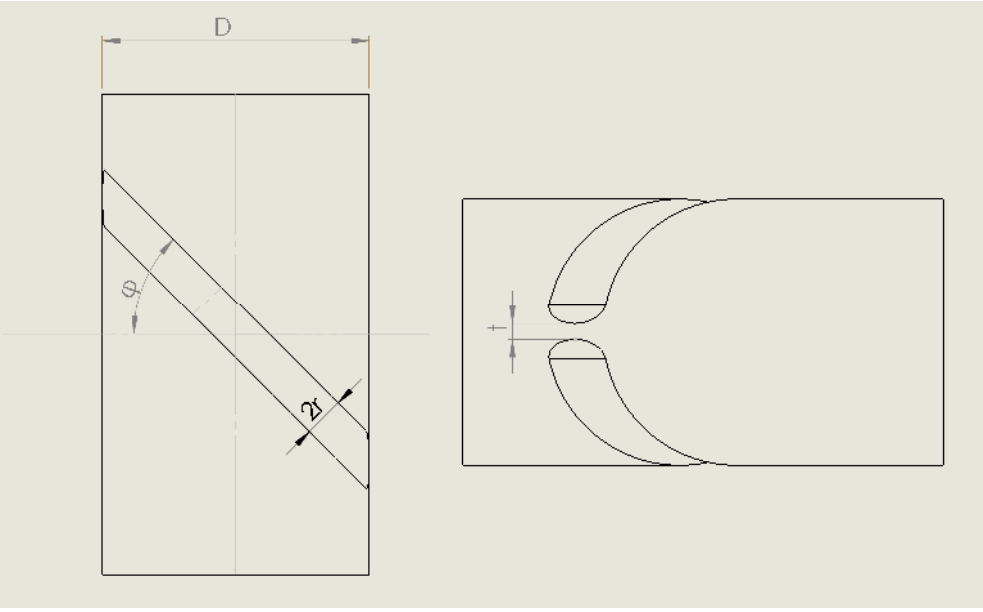

Figure 37 - Typical geometry of shear-compression sample

However, to process the raw data of the tests, a specific method coupling numerical simulations and experimental observations is required. Firstly, the geometry of the sample and of the experimental setup are created and assembled in a FEM software (ABAQUS® for this work) and a compressive load is applied on the sample. The results of the simulation will give the values (in function of the time) of the displacement of the two specimen interfaces d_1 and d_2 (and therefore the relative displacement of the specimen d), of the elastic strain of the output bar ε_{out} and of the equivalent plastic strain ε_{eq} and Mises equivalent stress σ_{eq} in the effective zone of the shear-compression sample (SCS). Some specific functions are introduced to evaluate ε_{eq} in function of d and of σ_{eq} in function of ε_{eq} and ε_{out} (Eq 2.17) [5].

$$\begin{cases} \varepsilon_{eq} = k_1\left(\frac{d-d_y}{h}\right) + k_2\left(\frac{d-d_y}{h}\right)^2 + k_3\left(\frac{d-d_y}{h}\right)^3 \\ \sigma_{eq} = k_4\left(1-k_5\varepsilon_{eq}\right)\frac{F^{k_6}}{Dt} \\ F = \pi R^2 E\varepsilon_{out} \end{cases} \quad (2.17)$$

With k_i empirical parameters linked to the geometry of the sample, r the radius of the groove, $h = \frac{2r}{\cos\varphi}$, d_y the displacement of the sample at yielding, D the diameter of the sample, t the thickness of the effective area, E the elastic modulus of the bar and R its radius (see Figure 10). The value of k_6 is set as 1 when the output force is important and computed when the force is low and need high precision.

The same procedure is used in quasi-static and dynamic (SHPB or Direct Impact): the output load and extension of the specimen are measured and then injected into the polynomial expressions for data processing.

The triaxiality through the whole effective section can be approximated by using Eq 2.18 (considering Von Mises criterion):

$$\sigma^* \sim -\frac{1}{3} - \ln\left(1 + \frac{R}{3r}\right)(1-\sin\varphi)^{\frac{1}{3}} \quad (2.18)$$

C. Analysis of the mechanical behavior of the materials

1. Analysis of the mechanical behavior of the F7020 aluminum alloy

a. Strain rate sensitive phenomena

It has been explained previously that the mechanical behavior of metallic materials is composed of two different stress responses: athermal and thermal stresses [25]. It has been observed that only the thermal stress presents a strain rate sensitivity. In fact, the two stress components of the thermal stress (internal and effective stresses) have their own specific strain rate response which have to be studied separately [26]. The mechanical behavior of the F7020 is studied here with compression tests (see Figure 38). The material is assumed isotropic due the nature of the SPS process.

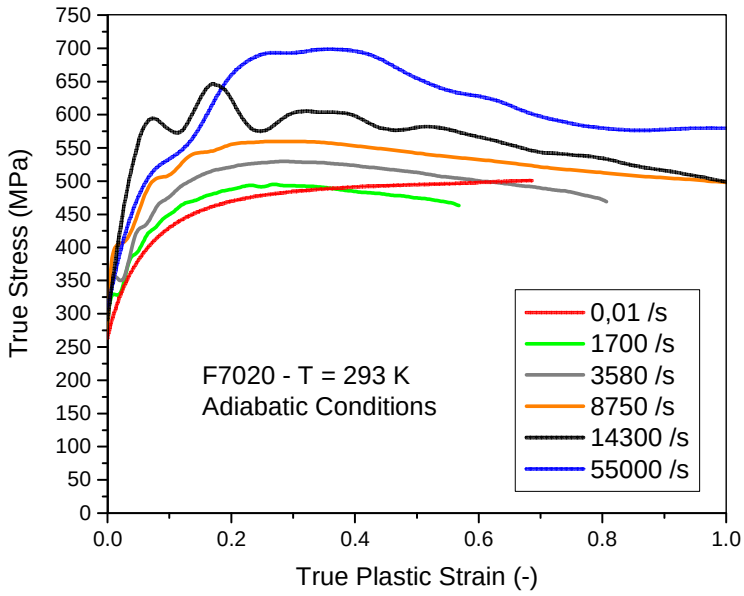

Figure 38 - Evolution of the stress vs strain curves of the F7020 with the strain rate in compression

1. Internal stress

The internal stress is the part of the stress corresponding to the contribution of the structural hardening of the metal. The strain rate sensitivity observed is caused by the difference of dislocation history between the samples which can be represented by the increase of the density of forest dislocations [27]. Therefore, this phenomenon can be observed for the FCC and HCP metals but not for the BCC metals

[28]. The experimental data (Figure 39) have been obtained through compression at room temperature with a uniaxial press for the quasi-static and intermediate conditions. The tests in dynamic conditions (from 0.0001 /s to 1 /s) have been carried out with a SHPB setup (from 500 /s up to 15,000 /s) and Direct Impact setup (from 10,000 /s to 55,000 /s). Other tests have been performed in shear-compression state of stress with the same experimental setups.

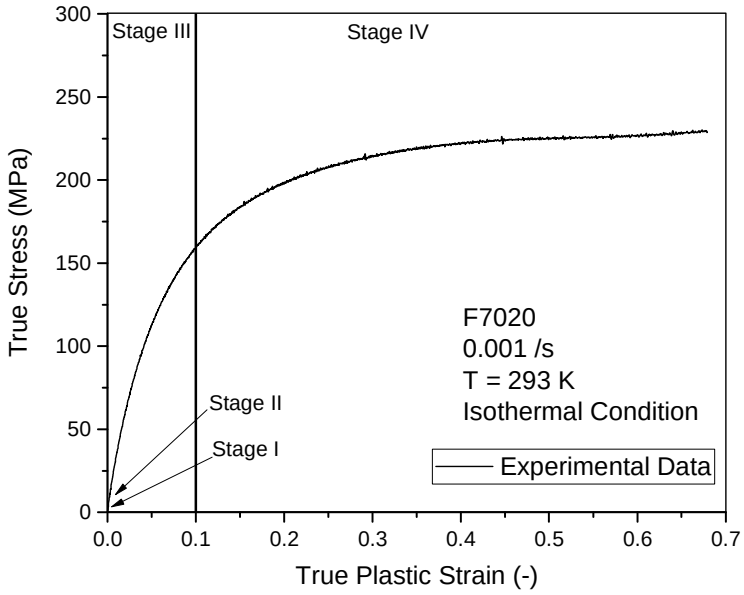

Figure 39 - Stress vs strain curve in quasi-static condition and room temperature of F7020 aluminum alloy

The Figure 39 shows the plastic hardening behavior due the multiplication of stored dislocations due to the propagation of the mobile dislocations (and Frank and Read sources) [27]. This kind of behavior is typical of metals presenting a kinematic hardening with a linear hardening at high strain. The stages III and IV of hardening are clearly visible on this curves, however, the stages I and II seem to be negligible [29].

An interesting phenomenon called Portevin-Lechâtelier effect [30, 31] can be observed on this stress vs strain curve (Figure 39). Indeed, the “noise” on the curve is in fact caused by the diffusion of atoms in the aluminum matrix which may cause the germination or the annihilation of dislocations (both phenomena are globally canceling each other). Due to the long characteristic time of diffusion phenomena, this effect generally only happens at low strain rates [32]. Indeed, at higher strain rates, the mechanical energy provided rapidly increases up to several order of magnitude higher than the one concerned in the Portevin-Lechâtelier phenomenon and the dislocations are not impacted anymore by this effect [33].

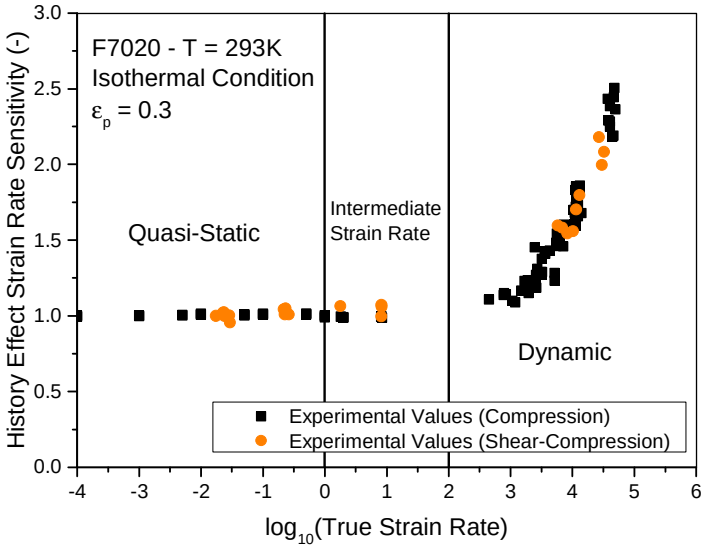

Figure 40 - Strain rate sensitivity of the internal stress due to history effect of F7020 aluminum alloy

Two main domains of strain rate sensitivities can be experimentally observed (Figure 40). In the quasi-static domain and up to the domain of intermediate strain rates, the strain rate dependency of the internal stress is quasi nonexistent. It can be interpreted that the thermo-activated phenomena concerning the evolution of the dislocation density require a constant level of energy to occur [34]. For the FCC metals, the phenomena leading to the strain rate sensitivity of the structural hardening is the creation and propagation of the forest of stored dislocations which are defining the stress history of the material [35, 36]. The density of forest dislocations is higher, at the same level of strain, for a stronger strain rate. If the increase of the strain rate over a considered range does not impact the stress history of the metal, it means that the velocity of the dislocations is slow or that the initial dislocation density is low [27]. Indeed, if the distance between two mobile dislocations which can create a forest dislocation is important (or if their velocity is low), the increase of the density of forest dislocations will be hardly visible leading to a quasi-inexistent strain rate sensitivity of the internal stress.

Another hypothesis about the non-sensitivity of the internal stress for the low strain rate range is the presence of several phenomena in competition. As explained above, if the initial density of dislocation is high enough, the density of forest dislocations may increase rapidly leading to a positive and observable strain rate sensitivity. But another phenomenon called Dynamical Strain Ageing (DSA) [37] can also cause a negative strain rate sensitivity. DSA is a common effect among aluminum alloys (e.g. AA5083 [37]). The negative sensitivity is explained by the presence of specific inclusions (such as precipitates) which are harder than the metallic matrix. At low rates, the mechanical energy provided to the dislocations is not sufficient to yield the hard precipitates. Therefore, the dislocations propagate around the inclusions in a restricted volume which is increasing the probability of mutual annihilation. The smaller the volume of free propagation is and the higher the strain rate is, the strongest will be the

rate of mutual annihilation. This leads to a decrease of the dislocation density and consequently of the internal stress. For a given microstructure, the DSA causes a negative strain rate sensitivity which can cancel the positive one caused by the increase of forest of dislocations density.

At higher strain rate (> 1000 /s), the other observable domain of strain rate sensitivity can be studied. Indeed, a sudden and exponentially positive sensitivity characterizes the dynamic domain. Such behavior can be explained by the stress originated from viscous drag effect [34] which as acquire a sufficient level to greatly influence the stress. This increase of the internal stress is considered monotonous for the strain rates above the highest one tested (55.000 /s) up to a saturation level (around 10^7 /s) caused by the overdriven shock regime [34, 38, 39].

It can also been noted that the strain rate sensitivity of the internal stress is the same in compression and shear-compression states of stress. It can therefore be concluded that the F7020 does not present an anisotropic sensitivity to the state of stress, that the triaxiality and the strain rate can be uncoupled.

2. Effective stress

The effective stress is the part of the thermal stress representing the contribution of the resistance of the lattice system to the strain. The main phenomenon responsible of this resistance is the presence of the energy required to move a dislocation, called the Peierls' energy E_P [27, 40, 41]. The higher E_P is the stronger the strain rate sensitivity will be.

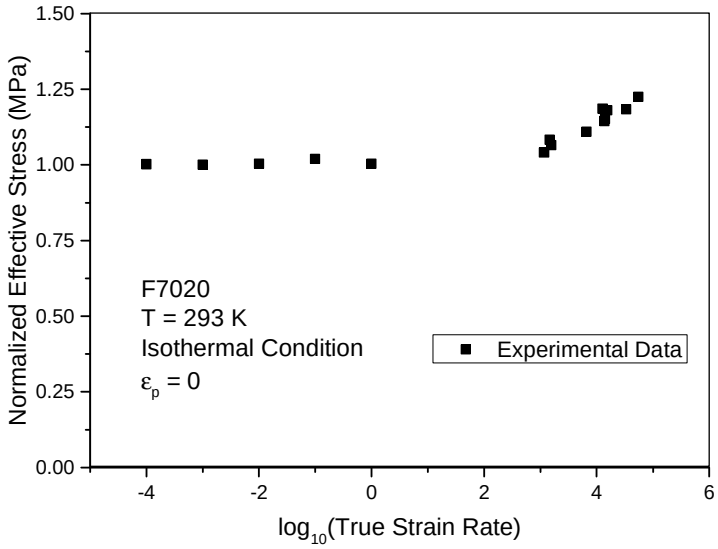

Figure 41 - Strain rate sensitivity of the effective stress of the F7020 aluminum alloy

The strain sensitivity of the effective stress is here analyzed as the normalized yield stress of the material at a given temperature (Figure 41). It can be seen that the effective stress displays hardly no rate

sensitivity over the quasi static range of strain rate. The rate dependency stays limited even in dynamic conditions. This behavior is typical of the FCC based metallic alloys which have generally a low Peierls' energy leading to a very little lattice resistance [28, 42]. The strain rate hardening caused by this phenomenon have a very low impact on the overall stress because of the very small base value of the lattice resistance.

b. Temperature sensitive phenomena

3. Athermal stress

The athermal stress is the part of stress which does not depend on the temperature [34]. For FCC metals, the assumption of the absence of athermal hardening is done [43]. Therefore, only the athermal yield stress (or effective yield stress) has to be determined. In this manuscript, the Eq 2.19 depending on the grain size is used [44]:

$$Y_a = \alpha\mu\left(\frac{b}{\langle D_g \rangle}\right)^2 \qquad (2.19)$$

With $\alpha = 0.3$ an empirical parameter, $\mu = 26.9$ GPa the shear modulus, $b = 0.286$ nm the Burgers' vector and $\langle D_g \rangle = 14$ µm the average grain size.

The value of the athermal yield stress can be easily computed and is: $Y_a = 36.5$ MPa

4. Thermal stress

In order to study the evolution of the thermal stress with the temperature, the calorific ratio [45, 46] needs to be introduced.

The calorific ratio f consists into the normalized evolution of the thermal stress with the temperature (in isothermal condition). It allows to visualize the thermal softening (or hardening) of a material and the potential microstructural changes (Figure 42.a).

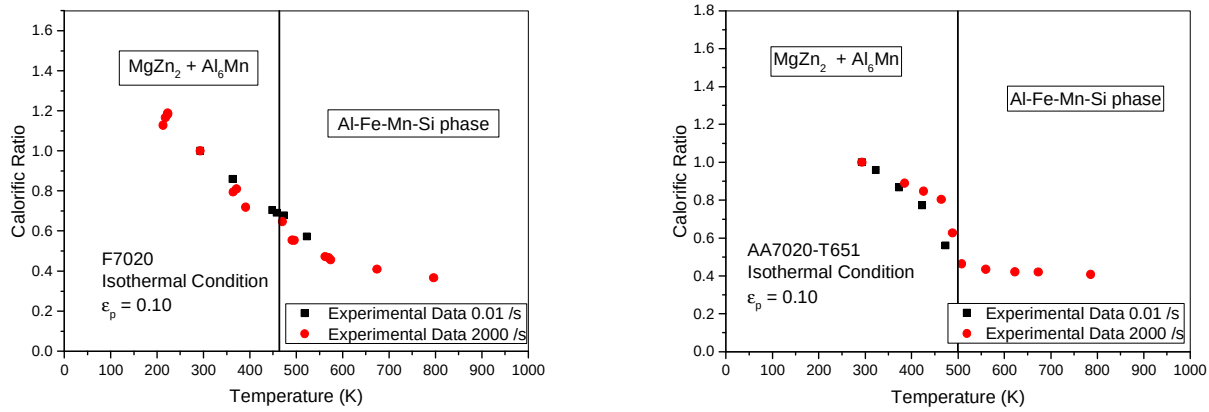

(a) (b)

Figure 42 - Evolution of the normalized thermal stress (calorific ratio) with the temperature in QS and dynamic cases of (a) the F7020 aluminum alloy and (b) the AA7020-T651 aluminum alloy

Two domains of thermal softening can be observed concerning the F7020. From room temperature (Figure 43.a) to around 490 K (temperature of dissolution of the $MgZn_2$ precipitates in the matrix [1, 2]), the thermal softening of the material is quite steep due to the progressive diffusion of the precipitate components into the matrix leading to the annihilation of dislocations (Figure 43.b). Around 490 K (Figure 43.c), the dissolution of the precipitates occurs. However the drop of the stress is very smooth and hardly visible unlike for the AA7020-T651 (Figure 42.b). Indeed, this last is a laminated material presenting a very high density of dislocations and especially around the precipitates. Therefore, during the dissolution of the precipitates, much less dislocations are annihilated for the F7020 than for the AA7020-T651 due to its more homogeneous density of dislocations.

After the dissolution of precipitates, the material is mainly composed of a dominant Al phase and a Al-Fe-Mn-Si phase [2] (Figure 43.d). The diffusion mechanisms are limited and the thermal softening of the F7020 is less steep than before the dissolution until reaching an athermal plateau around 700 K. A last massive diffusion mechanism occurs just before the melting point of the material (940 K), leading to the fusion of the F7020. The mechanical behavior is the then one of a fluid and is characterized by its viscosity.

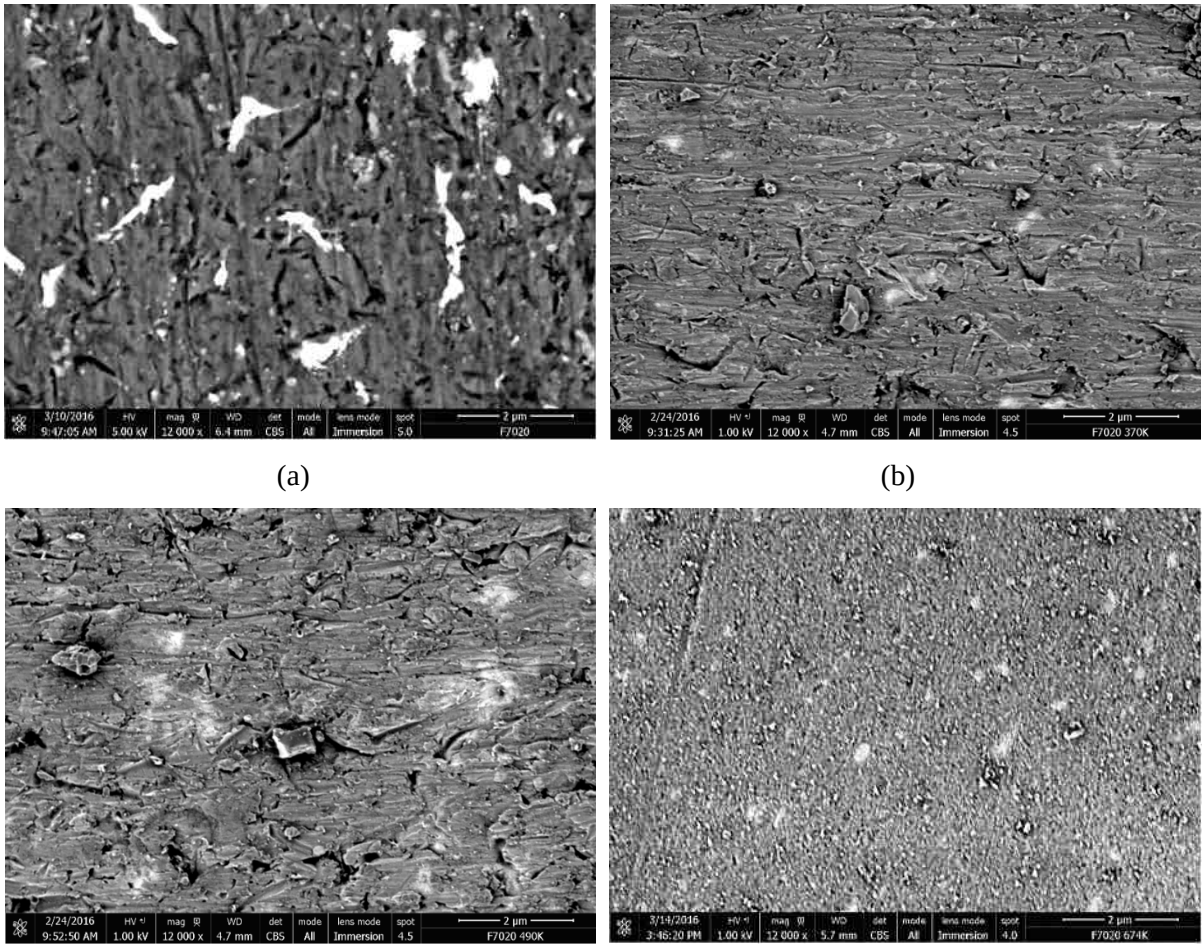

Figure 43 - SEM pictures of the F7020 (a) at 293K, (b) at 385K, (c) at 488K and at (d) 673K

The temperature/strain rate coupling of the F7020 seems to be limited but is still visible. It can be noted that the calorific ratio slightly decreases with the strain rate (between quasi-static and dynamic cases) showing a little rate dependency of the diffusion mechanisms. A much greater rate sensitivity has been observed with the AA7020-T651 concerning the temperature of dissolution of precipitates and of the diffusion mechanisms.

5. Adiabatic heating

The adiabatic heating is measured through the elevation of the sample temperature. Indeed, at high strain rates, a large fraction of the plastic work is converted into heat and is characterized by the adimensional Taylor-Quinney factor χ [38, 47-49]. In most cases, the value of the Taylor-Quinney factor is considered as equal to $\chi = 0.9$. However, it has been established that the value of the Taylor-Quinney coefficient is not constant with the strain and also shows temperature and strain rate dependencies [38, 49]. Some experimental methods exist to determine the evolution of χ during a dynamic tests such as measuring the temperature of the sample trough thermocouples (local measurement) or using optic methods such

as thermal high speed camera or emissivity measurement (surface measurement). Another method is suggested here by realizing repeated tests at small strain on the same sample [50] in order to prevent adiabatic heating softening effect on the stress (Figure 44).

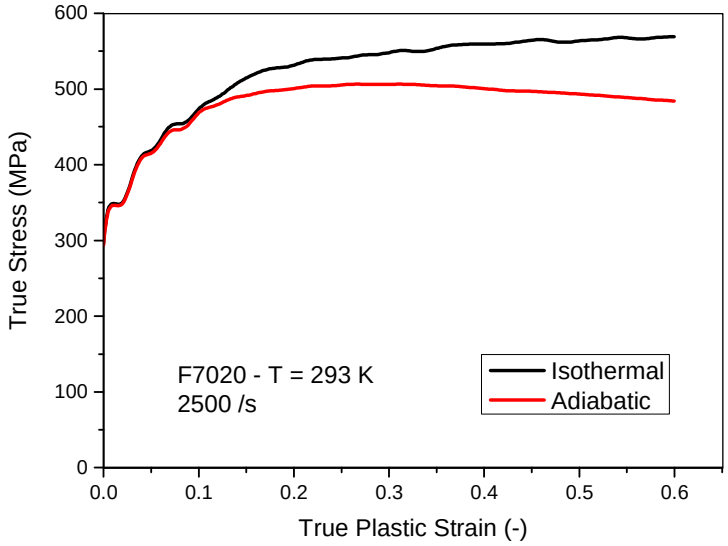

Figure 44 - Difference between isothermal and adiabatic stress vs strain curves of F7020 aluminum alloy

This method does not need any temperature measurement to operate. The isothermal test is then confronted to the adiabatic test performed at the same strain rate and through thermodynamic consideration, the Taylor-Quinney factor can be computed (see Appendix A). The method used to obtain the smoothed curve is explained as well in Appendix A.

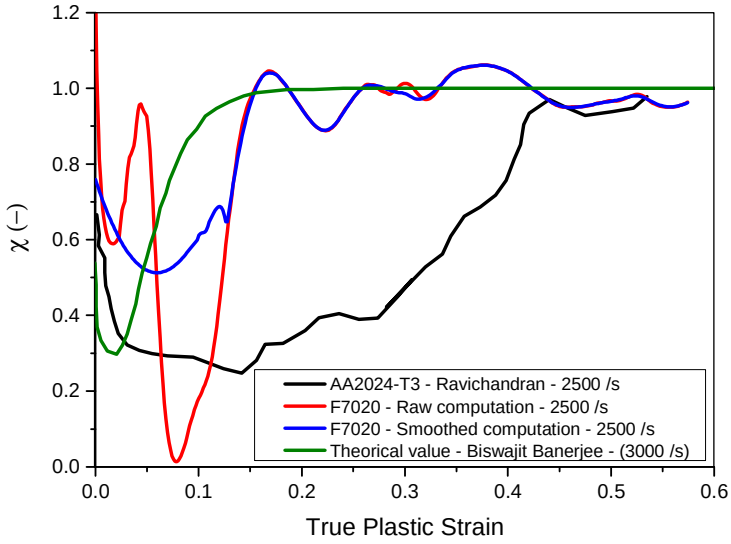

Figure 45 - Evolution of the Taylor-Quinney coefficient with the strain of F7020 aluminum alloy

It can be seen that the raw computation using the suggested method (Figure 45) gives highly variable results at small strain due to the very close values of isothermal and adiabatic stresses. Consequently, the computation is very sensitive at low strain.

Concerning the evolution of the Taylor-Quinney factor (Figure 45), the tendencies between the suggested method and the results obtained by Ravichandran on the AA2024-T3 [51] are similar: a decrease from an initial value around 0.7 down to a minimum and an increase up to 1 meaning a total conversion of the plastic work into heat. The average value $\langle\chi\rangle$ of the Taylor-Quinney coefficient of the F7020 over the computed range of strain is of $\langle\chi\rangle = 0.86$ for the raw computation and $\langle\chi\rangle = 0.88$ for the smoothed computation. The difference with other methods might come from the fact that it does not rely on temperature measurement which is not homogeneous through the sample and is difficult to estimate due to thermal resistivity and inertia depending on the studied material. However, the suggested method is closer to the theorical tendency [38].

It can be noted that the suggested method can only be applied for materials presenting only a negligible contribution of reversible strain phenomena. The Taylor-Quinney factor of polymers cannot be determined through this method due to generally the high viscoelastic strain range (around 0.1) and hyperelastic phenomenon generally encountered in the mechanical behavior of such materials.

Another interesting aspect to be studied about the adiabatic heating is the softening sensitivity of the material to this particular self-heating. Indeed, it can be noted that the loss of internal stress corresponding to the stored energy due strain hardening of the F7020 is increasing exponentially with the elevation of temperature due to adiabatic heating (Figure 46). This energy is in fact released as heat due to the viscous drag effect and causes the adiabatic heating effect.

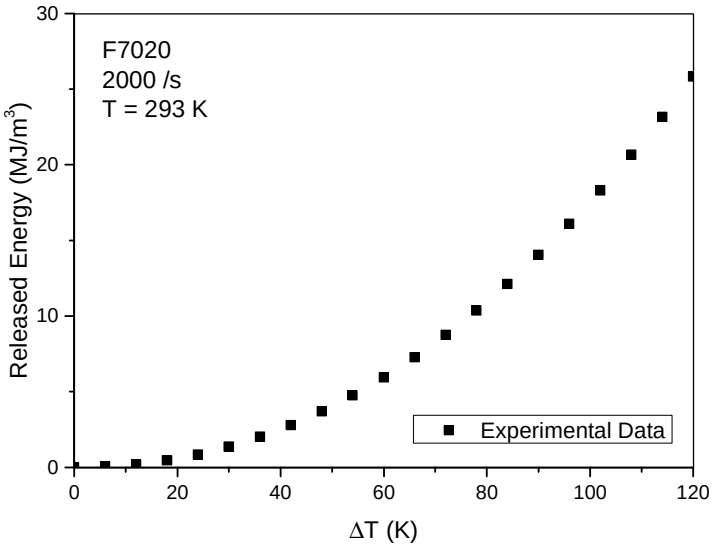

Figure 46 - Evolution of the amount of volumic energy released by the F7020 as heat due adiabatic effect

2. Analysis of the mechanical behavior of the sintered polyimides

The mechanical behavior of amorphous polymers can be explained through four main phenomena (Figure 47):

- The viscoelasticity phenomenon
- The yield stress defining the global level of stress (temperature and strain rate dependent)
- The hyperelasticity representing the resistance to the strain of the chain network (temperature and strain rate dependent)
- The strain softening is the results of relaxation phenomenon of the chains which causes a liberation of stored energy in the chains and a decrease of the stress.

The polyimide exhibits clearly each of these mechanical phenomena which can therefore be studied, interpreted and then modeled. Besides, this particular polymer shows a very strong mechanical behavior for a polymer. The mechanical behavior of the Polyimide is studied here with compression tests (the material is assumed isotropic due the nature of the SPS process).

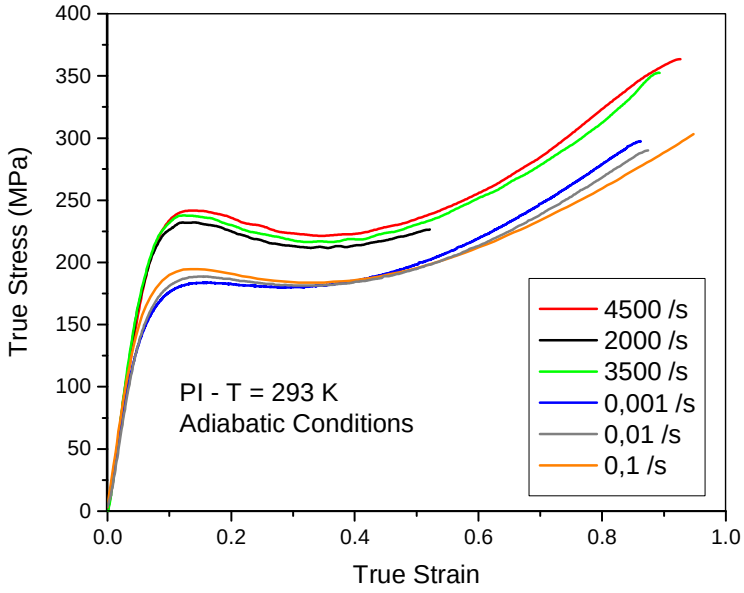

Figure 47 - Evolution of the stress vs strain curves of the sintered polyimide with the strain rate in compression

a. Thermo-elastic behavior of polyimide

The evolution of the equivalent elastic modulus of the polyimide with the temperature is reported in the Figure 48. It can be seen that the softening of the elastic properties of the polymer follows a nearly linear trend from room temperature up to the temperature of glass transition $T_g = 310°C$. This softening is due

to the diminution of the cross-linking of the chains with the temperature, leading to a loss of material rigidity [52].

No particular strain rate sensitivity of the elastic modulus has been measured during the tensile and compression tests. The elastic modulus will therefore be assumed strain rate independent for this study.

The elastic modulus has been evaluated as the mean slop of the elastic domain.

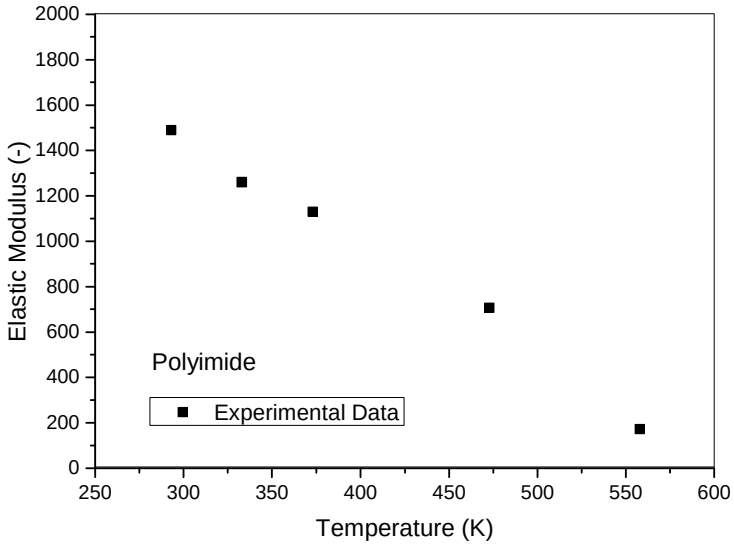

Figure 48 - Evolution of the average elastic modulus of the sintered polyimide with the temperature

b. Temperature/strain rate coupled behavior of the yield stress

The yield stress of polymers presents generally a strong temperature/strain rate coupled dependency [53-55]. Indeed, the level of stress is strongly dependent on the value of the free volume of the chains which depend greatly on the temperature [56]. Furthermore, the influence of the strain rate increases the stress threshold for yielding due to the higher resistance of the chains to the imposed movement.

The strain rate dependency of the yield stress of the polyimide is composed of two domains (Figure 49) at a given temperature (for the range of tested strain rate). Both domains are increasing monotonously with a steeper slop in the dynamic domain. This observation can be done for all the tested temperature, even if the slop in the dynamic domain becomes steeper when increasing the temperature and reveals the temperature/strain rate coupling [53, 57]. The stronger the entanglement of the chains is, the stronger the strain rate sensitivity will become [52].

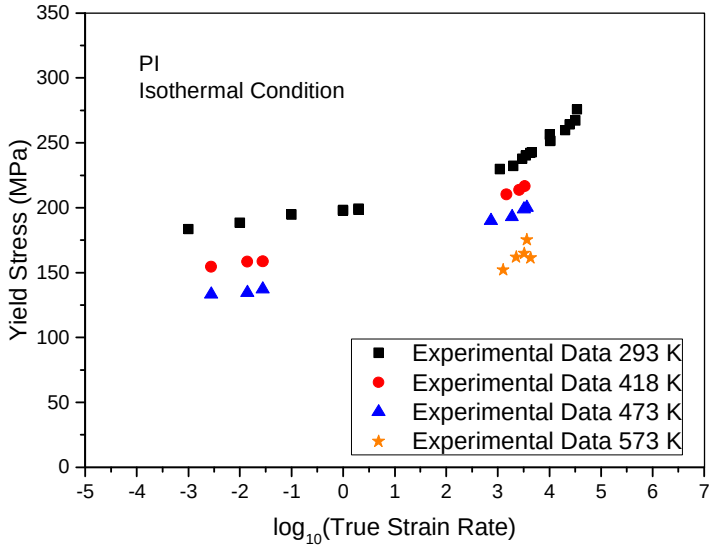

Figure 49 - Strain rate and temperature coupled sensitivities of the yield stress of the sintered polyimide

The polyimide presents only a linear thermal softening behavior (Figure 50) due to the diminution of the cross-linking of the chains [52]. However, the range of temperature tested starts at 293 K and finishes at 573 K which is below the temperature of glass transition ($T_g = 583$ K). The mechanical transition between the glassy state and the rubber state should therefore be very steep due to the quasi-absence of non-linearity even 10 K below T_g.

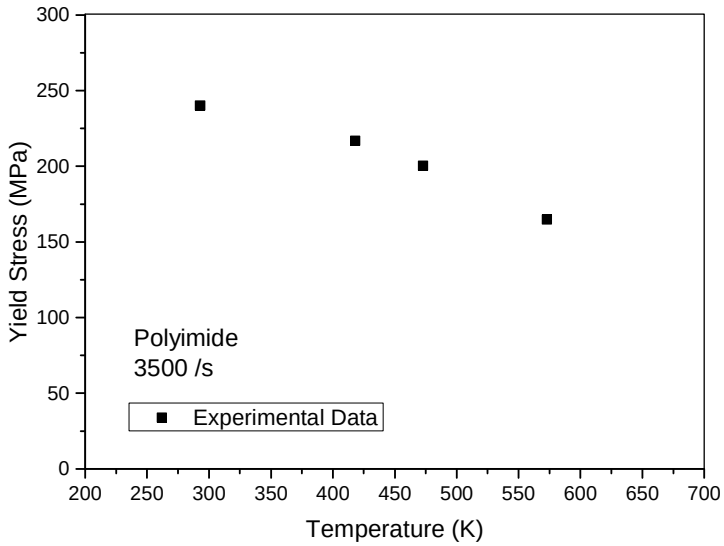

Figure 50 – Evolution of the yield stress with the temperature of the sintered polyimide

c. Hyperelasticity phenomenon

The hyperelasticity phenomenon is clearly visible on the mechanical behavior of the polyimide and is strongly dependent on the temperature [57, 58]. Indeed, the hyperelasticity response of the polymer decreases with the temperature and the limit at failure increases. These two phenomena can be evaluated through two figures: the rubber modulus C_R for the intensity of the hyperelasticity response and the locking parameter $N = e^{2\varepsilon_p^f}$.

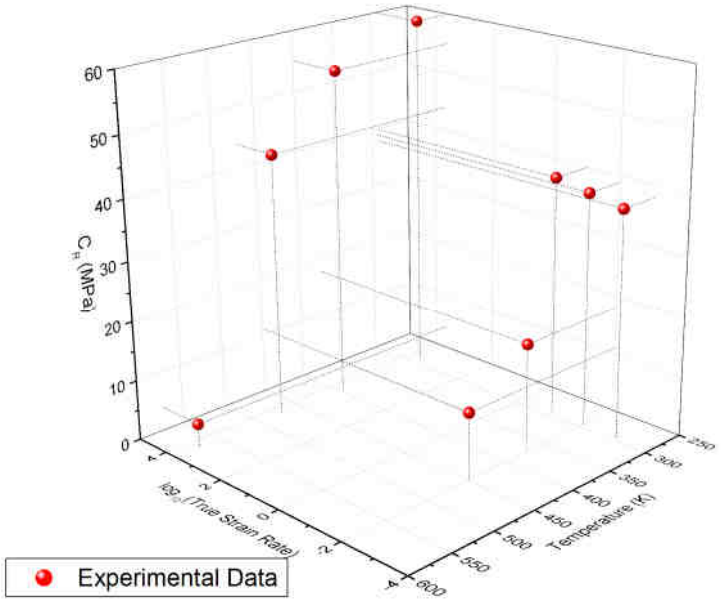

Figure 51 - Temperature and strain rate sensitivities of the rubber modulus of the sintered polyimide

The Figure 51 shows the experimental sensitivity of the rubber modulus C_R to the temperature [57] and the strain rate. It can be seen that the hyperelasticity behavior results in a hardening of the material when decreasing the temperature and increasing the strain rate. The softening of C_R with increasing temperatures is due to the much higher vibrations of the chains which cause an easier crawling phenomenon reducing the cross-linking level of the polymer chains [52]. The hardening of C_R with increasing strain rates is caused by the duration of the local strain of the chains which becomes shorter than the relaxation time of these lasts (which should allow an optimal reorganization of the molecules). Therefore, at high strain rates, the chains are interfering in the motion of the others more than at low strain rates. It can be assumed that the rubber modulus becomes null above the glass transition temperature for the polyimide. The observed temperature/strain rate coupled behavior of C_R has to be carefully modeled.

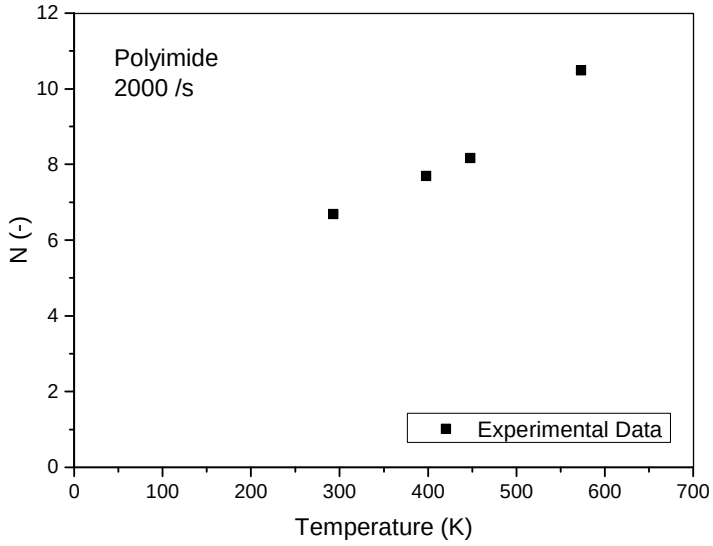

Figure 52 - Evolution of the locking parameter N of the sintered polyimide with the temperature

The locking parameter N is determined by evaluating the ultimate strain at failure of the polymer (Figure 52). It is increasing linearly with the temperature up to the glass transition temperature where it should stay constant [57]. The increase of N with the temperature can be explained by the easiest crawling phenomenon than for lower temperatures which limits chain interactions and therefore the strength imposed on them. No strain rate sensitivity has been detected for the polyimide. Therefore, the chain structure seems to have no entanglement high enough to get its locking influenced by the strain rate (except at the higher strain rates tested above 10.000 /s) [59].

d. Strain softening phenomenon

The strain softening corresponds to the effect of chain relaxation after yielding which leads to an optimal reorganization of the chain network [3, 56, 60]. A lot of molecules are less stretched during this phenomenon and it results in a release of energy of the material at the macroscopic level. The balance of energy can be observed by considering the ratio of the energetic balance of the full experimental mechanical behavior of the polymer and of the estimated behavior considering only the yield stress and hyperelasticity phenomena. More explanation are provided in the next chapter about the mathematical modeling of the phenomenon.

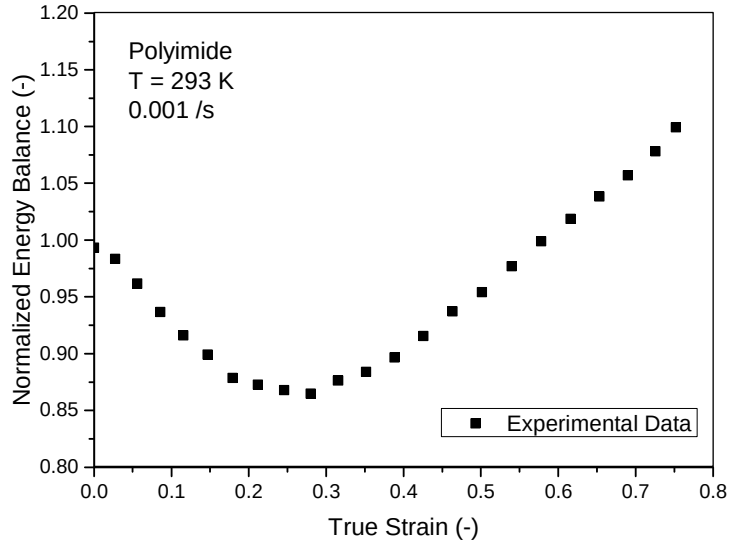

Figure 53 - Evolution of the normalized energy balance with the strain of the sintered polyimide

Figure 53 shows the evolution of the normalized energetic balance with the strain. It can be seen that the material releases some stored energy to reach a minimum balance at $\varepsilon_p \sim 0.27$ and then increases up to the ultimate failure of the material. This increase can be interpreted as the opposite phenomenon of the relaxation which is the friction between the stretched molecules.

A slight temperature dependency can be observed between the experimental curves at different temperatures (Figure 54). Indeed, it can be clearly seen that intensity of the strain softening phenomenon is decreasing with the temperature.

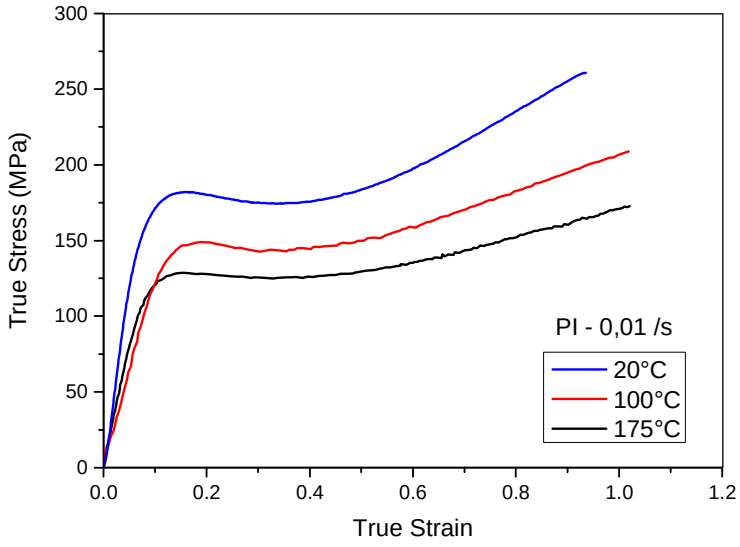

Figure 54 - Stress vs strain curves of the sintered polyimide at low strain rate and different temperatures

3. Analysis of the mechanical behavior of the epoxy resin

The mechanical behavior of the epoxy resin is studied here (Figure 55) with compression tests (the material is assumed isotropic due the nature of the shaping process).

The mechanical behavior of the epoxy resin shows the same phenomena as the polyimide (yield stress, strain softening and hyperelasticity). However, it can be noted a few differences. Firstly, the epoxy resin is much more strain rate sensitive than the polyimide. This is mainly due to the fact that the epoxy resin is a thermoset polymer which presents a stronger entanglement than the thermoplastic polyimide. Secondly, the impact of the adiabatic heating is much more important for the epoxy resin than for the polyimide causing a strong thermal softening of the material for high strain rate conditions. This is due to the low temperature of glass transition which is quickly reached in dynamic conditions and the rubber behavior of the polymer becomes preponderant.

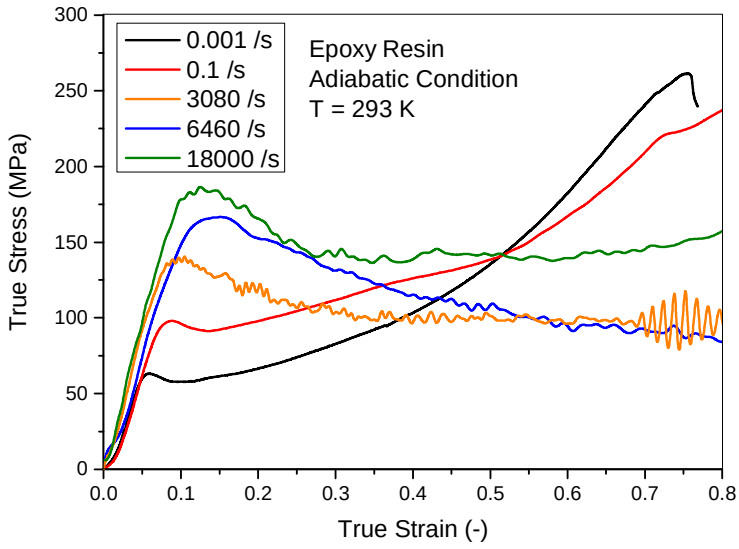

Figure 55 - Evolution of the stress vs strain curves of the epoxy resin with the strain rate

a. Thermo-elastic behavior

The studied epoxy resin also exhibits a strong softening of the elastic properties with the temperature (up to the temperature of glass transition $T_g = 333$ K) due to the very high initial level of entanglement of the chains which decreases rapidly with the temperature [52]. The T_g being close to room temperature, the softening is highly non-linear. However, contrary to the polyimide, the elastic properties of the epoxy resin show a strong strain rate dependency with an elastic modulus increasing from 0.2 GPa up to 2 GPa from quasi-static to dynamic conditions (at room temperature) [52, 61]. The elastic modulus has been evaluated as the mean slop of the elastic domain (Figure 56).

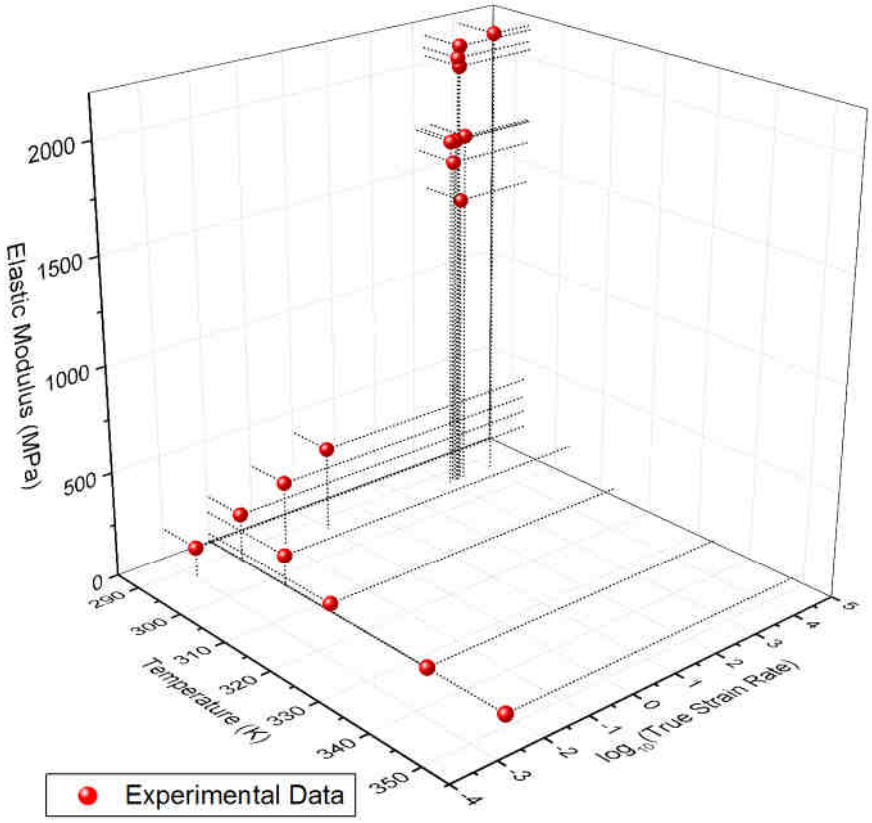

Figure 56 - Evolution of the average elastic modulus of the epoxy resin with the temperature and the strain rate

b. Temperature/strain rate coupled behavior of the yield stress

The evolution of the yield stress with the strain rate of the studied epoxy resin is nearly linear for all the tested temperatures (Figure 57). However, as for the polyimide, two domains exist with two different slops (which are here nearly the same). The first one characterizes the quasi-static domain and the other one the dynamic domain of strain rates (above 100 /s). In both domains, the strain rate sensitivity is very strong and can be explained by the high entanglement of the chains in such thermoset polymer [52].

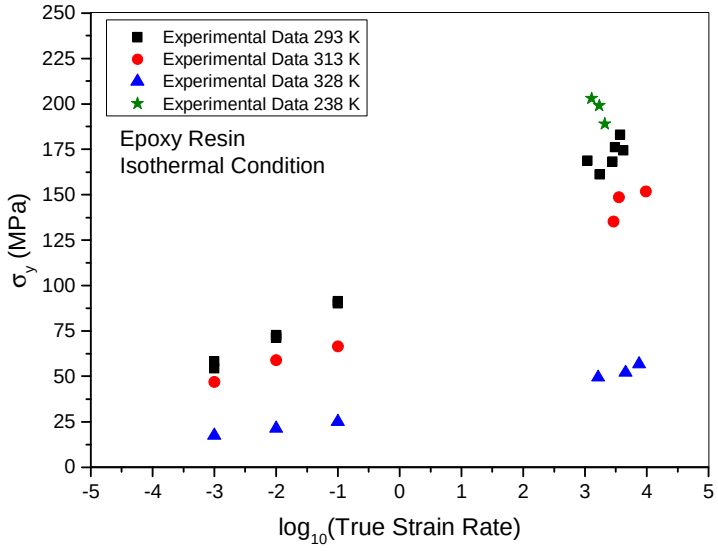

Figure 57 - Temperature and strain rate sensitivities of the yield stress of the epoxy resin

The figure 58 shows that the thermal sensitivity of the yield stress is highly nonlinear over the tested range of temperatures. This is due to the fact that the glass transition temperature of the epoxy resin is low and the mechanisms of chain diffusion from glassy state to rubber state greatly soften the polymer by the diminution of the level of cross-linking (Figure 58) [52]. In the case of this epoxy resin, the yield stress cannot be observed above T_g (Figure 59). Therefore, the mechanical behavior can be represented by a hyperelastic law above this temperature (in the quasi-static case).

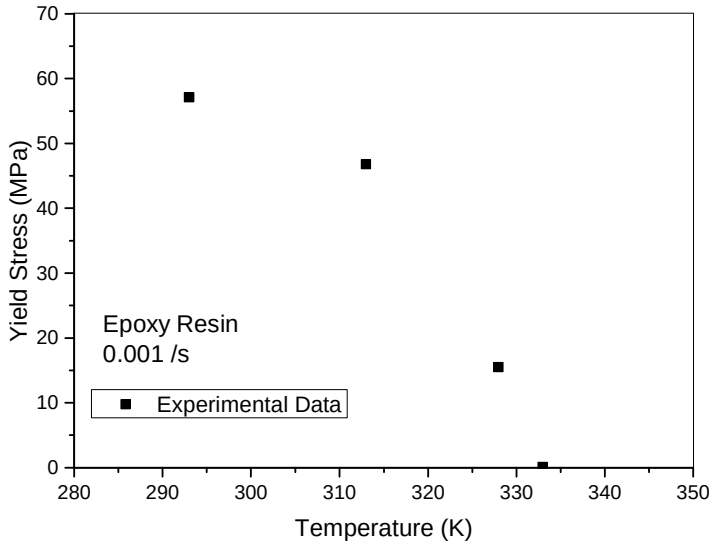

Figure 58 - Evolution of the yield stress of the epoxy resin with the temperature at low strain rate

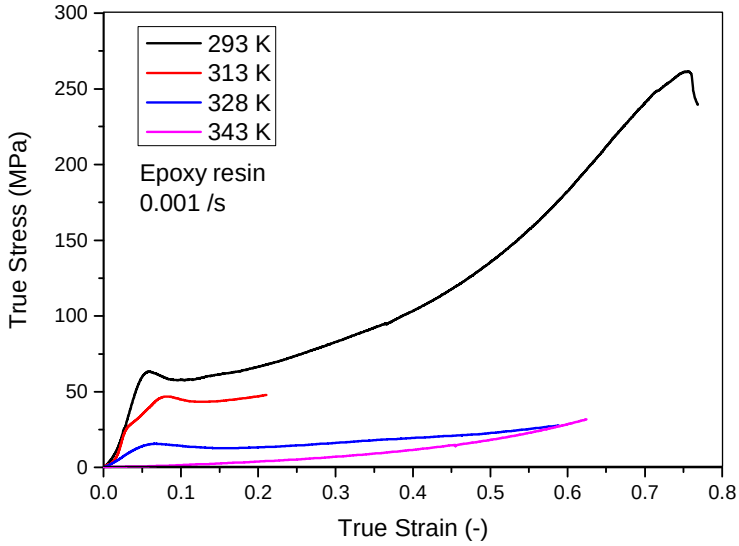

Figure 59 - Stress vs strain curves of the epoxy resin at low strain rate and different temperatures

c. Hyperelasticity phenomenon

The strain rate sensitivity of the hyperelasticity behavior of the epoxy resin is difficult to study due to the low temperature of glass transition. Indeed, the adiabatic heating encountered at high rates of deformation allows to observe only the rubber behavior of the polymer which does not seem to present any hyperelasticity phenomenon in this domain of strain rates (see Figure 60). However, the quasi-static cases provide exploitable data due to the high strain rate sensitivity of the overall mechanical behavior of the polymer.

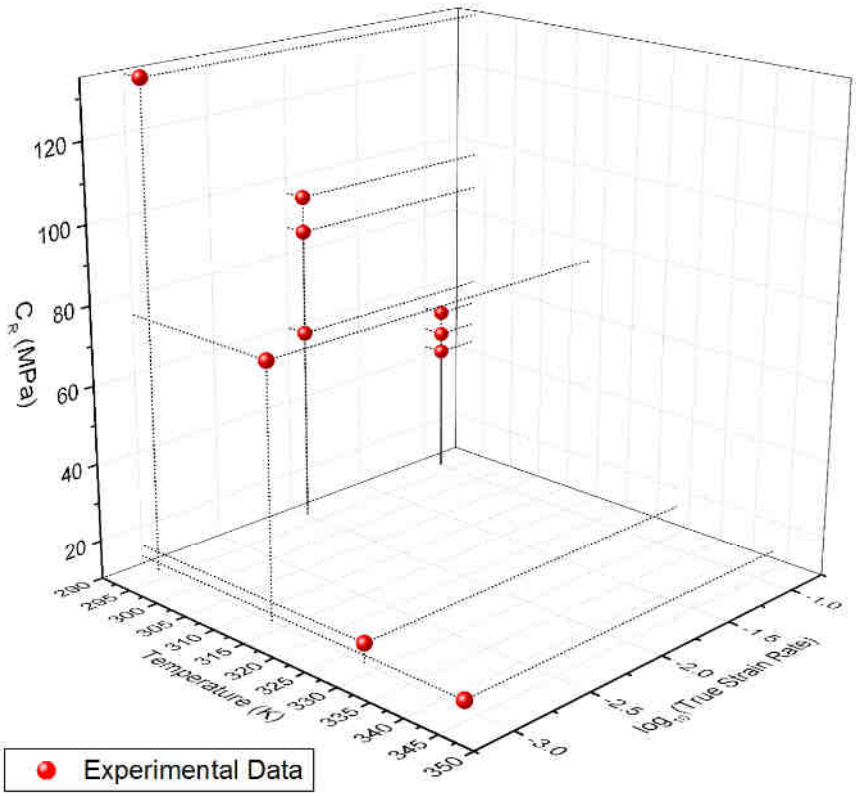

Figure 60 - Temperature and strain rate sensitivities of the rubber modulus C_R of the epoxy resin

It can be observed on the figure 60 that the rubber modulus C_R [57] decreases with the strain rate. The thermal sensitivity of C_R is also strictly negative up to the temperature of glass transition (for the same reason as for the polyimide, see d.iv section) where it seems to get an athermal behavior around 12 MPa for the quasi static behavior. At high strain rates (at temperature above T_g), the hyperelasticity phenomenon is not visible (see Figure 61) and this observation is in agreement with the temperature/strain rate coupled behavior studied at the lower rates of deformation. The negative strain rate sensitivity of C_R could be explained by a slight adiabatic heating leading to the softening of the hyperelastic behavior leading to the decrease of the level of chains entanglement and therefore of the material rigidity [52]. Such early adiabatic heating phenomenon can be explained by this same particularly high level of cross-linking in the epoxy resin causing a lot of internal friction during the deformation. The validation of this hypothesis can only be done by knowing the Taylor-Quinney coefficient of the polymer for this range of intermediate strain rate. Therefore, for the simplification of the study, the C_R of the epoxy resin will be assumed to have the experimentally studied negative strain rate sensitivity.

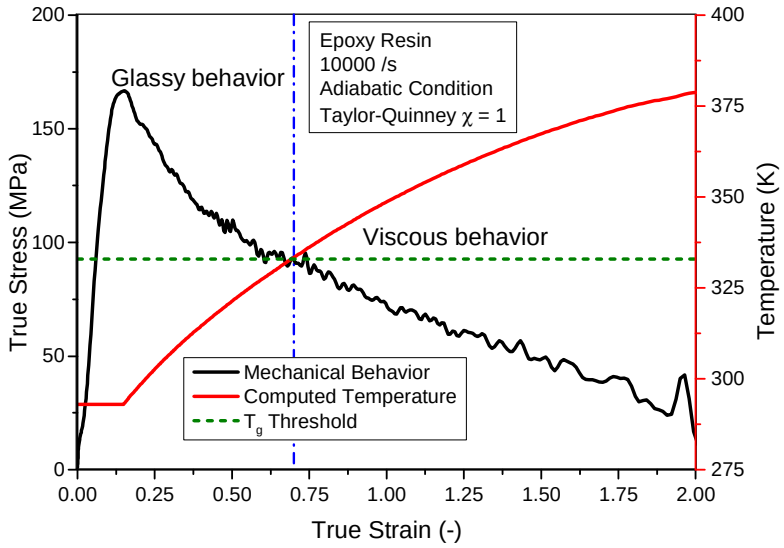

Figure 61 - Illustration of the phase transition from glassy to rubbery of the epoxy resin due to adiabatic heating

Concerning the locking parameter N [57], it can be observed, contrary to the polyimide, a strain rate and a temperature sensitivities of this parameter for the epoxy resin (Figure 62). This study leads to the assumption of a rate/temperature coupled behavior of the locking parameter. The high dispersion of the strain rate sensitivity can be explained by the high level of chain entanglement. In those conditions, the spatial organization of the molecules due the strain rate cannot be neglected. Indeed, for such large structure of chains, the characteristic time of relaxation is very high and therefore a small increase of the strain can lead to premature locking of the structure and to the failure of this last. The failure of such structure being more brittle than ductile, it results into a large dispersion of the value of N.

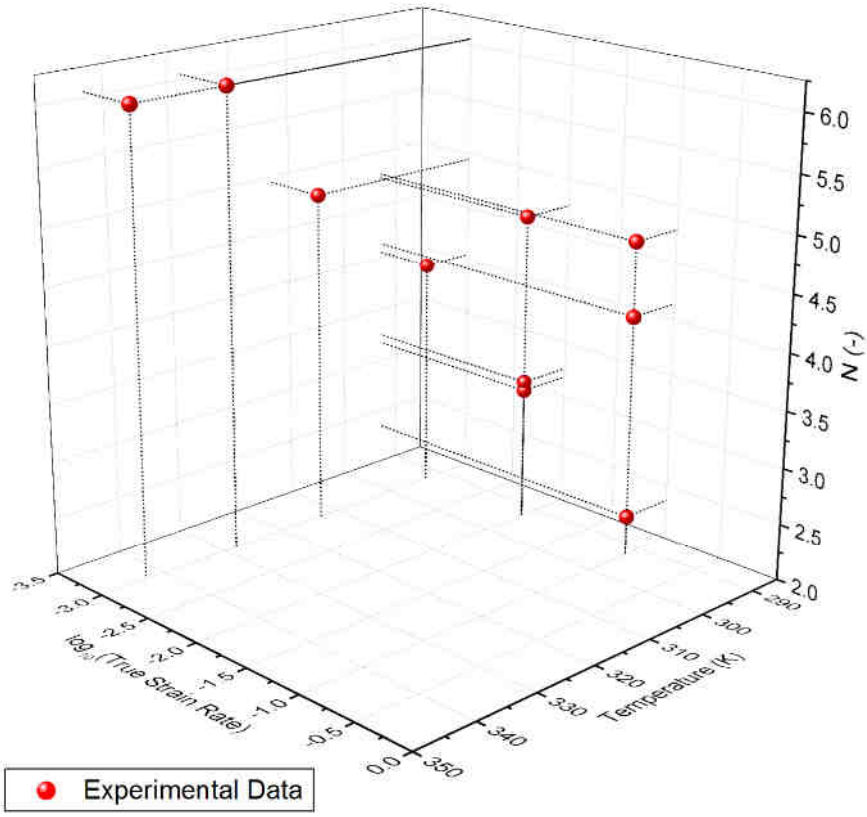

Figure 62 - Evolution of the locking parameter N of the epoxy resin with the temperature and the strain rate

d. Strain softening phenomenon

As for the polyimide, a strain softening phenomenon can be observed for the epoxy resin. The level of the normalized energetic balance (Figure 63) is nearly the same as for the polyimide (Figure 53). However, the minimal energetic "plateau" is reached before ($\varepsilon_p \sim 0.125$) and lasts for a longer range of strain than for the polyimide (up to around $\varepsilon_p \sim 0.3$). Therefore, it can be deduced than the epoxy resin (thermoset) releases its stored energy during the relaxation phenomenon in a different way than the polyimide (thermoplastic).

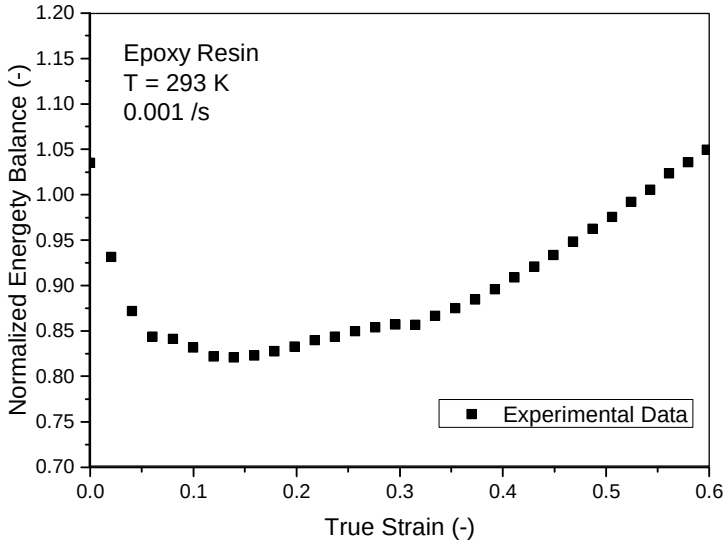

Figure 63 - Evolution with the strain of the normalized energy balance of the epoxy resin

D. Analysis of the failure and damage behavior of the materials

The characterization of the mechanisms leading to the failure of the materials are of the upmost importance in mechanical modeling of critical parts in structure. The criterion used in this work is the plastic strain at initiation of failure ε_p^f. However, the term "plastic" maybe removed to alleviate the text.

1. Analysis of the failure and damage behavior of the F7020 aluminum alloy

a. Triaxiality sensitivity of the strain at initiation of failure

The sensitivity to the state of stress of the strain at initiation of failure of the F7020 has been studied with different kind of tests in quasi-static conditions (see technical drawings Appendice B):

- Tension tests

The tensile samples used in this study have been designed through numerical simulation for the F7020 in order to prevent plastic deformation outside of the effective zone. The geometry has been validated through Digital Image Correlation (with GOM Correlate® software) during the test (Figure 64). The criteria for the validation were the homogeneity of the strain field in the effective zone and the absence of plasticity outside of the effective zone.

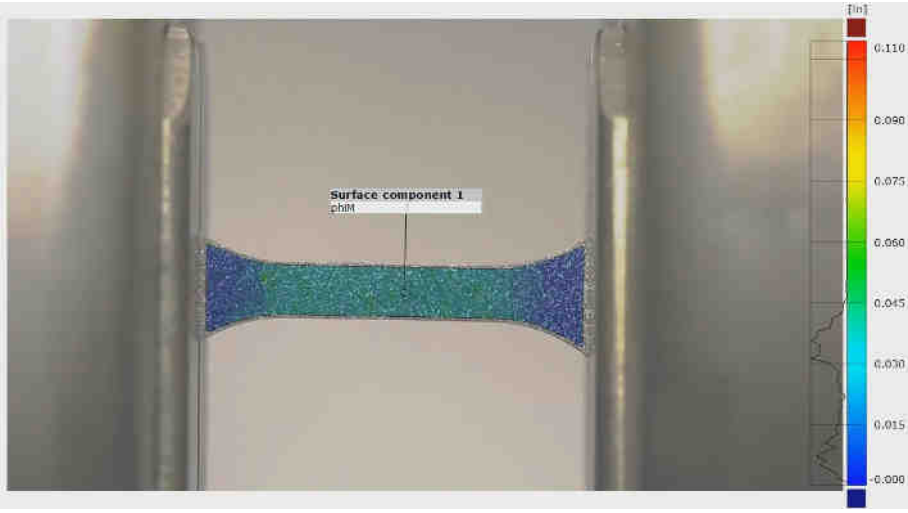

(a)

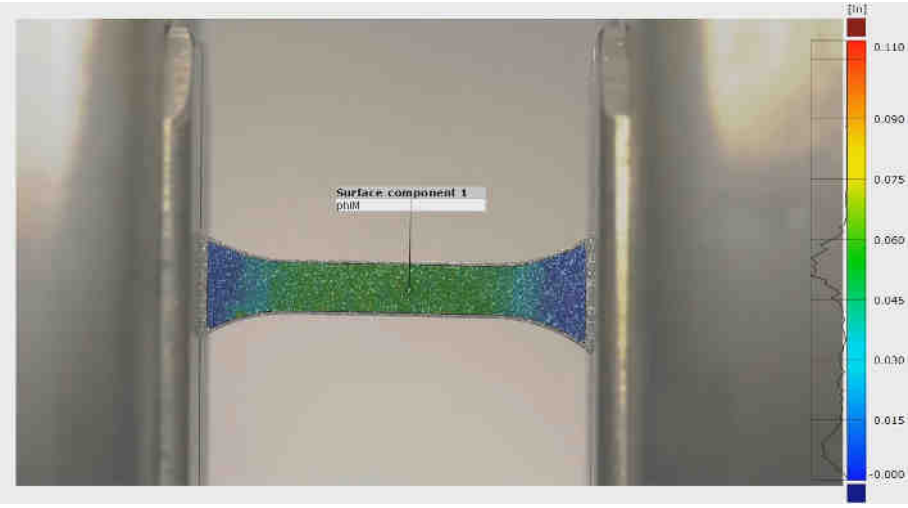

(b)

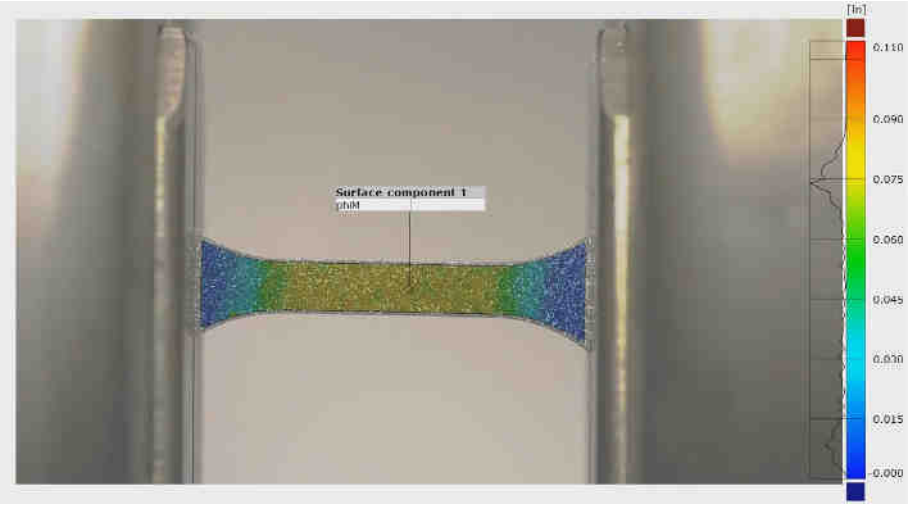

(c)

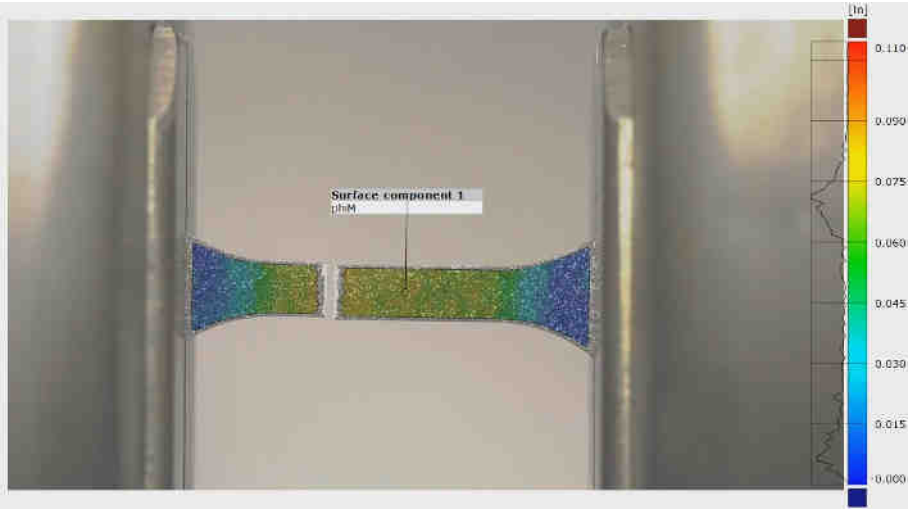

(d)

Figure 64 - Digital Image Correlation on tensile tests of F7020 at (a) beginning of the test, (b) during the test, (c) just before failure and (d) just after failure

The stress vs strain curves of the quasi-static tensile tests (Figure 65) show a brittle failure mode even before reaching the Consider criterion. Therefore, no visible ductile damage have been measured before failure. The Digital Image Correlation analysis shows a good homogeneity of the strain field and no necking (revealing the presence of damage mechanisms) has been observed over the duration of the test. These observations validate the recorded data and confirms the absence of ductile failure. The energy absorbed by the material between the initiation of failure and the ultimate failure can therefore be neglected in the case of tensile state of stress. The triaxiality of tensile test can be highly variable during the deformation in the presence of necking phenomenon [62, 63]. However, due to the absence of such effect and the relatively low strain at initiation of failure, the state of stress is assumed constant over the whole test with $\sigma^* = \frac{1}{3}$. The normalized third stress invariant and the Lode parameter of such solicitation have also been evaluated through numerical simulation for the whole section and worth respectively $\xi = 1$ and $\theta = 1$.

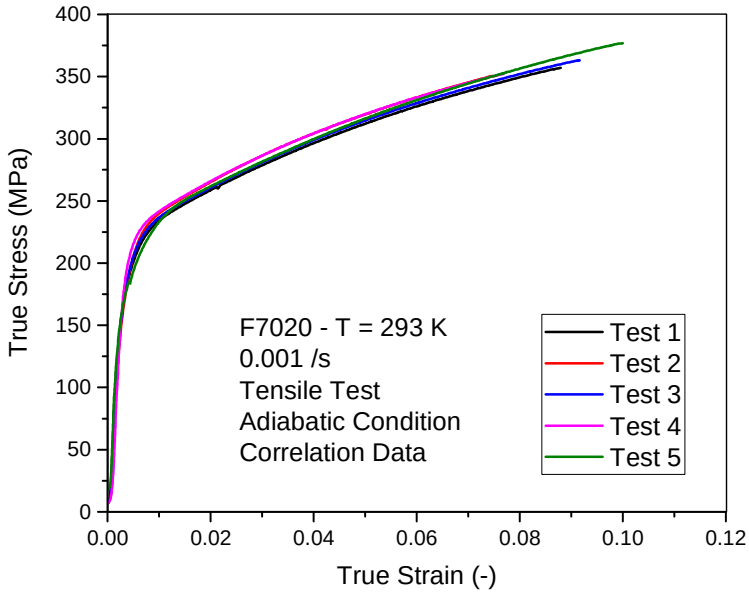

Figure 65 – Quasi-static tensile stress vs strain curves of F7020

The mechanism responsible of the failure for positive state of stress solicitation is the decohesion of the sintered powder grains (see Figure 66). Therefore, such tests are only giving the mechanical response of the sintered structure and not the intrinsic material properties. The temperature and strain rate sensitivities of ε_p^f cannot be studied through this kind of tests with positive state of stress.

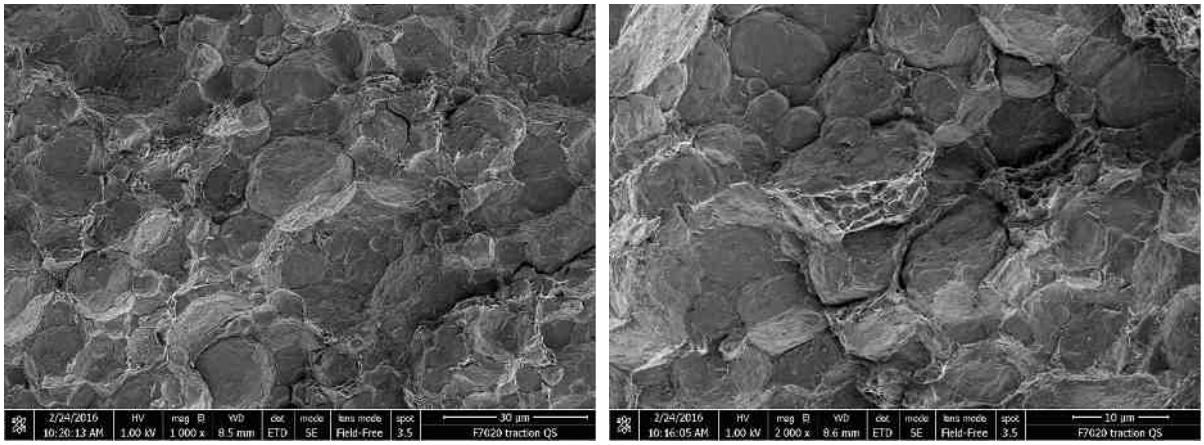

(a) (b)

Figure 66 - SEM pictures of fracture profile of F7020 tensile samples (ET detector) (a) x1000 and (b) x2000

The SEM pictures (Figure 66) show the fracture profile of the F7020 after a loading with a positive state of stress (tensile quasi-static). It can clearly be seen that the failure is due to the essentially decohesion of the powder grains [64-66] (Figure 66.a). The tensile resistance of the intergranular structure is therefore much lower than the one of the sintered powder grains (intragranular mesoscopic scale). These properties lead to a brittle failure of the material due to a structural effect and this kind of tests cannot be used for the study of the material properties (sensitivity to the temperature or to the strain rate). Another kind of test leading to the yielding of the grains powder has to be used for this purpose. It can be noted that few powder grains are presenting the signs of a yielding process (see cupules in Figure 66.b). These particular grains were surrounded by other grains and could not be submitted to the process of decohesion like the others. The yielding process was the only mean for these grains to allow the failure of the material.

- Axisymmetric notched tension

The axisymmetric notched tension tests have been carried out with the same experimental setup as the classic tension tests. The geometries have also been developed using numerical simulation and validated with experimental tests with the same criteria used for the tensile tests. For this test, the Digital Image Correlation (Figure 67) was clearly the most accurate mean of measurement for the extension due to the very small dimensions of the notches.

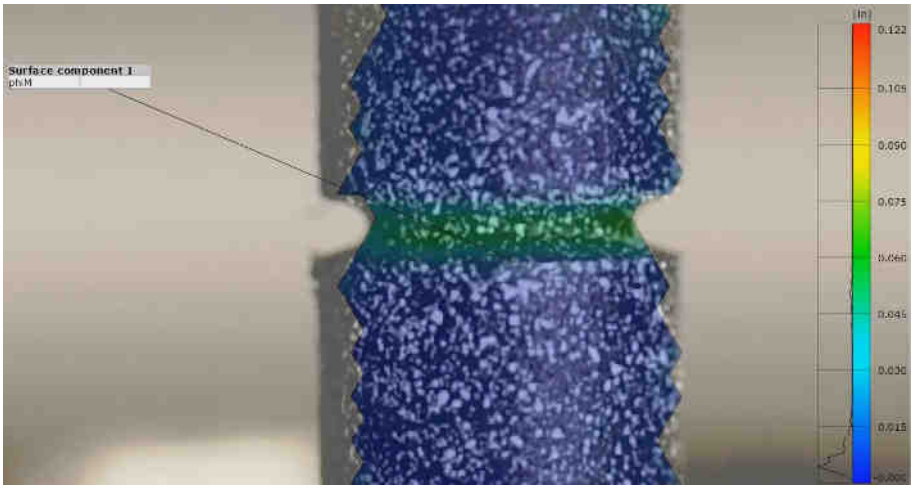

(a)

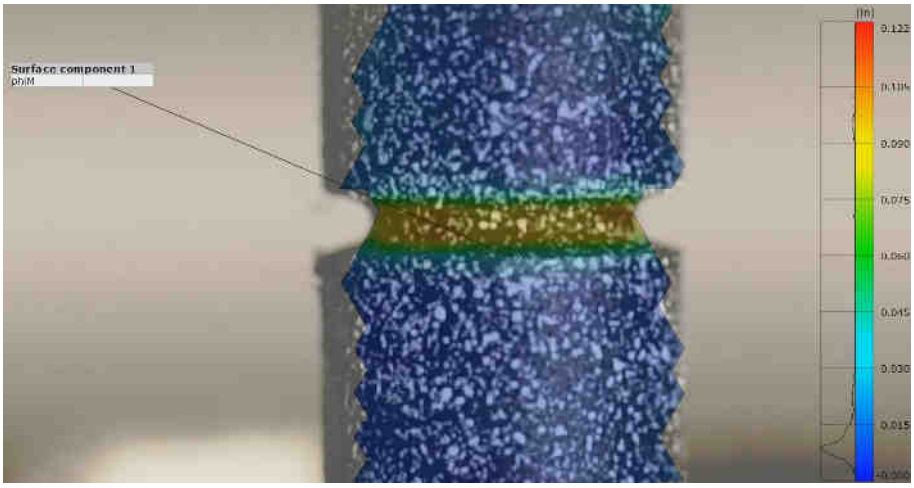

(b)

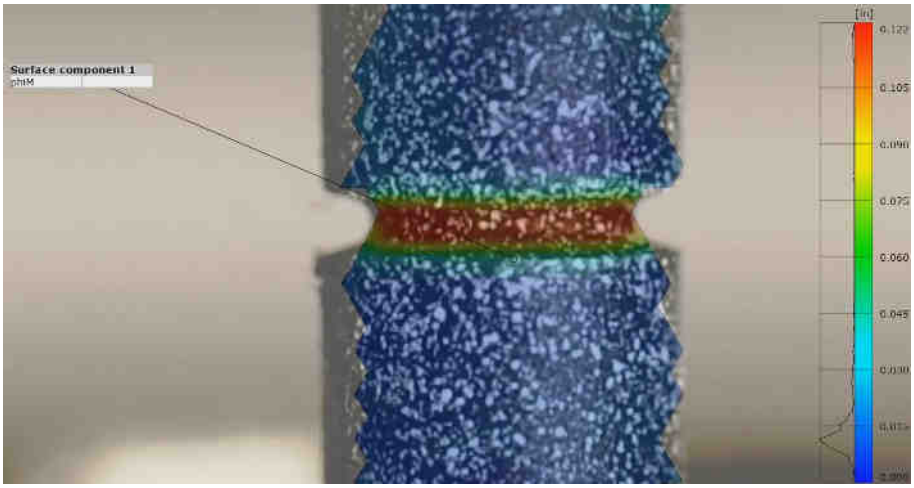

(c)

Figure 67 - Digital Image Correlation on notched tensile tests of F7020 at (a) beginning of the test, (b) during the test and (c) just before failure

The stress vs strain curves (Figure 68) display a mechanical behavior similar to the classic tension tests: the absence of ductile damage after the initiation of failure leading to a very small damage energy. This behavior is confirmed with the observation of the results obtained with the Digital Image Correlation analysis with the absence of necking or any other important modification of the local geometry have been noticed. It can be noted that the level of stress for the test with the smaller notch radius is much higher (see technical drawing in the Appendice B).

The values of triaxiality of both notched tension specimen have been computed for the whole duration of the test over the whole section with ABAQUS® simulation and no significant variation over the range of experimental strain has been revealed. The mean value of triaxiality of the section are $\sigma^* = 0.68$ for a notch radius of $R = 0.8$ mm and $\sigma^* = 0.98$ for a notch radius of $R = 0.4$ mm. The normalized third stress invariant and the Lode parameter have also been computed through the whole section and worth respectively, as for the classic tension tests, $\xi = 1$ and $\theta = 1$.

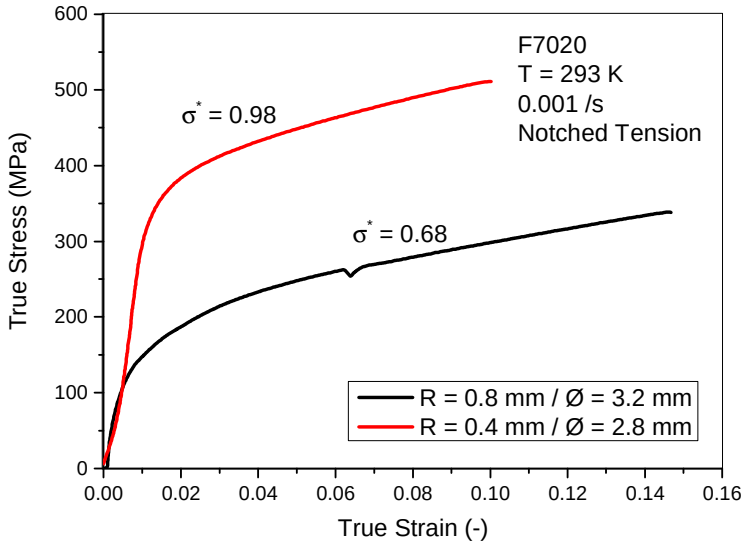

Figure 68 - Equivalent stress vs strain curves of F7020 for notched tension tests

- Shear-compression

The shear compression tests [5] have been used to get the values of strain at failure for negative triaxiality cases (propagation of cracks generated through the germination of adiabatic shear band). For this purpose, different kind of geometries of sample have been developed through numerical simulations (ABAQUS®). The criterion of validation of the test is a homogeneous stress/strain field through the whole effective section. These geometries differ by the angle of the notch with the perpendicular with the cylinder axis. Four different angles have been tested: 45° (classic shear-compression), 30°, 20° and 10° (no failure measured) with a thickness of the effective section of t. The respective mean triaxialities,

normalized third stress invariant and Lode parameter have been computed over the whole effective section and are reported in Table 8.

Table 8 - State of stress characteristic values of the different shear-compression tests

t = 0.6 mm	σ^*	ξ	θ
45°	-0.358	-0.83	-0.965
30°	-0.427	-0.57	-0.780
20°	-0.593	-0.24	-0.368
10°	-1.059	-0.03	-0.061
t = 1.6 mm	σ^*	ξ	θ
45°	-0.293	-0.86	-0.976

The main advantage of the shear-compression tests is the shearing of the powder grains and therefore the existence of ductile damage. It can also be noticed that the strain at initiation of failure increases with decreasing state of stress until becoming non measurable for the geometry presenting the smaller angle.

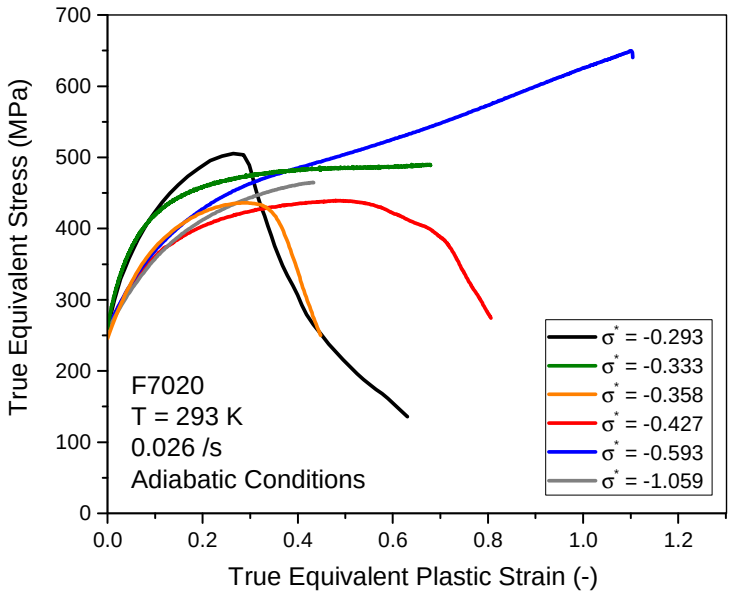

Figure 69 - Equivalent stress vs strain curves for the different shear-compression tests

The equivalent stress vs strain curves (Figure 69) show a particular behavior of the material over the negative range of tested states of stress. Indeed, two different levels of stress can be noticed. The first one gathers the tests with a triaxiality above the state of compression ($\sigma^* \geq -0.33$) which is higher than the second category which brings together the cases below the state of compression. It can be concluded

from these observations the existence of a cut-off value of triaxiality (which seems to correspond to the compression state) for which the flow stress behaves slightly differently.

The Table 9 gathers the values of the k_i parameters (Eq 2.17) for several values of φ with $D = 10$ mm, $r = 0.75$ mm and $t = 0.6$ mm in quasi-static conditions (see technical drawing Appendice B):

Table 9 – Polynomial coefficient values for shear-compression tests processing in quasi-static condition

φ	45°	30°	20°	10° (r=0.2 mm)	45° (t=1.6mm)
k_1	2.417	1.757	2.146	1.034	1.395
k_2	-1.26	0.2918	-0.9954	-0.7197	0.08598
k_3	0.4953	-1.392	0.02424	0.2987	-0.9523
k_4	0.9016	0.8483	0.8117	0.5515	0.901
k_5	0.2657	0.4087	0.5187	0.8891	0.2192
k_6	1	1	1	1	1

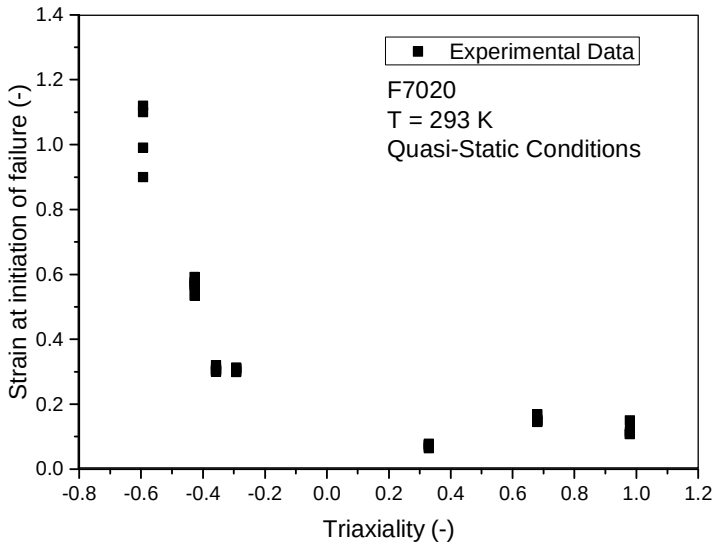

Figure 70 - Evolution of the strain at initiation of failure of the F7020 with the triaxiality

To sum up the behavior of the strain at initiation of failure of the F7020 (Figure 70), it can be seen that it decreases exponentially with the value of triaxiality. The complex behavior for the positive state of stress [67, 68] has not been fully studied but a nonlinear relation can be observed between the failure behavior and the triaxiality over this particular range. No failure has been observed in the compression state of stress ($\sigma^* = -\frac{1}{3}$).

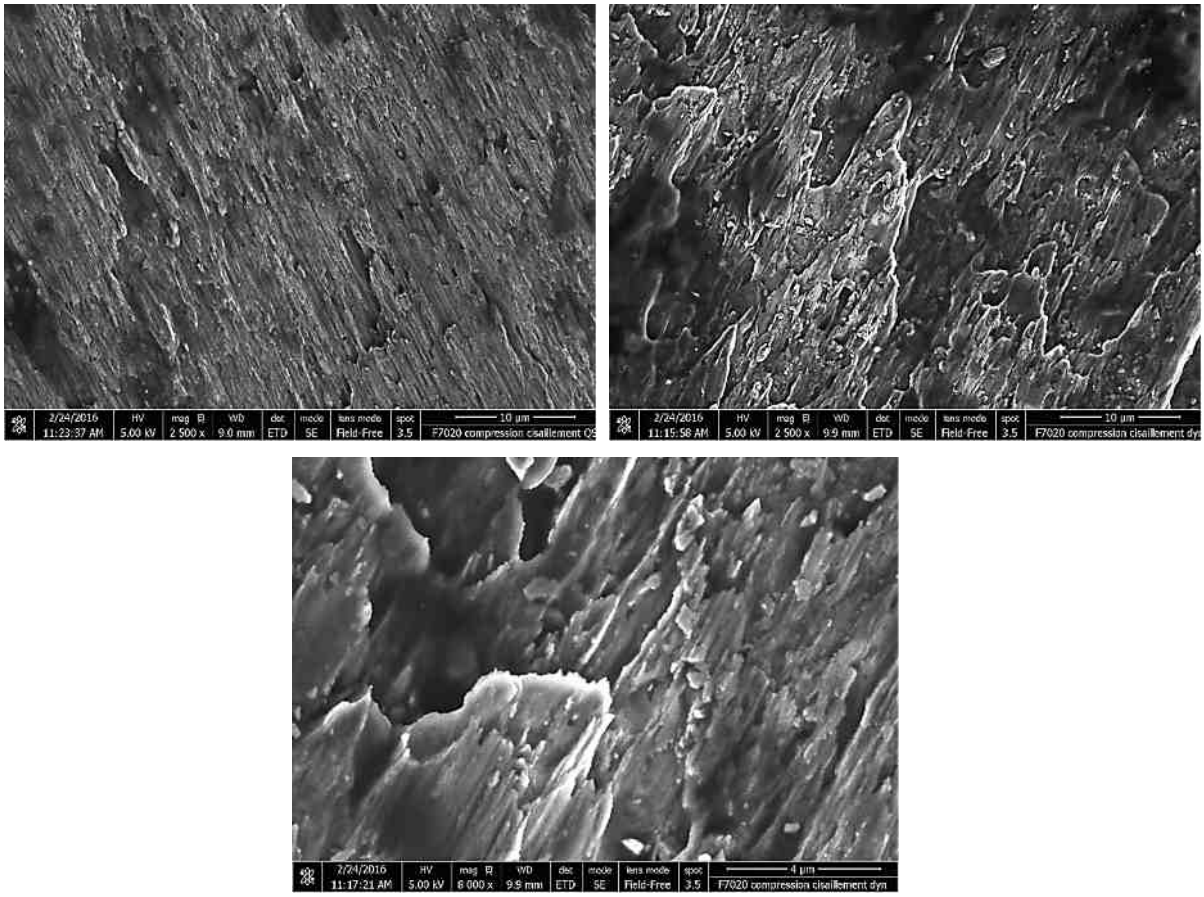

Figure 71 - SEM pictures of shear-compression profiles fracture of F7020 in (a) QS state and (b) dynamic case. (c) Focus on an adiabatic shear band fracture profile (ET detector)

Unlike the tests at positive state of stress (e.g. tension test) presented before, the shear-compression allows yielding of the powder grains through shear mechanisms. As it can be seen (Figure 71.a and 71.b), the failure is performed through the deformation of powder grains and more particularly by the germination of adiabatic shear bands [69, 70] (Figure 71.c). In those conditions, the mechanical properties of the F7020 are involved in the mechanisms of failure. The sensitivities to the temperature and to the strain rate of the failure mechanisms can therefore be studied.

b. Strain rate sensitivity of the strain at initiation of failure

The strain rate sensitivity of the F7020 failure has been studied by using 45° shear-compression samples ($t = 0.6$ mm and $r = 0.75$ mm). Different kind of tests have been performed with this particular geometry on quasi-static testing machine and Hopkinson bars. The parameters required to process the raw data are reported in Table 10.

Table 10 - Polynomial coefficient values for the processing of the shear-compression testes used for the strain rate sensitivity

φ	45° Quasi-static	45° Dynamic
k_1	2.417	1.868
k_2	-1.26	0.2985
k_3	0.4953	0.9001
k_4	0.9016	1.111
k_5	0.2657	0.2192
k_6	1	1

The equivalent stress vs strain curves (Figure 72) reveal an important strain rate sensitivity in the dynamic domain. This is also the case for the strain at initiation of failure at high strain rates and hardly no sensitivity is observable in the quasi-static domain (Figure 73). However, the curves represent the adiabatic behavior of the material and display an important adiabatic softening. Therefore an adiabatic strain at initiation of failure is greater than it should be in isothermal condition (which is required for proper modeling).

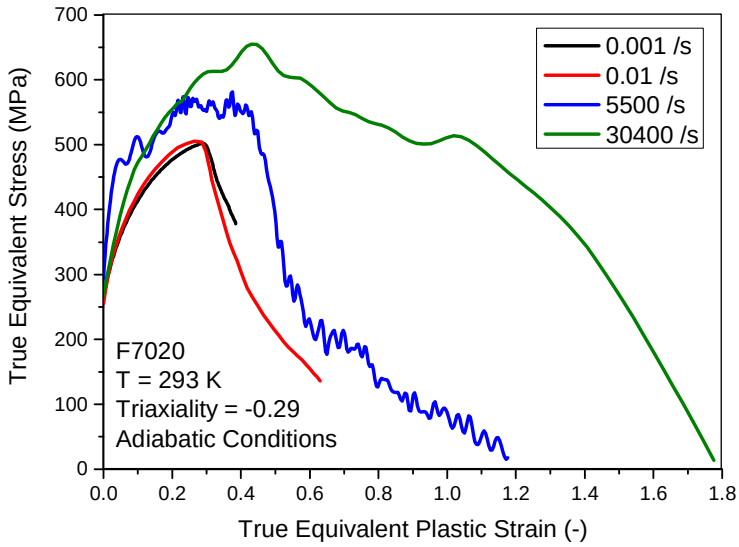

Figure 72 - Equivalent stress vs strain curves of the shear-compression tests at various strain rates

A specific method using the calorific ratio [45, 46] (see Appendix C) allows an accurate physical computation of the isothermal curves in order to evaluate the proper values of ε_p^f for the dynamic tests. The dynamic increase of the strain at initiation of failure is reported in Figure 73. Its exponential increase is essentially due to inertia effect of the dislocations caused by their high velocity [27] at high strain rates and linked to viscous drag effect [34].

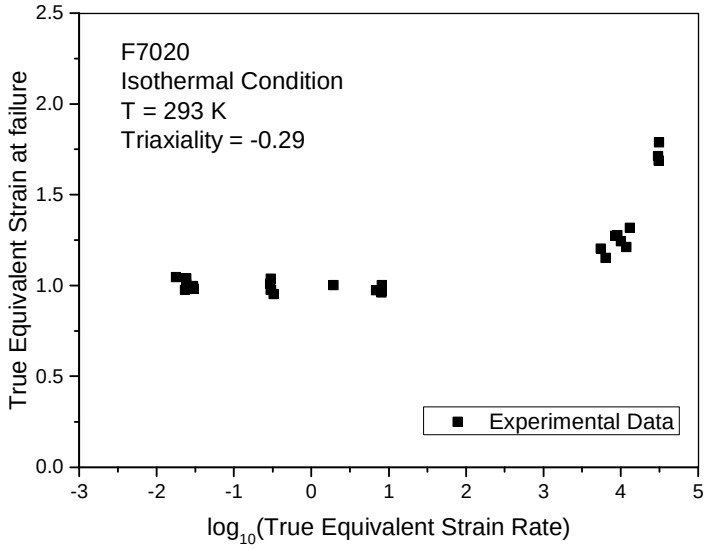

Figure 73 - Strain rate sensitivity of the strain at initiation of failure of the F7020

c. Temperature sensitivity of the strain at initiation of failure

The temperature sensitivity of the strain at initiation of failure has also been studied by using shear-compression tests ($\theta = 45°, t = 0.6\ \text{mm}, r = 0.75\ \text{mm}$). The heating system used was based on high speed induction heating ($\sim 50℃$ per second) and allows mechanical tests with limited microstructure changes. The equivalent stress vs strain curves of the tests can be seen in the Figure 74.

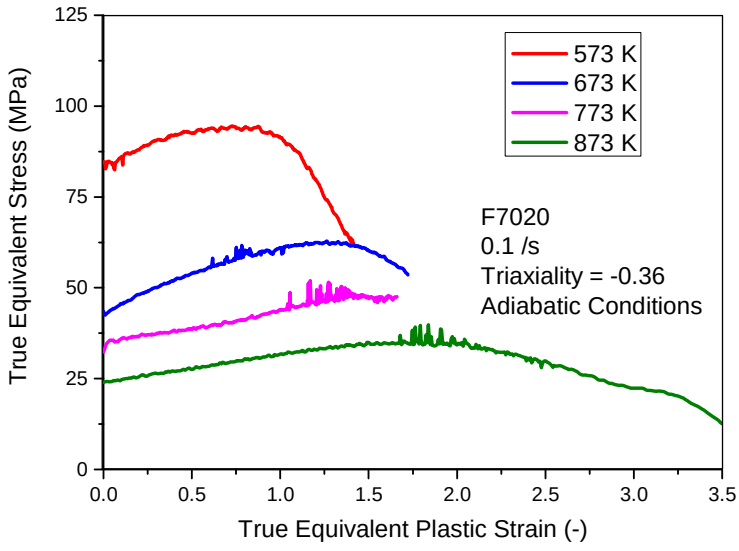

Figure 74 - Equivalent stress vs strain curves of shear-compression tests at various temperatures

On the figure 75, it can be clearly seen the evolution of the initiation of strain at failure with the temperature: a decrease between room temperature and around 490 K [1, 2], followed by an athermal plateau up to 773 K, and finally a very steep increase up to the complete fusion of the material. The presence of the athermal plateau can be explained by the microstructure of the material. Indeed, the dissolution of the hardening precipitates in the aluminum matrix has happened around 490 K and after this temperature, the microstructure presents few evolutions. Indeed, the diffusion mechanisms due to the elevation of temperature do not impact the hardening precipitates anymore since they are completely dissolved in the matrix. Therefore, the mechanical behavior does not change in this range of temperature until approaching the melting temperature (940 K) where diffusion mechanisms of the atoms lead to the physical decohesion at the atomic level. The strain rate sensitivity of ε_p^f is considered in its isothermal condition and is computed though the consideration of the expression of the calorific ratio presented in the next chapter.

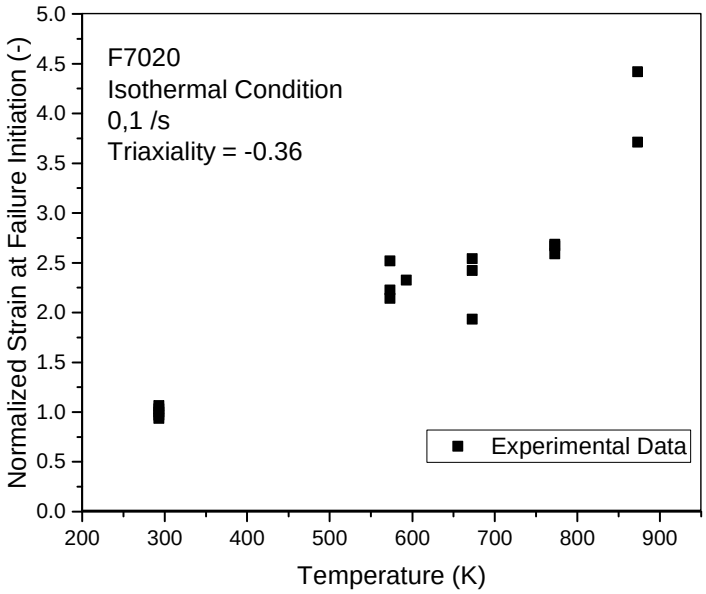

Figure 75 - Temperature sensitivity of the strain at initiation of failure of the F7020

d. Triaxiality sensitivity of the damage evolution energy

In this study, the quantification of the damage is performed through the evaluation of a damage energy after the initiation of failure. The amount of energy absorbed by the material after the Consider criterion is computed for each test and its evolution with the state of stress is studied (Figure 76). In the cases of positive states of stress, the energy of damage [71] is assumed as non-existent due to the brittle behavior of the failure (the Consider criterion is not even reached). However, it can be easily computed with the

tests presenting a negative triaxiality (shear-compression tests). Furthermore, the evolution of this energy with the strain rate has not revealed any particular strain rate or temperature sensitivity. Therefore, only the triaxiality dependency is reported for the F7020.

The state of stress sensitivity of the damage energy [71] seems to follow a decreasing exponential law. The lower the triaxiality is, the greater the energy will become. The dispersion of the measured energy of damage is mainly due to random properties of crack propagation (generated through the germination of adiabatic shear band) which leads to different path of cracks and depending on particular defects of the sample.

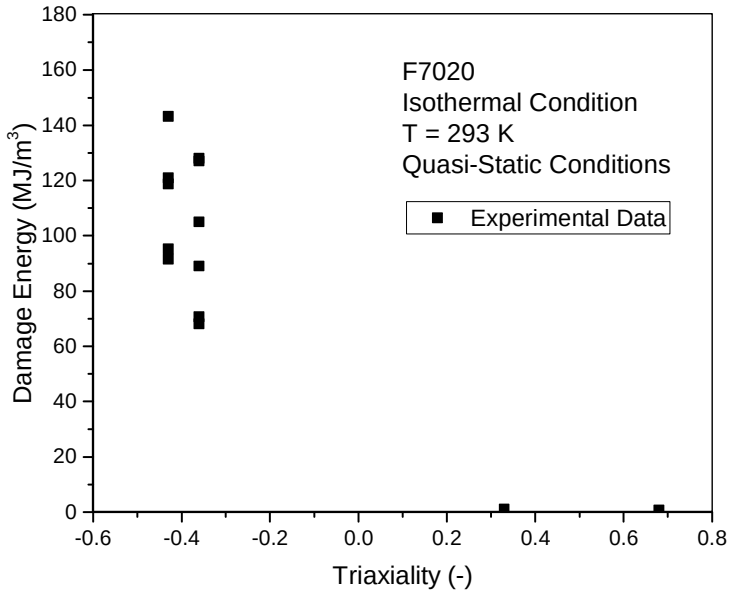

Figure 76 - Evolution of the damage energy with the state of stress of the F7020

2. Analysis of the failure and damage behavior of the sintered polyimide

a. Triaxiality sensitivity of the strain at initiation of failure

- Tensile tests

Tensile tests have been carried out on the sintered Polyimide in order to evaluate its response to positive triaxiality. Digital Image Correlation was also used for these tests to measure accurately the strains of the sample (Figure 77).


Surface component 1
phiM
[ln]
0.070
0.060
0.053
0.045
0.038
0.030
0.023
0.015
0.008
0.000

(a)


Surface component 1
phiM
[ln]
0.070
0.060
0.053
0.045
0.038
0.030
0.023
0.015
0.008
0.000

(b)

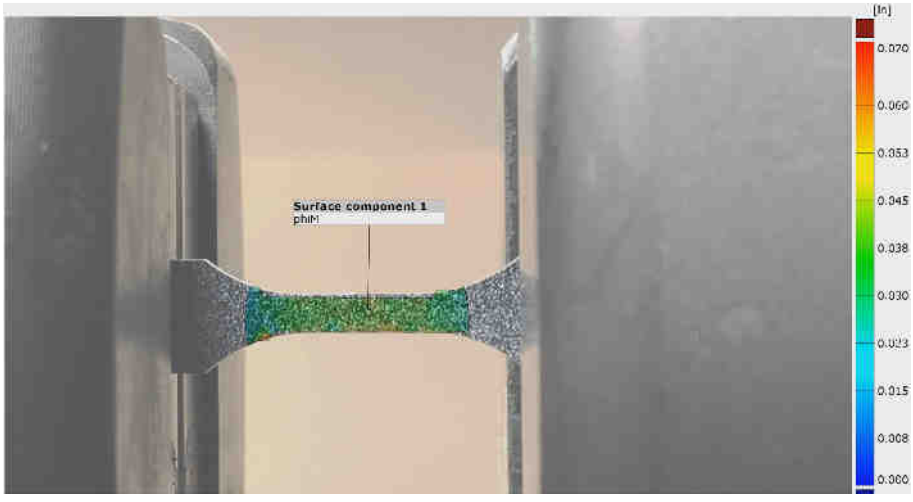
Surface component 1
phiM
[ln]
0.070
0.060
0.053
0.045
0.038
0.030
0.023
0.015
0.008
0.000

(c)

(d)

Figure 77 - Digital Image Correlation on tensile tests of sintered PI at (a) beginning of the test, (b) during the test, (c) just before failure and (d) just after failure

The stress vs strain curves (Figure 78) reveal a large dispersion (around 25 %) of the failure behavior of the sintered Polyimide in tensile loading mode. The failure of the material happens before reaching yielding phenomenon and leads the characterization of an elastic-brittle material. Furthermore, no progressive damage phenomenon can be observed on the stress vs strain curves (Figure 78). The damage energy [71] can therefore be neglected in these conditions. This failure elastic-brittle behavior is observed over the range of positive triaxiality due to the opening of voids phenomenon and "ductile" failure caused by locking phenomenon [59] is observed only for negative triaxiality cases such as compressive state.

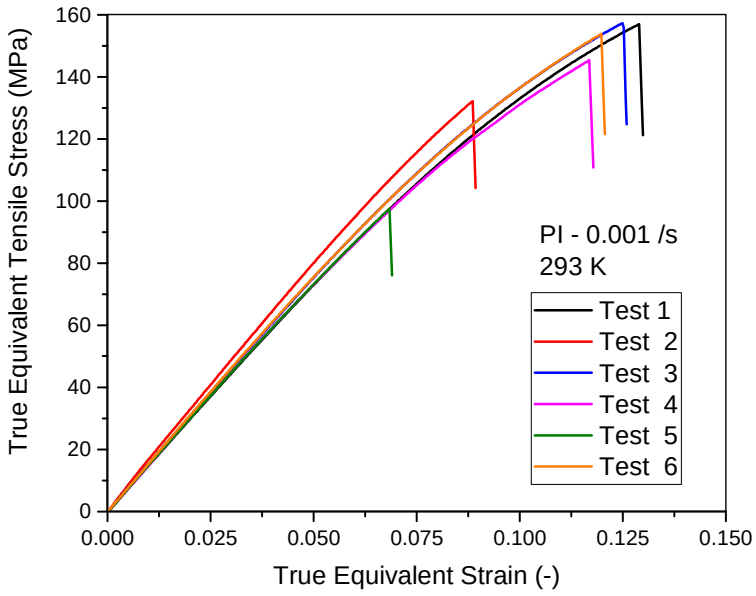

Figure 78 - Stress vs Strain curves of tensile tests on the sintered PI

Figure 79.a and 79.b are SEM pictures of tensile profile fracture of sintered polyimide at room temperature. As for the F7020, the mechanism leading to the failure of the material is the decohesion of the sintered grains of powder [65]. Besides, SEM observations (Figure 79.c and 79.d) have also been carried out at higher temperature (573 K) which is just below the glass transition temperature. The same failure mechanism is observed for both temperatures conditions leading to failure at the yield stress (brittle failure). Therefore, it can be concluded that the failure in tensile condition of the sintered polyimide is temperature independent due to this particular mode of failure (intergranular decohesion at mesoscopic scale). Another type of failure mode has to be investigated to evaluate the temperature sensitivity of the failure mechanisms of this material.

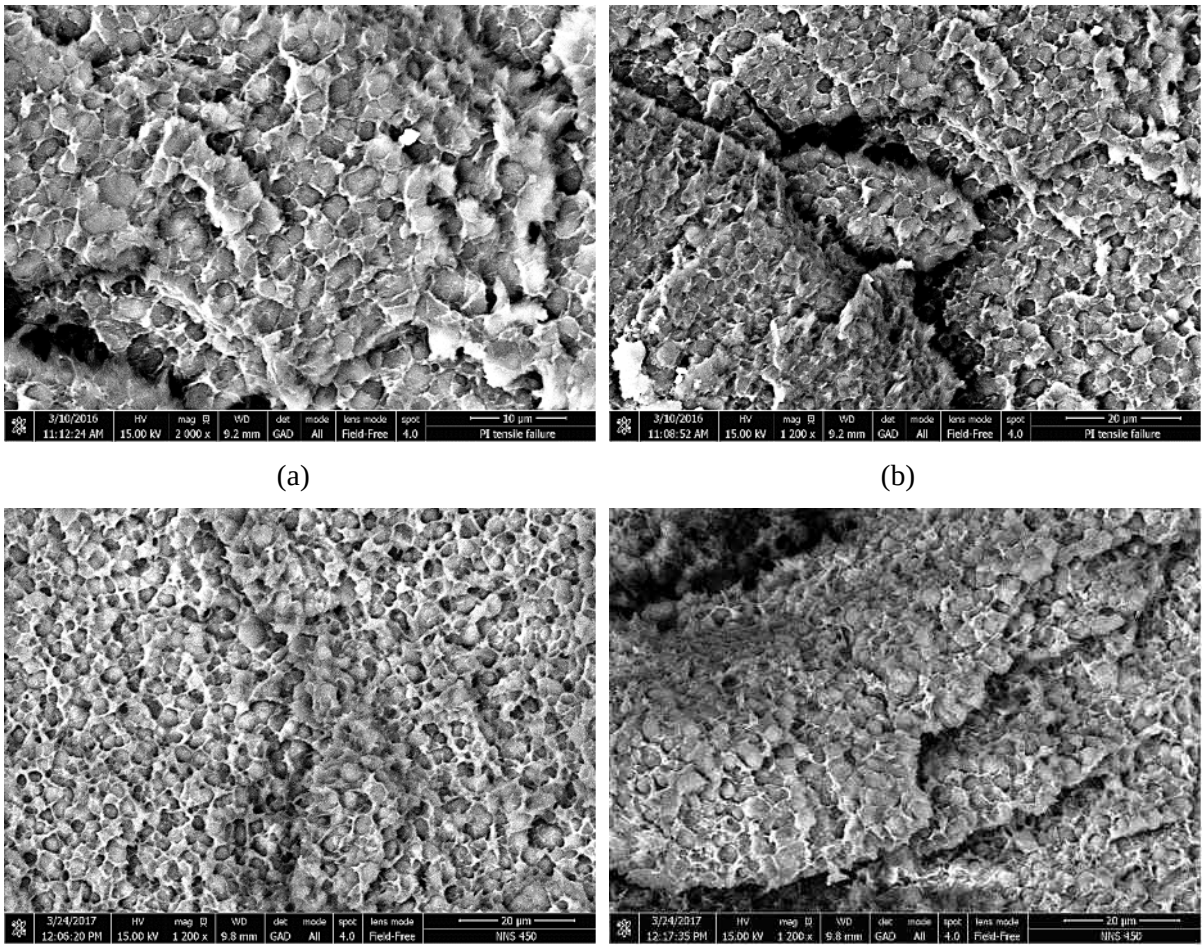

(a) (b)

(c) (d)

Figure 79 - SEM pictures of fracture profile of sintered PI tensile samples at (a,b) room temperature and (c,d) 573 K with chemical contrast (GA detector)

- Compressive state

In compression condition, the polymer reaches a critical value of strain at which the sample bursts due to the locking of the chains structure [59]. Furthermore, the higher the stress at failure is, the higher the propagation velocity of the cracks will be. Besides, due to inertia effect, the sample might fragments and it is the case for the sintered polyimide. The figure 80.a and 80.b shows the fracture profile of fragments of sintered polyimide after a compression test at 0.001 /s and at room temperature using a chemical contrast detector (GAD). No intergranular decohesion can be seen on the SEM pictures. The failure seems to occur through cracks propagation [72] (along the black arrow), only along one general direction and with wide crack steps. SEM observations through a topological detector (LVD) has also been carried out (Figure 80.c and 80.d). These pictures show a global ductile failure of the sintered powder grains with large deformation (Figure 80.d). Thus, the locking phenomenon [59] leading to the failure in compressive state is temperature and strain rate dependent and allows the study of the failure mechanisms.

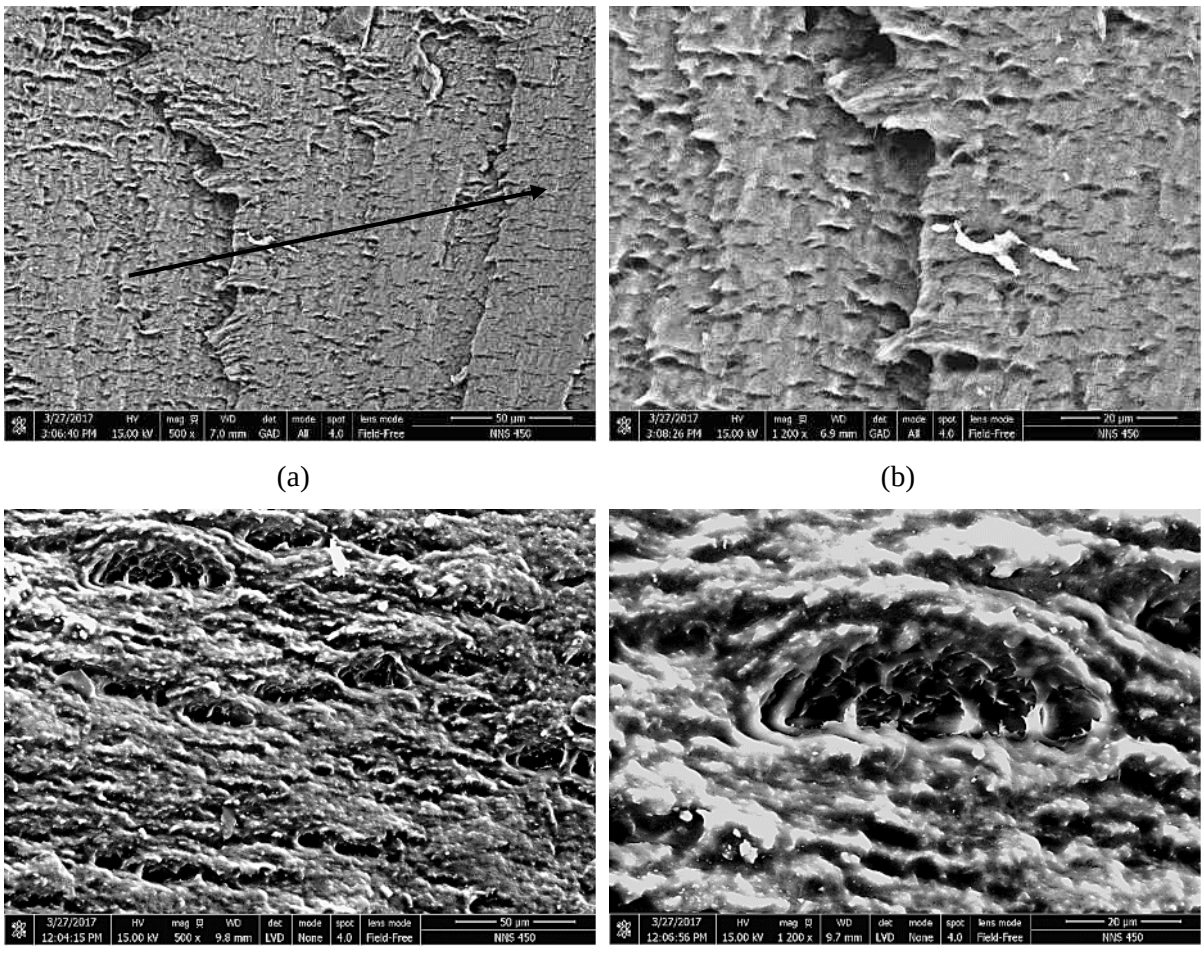

(a) (b)

(c) (d)

Figure 80 - SEM pictures of fracture profile of sintered PI compressive samples with (a,b) chemical contrast (GA detector) and (c,d) topologic contrast (LV detector)

The summary of the mechanical behavior of the strain at initiation of failure of the sintered polyimide can be found in Figure 81.

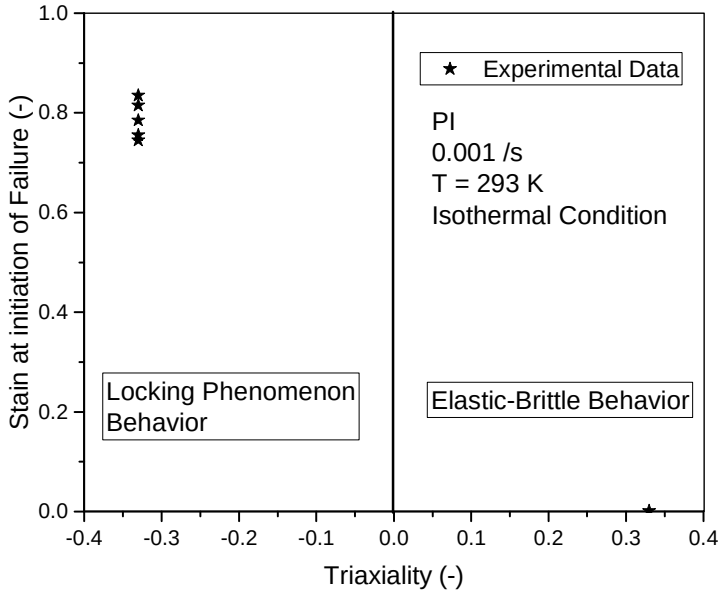

Figure 81 - Evolution of the strain at initiation of failure of the sintered PI with the triaxiality

b. Strain rate sensitivity of the strain at initiation of failure

The strain rate sensitivity of the initiation of the strain at failure of the polyimide has been studied with the compression tests. Indeed, as for the F7020, the polyimide is a sintered material presenting intergranular decohesion for solicitations presenting a positive state of stress such as tension tests. The mechanisms of failure for such materials is controlled by the local stretching of the chains caused by a constrained stress transfer along their entangled molecule segments [59, 72, 73]. The strain rate sensitivity is nearly nonexistent over a wide range of strain rate and suddenly decreases over $\dot{\varepsilon}_p^{trans} = 10^4\ /s$ due to the locking of the chains structure (Figure 82). The stronger the cross-linking is, the lower the transition strain rate $\dot{\varepsilon}_p^{trans}$ will be [52]. The high value of the transition strain rate means that the characteristic time of relaxation of the chains structure is quite low and allows a quick reorganization of the chains [59, 74].

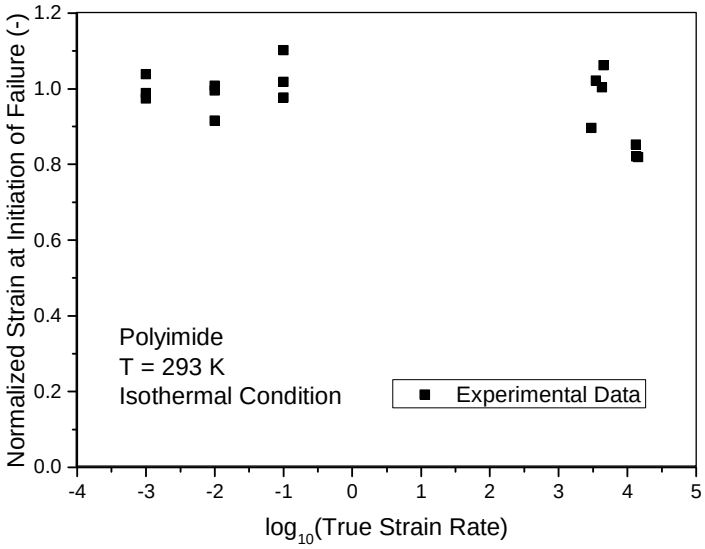

Figure 82 - Evolution of the strain at initiation of failure with the strain rate of the polyimide

c. Temperature sensitivity of the strain at initiation of failure

The temperature sensitivity has also been studied with the compression experiments. The strain rate sensitivity of ε_p^f is considered here in its isothermal condition. The value of the strain at initiation of failure ε_p^f is directly linked to the locking parameter N ($\varepsilon_p^f = \frac{\ln N}{2}$) [57]. The temperature sensitivity (Figure 83) seems to be linear over the range of tested temperatures. This tendency is mainly due to the faster and easier crawling of the chains at higher temperature leading to a higher mobility of the chain in the fibrils and therefore to the decrease of the characteristic time of chains relaxation (augmentation of the value of the locking parameter N). The locking phenomenon is therefore reached later in the fibrils due to their high mobility and the cracks propagate slow, delaying the failure of the material [54, 72, 75].

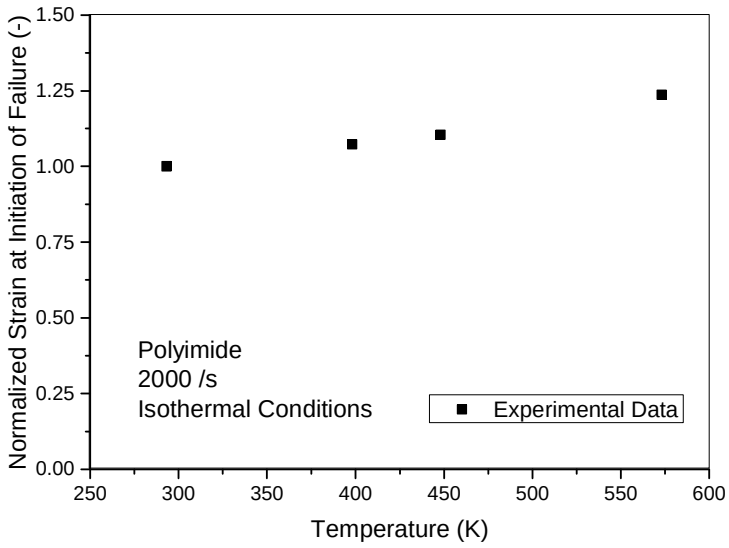

Figure 83 - Temperature sensitivity of the strain at initiation of failure of the polyimide

d. Triaxiality sensitivity of the damage evolution energy

The evolution of the damage energy (after the initiation of the failure mechanisms) is studied as a function of the state of stress. Indeed, the difference of failure mode between positive and negative triaxiality (grain powder decohesion) leads as well to two very different damage behavior:

- At positive triaxiality, the failure is brittle and no damage energy is observed. The mechanisms of failure are nearly instantaneous due to the simultaneous decohesion of the grain powder under the loading (intergranular decohesion).
- At negative triaxiality, the mechanisms of failure leads to the occurrence of the locking phenomenon of the polymer chains and to a progressive failure: a damage energy can be observed (intragranular decohesion).

The summary of such damage behavior [71] can be seen in Figure 84.

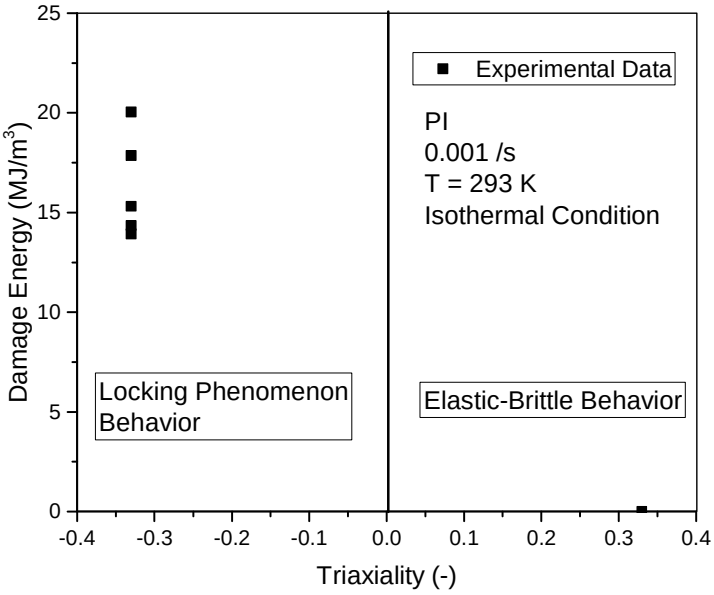

Figure 84 - Evolution of the damage energy of the sintered PI with the triaxiality

3. Analysis of the failure and damage behavior of the epoxy resin

a. Triaxiality/strain rate coupled sensitivities of the strain at initiation of failure

- Tensile tests

Tensile tests have also been carried out on the epoxy resin to determine its response to positive triaxiality. The study of the fracture profile has revealed a failure caused by cracks propagation in the epoxy matrix. Digital Image Correlation was also used for these tests to measure accurately the strains of the sample (Figure 85).

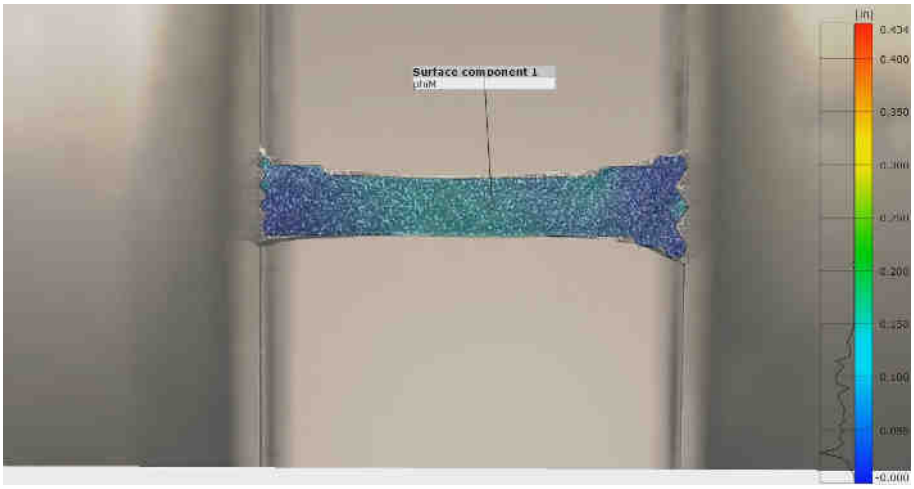
Surface component 1
[in]
0.400
0.350
0.200
0.100
-0.000

(a)

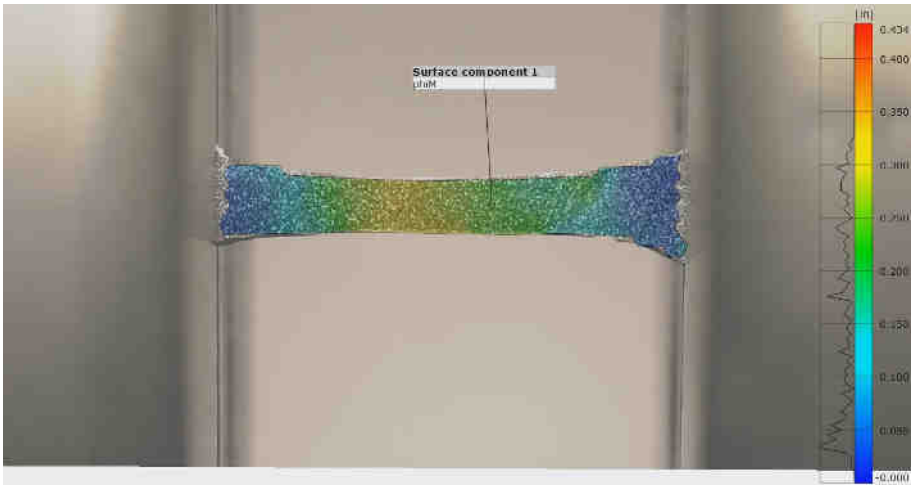
Surface component 1
[in]
0.400
0.350
0.200
0.100
-0.000

(b)

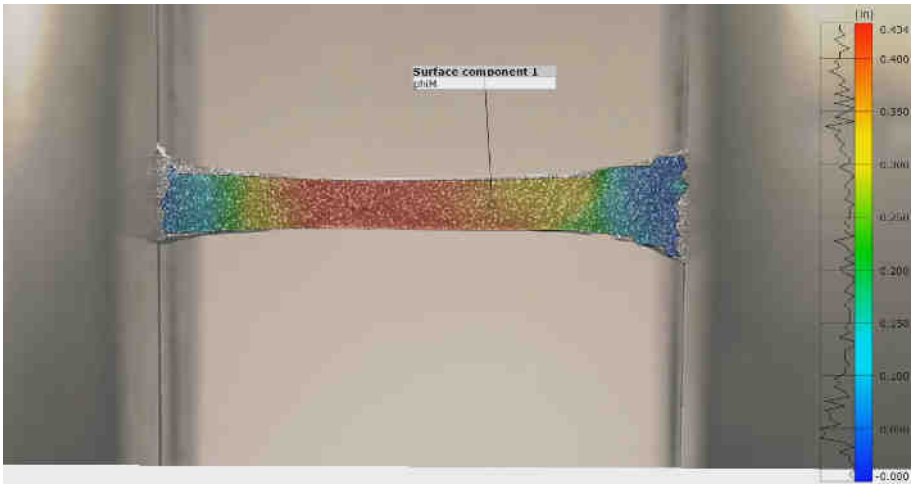
Surface component 1
[in]
0.400
0.350
0.200
0.100
-0.000

(c)

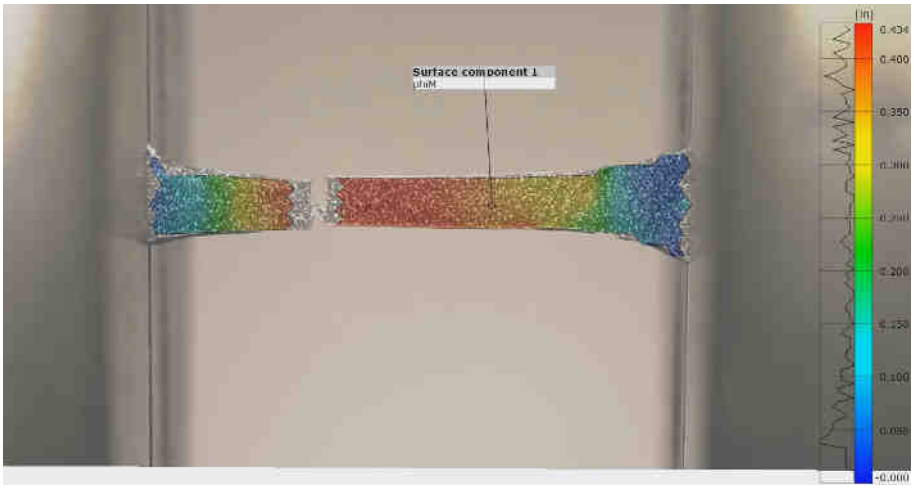

(d)

Figure 85 - Digital Image Correlation on tensile tests of the Epoxy Resin at (a) beginning of the test, (b) during the test, (c) just before failure and (d) just after failure

The stress vs strain curves (Figure 86) of the tests performed at different strain rates reveals a very high strain rate sensitivity of the strain at initiation of failure. In the case of the epoxy resin, it can also be clearly seen that the evolution of the failure phenomena begins with ductile characteristics at low strain rates (0.001 /s) until becoming quasi-brittle at higher strain rates (1 /s).

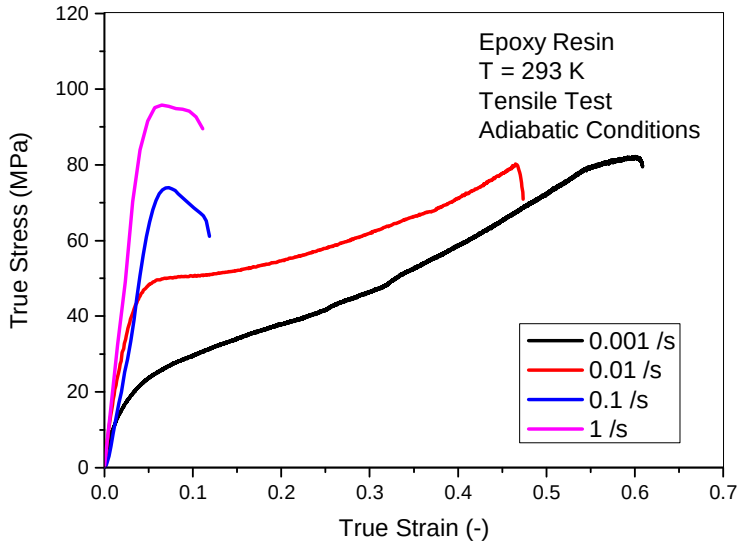

Figure 86 - Stress vs Strain curves of tensile tests on the epoxy resin

As for the polyimide, the strain rate sensitivity of the strain at initiation of failure is negative over the whole range of tested strain rates (Figures 86 and 90). However, the transition strain rate leading to quasi-brittle failure at low plastic strain is much lower than for the polyimide $\dot{\varepsilon}_p^{trans} \sim 10^4$ /s (thermoplastic polymer). Indeed, for the epoxy resin, in tensile condition, its value is around 10^{-2} /s. After this value of strain rate, the strain at initiation of failure stays around $\varepsilon_{lim}^f = 0.05$. It can be

explained by the very high entanglement of the thermoset epoxy resin which is much more sensible to the chain locking phenomenon [52, 59] than the thermoplastic polyimide. At “high” strain rate, the value of the strain at initiation of failure seems to stays constant. The assumption of an asymptotic behavior toward a value of zero can be eventually done.

Contrary to the two other materials, the epoxy resin has not been sintered and therefore cannot present a decohesion failure mechanism. Indeed, the figures 87.a and 87.b show a failure profile created by propagation of cracks through the polymeric matrix at room temperature (0.01 /s) as it was reported in [76] and [77]. The propagation of the cracks (along the black arrows) is performed by successive steps along a preferential direction depending on the topology of the already created profile failure and always on the plane of this last. It can also be noted that the porosities inside the epoxy matrix seem to have no crucial role in the germination and propagation of the cracks. Indeed, a crack seems to encounter a porosity only if it is on its propagation direction. This might be due to the fact that the porosities are spherical (formed by trapped air) and present therefore a very low stress concentration factor and to the rather higher pressure sensitivity of the epoxy resin leading to a good tenacity. It is certainly due to the much higher tenacity of the epoxy resin in the crack tip opening zone due to the high level of pressure.

The same crack propagation phenomenon can be observed at higher temperature (313 K) on the figures 87.c and 87.d. However, the intensity of the crack steps seems to be less important than at room temperature and the crack patterns seem to be smoother. The failure might therefore be more ductile at higher temperature [54, 75].

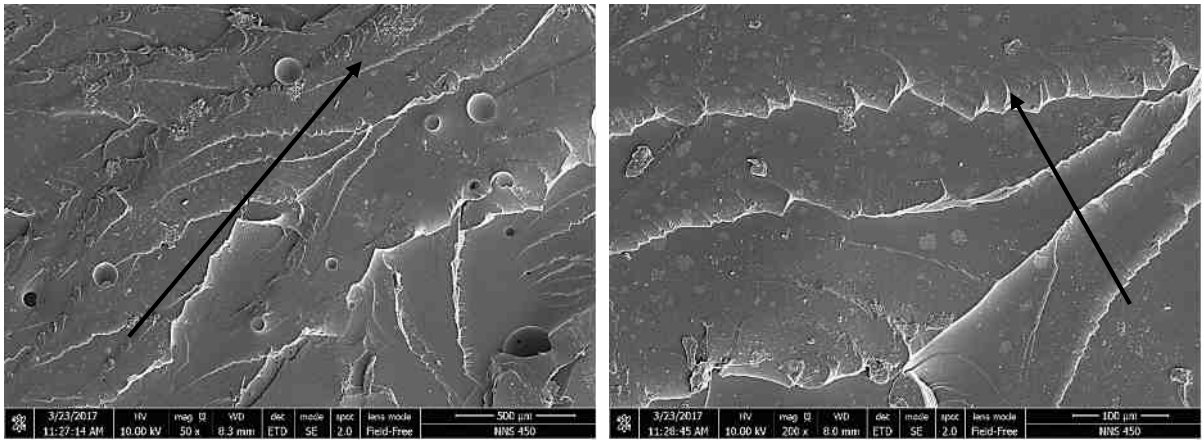

(a) (b)

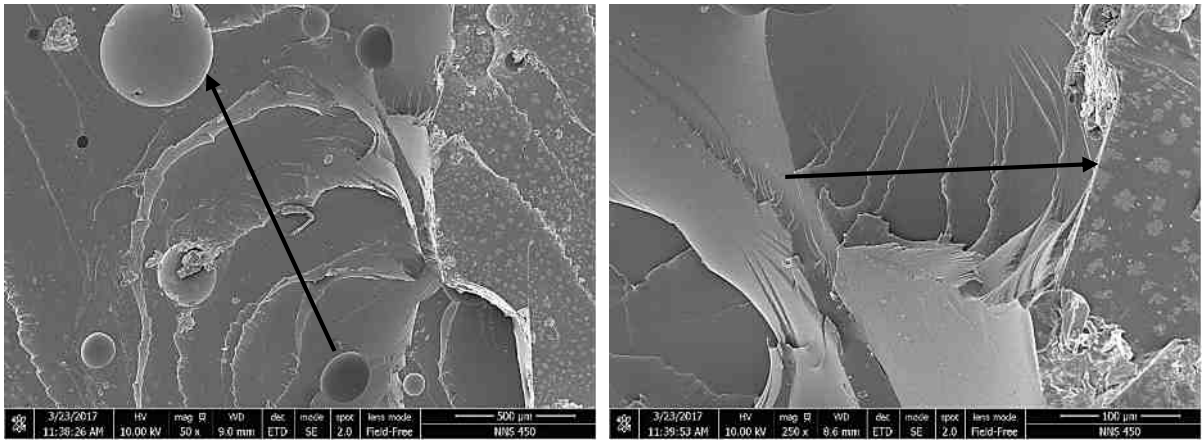

(c) (d)

Figure 87 - SEM pictures of fracture profile of epoxy resin tensile samples at (a,b) room temperature and (c,d) 313K (ET detector), direction of crack propagation given by the arrows

- Compression state

The failure in compression state of the epoxy resin shows a clearly different behavior than in tensile loading mode. Indeed, no significant strain rate sensitivity of the strain at initiation of failure can be observed over the range of 0.001 /s to 0.1 /s (Figure 90). This behavior means a different response to the locking phenomenon [59, 72] of the polymer structure between the different loading modes. The study of the strain at initiation of failure was not possible in dynamical condition due to the very low temperature of glass transition. Indeed, this temperature is rapidly reached due to adiabatic heating and the mechanisms change drastically in rubber conditions and the value of ε_p^f increases.

Figures 88.a and 88.b show the profile failure of remaining fragments of epoxy resin after compression tests at room temperature (0.01 /s). As for the sintered polyimide, the germination and propagation of cracks due to the phenomenon of chains locking is responsible of the failure [59, 72]. However, it can be seen for the epoxy resin, different directions of crack propagation (along the black arrows) with narrow crack steps (certainly due to the much higher tenacity of the epoxy resin in the rack tip opening zone due to the high level of pressure). It can be noted that this kind of fracture profile have been reported in the literature [77] and also for other type of polymers such as PMMA [78].

However, the same mechanisms as observed in tensile condition are responsible of the failure of the material. The tension state, being more specific to study the failure, will be used further in this work to study the sensitivity to the temperature.

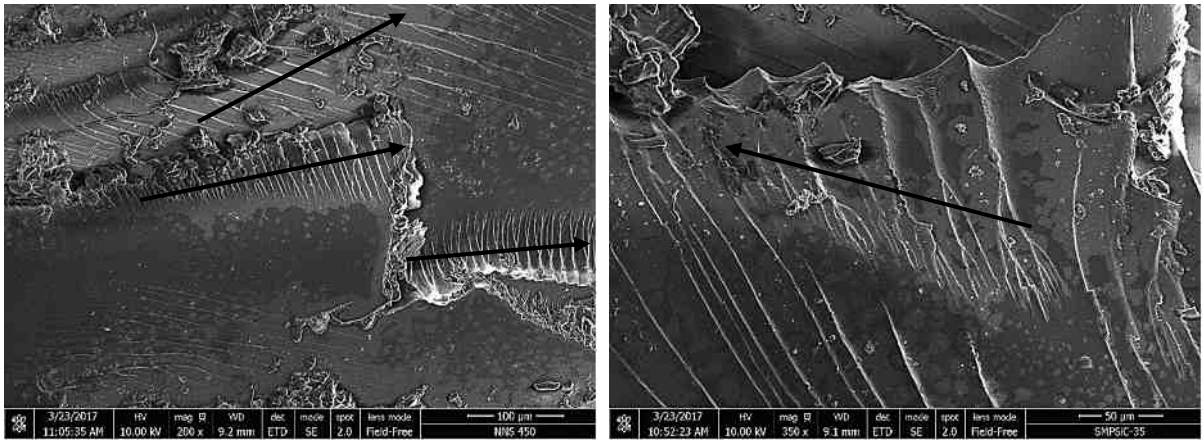

(a) (b)

Figure 88 - SEM pictures of fracture profile of epoxy resin compressive samples (ET detector)

- Notched flexural tests

To complete the study of the triaxiality sensitivity, a third state of stress condition has to be studied. Therefore, notched flexural tests have been performed and allows the study of the failure phenomena at a triaxiality of $\sigma^* = 0.55$ (Abaqus® simulation) in the notch where the crack is initiated. The choice of this particular value of triaxiality is justified by the particular behavior of the epoxy resin toward the strain rate and the triaxiality revealed by the previous results in other states of stress which have shown that additional values at strain rate around 0.01 /s and at $\sigma^* \sim 0.5\text{-}0.6$ would be of high interest for a better modeling. The local measurement of the strain has been carried out using Digital Image Correlation method (Figure 89). The bottom notch aims to reduce the compressive effect during the flexion in this particular region of the sample.

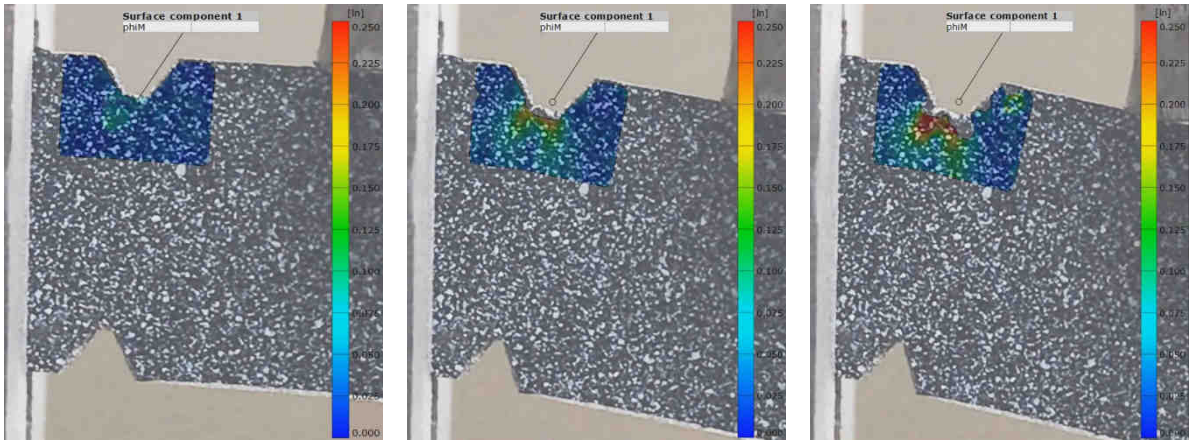

(a) (b) (c)

Figure 89 - Digital Image Correlation on tensile tests of epoxy resin (a) beginning of the test, (b) during the test and (c) at the failure initiation

The Digital Image Correlation reveals a stress concentration in the upper notch due to the flexural loading mode (5 mm/min) and leading to an increasing deformation at the tip of the notch which is concluded by the initiation of a crack (Figure 89.c). The strain rate measured in this area was 0.0086 /s.

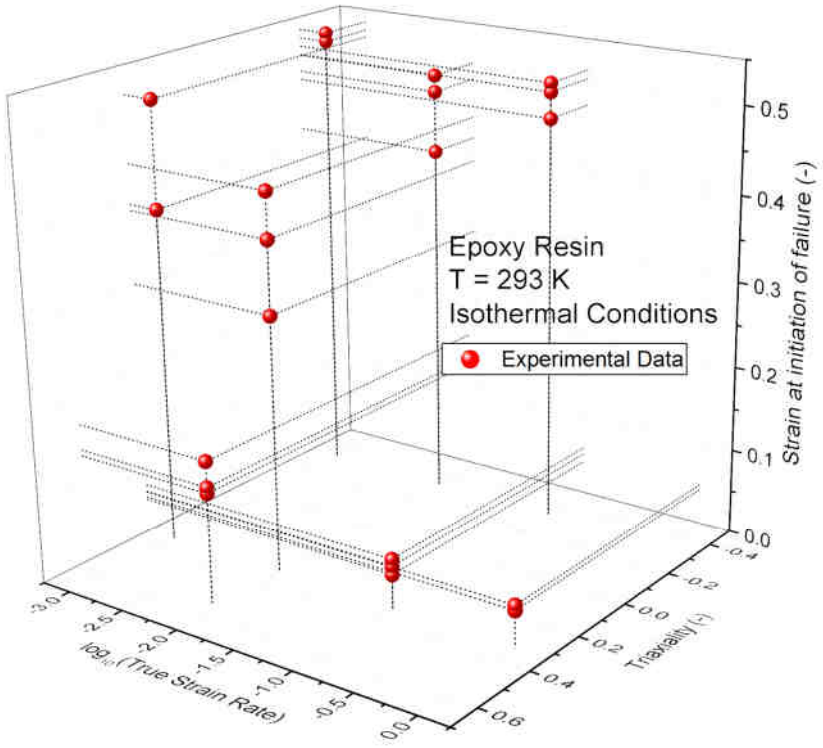

Figure 90 - Evolution of the strain at initiation of failure of the epoxy resin with the triaxiality and the strain rate

The Figure 90 shows the strain rate – state of stress coupling between tensile and compressive conditions. Indeed, the work of Fiedler et al. [77] have shown that the strain and failure modes are highly dependent on the type of loading (e.g. tension, torsion, compression). It can be seen that, despite a quasi-absence of rate sensitivity in compressive state of stress, the strain at initiation of failure shows a very high dependency with the rate of deformation and at low strain rates. It leads to a quasi-brittle behavior for strain rates above 0.1 /s even if this phenomenon is not observed in compression for this range of strain rate. The additional results obtained through notched flexural tests ($\sigma^* = 0.55$) show a quick decrease of the strain at initiation of failure with the increase of the triaxiality.

b. Temperature sensitivity of the strain at initiation of failure

As for the polyimide, the failure behavior of the epoxy resin is closely linked to the locking effect of the polymer chains. The values of the locking parameter N obtained previously with the compression tests are then used to compute the equivalent strain at failure $\varepsilon_p^f = \frac{\ln N}{2}$ [57]. The resulting temperature sensitivity seems to be linear from room temperature up to the temperature of glass transition (Figure

91). After reaching T_g, the variation of the failure phenomenon in the rubber domain is negligible. The locking phenomenon is reached later in the fibrils at higher temperature due to their high mobility and the cracks propagate is slow, delaying the failure of the material [54, 72, 75].

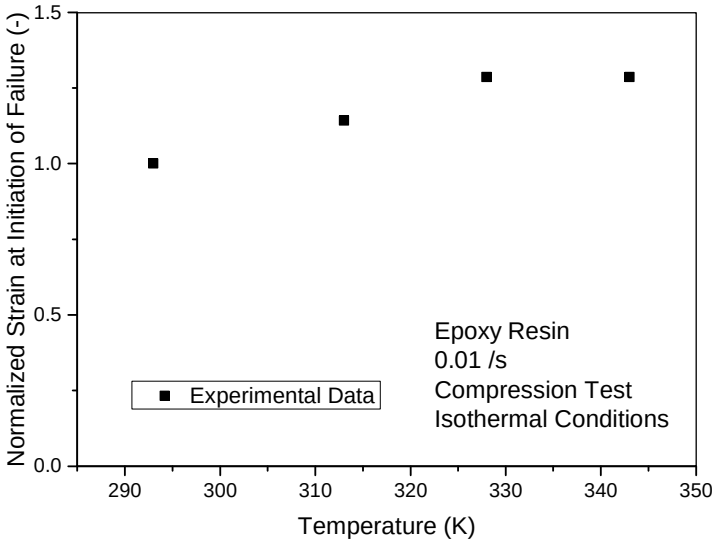

Figure 91 - Temperature sensitivity of the strain at initiation of failure of the epoxy resin

c. Triaxiality sensitivity of the damage evolution energy

The evolution of the damage energy of the epoxy resin decreases with the increase of the triaxiality (Figure 92). No particular strain rate dependency has been observed, certainly due to the dispersion of the experimental data. It can be seen, contrary to the sintered materials, that the damage energy [71] is not null in the positive triaxiality cases. This is due to the crack propagation failure mode observed over the whole range of tested triaxialities. The higher hydrostatic pressure at low triaxiality increases the amount of energy required for the crack to propagate.

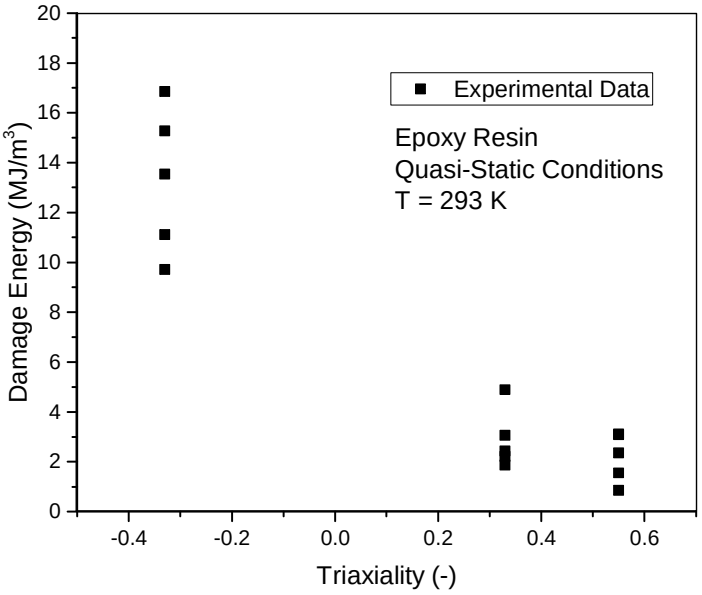

Figure 92 - Evolution of the damage energy of the epoxy resin with the triaxiality

E.CONCLUSION OF THE CHAPTER

In this chapter, the different experimental methods used to evaluate the mechanical behavior of each material (the F7020 aluminum alloy, the sintered polyimide and the epoxy resin) have been presented and explained. Thanks to these several experimental tests, the different phenomena responsible of the mechanical responses of the materials were able to be studied:

- The mechanical behavior F7020 aluminum alloy can be decomposed into two parts which are the athermal stress and the thermal stress [25]. This latter is itself divided into an effective stress (the friction resistance of the lattice to the strain) and the internal stress (the structural strain hardening) [26]. Furthermore, the complex microstructure of metallic alloys and their evolution with the temperature lead to highly nonlinear thermal behavior [45, 46].
- The sintered polyimide and the epoxy resin are polymers presenting a very different mechanical behaviors but which can be explained by the same phenomena and their very different level of cross-linking [52, 59]. The yield stress is in both cases caused by the overcoming of a loading threshold which leads to the crawling of the polymer chains and to an irreversible deformation. The second phenomenon is the strain softening which is caused by the relaxation of the chains after reaching the yield stress. The last main phenomenon is called the hyperelasticity and is due to the overall resistance of the chains network to their alignment under the loading. The significant difference of mechanical responses between the two polymers can be explained by their degree of chain entanglement which is much higher for the epoxy resin (thermoset) than for the sintered polyimide (thermoplastic).

The other aspect of the mechanical study of the different materials is the failure mechanisms. Indeed, knowing the conditions of loading leading to the fracture of the materials is of the upmost importance for impact simulation. For each material, the sensitivities of the plastic strain at initiation of failure to the triaxiality, the strain rate and the temperature have been studied. However, the mode of failure observed for the sintered materials (F7020 and polyimide) was the intergranular decohesion of the powder grains for positive triaxiality [64-66]. In these cases of loading, the study of the dependencies of the failure mechanisms to the temperature and strain rate were not possible and tests such as shear-compression or compression (negative triaxiality) have been chosen. However, for all materials, a similar behavior can be observed: an exponential increase of the plastic strain at initiation of failure with decreasing triaxiality. Concerning the sensitivity to the strain rate, the behavior is clearly different between the metal for which the value of ε_p^f increases and the polymers for which it decreases due an earlier locking effect [59, 72] of the chain leading to a constrained stress transfer through the molecules segments.

The gathered experimental data of each studied phenomenon now needs to be modeled through the development of specific mathematical expressions in order to be implemented in FORTRAN subroutine for ABAQUS® simulation of impact.

References

1. Belov, N.A., D.G. Eskin, and A.A. Aksenov, *Multicomponent phase diagrams: applications for commercial aluminum alloys*2005: Elsevier.
2. Chinella, J.F. and Z. Guo, *Computational Thermodynamics Characterization of 7075, 7039, and 7020 Aluminum Alloys Using JMatPro*, 2011, DTIC Document.
3. Bergstrom, J.S., *Mechanics of solid polymers: theory and computational modeling*2015: William Andrew.
4. Dieter, G.E. and D.J. Bacon, *Mechanical metallurgy*. Vol. 3. 1986: McGraw-Hill New York.
5. Dorogoy, A., D. Rittel, and A. Godinger, *Modification of the shear-compression specimen for large strain testing.* Experimental mechanics, 2015. **55**(9): p. 1627-1639.
6. Kuwabara, T. and F. Sugawara, *Multiaxial tube expansion test method for measurement of sheet metal deformation behavior under biaxial tension for a large strain range.* International Journal of Plasticity, 2013. **45**: p. 103-118.
7. Jankowiak, T., A. Rusinek, and T. Lodygowski, *Validation of the Klepaczko–Malinowski model for friction correction and recommendations on Split Hopkinson Pressure Bar*. Finite Elements in Analysis and Design, 2011. **47**(10): p. 1191-1208.
8. G.Gary, *Testing with bars from dynamic to quasi-static.* 2011.
9. Gama, B.A., S.L. Lopatnikov, and J.W. Gillespie Jr, *Hopkinson bar experimental technique: a critical review.* Appl. Mech. Rev, 2004. **57**(4): p. 223-249.
10. Chen, W.W. and B. Song, *Split Hopkinson (Kolsky) bar: design, testing and applications*2010: Springer Science & Business Media.
11. Klepaczko, J. and Z. Malinowski, *Dynamic frictional effects as measured from the split Hopkinson pressure bar*, in *High velocity deformation of solids*1979, Springer. p. 403-416.
12. Malinowski, J. and J. Klepaczko, *A unified analytic and numerical approach to specimen behaviour in the split-Hopkinson pressure bar.* International Journal of Mechanical Sciences, 1986. **28**(6): p. 381-391.
13. Safa, K. and G. Gary, *Displacement correction for punching at a dynamically loaded bar end.* International Journal of Impact Engineering, 2010. **37**(4): p. 371-384.
14. Lee, W.-S., C.-F. Lin, and G.-L. Xiea, *Dynamic shear deformation and failure behaviour of pure polycrystalline tungsten.* Materials Science and Engineering: A, 1998. **247**(1): p. 102-112.
15. Rubio, L., J. Fernández-Sáez, and C. Navarro, *Determination of dynamic fracture-initiation toughness using three-point bending tests in a modified Hopkinson pressure bar*. Experimental mechanics, 2003. **43**(4): p. 379-386.
16. Nie, X., et al., *Dynamic tensile testing of soft materials.* Experimental mechanics, 2009. **49**(4): p. 451-458.
17. Gerlach, R., C. Kettenbeil, and N. Petrinic, *A new split Hopkinson tensile bar design.* International Journal of Impact Engineering, 2012. **50**: p. 63-67.
18. CAMPBELL, J., *On the Use of a Torsional Split Hopkinson Bar to Study Rate Effects in.* 1970.
19. Lewis, J. and J. Campbell, *The development and use of a torsional Hopkinson-bar apparatus.* Experimental mechanics, 1972. **12**(11): p. 520-524.
20. Dharan, C.K. and F. Hauser, *Determination of stress-strain characteristics at very high strain rates*. Experimental mechanics, 1970. **10**(9): p. 370-376.
21. Malinowski, J., J. Klepaczko, and Z. Kowalewski, *Miniaturized compression test at very high strain rates by direct impact.* Experimental mechanics, 2007. **47**(4): p. 451-463.
22. Rittel, D., S. Lee, and G. Ravichandran, *A shear-compression specimen for large strain testing.* Experimental mechanics, 2002. **42**(1): p. 58-64.
23. Dorogoy, A. and D. Rittel, *Numerical validation of the shear compression specimen. Part I: Quasi-static large strain testing.* Experimental mechanics, 2005. **45**(2): p. 167-177.
24. Dorogoy, A. and D. Rittel, *Numerical validation of the shear compression specimen. Part II: Dynamic large strain testing.* Experimental mechanics, 2005. **45**(2): p. 178-185.
25. Follansbee, P. and U. Kocks, *A constitutive description of the deformation of copper based on the use of the mechanical threshold stress as an internal state variable.* Acta Metallurgica, 1988. **36**(1): p. 81-93.

26. Rusinek, A. and J.R. Klepaczko, *Shear testing of a sheet steel at wide range of strain rates and a constitutive relation with strain-rate and temperature dependence of the flow stress.* International Journal of Plasticity, 2001. **17**(1): p. 87-115.
27. Hull, D. and D.J. Bacon, *Introduction to dislocations*. Vol. 257. 1984: Pergamon Press Oxford.
28. Abed, F.H. and G. Voyiadjis, *A consistent modified Zerilli-Armstrong flow stress model for BCC and FCC metals for elevated temperatures.* Acta mechanica, 2005. **175**(1-4): p. 1-18.
29. Kocks, U. and H. Mecking, *Physics and phenomenology of strain hardening: the FCC case.* Progress in materials science, 2003. **48**(3): p. 171-273.
30. Louat, N., *On the theory of the Portevin-Le Chatelier effect.* Scripta Metallurgica, 1981. **15**(11): p. 1167-1170.
31. Cottrell, A., *LXXXVI. A note on the Portevin-Le Chatelier effect.* The London, Edinburgh, and Dublin Philosophical Magazine and Journal of Science, 1953. **44**(355): p. 829-832.
32. Kubin, L., K. Chihab, and Y. Estrin, *The rate dependence of the Portevin-Le Chatelier effect.* Acta Metallurgica, 1988. **36**(10): p. 2707-2718.
33. Kubin, L. and Y. Estrin, *Evolution of dislocation densities and the critical conditions for the Portevin-Le Chatelier effect.* Acta Metallurgica et Materialia, 1990. **38**(5): p. 697-708.
34. Klahn, D., A. Mukherjee, and J. Dorn, *STRAIN-RATE EFFECTS*, 1970, California Univ., Berkeley. Lawrence Radiation Lab.
35. Klepaczko, J. and C. Chiem, *On rate sensitivity of fcc metals, instantaneous rate sensitivity and rate sensitivity of strain hardening.* Journal of the Mechanics and Physics of Solids, 1986. **34**(1): p. 29-54.
36. Klepaczko, J., *Thermally activated flow and strain rate history effects for some polycrystalline FCC metals.* Materials Science and Engineering, 1975. **18**(1): p. 121-135.
37. Rusinek, A. and J.A. Rodríguez-Martínez, *Thermo-viscoplastic constitutive relation for aluminium alloys, modeling of negative strain rate sensitivity and viscous drag effects.* Materials & Design, 2009. **30**(10): p. 4377-4390.
38. Biswajit Banerjee, A.S.B., *An extended mechanical threshold stress plasticity model: modeling 6061-T6 aluminum alloy.* Journal of Mechanics of Materials and Structures, 2008. **3**(3).
39. Wallace, D.C., *Nature of the process of overdriven shocks in metals.* Physical Review B, 1981. **24**(10): p. 5607.
40. Wang, G., et al., *Calculating the Peierls energy and Peierls stress from atomistic simulations of screw dislocation dynamics: application to bcc tantalum.* Modelling and Simulation in Materials Science and Engineering, 2004. **12**(4): p. S371.
41. Nabarro, F.R., *Theory of crystal dislocations.* 1967.
42. Voyiadjis, G.Z. and F.H. Abed, *Microstructural based models for bcc and fcc metals with temperature and strain rate dependency.* Mechanics of Materials, 2005. **37**(2): p. 355-378.
43. Abed, F.H., *Physically based multiscale-viscoplastic model for metals and steel alloys: theory and computation*, 2005, Jordan University of Science and Technology.
44. Klepaczko, J., *Physical-state variables—the key to constitutive modeling in dynamic plasticity.* Nuclear engineering and design, 1991. **127**(1): p. 103-115.
45. Francart, C., et al., *Application of the Crystallo-Calorific Hardening approach to the constitutive modeling of the dynamic yield behavior of various metals with different crystalline structures.* International Journal of Impact Engineering, 2017.
46. FRANCART, C., et al., *Constitutive modelling of high thermal softening phenomenon in metallic materials*, in *ICILSM*2016: Torino.
47. Hodowany, J., et al., *Partition of plastic work into heat and stored energy in metals.* Experimental mechanics, 2000. **40**(2): p. 113-123.
48. Zaera, R., J.A. Rodríguez-Martínez, and D. Rittel, *On the Taylor–Quinney coefficient in dynamically phase transforming materials. Application to 304 stainless steel.* International Journal of Plasticity, 2013. **40**: p. 185-201.
49. Rittel, D., et al., *On the dynamically stored energy of cold work in pure single crystal and polycrystalline copper.* Acta Materialia, 2012. **60**(9): p. 3719-3728.
50. Nemat-Nasser, S. and J.B. Isaacs, *Direct measurement of isothermal flow stress of metals at elevated temperatures and high strain rates with application to Ta and TaW alloys.* Acta Materialia, 1997. **45**(3): p. 907-919.

51. Hodowany, J., et al., *Partition of plastic work into heat and stored energy in metals.* Experimental mechanics, 2000. **40**(2): p. 113-123.
52. Nielsen, L.E., *Cross-linking–effect on physical properties of polymers.* 1969.
53. Richeton, J., et al., *Influence of temperature and strain rate on the mechanical behavior of three amorphous polymers: Characterization and modeling of the compressive yield stress.* International Journal of Solids and Structures, 2006. **43**(7–8): p. 2318-2335.
54. Ward, I. and J. Sweeney, *An Introduction to the Mechanical Properties of Solid Polymers 2004.* England: John Wiley & Sons, Ltd.
55. Ward, I.M., *Review: The yield behaviour of polymers.* Journal of Materials Science, 1971. **6**(11): p. 1397-1417.
56. Struik, L.C.E., *Dependence of relaxation times of glassy polymers on their specific volume.* Polymer, 1988. **29**(8): p. 1347-1353.
57. Richeton, J., et al., *Modeling and validation of the large deformation inelastic response of amorphous polymers over a wide range of temperatures and strain rates.* International Journal of Solids and Structures, 2007. **44**(24): p. 7938-7954.
58. Van Melick, H., L. Govaert, and H. Meijer, *On the origin of strain hardening in glassy polymers.* Polymer, 2003. **44**(8): p. 2493-2502.
59. Karger-Kocsis, J. and T. Czigány, *Strain rate dependence of the work of fracture response of an amorphous poly (ethylene-naphthalate)(PEN) film.* Polymer Engineering & Science, 2000. **40**(8): p. 1809-1815.
60. Williams, M.L., R.F. Landel, and J.D. Ferry, *The temperature dependence of relaxation mechanisms in amorphous polymers and other glass-forming liquids.* Journal of the American Chemical society, 1955. **77**(14): p. 3701-3707.
61. Richeton, J., et al., *A unified model for stiffness modulus of amorphous polymers across transition temperatures and strain rates.* Polymer, 2005. **46**(19): p. 8194-8201.
62. Hopperstad, O., et al., *On the influence of stress triaxiality and strain rate on the behaviour of a structural steel. Part I. Experiments.* European Journal of Mechanics-A/Solids, 2003. **22**(1): p. 1-13.
63. Børvik, T., O. Hopperstad, and T. Berstad, *On the influence of stress triaxiality and strain rate on the behaviour of a structural steel. Part II. Numerical study.* European Journal of Mechanics-A/Solids, 2003. **22**(1): p. 15-32.
64. Skiba, T., et al., *Mechanical properties of spark plasma sintered FeAl intermetallics.* Intermetallics, 2010. **18**(7): p. 1410-1414.
65. Kubicki, B., *Stress concentration at pores in sintered materials.* Powder metallurgy, 1995. **38**(4): p. 295-298.
66. Dudrová, E. and M. Kabátová, *Fractography of sintered iron and steels.* Powder Metallurgy Progress, 2008. **8**(2): p. 59-75.
67. Bao, Y. and T. Wierzbicki, *On the cut-off value of negative triaxiality for fracture.* Engineering fracture mechanics, 2005. **72**(7): p. 1049-1069.
68. Bao, Y. and T. Wierzbicki, *On fracture locus in the equivalent strain and stress triaxiality space.* International Journal of Mechanical Sciences, 2004. **46**(1): p. 81-98.
69. Rittel, D. and S. Osovski, *Dynamic failure by adiabatic shear banding.* International Journal of Fracture, 2010. **162**(1): p. 177-185.
70. Osovski, S., et al., *Microstructural effects on adiabatic shear band formation.* Scripta Materialia, 2012. **66**(1): p. 9-12.
71. Abaqus, *Damage evolution and element removal for ductile metals.* Abaqus Documentation, 2014.
72. Rottler, J. and M.O. Robbins, *Growth, microstructure, and failure of crazes in glassy polymers.* Physical Review E, 2003. **68**(1): p. 011801.
73. Kinloch, A.J., *Fracture behaviour of polymers*2013: Springer Science & Business Media.
74. Arruda, E.M., M.C. Boyce, and R. Jayachandran, *Effects of strain rate, temperature and thermomechanical coupling on the finite strain deformation of glassy polymers.* Mechanics of Materials, 1995. **19**(2): p. 193-212.
75. Christian G'SELL, J.-M.H., *Introduction à la mécanique des polymères*1995.

76. Selby, K. and L. Miller, *Fracture toughness and mechanical behaviour of an epoxy resin.* Journal of Materials Science, 1975. **10**(1): p. 12-24.
77. Fiedler, B., et al., *Failure behavior of an epoxy matrix under different kinds of static loading.* Composites Science and Technology, 2001. **61**(11): p. 1615-1624.
78. Van Noort, R. and B. Ellis, *The fracture topography of poly (methyl methacrylate).* Journal of materials science letters, 1984. **3**(12): p. 1031-1034.

Chapter 3

CONSTITUTIVE MODELING OF MECHANICAL BEHAVIOR

The constitutive modeling of the mechanical behavior of materials such as metals or polymers has to take into account several phenomena in order to achieve an accurate numerical modeling in Finite Element software:

- The elasticity strain domain which is generated by different phenomena in metals and in polymers. It is always temperature T but may also be strain rate $\dot{\varepsilon}_e$ sensitive (depending on the studied material).
- The plasticity strain domain which characterizes the way how the material flows under a specific loading and involves a lot of complex phenomena (different in metals and in polymers). These phenomena show complex temperature T and strain rate $\dot{\varepsilon}_p$ dependencies.
- The initiation of failure which characterizes the beginning of the damage strain domain and, as the other phenomena, is temperature T and strain rate $\dot{\varepsilon}_p$ sensitive. Besides, the initiation of failure depends also greatly on the state of stress σ^*.
- The damage evolution $\dot{D}$ leading to the ultimate failure of the material is dependent to the state of stress σ^* and maybe to temperature T and to the strain rate $\dot{\varepsilon}_p$. However, only the state of stress sensitivity is studied in this work.

For all materials, the plasticity criterion used is the von Mises criterion [1]. This choice has been motivated for its general usage in mechanics of materials. However, other criteria might be used, especially for the epoxy resin (e.g. Drucker-Prager [2], Raghava [3, 4]).

In this chapter, the different phenomena explained in the previous part for the different materials (F7020, polyimide and epoxy resin) are modeled through different specific expressions which are thoroughly discussed and then applied. In each case, the full set of parameters is provided.

A. Constitutive modeling of elastic behavior

1. F7020 aluminum alloy

The constitutive modeling of the elasticity behavior of metallic material is generally performed by considering the linear elasticity hypothesis (Eq 3.1 – 1D case for isotropic materials).

$$\sigma = E\varepsilon \qquad (3.1)$$

The strain rate sensitivity of the elastic properties of metals has not been brought to light and can therefore be neglected if it exists. However, an important thermal dependency can be observed for all metals with a monotonous softening leading to a zero stiffness at the melting point T_m following Eq 3.2 for the elasticity modulus E [5, 6].

$$E(T) = E_0\left(1 - \frac{T}{T_m}e^{\theta^*\left(1-\frac{T_m}{T}\right)}\right) \qquad (3.2)$$

With E_0 the value of the elasticity modulus at 0 K and θ^* the temperature dependency parameter ($\theta^* = 0.9$ for FCC metals [5, 7] and $\theta^* = 0.6$ for BCC metals [5, 6]).

The theoretical evolution of E for an aluminum alloy ($E(293K) = 72\ GPa$) with the temperature is shown on Figure 93. The parameters can be found in Table 11. The value of T_m is the melting temperature and E_0 has been determined using the expression Eq 3.2 with $E(T = 293\ K) = 72\ GPa$.

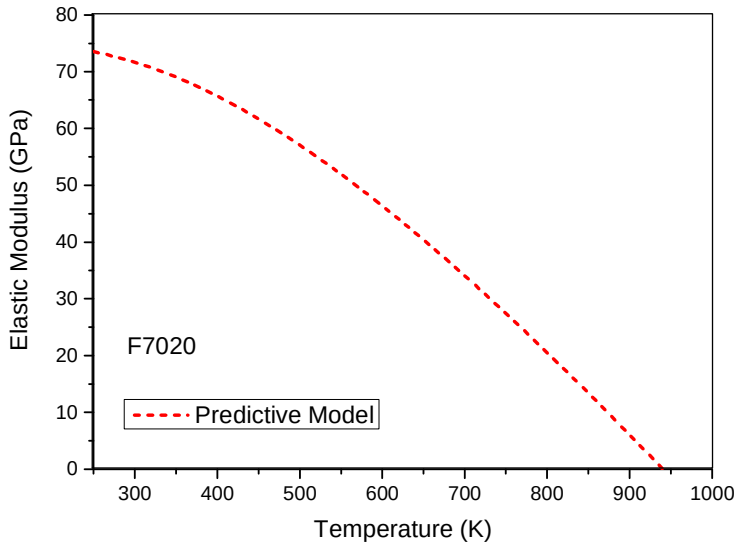

Figure 93 - Theoretical evolution of the elastic modulus of the F7020 with the temperature

Table 11 - Elastic modulus parameters of the F7020

$E_0(GPa)$	$\theta^*(-)$	$T_m\ (K)$
75.2	0.9	940

2. Sintered polyimide

The elasticity of polymers does not follow the linearity hypothesis as for the metallic materials. Indeed, the elastic behavior follows a viscoelastic law which is caused by the independent contribution of a great number of individual loading steps and generally computed by using the Boltzmann's superposition principle [8].

However, for numerical implementation purposes, the assumption of linear elasticity will still be used in this work by considering the average value of the stress slop over the range of the viscoelastic domain (Figure 94). Besides, the elastic properties of the sintered polyimide do not present any strain rate dependency. However, a strong temperature sensitivity of the average elastic modulus is observed up to

the temperature of glass transition T_g where it reaches a zero value. The same expression used for the linear elasticity of metallic material (Eq 3.3) is used to model the average elastic modulus $\langle E(T)\rangle$ [5]. The parameters are listed in Table 12 which have been determined using the least square method.

$$\langle E(T)\rangle = \langle E_0\rangle \left(1 - \frac{T}{T_g} e^{\theta^* \left(1 - \frac{T_g}{T}\right)}\right) \quad (3.3)$$

With E_0 the value of the elasticity modulus at 0 K and θ^* the temperature dependency parameter.

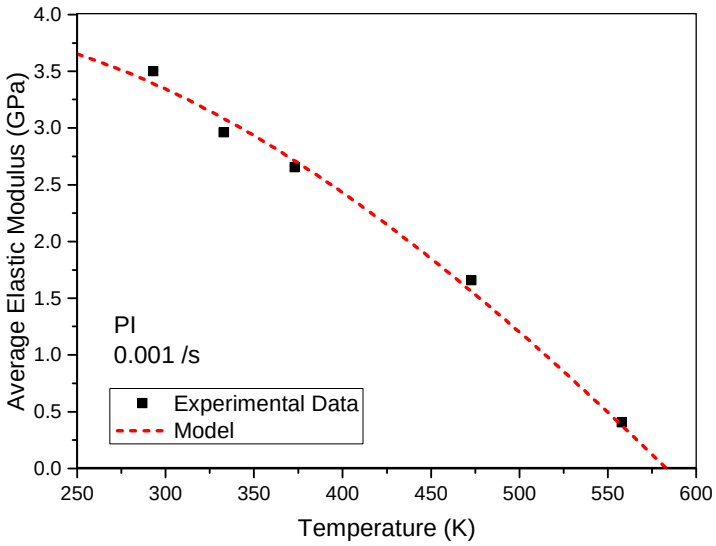

Figure 94 - Evolution of the average elastic modulus of the sintered PI with the temperature

Table 12 - Elastic modulus parameters of the sintered PI

$\langle E_0\rangle\ (GPa)$	$\theta^*\ (-)$	$T_g\ (K)$
1.693	1.241	583

3. Epoxy resin

The same hypothesis of linearity of an average elastic modulus computed over the viscoelastic domain done for the sintered polyimide is used for the epoxy resin. However, in this case, the material presents a temperature-strain rate coupled behavior (Figure 95).

The model used for the modeling of the average elastic modulus $\langle E(\dot{\varepsilon}_p, T)\rangle$ is performed using Eq 3.4.

$$\langle E(\dot{\varepsilon}_p, T)\rangle = \langle E_0\rangle \left(1 - \frac{T}{T_g} e^{\theta^* \left(1 - \frac{T_g}{T}\right)}\right)\left(1 + l_v \ln\left(\frac{\dot{\varepsilon}_e}{\dot{\varepsilon}_{e0}}\right) + v\left(\frac{\dot{\varepsilon}_e}{\dot{\varepsilon}_{e0}}\right)^{n_v}\right) \quad (3.4)$$

With E_0 the value of the elasticity modulus at 0 K and θ^* the temperature dependency parameter, $\dot{\varepsilon}_{e0}$ a reference elastic strain rate and l_v, v and n_v are empirical parameters modeling the strain rate sensitivity. The value of the parameters are reported in Table 13 which have been determined using the least square method.

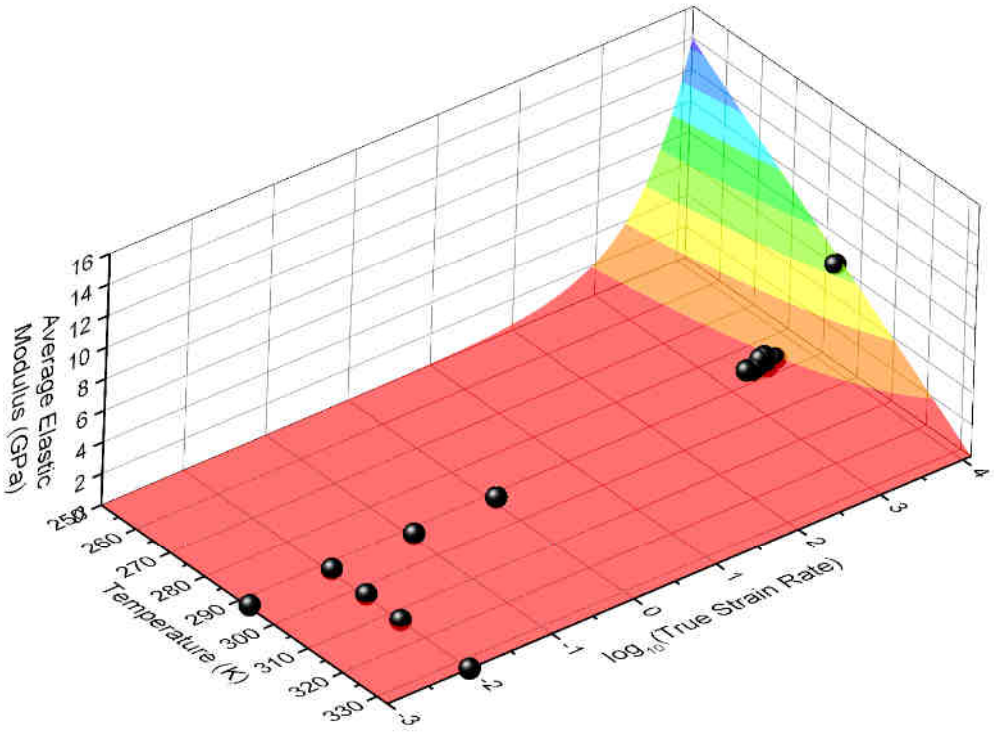

Figure 95 - Evolution of the average elastic modulus of the epoxy resin with the strain rate and the temperature

The strain rate sensitivity of the elastic properties decreases with the temperature due to the softening caused by this last. Indeed, the cross-linking of the chains (entanglement) decrease with the temperature and greatly conditions the strain rate sensitivity of the rigidity of the polymer [9]. This explains the very high values of $\langle E \rangle$ at high strain rates near the temperature of glass transition T_g.

Table 13 - Elastic modulus parameters of the epoxy resin

$\langle E_0 \rangle\ (MPa)$	$\theta^*\ (-)$	$T_g\ (K)$	$l_v\ (-)$	$v\ (-)$	$n_v\ (-)$	$\dot{\varepsilon}_{e0}\ (/s)$
0.9055	0.01932	333	0.7018	0.2984	0.7474	0.001

B. Constitutive modeling of inelastic behavior

1. Development of the Crystallo-Calorific Hardening approach for FCC metals (CCH-FCC)

In order to take into account all the different phenomena observed and discussed in the previous part, a method to obtain constitutive models for a specific metallic material has been developed. Only the FCC case will be discussed in this work.

The overall analytical expression of the overall constitutive model of the stress can be written as Eq 3.5 [10, 11].

$$\sigma(\varepsilon_p, \dot{\varepsilon}_p, T) = \sigma_{ath}(\varepsilon_p) + \sigma_{eff}(\dot{\varepsilon}_p, T)\Omega(\dot{\varepsilon}_p, T) + \sigma_{int}(\varepsilon_p, \dot{\varepsilon}_p, T)\Omega(\dot{\varepsilon}_p, T_0) \quad (3.5)$$

With σ_{ath} the athermal stress, σ_{eff} the effective stress, σ_{int} the internal stress, Ω the calorific ratio and T_0 the initial temperature.

Each of the above stress contributions ($\sigma_{int}, \sigma_{eff}, \Omega(\dot{\varepsilon}_p, T)$ and $\sigma_{ath}(\varepsilon_p)$) can be modeled using different and appropriate expressions [11]. The expressions suggested in this work to describe each of these phenomena can be replaced by any other which could be considered more adapted for the considered material. The expression presented in this chapter have been chosen to obtain a high level of accuracy for the modeling of the overall stress.

a. Introduction to the calorific ratio

The calorific ratio Ω corresponds to the evolution of the isothermal normalized thermal stress with the temperature at given strain rate and strain [10, 11]. It reveals the impact of thermally dependent microstructural phenomena (e.g. precipitation or dissolution) on the mechanical behavior. Therefore, the thermal mechanical behavior can become extremely complex in the case of alloys presenting a large number of microstructural changes over the studied range of temperature.

Thus, a specific expression allowing the constitutive modeling has been developed. It provides a method which permits the modeling of the influence of N changes of microstructure on the stress. The expression is based on Eq 3.6 [5, 11].

$$\Omega(T) = \frac{\sigma_{th}}{\sigma_{th_{ref}}} = 1 - (-1^n)\frac{T}{T_m}e^{\theta^p\left(1-\frac{T}{T_m}\right)} \quad (3.6)$$

With $n = 0$ in case of dissolution of precipitates and $n = 1$ in case of precipitation

Eq 3.6 is generally not determined at a reference temperature T_r of $0K$. It is therefore normalized for a reference value of temperature called T_r (Eq 3.7).

$$\Omega(T) = \frac{1-(-1^n)\frac{T}{T_m}e^{\theta^p\left(1-\frac{T}{T_m}\right)}}{1-(-1^n)\frac{T_r}{T_m}e^{\theta^p\left(1-\frac{T_r}{T_m}\right)}} \quad (3.7)$$

However, it has been stated that the thermal softening of a metal does not follow a relation directly linked to the melting temperature T_m. Indeed, another specific temperature called the critical temperature $T_C(\dot{\varepsilon}_p)$ has been introduced for mechanical modeling (Eqs 3.7 and 3.8) [12]. The critical temperature T_C corresponds to the temperature at which the mechanical response of the material becomes theoretically zero (without taking into account fusion phenomenon).

$$T_c(\dot{\varepsilon}_p) = \left(-\frac{k_B}{G_0}\ln\left(\frac{\dot{\varepsilon}_p}{\dot{\varepsilon}_m}\right)\right)^{-1} \quad (3.7)$$

$$\dot{\varepsilon}_m = b\rho_m l\omega_0 \quad (3.8)$$

With k_B the Boltzmann constant, G_0 the free energy, $\dot{\varepsilon}_m$ the athermal strain rates above which no thermal energy is required for the dislocations to overcome the obstacles, b the Burger vector, ρ_m the density of mobile dislocations, l the interdislocation distance and ω_0 the attempt frequency (the number of attempts a dislocation done per second to overcome an obstacle).

The parameter θ^p models the steepness of the softening (or hardening) of the metals with the temperature between two microstructural changes. It is therefore directly linked to the kinetics of microstructural changes and a strain rate sensitivity is physically justified. The higher the strain rate is, the less the microstructural change has the time to occur. Eq 3.9 allows a good estimation of the evolution of θ^p with the strain rate up to very high strain rates (above 10^7 /s) [10, 11].

$$\theta^p\left(\dot{\varepsilon}_p\right) = \theta^p{}_0 + \zeta\left(1+\ln\left(\frac{\dot{\varepsilon}_p}{\dot{\varepsilon}_0}\right)\right) \quad (3.9)$$

The element of modeling discussed (Eq 3.7) allow only the modeling of the thermal behavior between the microstructural changes. To model these changes, the factor $r(T)$ (Eq 3.10) [13] is introduced in order to model the transition mechanical behavior between two thermally dependent stable phases.

$$r(T) = e^{-\left(\frac{T}{T_p-T_t}\right)^a} \quad (3.10)$$

With T_p, the temperature of end of microstructural change, T_t the range of temperatures corresponding to this phenomenon and a is a parameter describing the kinetics of dissolution of the precipitates.

Furthermore, the value of T_p increases with the strain rate and a law similar to the one used to model the strain rate sensitivity of θ^* can be used (Eq 3.11) [11, 14].

$$T_p(\dot{\varepsilon}_p) = T_{p0} + \varpi\left(1+\ln\left(\frac{\dot{\varepsilon}_p}{\dot{\varepsilon}_0}\right)\right) \quad (3.11)$$

With T_{p0} the value of T_p at $\dot{\varepsilon}_0$ and ϖ a fitting parameter representing the strain sensitivity of T_p.

Finally, the expression can be generalized in order to take into account *N* changes of microstructure over the range of tested temperatures. The final expression of the calorific ratio used for *N* microstructural changes can be written as Eq 3.12 [11].

$$\Omega(\dot{\varepsilon}_p, T) = \frac{1}{N}\sum_{i=1}^{N}\left[\frac{1-(-1^{n_i})\frac{T}{T_{c_i}(\dot{\varepsilon}_p)}e^{\theta^{p}{}_i(\dot{\varepsilon}_p)\left(1-\frac{T}{T_{c_i}(\dot{\varepsilon}_p)}\right)}}{1-(-1^{n_i})\frac{T_r}{T_{c_i}(\dot{\varepsilon}_p)}e^{\theta^{p}{}_i(\dot{\varepsilon}_p)\left(1-\frac{T_r}{T_{c_i}(\dot{\varepsilon}_p)}\right)}}e^{-\left(\frac{T}{T_{p_i}(\dot{\varepsilon}_p)-T_{t_i}}\right)^{a_i}}\right] \quad (3.12)$$

The application of such modeling can become very complex if the metallic alloy presents a lot of microstructure changes. In those conditions, it is easier to operate on the thermal behavior for each stable range of temperature to find the approximate value of the parameters before adjusting over the whole range of temperatures. The temperature parameters can be generally easily found on the phase diagram of the corresponding metallic alloy.

The calorific ratio modeling has been applied on the thermal behavior of the F7020 aluminum alloy and the computed parameters are listed in Table 14. The values of these parameters have been determined, in this study, with a custom Matlab® program using the least square method considering physical boundaries of the values of the parameters through several steps of fitting: the temperature sensitivity is firstly fitted for each strain rate and then the strain rate sensitivity of the computed parameters is calculated to obtain the missing parameters.

Table 14 - Parameters of the calorific ratio of the F7020, N=1

Dissolution	**n**	G_{01}**(eV)**	$\dot{\varepsilon}_{m1}$ **(/s)**	θ_{01}^{p}	ζ_1 **(/K)**	$\dot{\varepsilon}_0$ ($/s$)	a_1	T_{p0} **(K)**	T_{t1} **(K)**	ϖ_1
	0	3.477	4.84e16	0.25	0.06	0.01	7	566.9	37	0.238
Fusion	**n**	G_{02}**(eV)**	$\dot{\varepsilon}_{m2}$ **(/s)**	θ_{02}^{p}	ζ_2 **(K)**	$\dot{\varepsilon}_0$ ($/s$)	a_2	T_m **(K)**	T_{t2} **(K)**	ϖ_2
	0	8.82	2.96e10	0.32	0.06	0.01	60	940	30	0

The results of the modeling of the calorific ratio can be observed on the Figure 96. It can be seen that the suggested model is accurate over the whole range of temperatures due to its capability to take separately into account the behavior before and after the dissolution of the precipitates (around 490 *K*) [15]. The athermal plateau observed at high temperatures, caused by the absence of the phase dissolution, is therefore correctly modeled. Models such as the Johnson-Cook model [16] or the Arrhenius law are not able to represent such behavior as well as the strain rate dependency. This last is less important concerning the F7020 contrary to the BCC metals. The expression of the critical

temperature T_c can explain this observation by the implication of the interdislocation distance l in the computation. Indeed, the value of l is around $500b$ in the case of FCC metals but is around the same magnitude of b for the BCC metals. Thus, the critical temperature T_c is much more strain rate sensitive for the CCC metals than for the FCC metals leading to the observed behavior of the calorific ratio of the F7020.

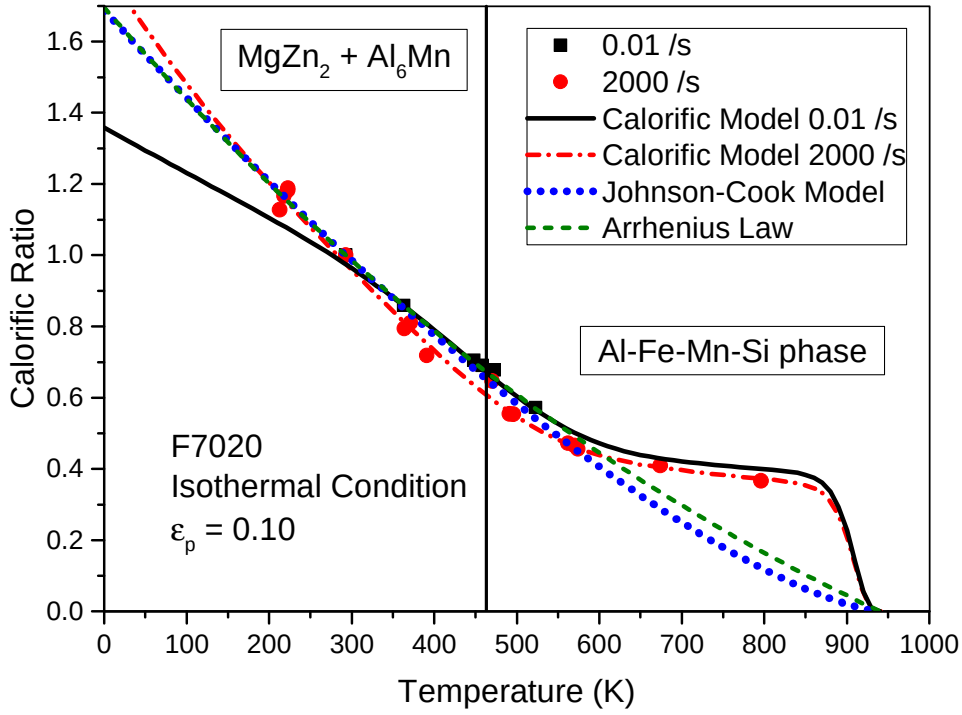

Figure 96 - Evolution of the calorific ratio of the F7020 in quasi-static and dynamic conditions

b. Constitutive modeling of the effective stress

The effective stress corresponds to the part of the overall thermal stress which does not depend on the structural hardening and therefore to the history effects. The overall contribution of each phenomenon (e.g. overcoming of Peierls' barriers) responsible of such stress can be modeled through Eq 3.13 (for M different phenomena) [17].

$$\sigma_{eff}(\dot{\varepsilon}_p, T_r) = \sum_{i=1}^{M}\left[\sigma_{e_i}\left(1-\left(\frac{k_B}{g_{0_i}\mu b^3}T_r \ln\left(\frac{\dot{\varepsilon}_r}{\dot{\varepsilon}_p}\right)\right)^{\omega_i}\right)^{\kappa_i}\right] \quad (3.13)$$

With σ_{e_i} the characteristic resulting stress of the phenomenon i at the reference temperature T_r and strain rate $\dot{\varepsilon}_r$, ω_i and κ_i are the form factors of the considered obstacles linked to the phenomenon i, g_{0_i} is the normalized inversed characteristic energy of the phenomenon i, b is the Burger's vector and μ is the shear modulus.

However, in most cases, only the contribution of the overcoming of the Peierls' barriers [18] is considered. Thus, the effective stress of FCC metals is modeled with Eq 3.14.

$$\sigma_{eff}(\dot{\varepsilon}_p, T_r) = (Y_r - Y_a)\left(1 - \left(\frac{k_B}{g_0 \mu b^3} T_r \ln\left(\frac{\dot{\varepsilon}_r}{\dot{\varepsilon}_p}\right)\right)^{\omega}\right)^{\kappa} \quad (3.14)$$

With Y_r the observable yield stress at T_r and $\dot{\varepsilon}_r$ and Y_a the athermal yield stress of the metal.

Concerning the F7020, the parameters are reported in Table 15. The values of ω and κ are arbitrary set to these values. The value of b is taken from the literature and μ is computed from the other elastic properties E and ν using Eq 3.15.

$$\mu = \frac{E}{2(1+\nu)} \quad (3.15)$$

Y_r is obtained from the measurable yield stress at reference temperature T_r and reference strain rate $\dot{\varepsilon}_r$. The athermal yield stress Y_a is determined using Eq. 3.16 [19].

$$Y_a = \alpha \mu \left(\frac{b}{D_g}\right)^{\frac{1}{2}} \quad (3.16)$$

With α an empirical parameter generally taken as $\alpha = 0.3$ and D_g the average grain size.

The parameter g_0 is then computed using the least square method.

Table 15 - Parameters of the effective stress of the F7020

$g_0\ (-)$	$b\ (nm)$	$\mu\ (GPa)$	ω	κ	$Y_r\ (MPa)$	$Y_a\ (MPa)$	$T_r\ (K)$	$\dot{\varepsilon}_r\ (/s)$
1.143	0.286	26.92	1	1.5	260	36.3	293	0.001

The suggested model has a linear sensitivity with the logarithm of the strain rate but the strain rate sensitivity of the normalized effective stress (with its value at $\dot{\varepsilon}_r$) seems to be nonlinear (Figure 97). This behavior can be explained by the influence of other phenomena than the overcoming of the Peierls' barriers. However, the strain rate sensitivity of the effective stress of the F7020 is not very strong and this behavior is characteristic of the FCC metals [20, 21]. Therefore, the usage of the simplified expression (Eq 3.14) taking into account only the main phenomena can still be used with a satisfying accuracy.

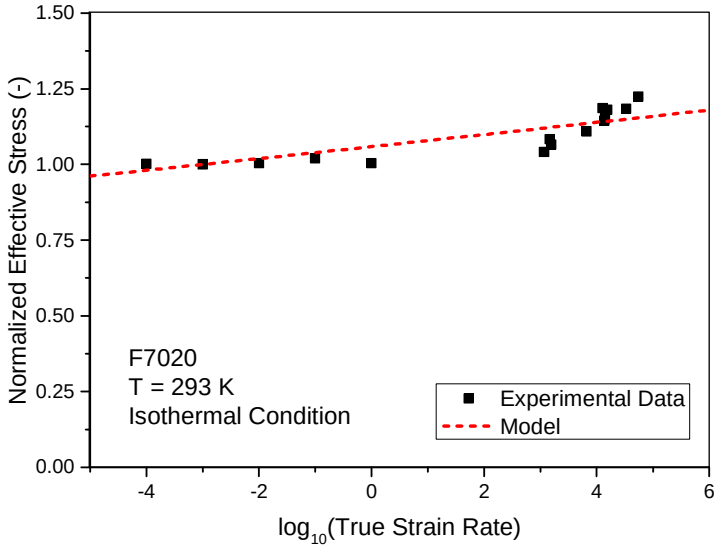

Figure 97 - Evolution of the normalized effective stress of the F7020 with the strain rate

c. Constitutive modeling of the internal stress

The modeling of the internal stress $\hat{\sigma}_{int}$ is performed through the consideration of each of the phenomena discussed in the previous chapter:

- The structural strain hardening $f_H(\varepsilon_p)$
- The strain rate sensitivity due to history effect $f_{SR}(\dot{\varepsilon}_p)$
- The adiabatic heating sensitivity $f_A\left(T, f_H(\varepsilon_p), f_{SR}(\dot{\varepsilon}_p)\right)$

With Eq 3.17 [11]:

$$\sigma_{int}(\varepsilon_p, \dot{\varepsilon}_p, T) = f_H(\varepsilon_p) f_{SR}(\dot{\varepsilon}_p) f_A\left(T, f_H(\varepsilon_p), f_{SR}(\dot{\varepsilon}_p)\right) \quad (3.17)$$

i. **Structural strain hardening**

The structural strain hardening of the internal stress corresponds to the multiplication of the mobile dislocations and to the propagation of the forests of dislocations in the case of FCC metals. These two phenomena cause a kinematic hardening which is different from the isotropic hardening of the BCC metals. During the strain of the FCC material, the dislocation texture generated is very heterogeneous due to the forests of dislocations [20, 21].

The modeling of such heterogeneous kinematic hardening can be taken into account through the following strain dependent function f_H (Eq 3.18).

$$f_H(\varepsilon_p) = B\left(1 - e^{-k\varepsilon_p}\right) + R\varepsilon_p \qquad (3.18)$$

With B the plastic modulus, k the coefficient of annihilation of dislocations and R the kinematic modulus. These parameters are determined using the least square method.

The value of the internal stress at a given strain is computed by removing the values of the effective and athermal stresses at the conditions of temperature and strain rate at this strain to the overall stress (Eq 3.5) [11].

The comparison between the experimental data and the model described by the previous expression can be found on the Figure 98 and the parameters used in Table 16.

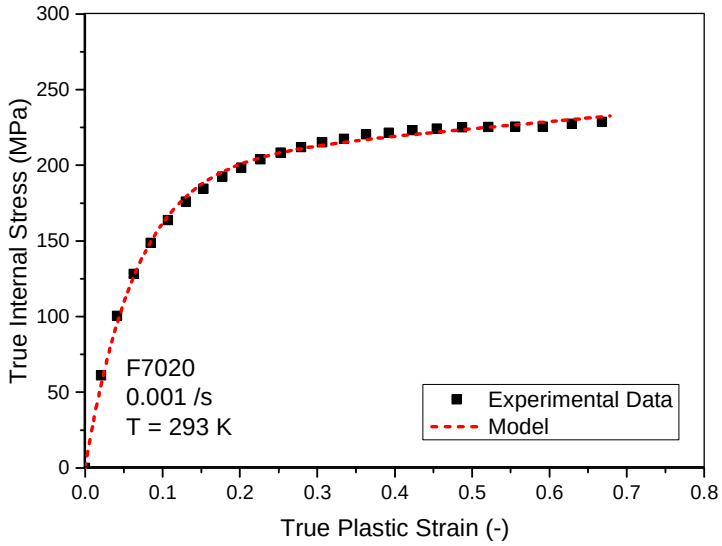

Figure 98 - Modeling of the structural strain hardening of the F7020

The suggested model (Eq 3.18) allows to evaluate the contribution of the isotropic hardening and of the kinematic hardening with the values of the parameters B and R. Concerning the F7020, it can be seen that the hardening due to the isotropic hardening is much more important than the contribution of kinematic hardening.

Table 16 - Strain hardening parameters of the F7020

$B\ (MPa)$	$k\ (-)$	$R\ (MPa)$
200.8	15.22	46.84

ii. Strain rate sensitivity of internal stress

The strain rate sensitivity of the internal stress due to history effect is modeled through a phenomenological expression taking into account quasi-static and dynamic behavior. Eq 3.19 allows

also the modeling of phenomena such viscous drag at high strain rates and dynamical stress ageing in the range of the low and intermediate strain rates (see Figure 99) [11, 17].

$$f_{SR}(\dot{\varepsilon}_p) = 1 + l_v \ln\left(\frac{\dot{\varepsilon}_p}{\dot{\varepsilon}_0}\right) + v\left(\frac{\dot{\varepsilon}_p}{\dot{\varepsilon}_0}\right)^{n_v} \quad (3.19)$$

With l_v, v and n_v phenomenological parameters and $\dot{\varepsilon}_0$ a reference value of strain rate. The value of these parameters are reported in Table 17. These parameters are computed using the least square method.

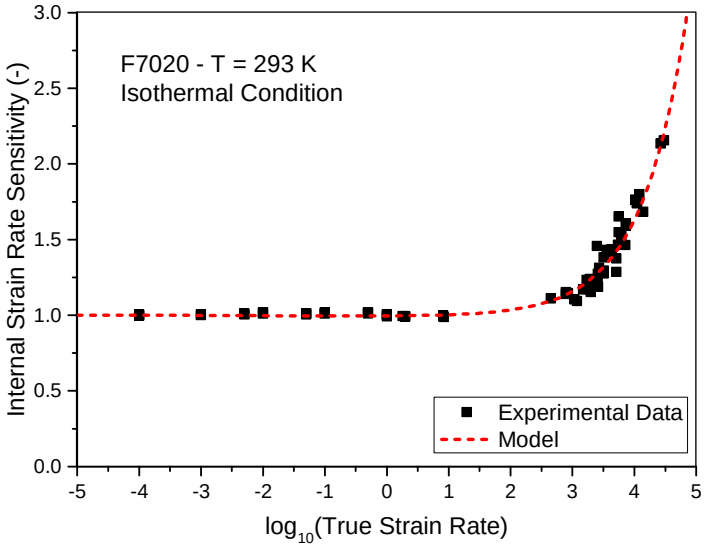

Figure 99 - Evolution of the strain rate sensitivity of the internal stress of the F7020

Table 17 - Parameters of the internal stress strain rate sensitivity of the F7020

$l_v\ (-)$	$v\ (-)$	$n_v\ (-)$	$\dot{\varepsilon}_0\ (/s)$
-0.003459	0.00008508	0.4889	0.0001

iii. **Adiabatic heating sensitivity**

The distinction between temperature sensitivity and adiabatic heating sensitivity can be done for modeling purpose. Indeed, the loss of stress caused by the elevation of the material temperature due to environmental effect (thermodynamic external source) can be very different than the one caused by self-heating (thermodynamic internal source). The environmental cases are modeled with the calorific ratio and the self-heating effect case is modeled through a specific expression which is applied on the isothermal value of the internal stress. The modeling of its impact on the internal stress is based on an energy method which consists in computing the dissipated energy $\Delta\hat{E}_T$ between the isothermal state $\hat{E}_{iso}$ and the adiabatic state $\hat{E}_{adia}$ of the internal stress (Eq 3.20).

$$\Delta\hat{E}_T = \hat{E}_{iso} - \hat{E}_{adia} \quad (3.20)$$

With Eq 3.21:

$$\hat{E}_{iso} = \int \widehat{\sigma_{iso}}\, d\varepsilon_p \text{ and } \hat{E}_{adia} = \int \widehat{\sigma_{adia}}\, d\varepsilon_p \quad (3.21)$$

From experimental data, $\hat{E}_{iso}$ and $\hat{E}_{adia}$ are calculated using Eqs 3.21 and 3.22.

$$\hat{E}_{iso} = \int \left(\sigma_{exp_{iso}} - f(\dot{\varepsilon}_p, T_0)\sigma_{eff} - \sigma_{ath}\right) d\varepsilon_p \quad (3.21)$$

$$\hat{E}_{adia} = \int \left(\sigma_{exp} - f(\dot{\varepsilon}_p, T)\sigma_{eff} - \sigma_{ath}\right) d\varepsilon_p \quad (3.22)$$

The experimental isothermal values of stress are obtained through repeated tests at small stress to avoid adiabatic heating. The evolution of $\Delta\hat{E}_T$ can be nicely fitted with a power law (Eq 3.23) (see Figure 100). The parameters are reported in Table 18 and are determined using the least square method.

$$\Delta\hat{E}_T = E_A(T - T_0)^{n_T} \quad (3.23)$$

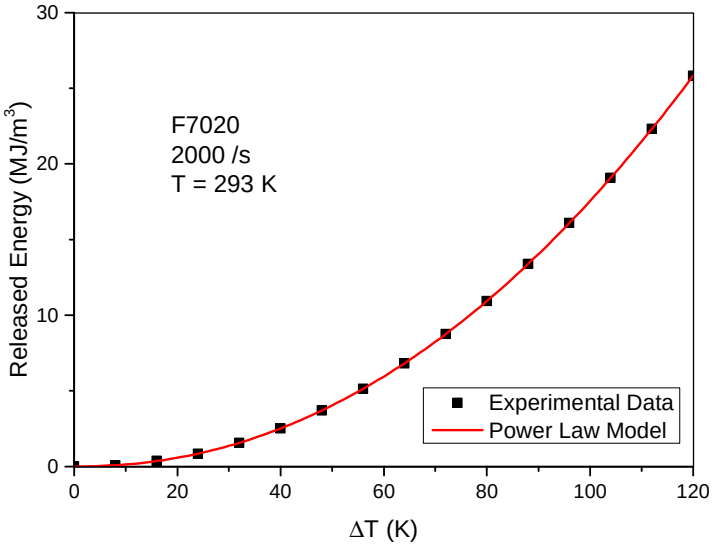

Figure 100 - Evolution of the energy released by the F7020 with the gradient of temperature due to the adiabatic heating

The evolution of the temperature with the strain is computed with Eq 3.24.

$$\Delta T = \frac{\chi}{\rho C_p}\int \sigma d\varepsilon_p \quad (3.24)$$

With χ the Taylor-Quinney coefficient, ρ the density of the material and C_p its specific heat. The value of ρ and C_p are temperature dependent but will be assumed constant in this work.

Table 18 - Adiabatic heating softening parameters of the F7020

$E_A\ (MPa.K^{-n_T})$	$n_T\ (-)$
0.00101	2.12

By considering the previous equations, the adiabatic energy can be written with Eq 3.25.

$$\hat{E}_{adia} = \hat{E}_{iso} - \Delta\hat{E}_T \quad (3.25)$$

By derivation of $\hat{E}_{adia}$, the values in terms of stress can be obtained and the impact of the adiabatic heating can be evaluated using Eq 3.26.

$$\sigma_{int} = \hat{\sigma}_{iso} - \frac{d\Delta\hat{E}_T}{d\varepsilon_p} \quad (3.26)$$

With Eq 3.27:

$$\frac{d\Delta\hat{E}_T}{d\varepsilon_p} = \frac{d}{d\varepsilon_p}(E_A(T-T_0)^{n_T}) = \frac{d}{d\varepsilon_p}\left(E_A\left(\frac{\chi\sigma}{\rho C_p}\varepsilon_p\right)^{n_T}\right) = \frac{n_T E_A\left(\frac{\chi\sigma\varepsilon_p}{\rho C_p}\right)^{n_T}}{\varepsilon_p} \quad (3.27)$$

The internal stress can therefore be expressed with Eq 3.28:

$$\sigma_{int} = \hat{\sigma}_{iso} - \frac{n_T E_A(T-T_0)^{n_T}}{\varepsilon_p} = f_H f_{SR} - \frac{n_T E_A(T-T_0)^{n_T}}{\varepsilon_p} \quad (3.28)$$

This can be rewritten into a multiplicative factor more suited to follow the impact of the thermal softening on the internal stress (Eq 3.29).

$$\sigma_{int} = f_H f_R\left(1 - \frac{n_T E_A(T-T_0)^{n_T}}{\varepsilon_p f_H f_R}\right) = f_H f_R f_A(T) \quad (3.29)$$

With Eq 3.30:

$$f_A(T) = \left(1 - \frac{n_T E_A(T-T_0)^{n_T}}{\varepsilon_p f_H f_R}\right) \quad (3.30)$$

This step only needs one test under adiabatic condition exhibiting the highest adiabatic heating (high strain state). The isothermal condition can be computed from the quasi-static state using the strain rate sensitivity factor determined previously (Eq 3.19) or more accurately by performing repeated impact tests at small strain on the same sample to limit a maximum adiabatic heating [22].

d. Overall constitutive modeling of the stress behavior

The different expressions used to model the different phenomena are gathered in the comprehensive model of the overall stress σ (Eq 3.5). The accuracy of the constructed CCH model is then checked over wide ranges of temperature and strain rates.

The modeling in quasi-static and dynamic conditions (Figure 101.a and 101.b) with different initial temperature presents an excellent result due to the ability of the calorific ratio to take into account the changes of microstructure, and to the nonlinear expression suggested for the modeling of the strain rate sensitivity of the internal stress.

It can be seen on the Figure 101.c, that the suggested CCH model is in good correlation with the experimental data even at very high strain rates (55000 /s). Therefore, the level of stress of the F7020 is very well modeled with the proposed CCH model.

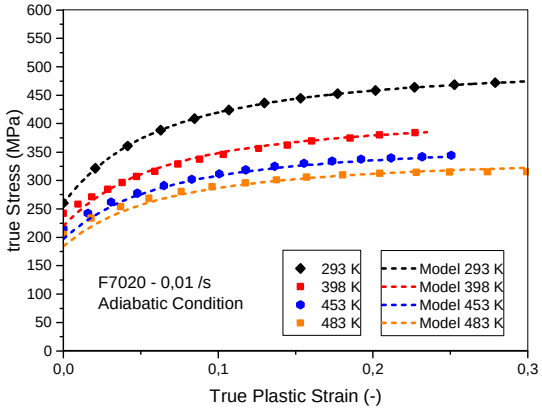

(a)

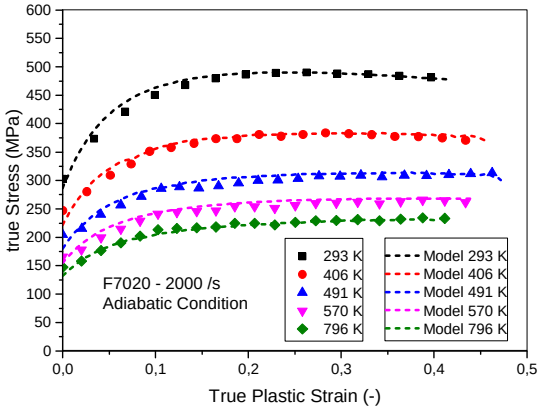

(b)

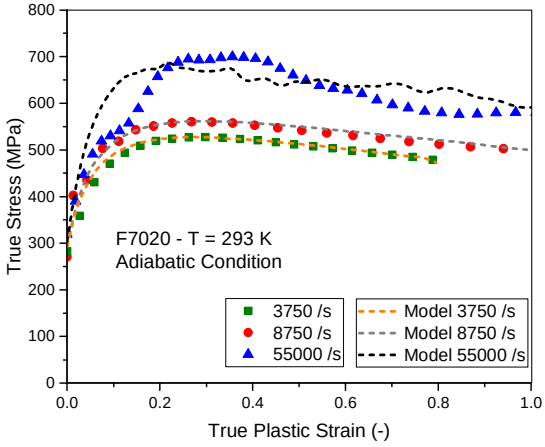

(c)

Figure 101 - Comparisons between the experimental data and the CCH model for the F7020 in (a) quasi-static, (b) dynamic at different temperatures and (c) at higher strain rates

e. Other possible expressions for constitutive modeling using the CCH approach

The expressions to model the different parts of the overall stress σ ($\hat{\sigma}_{int}(\varepsilon_p, \dot{\varepsilon}_p, T)$, σ_{eff}, $\Omega(\dot{\varepsilon}_p, T)$ and $\sigma_{ath}(\varepsilon_p)$) suggested previously in this chapter can be easily substitutes by other expressions to obtain a more appropriate model for another materials are a simpler expression of σ.

Expressions are suggested (Table 19) according to the lattice structure of the studied material (FCC or BCC).

Table 19 - Other expression for constitutive modeling of FCC and BCC models using the CCH approach

Lattice Structure	$\hat{\sigma}_{int}(\varepsilon_p, \dot{\varepsilon}_p, T)$	$\sigma_{eff}(\dot{\varepsilon}_p, T)$	$\Omega(\dot{\varepsilon}_p, T)$	$f_{SR}(\dot{\varepsilon}_p)$	$f_A(T)$
FCC	Eq 3.18	Y	$\left(1-\frac{T-T_r}{T_m-T_r}\right)^m$ [16]	Eq 3.19	Eq 3.30
	$B\sqrt{1-e^{-k\varepsilon_p}}$ [23]	Eq 3.14	Eq 3.12		1
BCC	$B{\varepsilon_p}^n$ [24]	Eq 3.14	$\left(1-\frac{T-T_r}{T_m-T_r}\right)^m$ [16]	1	1
			Eq 3.12		

Therefore, simple expressions to model σ can be built for FCC (Eq 3.31) and BCC (Eq 3.32) metals:

$$\sigma_{FCC}(\varepsilon_p, \dot{\varepsilon}_p, T) = \left[Y + B\sqrt{1-e^{-k\varepsilon_p}}\left(1 + l_v \ln\left(\frac{\dot{\varepsilon}_p}{\dot{\varepsilon}_r}\right) + v\left(\frac{\dot{\varepsilon}_p}{\dot{\varepsilon}_r}\right)^{n_v}\right)\right]\left(1-\frac{T-T_r}{T_m-T_r}\right)^m \quad (3.31)$$

7 parameters for calibration

$$\sigma_{BCC}(\varepsilon_p, \dot{\varepsilon}_p, T) = B{\varepsilon_p}^n + Y\left(1-\left(\varphi T_r \ln\left(\frac{\dot{\varepsilon}_r}{\dot{\varepsilon}_p}\right)\right)\right)^{\frac{3}{2}}\left(1-\frac{T-T_r}{T_m-T_r}\right)^m \quad (3.32)$$

5 parameters for calibration

The parameters for Eq 3.31 have been determined for the F7020 aluminum alloy and can be found in the APPENDIX C. The expression has been slightly modified from Eq 3.31 to take into account the increase of the effective stress between QS and dynamic conditions which cannot be neglected ($\sim 25\ MPa$). Indeed, Eq 3.31 can be used efficiently as written only if the strain rate sensitivity of the effective stress is negligible (e.g. AA7020-T651 or AA7075-T6 [25]). If not an expression such as Eq 3.14 has to be used in factor of Y to avoid too much inaccuracy at high strain rates.

Besides, as explained in the first chapter, the expression defining the thermal sensitivity used in Eq 3.31 and Eq 3.32 cannot model the athermal plateau at high temperatures, the overall mechanical response of the material is underestimated in this range of temperatures which can be found in high velocities impact experiments. Therefore, the impact simulations will underestimates the ballistic performances of the F7020 aluminum alloy target if Eq 3.31 is used.

Concerning the Eq 3.32, the usage of the expression $\left(1-\frac{T-T_r}{T_m-T_r}\right)^m$ for the temperature sensitivity might provide high inaccuracies at high strain rates and high temperatures due to the fact that the calorific ratio is much more sensitive to the strain rate for BCC metals than for FCC metals [11] (it is caused by the interdislocation distance which is much lower in the BCC case). In simulation involving relatively high temperatures (for the studied BCC metals) and high strain rates, the model will greatly underestimates the mechanical response of the structure. The usage of a strain rate dependent calorific ratio is advised for such BCC materials submitted to this kind of loading.

f. Parameters sensitivity and number of experimental tests for their determination

The sensitivity study of accuracy of the models to the parameters has been carried out and the results are shown in Table 20. The loss of accuracy on the model is calculated for positive and negative offsets of 50% on each parameter (the mean value is shown). The loss of accuracy in Table 20 corresponds to the global normalized difference between the modeling with the optimized parameters and an offset of $\mp$50% on their optimized value. It is difficult to set up universal loss of accuracy for the suggested CCH model since all materials have their own particularities. However, concerning the F7020 aluminum alloy, the most critical parameters are n_t, n_v and θ_0^p for FCC metals and mainly correspond to the internal stress (strain hardening).

Table 20 - List of model parameters for modeling of FCC metals using the suggested expressions of the F7020 aluminum alloy and their normalized sensitivity on the overall stress

Parameters	Loss of accuracy (%)	Parameters	Loss of accuracy (%)	Parameters	Loss of accuracy (%)
θ_0^p	18.7	D_g	0.07	E_{T_0}	1.9
ζ	1.6	g_0	3.1	n_T	> 100
k	1.8	μ	2.2	/	/
R	2.1	l_v	0.3	/	/
B	8.7	v	8.1	/	/

b	10.3	n_v	> 100	/	/

The number of experimental tests to achieve the determination of the model parameters depends greatly on the use of the expression defining the calorific ratio (Eq 3.12 or the simplified expression $\left(1-\frac{T-T_r}{T_m-T_r}\right)^m$). The details about the number of required tests are gathered in Table 21.

Table 21 - Number of experimental tests required for the determination of model parameters

Model / Variable		Eq 3.5 with Eq 3.12		Eq 3.5 with $\Omega(\dot{\varepsilon}_p,T)=\left(1-\frac{T-T_r}{T_m-T_r}\right)^m$		Eq 3.31	
$\dot{\varepsilon}_p$	Tests at different strain rates (QS and dynamic)	Mini	Recommended	Mini	Recommended	Mini	Recommended
		3	5	3	5	3	5
T	Tests at different temperatures (other than T_r and QS)	2	4	2	4	2	4
$\dot{\varepsilon}_p$ and T	Tests at different temperatures (other than T_r) and strain rates (dynamic)	2	4	0	0	0	0
Other		Grain size measurement	Grain size measurement + isothermal dynamic test	Grain size measurement	Grain size measurement + isothermal dynamic test	0	0
Total		7	14	5	10	5	9

2. Application of the cooperative model in a strain dependent constitutive model for polymers

The mechanical behavior of the amorphous polymers can be represented by the following three phenomena (detailed in Chapter 2):

- The yield stress σ_y which is temperature and strain rate dependent.
- The hyperelasticity generating temperature and strain rate sensitive a back stress σ_B which increases exponentially with the strain.
- The strain softening phenomenon which can be observed as a normalized energetic balance ψ. It is assumed, in this work, temperature and strain rate insensitive.

The overall stress σ corresponding to the macroscopic mechanical behavior is computed with a specific model which takes into account the three previous phenomena (Eq 3.33).

$$\sigma(\varepsilon_p, \dot{\varepsilon}_p, T) = \left(\sigma_y(\dot{\varepsilon}_p, T) + \sigma_B(\varepsilon_p, \dot{\varepsilon}_p, T)\right)\psi(\varepsilon_p) \quad (3.33)$$

a. Constitutive modeling of the yield stress

The modeling of the yield stress σ_y of the polymers defines the global level of stress and is greatly influenced by the temperature and the strain rate. It corresponds to the level of stress from which the chain motion is assumed irreversible [8, 26]. The model used in this work to describe this phenomenon is the cooperative model developed for amorphous polymers [27, 28]. It allows the modeling of the change of mechanical behavior before and after the temperature of glass transition through considerations on the variation of the free volume in the polymer with the temperature and the strain rate. However, the temperature sensitivity of the yield stress of the polymer becomes highly nonlinear near the temperature of glass transition. Therefore, the expression will be slightly modified concerning the modeling of the epoxy resin.

i. Sintered polyimide

The temperature sensitivity of the yield stress of the sintered polyimide can be assumed as linear over the range of tested temperature. Therefore, the original expression of the cooperative model is used to model the mechanical behavior (Eq 3.34) [27, 28]. The parameters used can be found in Table 22.

$$\begin{cases} \sigma_y(\dot{\varepsilon}_p, T) = \sigma_0 - mT + \dfrac{2k_bT}{V}\sinh^{-1}\left(\dfrac{\dot{\varepsilon}_p}{\dot{\varepsilon}_0 e^{-\frac{\Delta H_\beta}{RT}}}\right)^{\frac{1}{n}} & ,T < T_g - T_t \\ \sigma_y(\dot{\varepsilon}_p, T) = \dfrac{2k_bT}{V}\sinh^{-1}\left(\dfrac{\dot{\varepsilon}_p}{\dot{\varepsilon}_0 e^{-\frac{\Delta H_\beta}{RT_g}} e^{\frac{\ln(10)c_1^g(T-T_g)}{c_2^g+T-T_g}}}\right)^{\frac{1}{n}} & ,T \geq T_g - T_t \end{cases} \quad (3.34)$$

With σ_0 the yield stress at $0\,K$ and very low strain rate, m the linear temperature sensitivity, k_b the Boltzmann's constant, V the reference free volume of activation of chain motion, $\dot{\varepsilon}_0$ a reference strain rate, ΔH_β the enthalpy of activation, R the constant of perfect gas, n a phenomenological parameter, T_g the temperature of glass transition,c_1^g and c_2^g the constant of William-Landel-Ferry of the polymer [29] and T_t the temperature range between the beginning of the phenomenon of glass transition and T_g. These parameters are determined using the least square method.

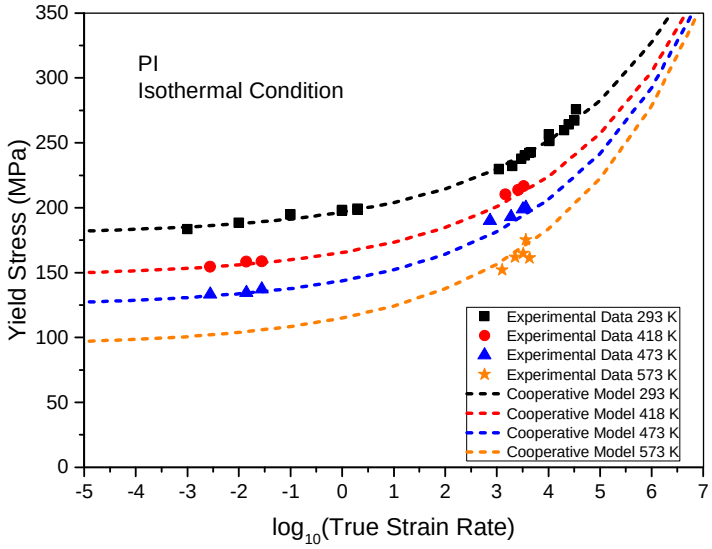

Figure 102 - Application of the cooperative model on the sintered PI below the glass transition temperature

The constitutive modeling has been only applied below the temperature of glass transition for the calibration of the parameters (Figure 102). The model predicts a convergence of the yield stress at very high strain for the different temperatures.

The values of the WLF parameters are taken as the universal values of c_1^g and c_2^g.

Table 22 - Cooperative model parameters for the sintered PI

$\sigma_0\ (MPa)$	$m\ (MPa/K)$	$V\ (m^3)$	$\dot{\varepsilon}_0\ (/s)$	$\Delta H_\beta\ (J/mol)$
268	0.307	3.82e-29	3.64e9	14400
$T_g\ (K)$	c_1^g	$c_2^g\ (°C)$	$n\ (-)$	$T_t\ (K)$
583	17.44	51.6	6.422	10

ii. Epoxy resin

The temperature sensitivity of the yield stress of the epoxy resin is highly nonlinear over the range of tested temperatures (around the temperature of glass transition). Therefore, the cooperative model [27, 28] is modified to take into account such thermal behavior [5] (Eq 3.33). The existence of a yield stress phenomenon has been observed only below the T_g in quasi-static regime and therefore the epoxy resin will be assumed as a purely hyperelastic material without any yield stress phenomenon at low strain rates (see Figure 103). The parameters are gathered in Table 23.

$$\begin{cases} \sigma_y(\dot{\varepsilon}_p, T) = \left[\sigma_0 - mT + \frac{2k_bT}{V}\sinh^{-1}\left(\frac{\dot{\varepsilon}_p}{\dot{\varepsilon}_0 e^{-\frac{\Delta H_\beta}{RT}}}\right)^{\frac{1}{n}}\right]\left(1 - \frac{T}{T_g}e^{\theta^*\left(1-\frac{T_g}{T}\right)}\right) & ,T < T_g - T_t \\ \sigma_y(\dot{\varepsilon}_p, T) = \frac{2k_bT}{V}\sinh^{-1}\left(\frac{\dot{\varepsilon}_p}{\dot{\varepsilon}_0 e^{-\frac{\Delta H_\beta}{RT_g}} e^{\frac{\ln(10)c_1^g(T-T_g)}{c_2^g+T-T_g}}}\right)^{\frac{1}{n}} & ,T \geq T_g - T_t \end{cases} \quad (3.35)$$

With θ^* the parameter modeling the nonlinear temperature sensitivity of the yield stress and T_t the temperature range between the beginning of the phenomenon of glass transition and T_g.

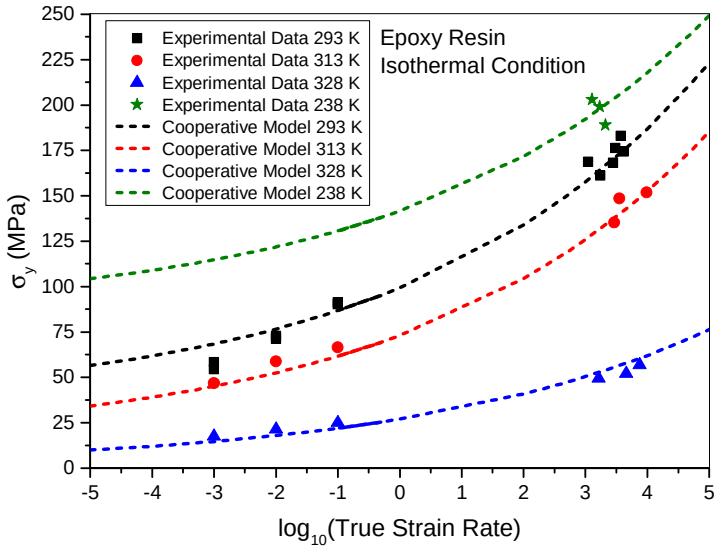

Figure 103 - Application of the modified cooperative model on the epoxy resin

Table 23 - Cooperative model parameters of the epoxy resin

$\sigma_0\ (MPa)$	$m\ (MPa/K)$	$V\ (m^3)$	$\dot{\varepsilon}_0\ (/s)$	$\Delta H_\beta\ (J/mol)$	$\theta^*\ (-)$
315.7	0.912	1.91e-29	4.92e9	5520	27.99
$T_g\ (K)$	c_1^g	$c_2^g\ (°C)$	$n\ (-)$	$T_t\ (K)$	/
333	17.44	51.6	10.83	8	/

b. Constitutive modeling of the hyperelasticity phenomenon

The hyperelastic phenomenon is present in all polymeric material due the intrinsic nature of the chains and their resistance to stretching [30, 31]. In this work, the same model is used for the sintered polyimide and for the epoxy resin: the Gent model [8, 32]. This model has been chosen due to its efficiency,

simplicity of use and of implementation in numerical code. The 8-chains model [33] can also be used but is more instable in numerical simulations. The uniaxial form of the model is used in this case (Eq 3.36).

$$\sigma_B\left(\varepsilon_p, \dot{\varepsilon}_p, T\right) = \frac{C_R\left(\dot{\varepsilon}_p, T\right)}{3}\left(\lambda^2 - \frac{1}{\lambda}\right)\frac{N(T)}{N(T) - \left(\lambda^2 + \frac{2}{\lambda} - 3\right)} \quad (3.36)$$

With Eq 3.37:

$$\lambda = e^{\varepsilon_p} \quad (3.37)$$

Here C_R is the rubber modulus of the polymer and N is the locking parameter.

It has been observed in the previous chapter, that the rubber modulus presents a double dependency to the temperature and to the strain rate. An expression is suggested here to take into account the full mechanical behavior of C_R over the ranges of tested temperatures and strain rates (Eq 3.38) [5, 11, 28].

$$\begin{cases} C_R\left(\dot{\varepsilon}_p, T < T_g - T_t\right) = C_{R0}\left(1 - \frac{T}{T_g}e^{\theta^*\left(1-\frac{T_g}{T}\right)}\right)\left(1 + l_v \ln\left(\frac{\dot{\varepsilon}_p}{\dot{\varepsilon}_r}\right) + v\left(\frac{\dot{\varepsilon}_p}{\dot{\varepsilon}_r}\right)^{n_v}\right) \\ C_R\left(\dot{\varepsilon}_p, T \geq T_g\right) = C_{R0}\left(1 - \frac{T_g - T_t}{T_g}e^{\theta^*\left(1-\frac{T_g}{T_g - T_t}\right)}\right)\left(1 + l_v \ln\left(\frac{\dot{\varepsilon}_p}{\dot{\varepsilon}_r}\right) + v\left(\frac{\dot{\varepsilon}_p}{\dot{\varepsilon}_r}\right)^{n_v}\right) \end{cases} \quad (3.38)$$

With C_{R0} the rubber modulus at 0K and very low strain rates, T_g the temperature of glass transition, θ^* a characteristic homologous temperature, $\dot{\varepsilon}_r$ the minimum reference strain rate, n_v, v and l_v phenomenological parameters defining the strain rate sensitivity of the rubber modulus and T_t the temperature range between the beginning of the phenomenon of glass transition and T_g.

The locking parameter N also exhibits a linear temperature dependency with a theoretical saturation when reaching the temperature of glass transition. The expression chosen for the modeling of this parameter is Eq 3.39 [28].

$$\begin{cases} N\left(T < T_g\right) = N_0 + b(T - 273.15) \\ N\left(T \geq T_g\right) = N_0 + b\left(T_g - 273.15\right) \end{cases} \quad (3.39)$$

With b the temperature sensitivity of N and N_0 the value of N at $T = 273.15\ K$

i. Sintered polyimide

The experimental observation of evolution of the rubber modulus of the sintered polyimide has led to the conclusion of an obvious temperature-strain rate coupled behavior. Indeed, the value of the rubber modulus increases exponentially with the strain rate at constant temperature but the intensity of this behavior decreases when this last increases (Figure 104).

The parameters allowing the modeling of the rubber modulus of the sintered polyimide are reported in Table 24. These parameters have been determined using the least square method.

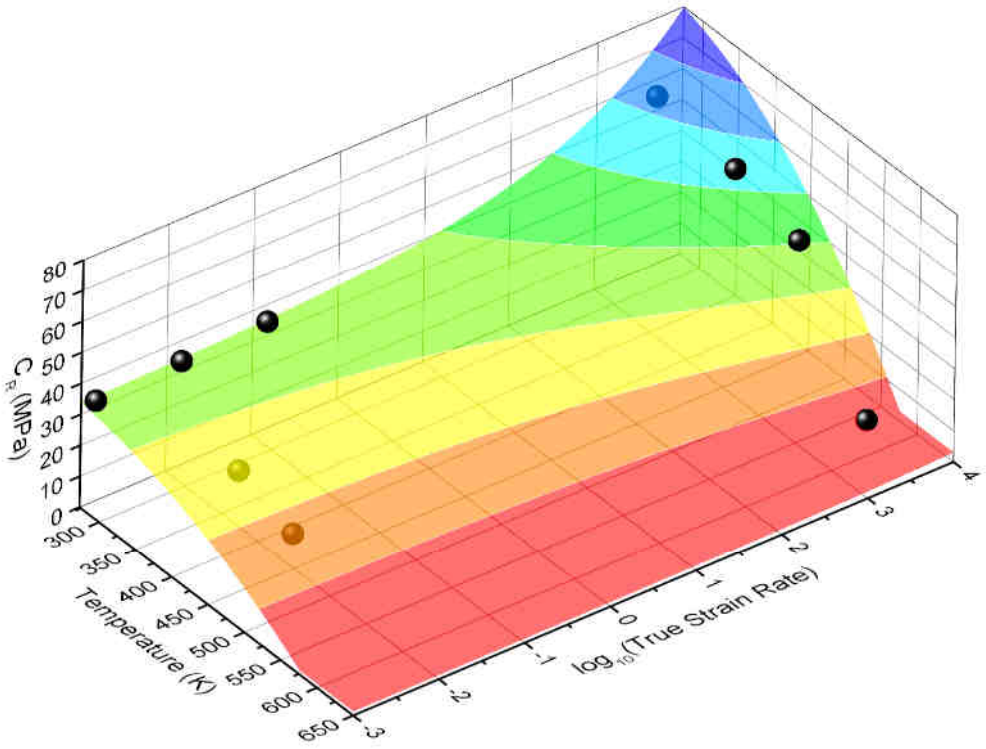

Figure 104 - Evolution of the rubber modulus of the sintered polyimide with the temperature and the strain rate

Table 24 - Parameters of rubber modulus modeling of the sintered PI

C_{R0} (MPa)	θ^* (-)	l_v (-)	v (-)	n_v (-)	$\dot{\varepsilon}_r$ (/s)	T_g (K)	T_t (K)
34.8	2.122	1.15e-5	3.49e-3	0.289	10^{-5}	583	10

The locking parameter N of the sintered polyimide has been observed as strain rate independent, therefore only the temperature sensitivity is considered (see Figure 105). It is assumed that the value of N above the temperature of glass transition stays constant and equal to $N = N_0 + b(T_g - 273.15)$. The values of N_0 and b can be found in Table 25.

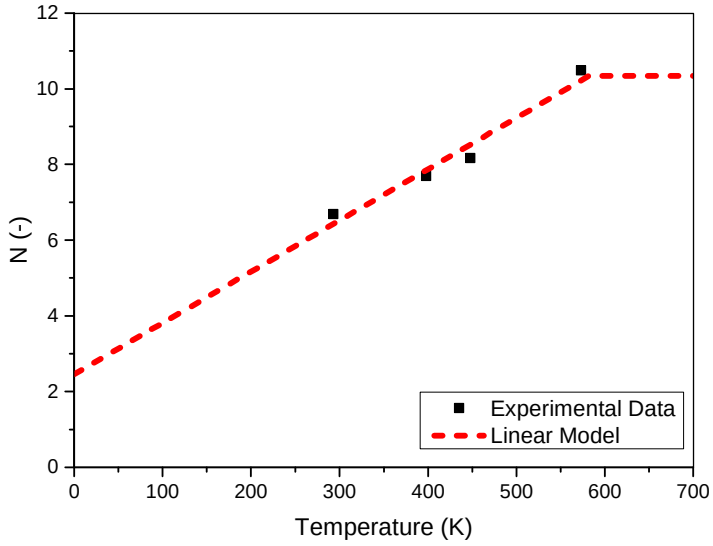

Figure 105 - Evolution of the locking parameter N of the sintered PI with the temperature

Table 25 -Parameters of locking parameters N modeling of the sintered PI

$N_0(-)$	$b\ (K^{-1})$	$T_g\ (K)$
6.158	0.01354	583

ii. Epoxy resin

The variation of the rubber modulus of the epoxy resin shows also a temperature-strain rate coupled behavior (Figure 106). However, contrary to the sintered polyimide, the value of C_R decreases with the strain rate over the range of tested strain rates (higher strain rates did not allow the observation of the hyperelasticity phenomenon). The softening may be caused a premature locking phenomenon which prevents the efficient stretching of the chains which leads to the failure of the material [34] or to premature adiabatic heating leading to decrease of the cross-linking and therefore to a global softening of the polymer [9]. In dynamic conditions, the rubber modulus will be assumed as zero.

Deeper microstructural investigation might reveal the actual cause of the strain rate behavior of the epoxy resin and allow the construction of a more physical model thanks to its understanding. However, the suggested phenomenological approach allows an efficient modeling of the rubber modulus over the evaluated ranges of temperatures and strain rates. The parameters of the used model are gathered in Table 26.

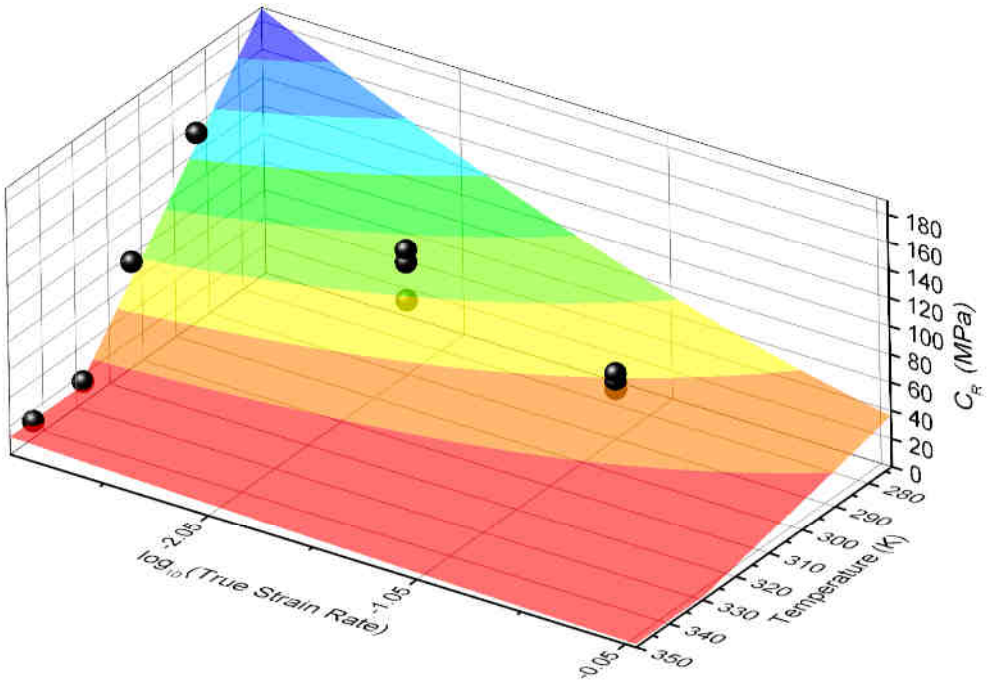

Figure 106 - Evolution of the rubber modulus of the epoxy resin with the temperature and the strain rate

Table 26 - Parameters of rubber modulus modeling of the epoxy resin

C_{R0} (MPa)	θ^* (-)	l_v (-)	v (-)	n_v (-)	$\dot{\varepsilon}_r$ (/s)	T_g (K)	T_t (K)
18.73	0.1537	-12.87	47.69	0.1031	10^{-3}	333	10

As for the sintered polyimide, the locking parameter N does not seem to present any strain rate sensitivity (even with the consideration of the high dispersion). Thus, only the linear temperature dependency is taken into account in the modeling (Figure 107) which is lower than for the polyimide. Above the temperature of glass transition, the value of N is assumed constant and equal to $N = N_0 + b(T_g - 273.15)$. The values of N_0 and b are reported in Table 27.

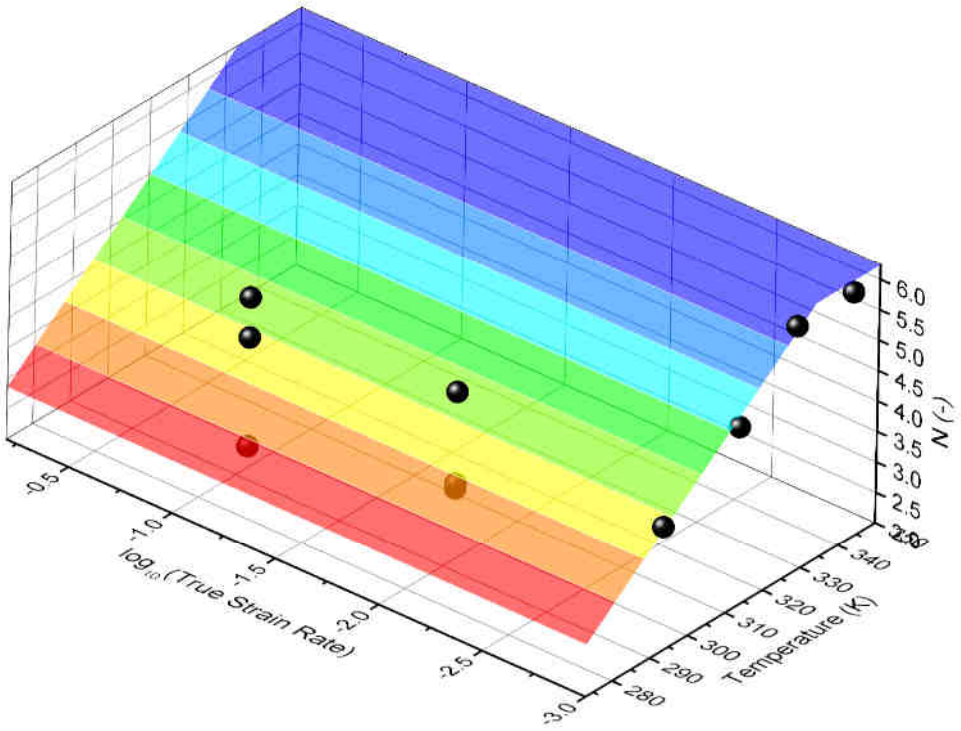

Figure 107 - Evolution of the locking parameter N of the epoxy resin with the temperature and the strain rate

Table 27 - Parameters of locking parameters N modeling of the epoxy resin

$N_0(-)$	$b\ (K^{-1})$	$T_g\ (K)$
2.869	0.05633	333

c. Constitutive modeling of the strain softening

The modeling of the yield stress and of the hyperelasticity is insufficient to take into account the full mechanical behavior of polymers. Indeed, an amount of energy is released during the strain softening phenomenon caused by the relaxation of the chains [8, 29, 35]. Therefore, to maintain the energy balance during the whole strain, the same amount of energy released during the relaxation of the chains has to be absorbed before the failure (Eq 3.40).

$$\int_0^{\ln \varepsilon_p^f} \left(\frac{\sigma_{exp}}{\sigma_y + \sigma_{hyp}} - 1 \right) d\varepsilon_p = 0 \qquad (3.40)$$

The evolution of the energy balance ψ is suggested by Eq 3.41. Only the strain dependency is taken into account here. Indeed, temperature and strain rate sensitivities on this phenomena seems negligible in the studied case.

$$\psi(\varepsilon_p) = \frac{\sigma_{exp}}{\sigma_y + \sigma_{hyp}} = Ae^{B\varepsilon_p} + Ce^{D\varepsilon_p} \quad (3.41)$$

With A, B, C and D phenomenological parameters.

i. Sintered polyimide

The evolution of the energy balance ψ (Eq 3.42) of the polyimide with the strain is represented on Figure 108. The expression suggested to model such a behavior seems to provide a good accuracy over the whole range of strains (from yield strain to strain at initiation of failure). The computed parameters are reported in Table 28 and are determined by the least square.

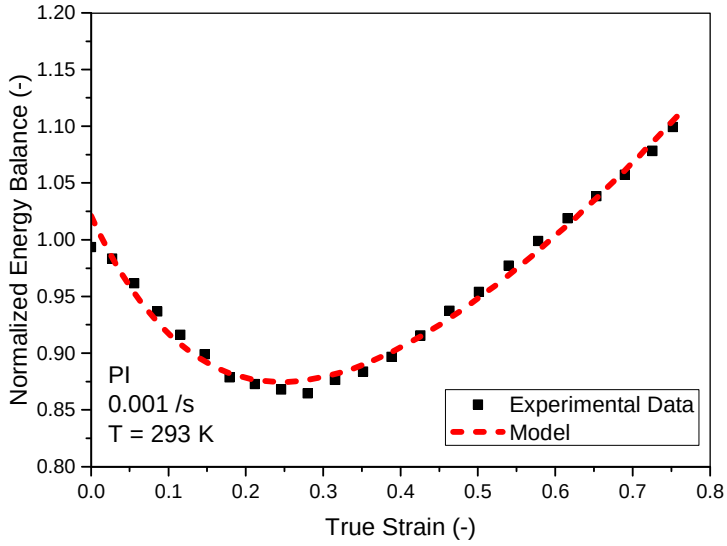

Figure 108 - Evolution of the normalized energetic balance with the strain of the sintered PI

Table 28 - Energetic balance parameters of the sintered PI

A $(-)$	B $(-)$	C $(-)$	D $(-)$
0.3709	-5.204	0.6502	0.6959

ii. Epoxy resin

The energy balance behavior of the epoxy resin follows the same trend as the sintered polyimide and the overall experimental curve is nicely fitted by the suggested phenomenological expression Eq 3.41 (Figure 109). However, it can be seen a slight nonlinear behavior in the range of strain between $\varepsilon_p = 0.1$ and $\varepsilon_p = 0.3$. This particular nonlinearity might be due to the fact that the epoxy resin is a biphasic material. Both phases may have a different behavior over this range of strains. The parameters are reported in Table 29 and determined using the least square method.

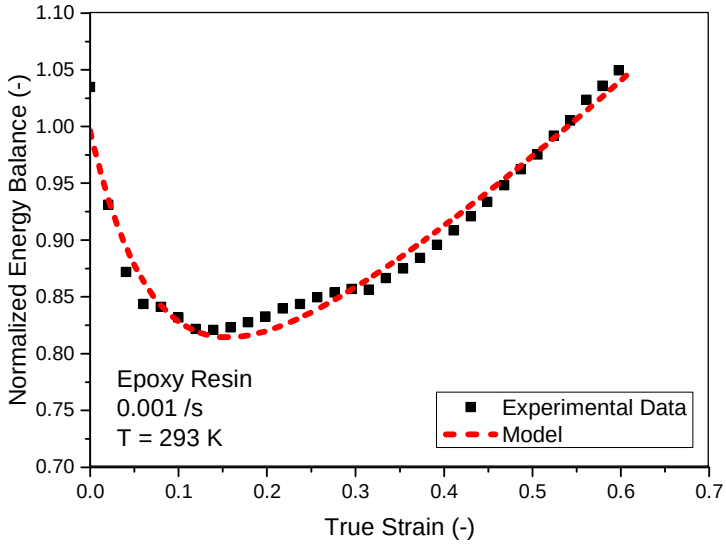

Figure 109 – Evolution of the normalized energetic balance with the strain of the epoxy resin

Table 29 - Energetic balance parameters of the epoxy resin

$A\ (-)$	$B\ (-)$	$C\ (-)$	$D\ (-)$
0.2978	-12.91	0.6984	0.6644

d. Overall constitutive modeling of the stress behavior

i. Sintered polyimide

Once all the different phenomena have been modeled separately, the different expressions are gathered in order to model the full level of stress σ of the polyimide (Eq 3.33).

Wide ranges of temperatures and strain rates have been tested and used for the validation of the suggested model (Figure 110.a and 110.b). It can be seen that the level of stress is correctly modeled for all the conditions due to the accurate prediction of the cooperative model for the yield stress. Furthermore, the thermal softening of the hyperelasticity phenomenon is well represented in all cases (even at high temperatures). The suggested model provides an efficient tool to evaluate the level of stress concerning the sintered polyimide.

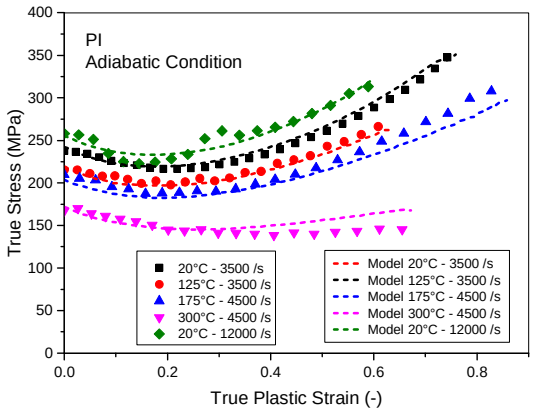

(a)

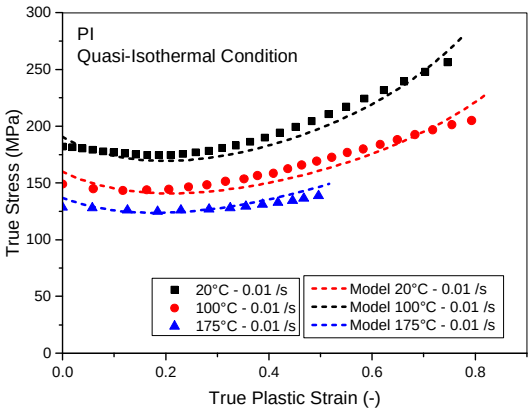

(b)

Figure 110 – Comparison between the experimental data and the suggested model for the sintered PI in (a) dynamic condition and (b) quasi-static condition

ii. Epoxy resin

The mechanical behavior of the epoxy resin is much more complex than the one of the polyimide. Indeed the important difference between quasi-static and dynamic conditions is due to two properties of the material (Figure 111.a and 111.b):

- The high entanglement of the chains of the thermoset polymers causes the high strain rate sensitivity of the yield stress [9].
- The low temperature of glass transition T_g causes a very high softening of the level of stress as soon as the temperature increases (due to adiabatic heating or environmental factors).

The model provides satisfying results to evaluate the level of stress of the epoxy resin over such wide ranges of temperatures and strain rates and up to very high strains (see Figure 111.b).

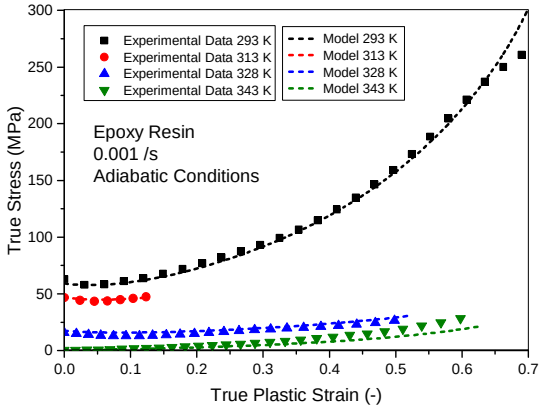

(a)

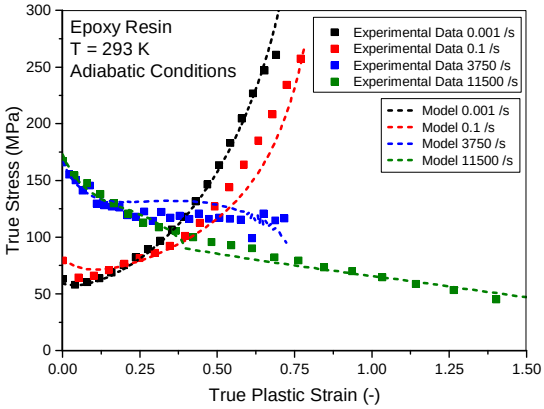

(b)

Figure 111 - Comparison between the experimental data and the suggested model for the epoxy resin over wide ranges of (a) temperatures and (b) strain rates

C. Constitutive modeling of the strain at initiation of failure

The constitutive modeling of the failure of the studied materials is performed through a similar approach which consists in two steps:

- The modeling of the plastic strain at initiation of failure as a function of the triaxiality, the strain rate and the temperature.
- The modeling of the damage energy after the initiation of failure as a function of the triaxiality in this work (the sensitivities to the temperature and strain rates can also be considered).

The overall modeling of the plastic strain at initiation of failure ε_p^f is modeled through a typical expression [36] which can be written using Eq 3.42.

$$\varepsilon_p^f(\sigma^*, \theta, \dot{\varepsilon}_p, T) = f_{\sigma^*}(\sigma^*, \theta) f_{vf}(\dot{\varepsilon}_p) f_{T_f}(\dot{\varepsilon}_p, T) \quad (3.42)$$

With f_{σ^*} a function defining the evolution of the plastic strain at initiation of failure with the state of stress at reference states of temperature and strain rate, f_{vf} a function corresponding to the strain rate sensitivity and f_{T_f} a function modeling the temperature sensitivity.

1. Triaxiality sensitivity

a. F7020 aluminum alloy

The F7020 aluminum alloy displays a classic exponential decreasing strain at initiation of failure with the triaxiality (Figure 112). No failure has been observed in compression state and this behavior is taken into account in the numerical model developed for the simulations. It can be added that the level of strain at initiation of failure is quite low for an aluminum alloy over the whole range of tested triaxialities. This behavior is mainly due to the intrinsic characteristic of the sintered materials [37, 38] leading to the low cohesion of the powder grains and a premature failure (intergranular failure at mesoscopic scale). The parameters are provided in the Table 30 (determined with the least square method). The expression chosen to model the triaxiality behavior of the studied materials is Eq 3.43 [36].

$$f_{\sigma^*}(\sigma^*) = d_1 + d_2 e^{d_3 \sigma^*} \quad (3.43)$$

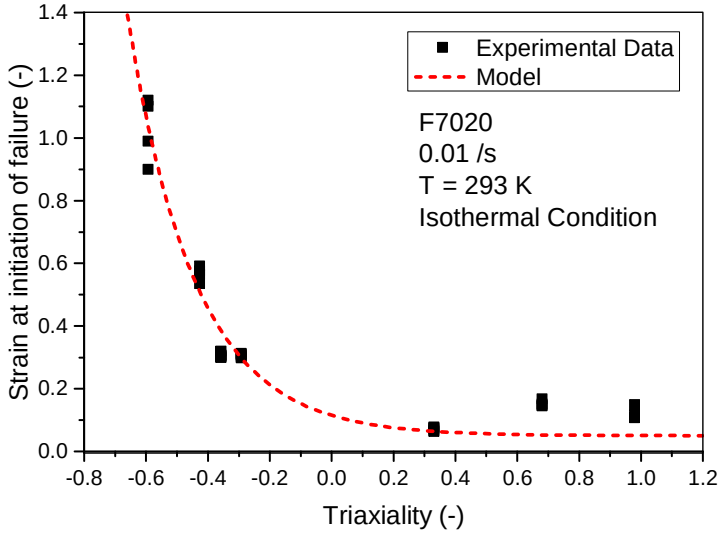

Figure 112 - Evolution and modeling of the plastic strain at initiation of failure with triaxiality of the F7020

Table 30 - Parameters for triaxiality sensitivity modeling of the F7020

$d_1\ (-)$	$d_2\ (-)$	$d_3\ (-)$
0.0459	0.06506	-4.586

b. Sintered polyimide

The failure behavior of the sintered polyimide can be divided into two parts (see Figure 113):

- An elastic-brittle behavior consisting into the domain of triaxiality corresponding to the phenomenon of voids nucleation and growth (positive triaxiality). This particular behavior is caused by the low cohesion of the sintered powder grains (mesoscopic scale) which has been observed in the previous chapter [37].
- A domain in negative triaxiality in which the failure is caused by the phenomenon of locking of polymer chains at relative high plastic strain [34]. The experimental data are provided by the compression tests.

The assumption of initiation of failure at the yield stress is assumed to model the elastic-brittle behavior (zero plastic strain). Therefore, the value of d_1 should be set to 0 but to avoid numerical problems, its value is set slightly above at $d_1 = 0.001$ (Table 31).

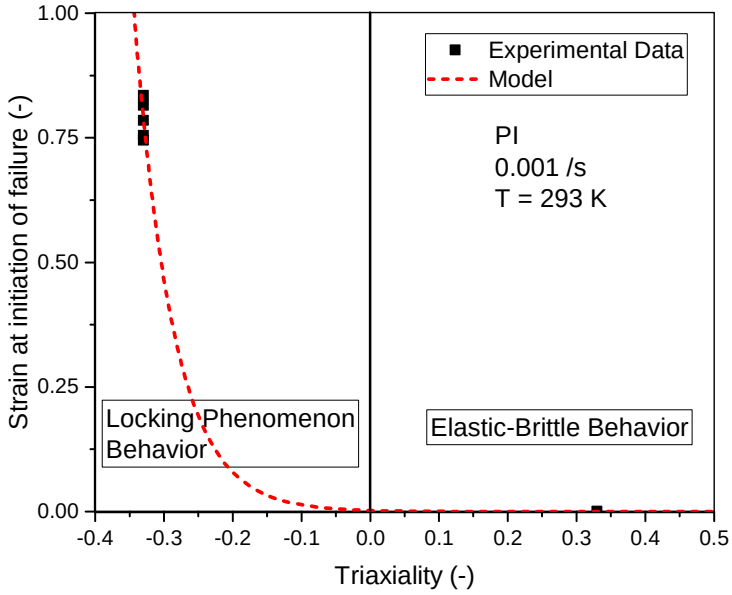

Figure 113 - Evolution and modeling of the plastic strain at initiation of failure with triaxiality of the sintered PI

Table 31 - Parameters for triaxiality sensitivity modeling of the sintered PI

$d_1\ (-)$	$d_2\ (-)$	$d_3\ (-)$
0.001	0.002312	-17.67

2. Strain rate sensitivity

In the previous chapter, it has been experimentally shown that the metals and the polymers present very different failure behaviors toward increasing strain rate. Indeed, the strain at initiation of failure of metallic materials increases with the rate of deformation due to phenomena such as micro-inertia. Polymer materials have a very different mechanical response: ε_p^f decreases suddenly at a transition strain rate due to the overcoming of the relaxation time of the chains structure [34]. The stronger the entanglement is, the lower the transition strain rate will be [9] (very low for thermoset polymers). In all cases, the same expression (Eq 3.44) to model the evolution of ε_p^f is used [11] (if no coupled behavior is assumed).

$$f_{vf}(\dot{\varepsilon}_p) = 1 + l_{vf} \ln\left(\frac{\dot{\varepsilon}_p}{\dot{\varepsilon}_{0ff}}\right) + v_f \left(\frac{\dot{\varepsilon}_p}{\dot{\varepsilon}_{0ff}}\right)^{n_{vf}} \quad (3.44)$$

With l_{vf}, vf and n_{vf} are phenomenological parameters defining the strain rate sensitivity of the strain at initiation of failure and $\dot{\varepsilon}_{0ff}$ is a reference strain rate. The parameters are determined using the least square method.

a. F7020 aluminum alloy

The strain rate sensitivity of the strain at initiation of failure of the F7020 aluminum alloy has been studied through shear-compression tests under different types of loading (quasi-static stress, SHPB and direct Impact).The shear-compression tests have been used in order to avoid the decohesion failure mode through shearing of the powder grain. The Figure 114 shows an exponential increase of the strain at failure initiation with the logarithm of the strain rate which may be linked to the viscous drag effect [39] and the dislocations velocities. It can be also seen that the values at the highest rates (around 40.000/s) are mandatory to obtain an accurate modeling for the even greatest rates of deformation which are involved in perforation tests at high velocities. The parameters of the strain sensitivity functions are provided in the Table 32.

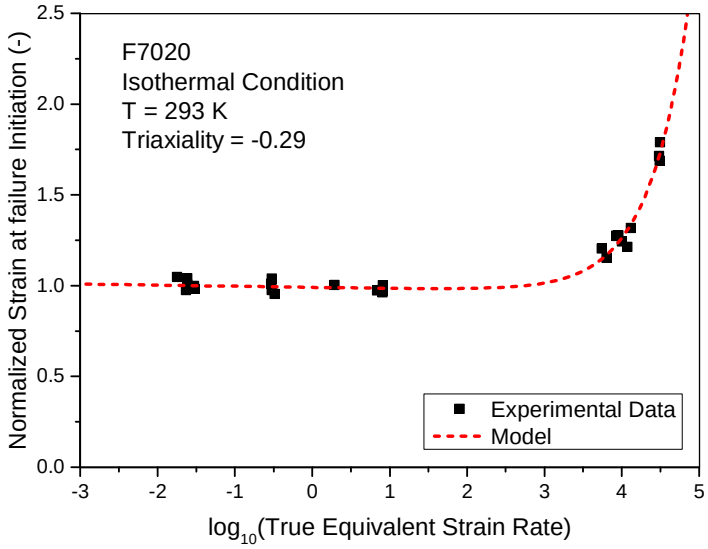

Figure 114 - Evolution and modeling of the plastic strain at initiation of failure with the strain rate of the F7020

Table 32 - Parameters for strain rate sensitivity modeling of the F7020

$l_{vf}\ (-)$	$v_f\ (-)$	$n_{vf}\ (-)$	$\dot{\varepsilon}_{0ff}\ (/s)$
-0.001156	2.069e-7	0.8754	0.001

b. Sintered polyimide

The strain at initiation of failure of the sintered polyimide follows the inverse trend of the metals: its value decreases with increasing strain rate due to the chains locking phenomenon [34] (Figure 115). The modeling of ε_p^f of the sintered polyimide is performed using the same expression used for the metallic material. However, another aspect of modeling has to be taken in consideration: a minimum value of ε_p^f at very high strain rate due to the locking phenomenon. In this case, a small minimal value set as $\varepsilon_{min}^f = 0{,}05$ is used (same value as for the epoxy resin). The values of the parameters can be found in Table 33.

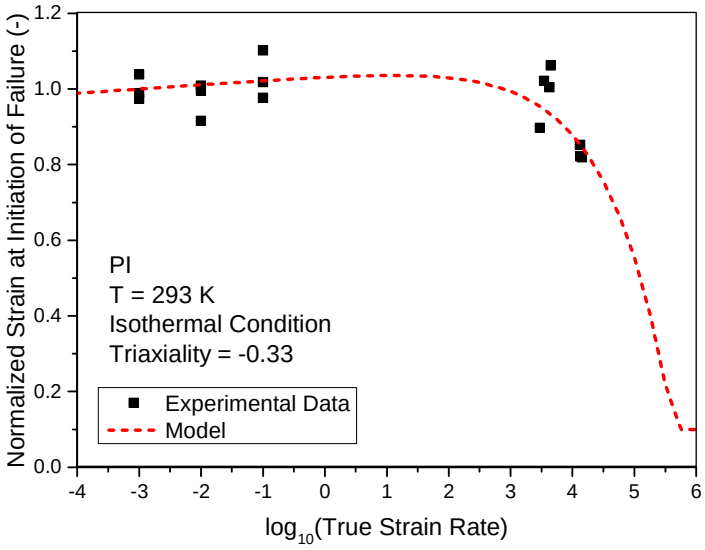

Figure 115 - Evolution and modeling of the plastic strain at initiation of failure with the strain rate of the sintered PI

Table 33 - Parameters for strain rate sensitivity modeling of the sintered PI

$l_{vf}\ (-)$	$v_f\ (-)$	$n_{vf}\ (-)$	$\dot{\varepsilon}_{0ff}\ (/s)$	$\varepsilon_{min}^f\ (-)$
0.005	-0.0002088	0.4264	0.001	0.05

c. Epoxy resin

The epoxy resin presents a particular behavior of its plastic strain at initiation of failure ε_p^f. Indeed, a triaxiality-strain rate coupled sensitivity of the phenomenon leading to the failure is experimentally observed in this work and in the literature [40] (Figure 116). For this purpose, a new expression (Eq 3.45) has been developed on the assumption of a decomposition of the triaxiality sensitivity of ε_p^f in two parts with one rate insensitive (d_1 and d_2) and the other one strain rate dependent (d_3 and d_4).

$$f_{\sigma^* vf}(\sigma^*, \dot{\varepsilon}_p) = d_1 e^{d_2 \sigma^*} + d_3 \left(l_{vf} \ln\left(\frac{\dot{\varepsilon}_p}{\dot{\varepsilon}_{0ff}}\right) + v_f \left(\frac{\dot{\varepsilon}_p}{\dot{\varepsilon}_{0ff}}\right)^{n_{vf}} \right) e^{d_4 \sigma^*} \quad (3.45)$$

With d_1 and d_2 phenomenological parameters defining the triaxiality sensitivity of the rate insensitive part, d_3 and d_4 phenomenological parameters corresponding to the triaxiality sensitivity of the rate sensitive part, l_{vf}, vf and n_{vf} are phenomenological parameters defining the strain rate sensitivity of the strain at initiation of failure and $\dot{\varepsilon}_{0ff}$ is a reference strain rate.

At relative high strain rates, the plastic strain at failure of the epoxy resin reaches a minimum value of $\varepsilon^f_{min} = 0.05$ due to the very early locking phenomenon [34] due to the high level of chains cross-linking [9] and this has to be taken into account in the model. The parameters can be found in the Table 34.

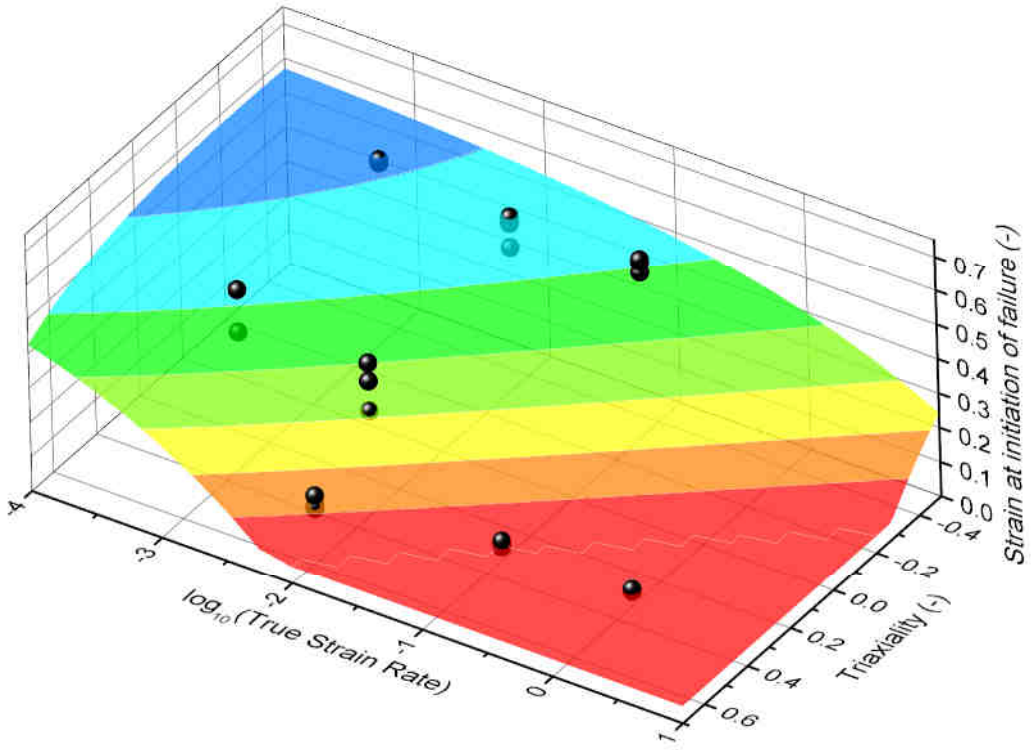

Figure 116 - Evolution and modeling of the plastic strain at initiation of failure with the temperature and the strain rate of the epoxy resin

Table 34 - Parameters for triaxiality and strain rate sensitivities modeling of the epoxy resin

$d_1\ (-)$	$d_2\ (-)$	$d_3\ (-)$	$d_4\ (-)$	$l_v\ (-)$
0.6284	0.1163	0.2476	2.02	0.01044
$v\ (-)$	$n_v\ (-)$	$\dot{\varepsilon}_{0f}\ (/s)$	$\varepsilon^f_{min}\ (-)$	/
-0.4039	0.2485	0.001	0.05	/

3. Temperature sensitivity

For all materials, the thermal softening of the stress behavior leads to an augmentation of the plastic strain at initiation of failure. Indeed, the value of ε_p^f of the polymers increases with the temperature due to the absence of thermal hardening phenomenon. However, concerning the metallic materials, some microstructural changes at higher temperatures can lead to a structural hardening effect [14, 41] (apparition of precipitates generating dislocations) and the value of ε_p^f decreases over the range of temperature covered by these phenomena.

In this work, the modeling of the temperature sensitivity of ε_p^f is performed differently for the metals and for the polymers.

a. F7020 aluminum alloy

The thermal softening of the thermal mechanical behavior σ_{th} of the F7020 aluminum alloy follows the calorific ratio describes in the section B.1.a of this chapter and is highly non-linear due to the complex evolution of the microstructure of this material with the temperature, and particularly the dissolution of the $MgZn_2$ and $AlMn_6$ precipitates [15]. The modeling of ε_p^f is performed using a similar expression of the calorific ratio Ω used for the stress (Figure 117). The evolution of the normalized strain at failure initiation is modeled with the function $\mho$ corresponding to the inverse of Ω (Eq 3.46). The same parameters determined for the modeling of the thermal stress are used for $\mho(\dot{\varepsilon}_p, T)$ and can be found in the Table 14. Therefore, the calorific model in the Figure 117 has not been calibrated using the experimental data displayed on the same graphic which have been obtained through shear-compression tests.

$$f_{T_f}(\dot{\varepsilon}_p, T) = \mho(\dot{\varepsilon}_p, T) = \left[\Omega(\dot{\varepsilon}_p, T)\right]^{-1} \quad (3.46)$$

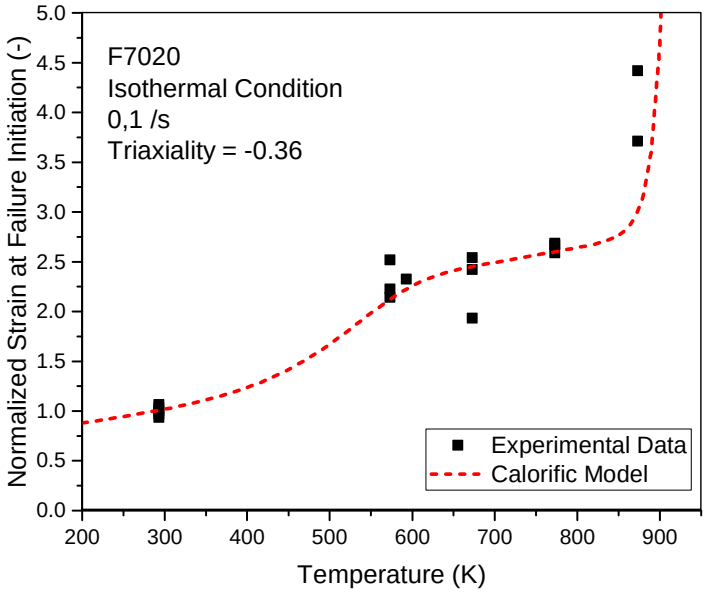

Figure 117 - Evolution and modeling of the plastic strain at initiation of failure with the temperature of the F7020

b. Sintered polyimide and epoxy resin

The value of ε_p^f of the polymers is increasing monotonously with the temperature due to the augmentation of the value of locking parameter N. Indeed, the sliding between the chains becomes easier at higher temperature leading to a decrease of the level of chain entanglement [9]. Therefore, the locking phenomenon [42] is delayed up to a specific value at the glass transition temperature T_g. For this purpose a simple expression (Eq 3.47) aiming to model the evolution of the normalized plastic strain at initiation of failure ε_p^f is used in this work for the two polymers: sintered polyimide (Figure 118.a) and epoxy resin (Figure 118.b).

$$f_{T_f}(T) = \left(1 + \frac{T - T_r}{T_g - T_r}\right)^m \qquad (3.47)$$

With m a phenomenological parameter. The parameters are gathered in Table 35.

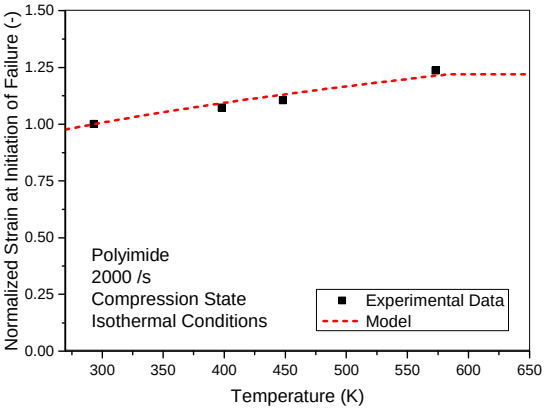

(a)

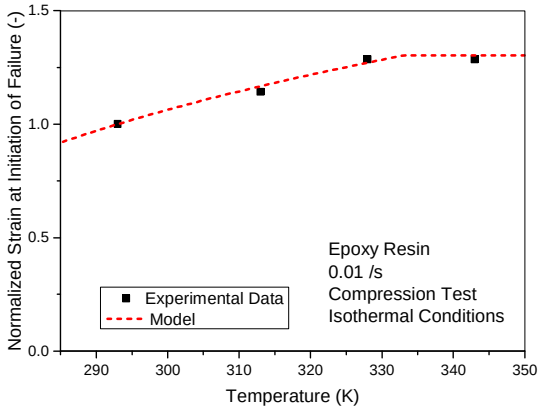

(b)

Figure 118 – Evolution and modeling of the normalized plastic strain at initiation of failure with the temperature of (a) the sintered PI and (b) the epoxy resin

Table 35 - Parameters used for the temperature sensitivity of the normalized plastic strain at initiation of failure of the sintered polyimide and the epoxy resin

Material	$m\ (-)$	$T_r\ (K)$	$T_g\ (K)$
Sintered PI	0.2862	293	583
Epoxy Resin	0.3817	293	333

D. Constitutive modeling of the damage evolution

In this work the damage evolution $\dot{D}$ is taken as a function of the evolution of the absorbed energy E_M by the material between the plastic strain at initiation of failure ε_p^f and the plastic strain at ultimate failure ε_p^u. The following expression [43] (Eq 3.48) defines an exponential evolution of the evolution of D in function of E_M.

$$D = 1 - e^{\frac{\int_{\varepsilon_p^u}^{\varepsilon_p^f} \sigma d\varepsilon_p}{E_M(\sigma^*)}} \quad (3.48)$$

With E_M the absorbed energy at ε_p^u and is a function of the triaxiality σ^*.

The damage D is then implemented in the overall model as a multiplicative factor of the computed stress σ in order to obtain the true stress including damage evolution σ_v (Eq 3.49).

$$\sigma_v = \sigma(1 - D) \quad (3.49)$$

The evolution of E_M with the triaxiality is modeled with a simple exponential function (Eq 3.50) (see Figure 119):

$$E_M(\sigma^*) = A_E e^{B_E \sigma^*} \quad (3.50)$$

With A_E and B_E phenomenological parameters.

The parameters of the model for each material are gathered in Table 36.

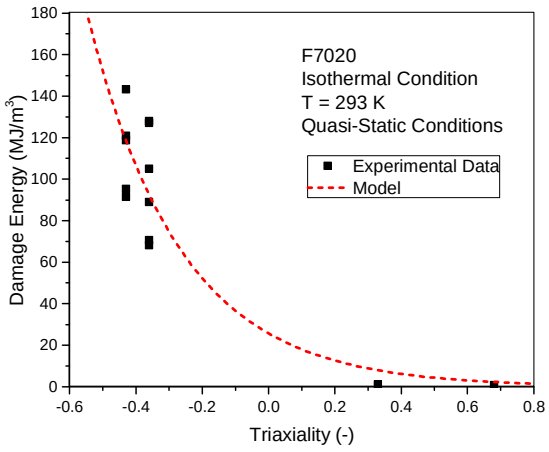

(a)

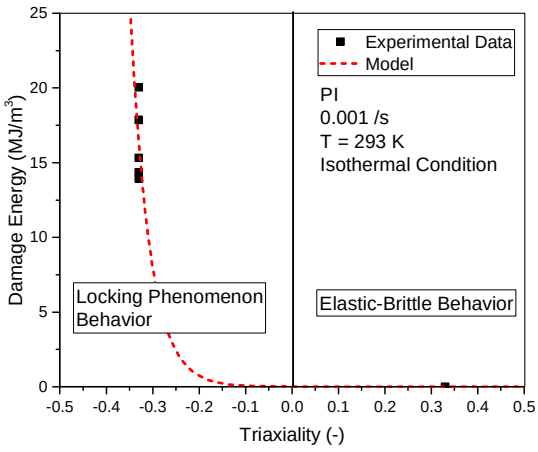

(b)

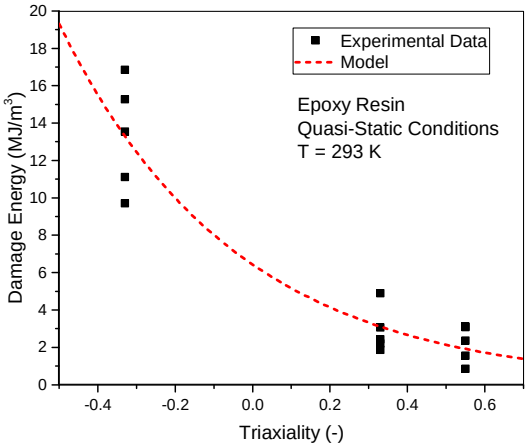

(c)

Figure 119 - Evolution and modeling of the damage energy with the triaxiality for (a) F7020, (b) the sintered PI and (c) the epoxy resin

Table 36 – Parameters used to model the evolution of the damage energy of the different materials studied in this work

Material	$A_E\ (MJ.m^{-3})$	$B_E(-)$
F7020	17.68	-3.558
Sintered PI	0.006151	-23.88
Epoxy Resin	6.431	-2.199

E.CONCLUSION OF THE CHAPTER

Through this chapter, the mathematical expressions developed and chosen to model the different phenomena of each material have been discussed and the parameters given.

Concerning the F7020 aluminum alloy, a new analytical approach aiming to developed specific models for each material has been presented [10, 11] (for the FCC case). This approach is based onto two main aspects: the calorific ratio aiming to model the complex thermal behavior of the alloy (due to microstructure changes) over a wide range of temperature and the identification of the correct hardening function regarding the type of strain hardening of the metal (homogeneous or heterogeneous). The constitutive modeling of the plastic strain at initiation of failure of the F7020 has also been performed using the calorific ratio and does not require any parameter calibration since it is using the same parameters set as for the stress.

The modeling of the two polymers (sintered polyimide and epoxy resin) have been modeled following a similar approach:

- The yield stress has been modeled using the cooperative model for amorphous [27, 28] (with a small thermal modification for the resin epoxy).
- The hyperelasticity has been modeled using the well-known Gent model [32] coupling simplicity and efficiency.
- The strain softening has been modeled using an energetic balance assumption.

The modeling of the plastic strain at initiation of failure of polymers has been carried out using classic expressions for the triaxiality [36], strain rate [11] and temperature sensitivities.

The next step to obtain a numerical model designed to develop impact experiments on these materials is the implementation of the suggested expressions into a VUMAT subroutine in FORTRAN code for ABAQUS®/explicit.

References

1. Hill, R., *The mathematical theory of plasticity*. Vol. 11. 1998: Oxford university press.
2. Drucker, D.C. and W. Prager, *Soil mechanics and plastic analysis or limit design.* Quarterly of applied mathematics, 1952. **10**(2): p. 157-165.
3. Raghava, R.S. and R.M. Caddell, *A macroscopic yield criterion for crystalline polymers.* International Journal of Mechanical Sciences, 1973. **15**(12): p. 967-974.
4. Caddell, R.M., R.S. Raghava, and A.G. Atkins, *Pressure dependent yield criteria for polymers.* Materials Science and Engineering, 1974. **13**(2): p. 113-120.
5. Klepaczko, J., *A practical stress-strain-strain rate-temperature constitutive relation of the power form.* Journal of Mechanical Working Technology, 1987. **15**(2): p. 143-165.
6. Rusinek, A. and J.R. Klepaczko, *Shear testing of a sheet steel at wide range of strain rates and a constitutive relation with strain-rate and temperature dependence of the flow stress.* International Journal of Plasticity, 2001. **17**(1): p. 87-115.
7. Rusinek, A. and J.A. Rodríguez-Martínez, *Thermo-viscoplastic constitutive relation for aluminium alloys, modeling of negative strain rate sensitivity and viscous drag effects.* Materials & Design, 2009. **30**(10): p. 4377-4390.
8. Bergstrom, J.S., *Mechanics of solid polymers: theory and computational modeling*2015: William Andrew.
9. Nielsen, L.E., *Cross-linking–effect on physical properties of polymers.* 1969.
10. FRANCART, C., et al., *Constitutive modelling of high thermal softening phenomenon in metallic materials*, in *ICILSM*2016: Torino.
11. Francart, C., et al., *Application of the Crystallo-Calorific Hardening approach to the constitutive modeling of the dynamic yield behavior of various metals with different crystalline structures.* International Journal of Impact Engineering, 2017.
12. Nemat-Nasser, S. and M. Hori, *Micromechanics: overall properties of heterogeneous materials*. Vol. 2. 1999: Elsevier Amsterdam.
13. Rodríguez-Martínez, J., et al., *Extension of R–K constitutive relation to phase transformation phenomena.* Materials & Design, 2009. **30**(7): p. 2513-2520.
14. Wang, J., et al., *Dynamic tensile properties of a single crystal Nickel-base superalloy at high temperatures measured with an improved SHTB technique.* Materials Science and Engineering: A, 2016. **670**: p. 1-8.
15. Chinella, J.F. and Z. Guo, *Computational Thermodynamics Characterization of 7075, 7039, and 7020 Aluminum Alloys Using JMatPro*, 2011, DTIC Document.
16. Johnson, G.R. and W.H. Cook. *A constitutive model and data for metals subjected to large strains, high strain rates and high temperatures*. in *Proceedings of the 7th International Symposium on Ballistics*. 1983. The Netherlands.
17. Follansbee, P. and U. Kocks, *A constitutive description of the deformation of copper based on the use of the mechanical threshold stress as an internal state variable.* Acta Metallurgica, 1988. **36**(1): p. 81-93.
18. Wang, G., et al., *Calculating the Peierls energy and Peierls stress from atomistic simulations of screw dislocation dynamics: application to bcc tantalum.* Modelling and Simulation in Materials Science and Engineering, 2004. **12**(4): p. S371.
19. Klepaczko, J., *Physical-state variables—the key to constitutive modeling in dynamic plasticity.* Nuclear engineering and design, 1991. **127**(1): p. 103-115.
20. Abed, F.H. and G. Voyiadjis, *A consistent modified Zerilli-Armstrong flow stress model for BCC and FCC metals for elevated temperatures.* Acta mechanica, 2005. **175**(1-4): p. 1-18.
21. Voyiadjis, G.Z. and F.H. Abed, *Microstructural based models for bcc and fcc metals with temperature and strain rate dependency.* Mechanics of Materials, 2005. **37**(2): p. 355-378.
22. Nemat-Nasser, S. and J. Isaacs, *Direct measurement of isothermal flow stress of metals at elevated temperatures and high strain rates with application to Ta and Ta W alloys.* Acta Materialia, 1997. **45**(3): p. 907-919.
23. Abed, F.H., *Physically based multiscale-viscoplastic model for metals and steel alloys: theory and computation*, 2005, Jordan University of Science and Technology.

24. Ludwik, P., *Elemente der technologischen Mechanik*1909: J. Springer.
25. Børvik, T., O.S. Hopperstad, and K.O. Pedersen, *Quasi-brittle fracture during structural impact of AA7075-T651 aluminium plates.* International Journal of Impact Engineering, 2010. **37**(5): p. 537-551.
26. Ward, I.M., *Review: The yield behaviour of polymers.* Journal of Materials Science, 1971. **6**(11): p. 1397-1417.
27. Richeton, J., et al., *Influence of temperature and strain rate on the mechanical behavior of three amorphous polymers: Characterization and modeling of the compressive yield stress.* International Journal of Solids and Structures, 2006. **43**(7–8): p. 2318-2335.
28. Richeton, J., et al., *Modeling and validation of the large deformation inelastic response of amorphous polymers over a wide range of temperatures and strain rates.* International Journal of Solids and Structures, 2007. **44**(24): p. 7938-7954.
29. Williams, M.L., R.F. Landel, and J.D. Ferry, *The temperature dependence of relaxation mechanisms in amorphous polymers and other glass-forming liquids.* Journal of the American Chemical society, 1955. **77**(14): p. 3701-3707.
30. Manuel J. Garcia R., O.E.R.S., Carlos Lopez, *Hyperelastic Material Modeling*, 2005, Departamento de Ingenieria Mecanica: Medellin.
31. Boyce, M.C. and E.M. Arruda, *Constitutive models of rubber elasticity: a review.* Rubber chemistry and technology, 2000. **73**(3): p. 504-523.
32. Horgan, C.O., *The remarkable Gent constitutive model for hyperelastic materials.* International Journal of Non-Linear Mechanics, 2015. **68**(0): p. 9-16.
33. Arruda, E.M. and M.C. Boyce, *A three-dimensional constitutive model for the large stretch behavior of rubber elastic materials.* Journal of the Mechanics and Physics of Solids, 1993. **41**(2): p. 389-412.
34. Karger-Kocsis, J. and T. Czigány, *Strain rate dependence of the work of fracture response of an amorphous poly (ethylene-naphthalate)(PEN) film.* Polymer Engineering & Science, 2000. **40**(8): p. 1809-1815.
35. Struik, L.C.E., *Effect of thermal history on secondary relaxation processes in amorphous polymers.* Polymer, 1987. **28**(1): p. 57-68.
36. Johnson, G.R. and W.H. Cook, *Fracture characteristics of three metals subjected to various strains, strain rates, temperatures and pressures.* Engineering fracture mechanics, 1985. **21**(1): p. 31-48.
37. Dudrová, E. and M. Kabátová, *Fractography of sintered iron and steels.* Powder Metallurgy Progress, 2008. **8**(2): p. 59-75.
38. Skiba, T., et al., *Mechanical properties of spark plasma sintered FeAl intermetallics.* Intermetallics, 2010. **18**(7): p. 1410-1414.
39. Klahn, D., A. Mukherjee, and J. Dorn, *STRAIN-RATE EFFECTS*, 1970, California Univ., Berkeley. Lawrence Radiation Lab.
40. Fiedler, B., et al., *Failure behavior of an epoxy matrix under different kinds of static loading.* Composites Science and Technology, 2001. **61**(11): p. 1615-1624.
41. Klepaczko, J.R., et al., *Modelling of thermo-viscoplastic behaviour of DH-36 and Weldox 460-E structural steels at wide ranges of strain rates and temperatures, comparison of constitutive relations for impact problems.* Mechanics of Materials, 2009. **41**(5): p. 599-621.
42. El-Qoubaa, Z. and R. Othman, *Characterization and modeling of the strain rate sensitivity of polyetheretherketone's compressive yield stress.* Materials & Design, (0).
43. Abaqus, *Damage evolution and element removal for ductile metals.* Abaqus Documentation, 2014.

Chapter 4

NUMERICAL VALIDATION OF MODELING THROUGH APPLICATION TO BALL IMPACT

The constitutive modeling of the mechanical behavior of each material (F7020 aluminum alloy and sintered polyimide) was performed with the aim to be applied to high velocity impacted structures. For this purpose some validation tests of ball impacts have been carried out on monolayers (F7020 and sintered PI).

The experimental results obtained on structures impacted by spherical steel projectiles and then compared to the simulations computed with ABAQUS®/Explicit using the VUMAT subroutines in FORTRAN. The constitutive models suggested in the previous part is used in the simulation in order to evaluate the performances of the numerical model.

Several relevant parameters are studied in this work: the residual velocity of the projectile, the velocity of the ejected plug. Each of these parameters will be described in this chapter and a comparison between experimental data and simulation computations will be displayed.

In a second part of this chapter, numerical simulations on multilayers materials (sintered PI and F7020 assembled using epoxy resin) are investigated in order to evaluate the potential of such structures.

A. Experimental performing of ball impacts

1. Experimental setup

a. Gas gun

The projectile used for the test consists into a 8 mm diameter 100C6 steel ball. It is launched using a 1.7 m long gas gun (Figure 120). The launching system allows impact velocities ranging from 70 m/s up to 400 m/s with this projectile. The gas used for the tests is compressed helium which permits to reach higher velocities than compressed air due to its lower inertia.

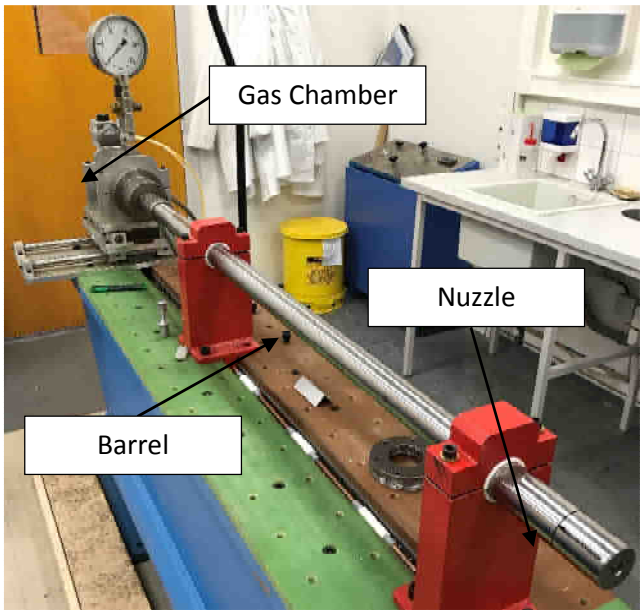

Figure 120 - Gas gun used for the impact tests

b. Target fixation setup

The target consists into an 80 mm diameter disk of several thicknesses (2 mm, 2.5 mm, 3 mm and 4 mm for the F7020 aluminum alloy). To avoid any mounting hole in the target, the disk is fitted between the frame and a target holder (see Figure 121). A target wedge is also added around it to get a linear and homogeneous contact with the target and to center it.

The target holder, the target wedge and frame are screwed together and the frame is then fixed at the bottom of a security box (see Figure 122). Transparent windows on the sides of the box allows video recording of the projectile and target fragments from the back side of the target.

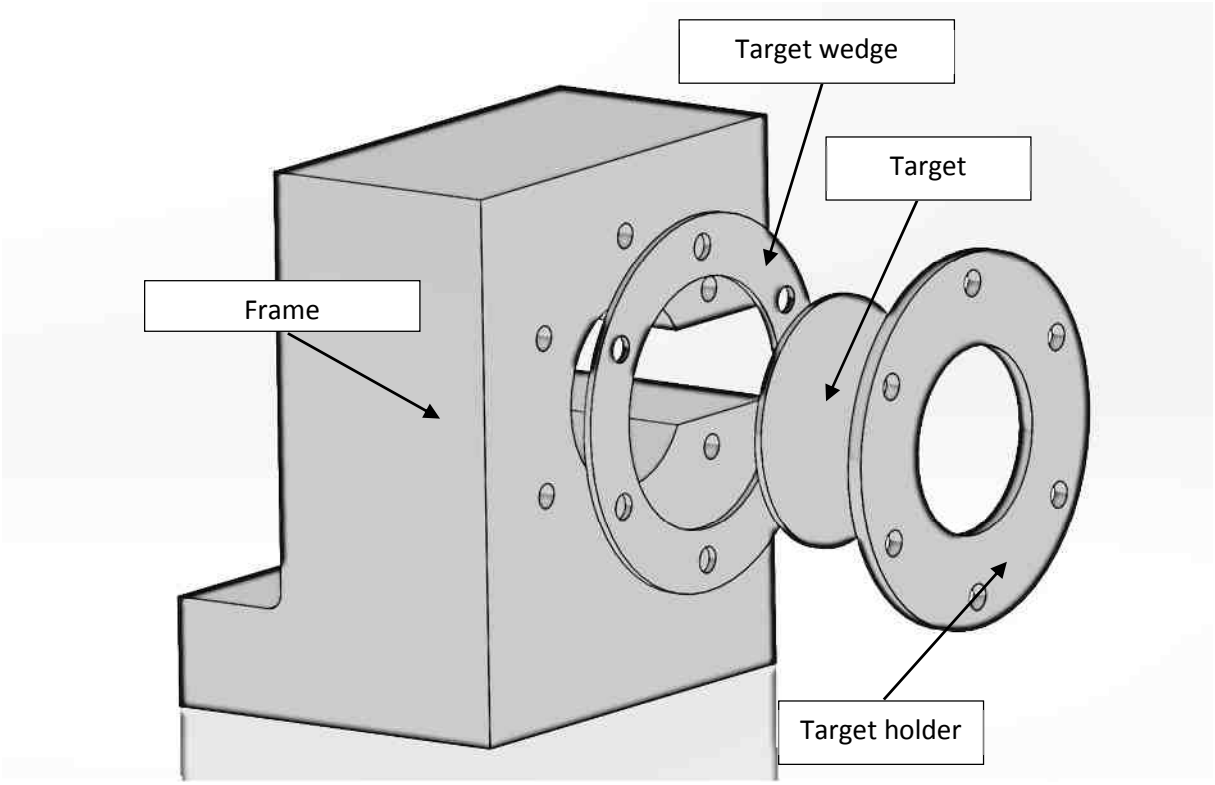

Figure 121 - CAD representation of the fixation setup of the setup

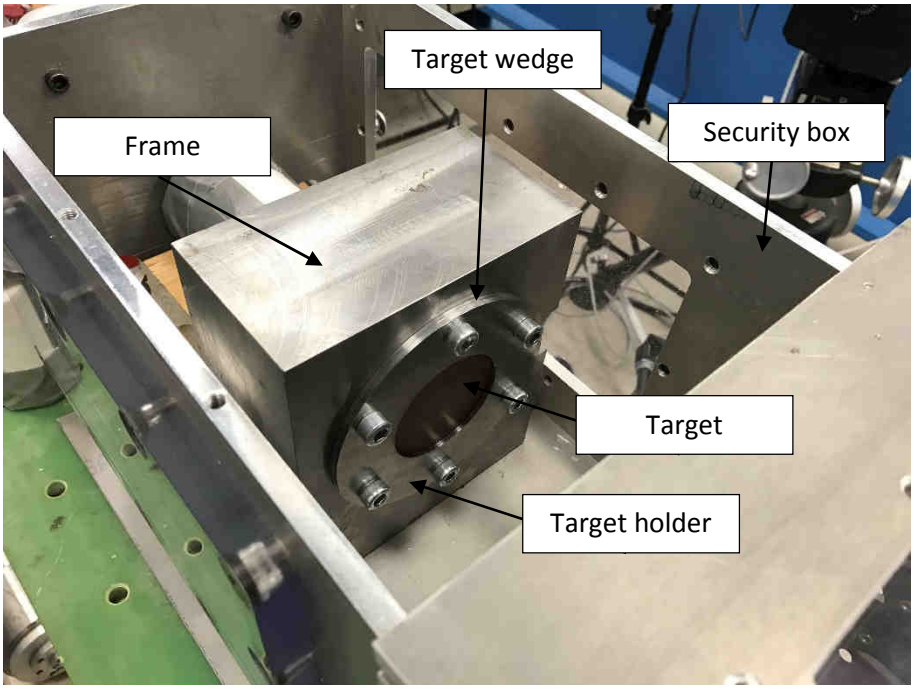

Figure 122 - Target fixation setup fixed in the security box

2. Measurement methods

a. Optical barrier

The optical barrier consists into two laser lines separated, in this case, by a distance $l = 72$ mm (see Figure 123). When the projectile passes through the laser beams, the signal from the photodiodes at the other side decreases drastically and the crossing of the ball is therefore detected. By using two laser beams, it is possible to compute the impact velocity V_0 of the projectile from the delay Δt between the drops of the two measured signals (Eq 4.1).

$$V_0 = \frac{l}{\Delta t} \qquad (4.1)$$

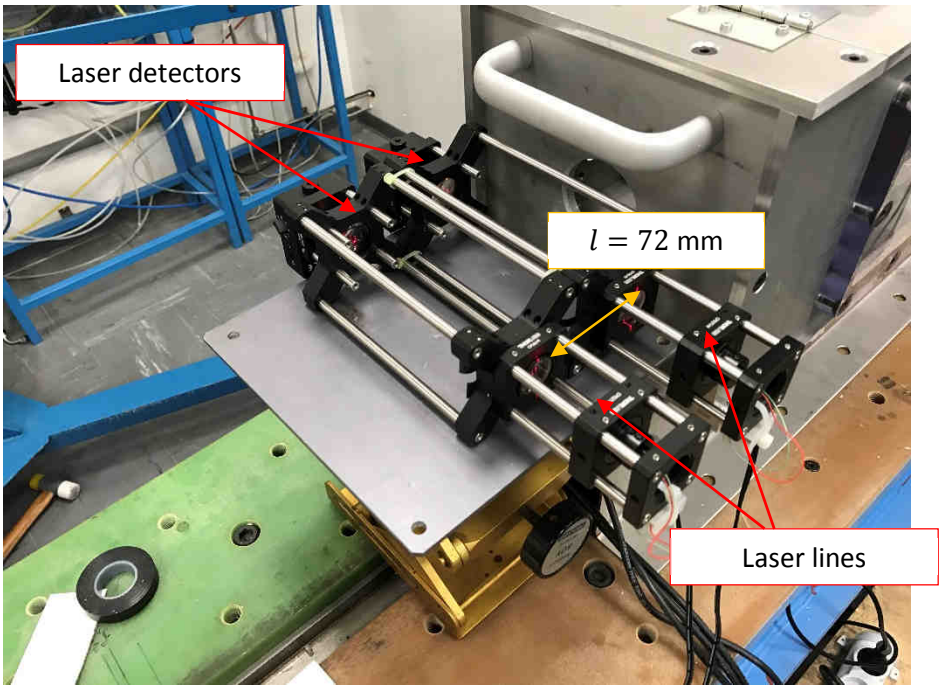

Figure 123 - Optical barrier

b. High speed camera

The velocities of post-impact objects are measured using a high speed camera (Shimadzu HPV-X). The recording of the camera is triggered using the optical barrier and a delay is generated using an oscilloscope (Figure 124). A flash generator is also used to ensure a correct visibility of the video recording. It is triggered using the same process as the high speed camera. The camera is setup to record 128 frames per recording and the frame rate is therefore computed depending on the test (essentially the

impact velocity V_0 which conditions the residual velocity of the objects). The range of frame rates used for these experiments starts from 50.000 frames/s up to above 100.000 frames/s.

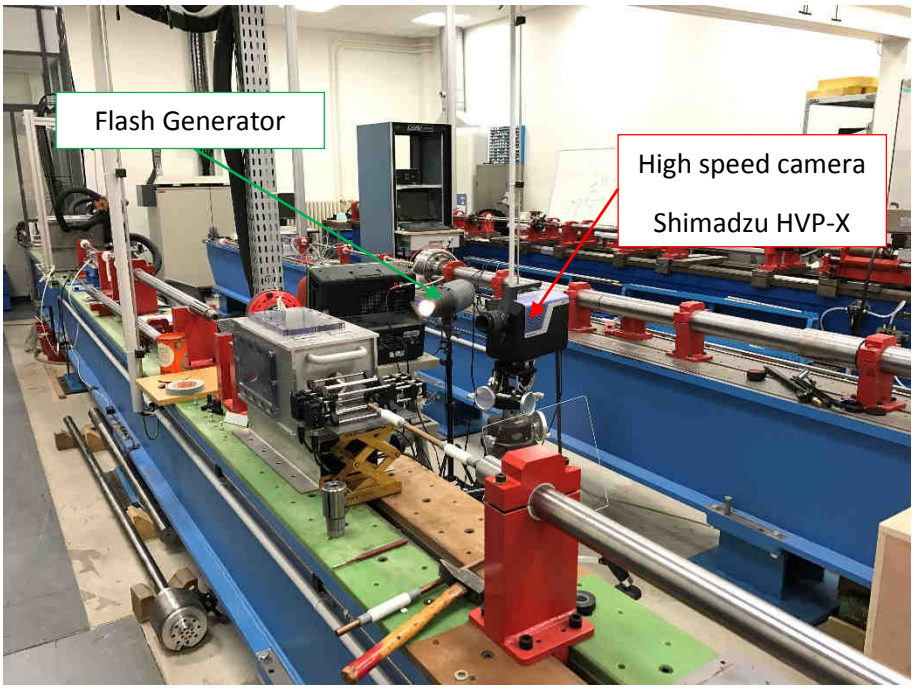

Figure 124 - High speed video recording setup

B. Simulation parameterization

The simulations are processed using the commercial software ABAQUS/Explicit®. The same target assembly used for the experiments has been modeled to keep the same boundary conditions (Figure 125). Embedment condition is set through the internal threads of the target holder, target wedge and the frame. The frame is also embedded to its base. Only contact conditions are set as boundary conditions for the target (without friction). The 100C6 steel ball (8 mm diameter) is assumed rigid through constraint condition (hypothesis verified after experiment) but is still meshed with C3D6 linear tetrahedron elements (size ~ 0.5 mm) and material properties are given ($E = 210$ GPa, $\nu = 0.3$ and $\rho = 7800$ kg. m^{-3}) in order to allow wave propagation in it. The initial velocity of the projectile is set by defining a predefined field on a reference point placed onto the ball.

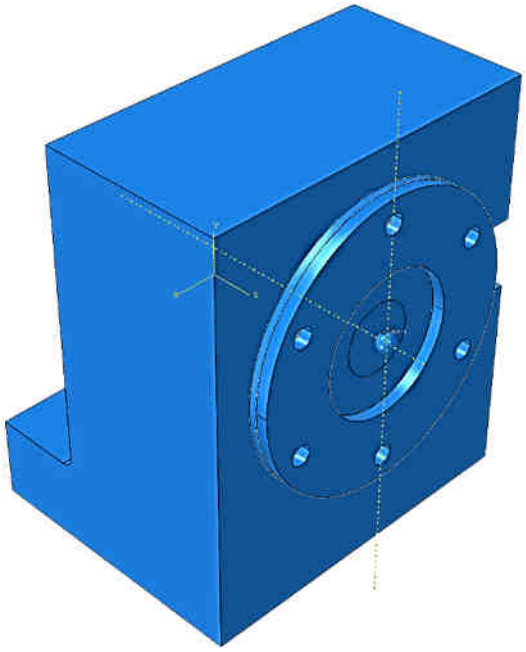

Figure 125 - Simulation setup used

The target and the fixation setup (same material properties as the projectile) are meshed using C3D8R elements (8-node linear brick element with reduced integration and default hourglass control, see Figure 126). The element size in the impacted area of the target has been set as size ~ 0.2 mm for all target thicknesses (Figure 127). The contact between the projectile and the target is set between their respective meshes (volumic contact) and a self-contact is taken into account for the target. The failure is processed through element deletion (when the damage evolution variable D is equal to 1).

The material of the target is defined by the model associated to the VUMAT subroutine in FORTRAN (CCH model for the F7020 aluminum alloy (Eq 3.5 + Eq 3.42) and Cooperative model for the sintered PI (Eq 3.33 + Eq 3.42)). The Johnson-Cook models for the stress and the failure behaviors are as well used in this work as a comparison with the CCH model for the F7020 aluminum alloy. The parameters

can be found in the APPENDIX C. The global algorithm used for these VUMAT subroutines is given in APPENDIX F.

To allow the penetration through the whole target of the projectile, the contact condition between the two entities has to be defined in the input file. The two “surfaces” involved are created from the element sets of the target and of the projectile (the “surfaces” are therefore volumes).

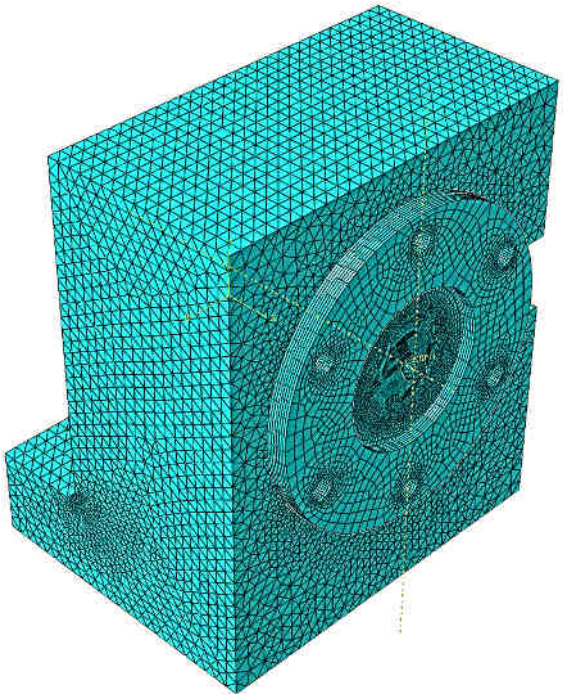

Figure 126 - Mesh of the overall simulation setup

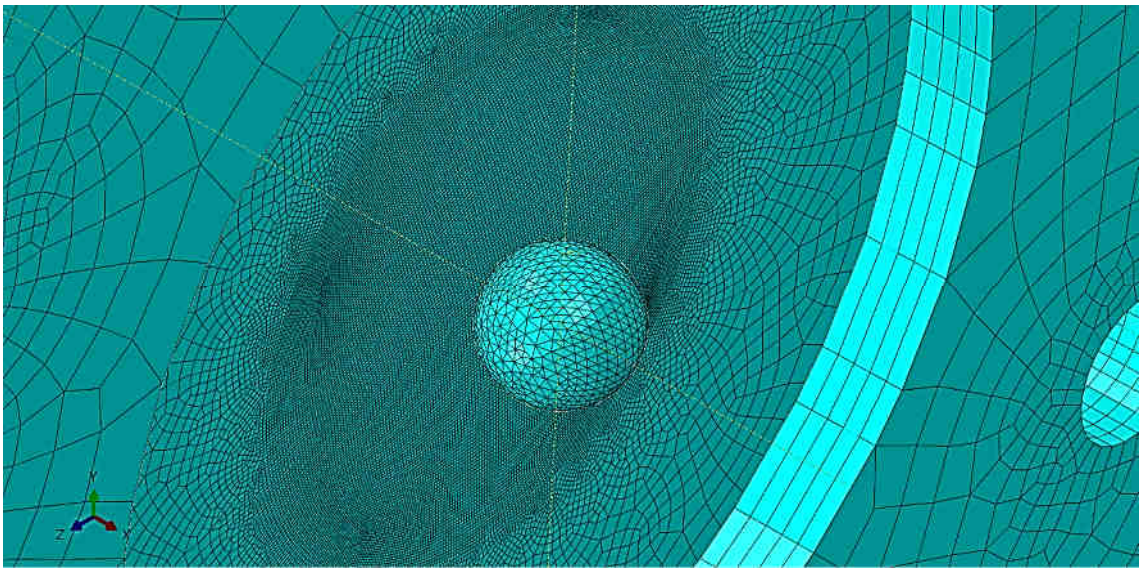

Figure 127 - Focus on the mesh of the target

C. Monolayer cases

The impact tests of a steel ball on the monolayers allow to separately check the accuracy of the constitutive models before the modeling of the multilayer material.

1. F7020 aluminum alloy

a. Observations of the experimental tests

The video recordings obtained with the high-speed camera enable to observe, from the back side, the different structural mechanisms leading to the perforation of the targets (Figure 128.a to 128.d).

The different steps of perforation seen from the back side of the target of F7020 by a steel ball (hemispherical nose-shaped projectile) are commented in this section.

The involved material displays a quasi-brittle behavior in the area consisting in positive triaxialities which can be found at the back of the target due to the deflection. Other aluminum presenting this kind of behavior have been reported in the literature such as the AA7075-T651 aluminum alloy [1, 2] or AA6070 [3] but the observed fragmentation phenomenon [4] of these alloys is not due to decohesion of the powder grains (intergranular failure) as it has been observed for the F7020 in this work (Chapter 2). The behavior of the targets of F7020 aluminum alloy is very different than the one of the commercial AA7020-T651 which presents a much more ductile failure mode of perforation [5, 6].

Therefore, concerning the F7020 aluminum alloy, the failure mechanisms start early (Figure 128.a) and consist here in the formation of numerous radial cracks starting from the center of the target (their number depends on the impact velocity and the target thickness). The ball velocity decreases drastically during this step.

The steel ball continues its trajectory through the target, creating a channel and pushing the different fragments at the back of the target previously formed by the cracks. This observed phenomenon leads to the formation of petals [4, 7] (between 8 and 10 in the tested conditions). Some fragments (plug [8]) of the inner section of the target are as well pushed away by the projectile (Figure 128.b). The presence of an ejected plug is normal when spherical or hemispherical projectiles are used [7].

The ball is at the limit of being released by the target and its deceleration is almost zero (Figure 128.c). However, this step is very important because it conditions the final state of the target after the perforation by the projectile (petals might be torn off the plate).

The ball is then totally released from the contact of the petals (Figure 128.d), its velocity will not vary anymore: its value is called the residual velocity V_r. The different fragments are expulsed in a cone-shaped volume.

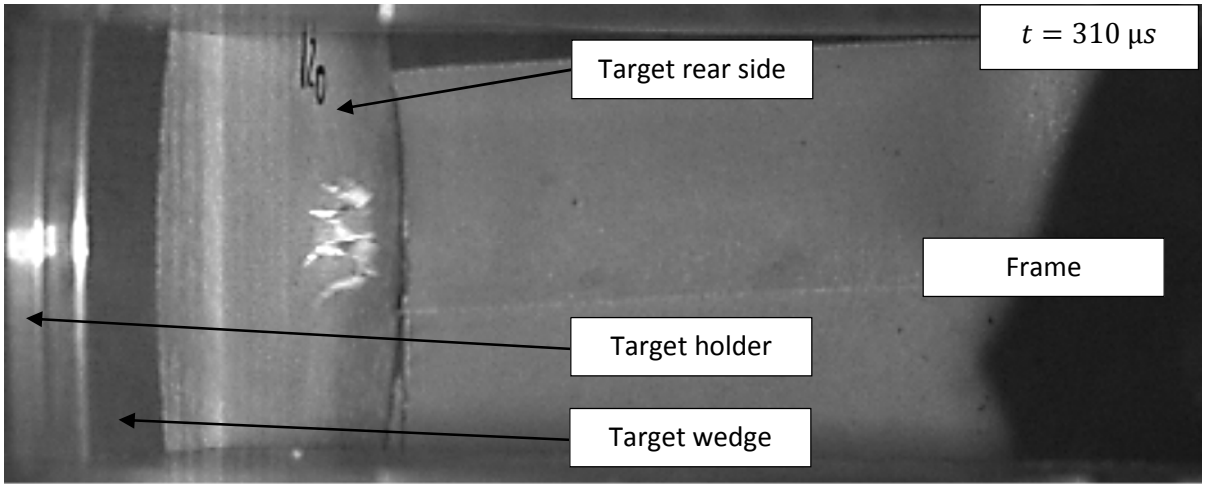
$t = 310\ \mu s$
Target rear side
Frame
Target holder
Target wedge

(a)

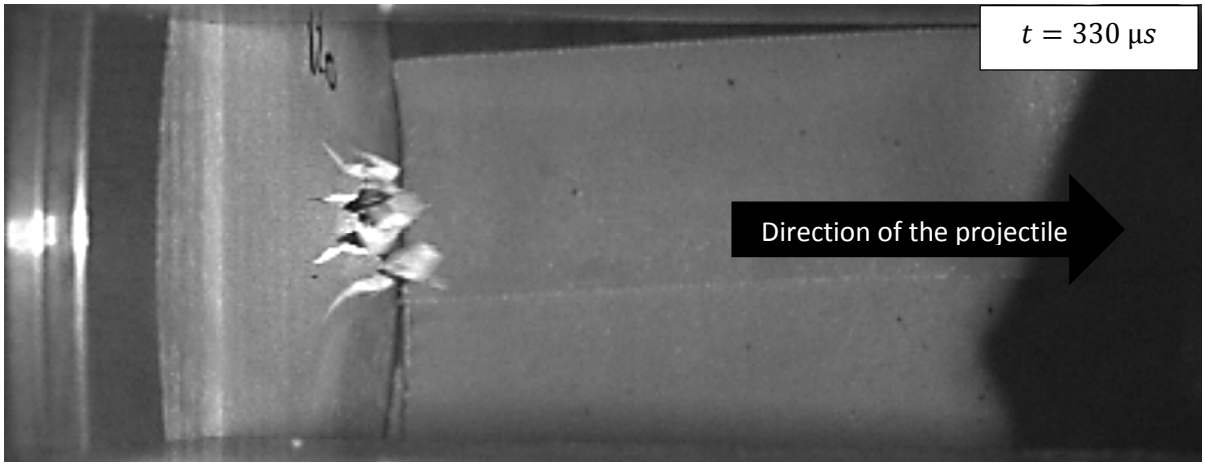
$t = 330\ \mu s$
Direction of the projectile

(b)

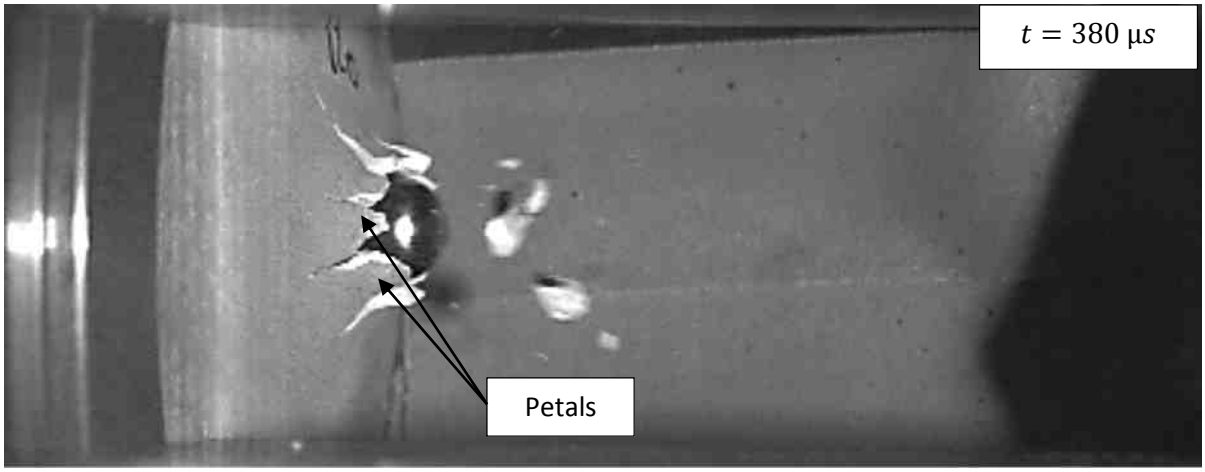
$t = 380\ \mu s$
Petals

(c)

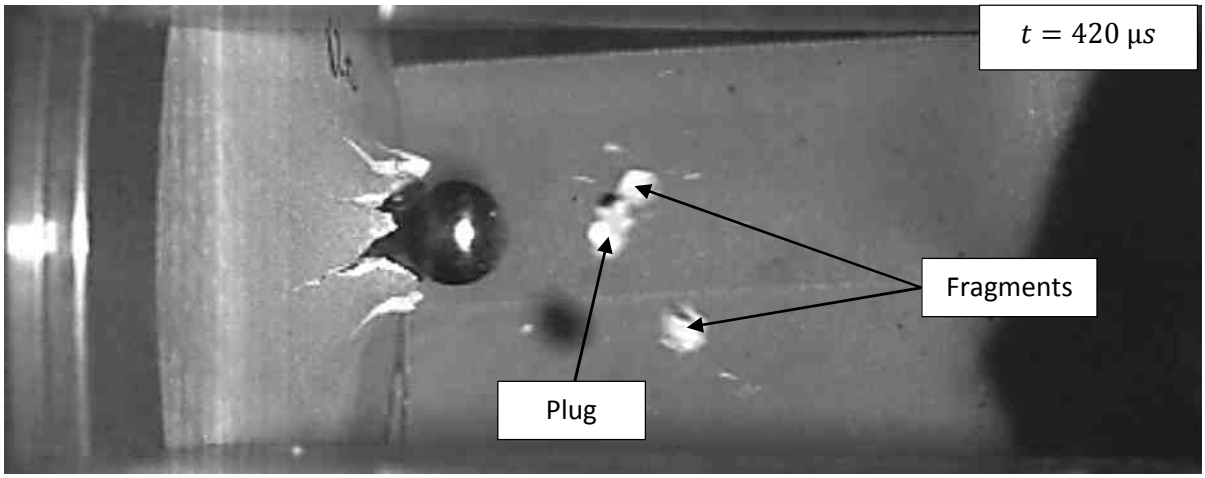

(d)

Figure 128 - Pictures of the video recording of the perforation processes of a F7020 aluminum plate (3 mm thick) by a 8 mm diameter ball at 298 m/s at (a) 310 µs, (b) 330 µs,(c) 380 µs and (d) 420 µs after the beginning of recording

b. Comparison with numerical results

Concerning the F7020 aluminum alloy, 12 tests have been carried out for model validation in different configurations. Two parameters have been changed for the tests: the impact velocity and the target thickness (2 mm, 2.5 mm, 3 mm and 4 mm). The number of experimental impact tests is limited to 12 due to the complex shaping process (Spark Plasma Sintering) which does not allow mass production of the studied materials.

i. Residual velocity

The residual velocity V_r corresponds to the velocity of projectile after the perforation of the target. The highest impact velocity for which $V_r = 0$ is called the ballistic limit velocity V_{bl} [7]. The experimental results have been confronted to two numerical models: the suggested CCH model [9] and the classic Johnson-Cook model [10] (see parameters in APPENDICE C). The Johnson-Cook model has been chosen due to its universal use in ballistic problematic for all kinds of metallic materials [1, 5, 11, 12] and to represent the models from the literature which does not take into account the microstructural changes which can be encountered at high temperatures (e.g. MTS model [13], ZA model [14], RK model [15]). The Johnson-Cook model means in this work, the Johnson-Cook model for the stress [10] coupled to the failure Johnson-Cook model [16]. However, these microstructural changes are modeled in the suggested CCH model by using the calorific ratio approach [9]. It can be seen on the Figure 129 that the CCH model is very accurate over the ranges of thicknesses and experimental impact velocities with a mean error percentage of 3.8% (see Figure 131). The simulations using the classic Johnson-Cook model (determined using the same experimental data) show an important inaccuracy (Figure 130) with increasing thicknesses with a mean error of 15.9% (see Figure 131).

Besides, the error measured for CCH models stays constant over the range of tested thicknesses but the one of the Johnson-Cook model increases. It can therefore be said that the CCH model might be more

accurate than the Johnson-Cook model for a wider range of target thicknesses. The estimated value of V_{bl} using the CCH model for each thickness can be found in the Table 37.

Table 37 - Ballistic limit velocities according to CCH modeling for the different tested thicknesses of F7020 aluminum alloy

Thickness (mm)	2	2.5	3	4
V_{bl} (m/s)	170	215	265	350

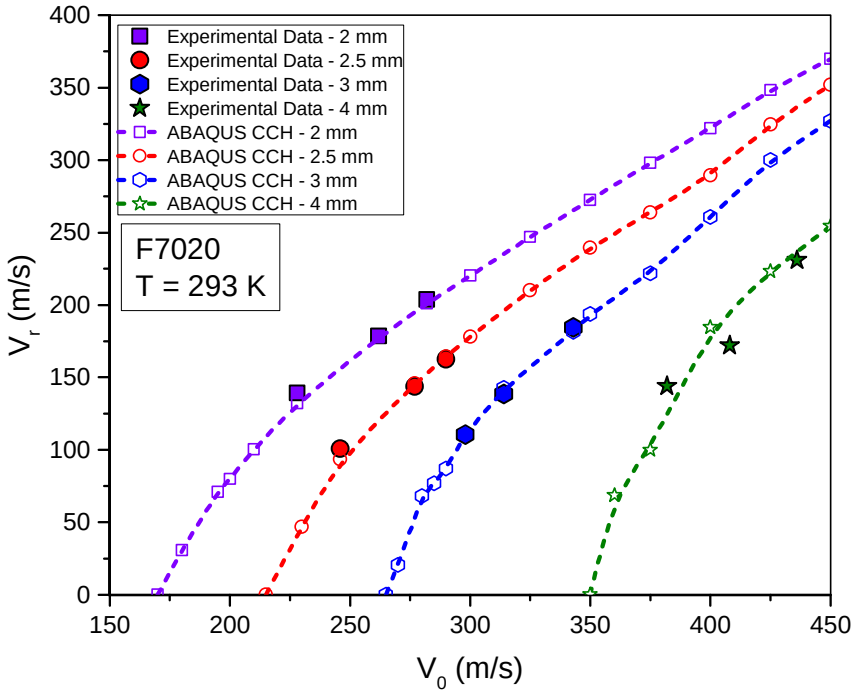

Figure 129 - Comparison between the experimental results and the numerical results with CCH model of the residual velocity V_r for the F7020 aluminum alloy target

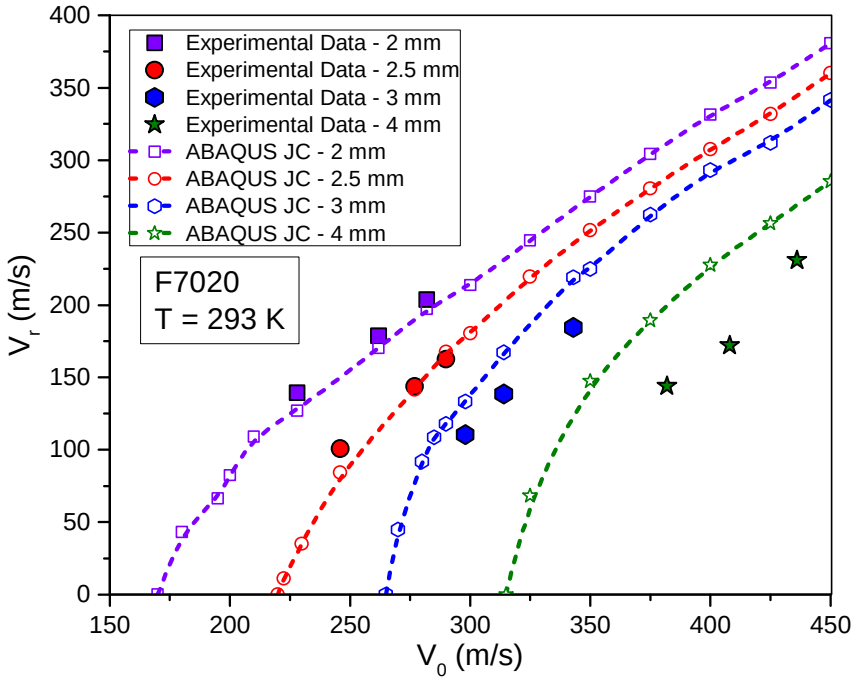

Figure 130 - Comparison between the experimental results and the numerical results with JC model of the residual velocity V_r for the F7020 aluminum alloy target

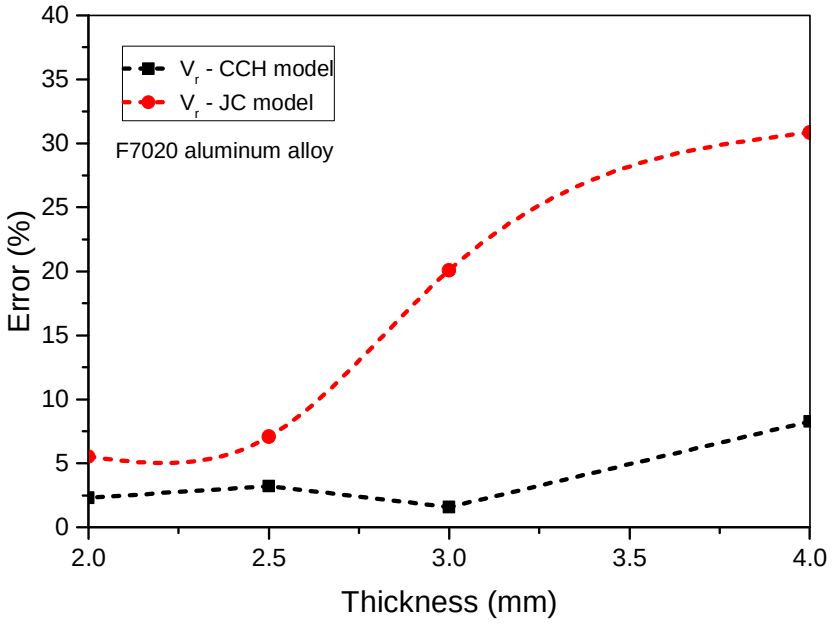

Figure 131 – Evolution of the error percentage between the experimental data and the used model for the residual velocity of the projectile with the thickness of the target

Several points can explain the reasons of the important error of the Johnson-Cook model:

- For these thicknesses and for such quasi-brittle aluminum, the modeling of failure and damage evolution behavior has an important impact on the results. In the case of the Johnson-Cook failure model [16], the sensitivity to the strain rate of the plastic strain at initiation of failure underestimates greatly its real value and the material will fail prematurely.
- Concerning the Johnson-Cook stress model, the strain rate sensitivity expression [16] also strongly underestimates the stress.

The more the thickness increases, the more the influence of the stress modeling is important. Therefore, the error contributions of the failure and stress modeling are summed and the total error increases. Besides, higher impact velocities are generally used on the target with the greater thicknesses and the involved strain rate increases and so the error continues to augment.

The experimental data have also been compared with the analytical Rosenberg model [7] with the spherical nosed projectiles ($D = 8$ mm (diameter of the projectile) and $L_{eff} = 5.33$ mm (equivalent length of a cylinder of same volume as the projectile)). The density of the steel ball is taken as $\rho_p = 7800\ \text{kg.m}^{-3}$. The target material (of thickness H) reference yield stress is taken as $Y = 260$ MPa, its density as $\rho_t = 2880\ \text{kg.m}^{-3}$ and its elastic modulus as $E_t = 72$ GPa. The projectile is assumed rigid.

The residual velocity is computed from the projectile and target geometrical and mechanical properties. The expressions used are Eqs 4.2, 4.3 and 4.4 [7].

$$V_r = V_{bl}\sqrt{\frac{1}{1+\frac{3\rho_t H}{2\rho_p D}}\left(\frac{V_0}{V_{bl}}\right)^2 - 1} \quad (4.2)$$

$$V_{bl} = \sqrt{\frac{2H\sigma_r}{\rho_p L_{eff}}} \quad (4.3)$$

$$\begin{cases} \sigma_r = \sigma_y\left(\frac{2}{3} + 4\left(\frac{H}{D}\right)\right) & \text{for } \frac{H}{D} \leq \frac{1}{3} \\ \sigma_r = 2\sigma_y & \text{for } \frac{1}{3} \leq \frac{H}{D} \leq 1 \\ \sigma_r = \sigma_y\left(2 + 0.8\ln\left(\frac{H}{D}\right)\right) & \text{for } \frac{H}{D} \geq 1 \end{cases} \quad (4.4)$$

The quantity σ_r corresponds to the effective resistive stress of the target and is greatly dependent on the H/D ratio.

The model results can be found in the Figure 132. A clear shift of the model can be observed for the 2 mm and 2.5 mm thicknesses. It underestimates the real residual velocity of the projectile but is correct for the 3 and 4 mm thicknesses. This inaccuracy for thinner targets is greatly due to the enhanced effect of the brittle failure toward the stress response in those conditions and the model is not designed to take into account such energy loss caused by the numerous crack propagation.

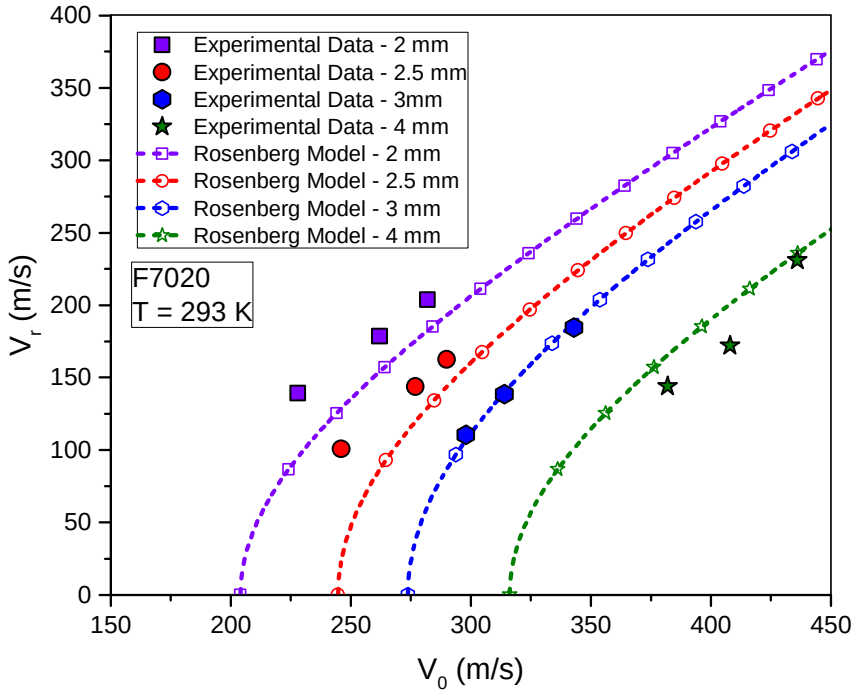

Figure 132 - Comparison between the experimental results and the analytical results with Rosenberg model of the residual velocity V_r for the F7020 aluminum alloy target

ii. Plug velocity

A plug is generally formed in cases of impact of hemispheric or blunt projectiles [8] and its output velocity V_p is higher than the residual velocity V_r of the projectile [7]. Therefore, being able to predict accurately the quantity V_p through a numerical or analytical model is an important asset to evaluate the protection performances of the target. For this purpose, the velocity of the plug is experimentally measured through a high speed camera recording, and numerical simulations with CCH [9] and Johnson-Cook [10] models are performed for comparison (see Figure 133 and Figure 134). The numerical results using the CCH model can be found in the Figure 14 and it can be observed that the modeling suggested in the previous chapter allows an accurate evaluation of the plug velocity in all the tested cases (global error around 3.6% with the experimental data, see Figure 135). However, concerning the Johnson-Cook model (Figure 135), the thicker the target becomes, the higher the error with the experimental data increases (mean error of 11.3%, see Figure 135). However, for the case for 4 mm target thickness, the gap between the CCH model and JC model is reduced. Indeed, the JC model manages to be quite efficient to evaluate the plug velocity for this particular thickness.

The gap between the simulations using the Johnson-Cook model and the real velocities of the plug is mainly due to the underestimation of global mechanical behavior of the material at the very high strain

rates involved during the experiments. Indeed, both stress and strain at initiation of failure [16] becomes much lower than the actual mechanical behavior. With such modeling, the formation of the plug starts earlier as well as its detachment from the target. Then, it keeps the projectile velocity from this particular instant which is higher than the ones of the experiments due to the underestimation of the stress behavior.

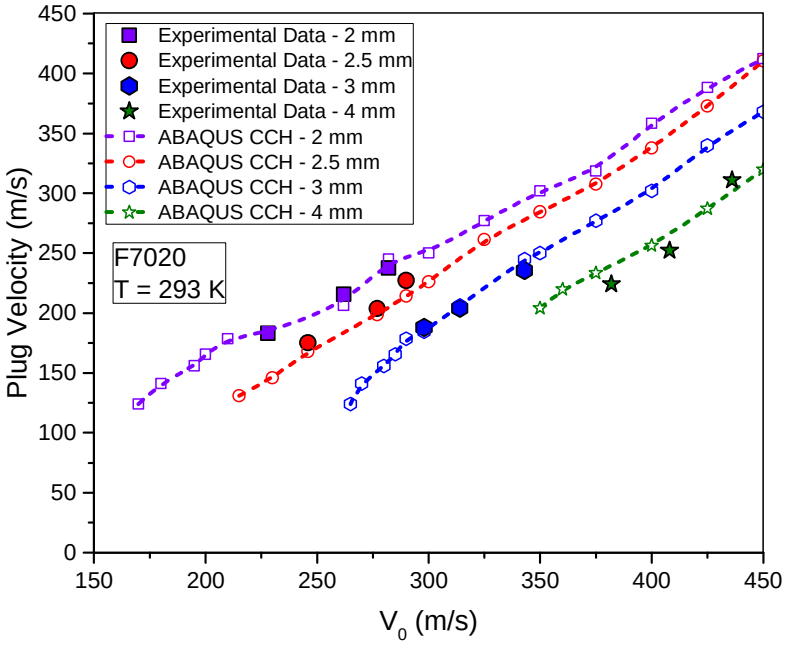

Figure 133 - Comparison between the experimental results and the numerical results with CCH model of the velocity of the plug V_p for the F7020 aluminum alloy target

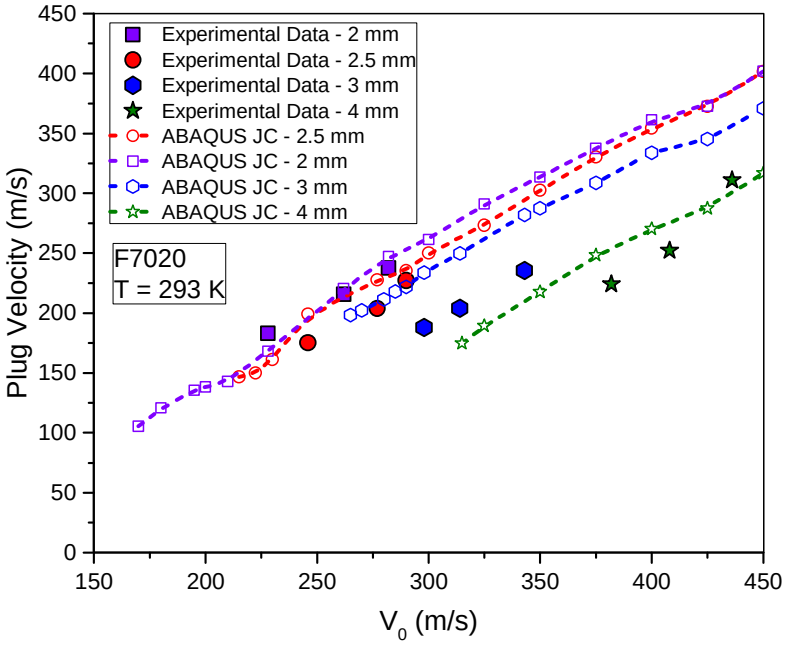

Figure 134 - Comparison between the experimental results and the numerical results with JC model of the velocity of the plug V_p for the F7020 aluminum alloy target

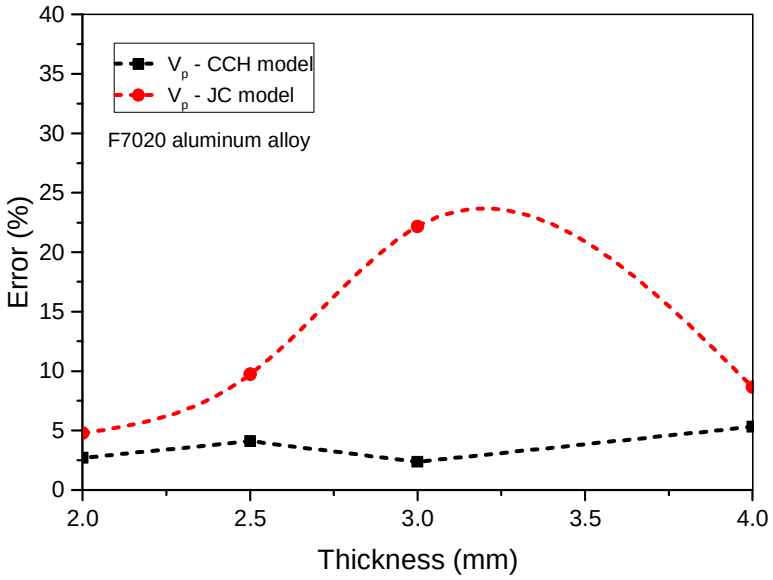

Figure 135 - Evolution of the error percentage between the experimental data and the used model for the residual velocity of the projectile with the thickness of the target for the F7020 aluminum alloy target

An analytical approach allowing to evaluate the plug velocity V_p without having to perform numerical simulations has been developed for this work. The concept is based on a critical projectile depth penetration h_{lim} in the target before reaching a characteristic strain at failure ε_C^{plug} leading to the detachment of the plug. A coupling of this modeling concept with the Rosenberg model [7] leads to know the value of the residual velocity V_r at h_{lim} (and more generally for any value h of penetration depth) which will correspond to the value of V_p. In the case of a hemispherical nosed projectile, the main state of stress occurring near the zone of plug detachment is closed to the shear-compression σ^*~-0.4 (shear state of stress in case of a blunt projectile). Therefore, the value of ε_C^{plug} used will be the one measured experimentally for the tests in shear-compression in quasi-static $\varepsilon_C^{plug} = 0.31$. However, the value of the strain at failure increases with the strain rate and has to be multiplied with a rate dependent factor $f_{vf}(\dot{\varepsilon}_p)$ which may correspond to the expression suggested in the previous chapter (Eq 3.42) to model the rate sensitivity of the strain at initiation of failure (or replaced by a fixed factor f_{vf}~2.15). An approximation of the strain in this particular zone can be computed as follows: $\varepsilon = \frac{h}{H}$ with H the thickness of the target and the strain rate will be $\dot{\varepsilon} = \frac{V_r}{h}$. The value of the critical projectile depth penetration h_{lim} is then computed considering $f_{vf}\left(\frac{V_r}{h}\right)$ as shown in the Eq 4.5.

$$h_{lim} = H\varepsilon_C^{plug} f_{vf}\left(\frac{V_r}{h}\right) \qquad (4.5)$$

If $h_{lim} < h$ then the plug is fully detached and $V_p = V_r$. The results can be found in the Figure 136.

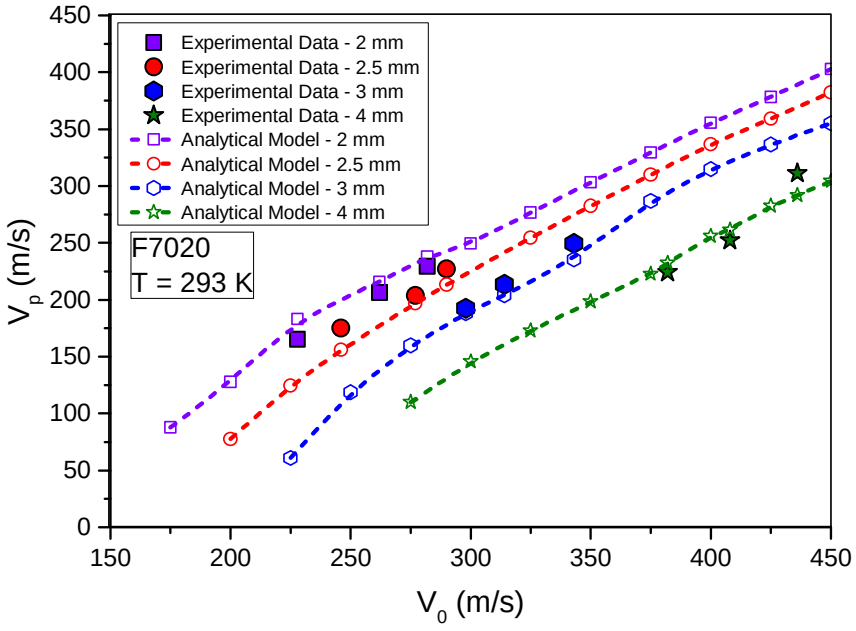

Figure 136 - Comparison between the experimental results and the analytical results using the suggested model of the velocity of the plug V_p for the F7020 aluminum alloy target

iii. Perforation mode

The perforation mode consists, in this work, into the failure process undergone by the target during the perforation of the projectile. In the case of the F7020 aluminum alloy, two different structural mechanisms have been observed over the ranges of impact velocities and target thicknesses.

The first structural failure behavior consists into the formation of multiple petals [4, 7] (between 8 and 10 depending on the target thickness and impact velocity) and the ejection of a main plug [8] (see Figure 137.a). The impact velocity of the projectile in the Figure 137.a for the experiment and the simulation shown is 282 m/s and the target thickness is 2 mm. It can be seen that the numerical model (model suggested in this work) predicts the experimental perforation mode as well as the number of petals in most cases (see Figure 137.b). The high number of petals is mainly due to the quasi-brittle behavior of the material r (but not brittle enough to lead to a fragmentation in this case) and its very low damage energy in positive triaxialities. This particular range of triaxialities characterizes the state of stress at the back of the target due to the deflection of this last. The petaling effect can be clearly seen on Figure 137.c and 137.d from both sides of the target after impact.

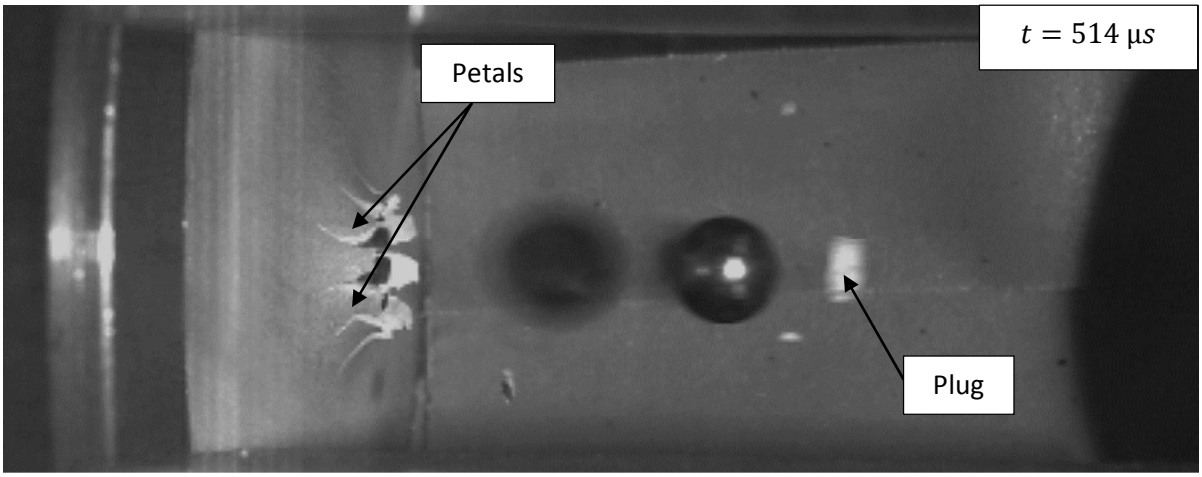

(a)

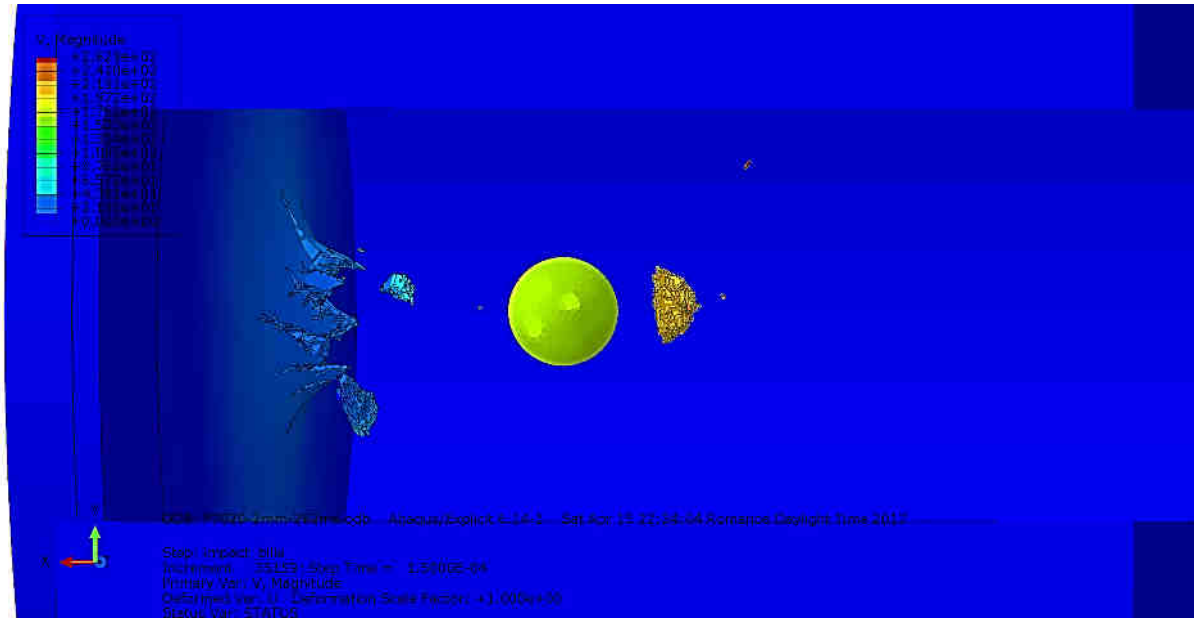

(b)

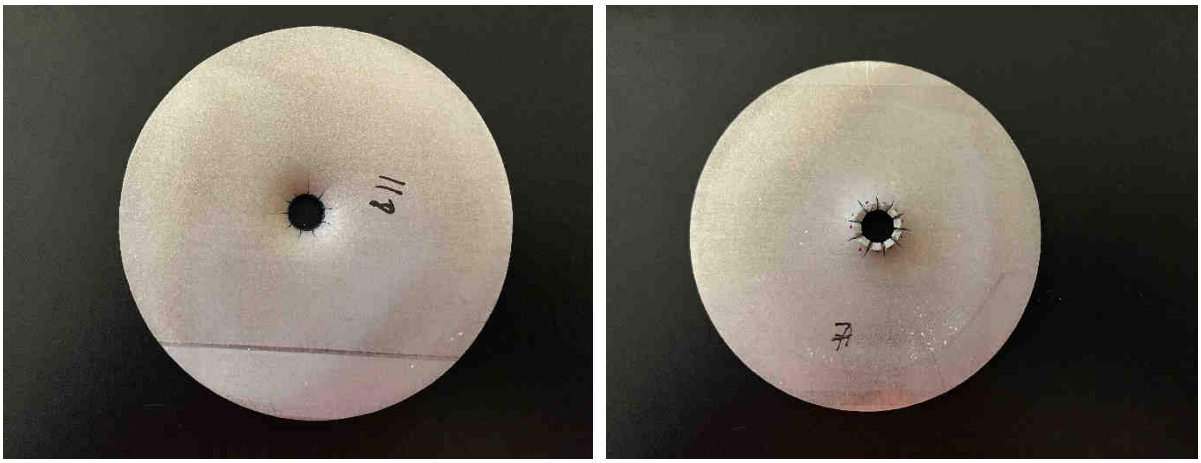

(c) (d)

Figure 137 – Comparison of the impact mechanisms between (a) the experimental results at 514 µs after the beginning of recording, (b) the numerical results (CCH model) on a 2 mm F7020 aluminum alloy at 282 m/s, (c) the front side of the impacted target and (d) the rear side of the impacted target

The second structural failure behavior, observed for the F7020 aluminum alloy, is similar to the first one but the petals are torn off the target and become fragments due to inertial effect (Figure 138.a). This phenomenon happened only in the cases of 3 mm thick plates and at relatively high impact velocities (above approximately 325 m/s). For all the 4 mm thick plates, this fragmentation phenomenon is even more important (Figure 139). It is mainly caused by the fact that the involved petals are too thick to be bent without breaking. The ejection of a plug still occurs [8]. The experiment and simulation (model suggested in this work) involved a 3 mm thick target and an impact velocity of 343 m/s (Figure 138.b) respectively. In this condition, all the petals have been torn off but for a test at 314 m/s, some petals stayed attached to the target. The phenomenon can be observed post-mortem on the two faces of the impacted target. Figures 138.c and 138.d show clearly the absence of petals which have been ripped of the rear side of the target.

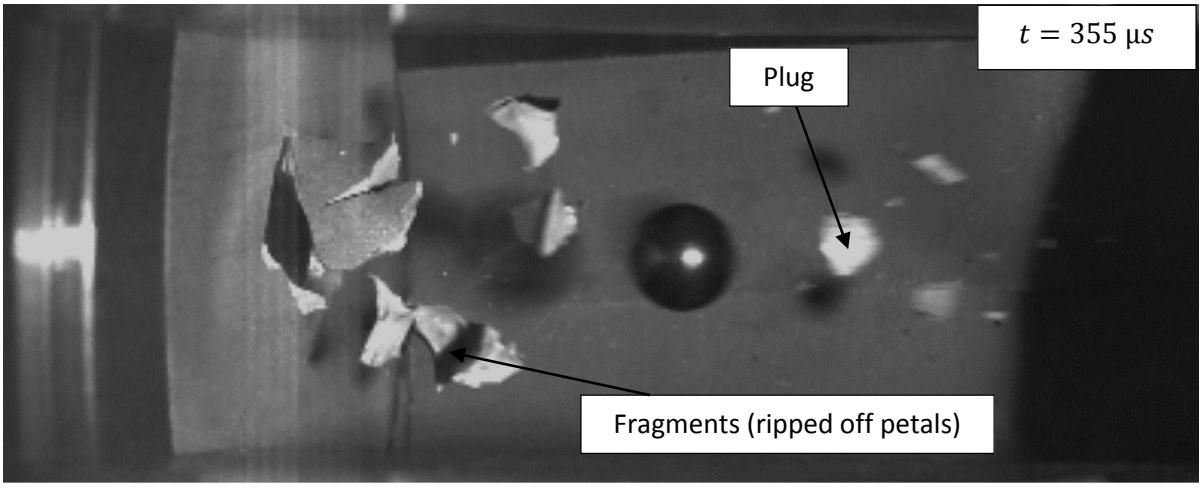

(a)

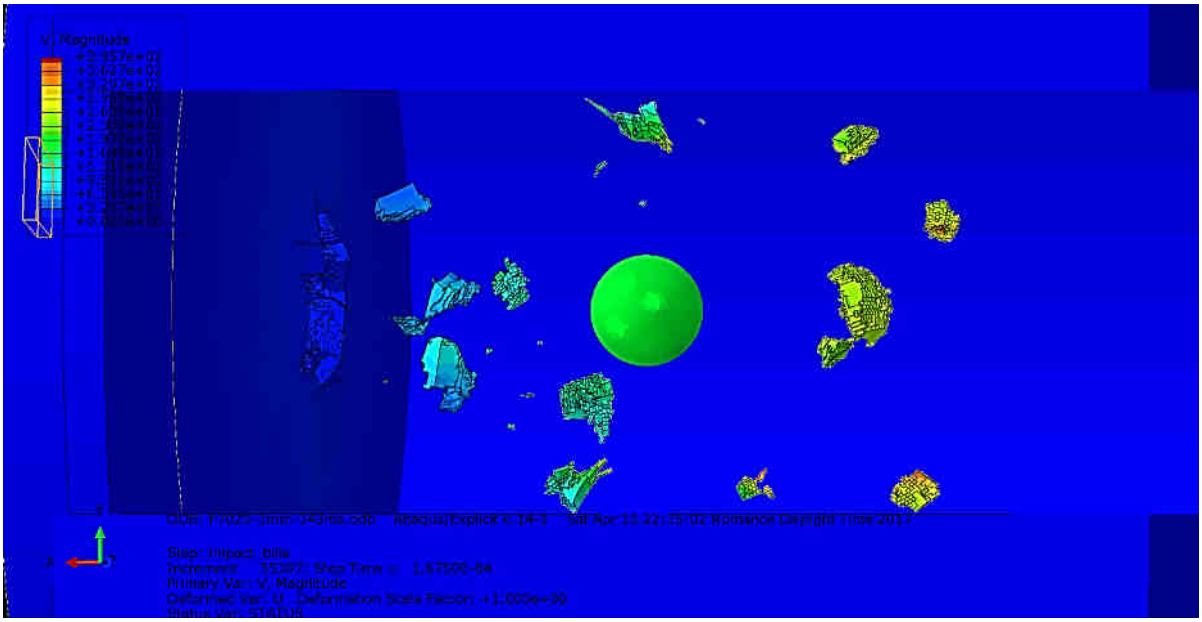

(b)

(c) (d)

Figure 138 - Comparison of the impact mechanisms between (a) the experimental results at 355 µs after the beginning of recording, (b) the numerical results (CCH model) on a 3 mm F7020 aluminum alloy at 343 m/s, (c) the front side of the impacted target and (d) the rear side of the impacted target

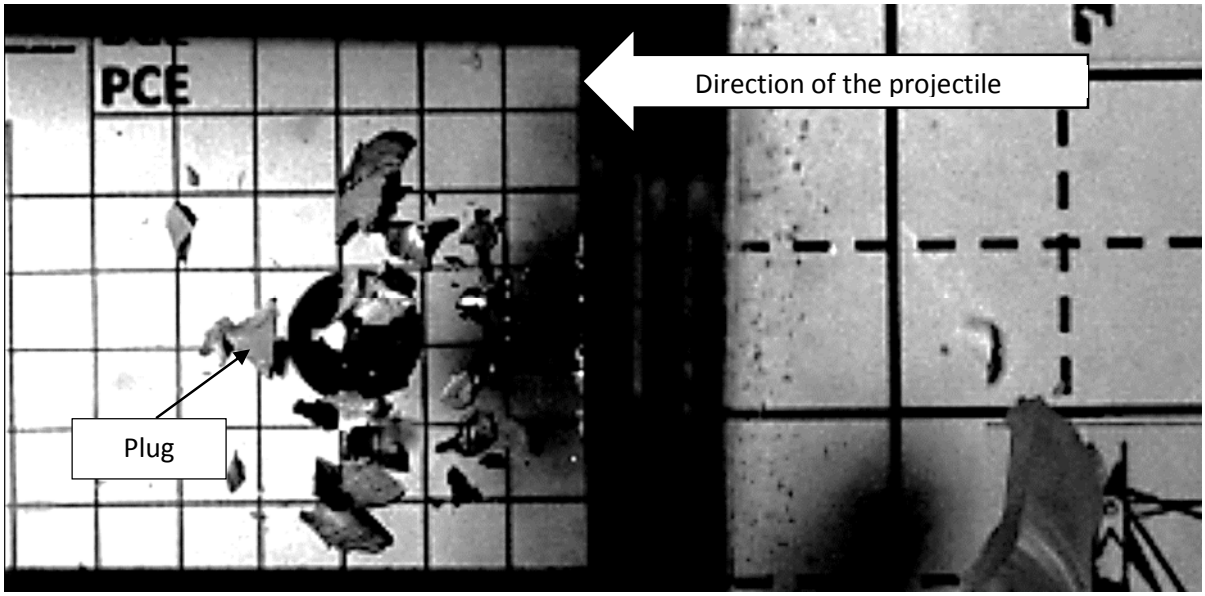

(a)

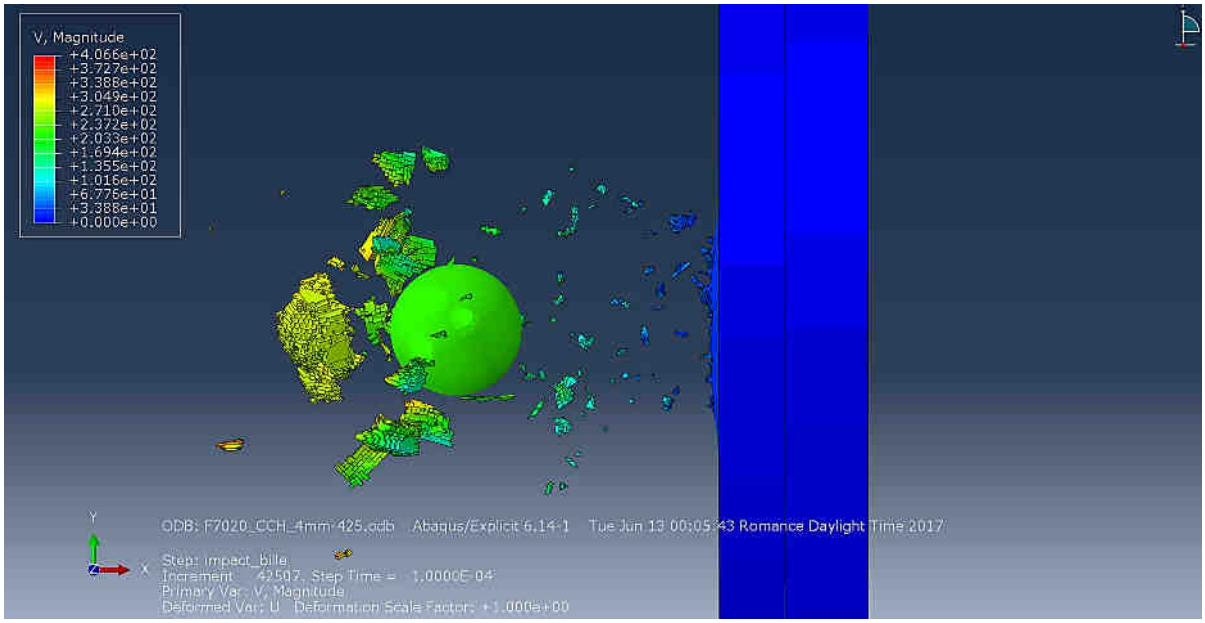

(b)

Figure 139 - Fragmentation of the rear side of a 4 mm thick target of F7020 aluminum alloy due to the perforation of a spherical projectile at 436 m/s (a) experiment and (b) simulation

As a conclusion, the mode of perforation of the F7020 targets greatly depends on the impact velocity and on the thickness. Plugging is observed for all the tested conditions. However, petaling can only be seen for the thinner cases (2 and 2.5 mm – see Figure 137). The 3 mm thickness cases show a transition phenomenon from petaling (for $V_0 \lesssim 325\ m/s$) to fragmentation (Figure 138). For the above tested thickness (4 mm) only fragmentation is always observed and is more and more preponderant (Figure 139).

Figures 140.a and 140.b display the numerical results using the Johnson-Cook model in the same conditions than Figures 137 and 138. It can be seen that the modes of perforation using JC model is

clearly different than the ones observed in the experimental conditions (Figures 137.a and 138.a) contrary to the ones obtained with simulations using CCH model (Figures 137.b and 138.b). Indeed, the fragmentation starts too early in Figure 140.a: the petals are not ripped off in experimental (Figure 137.a) and CCH simulation (Figure 137.b) in these conditions. Concerning the Figure 140.b, the fragmentation is much less important than in experimental results (Figure 138.a) and CCH simulations (Figure 138.b) which are very much alike. This is due to a lesser length of formed petals in the JC simulation caused by an underestimation of the strain at initiation of failure at very high strain rates by the JC model (linear sensitivity with the logarithm of the strain rate). This leads to premature failure in the tested conditions: ripped of petals in Figure 140.a and much shorter petals in Figure 140.b. Therefore, it can be said that the CCH model ability to reproduce the perforation modes is much higher than the JC model in this case.

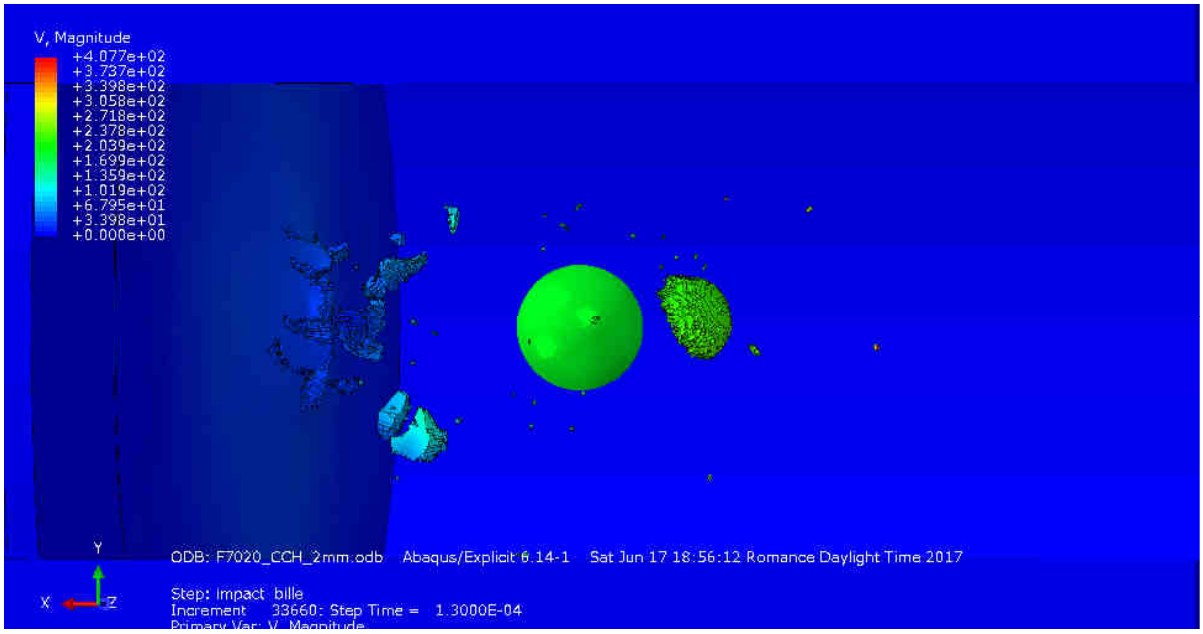

(a)

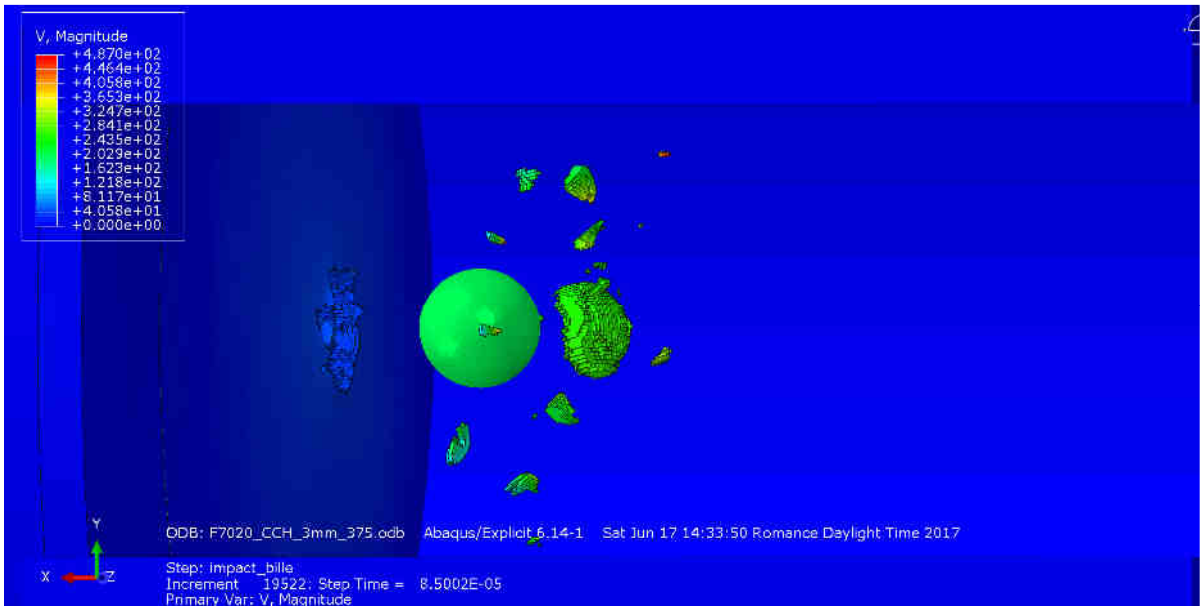

(b)

Figure 140 - Simulation results using Johnson-Cook F7020 model on at (a) 282 m/s on 2 mm thick target plate and (b) 343 m/s on 3 mm thick target plate

2. Sintered polyimide

a. Observations of the experimental tests

The different steps of perforation seen from the backside of the target of sintered polyimide by a steel ball (hemispherical nose-shaped projectile) are being commented in this section.

The sintered polyimide shows a very brittle behavior at the rear side of the target which presents positive state of stress due the deflection during the impact. Therefore, the fragmentation process of the target begins very early (Figure 141.a). Orthoradial cracks are generated at the opposite side of the impacted side (which can be well seen on Figure 141.b).

The propagation of the fragments is caused by the energy released by the crack generation (Figure 141.b and 141.c). The observed spatial repartition of the fragments is caused by the generation of orthoradial cracks under the loading and the phenomenon created a cup cone of fragmentation at the rear side of the target. This kind of behaviors (orthoradial cracks and cup cone failure mode) has been well reported in the literature for brittle polymers subjected to this kind of dynamic solicitation such as PMMA [17, 18] which presents a very different failure behavior than PE [19] or PC [18, 20, 21] (ductile perforation). However, the PMMA displays a much more brittle behavior [18] than the sintered polyimide studied in this work (due to its very high level of chain cross-linking leading a generalized locking phenomenon [22, 23]). The velocity of the generated fragments is higher than the one of the projectile.

After an important traveling time, the projectile and the fragments filled an important volume behind the target (Figure 22.d). The observation of the detachment of large fragments from the target can also been noted. This phenomenon might be caused by the crack propagation due to the target vibration after the loading, coupled with inertia effect.

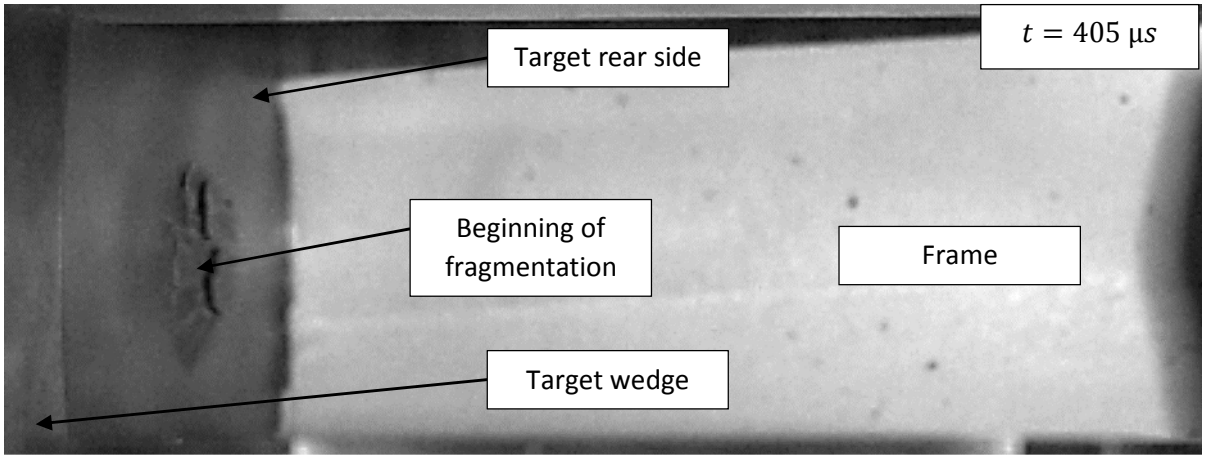

(a)

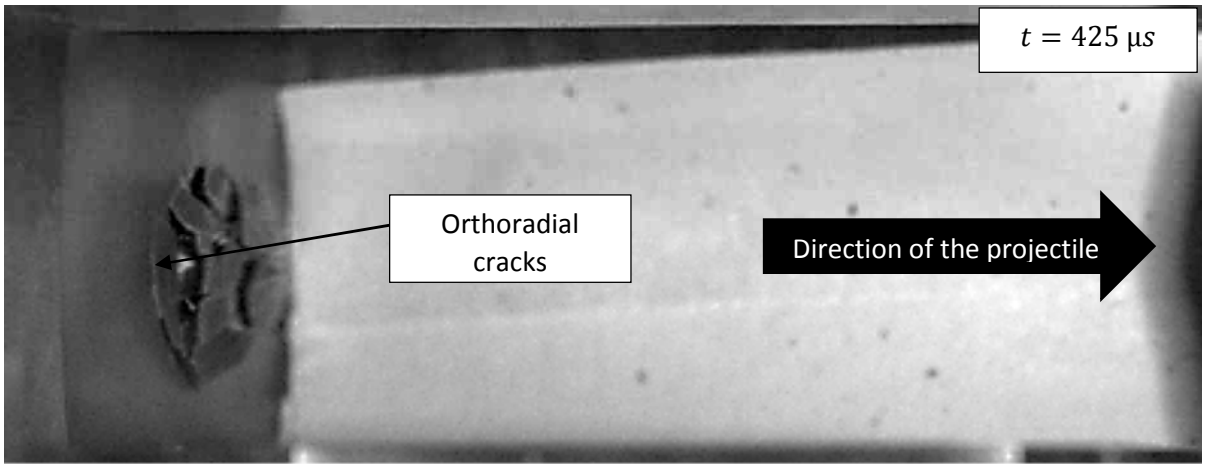

(b)

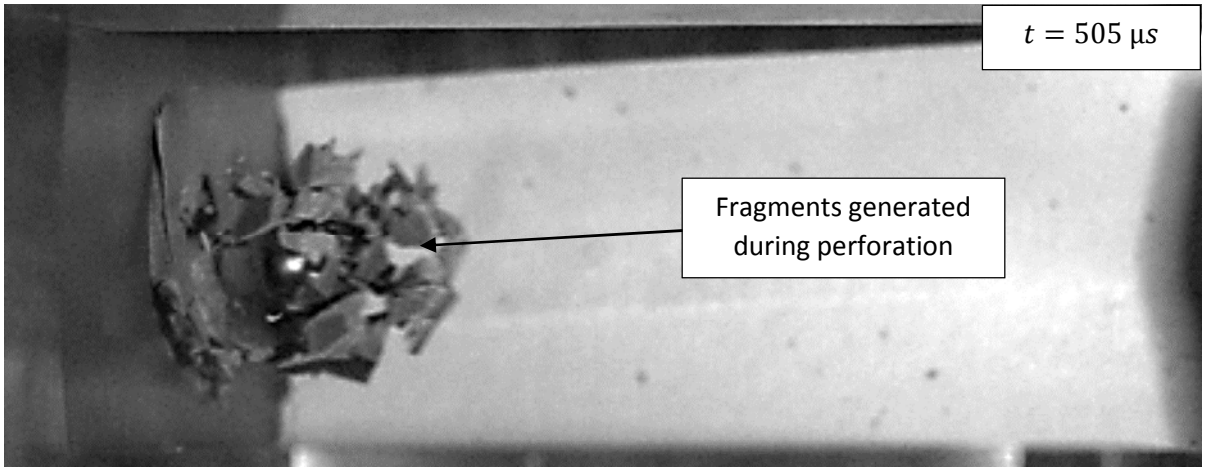

(c)

$t = 785\ \mu s$

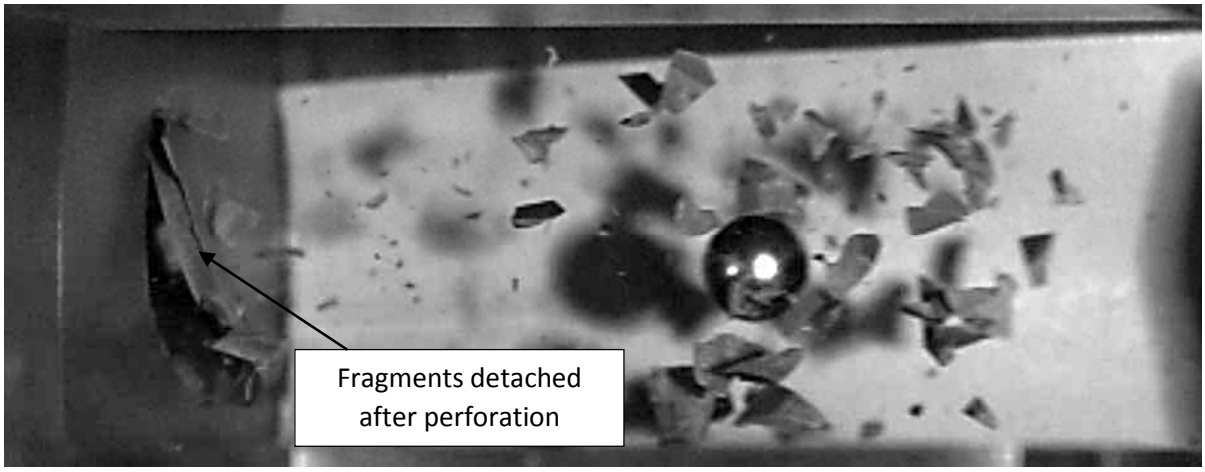

(d)

Figure 141 - Pictures of the video recording of the perforation processes of a sintered PI plate (2.5 mm thick) by a 8 mm diameter ball at 143 m/s at (a) 405 µs, (b) 425 µs,(c) 505 µs and (d) 785 µs after the beginning of recording

b. Comparison with numerical results

Concerning the sintered polyimide, 12 tests have been carried out for the model validation in different configurations. As previously said for the F7020, two parameters have been changed for the tests: the impact velocity and the target thickness (2 mm, 2.5 mm and 3 mm). The number of experimental impact tests is limited to 12 due to the complex shaping process (Spark Plasma Sintering) which does not allow mass production of the studied materials.

i. Residual velocity

As for the F7020 aluminum alloy, the residual velocity V_r of the steel ball after target perforation is recorded. The overall behavior of this material during the ball impacts is characterized by a global fragmentation of the impacted area generating a large number of fragments and the formation of a cup cone of fragmentation [17, 18].

In this work, due to the specific failure behavior of the material related to the shaping process, only the modified cooperative [24, 25] suggested modeling (Eq 3.31) has been implemented for the numerical simulations (Figure 142). It can be observed that the decrease of the residual velocity of the projectile with the thickness is limited (a decrease of only 15% for a weight increase of 50%). The results of the numerical simulations display a good correlation (5.5% of overall error, see Figure 143) with the experimental data despite the fragmentation perforation mode. The numerical model predicts a behavior highly nonlinear around the ballistic limit velocity V_{bl} (see Table 38) due to the fragmentation phenomenon which may lead to different scenarios in this range of low impact velocities V_0.

Table 38 - Ballistic limit velocities according to sintered PI modeling for the different tested thickness

Thickness (mm)	2	2.5	3
V_{bl} (m/s)	65	82	92

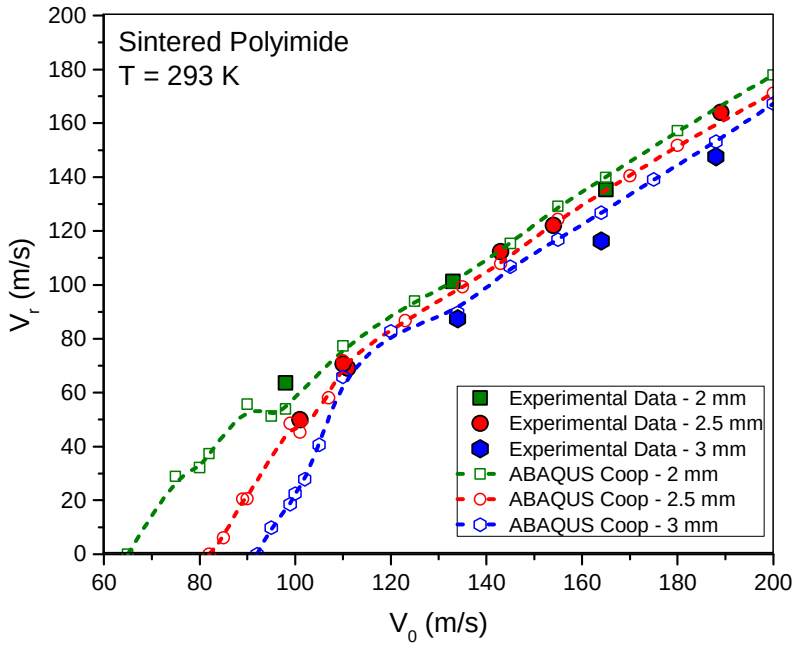

Figure 142 - Comparison between the experimental results and the numerical results for the sintered PI using the cooperative model of the residual velocity V_r

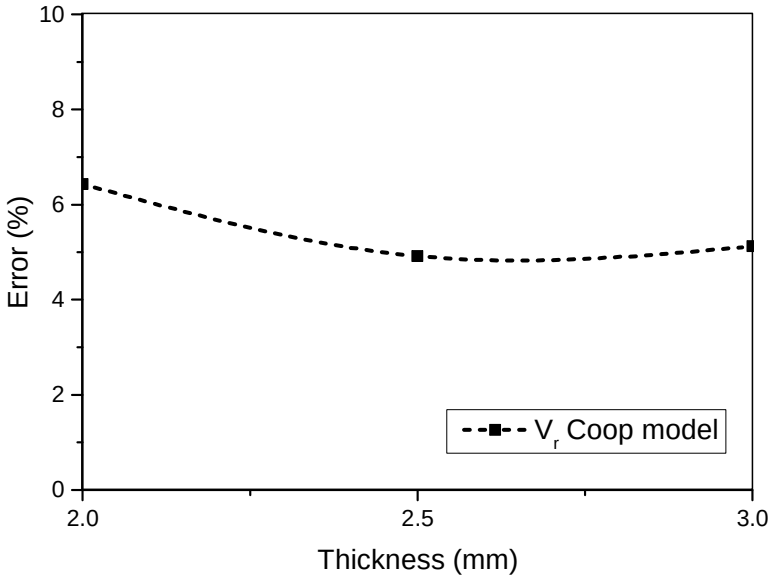

Figure 143 - Evolution of the error percentage between the experimental data and the cooperative model for the residual velocity of the projectile with the thickness of the target (sintered PI)

ii. Perforation mode and back channel diameter

In the case of the sintered polyimide, one global structural mechanism has been observed over the ranges of impact velocities and target thicknesses.

The structural mechanism observed leading to the failure of the sintered polyimide target is the fragmentation around the impacted area [17, 18]. The case exposed in the Figures 144.a and 144.b is a 2.5 mm thick plate impacted by the 8 mm diameter steel ball at 143 m/s. The simulation shows correctly the fragmentation phenomenon of the rear of the target. However, even if the bigger fragments are well represented, the average size of the small fragments is not well modeled. This is mainly due to the method used in the simulation to model the facture phenomenon: element deletion. Indeed, the smaller the fragments are the more the impact of the element deletion around its surface will be (some fragments may even disappear due to this method).

Furthermore, some bigger fragments are torn of the rear of the target after the crossing of the projectile. This phenomenon can be observed in the experimental case but is not reproduced in the simulation. This might be due to some specific experimental boundary conditions which are not taken into account in the simulation. This phenomenon is also amplified by the effect of target vibration leading to the detachment of more fragments (due to the extreme brittleness of the material).

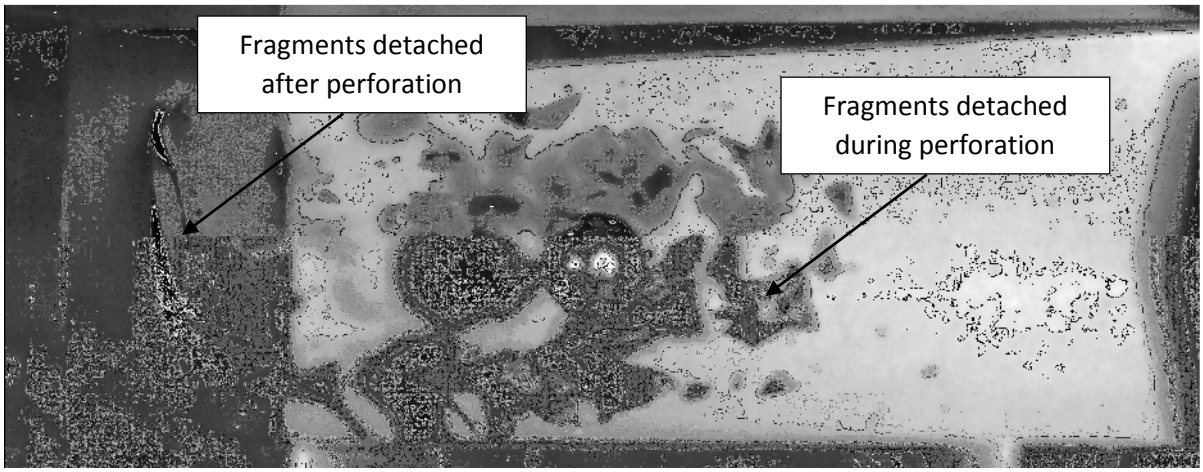

(a)

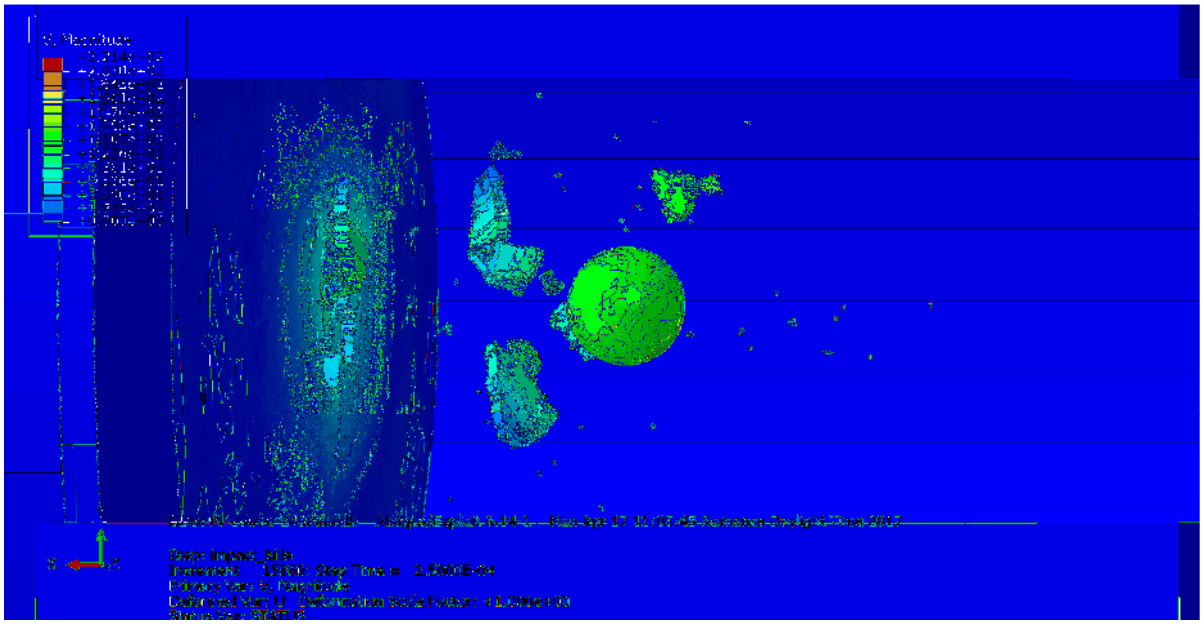

(b)

Figure 144 - Comparison of the impact overall results between (a) the experimental results and (b) the numerical results (suggested model) on a 2.5 mm sintered PI at 143 m/s

Due to the modeling using the element deletion method, it is not relevant to compare the mass or volume of the fragments between the simulation and the experimental case. Another data has therefore been chosen to evaluate the global volume of fragments: the diameter of the channel at the rear of the target created by the formation of the cup cone of fragmentation [17] (Figure 145.a). The measurement of the diameter is performed after the reassembling of the fragments detached after the passage of the ball (not represented by the simulation) and in each case, the mean value of the diameter of the rear hole of the cup cone [17, 18] is taken (10 measurements for each impacted plate). The same procedure is done for the simulated results. The results are shown in the Figure 146.

(a)

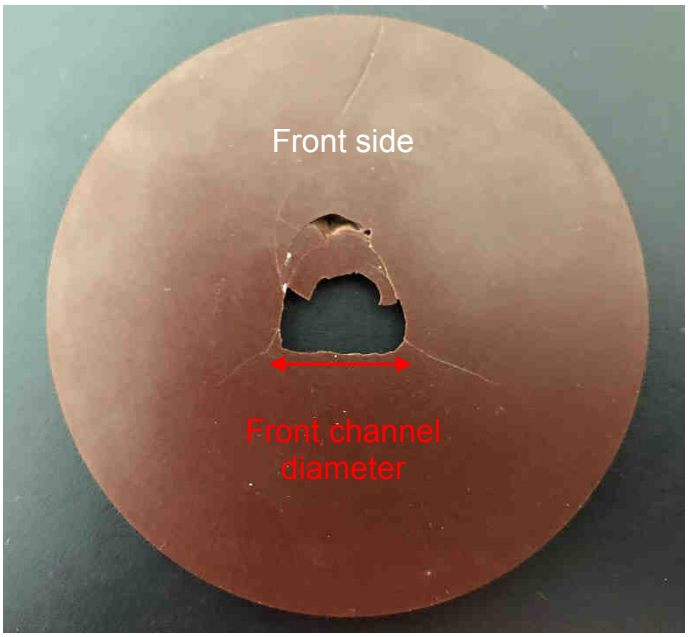

(b)

Figure 145 - Sintered PI plate after impact at 180 m/s (3 mm thick) (a) rear side and (b) front side

Two different behaviors can be observed:

- For the 2.5 mm and 3 mm thick plates, the diameter of the back channel increases exponentially with the decrease of the impact velocity V_0
- For the 2 mm thick target, the diameter of the back channel increases up to around $V_0 = 140\ \mathrm{m/s}$ and then slowly decreases.

It can be seen that the numerical modeling results are closed to the experimental data concerning the rear channel diameter. It can therefore be said that the model efficiently represents the fracture

phenomena during the perforation of the target by the projectile. It reveals a representative modeling of the mechanical behavior of the material. Therefore, the assumption which may explain the detachment of the big fragments after the projectile traveling due to the high sensitivity of the boundary conditions is heightened.

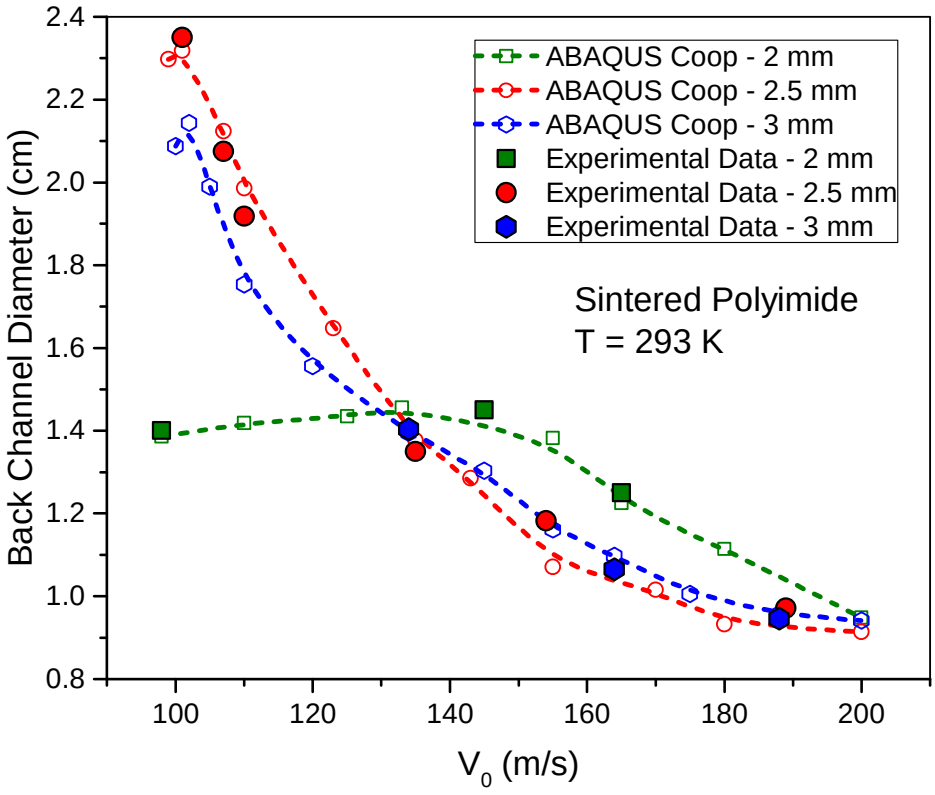

Figure 146 - Evolution of the back channel diameter with the impact velocity V_0 for the different thicknesses tested and the correlation with the numerical model

3. Ballistic performances of the monolayer targets

The impact tests previously presented on the monolayer targets of sintered polyimide and F7020 aluminum alloy have allowed the construction of V_r versus V_0 curves for the different tested thicknesses. However, these curves do not display the ballistic performance regarding the increase of the areal density A_d with the thickness.

For this purpose, a simple reasoning considering the variation of kinetic energy of the projectile before and after the perforation of the target is applied and then normalized with the kinetic energy before the

impact. The value obtained is then divided by the value of the areal density A_d (see Table 39) and corresponds to the ballistic performance P_B (Eq 4.6).

$$P_B = \frac{\frac{0.5m_p(V_0^2 - V_r^2)}{0.5m_p V_0^2}}{A_d} = \frac{V_0^2 - V_r^2}{A_d V_0^2} \quad (4.6)$$

The value of P_B is therefore dependent on the impact velocity V_0. The results obtained from the simulations using ABAQUS®/Explicit are shown in Figures 147.a and 147.b for both materials. The higher the value of P_B is, the better the ballistic performance becomes.

Table 39 - Value of areal density of the different targets

Material	F7020 – 2 mm	F7020 – 2.5 mm	F7020 – 3 mm	F7020 – 4 mm	PI – 2 mm	PI– 2.5 mm	PI – 3 mm
A_d $(\frac{kg}{m^2})$	5.76	7.2	8.64	11.52	2.76	3.45	4.14

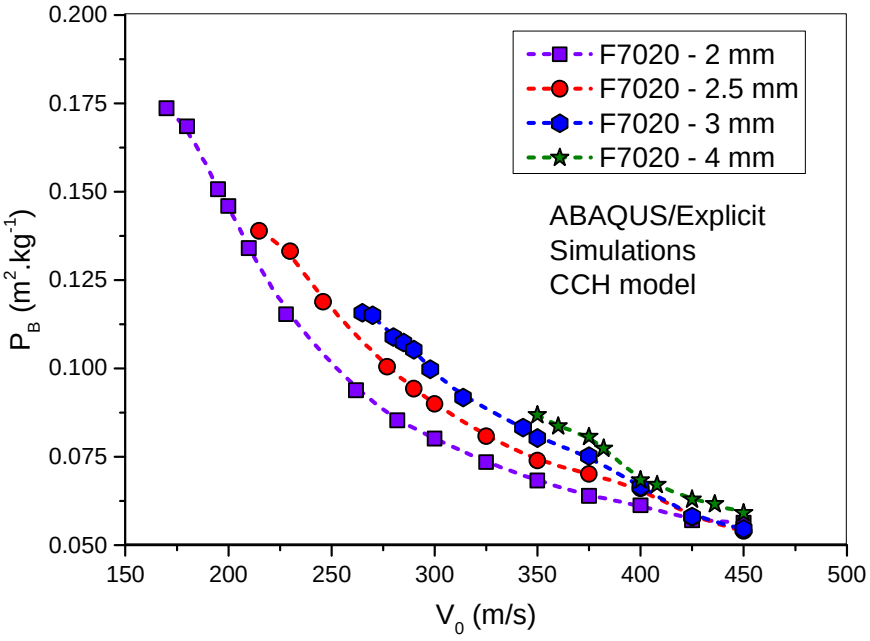

(a)

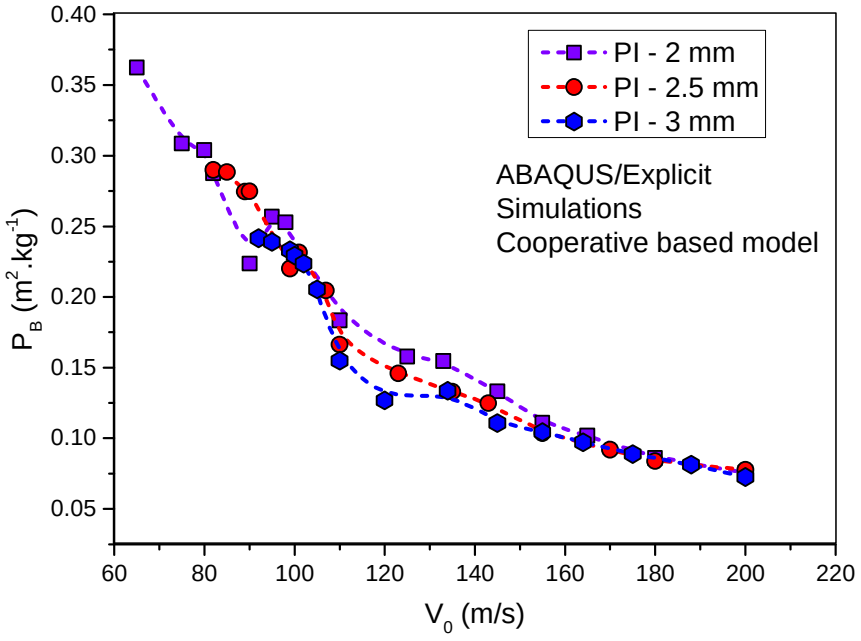

(b)

Figure 147 - Evolution of the ballistic performance P_B with the impact velocity of the projectile V_0 for the (a) F7020 aluminum alloy and (b) sintered polyimide

The Figure 147.a shows that the ballistic performance of the F7020 aluminum alloy increases with the thickness of the target (for a ball impact). This observation can be interpreted by a change in the failure phenomena leading to the failure of the target due an improved stiffness caused by the higher thickness which limits the deflection of the impacted plate. The failure at the rear side of the target is therefore delayed with increasing stiffness and the ballistic performance increases. At higher impact velocities, the value of P_B for the different thicknesses seems to converge to a unique value.

However, the behavior of the ballistic performance of the sintered polyimide shows a very different trend (see Figure 147.b). Indeed, it can be seen that the value of P_B decreases with increasing target thickness. This phenomenon can be observed above 110 m/s. Below this impact velocity, the brittle response of the sintered polyimide under such impact loadings leads to a transition regime of P_B which is difficult to interpret. However, above 110 m/s, it can be clearly seen that the 3 mm thick target has a worse ballistic performance than the two other tested thicknesses. This particular behavior can be caused by the fact that the mass increase brought by the higher thickness is not compensated by the improved stiffness of the target. Therefore, the ballistic performance decreases over this range of thickness. It can be noted that the behavior of the different thicknesses converge to a unique value above $V_0 \approx 180$ m/s. Besides, at 200 m/s, the value of P_B for the sintered PI is around 0.07 and for the F7020 aluminum alloy around 0.15. It can therefore be said that the F7020 is about twice more performant than the sintered polyimide in case of ball impacts at the tested velocities.

D. Application to numerical modeling of multilayer targets

After the validation of the numerical modeling of the two main materials in impact conditions (F7020 aluminum alloy and sintered polyimide), the numerical model of the multilayer material can be performed. This modeling allows to identify the evolution of the residual velocity of the projectile with its impact velocity for different configurations of layers and to identify the structural phenomena leading to the failure of the impacted target.

Unfortunately, some difficulties in material manufacturing and provifing did not allow experimental tests of high velocity impacts on the bilayer composites. Therefore, only the numerical parametric study of different configurations of multilayer composites has been carried out in this work.

1. Numerical simulation setup

The simulation setup used from the monolayer targets has been slightly modified for multilayer materials impact experiments. The modification has been performed on the target design which has become a three layer material with different configuration setups (Figure 148):

- A F7020 aluminum alloy layer with the mechanical properties used for this material in the simulations of the monolayer material (and the associated VUMAT). Its thickness can be 2 mm, 2.5 mm or 3 mm.
- A sintered polyimide layer with the mechanical properties used for this material in the simulations of the monolayer material (and the associated VUMAT). Its thickness can be 2 mm, 2.5 mm or 3 mm (as for the F7020 aluminum alloy layer).
- An epoxy resin layer of 0.5 mm with the mechanical properties used for this material and determined during this work as well as the associated VUMAT.

A tie condition is intrinsically assumed between each layer (F7020/epoxy resin and epoxy resin/PI) (Figure 148.a). Any failure in the joint is therefore piloted by the mechanical behavior of the epoxy resin.

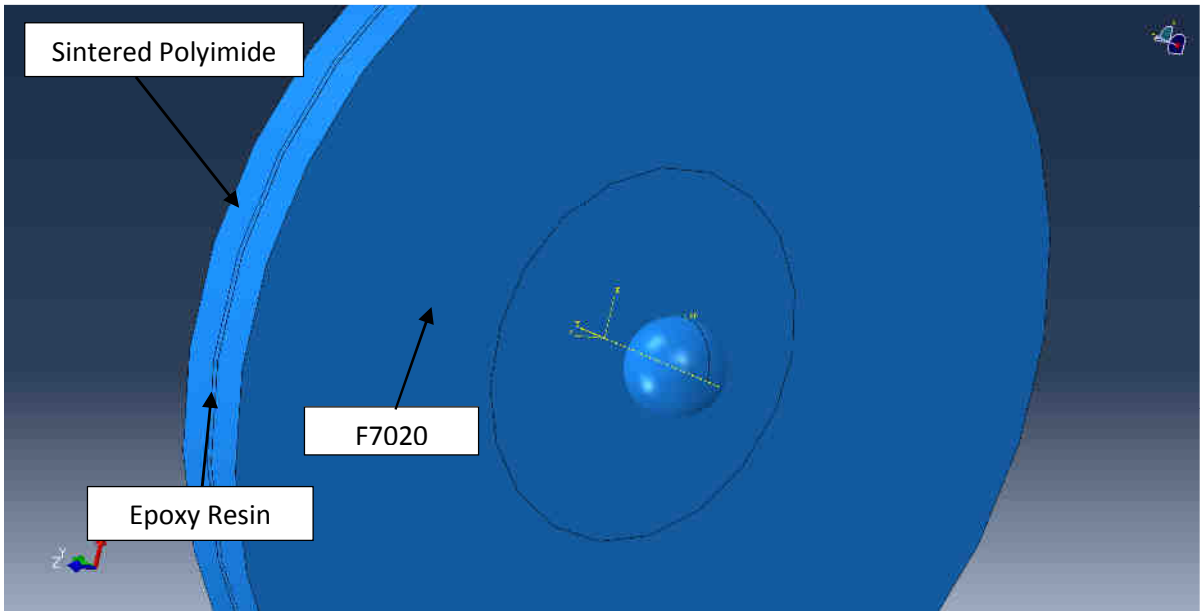

(a)

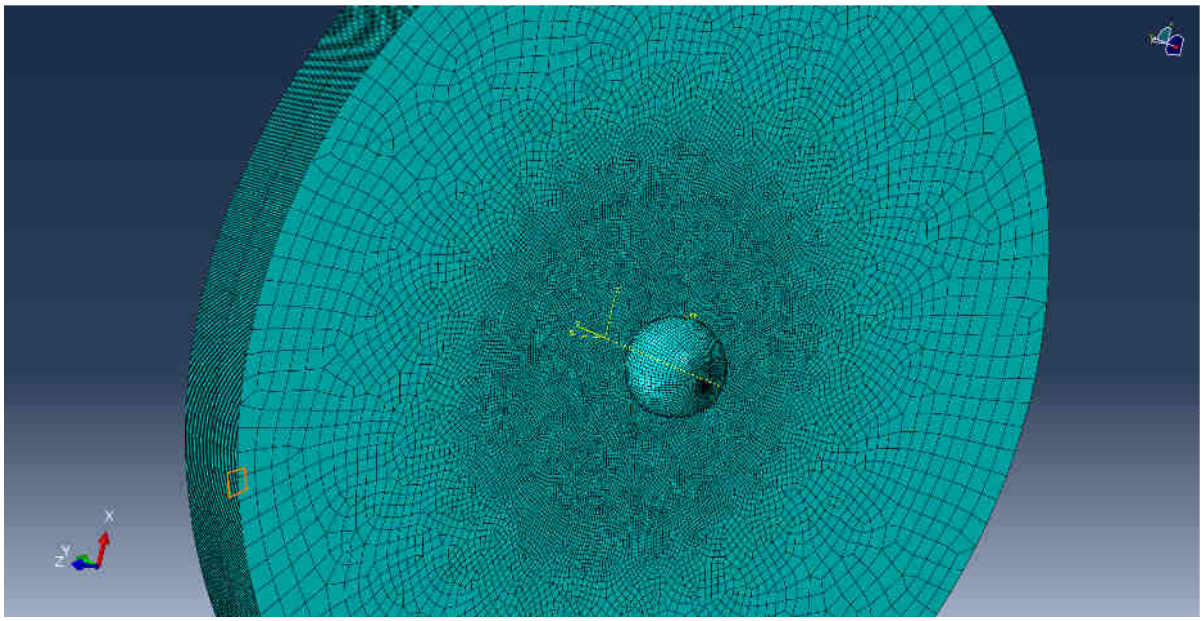

(b)

Figure 148 - Numerical setup used for the multilayer target (a) topologic modeling and (b) mesh

The impacted multilayer material can have different configurations: different combinations of layer thicknesses of F7020 aluminum alloy and sintered polyimide or their relative position (front side or rear side).

It can be noted that ABAQUS does not allow the use of several subroutines at the same time. Therefore, a master subroutine is used. This master subroutine only checks the material defined for each element and then calls the appropriate VUMAT subroutine provided.

A notation system is used: X1_T1/X2_T2 with X1 the material at the impacted side and X2 the material at the rear side (F7020 or PI) and T1 and T2 their respective thicknesses. The thickness of epoxy resin is always 0.5 mm and is located between X1 and X2.

2. Numerical modeling according to different multilayer configurations

a. Bilayer configurations

The bilayer configurations consist into a layer of F7020 aluminum alloy and a layer of sintered polyimide stacked together. Several parameters can be adjusted such as the thickness of each layer and the respective position in the target (rear or front sides). The following work presents the ballistic response of such bilayer materials over a wide range of impact velocities (from ballistic limit velocity to 400 m/s).

i. Front side – F7020 aluminum alloy

The thickness of the complete composite target is 5.5 mm for all simulated configurations (including the epoxy resin layer). In these cases, the F7020 aluminum alloy is set on the impacted front side of the target. The typical behavior of such target under ball impact loading can be observed on the Figure 149. Large polymer fragments are ripped of the rear side of the target and small aluminum fragments also propelled.

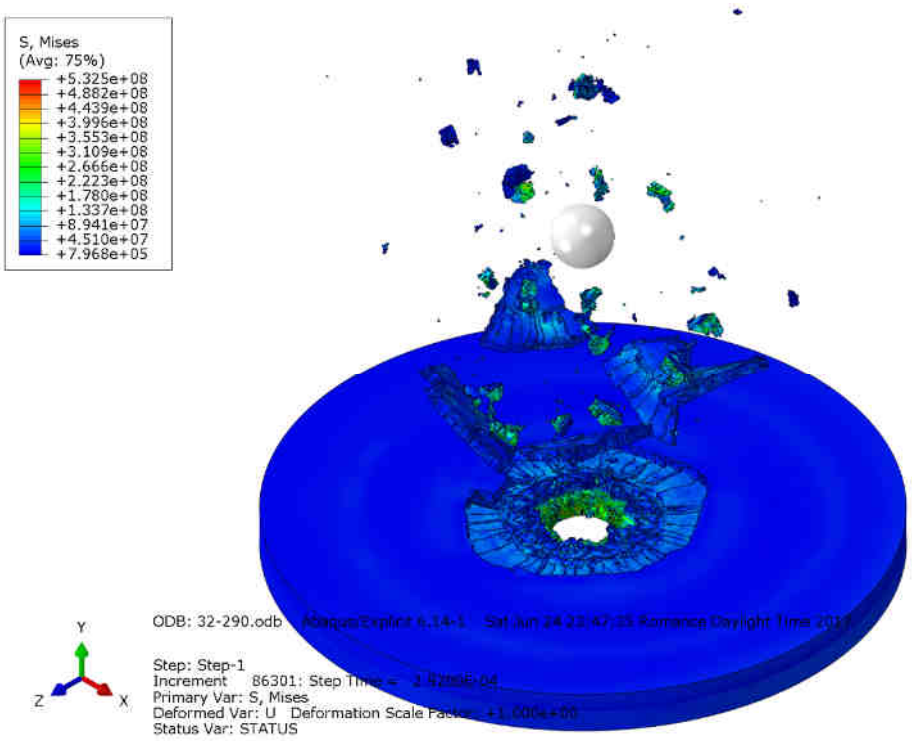

Figure 149 - Typical behavior of F7020_X/PI_Y bilayer targets (in this case F7020_3/PI_2 impacted at 290 m/s)

In order to compare the influence of the material volume ratio on the mechanical behavior of the bilayer target composite (F7020 at the front side), simulation cross sections of each studied case (F7020_2/PI_3, F7020_2.5/PI_2.5 and F7020_3/PI_2) are observed to identify the different phenomena occurring during the perforation (Figure 150). In each case, the impact velocity of the steel ball projectile is 300 m/s and the shown data corresponds to the normalized Mises stress.

F7020_2/PI_3

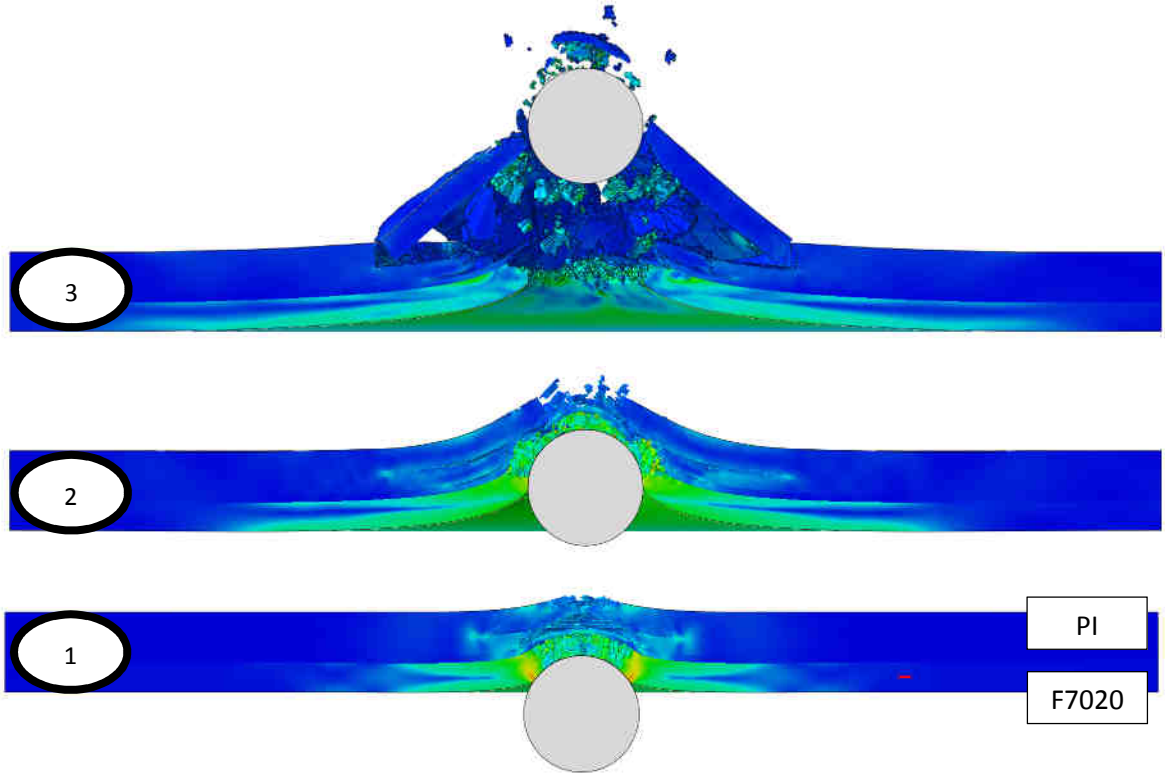

(a)

F7020_2.5/PI_2.5

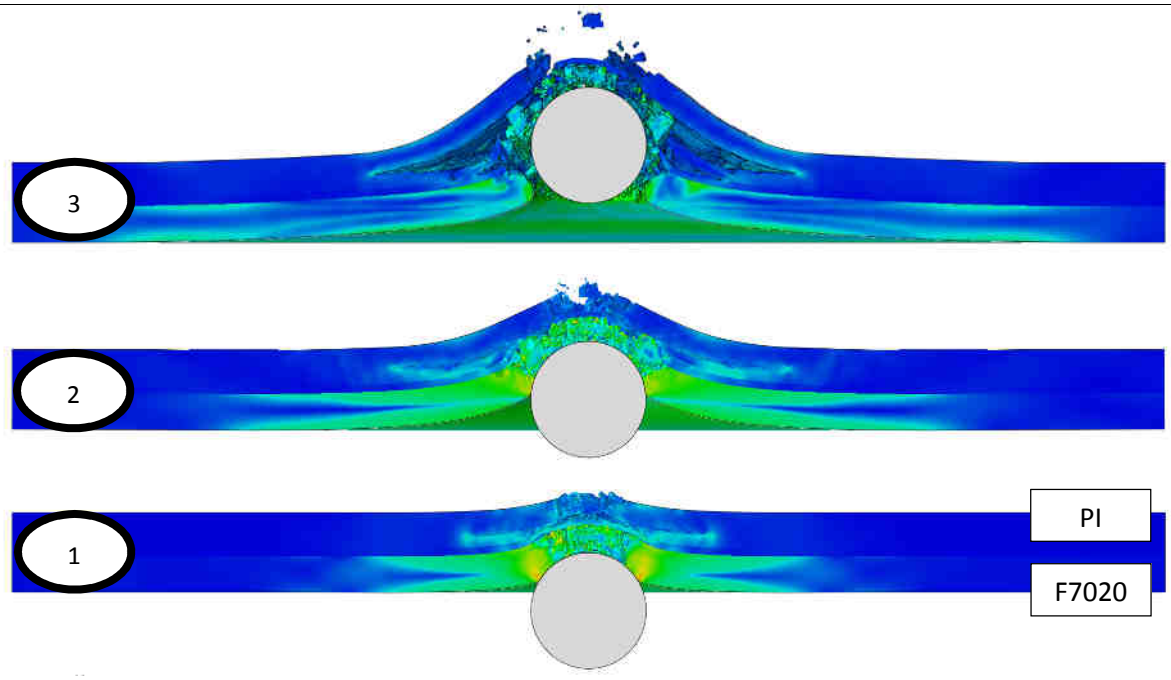

(b)

F7020_3/PI_2

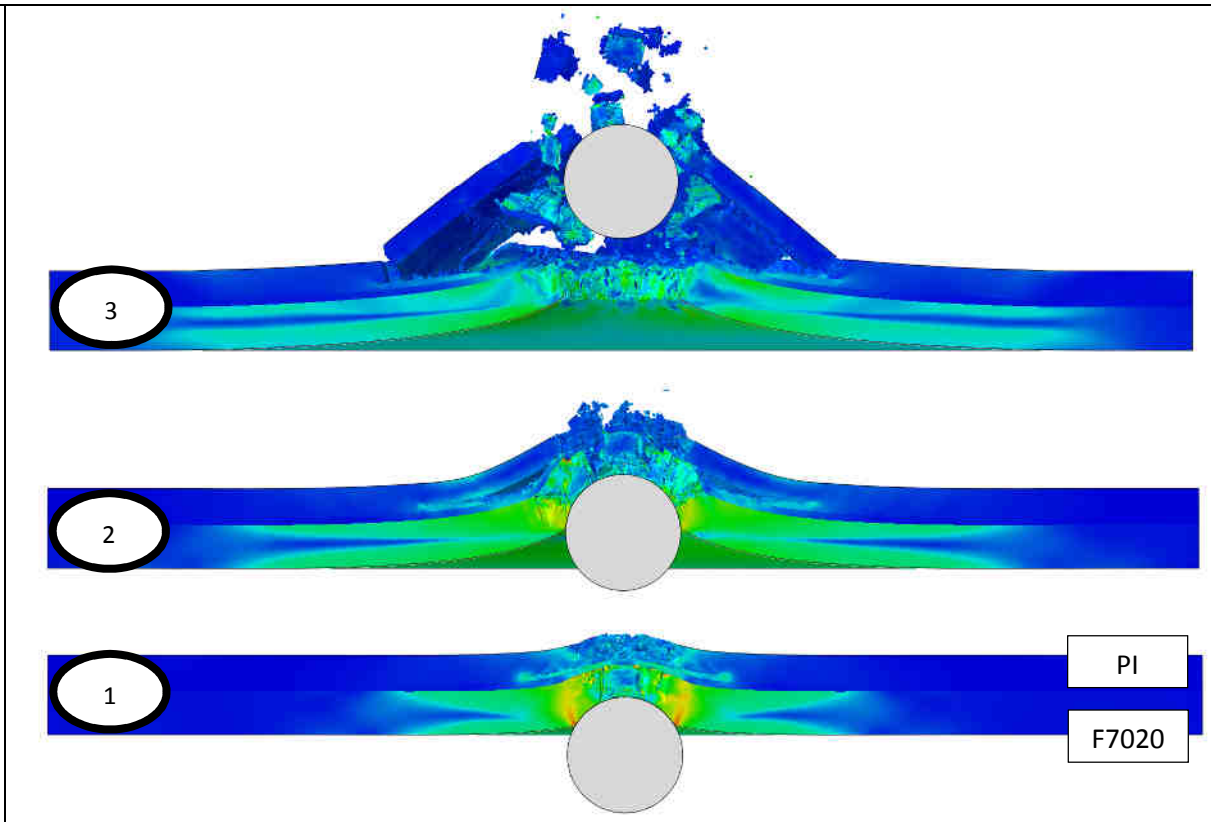

(c)

Figure 150 - Evolution of the simulated perforations by a steel ball projectile at 300 m/s of (a) F7020_2/PI_3, (b) F7020_2.5/PI_2.5 and (c) F7020_3/PI_2 bilayer targets

On the Figure 150, one can see the different steps of perforation of the different F7020_X/PI_Y bilayer composite targets. For each target configuration, the perforation is shown at three different states, the order being from bottom to top. For each case, the behavior of the target consists into a relatively ductile perforation of the impacted F7020 layer. The metallic layer is fragmented for the all cases but larger fragments are created for the configuration using the thickest F7020 layer (Figure 150.c). The deflection of the F7020 layer leads to the premature failure of the sintered polyimide rear layer even before the projectile becomes in contact with it. Then, the advancement of the projectile activates a delamination phenomenon of the sintered polyimide with the epoxy resin. This is due to the high elastic strain range of the polymer which allows a high deformation of the polyimide before the failure of the delaminated sections as it can be seen for all the presented configurations. Large fragments of sintered polyimide are then propelled with small fragments of F7020 aluminum alloys (except for Figure 150.c due to the thickness of the metallic layer).

The impact velocity versus residual velocity curves for each configuration are displayed on Figure 151.a. It can be seen that the mechanical response of the target under the impact loading decreases with the amount of sintered polyimide. Indeed, the relatively high mechanical resistance of the polymer layer prevents the metallic layer from deforming as in the monolayer case. Therefore, the projectile is

decelerated over a smaller distance than if the metallic layer was used alone. The area of interest of the sintered polyimide layer being already highly damaged, the impact of this last on the deceleration of the projectile during its perforation is negligible. This explains the lower ballistic performance of the different bilayer composite targets than the monolithic F7020_3 case (see Figure 151.b). Besides, it can be observed that the values of P_B do not evolve a lot with the volume ratio of sintered polyimide (40%, 50% and 60%) and stay close to the one of the polymer monolayer case.

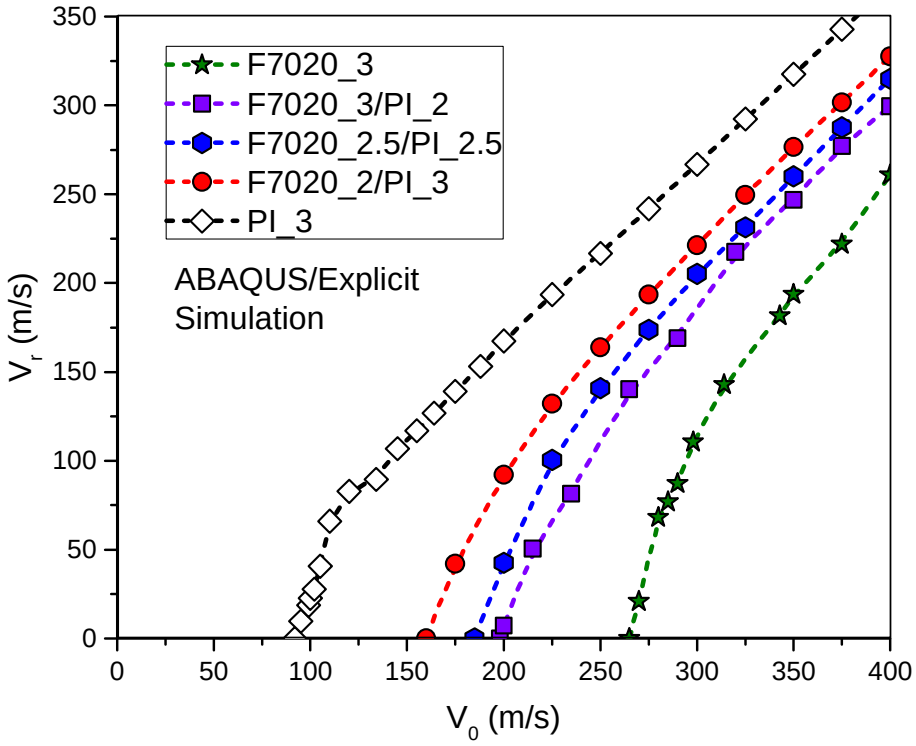

(a)

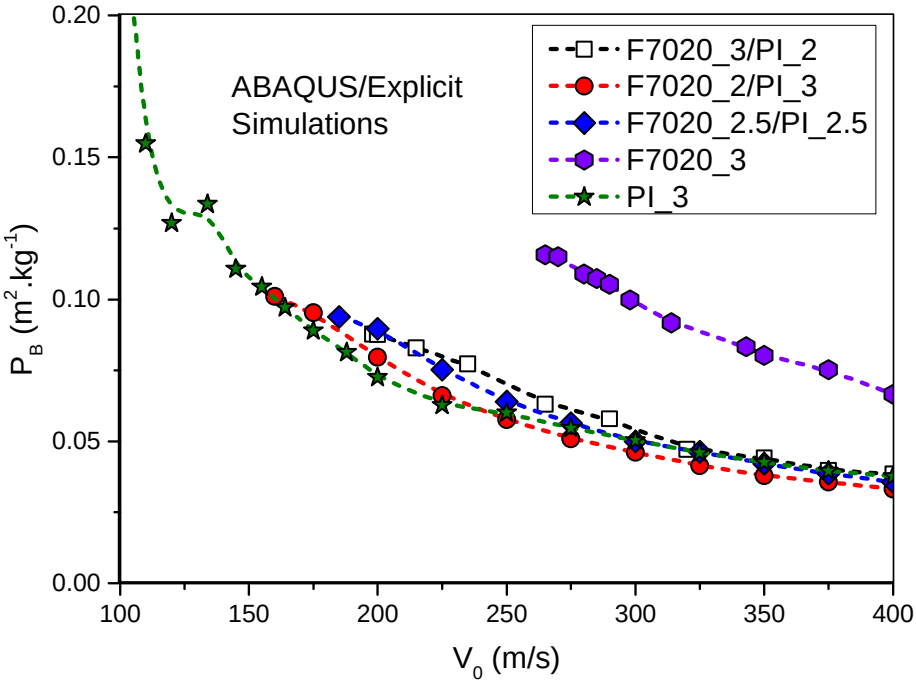

(b)

Figure 151 - Evolution of (a) the simulated residual velocity of the projectile and (b) of the ballistic performance with the impact velocity for the different F7020_X/PI_Y chosen composite target configurations

ii. Front side – Sintered polyimide

The thickness of the complete composite target is 5.5 mm for all simulated configurations (including the epoxy resin layer). In these cases, the sintered polyimide is set on the impacted front side of the target. The typical behavior of such target under ball impact loading can be observed on the Figure 152. The only fragments observed come from the brittle petals which have been ripped off the F7020 aluminum alloy at the rear side of the target. Hardly no sintered polyimide fragments from the target front side are observed through the simulations.

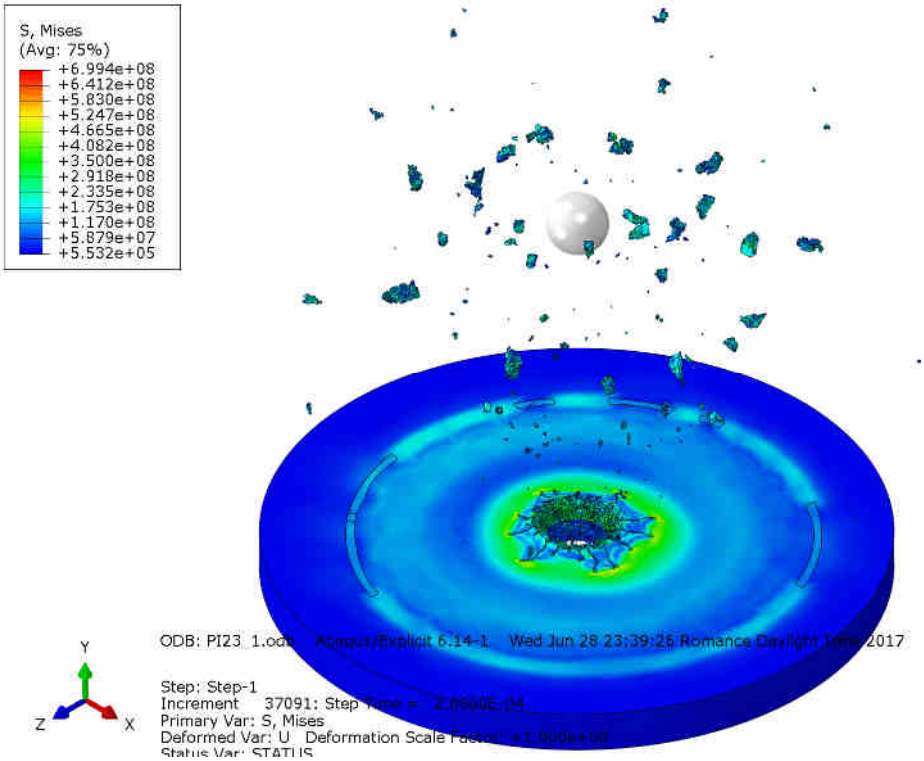

Figure 152 - Typical behavior of PI_X/F7020_Y bilayer targets (in this case PI_2/F7020_3 impacted at 375 m/s)

PI_2/F7020_3	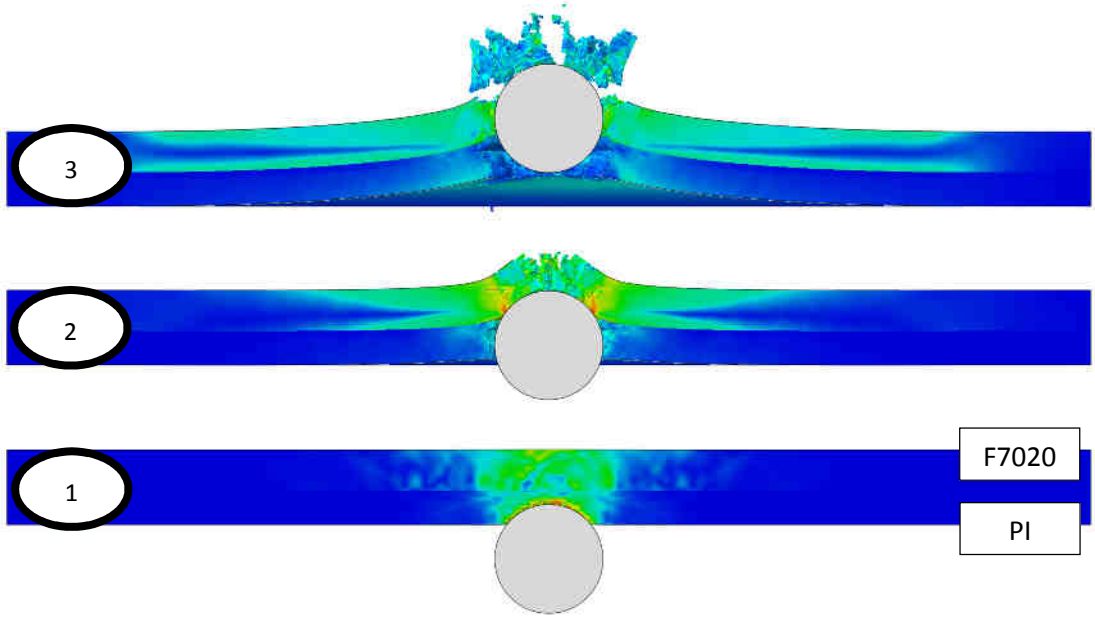

(a)

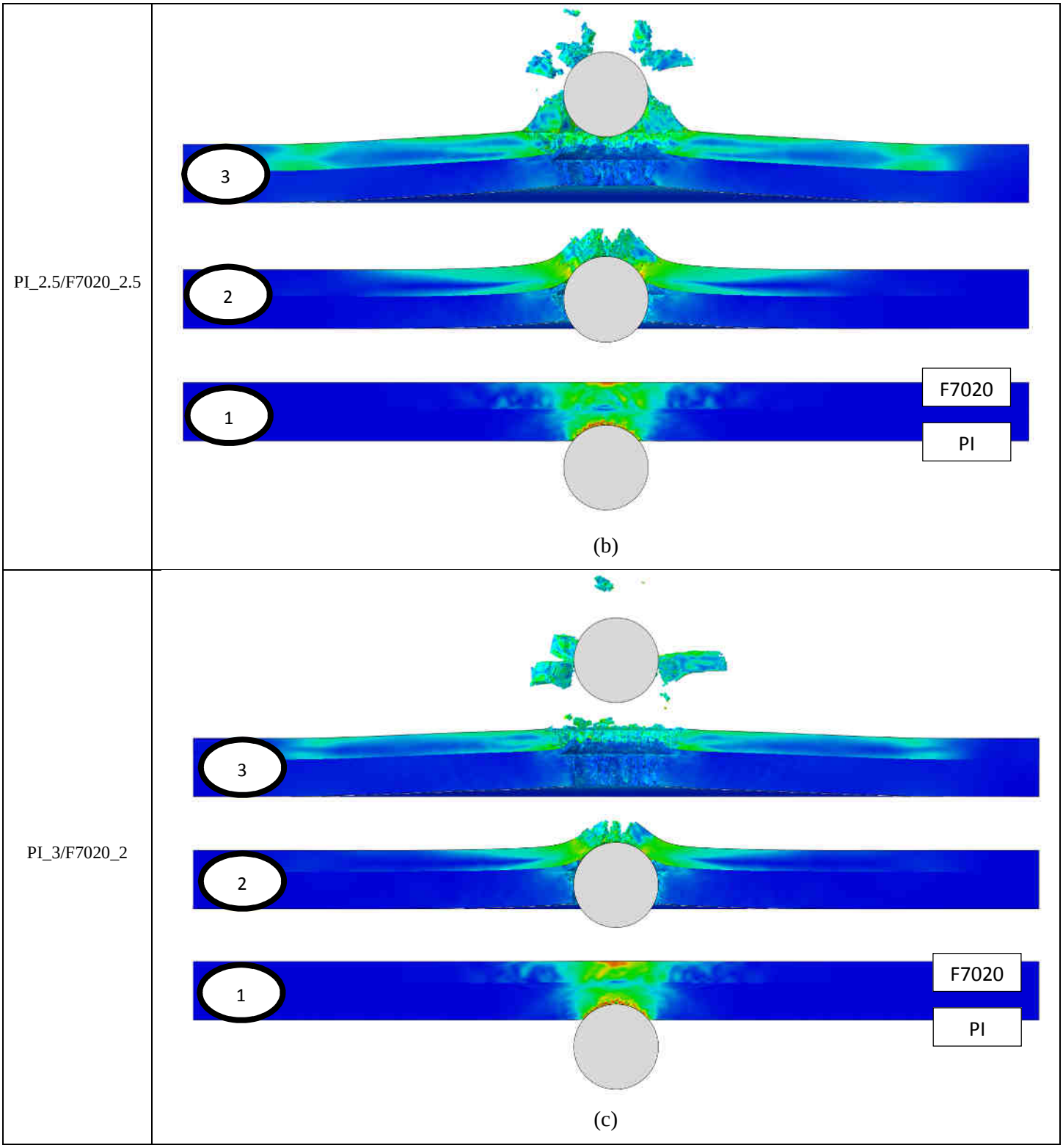

Figure 153 - Evolution of the simulated perforations by a steel ball projectile at 300 m/s of (a) PI_2/F7020_3, (b) PI_2.5/F7020_2.5 and (c) PI_3/F7020_2 bilayer targets

In order to compare the influence of the material volume ratio on the mechanical behavior of the bilayer target composite (sintered polyimide at the front side), simulation cross sections of each studied cases (PI_2/F7020_3, PI_2.5/F7020_2.5 and PI_3/F7020_2) are observed to identify the different phenomena

occurring during the perforation (Figure 153). In each case, the impact velocity of the steel ball projectile is 300 m/s and the shown data corresponds to the normalized Mises stress.

On the Figure 153, one can see the different steps of perforation of the different PI_X/F702_Y bilayer composite targets. For each target configuration, the perforation is shown at three different states, the order being from bottom to top. The mechanisms of perforation of the sintered polyimide layer is similar for the three simulated configurations. Indeed, the high brittleness of the material leads to an important erosion of the element composing the polymer front layer. The deceleration of the projectile caused by this layer is not very significant due to the relatively high impact velocity. Meanwhile, the deflection of the rear F7020 aluminum alloy is negligible and begins only when the projectile comes in contact. The mechanisms of failure of the rear layer starts and is slightly different for each case. Indeed, the thicker the layer is, the more the damaged zone becomes “narrow” (Figure 153.a) and the number of fragments increases. Indeed, the last steps of perforation displayed for the each case show different behavior, from few propelled fragments (Figure 34.c) up to a dozen of ripped off petals (Figure 153.a). The Figure 153.b consists into an intermediate state between the two others studied in this work.

The impact velocity versus residual velocity curves for each configuration are displayed on Figure 154.a. Like the cases involving the F7020 front side layer, it can be seen that the mechanical response of the target under the impact loading decreases with the amount of sintered polyimide. However, this trends is due to a different reason. Indeed, for the configurations involving the sintered polyimide layer at the impacted side, this last cannot slow down significantly the projectile for such impact velocities and therefore, its influence is negligible. For instance, at $V_0 = 300\ \mathrm{m/s}$, the residual velocity of the projectile in the case of PI_3 is $V_r = 267\ \mathrm{m/s}$ which is around 60% more than the V_{bl} of the 2 mm thick F7020 rear layer. Besides, the presence of the rear metallic layer prevents any deflection of the polymer layer, reducing even more its performance. This explains the lower ballistic performance of the different bilayer composite targets than the monolithic F7020_3 case (see Figure 154.b). Besides, it can be observed that the values of P_B do not evolve a lot with the volume ratio of sintered polyimide (40%, 50% and 60%) and stay close to the one of the polymer monolayer case. The PI_3/F7020_2 configuration is even significantly less efficient than the PI_3 monolayer target. It can also be noted that the ballistic performances of the PI_X/F7020_Y configurations are slightly lower than the F7020_X/PI_Y configurations.

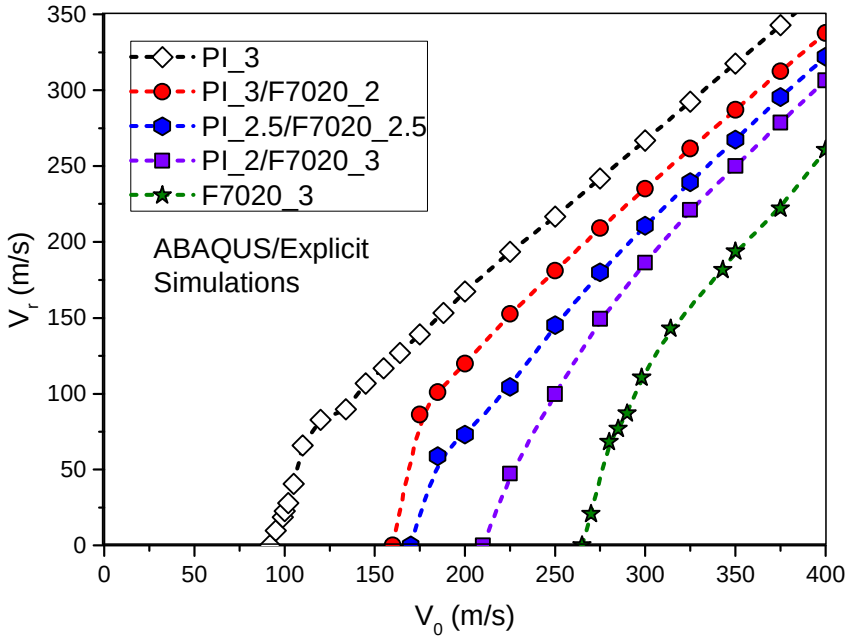

(a)

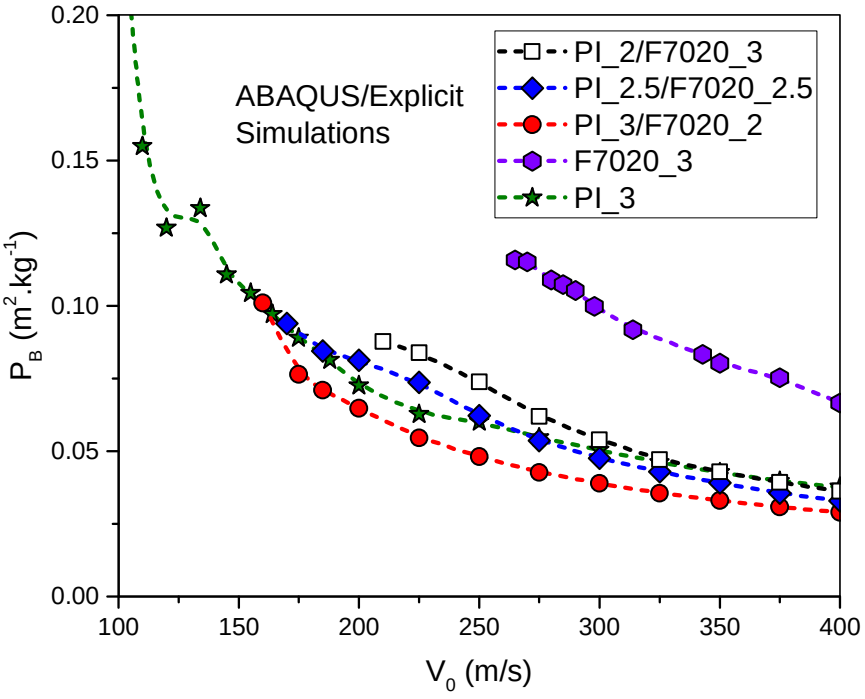

(b)

Figure 154 - Evolution of (a) the simulated residual velocity of the projectile and (b) of the ballistic performance with the impact velocity for the different PI_X/F7020_Y chosen composite target configurations

iii. Variation of the overall thickness (ratio F7020/PI =1)

After the study of the influence of the impacted material, the influence of the overall thickness of the bilayer target is studied through ABAQUS®/Explicit simulation. In this study, the same layer thicknesses for the two materials are considered. In addition to the F7020_2.5/PI_2.5 and PI_2.5/F7020_2.5 cases already studied in the previous sections, the results for four other configurations are shown here: PI_2/F7020_2, F7020_2/PI_2, PI_3/F7020_3 and F7020_3/PI_3.

In order to compare the influence of the overall thickness on the mechanical behavior of the bilayer target composite, simulation cross sections of each studied case (PI_2/F7020_2, F7020_2/PI_2, PI_3/F7020_3 and F7020_3/PI_3) are observed to identify the different phenomena occurring during the perforation (Figure 155). In each case, the impact velocity of the steel ball projectile is 300 m/s and the shown data corresponds to the normalized Mises stress.

PI_2/F7020_2	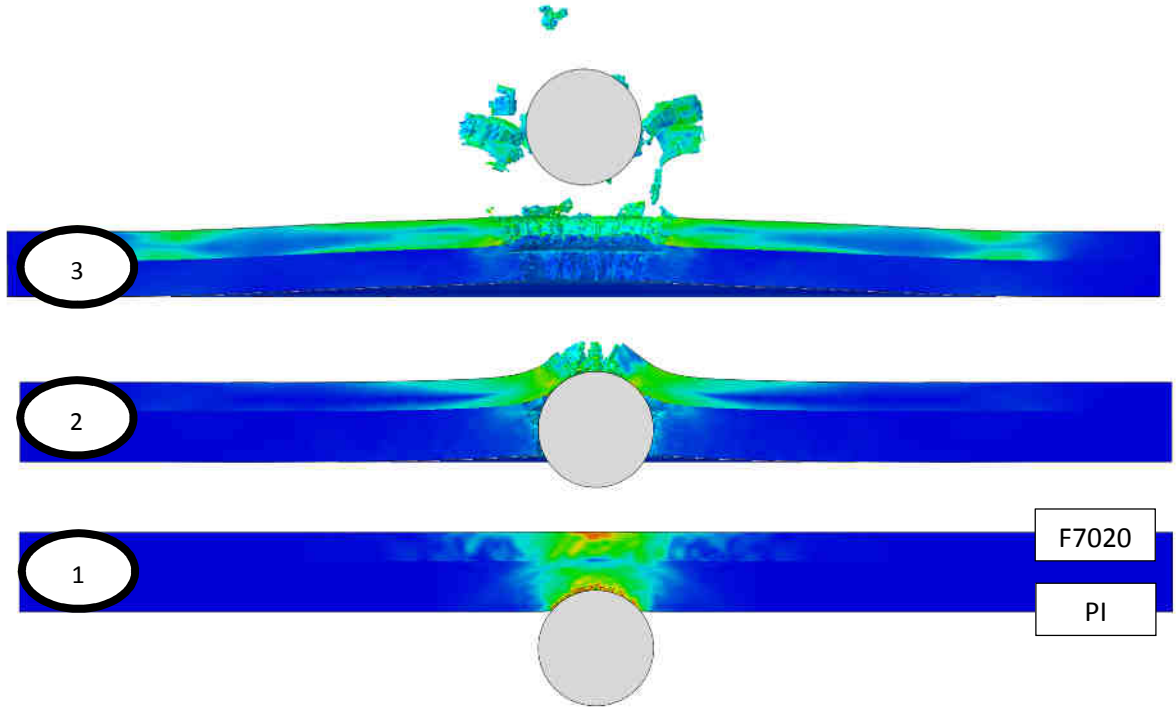 (a)
F7020_2/PI_2	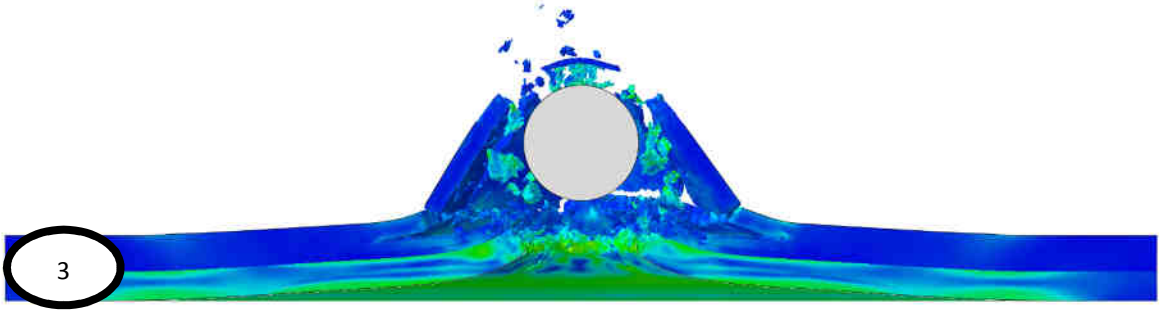

	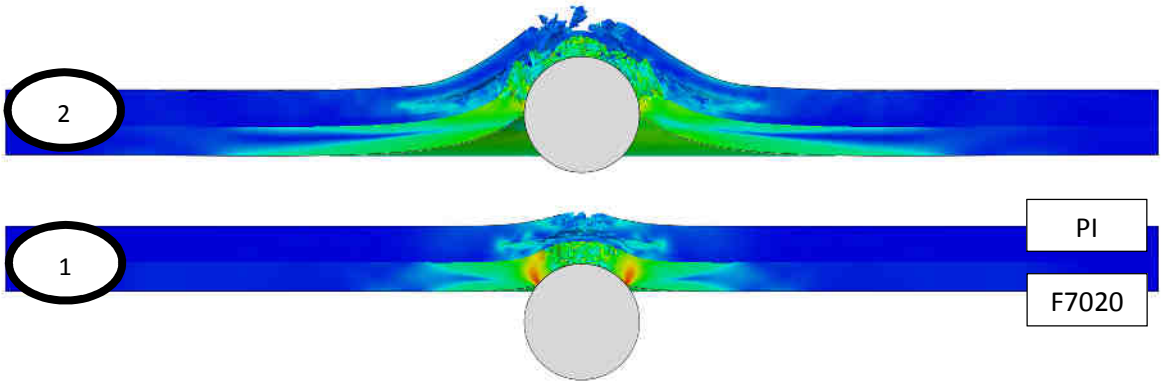 (b)
PI_3/F7020_3	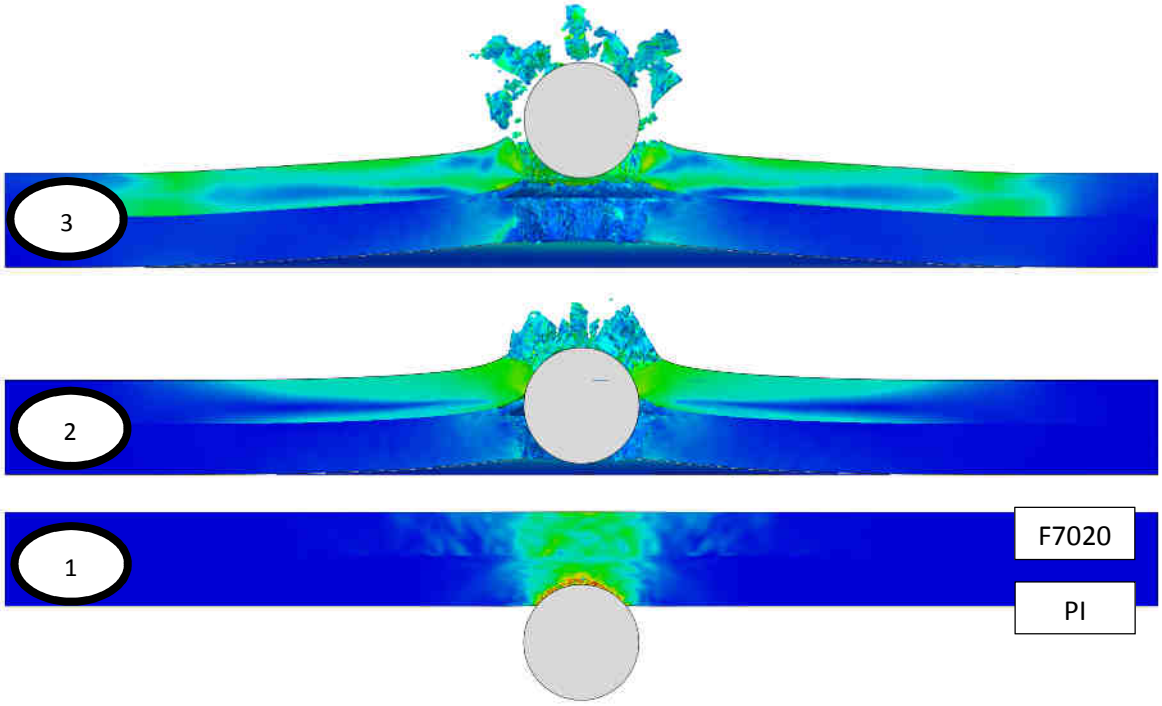 (c)
F7020_3/PI_3	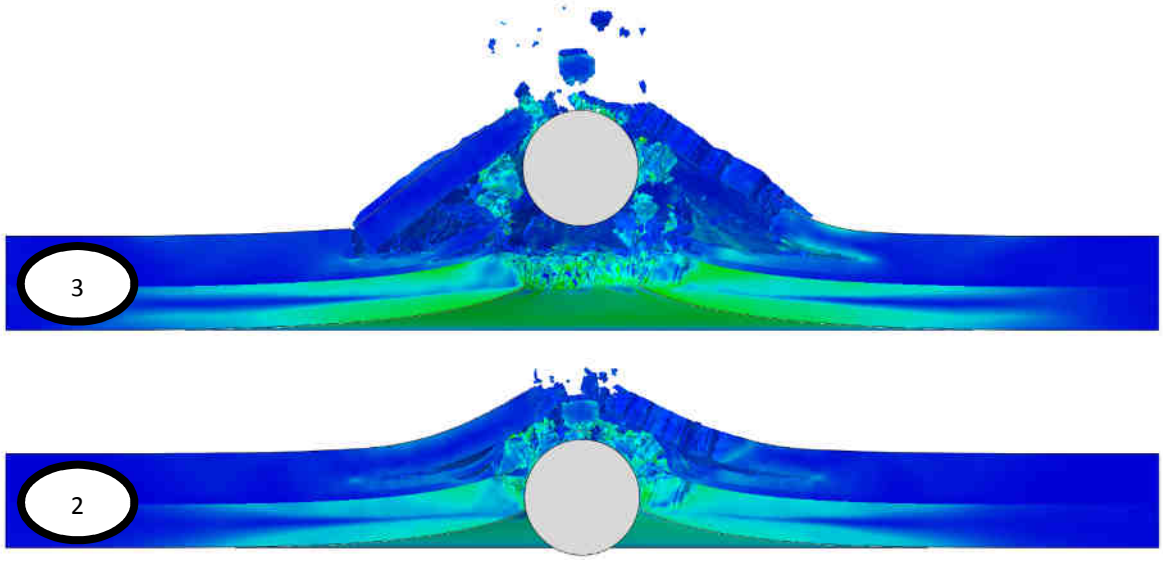

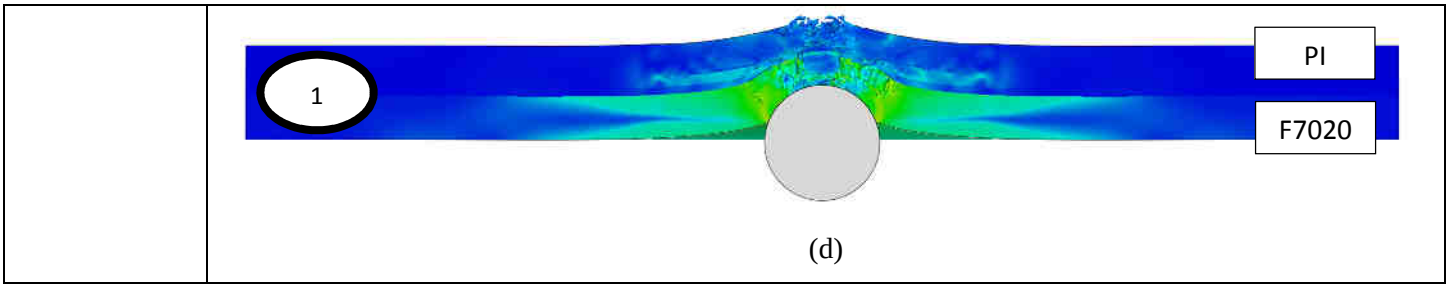

Figure 155 - Evolution of the simulated perforations by a steel ball projectile at 300 m/s of (a) PI_2/F7020_2, (b) F7020_2/PI_2, (c) PI_3/F7020_3 and (d) F7020_3/PI_3 bilayer targets

The comparison of the perforation mechanisms between the configurations PI_2/F7020_2 (Figure 155.a) and PI_3/F7020_3 (Figure 155.c) reveals a phenomenon which has been observed in the previous section: the thicker the F7020 aluminum alloy rear layer is, the higher the fragmentation phenomenon of this last becomes. The PI_2.5/F7020_2.5 configuration (Figure 153.b) can also be observed as an intermediate state.

Concerning the F7020_2/PI_2 (Figure 155.b) and F7020_3/PI_3 (Figure 155.d), the same perforation phenomena than for the F7020_X/PI_Y (Figure 150) are observed. However, a clear difference between the different configurations can be observed (including the F7020_2.5/PI_2.5 case): the increase of the fragmentation cup cone diameter of the sintered polyimide rear layer with the overall thickness of the target. This is due to the coupled increase of the metallic front layer thickness for which the deflection zone is wider for the thickest case (Figure 155.d).

The difference of mechanical response between the PI_X/F_7020_X and F7020_X/PI_X bilayer targets can be seen on the Figure 156.a. For each overall thickness, the one with the F7020 aluminum alloy layer as front layer presents slightly better performance. It can also be noted that the gap of performance between the two configurations decreases with increasing overall thickness (it nearly disappears between F7020_3/PI_3 and PI_3/F7020_3). However, the ballistic performance P_B of all the studied cases stays lower than the one of the monolithic F7020_3 case due to the different characteristic structural phenomena discussed in the previous sections. Indeed, as soon as, a sintered polyimide layer is involved, the value of P_B becomes close to the one of PI_3 alone (Figure 156.b).

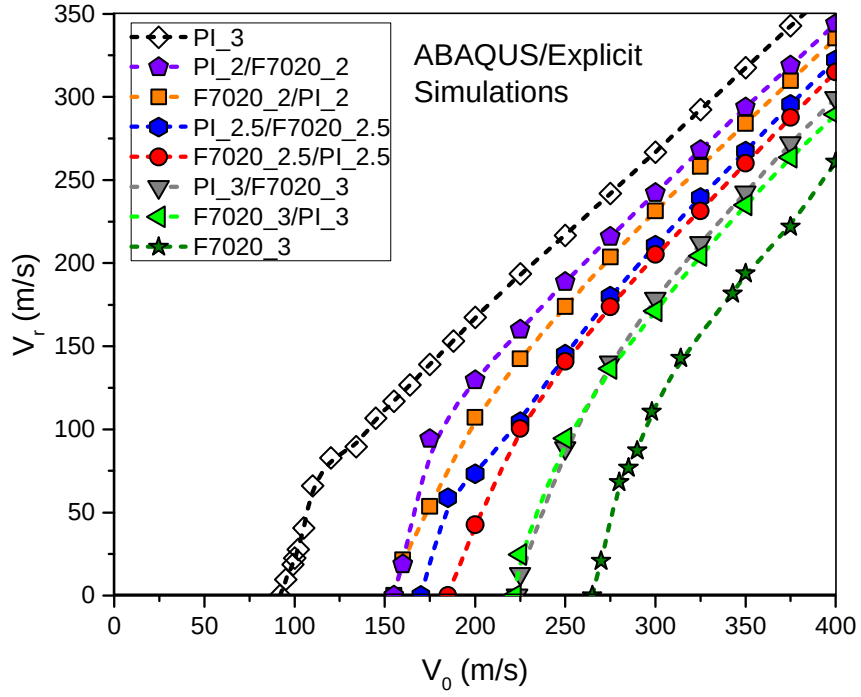

(a)

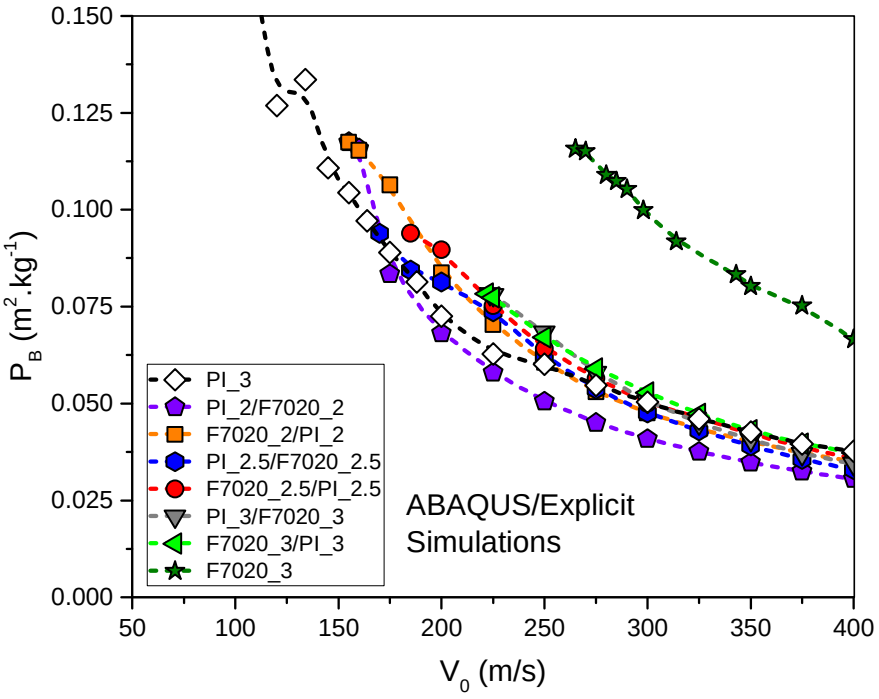

(b)

Figure 156 - Evolution of (a) the simulated residual velocity of the projectile and (b) of the ballistic performance with the impact velocity for the different considered composite target configurations

E.CONCLUSION OF THE CHAPTER

In this chapter, the analytical constitutive model expressions developed in the previous section of the manuscript have been implemented in the form of VUMAT subroutine in FORTRAN code for ABAQUS®/Explicit. The validations of the individual model (sintered polyimide and F7020 aluminum alloy) have been carried out through high velocity impact experiments of steel ball projectile on single layer targets up to around 450 m/s.

The CCH model has been confronted to the well-known Johnson-Cook model (and its associated failure model). The simulation results have revealed a better correlation with the experimental results of the CCH model than the JC model concerning the evaluation of the residual velocity of the projectile and the plug velocity according to the impact velocity. The validation has been performed over a wide range of impact velocities (from 250 m/s to 450 m/s) and thicknesses (for 2 mm, 2.5 mm, 3 mm and 4 mm).The suggested model also shows a much better ability to model the fragmentation of the F7020 aluminum alloy targets under such impact loadings. A normalized absorbed kinematic energy criterion taking into account the areal density of the targets has been used to compare the ballistic performance for different thicknesses. It allows to see that the resistance of the F7020 aluminum targets to the impact increase with its thickness.

Concerning the impact on the sintered polyimide targets, the model suggested in this work has been successfully validated in the same conditions as for the F7020 aluminum alloy (from 90 m/s to 200 m/s and for 2 mm, 2.5 mm and 3 mm thick targets). The fragmentation phenomenon of the highly brittle polymer is nicely modeled and the low sensitivity of the residual velocity of the projectile with the increase of the target thickness is well represented. It has been shown that the ballistic performance of the sintered polyimide decreases slightly with increasing thickness. This means that the increase of material stiffness is not enough to compensate its increase in areal density.

The validation of the numerical of each individual constitutive model has led to the construction of the numerical model of different configurations of bilayer materials. The two involved main layers consists into the sintered polyimide and the F7020 aluminum alloy. These two materials are assembled using the epoxy resin. Unfortunately, some difficulties in material manufacturing and providing did not allow experimental tests of high velocity impacts on the bilayer composites. Therefore, only the parametric study of different configurations of multilayer composites has been carried out in this work. The attention has therefore be centered on the numerical modeling of such composite through a parametric numerical study. Three parameters have been modified on the bilayer materials: the material in front side, the volume ratio of each material and the overall thickness of the target. In order, to compare the numerical results between materials presenting different areal density, the criterion to evaluate the

ballistic performance of the different configurations has been used. This method allows to see that all bilayer materials have a ballistic performance close to the one of the sintered polyimide alone which is below the one of the monolithic F7020 targets. Such behavior can be explained by the fact that the sintered polyimide layer is far too brittle to rise its ballistic performance with increasing thickness. Indeed, in front layer, the impact velocities are far too high for such material and its deflection is completely prevented by the F7020 rear layer thus limiting greatly its influence on the projectile. As rear layer, the sintered polyimide is rapidly fragmented by the deflection of the F7020 front layer and its influence on the projectile during its preformation becomes negligible. Moreover, the presence of the sintered polyimide as rear layer prevents partially the deflection of the F7020 front layer. The ballistic performance of the overall bilayer composite becomes therefore lower than the one of the monolayer F7020_3 targets. It can also be noted that ballistic performances of the target presenting the F7020 aluminum alloy in front layer are slightly better.

As it has be shown in this chapter, the high brittleness of the sintered polyimide is the main drawback of the studied multilayer composite. The increase of the ductility of the sintered polyimide by delaying the intergranular the failure between the powder grains would be an interesting way of improvement of such material. The simulation and experimental validation with three or more layers is also an interesting aspect of investigation toward the development of such advanced multilayer materials for protection.

References

1. Børvik, T., O.S. Hopperstad, and K.O. Pedersen, *Quasi-brittle fracture during structural impact of AA7075-T651 aluminium plates.* International Journal of Impact Engineering, 2010. **37**(5): p. 537-551.
2. Demir, T., M. Übeyli, and R.O. Yıldırım, *Investigation on the ballistic impact behavior of various alloys against 7.62 mm armor piercing projectile.* Materials & Design, 2008. **29**(10): p. 2009-2016.
3. Holmen, J., et al., *Effects of heat treatment on the ballistic properties of AA6070 aluminium alloy.* International Journal of Impact Engineering, 2013. **57**: p. 119-133.
4. Goldsmith, W., *Impact*2001: Courier Corporation.
5. Fras, T., et al., *Thick AA7020-T651 plates under ballistic impact of fragment-simulating projectiles.* International Journal of Impact Engineering, 2015. **86**: p. 336-353.
6. Fras, T., L. Colard, and P. Pawlowski, *Perforation of aluminum plates by fragment simulating projectiles (FSP).* The International Journal of Multiphysics, 2016. **9**(3).
7. Rosenberg, Z. and E. Dekel, *Terminal ballistics* 2016: Springer.
8. Awerbuch, J. and S. Bodner, *Analysis of the mechanics of perforation of projectiles in metallic plates.* International Journal of Solids and Structures, 1974. **10**(6): p. 671-684.
9. Francart, C., et al., *Application of the Crystallo-Calorific Hardening approach to the constitutive modeling of the dynamic yield behavior of various metals with different crystalline structures.* International Journal of Impact Engineering, 2017.
10. Johnson, G.R. and W.H. Cook. *A constitutive model and data for metals subjected to large strains, high strain rates and high temperatures*. in *Proceedings of the 7th International Symposium on Ballistics*. 1983. The Netherlands.
11. Meyer, H.W. and D.S. Kleponis, *Modeling the high strain rate behavior of titanium undergoing ballistic impact and penetration.* International Journal of Impact Engineering, 2001. **26**(1): p. 509-521.
12. Anderson, C.E., et al., *Time-resolved penetration of long rods into steel targets.* International Journal of Impact Engineering, 1995. **16**(1): p. 1-18.
13. Follansbee, P. and U. Kocks, *A constitutive description of the deformation of copper based on the use of the mechanical threshold stress as an internal state variable.* Acta Metallurgica, 1988. **36**(1): p. 81-93.
14. Zerilli, F.J. and R.W. Armstrong. *Constitutive relations for the plastic deformation of metals*. in *High-pressure science and technology—1993*. 1994. AIP Publishing.
15. Rusinek, A. and J.R. Klepaczko, *Shear testing of a sheet steel at wide range of strain rates and a constitutive relation with strain-rate and temperature dependence of the flow stress.* International Journal of Plasticity, 2001. **17**(1): p. 87-115.
16. Johnson, G.R. and W.H. Cook, *Fracture characteristics of three metals subjected to various strains, strain rates, temperatures and pressures.* Engineering fracture mechanics, 1985. **21**(1): p. 31-48.
17. Segreti, M., A. Rusinek, and J. Klepaczko, *Experimental study on puncture of PMMA at low and high velocities, effect on the failure mode.* Polymer Testing, 2004. **23**(6): p. 703-718.
18. Hsieh, A.J., et al., *The effects of PMMA on ballistic impact performance of hybrid hard/ductile all-plastic-and glass-plastic-based composites*, 2004, DTIC Document.
19. Mohagheghian, I., G. McShane, and W. Stronge, *Impact perforation of monolithic polyethylene plates: Projectile nose shape dependence.* International Journal of Impact Engineering, 2015. **80**: p. 162-176.
20. Wright, S., N. Fleck, and W. Stronge, *Ballistic impact of polycarbonate—an experimental investigation.* International Journal of Impact Engineering, 1993. **13**(1): p. 1-20.
21. Shah, Q.H., *Impact resistance of a rectangular polycarbonate armor plate subjected to single and multiple impacts.* International Journal of Impact Engineering, 2009. **36**(9): p. 1128-1135.

22. Karger-Kocsis, J. and T. Czigány, *Strain rate dependence of the work of fracture response of an amorphous poly (ethylene-naphthalate)(PEN) film.* Polymer Engineering & Science, 2000. **40**(8): p. 1809-1815.
23. Nielsen, L.E., *Cross-linking–effect on physical properties of polymers.* 1969.
24. Richeton, J., et al., *Influence of temperature and strain rate on the mechanical behavior of three amorphous polymers: Characterization and modeling of the compressive yield stress.* International Journal of Solids and Structures, 2006. **43**(7–8): p. 2318-2335.
25. Richeton, J., et al., *Modeling and validation of the large deformation inelastic response of amorphous polymers over a wide range of temperatures and strain rates.* International Journal of Solids and Structures, 2007. **44**(24): p. 7938-7954.

CONCLUSION

The results and discussions presented in this manuscript are the result of a three years of work at the ISL institute and ICube laboratory. The aim of the study was to develop a numerical model of a polymer/metal multilayer composite designed for lightweight structures submitted to extreme conditions. Both main materials (F7020 aluminum alloy and amorphous thermoplastic polyimide) have been sintered using Spark Plasma Sintering process at the ISL. The different layers of the composite have been assembled using an epoxy resin which has also been mechanically characterized. Impact loading involves generally high strain rates and high temperatures due to adiabatic heating. No occurrence of a numerical modeling involving this kind of materials has been found in the literature and more particularly concerning the dynamic characterization and modeling of a sintered polymer.

The mechanical characterization of the different materials involved in this work (F7020 aluminum alloy, sintered polyimide and epoxy resin) has revealed several different constitutive behaviors until the failure. The sintered materials can be studied over three different scales which are the macroscopic scale (sample size), the mesoscopic scale (powder grains scale) and microscopic-nanoscopic scale (crystal for metals and chains for the polymers).

- The strain mechanisms concerning the studied metal (F7020) are complex due to its particular microstructure which is highly non-linear temperature dependent. Besides, the FCC lattice structure of the dominant aluminum matrix presents different non-linear strain rate sensitivities for its yield stress (effective stress) and its strain hardening (internal stress). Concerning the failure behavior, the observed behavior is very specific to sintered material. Indeed, in the cases of positive triaxialities (e.g. tension), the failure is caused by decohesion of powder grains (intergranular failure) causing a quasi-brittle behavior. For the negative triaxiality cases (e.g. shear-compression), the failure is caused by shear yielding of the powder grains (intergranular failure). For this purpose, the temperature and strain rate sensitivities of failure phenomena have been carried out using shear-compression tests. A method to experimentally determine the value of the Taylor-Quinney coefficient with the strain (of material with negligible elastic work) has been presented in this manuscript.
- Concerning the sintered polyimide, the strain mechanisms are controlled by the chain displacement and not by the dislocations. The yield stress, defining the global level of stress of the polymer, presents important temperature and strain rate dependencies and is very important for an unfilled polymer ($\sigma_y \sim 250$ MPa in dynamic condition). The hyperelasticity behavior has been as well studied in this work with the dependencies of the rubber modulus to the thermal conditions and deformation rate. The failure behavior is very close to the one observed for the F7020 aluminum alloy: intergranular failure of the powder grains for positive stress triaxialities (e.g. tension) and yielding of these last in case of negative triaxialities (e.g. compression). The failure is governed at a different scale in comparison of the deformation mechanisms.
- However, the tests have revealed a much more significant brittleness of the sintered polyimide.

The epoxy resin, which used to assemble the F7020 aluminum alloy and the sintered polyimide layers in this work, presents a relatively low temperature of glass transition ($T_g = 333$ K) and the transition between glassy and rubber states is reached during dynamic conditions due to adiabatic heating. Therefore, the mechanical response of this material is very different regarding the strain rate involved. As for the sintered polyimide, the dependencies to temperature and deformation rate of the yield stress and hyperelasticity phenomena have been highlighted trough experimental tests and are much important the one identified for the polyimide. The failure mechanisms are also very different. Indeed, the epoxy resin has not been sintered and presents only failure created by crack propagation (in tension and compression). It can be noted that the epoxy resin is more ductile than the polyimide in tension but becomes quickly more brittle than this one in compression when the strain rate increases (above 0.1 /s). This is due to the fact that the epoxy resin is a thermoset polymer presenting a very high level of chain cross-linking and is very sensitive to the locking phenomenon leading to the failure of the chain structure.

Once the experimental data have been collected and the phenomena responsible of the deformation mechanism of each material have been identified and studied, the mechanical constitutive modeling has been achieved. For this purpose, a new approach to analytically model the complex and highly nonlinear thermally dependent stress response of metallic materials has been suggested: the Crystallo-Calorific Hardening approach (for FCC metals in this case). The approach is based on the classic separation of the overall stress response in athermal and thermal parts. The thermal part is itself divided into an effective stress (yield stress) and internal stress (structural strain hardening). The main contribution which can be found in the CCH approach is the use of the calorific ratio. It allows the modeling of highly nonlinear temperature sensitivities due to microstructure changes such as dissolution softening and/or precipitation hardening. The ability of the model to be easily adaptable to any type of metals just by changing the expression representative of a phenomenon is also an important asset of the suggested constitutive model. The obtained analytical expression can therefore be very complex or very simple according to the desired level of accuracy.

Concerning the two polymer materials, the constitutive modeling has been developed around the cooperative model describing the sensitivities of the yield stress to the temperature and the strain rate. However, this expression alone is not sufficient to take into account the whole strain behavior of the polymer. Therefore, a unified analytical expression taking into account the yield stress (cooperative model), the hyperelasticity (Gent model) and the strain softening (phenomenological expression) is suggested in this work to model the stress response of both polymers. The model has the ability to fit accurately the mechanical behavior of two very different polymers and over wide ranges of temperatures and strain rates.

Concerning the constitutive modeling of failure phenomena, the same approach has been used for the three materials: the development of a multiplicative expression modeling the value of the plastic strain at initiation of failure. This expression is dependent to the temperature, the strain rate and the state of stress. For each material, different expressions have been used in order to take into account more accurately the observed behaviors. For instance, the epoxy resin shows a strongly triaxiality-strain rate coupled response of its plastic strain at initiation of failure. Concerning the F7020 aluminum alloy, its evolution with the temperature can be modeled using the calorific ratio over a wide range of temperatures (with the same parameters identified for the stress). The triaxiality sensitivity of the brittle and quasi-brittle materials (sintered polyimide and F7020 aluminum alloy) has been taken into account with a suggested expression which allows to make the difference of mechanical responses between negative and positive stress triaxialities. Finally, the damage evolution between the plastic strain at initiation of failure and the strain at ultimate failure has been modeled considering the energy absorbed by the material during this range of strains (nearly zero in case of brittle failure).

After the determination of all the model parameters, the analytical expressions have been implemented in a VUMAT subroutine in FORTRAN code for ABAQUS®/Explicit. The validation of the numerical model has been firstly performed through comparisons with experimental results of high velocity impacts of a steel ball on monolayer materials (F7020 aluminum alloy and sintered polyimide). In each case, the suggested models where able to accurately represent the residual velocity and the fracture profile modes due to the perforation. Concerning the F7020 aluminum alloy, the velocity of the ejected plug has also been compared with the numerical model. It resulted that the suggested CCH model has a better accuracy than the widely broad used Johnson-Cook model. The failure profile of the channel is also more precisely reproduced when using the CCH model. The sintered polyimide presents a mode of perforation by fragmentation. Therefore, the comparison with the simulation of the fracture profile has been performed on the fragmentation cup at the rear side of the target. Unfortunately, difficulties in material providing did not allow experimental tests of high velocity impacts on the bilayer composites. Therefore, only the parametric study of different configurations of multilayer composites has been carried out in this work.

The numerical results on the bilayer composites have shown that the high brittleness of the sintered polyimide leads to a loss a ballistic performance of the protective material whatever are the thicknesses of the layers. The increase of the ductility of the sintered polyimide by delaying the intergranular the failure between the powder grains would be an interesting way of improvement of such material. The simulation and experimental validation with three or more layers is also an interesting aspect of investigation toward the development of such advanced multilayer materials for protection.

To go further in the project, it is mandatory to proceed to the experimental validation of the numerical model of impact on the multilayer material for several configurations (for each condition) and it would

be interesting to perform additional tests for the monolayer targets. Besides, the presented work is only about impacts of spherical steel projectile on thin targets. Therefore, the parameters to modify for a wider validation could be:

- The thickness of the targets (monolayer and multilayer targets)
- The relative position of the layer (e.g. sintered polyimide on the front side)
- The shape of the projectile (conical, ogival and blunt shaped projectile)
- The velocity of the projectile (very high velocities)
- The number of layers (more than two layers such as Al/PI/Al)
- The type of solicitation (e.g. bullets shot with an angle, blast solicitation …)

Many other aspects of the work can be brought further such as the characterization of the sintered polyimide above its temperature of glass transition or the implementation of the Lode parameter in the failure constitutive model by performing experimental tests in other conditions of state of stress (Butterfly specimen or punching tests). The SEM fracture profile can be analyzed in a quantitative way in order to develop specific intergranular model of failure for sintered materials.

APPENDICES

APPENDIX A – DETERMINATION METHOD OF THE TAYLOR-QUINNEY COEFFICIENT

This appendix aims to describe the measurement method used in this work to determine the evolution of the Taylor-Quinney coefficient during a dynamic deformation. The present method does not require the measure of the temperature of the sample. It is based on the difference of mechanical behavior between adiabatic and isothermal conditions (difference in energy absorption).

The isothermal dynamical test has to be performed at the same strain rate as the adiabatic test. To obtain the isothermal state, repeated tests at small strains are done on the same sample in order to avoid adiabatic heating. These tests are then processed, assembled and smoothed to get the usable isothermal stress-strain curve (Figure 157).

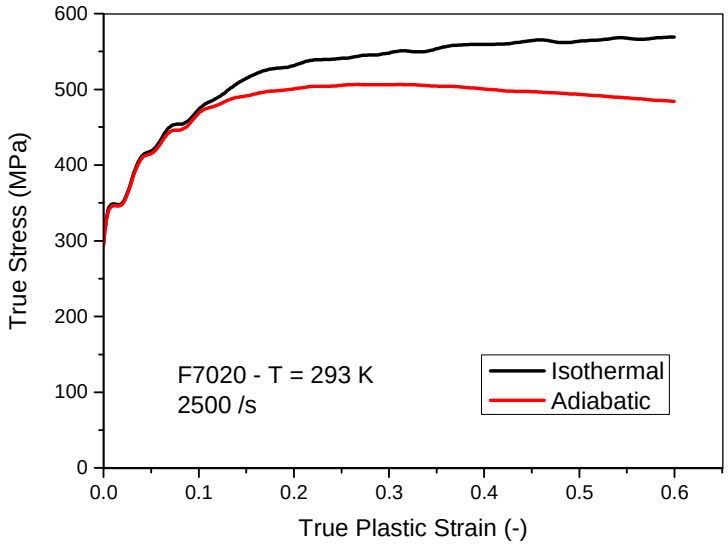

Figure 157 - Isothermal and adiabatic experimental true stress vs true strain curves

Once the experimental data have been obtained, some theorical considerations have to be taken into account to compute the Taylor-Quinney coefficient. In the case of metallic materials, the decomposition of the overall stress into athermal and thermal parts has to be firstly considered.

$$\sigma(\varepsilon_p, \dot{\varepsilon}_p, T) = \sigma_{athermal}(\varepsilon_p) + \sigma_{thermal}(\varepsilon_p, \dot{\varepsilon}_p, T)$$

The thermal stress is also composed of the effective (yield stress) and internal stresses (hardening) [1-3].

$$\sigma_{thermal}(\varepsilon_p, \dot{\varepsilon}_p, T) = \sigma_{effective}(\dot{\varepsilon}_p, T) + \sigma_{internal}(\varepsilon_p, \dot{\varepsilon}_p, T)$$

The computation of the evolution of the Taylor-Quinney coefficient with the strain needs the introduction of the notion of calorific potential p defining the energetic evolution of a medium submitted to a thermal transformation from a temperature T_0 to a temperature T_1.

$$p = \rho(T)C_p(T)(T_1\text{-}T_0)$$

With ρ the density of the material and C_p its specific heat. The value of the calorific potential p_0 from a reference temperature T_{ref} to another temperature T_{ext} by external heating is:

$$p_0 = \rho_0 C_{p_0}(T_{ext}\text{-}T_{ref})$$

During an adiabatic deformation, the elevation of temperature of the medium is calculated by using the following relation:

$$T = T_{ext} + \frac{\chi}{\rho C_p}\int \sigma d\varepsilon_p$$

With χ the Taylor-Quinney coefficient. And the new value of the calorific potential during the strain is therefore:

$$p = \chi \int \sigma d\varepsilon_p + p_0 = \rho C_p(T\text{-}T_{ext}) + p_0$$

Furthermore, a maximal calorific potential can be defined at the melting temperature of the material at which it cannot absorb more thermal energy.

$$p_{max} = \rho_f C_{p_f}(T_f\text{-}T_{ext}) + p_0$$

It is now possible to define the ratio of the calorific potential as follow:

$$\frac{p}{p_{max}} = \frac{\rho C_p(T\text{-}T_{ext}) + \rho_0 C_{p_0}(T_{ext}\text{-}T_{ref})}{\rho_f C_{p_f}(T_f\text{-}T_{ext}) + \rho_0 C_{p_0}(T_{ext}\text{-}T_{ref})} = \frac{\chi \int \sigma d\varepsilon_p + \rho_0 C_{p_0}(T_{ext}\text{-}T_{ref})}{\rho_f C_{p_f}(T_f\text{-}T_{ext}) + \rho_0 C_{p_0}(T_{ext}\text{-}T_{ref})}$$

And the adiabatic calorific ratio f_{cal} as:

$$f_{cal}(T) = 1\text{-}\frac{\rho(T)C_p(T)(T\text{-}T_{ext}) + \rho_0 C_{p_0}(T_{ext}\text{-}T_{ref})}{\rho_f C_{p_f}(T_f\text{-}T_{ext}) + \rho_0 C_{p_0}(T_{ext}\text{-}T_{ref})}$$

The Taylor-Quinney coefficient corresponds to the fraction of plastic work which is converted into heat during the deformation and involved in the evolution of the whole thermal plastic stress. The adiabatic and isothermal states can be linked by using the adiabatic calorific ratio.

$$\sigma_{th_{adia}}(\varepsilon_p, \dot{\varepsilon}_p, T) = \sigma_{th_{iso}}(\varepsilon_p, \dot{\varepsilon}_p, T) f_{cal}(T)$$

$$\frac{\sigma_{th_{adia}}}{\sigma_{th_{iso}}} = 1\text{-}\frac{\chi \int \sigma_{th_{adia}} d\varepsilon_p + \rho_0 C_{p_0}(T_{ext}\text{-}T_{ref})}{\rho_f C_{p_f}(T_f\text{-}T_{ext}) + \rho_0 C_{p_0}(T_{ext}\text{-}T_{ref})}$$

If $T_{ext} = T_{ref}$, the case becomes simpler and the Taylor-Quinney coefficient can be computed as:

$$\chi(\varepsilon_p) = \frac{\left(1-\frac{\sigma_{th_{adia}}}{\sigma_{th_{iso}}}\right)\rho_f C_{p_f}(T_f-T_{ext})}{\int \sigma_{th_{adia}} d\varepsilon_p}$$

And in the cases where $T_{ext} \neq T_{ref}$, the general expression is:

$$\chi(\varepsilon_p) = \frac{\rho_f C_{p_f}(T_f-T_{ext})-\frac{\sigma_{th_{adia}}}{\sigma_{th_{iso}}}\left(\rho_f C_{p_f}(T_f-T_{ext}) + \rho_0 C_{p_0}(T_{ext}-T_{ref})\right)}{\int \sigma_{th_{adia}} d\varepsilon_p}$$

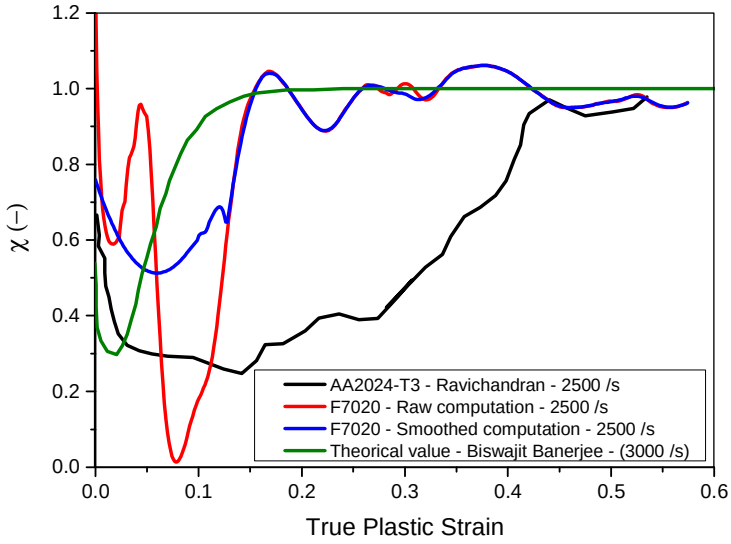

Figure 158 - Evolution of the Taylor-Quinney coefficient with the strain according to different methods

The evolution of the Taylor-Quinney coefficient with the strain follows a similar trend (see Figure 158) by using the suggested method and the method used by Ravichandran on the AA2024-T3 [4] but which involves temperature measurement during the test. Furthermore, the suggested method is closer to the theoretical computed value [3].

The smoothed curve of the raw computation is obtained through the Matlab® smooth function and using the 'rloess' option. This option consists into a robust local regression using weighted l inear least squares and 2nd degree polynomial model. It also assigns lower weight to outliers in the regression and zero weight to data outside six mean absolute deviations.

References

1. Follansbee, P. and U. Kocks, *A constitutive description of the deformation of copper based on the use of the mechanical threshold stress as an internal state variable.* Acta Metallurgica, 1988. **36**(1): p. 81-93.
2. Rusinek, A. and J.R. Klepaczko, *Shear testing of a sheet steel at wide range of strain rates and a constitutive relation with strain-rate and temperature dependence of the flow stress.* International Journal of Plasticity, 2001. **17**(1): p. 87-115.

3. Biswajit Banerjee, A.S.B., *An extended mechanical threshold stress plasticity model: modeling 6061-T6 aluminum alloy.* Journal of Mechanics of Materials and Structures, 2008. **3**(3).
4. Hodowany, J., et al., *Partition of plastic work into heat and stored energy in metals.* Experimental mechanics, 2000. **40**(2): p. 113-123.

APPENDIX B – TECHNICAL DRAWINGS OF SAMPLES

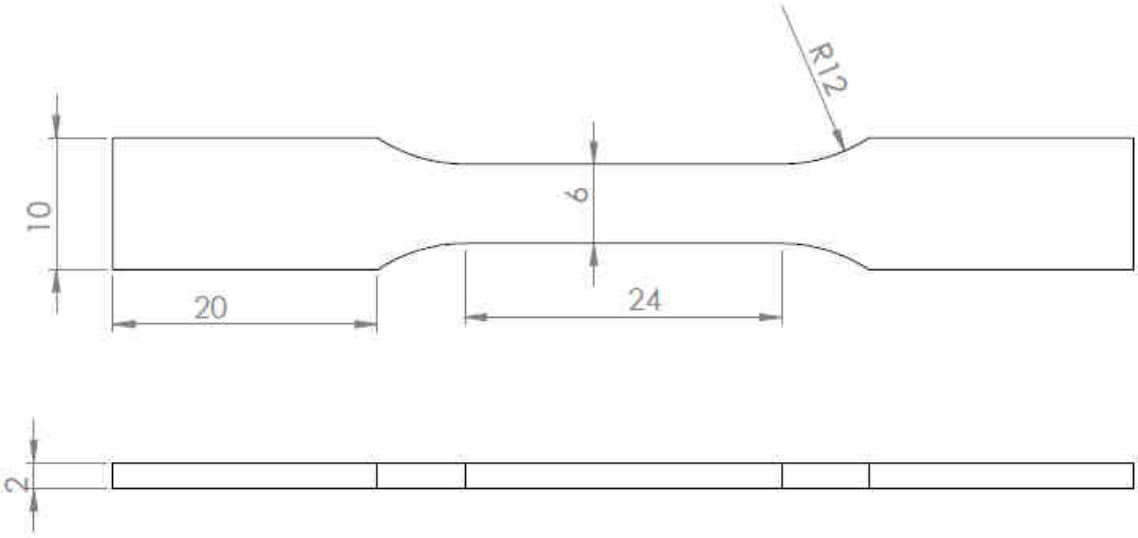

Figure 159 - Tensile specimen for F7020 aluminum alloy, epoxy resin and sintered polyimide

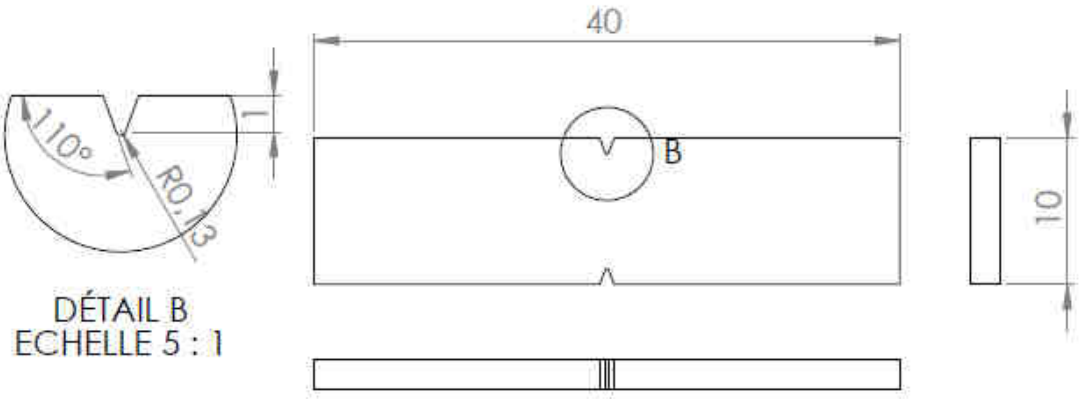

Figure 160 - Flexural notched sample for epoxy resin

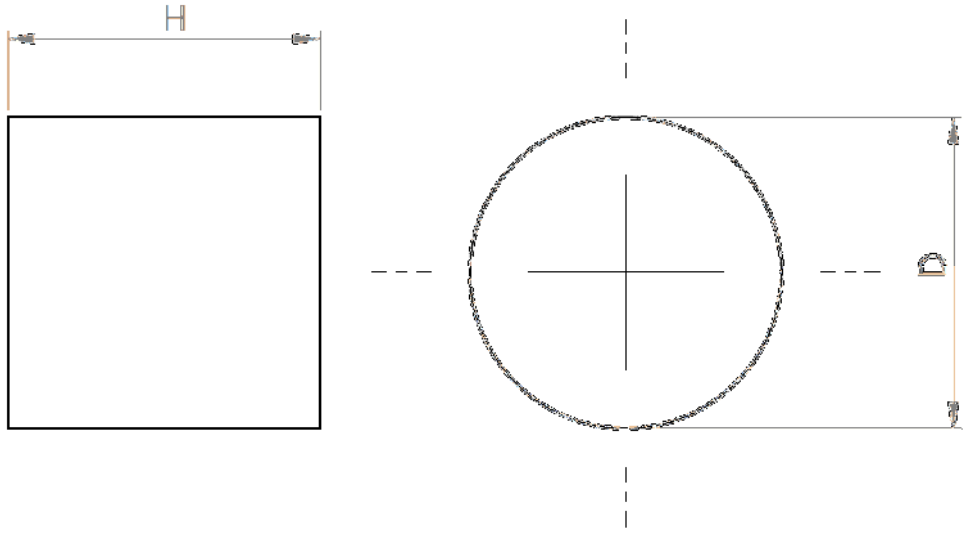

Figure 161 - Compression samples for F7020 aluminum alloy, epoxy resin and sintered polyimide

Table 40 - Dimension of compression samples according to materials and tests

Tests	Quasi-static		SHPB		Direct Impact	
	H (mm)	D (mm)	H (mm)	D (mm)	H (mm)	D (mm)
F7020	6	6	4	8	1	5
			3	6		
Epoxy Resin	10	10	5	10	1	5
Sintered Polyimide	6	6	4	8	1	5

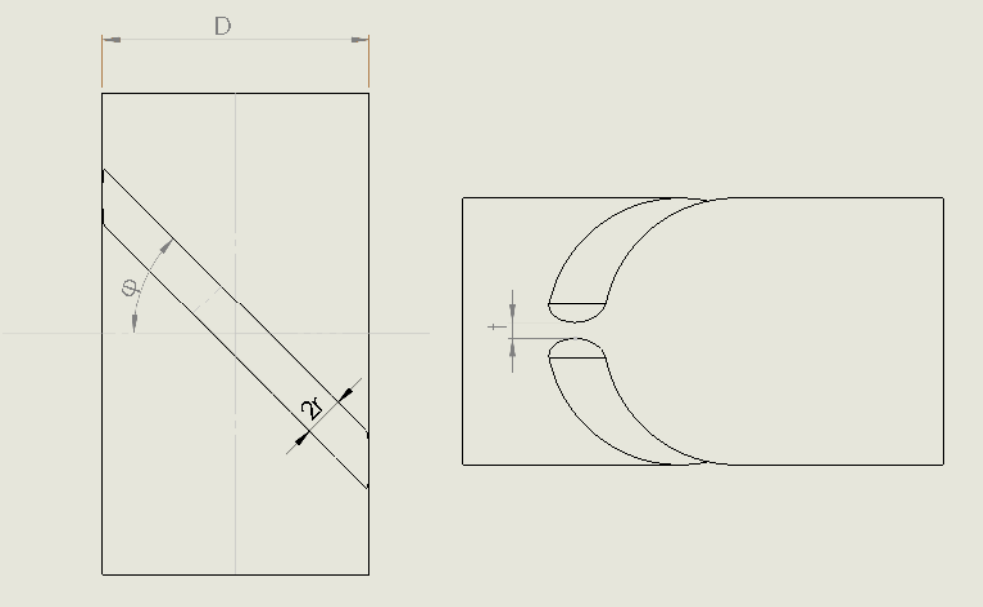

Figure 162 – Shear-compression samples for F7020 aluminum alloy

Table 41 - Dimension of shear-compression samples used for F7020 aluminum alloy

D = 10mm and r = 0.75mm				
t (mm)	φ			
0.6	45°	30°	20°	10°
1.6	45°			

APPENDIX C – JOHNSON-COOK PARAMETERS F7020

Stress behavior

$$\sigma(\varepsilon_p, \dot{\varepsilon}_p, T) = \left(A + B{\varepsilon_p}^n\right)\left(1 + C \ln\left(\frac{\dot{\varepsilon}_p}{\dot{\varepsilon}_0}\right)\right)\left(1 - \left(\frac{T - T_r}{T_m - T_r}\right)^m\right)$$

Material	A (MPa)	B (MPa)	n (-)	C (-)	m (-)	$\dot{\varepsilon}_0$ (/s)	T_r (K)	T_m (K)
F7020	260	278.9	0.2659	0.01929	0.915	0.001	293	940

Damage initiation

$$\varepsilon_p^f(\varepsilon_p, \dot{\varepsilon}_p, T) = \left(d_1 + d_2 e^{-d_3 \eta}\right)\left(1 + d_4 \ln\left(\frac{\dot{\varepsilon}_p}{\dot{\varepsilon}_0}\right)\right)\left(1 + d_5 \frac{T - T_r}{T_m - T_r}\right)$$

Material	d_1 (-)	d_2 (-)	d_3 (-)	d_4 (-)	d_5 (-)	$\dot{\varepsilon}_0$ (/s)	T_r (K)	T_m (K)
F7020	0.0459	0.06506	-4.586	0.027	2.71	0.026	293	940

CCH-FCC SIMPLIFIED EXPRESSION – PARAMETERS F7020

$$\sigma(\varepsilon_p, \dot{\varepsilon}_p, T) = \left[Y\left(1 - \varphi T_r \ln\left(\frac{\dot{\varepsilon}_r}{\dot{\varepsilon}_p}\right)\right)^{\frac{3}{2}} + B\sqrt{1 - e^{-k\varepsilon_p}}\left(1 + l_v \ln\left(\frac{\dot{\varepsilon}_0}{\dot{\varepsilon}_r}\right) + v\left(\frac{\dot{\varepsilon}_p}{\dot{\varepsilon}_r}\right)^{n_v}\right)\right]\left(1 - \frac{T - T_r}{T_m - T_r}\right)^m$$

Y (MPa)	φ (-)	B (MPa)	k (-)	l_v (-)	v (-)
260	1.9186e-5	232.7	6.042	-0.003459	0.00008508
n_v (-)	m (-)	$\dot{\varepsilon}_r$ (/s)	T_r (K)	T_m (K)	/
0.4889	1.307	0.0001	293	940	/

APPENDIX D – VISCOUS DRAG PHENOMENON

Viscous drag effect is present in all conditions of strain rates – dislocation velocity – and temperature (except at 0K). It is caused by various mechanisms at the nanometric level and are experimentally predominant (in metals) in dynamical conditions (above 1.000 /s). At the macroscopic level, the viscous drag effect results in a very strong strain rate sensitivity of the stress.

The mechanisms responsible of viscous drag can be seen as Newtonian drag forces per unit length of a moving dislocation $\tau_B b$ and is given by:

$$\tau_B b = Bv$$

With B the net drag coefficient and v the dislocation velocity.

The net drag coefficient B is the sum of each drag coefficient of the different mechanisms involved in the viscous drag effect such as electron scattering and viscosity (only in electronic conductors), thermoelastic damping effect (generally negligible) and phonons scattering and viscosity. In Physics, a phonon is a quantum of vibration energy of a crystalline solid.

The mechanisms related to phonons (and electrons for the electronic conductors) are the most predominant ones in metallic materials and more specifically viscosity factors which are around ten times greater than scattering.

Physically, phonons viscosity is caused by the augmentation of the different frequency modes of the phonons when they are crossed by a dislocation at a higher strain rate. The augmentation of modes of frequencies of the phonon leads to an increase of energy the crystalline solid and therefore the level of stress required for a dislocation to pass through it augments. The phonon scattering phenomenon consists in a momentum transfer between dislocations and phonons leading to a drag effect.

The influence of the electrons also causes (in electronic conductors) viscosity and scattering effects. The viscosity effect comes from the momentum transfer from electrons to phonons caused by the strain field. This phenomenon leads to a rise of the mode of vibrations of the phonons and a high heat dissipation which is strongly dependent on the electrical resistivity. This phenomenon is called, at the macroscopic level, the adiabatic heating effect. Electron scattering is similar to phonon scattering at the exception that it is athermal. Momentum transfer between phonons and electrons are always present amplifying the heat dissipation phenomenon even in nonconductor metals.

APPENDIX E – MODEL PARAMETERS FOR THE AA7020-T651 ALUMINUM ALLOY

The parameters of the constitutive models used in the Figure 11 for the AA7020-T651 have all been determined in this work and are gathered in the tables below:

Johnson-Cook

$$\sigma = (A + B{\varepsilon_p}^n)\left(1 + C\log\frac{\dot{\varepsilon}_p}{\dot{\varepsilon}_0}\right)\left(1-\left(\frac{T-T_r}{T_m-T_r}\right)\right)^m$$

A (MPa)	B (MPa)	n	C	m	T_r (K)	$\dot{\varepsilon}_0$ (/s)
400	136.9	0.2015	0.01506	1.036	293	0.001

Molinari-Clifton

$$\sigma = \sigma_0{\varepsilon_p}^n\left(\frac{\dot{\varepsilon}_p}{\dot{\varepsilon}_0}\right)^m\left(\frac{T}{T_0}\right)^\nu$$

σ_0 (MPa)	n	m	ν	T_0 (K)	$\dot{\varepsilon}_0$ (/s)
533.2	0.03931	0.01363	-0.9356	293	0.001

Zerilli-Armstrong

$$\sigma = \sigma_a + B_0\sqrt{\varepsilon^p}e^{-(\alpha_0-\alpha_1\ln\dot{\varepsilon}^p)T}$$

σ_a (MPa)	B_0 (MPa)	n	a_0	a_1
400	1777	0.2163	0.01	0.0002809

Rusinek-Klepaczko

$$\sigma = \frac{E(T)}{E_0}\left(\sigma_\mu + \sigma^*\right)$$

$$\begin{cases} \sigma_\mu = Y \\ \sigma^*\left(\varepsilon_p, \dot{\varepsilon}_p, T\right) = B\left(\dot{\varepsilon}_p, T\right){\varepsilon_p}^{n\left(\dot{\varepsilon}_p, T\right)}\left[1-D_1\frac{T}{T_m}\ln\left(\frac{\dot{\varepsilon}_{max}}{\dot{\varepsilon}_p}\right)\right]^{\frac{1}{m}} \end{cases}$$

$$\begin{cases} E(T) = E_0\left[1\text{-}\frac{T}{T_m}e^{\theta^*\left(1\text{-}\frac{T_m}{T}\right)}\right] \\ B\left(\dot{\varepsilon}_p, T\right) = B_0\left(\frac{T}{T_m}\ln\frac{\dot{\varepsilon}_{max}}{\dot{\varepsilon}_p}\right)^{\text{-}\nu} \\ n\left(\dot{\varepsilon}_p, T\right) = n_0\left(1\text{-}D_2\frac{T}{T_m}\ln\left(\frac{\dot{\varepsilon}_p}{\dot{\varepsilon}_{min}}\right)\right) \end{cases}$$

Y (MPa)	B_0 (MPa)	D1	D2	m	ν
400	270.3	0.1109	0.01	6.38	-0.1
n_0	T_m (K)	θ^*	$\dot{\varepsilon}_{min}$ (/s)	$\dot{\varepsilon}_{max}$ (/s)	E_0 (GPa)
0.2029	898	0.9	10^{-5}	10^7	75

Mechanical Threshold Stress

$$\sigma\left(\varepsilon_p, \dot{\varepsilon}_p, T\right) = \sigma_a + \left(\sigma_\varepsilon\left(\varepsilon_p, \dot{\varepsilon}_p, T\right)S_\varepsilon\left(\varepsilon_p, \dot{\varepsilon}_p, T\right) + \sigma_i\right)\frac{E(T)}{E_0}$$

$$E(T) = E_0\left[1\text{-}\frac{T}{T_m}e^{\theta^*\left(1\text{-}\frac{T_m}{T}\right)}\right]$$

$$S_\varepsilon = \left[1\text{-}\left(\frac{k_b T}{g_{0_\varepsilon}\mu b^3}\ln\left(\frac{\dot{\varepsilon}_{0_\varepsilon}}{\dot{\varepsilon}_p}\right)\right)^{\frac{1}{q_\varepsilon}}\right]^{\frac{1}{p_\varepsilon}}$$

$$\theta\left(\varepsilon_p, \dot{\varepsilon}_p, T\right) = \frac{d\sigma_\varepsilon\left(\varepsilon_p, \dot{\varepsilon}_p, T\right)}{d\varepsilon_p} = \theta\,[1\text{-}F(X)]$$

$$\theta = \theta_0 + \theta_1 \ln\dot{\varepsilon}_p + \theta_2\dot{\varepsilon}_p$$

$$F(X) = \frac{\sigma\text{-}\sigma_a}{\sigma_{\varepsilon s}\text{-}\sigma_a}$$

$$\ln\left(\frac{\dot{\varepsilon}_{\varepsilon s0}}{\dot{\varepsilon}_p}\right) = \frac{\mu b^3 g_{\varepsilon s0}}{k_b T}\ln\left(\frac{\sigma_{\varepsilon s}}{\sigma_{\varepsilon s0}}\right)$$

σ_a (MPa)	σ_i (MPa)	$\sigma_{\varepsilon s0}$ (MPa)	$g_{0\varepsilon}$	$g_{0\varepsilon s}$	p_ε	q_ε	μ (GPa)
24.8	398	280	1	0.2	2/3	1	27
b (nm)	θ^*	T_m (K)	$\dot{\varepsilon}_{\varepsilon 0}$ (/s)	$\dot{\varepsilon}_{\varepsilon s0}$ (/s)	θ_0 (MPa)	θ_1 (MPa)	θ_2 (MPa)
0.286	0.9	898	10^9	10^8	3525	14	0.044

APPENDIX F – VUMAT ALGORITHM

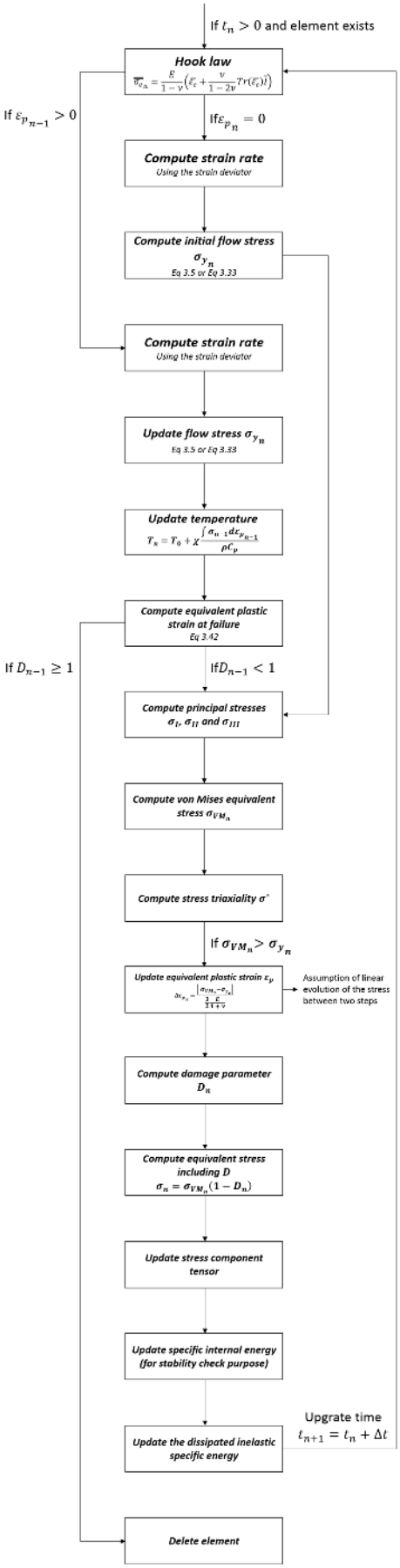

Charles FRANCART

Experimental and numerical study of the mechanical behavior of metal/polymer multilayer composite for ballistic protection

Résumé

L'étude présentée porte sur le développement d'un modèle numérique destiné à évaluer les performances balistiques d'une structure multicouche polymère/métal frittée par procédé SPS. Les matériaux sont un alliage d'aluminium 7020 et un polyimide thermoplastique amorphe qui sont ensuite assemblés avec une résine epoxy. Le comportement mécanique de ces trois matériaux a été étudié sur de larges gammes de vitesses de déformations (de 0.0001 /s à 50.000 /s) et de températures (de -70°C à 500°C) correspondant aux conditions extrêmes rencontrées lors d'impacts à hautes vitesses. Afin d'améliorer la précision des résultats, des approches analytiques ont été développées autant pour la modélisation du métal que pour celle les polymères. Après la calibration des modèles, ces derniers ont été implémenté dans ABAQUS®/Explicit (éléments finis) via des subroutines VUMAT en code FORTRAN. Des essais d'impacts de billes à hautes vitesses ont été réalisés sur des cibles monocouches pour valider les modèles numériques. De nombreuses configurations de composites multicouches ont ensuite été étudiées numériquement et leurs performances balistiques ont été comparées.

Comportement mécanique ; balistique ; VUMAT ; modélisation ; polymère ; métaux

Abstract

The present study deals with the development of a numerical model to evaluate the ballistic performance of a polymer/metal multilayer structure sintered by SPS. The materials are an aluminum alloy 7020 and an amorphous thermoplastic polyimide which are then assembled using an epoxy resin. The mechanical behavior of these three materials has been studied over wide ranges of strain rates (from 0.0001 / s to 50,000 / s) and temperatures (from -70 °C to 500 °C) corresponding to the extreme conditions encountered during impacts at high velocities. In order to improve the accuracy of the results, analytical approaches have been developed both for the modeling of the metal and for the polymers. After the calibration of the models, these models were implemented in ABAQUS® / Explicit (finite elements) via VUMAT subroutines in FORTRAN code. Ball impact tests at high velocities were performed on monolayer targets to validate numerical models. Numerous configurations of multilayer composites were then studied numerically and their ballistic performances have been compared.

Mechanical behavior; Ballistics; VUMAT; constitutive modeling; polymer; metals

UNIVERSITÉ DE STRASBOURG

ÉCOLE DOCTORALE ED269

ICUBE – Equipe MMB

THÈSE présentée par :

Charles FRANCART

soutenue le : **13th Octobre 2017**

pour obtenir le grade de : **Docteur de l'université de Strasbourg**

Discipline/ Spécialité : mécanique des matériaux

Etude expérimental et numérique du comportement mécanique de composites multicouches polymère/métal pour protection balistique

THÈSE dirigée par :

Mr AHZI Said	Pr., ICUBE – Université de Strasbourg
Mme BAHLOULI Nadia	Pr., ICUBE – Université de Strasbourg

JURY dirigé par :

Mme VERLEYSEN Patricia	Pr., University of Ghent

RAPPORTEURS :

Mr LAURO Franck	Pr., LAMIH – Université de Valenciennes
Mr RUSINEK Alexis	Pr., LEM3 – Université de Lorraine

AUTRES MEMBRES DU JURY :

Mme DEMARTY Yaël	Dr., French-German Institute of Saint-Louis (ISL)
Mr RITTEL Daniel	Pr., Technion (Israël)

INTRODUCTION

De nos jours, l'un des principaux problèmes abordés dans l'industrie du transport consiste à développer des matériaux légers visant à réduire la consommation de carburant et à accroître l'autonomie des véhicules. Cette problématique est également pertinente dans l'industrie militaire à des fins stratégiques. En effet, plus l'autonomie des véhicules est élevée, plus leur zone d'action sera importante. Par conséquent, le développement de matériaux de protection légers est actuellement à l'étude. Ce travail concerne plus précisément les structures légères soumises à des conditions extrêmes subies lors d'un chargement d'impact.

Cette étude vise à développer un modèle numérique (avec ABAQUS®/Explicit) permettant l'évaluation de la réponse mécanique dynamique d'un composite fritté polymère/métal multicouche dans des conditions d'impacts à hautes vitesses. Les deux matériaux (alliage d'aluminium 7020 [1] et polyimide thermoplastique [2]), ont été frittés à l'aide du procédé Spark Plasma Sintering (SPS) et sont développés à l'Institut franco-allemand de Saint-Louis (ISL). Ce travail a pour objectif d'évaluer leur potentiel de protection. À cette fin, la séquence d'empilement des couches leur nombre et leurs épaisseurs respectives doivent être étudiés numériquement pour optimiser l'efficacité et le coût de développement. Le comportement mécanique de l'interface résine époxy est abordé en tenant compte de la présence de ce matériau en tant que couche intermédiaire possédant ses propres propriétés matérielles. Cependant, l'étude mécanique concernant ce matériau n'est pas abordé cette version abrégé du manuscrit de thèse.

Ce travail vise à présenter une méthodologie de développement d'un modèle numérique prédictif qui pourrait être adapté à d'autres types de matériaux. L'outil numérique offrirait alors la possibilité d'optimiser les structures composites multicouches pour atteindre les spécifications ciblées (poids, volume et performances). Le premier chapitre de ce manuscrit vise à expliquer les principaux mécanismes liés à la résistance mécanique et à la rupture des métaux et des polymères amorphes ainsi que des modèles existants permettant de représenter ces mêmes mécanismes.

Le deuxième chapitre de ce travail concerne la caractérisation expérimentale du comportement mécanique de chaque matériau (alliage d'aluminium fritté 7020, polyimide thermoplastique et résine époxy). Les réponses mécaniques des comportements de la contrainte et de la rupture doivent être étudiées afin de comprendre les sensibilités des phénomènes à la déformation, à la vitesse de déformation et à la température. L'identification de ces différents phénomènes permet un meilleur développement de la modélisation constitutive du comportement mécanique (contrainte et rupture).

Dans le troisième chapitre, une nouvelle approche pour développer des modèles constitutifs décrivant le niveau de contrainte des métaux CFC est suggérée [3]. Le modèle qui en résulte permet une modélisation précise du comportement mécanique de l'alliage d'aluminium 7020 sur une large gamme de vitesse de déformation et tient compte des phénomènes microstructuraux tels que la dissolution des précipités. La modélisation du comportement mécanique polyimide fritté est basée sur l'expression du modèle coopératif [4] couplée au modèle hyperélastique de Gent [5]. Le comportement de la rupture est modélisé avec deux phénomènes couplés: l'évaluation de la déformation plastique à l'initiation de la rupture (en fonction de l'état de contrainte, de la température et de la vitesse de déformation) et ensuite de l'évolution de l'énergie d'endommagement.

Le dernier chapitre du manuscrit consiste en la mise en application des modèles identifiés dans le logiciel ABAQUS®/Explicit par le développement de subroutines VUMAT en code FORTRAN. Les simulations sont réalisées en modélisant la configuration expérimentale utilisée pour les essais d'impact afin d'assurer les mêmes conditions limites pour la validation du modèle numérique. Dans un premier temps, des essais sur des cibles de matériaux monolithiques sont réalisés afin de valider les modèles numériques séparément avant de traiter les cas multicouches dans un second temps.

Chapitre 1 – Comportement mécanique des matériaux métalliques et polymères

1. Modélisation des mécanismes liés à l'évolution de la contrainte

Dans cette étude, les matériaux étudiés sont un alliage d'aluminium, un polyimide thermoplastique et une résine époxy (polymères amorphes). Dans les cas, le critère de plasticité considéré est le critère de Von Mises et les déformations plastiques ε_p et contraintes équivalentes σ évoquées le sont suivant ce critère.

a. Matériaux métalliques

i. Mécanismes de déformation

La déformation des matériaux métalliques peut être divisée en deux parties principales : l'élasticité linéaire (phénomène réversible impliquant de petites déformations) et la viscoplasticité (phénomènes irréversible impliquant les grandes déformations). La limite entre ces deux domaines est caractérisée par une valeur de la contrainte appelée la limite d'élasticité Y.

Le domaine plastique de déformation est celui qui est le plus complexe. En effet, de nombreux phénomènes conduisent au niveau de contrainte macroscopique observé. La contrainte plastique équivalente σ (suivant le critère de plasticité de Von Mises) est composée d'une partie athermique σ_{ath} pouvant être sensible à la déformation plastique équivalente ε_p et d'une partie thermique σ_{th} sensible à la déformation plastique ε_p, à la température T et à la vitesse de déformation $\dot{\varepsilon}_p$ [6]. La contrainte thermique σ_{th} peut être également séparée en deux parties : une contrainte effective σ_{eff} décrivant la contrainte indépendante de l'état de déformation plastique ε_p et est sensible à la température T et à la vitesse de déformation $\dot{\varepsilon}_p$ ainsi qu'une contrainte interne σ_{int} décrivant l'écrouissage structural du métal avec la déformation plastique ε_p, la température T et la vitesse de déformation $\dot{\varepsilon}_p$ [7]. La contrainte interne σ_{int} est générée par l'évolution de la densité de dislocation ρ conduisant à l'écrouissage structurel du matériau et à sa déformation plastique [8] (déplacement des dislocations mobiles). Les mécanismes thermo-activés impliqués dans le déplacement et la multiplication des dislocations peuvent être fortement sensibles à la température et à la vitesse de déformation. La contrainte effective σ_{eff} peut correspond à la modélisation de l'évolution de la limite d'élasticité du matériau avec la température et la vitesse de déformation. Cependant, cette notion est plus complexe car elle vise à prendre en compte de nombreux phénomènes thermo-activés à l'échelle microscopique tels que le franchissement des barrières de Peierls [9]. L'énergie de Peierls étant l'énergie nécessaire pour qu'une dislocation se déplace d'une position d'équilibre à celle suivante.

La contrainte athermique σ_{ath} est provient principalement de propriétés intrinsèque du matériau considéré et de mécanismes impliquant de très faibles sensibilités à la température tels que les interactions entre les dislocations et les obstacles à très grandes distances (supposés alors athermiques).

D'autres contraintes provenant de phénomènes liés par exemple à l'élévation de la vitesse de déformation peuvent être considérées telle que la contrainte de « viscous drag » σ_{VD}. En effet, dans le domaine dynamique de vitesse de déformation, des phénomènes liés à des transferts

énergétiques entre les phonons et les dislocations se propageant à grande vitesse ralentissent ces dernières [9]. L'énergie nécessaire pour déformer le matériau augmente alors avec la vitesse de déformation d'où l'existence de σ_{VD}.

ii. Modèles constitutifs pour la contrainte

De nombreux modèles constitutifs visant à représenter l'évolution de la contrainte plastique σ des métaux avec la déformation ε_p, la température T et la vitesse de déformation $\dot{\varepsilon}_p$ ont été développés et sont trouvables dans la littérature. Un bref état de l'art est présenté dans ce rapport.

Le modèle phénoménologique de Johnson-Cook [10] (Eq. 1) est probablement celui qui est le plus utilisé dans l'industrie de par sa simplicité d'utilisation et du fait qu'il soit implémenté dans la plupart des codes de calculs par la méthode des éléments finis. Cependant, ce modèle considère une unique sensibilité linéaire à la vitesse de déformation pour les contraintes interne et effective. Conduisant à une validité limitée à une faible plage de vitesses de déformation. Ce n'est pas un modèle prédictif.

$$\sigma = (A + B{\varepsilon_p}^n)\left(1 + C\log\frac{\dot{\varepsilon}_p}{\dot{\varepsilon}_0}\right)\left(1 - \left(\frac{T - T_r}{T_m - T_r}\right)\right)^m \quad (1)$$

Avec A, B, C, n et m des paramètres phénoménologiques du modèle, T_r et $\dot{\varepsilon}_0$ sont respectivement une température et une vitesse de déformation de référence et T_m la température de fusion du métal. On peut noter que n est aussi appelé le coefficient d'écrouissage.

Le modèle de Zerilli-Armstrong [11] provient d'hypothèses physiques sur le mouvement des dislocations. Des expressions différentes existent pour les structures cristallines CFC et CC. L'expression pour les métaux CFC est présentée ici (Eq. 2). Cependant, le modèle de Zerilli-Armstrong présente des difficultés à représenter le comportement mécanique dans de nombreux cas. En effet, la contrainte effective σ_{eff} est considérée comme athermique et le matériau ne parviendra pas à représenter l'adoucissement du matériau à haute température. De plus, le coefficient d'écrouissage est ici considéré de base comme étant égal à 0.5 (racine carrée) pour limiter le nombre de paramètre. Cette hypothèse conduit souvent à une modélisation approximative du durcissement structurel dans de nombreux cas.

$$\sigma = \sigma_{ath} + B_0\sqrt{\varepsilon^p}e^{-(\alpha_0 - \alpha_1 \ln \dot{\varepsilon}^p)T} \quad (2)$$

Le modèle MTS [7] (Mechanical Threshold Stress) a été développé sur des bases physiques pour les matériaux CFC et CC. Ce modèle considère la séparation des contraintes interne σ_{int} et effective σ_{eff} ainsi que des contraintes athermique et thermique (Eq. 3). Ce modèle constitutifs et les autres basés également sur une telle décomposition (modèle Rusinek-Klepaczko [12]) proposent généralement un meilleur domaine de validité en température T et en vitesse de déformation $\dot{\varepsilon}_p$ et donc une meilleure prédictibilité que les modèles phénoménologiques tel que Johnson-Cook.

$$\sigma = \sigma_{ath} + \left(\sigma_{int}(\varepsilon_p, \dot{\varepsilon}_p, T)S_\varepsilon(\varepsilon_p, \dot{\varepsilon}_p, T) + \sigma_{eff}S_i(\varepsilon_p, \dot{\varepsilon}_p, T)\right)\frac{E(T)}{E_0} \quad (3)$$

b. Matériaux polymères amorphes

i. Mécanismes de déformation

Le comportement mécanique des polymères amorphes peuvent être, tout comme les métaux, décomposés suivant plusieurs domaines de déformation. Cependant, contrairement aux deux

principaux domaines des métaux, les polymères amorphes en présentent trois en plus de limite élastique σ_y : la viscoélasticité (faibles déformations), l'adoucissement plastique (moyennes déformations) et l'hyperélasticité (grandes déformations).

La viscoélasticité est, comme élasticité linéaire, un mécanisme réversible. Elle est basée sur le principe de superposition de Boltzmann selon lequel le comportement viscoélastique global est la superposition de nombreux mécanismes indépendants d'élasticité linéaire possédant des propriétés d'activations différentes [13]. Le concept de limite d'élasticité σ_y dans les polymères est basé sur l'activation de la reptation des chaînes moléculaires les unes par rapport aux autres [14]. Ce phénomène définissant alors le début de la déformation irréversible ε_p dans le matériau. La limite d'élasticité est, pour les polymères amorphes, fortement sensible à la vitesse de déformation $\dot{\varepsilon}_p$ et à la température T. L'adoucissement plastique est un phénomène débutant dès l'activation de la reptation des chaînes moléculaires à la limite d'élasticité mais prenant de plus en plus d'ampleur avec la déformation ε_p. En effet, une fois que les molécules commencent à glisser, la complexité du réseau de chaînes peut être observée. D'une part, un fort frottement, influencé par l'état de contrainte local entre les chaînes, augmente la résistance du matériau avec la déformation ε_p. D'autre part, les chaînes ne sont pas encore en tension et une importante liberté de mouvement des segments de chaîne est présente, entraînant alors une diminution de la résistance du polymère. Ce mouvement libre relatif des chaînes dure jusqu'à ce que la majorité de ces chaînes commence à être localement en tension, provoquant le phénomène d'hyperélasticité et la génération de la contrainte de recouvrement σ_B causée par la résistance du réseau de chaîne à la déformation [13].

ii. Modèles constitutifs pour la contrainte

Le nombre de modèles constitutifs visant à représenter l'évolution de la contrainte plastique σ des polymères avec la déformation ε_p, la température T et la vitesse de déformation $\dot{\varepsilon}_p$ est relativement faible. En effet, de par la décomposition des phénomènes de limite élastique σ_y et de contrainte hyperélastique σ_B, les approches physiques ont plus tendances à les traiter séparément. Un bref état de l'art est présenté dans ce rapport.

Le modèle de G'Sell-Jonas [15] est le principal modèle phénoménologique existant proposant une modélisation de l'ensemble du domaine de déformation plastique (Eq. 4). Cependant, il est à noter que les sensibilités à la vitesse de déformation et à la température ne permettent pas au modèle d'être valide sur de larges gammes de conditions de tests.

$$\sigma = K e^{h{\varepsilon_p}^n} e^{\frac{a}{T}} {\dot{\varepsilon}_p}^m \quad (4)$$

Concernant la modélisation de la limite élastique σ_y, le modèle le plus classiquement utilisé est le modèle de Ree-Eyring [16] (Eq. 5). Ce modèle est physiquement basé sur le concept de probabilité de « sauts » de segments de macromolécules d'une configuration à une autre conduisant alors à la reptation de la chaîne. Ce modèle considère donc un phénomène thermo-activé et dépendant de la vitesse de déformation.

$$\frac{\sigma_y}{T} = \sum_i^N A_i \sinh^{-1}\left(\frac{C_i \dot{\varepsilon}}{T} e^{\frac{\Delta H_i}{k_b T}}\right) \quad (5)$$

Un autre modèle, plus avancé, a été développé à partir de cette théorie. Il s'agit du modèle coopératif [4] (choisi pour cette étude), prenant en compte avec une meilleure précision les sensibilités à la vitesse de déformation et à la température. De plus le modèle coopératif est le seul modèle valide en-dessous et au-dessus de la température de transition vitreuse T_g (Eq. 6).

$$\begin{cases} \sigma_y = \sigma_i(0) - mT + \dfrac{2k_bT}{V}\sinh^{-1}\left(\dfrac{\dot{\varepsilon}}{\dot{\varepsilon}_0 e^{-\frac{\Delta H_\beta}{RT}}}\right)^{\frac{1}{n}} & for\ T \le T_g \\ \sigma_y = \dfrac{2k_bT}{V}\sinh^{-1}\left(\dfrac{\dot{\varepsilon}}{\dot{\varepsilon}_0 e^{-\frac{\Delta H_\beta}{RT}} e^{\frac{\ln(10)c_1^g(T-T_g)}{c_2^g+T-T_g}}}\right)^{\frac{1}{n}} & for\ T > T_g \end{cases} \quad (6)$$

La modélisation de la contrainte hyperélastique des polymères amorphes peut être réalisée avec un très grand nombre de modèles existant [17]. Cependant, seuls quelques-uns sont réellement utilisés dans le cadre pratique.

Le plus connu est certainement le modèle 8-chaînes [18] mais présentant, malgré des performances intéressantes, une non-linéarité dans son expression handicapante pour les cas d'implémentation numérique dans les codes de calculs par éléments finis. Dans cette étude le modèle choisi est le modèle de Gent [5], présentant une expression simple d'utilisation et de très bonnes performances en grandes déformations. L'expression dans le cas uniaxiale est présenté (Eq. 7) [13].

$$\sigma_{uniax} = \mu\left(\lambda^2 - \frac{1}{\lambda}\right)\frac{J_m}{J_m - \left(\lambda^2 + \frac{2}{\lambda} - 3\right)} \quad (7)$$

2. Modélisation des mécanismes liés à la rupture

i. Mécanismes de rupture

La rupture des matériaux est de la plus haute importance dans la modélisation du comportement mécanique. En effet, ces mécanismes représentent la limite des matériaux et permettent la conception efficace des éléments fonctionnels dans les systèmes mécaniques. À cette fin, le comportement de delà rupture doit être étudié en plus du comportement relatif à la contrainte pour compléter l'étude à l'égard d'un modèle numérique complet. Le comportement de la rupture des matériaux peut généralement être décomposé en deux étapes: l'initiation de la rupture à laquelle commence l'évolution de l'endommagement conduisant à la rupture finale du matériau.

L'initiation de l'échec correspond au critère de Considère mathématiquement représenté par l'expression suivante (Eq. 8).

$$\frac{d\sigma_n}{d\varepsilon_p} = 0 \quad (8)$$

Les mécanismes d'endommagement commencent à la valeur de déformation vraie ε_p^f pour laquelle le critère Considère est rempli. Ces mécanismes peuvent être de deux natures différentes:

- Apparition et expansion de bandes de cisaillement adiabatique conduisant à des segments de fissure localisés (pour un état de triaxialité inférieur à l'état de traction).
- La germination, la croissance et la coalescence des vides conduisant à la création de cupules (pour un état de triaxialité positif) (Figure 1).

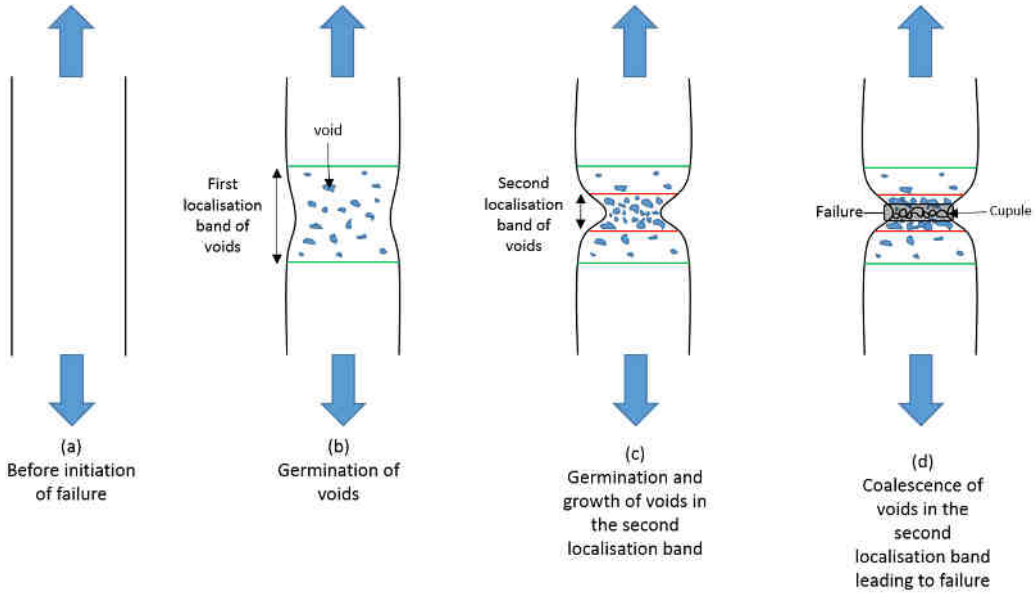

Figure 163 – Illustrations des différentes étapes de la rupture ductile

Une tendance générale de la sensibilité de la déformation plastique à l'initiation de la rupture ε_p^f avec la triaxialité peut être observée:

- La valeur de ε_p^f augmente exponentiellement avec une triaxialité décroissante jusqu'à une valeur de limite pour l'état de contrainte de compression pure $\sigma^* = -\frac{1}{3}$ en dessous de laquelle la valeur de ε_p^f est considérée comme infinie (Domaine 1 de la Figure 2).
- La valeur de ε_p^f converge de manière asymptotique à une faible valeur dépendant du matériau spécifique à une grande triaxialité (Domaine 2 de la Figure 2).

Cependant, la sensibilité à la triaxialité de ces matériaux est beaucoup plus complexe dans le domaine de l'état de stress positif. Une valeur de crête de ε_p^f dans l'état de tension pure ($\sigma^* = \frac{1}{3}$) peut être observée.

Dans le cas de matériaux présentant une faible cohésion interne (typiquement les matériaux frittés), une rupture intergranulaire mésoscopique entre les grains de poudre frittés peut être observée pour les états de triaxialité mettant en œuvre des mécanismes de germination et de coalescence de vides.

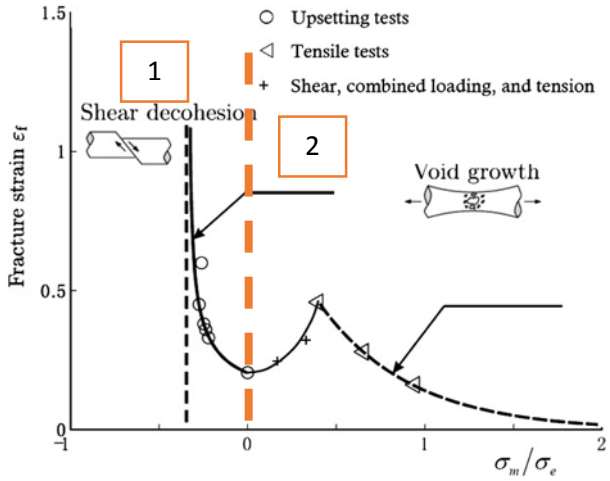

Figure 164 – Sensibilité typique à la triaxialité de la déformation à l'initiation de la rupture [19]

L'évolution de ε_p^f et celle de la contrainte σ du matériau est étroitement liée. En effet, l'énergie mécanique potentielle absorbée par le matériau reste la même pour toute température (dans le cas d'une rupture ductile impliquant un phénomène d'écoulement). Par conséquent, la valeur de ε_p^f augmente avec l'adoucissement thermique du matériau [20]. Cependant, pour les métaux, le comportement peut être beaucoup plus complexe car de nombreux phénomènes microstructural différents peuvent se produire avec l'élévation de la température [21] (durcissement par précipitation ou adoucissement par dissolution).

En ce qui concerne les polymères amorphes, le comportement de la contrainte du matériau a une incidence significative sur la propagation de la fissure à cause de la présence des fibrilles [22] (Figure 3). En effet, plus la résistance des fibrilles est faible (faible vitesse de déformation et/ou température élevée), plus la propagation des fissures sera plus lente. Le principal changement microstructural consiste en la transition de l'état vitreux à l'état caoutchoutique à la température de transition vitreuse T_g pendant laquelle le comportement mécanique du matériau baisse considérablement.

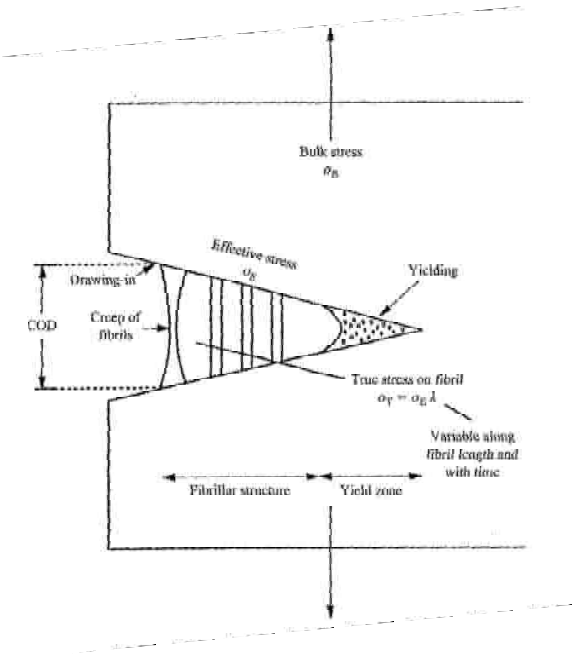

Figure 165 - Représentation schématique de propagation d'une fissure dans un polymère [23]

Pour les matériaux métalliques, la sensibilité positive à la vitesse de déformation de ε_p^f peut être divisée en deux domaines séparés par une vitesse de déformation de transition $\dot{\varepsilon}_{trans}$ ($\sim$1000 /s) au-dessus de laquelle l'effet de « viscous drag » ne peut être négligé.

- Au-dessous de $\dot{\varepsilon}_{trans}$, ε_p^f ne montre peu de sensibilité à la vitesse de déformation.
- Au-dessus de $\dot{\varepsilon}_{trans}$, la sensibilité de ε_p^f suit une tendance positive exponentielle qui est principalement due aux effets de micro-inertie rencontrés dans les phénomènes de « viscous drag »

Concernant les polymères amorphes, l'évolution ε_p^f avec la vitesse de déformation peut également être divisée en deux domaines. Cependant, la vitesse de déformation de transition $\dot{\varepsilon}_{trans}$, séparant ces deux comportements différents peut être très différente selon le polymère considéré [24]. En effet, plus l'enchevêtrement des chaînes est élevé, plus la valeur de $\dot{\varepsilon}_{trans}$ sera faible. À faible vitesse de déformation, le transfert de contraintes est efficacement redistribué sur toute la longueur des

chaînes enchevêtrées (Figure 4). Si la structure de la chaîne n'a pas assez de temps pour s'adapter à la déformation, l'endommagement commencera à apparaître dans le matériau de plus en plus tôt. Cet effet s'appelle le phénomène de verrouillage [25]. Par conséquent, les tendances sont opposées à celles observées pour les métaux: la valeur de ε_p^f diminue avec la vitesse de déformation.

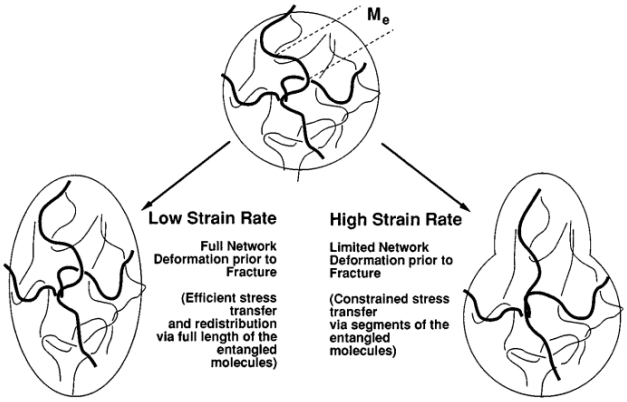

Figure 166 - Effet de la vitesse de déformation sur la structure de chaînes enchevêtrées des polymères [25]

ii. Modélisation de la rupture

La déformation plastique à l'initiation de la rupture ε_p^f est sensible à la triaxialité σ^*, à la vitesse de déformation $\dot{\varepsilon}_p$ et à la température T et montre un effet couplé entre ces deux derniers paramètres. La construction d'un modèle multiplicatif [26] qui prend en compte tous ces effets peut conduire à l'expression suivante (Eq. 9):

$$\varepsilon_p^f(\sigma^*, \dot{\varepsilon}_p, T) = f_\sigma(\sigma^*) f_{SR}(\dot{\varepsilon}_p) f_T(\dot{\varepsilon}_p, T) \quad (9)$$

La fonction f_σ modélise la sensibilité à l'état de contrainte et modélise la valeur de ε_p^f dans les conditions de vitesse de déformation et de température de référence. La fonction f_{SR} vise à modéliser l'évolution de ε_p^f en condition isotherme avec la vitesse de déformation et f_T décrit la sensibilité à la température de ε_p^f avec éventuellement un couplage avec la vitesse de déformation.

De nombreuses expressions pour chacune de ces fonctions peuvent trouvées dans la littérature [27] afin de développer un modèle sur mesure pour le matériau considéré.

L'évolution de l'endommagement est ensuite modélisée suivant des expressions telles que des modèles énergétiques ou tenants compte l'évolution de fraction volumique de vide (germination, croissance et coalescence de vides) comme les modèles de Tvergaard [28], Gurson [29] ou NAG [30].

Chapitre 2 – Caractérisation mécanique des matériaux métalliques et polymères

1. Matériaux

a. Alliage d'aluminium F7020

La dénomination F7020 correspond à un alliage d'aluminium spécifique mis en forme avec le procédé de frittage Spark Plasma Sintering (SPS). La densité du F7020 est $\rho = 2880\ kg.m^{-3}$ et sa chaleur spécifique est $C_p = 875\ J.kg^{-1}.K^{-1}$ Le module élastique est $E = 72\ GPa$ et le rapport Poisson $\nu = 0.3$. La composition chimique du F7020 se trouve dans le Tableau 1.

Tableau 42 – Composition chimique de l'alliage d'aluminium F7020

	Element	Al	Zn	Mg	Cu	Fe	Si
F7020	Wt. %	Bal.	4.80	1.20	<0.20	<0.35	<0.35

Les alliages d'aluminium sont considérés comme des métaux CFC qui présentent un durcissement structurel cinématique en raison de la germination et de la propagation des forêts de dislocations. A température ambiante, les principales phases en présence sont, en plus de matrice Al, $MgZn_2$ (6 %) et Al_6Mn (1.5 %) (Figure 5) [31, 32]. Ces deux phases se dissolvent dans la matrice à environ 500 K et une phase Al-Fe-Mn-Si apparaît.

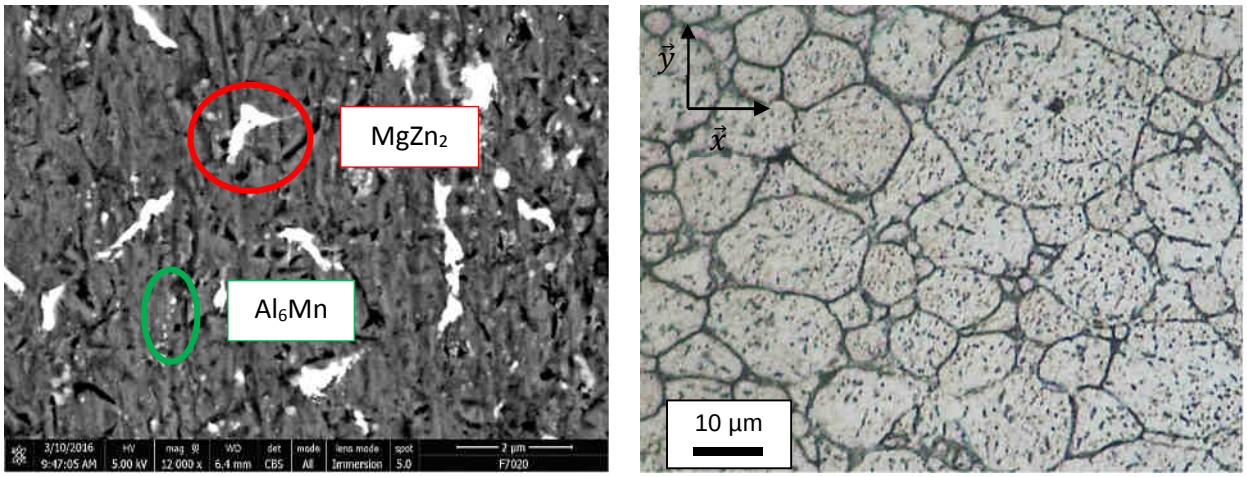

(a) (b)

Figure 167 – Images (a) MEB et (b) optique de l'alliage d'aluminium fritté F7020

b. Polyimide fritté

Le polyimide (PI) étudié dans ce travail a été fritté à l'aide du procédé Spark Plasma Sintering (SPS) (Figure 6.a). Le polyimide est un polymère thermoplastique amorphe avec des propriétés mécaniques très élevées (enchevêtrement limité). De telles performances mécaniques sont principalement dues à la très grande température de transition vitreuse du polyimide fritté ($T_g = 583\ K$ – Figure 6.b) qui permet une forte résistance à la déformation à température ambiante. À une

température encore plus élevée ($T_d \approx 683$ K), le polymère atteint son état de dégradation conduisant à une défaillance globale du matériau. La densité (à température ambiante) du PI $\rho = 1380\ kg.m^{-3}$ et sa chaleur spécifique est $C_p = 1170\ J.kg^{-1}.K^{-1}$. Le ratio de Poisson est pris comme $\nu = 0.4$.

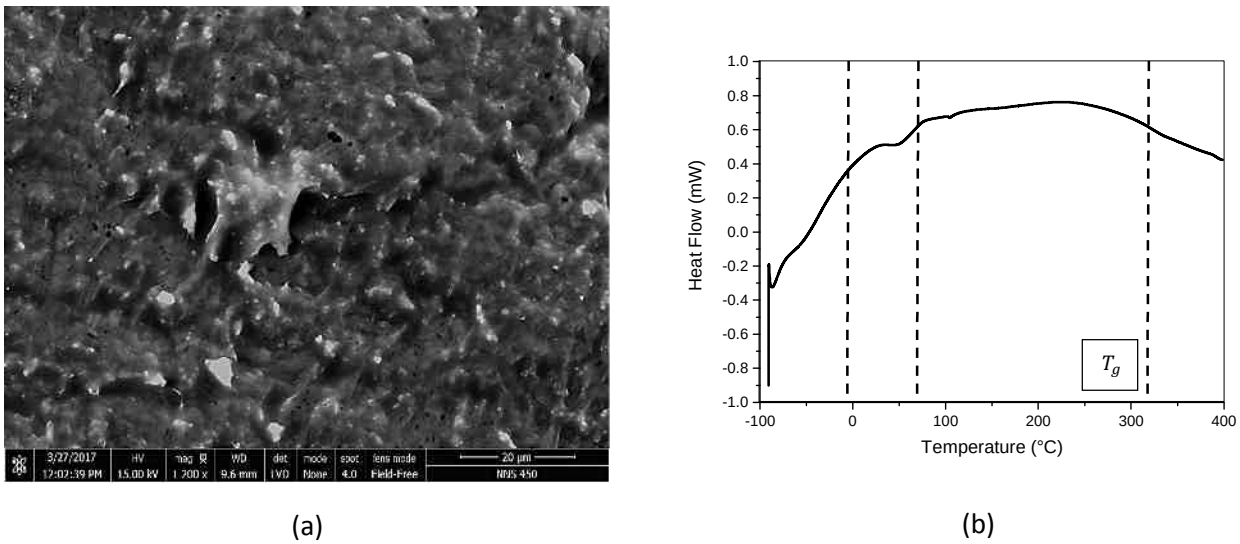

(a) (b)

Figure 168 - (a) Image MEB et (b) résultat DSC du polyimide fritté

2. Analyse du comportement mécanique des matériaux

a. Alliage d'aluminium F7020

Il a été expliqué précédemment que le comportement mécanique des matériaux métalliques se compose de deux contraintes différentes: contraintes athermique et thermique. Les deux composantes de contrainte de la contrainte thermique (contraintes interne et effective) ont leur propre réponse spécifique à la vitesse de déformation et doivent être étudiées séparément. Le comportement mécanique du F7020 est étudié ici avec des tests de compression. Le matériel est supposé isotrope en raison de la nature du processus SPS.

La contrainte interne est la partie de la contrainte thermique correspondant à la contribution du durcissement structurel du métal. La sensibilité à la vitesse de déformation observée est causée par la différence d'histoire de dislocations entre les différents tests qui peut être représentée par l'augmentation de la densité des dislocations forêt stockées. Les données expérimentales (Figure 7.a) ont été obtenues par compression à température ambiante avec une presse uniaxiale pour les conditions quasi-statiques et intermédiaires dynamiques (de 0,0001 / s à 1 / s). Les tests dans des conditions ont été effectués avec des essais SHPB [33] (de 500 / s à 15 000 / s) et avec des tests d'impact direct (de 10 000 / s à 55 000 / s). D'autres tests ont été effectués dans l'état de contrainte de compression-cisaillement [34].

La Figure 7.b montre le comportement de durcissement plastique dû à la multiplication des dislocations stockées en raison de la propagation des dislocations mobiles [8] (et des sources Frank et Read). Ce type de comportement est typique des métaux présentant un durcissement cinématique avec un durcissement linéaire à haute déformation. Les étapes III et IV de durcissement sont clairement visibles sur ces courbes [35], mais les étapes I et II semblent négligeables.

La sensibilité à la vitesse de déformation de la contrainte interne peut être considérée suivant une échelle logarithmique (Figure 7.c). Le régime de sensibilité à la vitesse de déformation peut être séparé en deux domaines. Le premier est essentiellement dans le domaine quasi-statique (jusqu'à environ 100 /s) et correspond au domaine où le mouvement des dislocations est régi par les mécanismes thermo-activés [9]. La sensibilité à la vitesse de déformation est quasi-nulle pour le F7020 sur cette gamme de vitesse de déformation. Le second domaine correspond aux vitesses de déformation plus élevées. La sensibilité à la vitesse de déformation y est beaucoup plus élevée que dans le premier domaine. Cela est causé par l'augmentation de l'effet de « viscous drag » avec la vitesse de déformation [9].

La contrainte effective a été étudiée séparément et présente une sensibilité linéairement positive à la vitesse de déformation.

Concernant la sensibilité de la contrainte thermique avec la température (Figure 7.d), l'adoucissement observé est non linéaire. En effet, autour de 500 K, la dissolution des précipités de $MgZn_2$ (au fort potentiel durcisseur) et d'Al6Mn et l'apparition de la phase Al-Fe-Mn-Si causent un changement important dans le comportement mécanique du F7020. Un plateau quasi-athermique est observé pour les températures supérieures à 500 K.

La contrainte est calculée à partir de la taille de l'obstacle aux dislocations le plus grand. Il s'agit de la taille moyenne de grains $\langle D_g \rangle = 14\ \mu m$ (Figure 5.b). Pour les matériaux CFC, elle est considérée comme étant constante et dans ce cas $Y_a = 36.5\ MPa$.

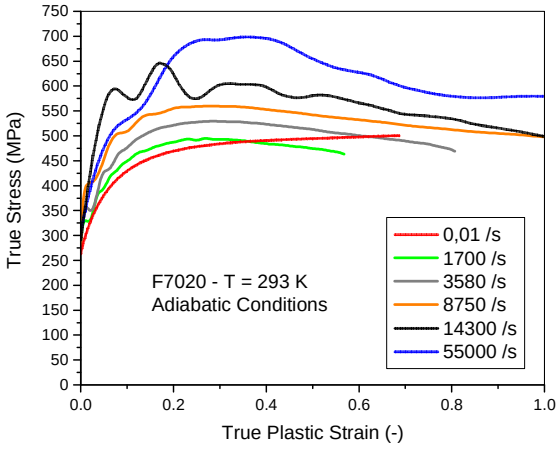

(a)

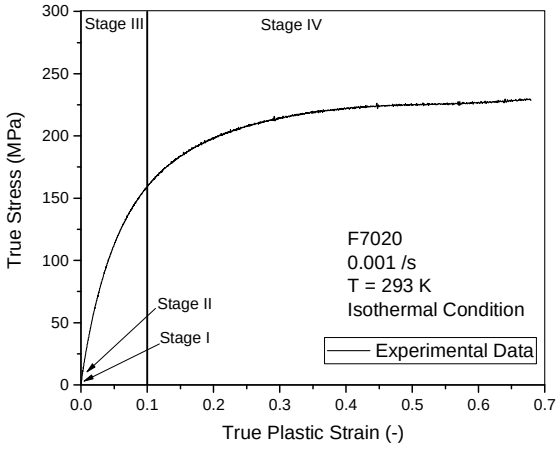

(b)

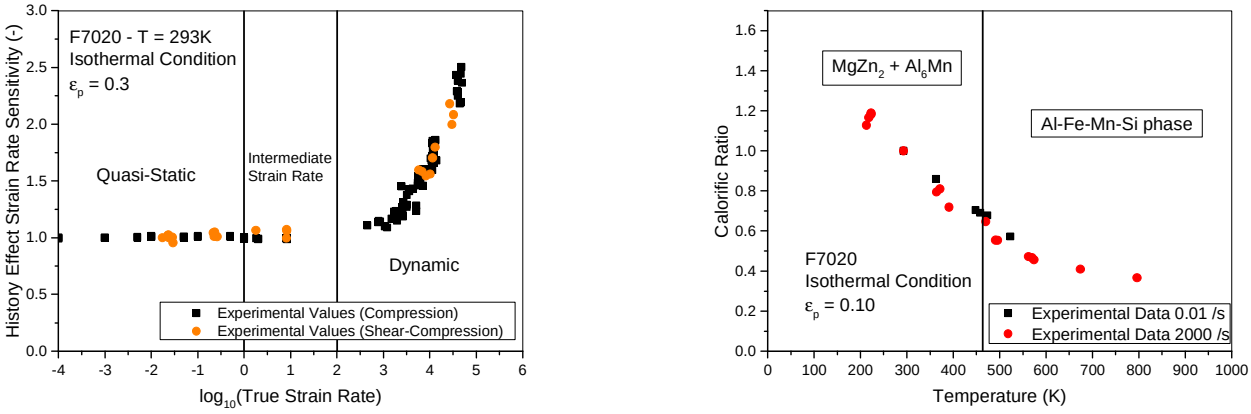

(c) (d)

Figure 169 – (a) Comportement de la contrainte à température ambiante sur une large gamme de vitesses de déformation du F7020, (b) focus sur l'écrouissage du F7020, (c) sensibilité normalisée à la vitesse de déformation de la contrainte interne du F7020 et (d) évolution du ratio calorifique avec la température du F7020

b. Polyimide fritté

Le comportement mécanique des polymères amorphes peut s'expliquer par quatre phénomènes principaux : le phénomène de viscoélasticité, la limite d'élasticité définissant le niveau de contrainte globale (dépend de la température et de la déformation), l'hyperélasticité représentant la résistance à l'alignement du réseau de chaînes (dépend de la température et de la déformation) et l'adoucissement plastique, résultat du phénomène de relaxation des chaînes provoquant une libération de l'énergie stockée dans les chaînes et une diminution de la contrainte.

Le polyimide présente clairement chacun de ces phénomènes mécaniques qui peuvent donc être étudiés, interprétés puis modélisés. De plus, ce polymère particulier présente un niveau de contrainte très élevé pour un polymère (Figure 8.a). Le comportement mécanique du polyimide est étudié ici avec des tests de compression (le matériau est supposé isotrope en raison de la nature du processus de frittage).

La dépendance à la vitesse de déformation de la limite élastique du polyimide se compose en deux domaines à une température donnée (Figure 8.b). Les deux domaines augmentent de façon monotone avec une pente plus raide dans le domaine dynamique [4]. Cette observation peut être effectuée pour toutes les températures testées, même si la pente dans le domaine dynamique devient plus raide lors de l'augmentation de la température et révèle un couplage de la vitesse de température/déformation. Plus l'enchevêtrement des chaînes est fort, plus la sensibilité à la vitesse de déformation est élevée.

La Figure 8.c montre la sensibilité expérimentale du module de caoutchouc C_R à la température et la vitesse de déformation [36]. On constate que le comportement hyperélastique entraîne un durcissement du matériau en diminuant la température et en augmentant la vitesse de déformation. L'adoucissement de C_R avec la température est dû aux vibrations beaucoup plus élevées des chaînes qui provoquent un phénomène de reptation plus facile réduisant alors le niveau de réticulation des chaînes polymères. Le durcissement de C_R avec la vitesse de déformation est causé par la durée de la déformation locale des chaînes qui devient plus courte que le temps de relaxation caractéristique

(qui permet une réorganisation optimale des molécules). Par conséquent, à des vitesses de déformation élevées, les chaînes interfèrent dans le mouvement des autres plus qu'à faibles vitesses. On peut supposer que le module caoutchoutique devient nul au-dessus de la température de transition vitreuse pour le polyimide. Le comportement couplé à la température/déformation observée de C_R doit être soigneusement modélisé.

L'adoucissement plastique correspond à l'effet de la relaxation du réseau de chaîne après la limite d'élasticité atteinte, ce qui conduit à une réorganisation optimale du réseau de la chaîne. Beaucoup de molécules sont moins étirées au cours de ce phénomène et il en résulte une libération d'énergie du matériau au niveau macroscopique. L'équilibre énergétique peut être observé en considérant le rapport de l'équilibre énergétique du comportement mécanique expérimental complet du polymère et du comportement estimé en considérant uniquement les phénomènes de limite élastique et d'hyperélasticité. La Figure 8.d montre l'évolution de l'équilibre énergétique normalisé en fonction de la déformation plastique. On peut voir que le matériau libère de l'énergie stockée pour atteindre un minimum à $\varepsilon_p \sim 0.27$ et augmente jusqu'à la rupture ultime du matériau. Cette augmentation peut être interprétée comme le phénomène opposé de la relaxation qui est le frottement entre les molécules étirées.

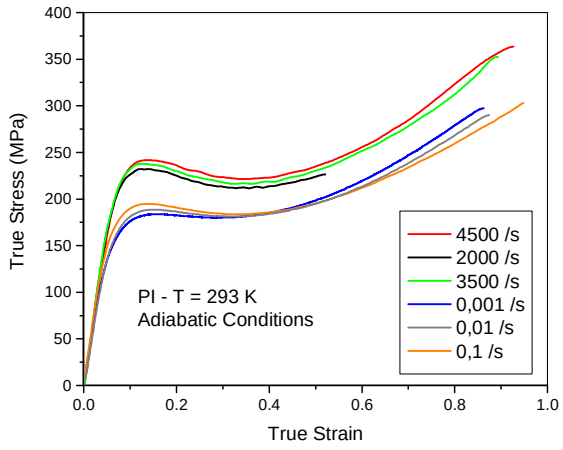

(a)

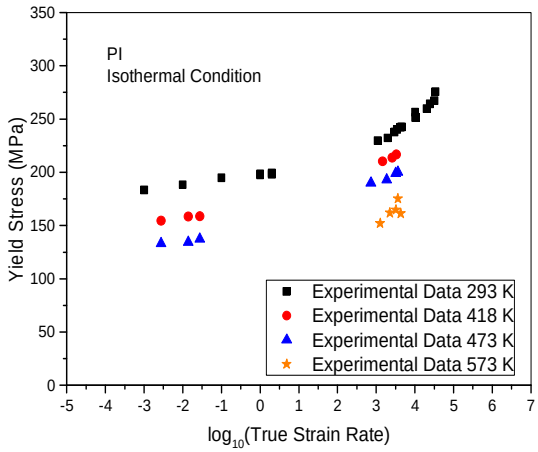

(b)

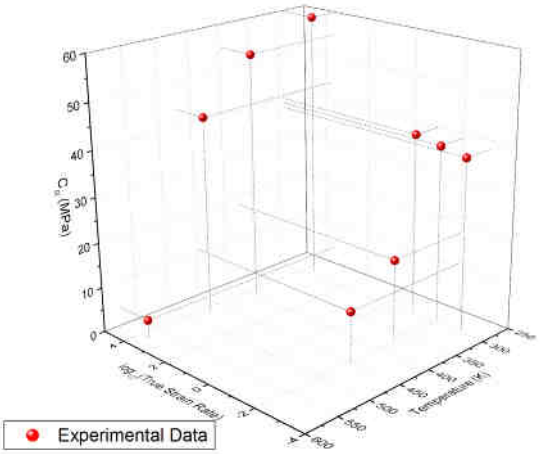

(c)

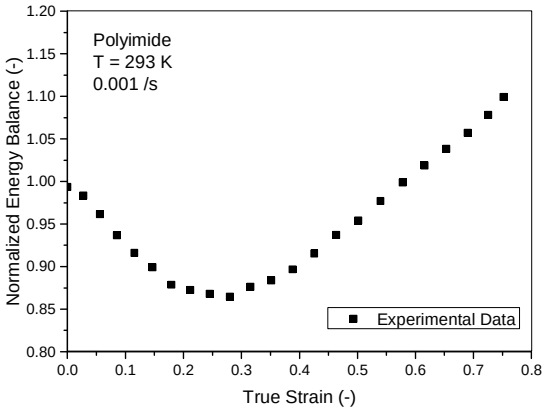

(d)

Figure 170 – (a) Comportement de la contrainte à température ambiante sur une large gamme de vitesses de déformation du polyimide fritté, (b) évolution de limite d'élasticité du polyimide fritté avec la vitesse de déformation et la température, (c) sensibilité du module caoutchoutique du polyimide fritté avec la température et la vitesse de déformation et (d) évolution de la balance énergétique de l'adoucissement plastique avec la déformation pour le polyimide fritté

3. Analyse du comportement à la rupture des matériaux

La caractérisation des mécanismes menant à la rupture des matériaux revêt une importance capitale pour la modélisation mécanique des structures. Le critère utilisé dans ce travail est la contrainte plastique à l'initiation de la rupture ε_p^f.

a. Alliage d'aluminium F7020

Le mécanisme responsable de la rupture pour les sollicitations ayant une triaxialité positive est la décohésion des grains de poudre frittés [37] (rupture intergranulaire mésoscopique – Figure 9.a). Par conséquent, ces tests ne donnent que la réponse mécanique de la structure frittée et non les propriétés intrinsèques du matériau. L'influence de la température et de la vitesse de déformation de ε_p^f ne peuvent être étudiées à travers ce type de tests avec un état de contrainte positif.

Pour cela, des essais de compression-cisaillement ont été réalisé [34]. Ces tests permettent la rupture des grains de poudre par des mécanismes de cisaillement (Figure 9.b). Comme on peut le voir, la rupture est effectuée par déformation des grains de poudre et plus particulièrement par la germination des bandes de cisaillement adiabatique. Dans ces conditions, les propriétés mécaniques du F7020 sont impliquées dans les mécanismes de la rupture. Les sensibilités à la température et à la vitesse de déformation des mécanismes de rupture peuvent donc être étudiées.

Pour résumer le comportement de ε_p^f du F7020 avec l'état de contrainte, on constate que sa valeur diminue exponentiellement avec la triaxialité (Figure 9.c). Aucune rupture n'a été observée dans l'état de contrainte de contrainte ($\sigma^* = -\frac{1}{3}$).

La sensibilité de ε_p^f à la vitesse de déformation est quasi-nulle jusqu'à environ 1000 /s où elle commence à augmenter exponentiellement (Figure 9.d). Cet effet est causé par des phénomènes de micro-inerties liés à l'effet de « viscous drag ».

Sur la figure 9.e, on peut voir clairement l'évolution de la déformation à l'initiation de la rupture avec la température: une augmentation entre la température ambiante et environ 490 K. Celle-ci est suivie d'un plateau athermique jusqu'à 773 K et enfin Une augmentation très importante jusqu'à la fusion complète du matériau. La présence du plateau athermique s'explique par la microstructure du matériau. En effet, la dissolution des précipités de durcissement dans la matrice d'aluminium s'est produite autour de 500 K et après cette température, la microstructure présente peu d'évolutions. En effet, les mécanismes de diffusion dus à l'élévation de température n'influencent plus les précipitations car ils sont complètement dissous dans la matrice.

Dans cette étude, la quantification de l'endommagement est effectuée grâce à l'évaluation d'une énergie absorbée par le matériau à partir de l'initiation de la rupture. La quantité d'énergie absorbée par le matériau après le critère Considère est calculée pour chaque test et est étudiée en fonction de l'état de contrainte (Figure 9.f) [38]. Dans les cas d'états de contrainte positifs, l'énergie d'endommagement est supposée inexistante en raison du comportement fragile de la rupture (le critère de Considère n'est même pas atteint). Cependant, il peut être facilement calculé avec les tests présentant une triaxialité négative (tests de cisaillement-compression). En outre, l'évolution de cette

énergie avec la vitesse de déformation n'a révélé aucune sensibilité particulière de même qu'avec la température. Par conséquent, seule la dépendance à la triaxialité est considérée pour le F7020.

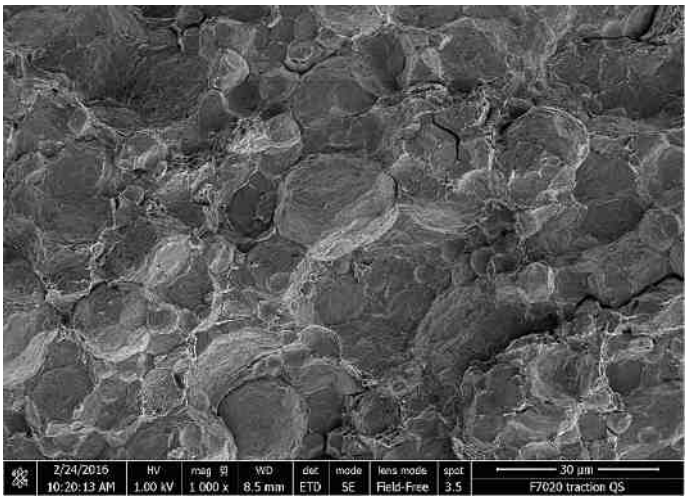

(a)

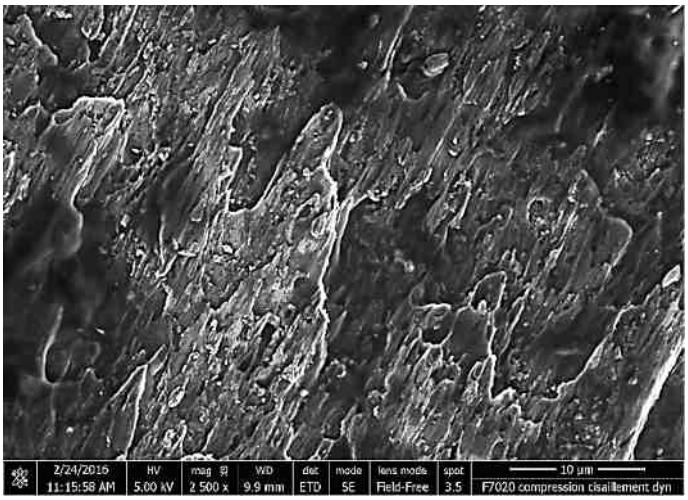

(b)

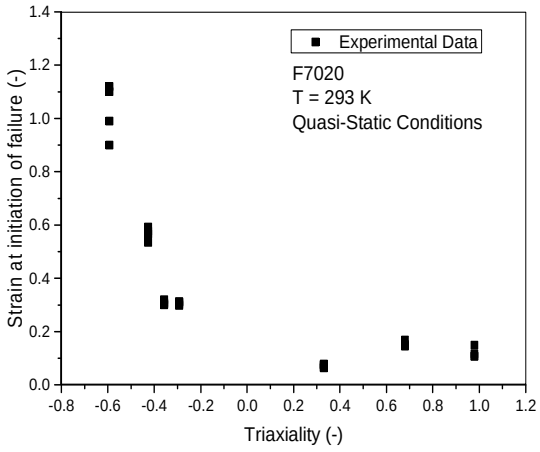

(c)

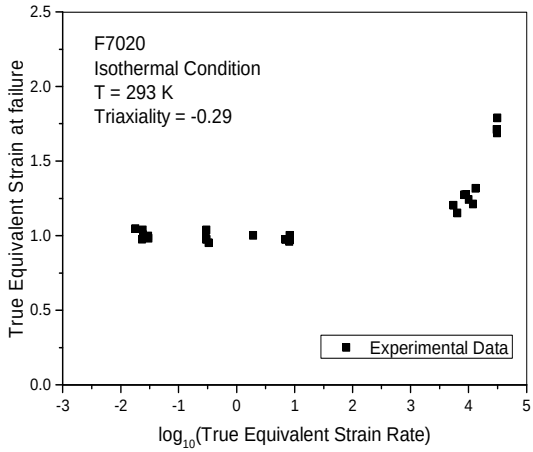

(d)

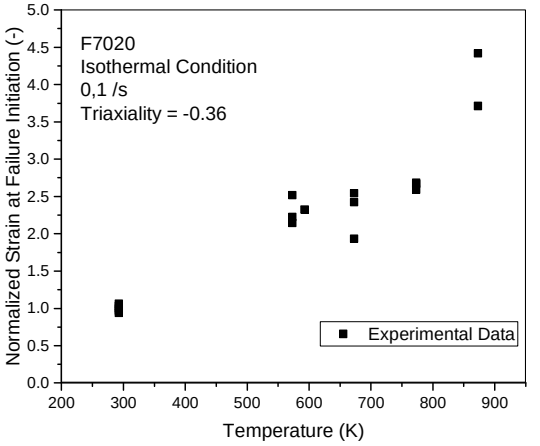

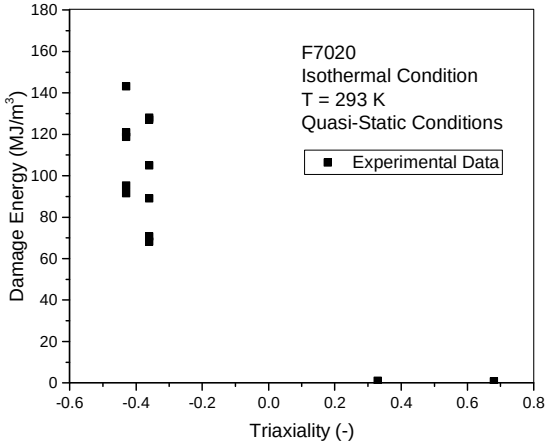

(e) (f)

Figure 171 – (a) Image MEB du faciès de rupture en traction et (b) en compression-cisaillement du F7020, sensibilité de la déformation à l'initiation de la rupture avec (c) la triaxialité, (d) la vitesse de déformation et (e) la température et (f) la sensibilité de l'énergie d'endommagement avec la triaxialité du F7020

b. Polyimide fritté

Le polyimide fritté présente le même type de rupture par décohésion des grains de poudres frittés que le l'alliage d'aluminium F7020 présenté précédemment pour des essais présentant un état de contrainte positif (comme la traction). Il peut être noté que le polyimide fritté est extrêmement fragile en traction où il ne présente même pas de domaine plastique (élastique-fragile). Par conséquent, un test présentant un état de contrainte permettant une rupture par déformation de ces grains est utilisé pour l'étude des sensibilités à la vitesse de déformation et à la température de ε_p^f. Il s'agit ici de l'état de compression. En effet, en état de compression, le polymère atteint une valeur critique de déformation à laquelle l'échantillon éclate en raison du blocage de la structure des chaînes (phénomène de verrouillage des chaînes). Le résumé du comportement mécanique en fonction de la triaxialité de la déformation à l'initiation de la rupture du polyimide fritté se trouve à la Figure 10.a.

La sensibilité à la vitesse de déformation de ε_p^f du polyimide a été étudiée à travers les essais de compression. Les mécanismes de rupture pour de tels matériaux sont contrôlés par l'étirement local des chaînes provoqué par un transfert de contraintes le long de leurs segments de molécule enchevêtrés. La sensibilité à la vitesse de déformation est pratiquement inexistante sur une large gamme de vitesses de déformation et diminue soudainement à partir de $\dot{\varepsilon}_p^{trans} = 10^4\ /s$ en raison du verrouillage de la structure des chaînes [25] (Figure 10.b). La valeur élevée de la vitesse de déformation de transition signifie que le temps caractéristique de relaxation de la structure des chaînes est assez faible et permet une réorganisation rapide des chaînes polymères. Plus l'enchevêtrement des chaînes est fort, moins la vitesse de déformation de transition $\dot{\varepsilon}_p^{trans}$ le sera.

La sensibilité à la température a également été étudiée avec les expériences de compression. La sensibilité à la vitesse de déformation de ε_p^f est considérée ici dans son état isotherme. La valeur de la contrainte lors de la rupture ε_p^f est directement liée au paramètre de verrouillage N ($\varepsilon_p^f = \frac{\ln N}{2}$). La sensibilité à la température (Figure 10.c) semble être linéaire sur la gamme des températures testées. Cette tendance s'explique principalement par la reptation plus rapide et plus facile des chaînes pour les températures plus élevées conduisant à une plus grande mobilité des chaîne dans les fibrilles et donc à la diminution du temps caractéristique de la relaxation des chaînes (augmentation de la valeur du paramètre de verrouillage N). Le phénomène de verrouillage est donc atteint plus tard dans les fibrilles en raison de leur grande mobilité et les fissures se propagent lentement, retardant la défaillance du matériau.

L'évolution de l'énergie d'endommagement (après l'initiation des mécanismes de rupture) est étudiée en fonction de l'état de contrainte [38] (Figure 10.d). En effet, la différence de mode de rupture entre la triaxialité positive (décohésion de la poudre de grain) et négative conduit également à deux comportements d'endommagement très différents:

- En cas de triaxialité positive, la rupture est fragile et aucune énergie d'endommagement n'est observée. Les mécanismes de rupture sont presque instantanés en raison de la décohésion simultanée de la poudre de grain sous le chargement (décohésion intergranulaire mésoscopique).

- En cas de triaxialité négative, les mécanismes de rupture entraînent l'apparition du phénomène de verrouillage des chaînes polymères et une rupture progressive: une énergie d'endommagement peut être observée (décohésion intragranulaire).

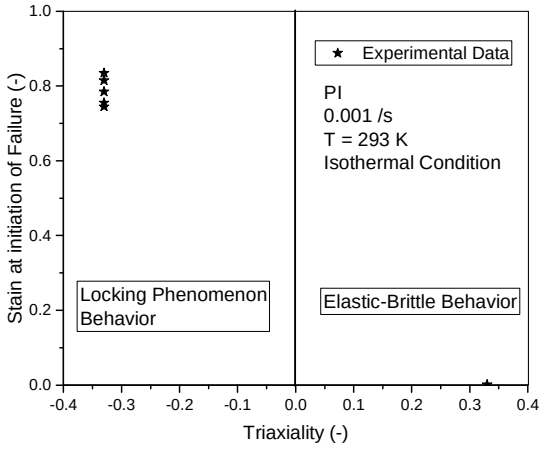

(a)

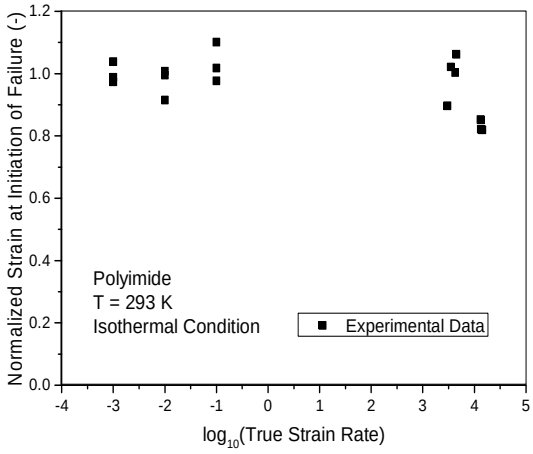

(b)

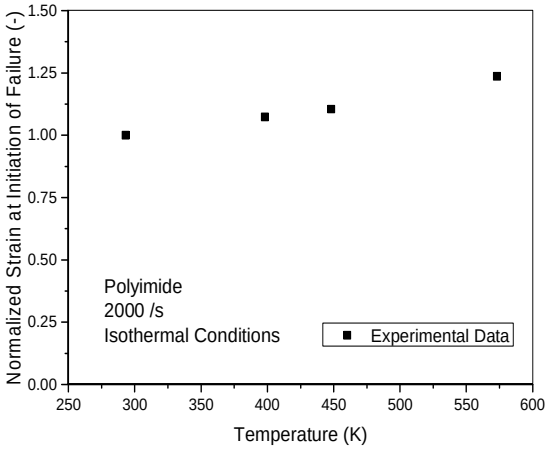

(c)

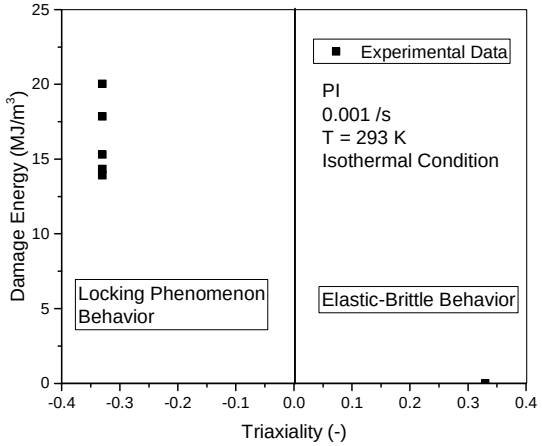

(d)

Figure 172 – Sensibilité de la déformation à l'initiation de la rupture du polyimide fritté avec (a) la triaxialité, (b) la vitesse de déformation et (c) la température et (d) la sensibilité de l'énergie d'endommagement avec la triaxialité du polyimide fritté

La même approche d'étude du comportement mécanique (contrainte et rupture) que celle utilisée pour le polyimide fritté a été employée pour la résine epoxy étudiée dans cette thèse.

Chapitre 3 – Modélisation du comportement mécanique

1. Modélisation de la contrainte plastique

a. Alliage d'aluminum F7020

Afin de tenir compte de tous les phénomènes observés et discutés dans la partie précédente, une approche pour construire des modèles constitutifs spécifiques pour un matériau métallique a été développée : l'approche Crystallo-Calorific Hardening (CCH) [3]. Seul le cas de la FCC sera discuté dans ce travail. L'expression analytique globale du modèle constitutif pour la contrainte peut être écrite avec Eq. 10.

$$\sigma(\varepsilon_p, \dot{\varepsilon}_p, T) = \sigma_{ath}(\varepsilon_p) + \sigma_{eff}(\dot{\varepsilon}_p, T)\Omega(\dot{\varepsilon}_p, T) + \sigma_{int}(\varepsilon_p, \dot{\varepsilon}_p, T)\Omega(\dot{\varepsilon}_p, T_0) \quad (10)$$

Avec σ_{ath}la contrainte athermique, σ_{eff} la contrainte effective, σ_{int} la contrainte interne, Ω le ratio calorifique et T_0 la température initiale.

Chacune des contributions à la contrainte globale σ (σ_{int}, σ_{eff}, Ω et σ_{ath}) peut être modélisée en utilisant des expressions appropriées. Les expressions suggérées dans ce travail pour décrire chacun de ces phénomènes peuvent être remplacées par tout autre qui pourrait être considérées comme plus adaptées pour le matériau considéré. L'expression présentée dans ce chapitre a été choisie pour obtenir un haut niveau de précision pour la modélisation de la contrainte globale σ.

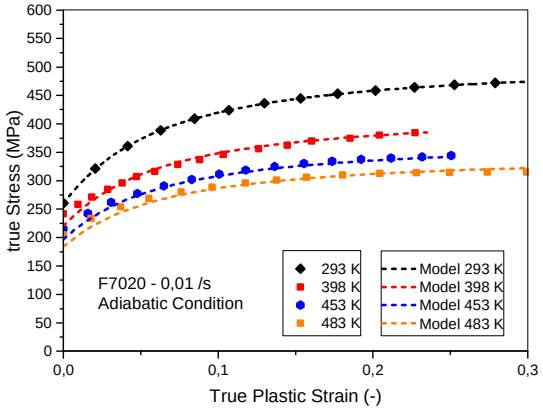

(a)

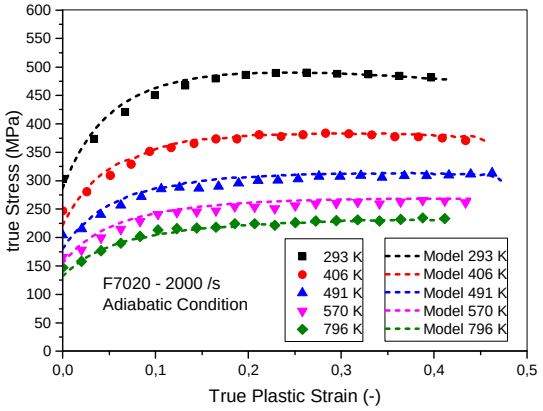

(b)

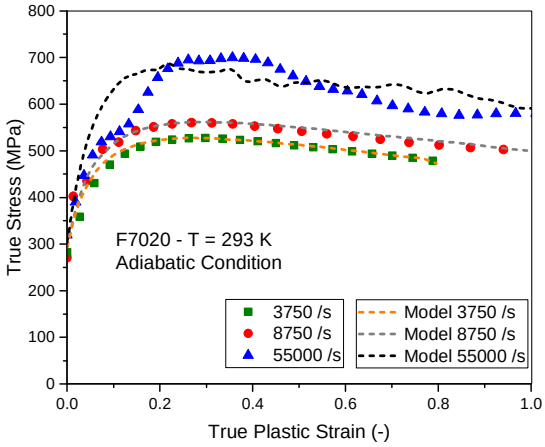

(c)

Figure 173 - Modélisation du comportement mécanique du F7020 (a) en quasi-statique, (b) en dynamique et (c) à très hautes vitesses de déformations

Les différentes expressions utilisées pour modéliser les différents phénomènes sont rassemblées dans le modèle complet du stress général σ (Eq. 10). La précision du modèle CCH construit est ensuite contrôlée sur de larges plages de température et de contraintes.

La modélisation dans des conditions quasi statiques et dynamiques (Figure 11.a et 11.b) avec une température initiale différente présente un excellent résultat en raison de la capacité du rapport calorifique à prendre en compte les changements de microstructure et à l'expression non linéaire suggérée pour la modélisation de la sensibilité à la vitesse de déformation de la contrainte interne.

On peut voir sur la Figure 11.c, que le modèle CCH suggéré est en bonne corrélation avec les données expérimentales même à des taux de contrainte très élevés (55000 / s). Par conséquent, l'évolution de la contrainte du F7020 est très bien modélisée avec le modèle CCH proposé.

b. Polyimide fritté

Le comportement mécanique des polymères amorphes peut être représenté par les trois phénomènes suivants (détaillés au chapitre 2):

- La limite d'élasticité σ_y dépendante à la température et à la vitesse de déformation.
- L'hyperélasticité générant une contrainte de recouvrement σ_B dépendant de la température et de la vitesse de déformation augmentant exponentiellement avec la déformation.
- Le phénomène d'adoucissement plastique de la contrainte qui peut être observé comme un équilibre énergétique normalisé ψ. On suppose, dans ce travail, ce phénomène indépendant de la température et de la vitesse de déformation.

La contrainte σ correspondant au comportement mécanique macroscopique est calculée avec un modèle spécifique qui prend en compte les trois phénomènes précédents (Eq. 11).

$$\sigma(\varepsilon_p, \dot{\varepsilon}_p, T) = \left(\sigma_y(\dot{\varepsilon}_p, T) + \sigma_B(\varepsilon_p, \dot{\varepsilon}_p, T)\right)\psi(\varepsilon_p) \quad (11)$$

Dans cette étude, la limité d'élasticité σ_y est modélisée suivant le modèle coopératif [4], la contrainte hyperélastique σ_B avec le modèle de Gent [5] et le bilan de l'équilibre énergétique définissant l'adoucissement plastique par une expression phénoménologique développée pour ce travail (Eq. 12).

$$\psi(\varepsilon_p) = \frac{\sigma_{exp}}{\sigma_y + \sigma_{hyp}} = Ae^{B\varepsilon_p} + Ce^{D\varepsilon_p} \quad (12)$$

Avec A, B, C et D des paramètres phénoménologiques.

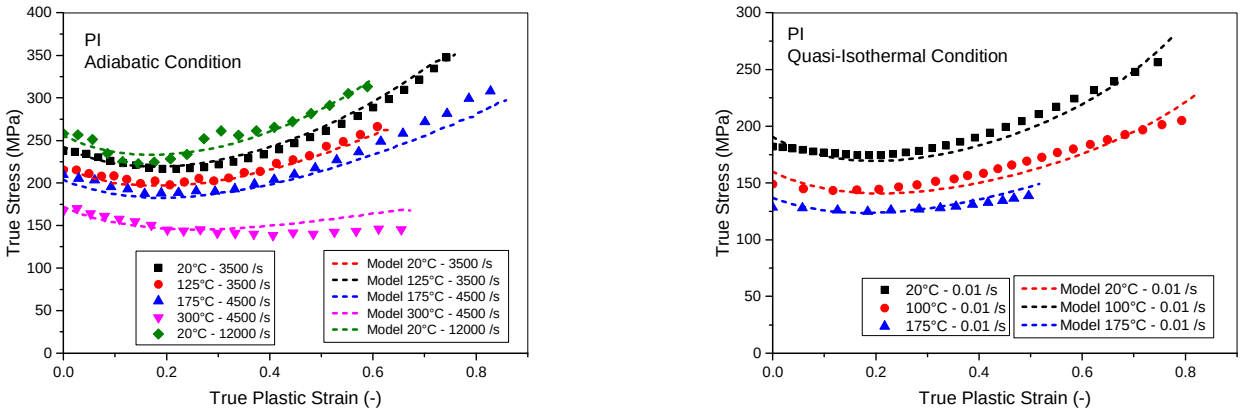

(a) (b)

Figure 174 - Modélisation du comportement mécanique du polyimide fritté (a) en dynamique et (b) en quasi-statique

Une fois que tous les phénomènes différents ont été modélisés séparément, les différentes expressions sont rassemblées afin de modéliser le niveau complet de contrainte σ du polyimide (Eq. 11).

De larges gammes de températures et de vitesses de déformation ont été testées et utilisées pour la validation du modèle suggéré (Figure 12.a et 12.b). On constate que le niveau de contrainte est correctement modélisé pour toutes les conditions en raison de la performance du modèle coopératif pour la limite d'élasticité. En outre, l'adoucissement thermique du phénomène d'hyperélasticité est bien représenté dans tous les cas (même à haute température). Le modèle suggéré fournit un outil efficace pour évaluer le niveau de stress concernant le polyimide fritté.

La résine epoxy étudiée dans cette thèse a été modélisée avec le même modèle.

2. Modélisation de la rupture

La modélisation constitutive de la rupture des matériaux étudiés s'effectue par une approche similaire qui consiste en deux étapes:

- La modélisation de la déformation plastique à l'initiation de la rupture en fonction de la triaxialité, de la vitesse de déformation et de la température.
- La modélisation de l'énergie d'endommagement après l'initiation de la rupture en fonction de la triaxialité (les sensibilités aux taux de température et de contrainte peuvent aussi être considérées).

La modélisation globale de la déformation plastique à l'initiation de la rupture ε_p^f est modélisée par une expression multiplicative qui peut être écrite par Eq. 9 [26].

Avec $f_{\sigma^*}(\sigma^*, \theta)$une fonction définissant l'évolution de ε_p^f avec l'état de contrainte aux états de référence de température et de vitesse de déformation (Figures 13.a et 13.b), f_{vf} une fonction correspondant à la sensibilité à la vitesse de déformation (Figures 13.c et 13.d) et f_{T_f} une fonction modélisant la sensibilité à la température (Figures 13.e et 13.f).

Les expressions choisies dans cette étude pour les différentes fonctions présentées sont les suivantes (Eqs. 13 à 16).

$$f_{\sigma^*}(\sigma^*) = d_1 + d_2 e^{d_3 \sigma^*} \quad (13)$$

$$f_{vf}(\dot{\varepsilon}_p) = 1 + l_{vf} \ln\left(\frac{\dot{\varepsilon}_p}{\dot{\varepsilon}_{0ff}}\right) + v_f \left(\frac{\dot{\varepsilon}_p}{\dot{\varepsilon}_{0ff}}\right)^{n_{vf}} \quad (14)$$

$$f_{T_f}(\dot{\varepsilon}_p, T) = \mho(\dot{\varepsilon}_p, T) = \left[\Omega(\dot{\varepsilon}_p, T)\right]^{-1} \quad (15)$$

$$f_{T_f}(T) = \left(1 + \frac{T - T_r}{T_g - T_r}\right)^m \quad (16)$$

L'énergie d'endommagement E_M est modélisée par l'expression suivante (Eq. 17) et utilisé suivant les Eqs. 18 et 19 [38] (Figures 13.g et 13.h) pour obtenir la contrainte tenant compte de l'endommagement σ_v.

$$E_M(\sigma^*) = A_E e^{B_E \sigma^*} \quad (17)$$

$$D = 1 - e^{\frac{\int_{\varepsilon_p^u}^{\varepsilon_p^f} \sigma d\varepsilon_p}{E_M(\sigma^*)}} \quad (18)$$

$$\sigma_v = \sigma(1 - D) \quad (19)$$

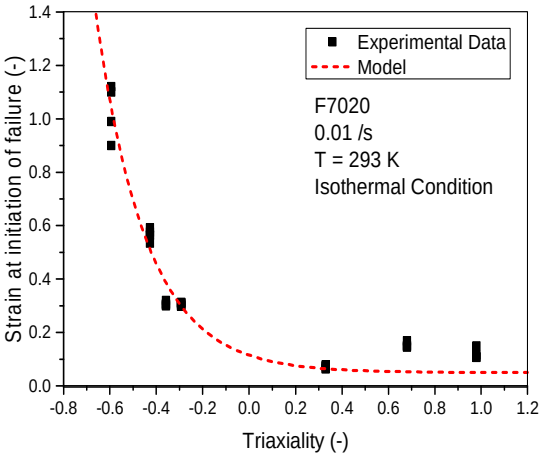

(a)

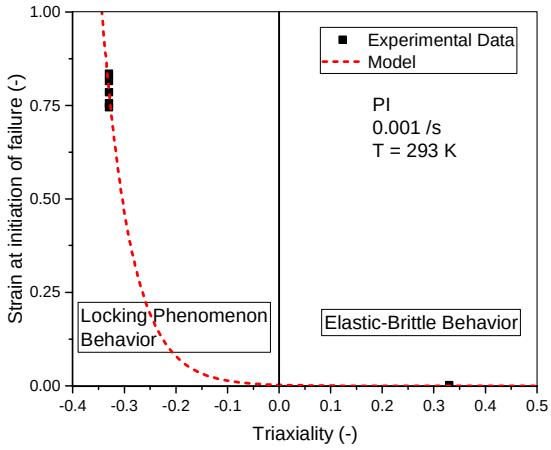

(b)

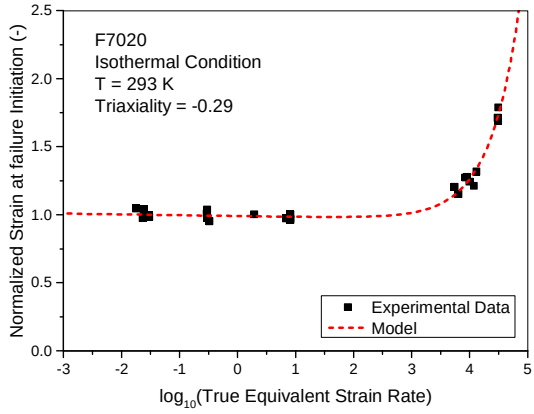

(c)

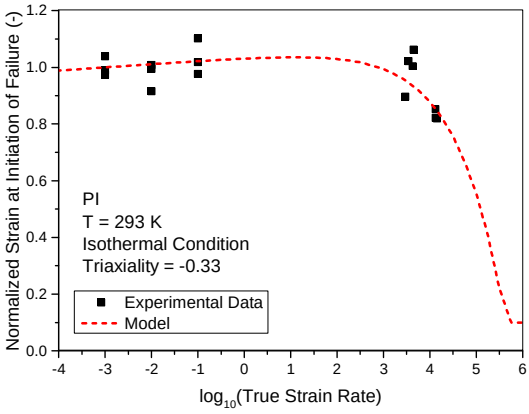

(d)

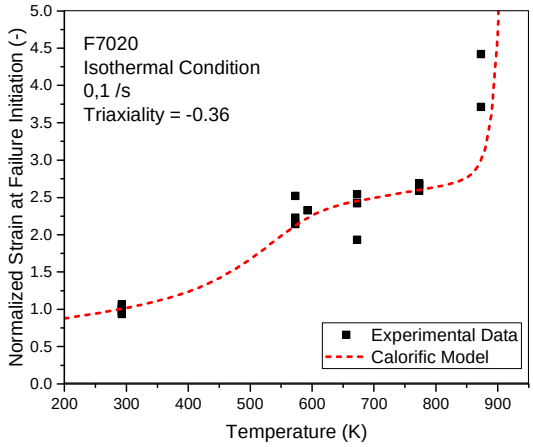

(e)

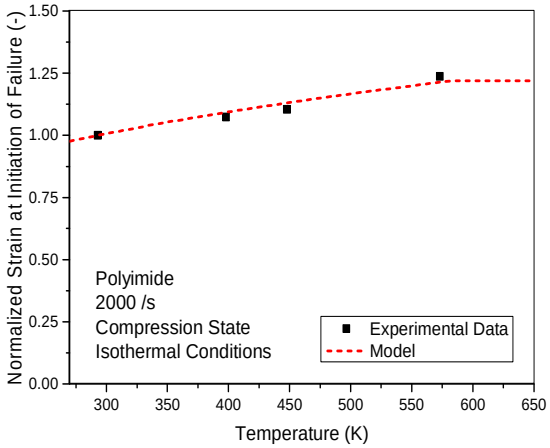

(f)

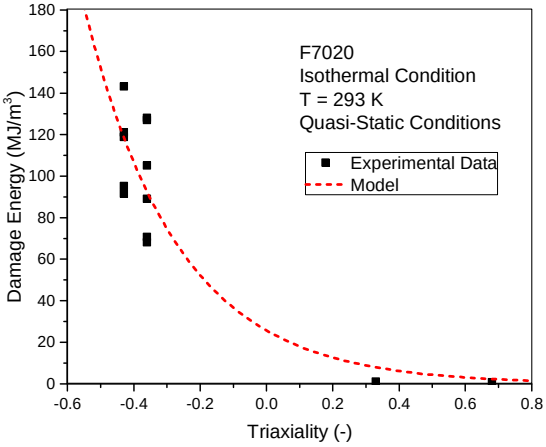

(g)

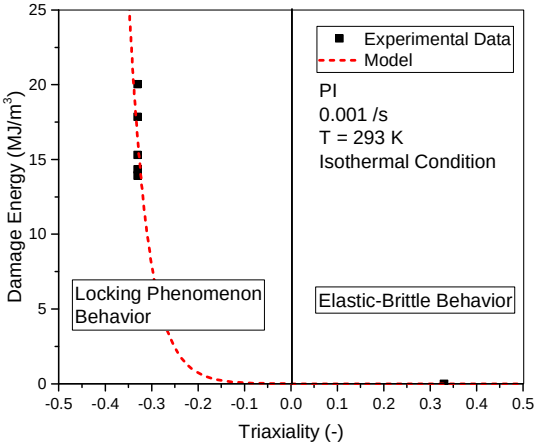

(h)

Figure 175 - Sensibilité de la déformation à l'initiation de la rupture à la triaxialité (a) du F7020 et (b) du polyimide fritté, à la vitesse de déformation (c) du F7020 et (d) du polyimide fritté et à la température (e) du F7020 et (f) du polyimide fritté ainsi que de l'énergie d'endommagement en fonction de la triaxialité pour (g) le F7020 et (h) le polyimide fritté

L'étude de caractérisation mécanique et de modélisation mécanique effectuée pour l'alliage d'aluminium F7020 et le polyimide thermoplastique fritté a également été faite pour la résine epoxy. Les résultats concernant ce matériau sont présents dans le manuscrit de thèse.

Chapitre 4 – Validation du modèle numérique par le biais d'essais d'impacts à hautes vitesses

Les résultats expérimentaux obtenus sur les structures impactées par les projectiles sphériques en acier, puis comparés aux simulations calculées avec ABAQUS®/Explicit en utilisant les subroutines VUMAT en code FORTRAN. Les modèles constitutifs suggérés dans la partie précédente sont utilisés dans la simulation afin d'évaluer les performances du modèle numérique.

1. Impact sur les matériaux monolithiques

Les essais d'impact d'une bille en acier sur les matériaux monocouches permettent de vérifier séparément la précision des modèles avant la modélisation du matériau multicouche.

a. Alliage d'aluminium F7020

Concernant l'alliage d'aluminium F7020, 12 essais ont été effectués pour la validation du modèle dans différentes configurations. Deux paramètres ont été étudiés pour les essais: la vitesse d'impact et l'épaisseur cible (2 mm, 2.5 mm, 3 mm et 4 mm). Le nombre d'essais d'impacts expérimentaux est limité à 12 en raison du processus de mise en forme complexe (Spark Plasma Sintering) qui ne permet pas la production en masse des matériaux étudiés.

Le modèle CCH (Eqs. 9 et 10) développé dans le cadre de la thèse et présenté dans le chapitre précédent a été utilisé dans les simulations. Les mesurables choisi pour évaluer l'efficacité du modèle numérique sont la vitesse résiduelle du projectile V_r et la vitesse du plug éjecté V_p. Ces derniers sont étudiés en fonction de la vitesse d'impact du projectile V_0.

Les Figures 14.a and 14.b montrent que le modèle CCH parvient à reproduire avec une excellente précision les phénomènes liés à la perforation à grande vitesses de l'alliage d'aluminium fritté F7020. On peut noter une convergence de la valeur de la vitesse résiduelle V_r vers la vitesse d'impact V_0 pour toutes les épaisseurs étudiées.

La Figure 14.c présente l'évolution d'un paramètre de performance balistique P_B (Eq. 20) en fonction de V_0 pour différentes épaisseurs de plaques. Ce paramètre permet de comparer les résultats balistiques pour des matériaux présentant des densités surfaciques A_d différentes.

$$P_B = \frac{{V_0}^2 - {V_r}^2}{A_d {V_0}^2} \qquad (20)$$

On observe que la valeur de P_B augmente avec l'épaisseur de la cible pour l'alliage d'aluminium fritté F7020. Cela signifie que le gain en rigidité de la cible compense l'augmentation de la densité surfacique.

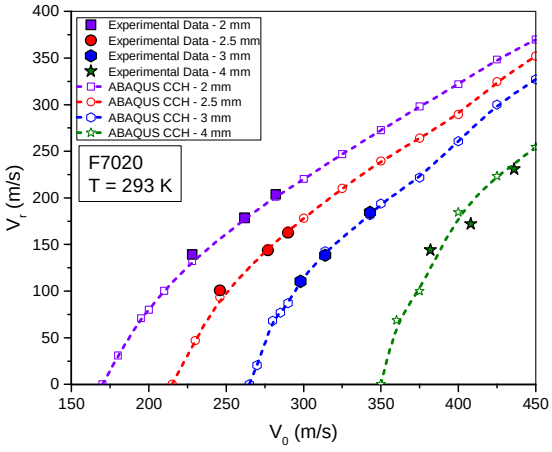

(a)

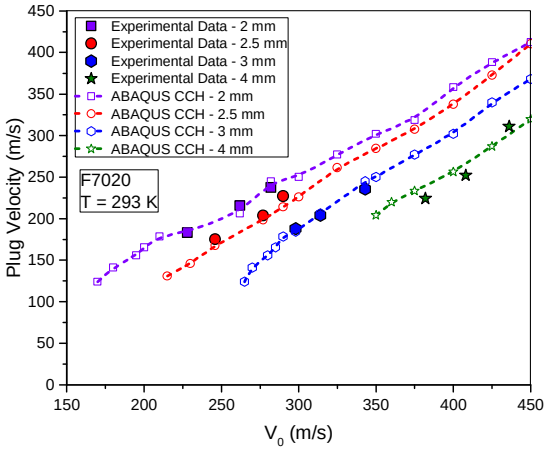

(b)

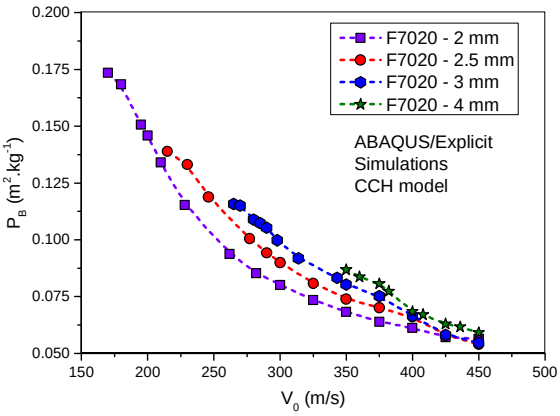

(c)

Figure 176 - Evolution en fonction de la vitesse d'impact du projectile de (a) la vitesse résiduelle du projectile, (b) la vitesse du plug et (c) de la performance balistique pour le F7020

b. Polyimide fritté

En ce qui concerne le polyimide fritté, 12 tests ont été effectués pour la validation du modèle dans différentes configurations. Comme indiqué précédemment pour l'alliage d'aluminium fritté F7020, deux paramètres ont été étudiés pour les essais: la vitesse d'impact et l'épaisseur cible (2 mm, 2.5 mm et 3 mm). Le nombre d'essais d'impacts expérimentaux est limité à 12 en raison du processus de mise en forme complexe (Spark Plasma Sintering) qui ne permet pas la production en masse des matériaux étudiés.

Le modèle utilisé pour les simulations est le modèle pour les polymères qui a été présenté dans le chapitre précédent (Eqs. 9 et 11). Les mesurables choisi pour évaluer l'efficacité du modèle numérique sont la vitesse résiduelle du projectile V_r et le diamètre arrière du cône de fragmentation (Back Channel Diameter). Ces derniers sont étudiés en fonction de la vitesse d'impact du projectile V_0.

Les Figures 15.a and 15.b montrent que le modèle unifié suggéré dans cette étude parvient à reproduire avec une excellente précision les phénomènes liés à la perforation à grande vitesses du polyimide fritté. On peut noter une convergence de la valeur de la vitesse résiduelle V_r vers la vitesse d'impact V_0 pour toutes les épaisseurs étudiées.

La Figure 15.c présente l'évolution d'un paramètre de performance balistique P_B (Eq. 20) en fonction de V_0 pour différentes épaisseurs de plaques. On observe que la valeur de P_B diminue avec l'épaisseur de la cible pour le poylimide fritté. Cela signifie que le gain en rigidité de la cible ne parvient pas à compenser l'augmentation de la densité surfacique.

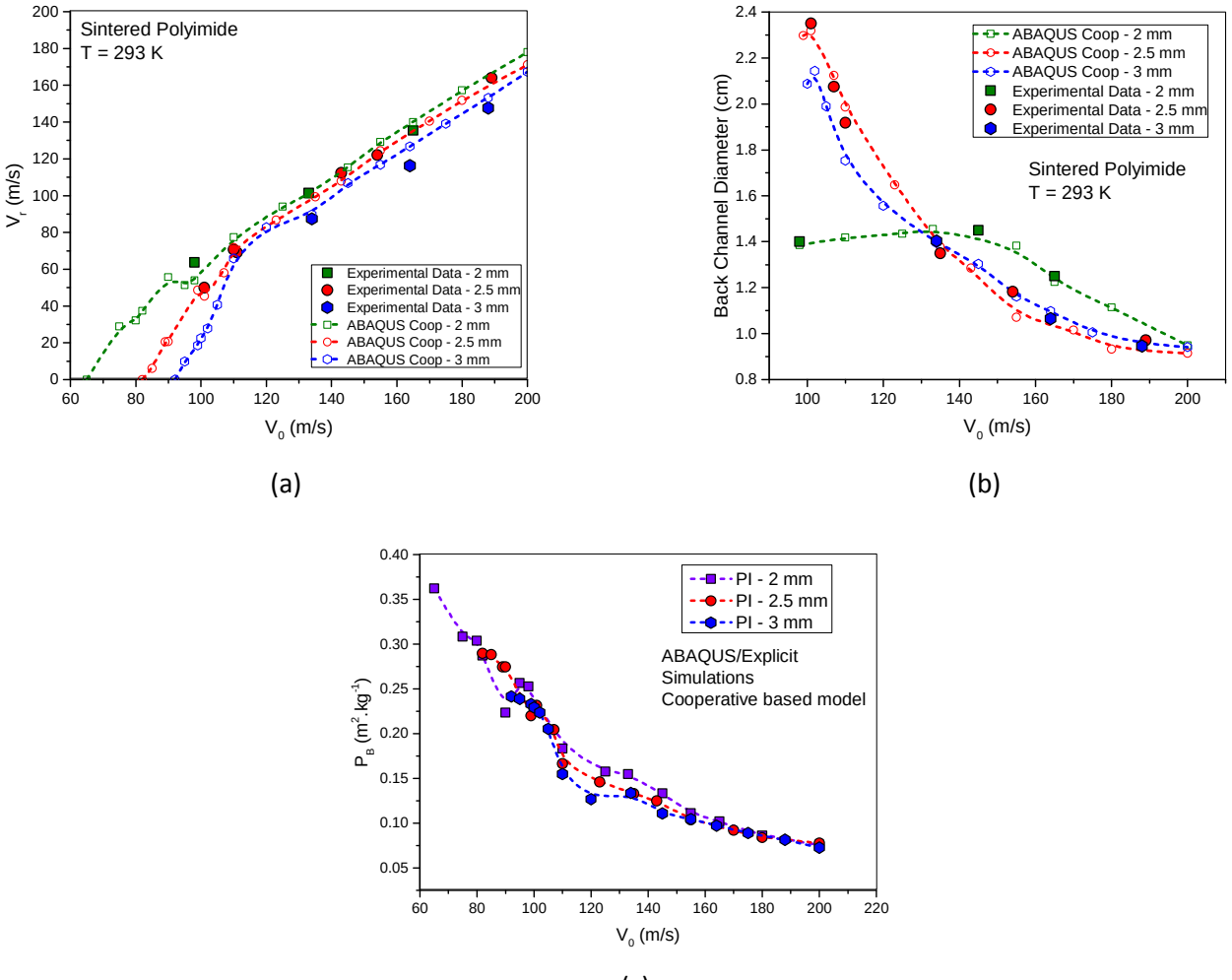

Figure 177 - Evolution en fonction de la vitesse d'impact du projectile de (a) la vitesse résiduelle du projectile, (b) diamètre arrière du cône de fragmentation de la cible et (c) de la performance balistique pour le polyimide fritté

2. Simulation d'impact sur les matériaux bicouches

Après la validation de la modélisation numérique des deux matériaux principaux dans les conditions d'impact (alliage d'aluminium F7020 et polyimide fritté), le modèle numérique des matériaux multicouches peut être effectué. Cette modélisation permet d'étudier l'évolution de la vitesse résiduelle du projectile V_r en fonction de sa vitesse d'impact V_0 pour différentes configurations de couches et d'identifier les phénomènes structurels conduisant à la perforation de la cible impactée.

Malheureusement, certaines difficultés dans la fabrication et la préparation des matériaux n'ont pas permis d'essais expérimentaux d'impacts à grande vitesse sur les composites multicouches. Par conséquent, seule l'étude numérique paramétrique de différentes configurations de composites multicouches a été réalisée dans ce travail.

Un système de notation est utilisé: X1_T1 / X2_T2 avec X1 le matériau du côté impacté et X2 le matériau à l'arrière (F7020 ou PI) et T1 et T2 leurs épaisseurs respectives. L'épaisseur de la résine époxy est toujours de 0.5 mm et se situe entre X1 et X2.

a. Perforation de différents types de configuration de cible multicouche

Les configurations bicouches consistent en une couche d'alliage d'aluminium F7020 et une couche de polyimide fritté assemblées ensemble par une couche de résine epoxy de 0.5 mm d'épaisseur. Plusieurs paramètres peuvent être ajustés tels que l'épaisseur de chaque couche et leur position respective dans la cible (côtés arrière ou avant). Les résultats suivants présentent la réponse balistique de ces matériaux bicouches sur une large gamme de vitesses d'impact (de la vitesse balistique limite à 400 m/s).

Dans le cas F7020_X/PI_Y, le comportement typique sous charge d'impact consiste en grands fragments de polymère arrachés de la face arrière de la cible et également de petits fragments d'aluminium (Figure X.a). Concernant le cas PI_X/F7020_Y, les seuls fragments observés proviennent des pétales qui ont été arrachés de l'alliage d'aluminium F7020 situé à l'arrière de la cible. Seulement quelques fragments de polyimide frittés provenant de la face avant cible sont observés à travers les simulations.

Afin de visualiser les mécanismes de perforation des cibles en fonction de la position des différents matériaux (face avant ou arrière), des coupes de simulation de deux cas typiques (F7020_2.5 / PI_2.5, et PI_2.5/F7020_2.5) sont présentées (respectivement Figure 16.a et 16.b). Dans chaque cas, la vitesse d'impact du projectile à bille en acier est de 300 m / s et les données représentées correspondent à la contrainte normalisée de Von Mises.

F7020_2.5/PI_2.5	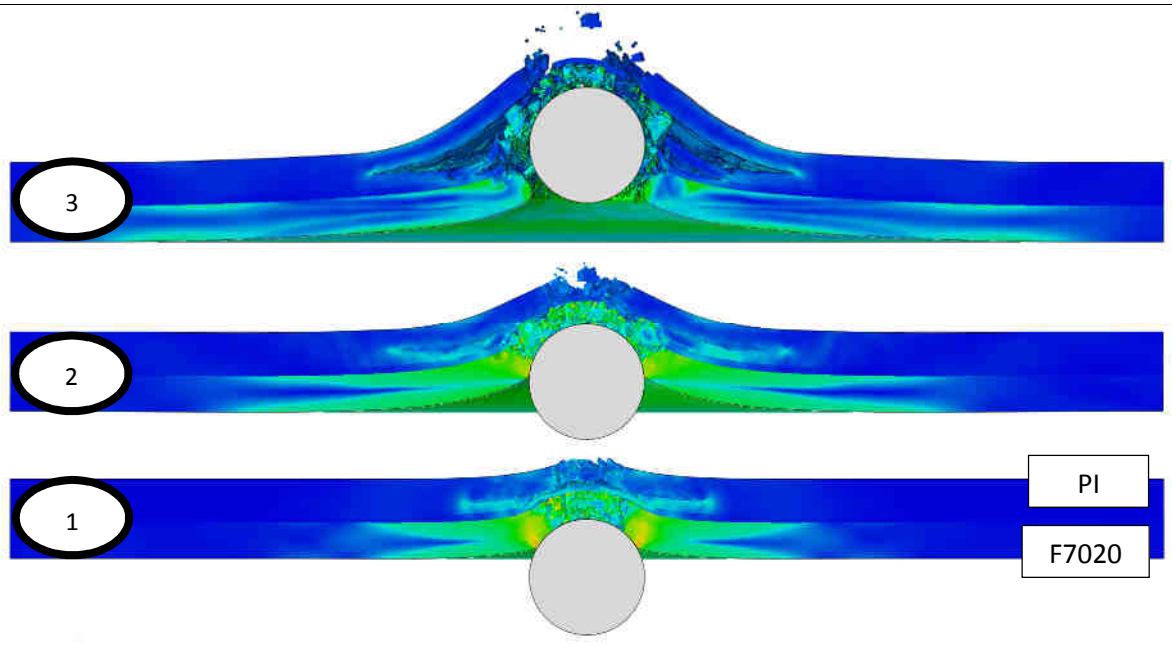 (a)

PI_2.5/F7020_2.5	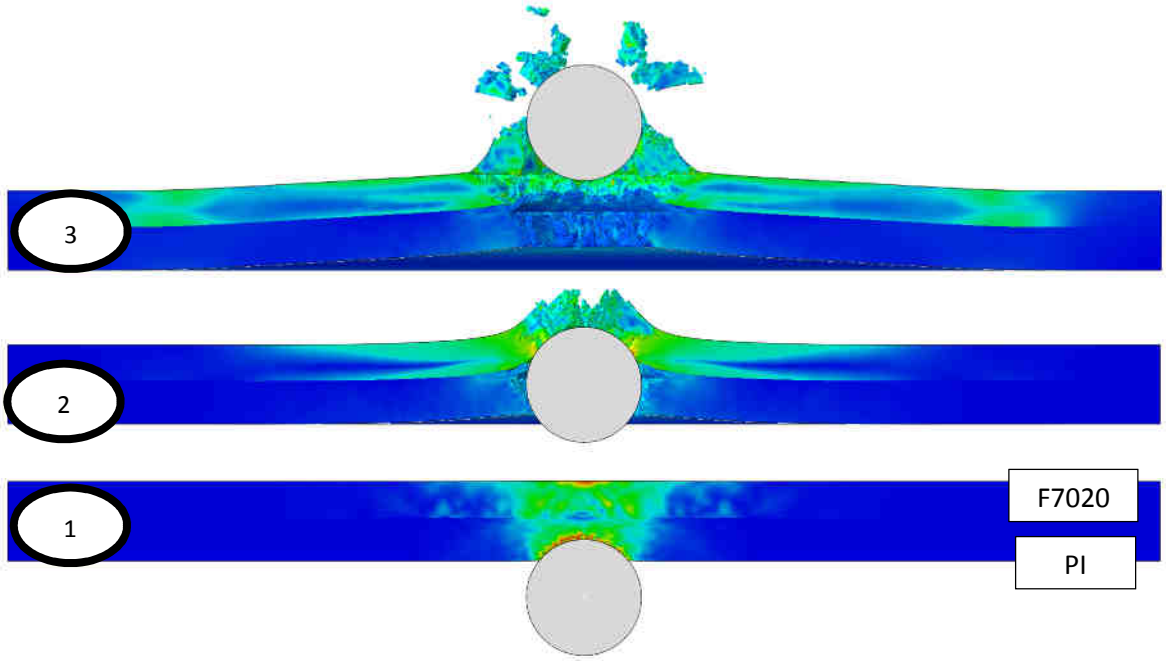 (b)

Figure 178 – Evolution de la perforation par une bille d'acier Ø8mm à $V_0 = 300\ m/s$ pour les configurations (a) F7020_2.5/PI_2.5 et (b) PI_2.5/F7020_2.5 avec ABAQUS®/Explicit

b. Performance balistique

Les courbes de la vitesse résiduelle du projectile V_r en fonction de la vitesse d'impact V_0 pour chaque configuration étudiée sont présentées sur la Figure 17.

On peut voir que quelques soit la configuration étudiée, la réponse mécanique de la cible sous la charge d'impact diminue avec la quantité de polyimide fritté.

En effet, dans le cas F7020_X/PI_Y, la résistance mécanique relativement élevée de la couche de polymère empêche la couche métallique de se déformer comme dans le cas monocouche. Par conséquent, le projectile est décéléré sur une distance plus petite que si la couche métallique était utilisée seule. La couche de polyimide fritté étant déjà fortement endommagé lorsque le projectile l'atteint, l'impact de cette dernière sur la décélération de ce dernier lors de sa perforation est négligeable. Cela explique les performances balistiques inférieures des cibles bicouches par rapport au cas monolithique F7020_3 (Figure 17.a). En outre, on constate que les valeurs de P_B n'évoluent pas beaucoup avec le rapport volumique du polyimide fritté (40%, 50% et 60%) et restent proches de l'un des cas de monocouche polymère (Figure 17.b).

Concernant les configurations de type PI_X/F7020_Y, on constate également que la réponse mécanique de la cible sous la charge d'impact diminue avec la quantité de polyimide fritté (Figure 17.c). Cependant, cette tendance est due à une raison différente. En effet, pour les configurations impliquant la couche de polyimide fritté sur le côté impacté, cette dernière ne peut parvient pas à ralentir significativement le projectile pour de telles vitesses d'impact et, par conséquent, son influence est négligeable. En outre, la présence de la couche métallique en face arrière empêche toute déformation de la couche de polymère, réduisant encore plus ses performances. Ceci explique les performances balistiques P_B inférieures des différentes cibles composites bicouches comparées au cas monolithique F7020_3 (Figure 17.d). Comme pour les configurations F7020_X/PI_Y, on constate que les valeurs de P_B n'évoluent pas beaucoup avec le rapport volumique du polyimide fritté (40%, 50% et 60%) et restent proches des cas de monocouche polymère PI_3. On notera également que les performances balistiques des configurations PI_X / F7020_Y sont légèrement inférieures aux configurations F7020_X/PI_Y.

Les Figures 17.e et 17.f montrent les résultats des simulations pour des configurations bicouches présentant des épaisseurs totales différentes mais des ratios volumiques 50%/50% pour chacun des matériaux principaux (F7020 et polyimide frittés). On observe les mêmes phénomènes que pour les autres configurations déjà étudiés : une performance balistique beaucoup plus faible que le cas F7020_3 à cause des faibles performances balistiques du polyimide fritté qui de plus empêche une déformation optimale de la couche d'alliage d'aluminium F7020. Cela conduit alors à une perte de performance balistique P_B par rapport au cas monolithique F7020_3 (renforcé par une augmentation importante de la densité surfacique du matériau bicouche).

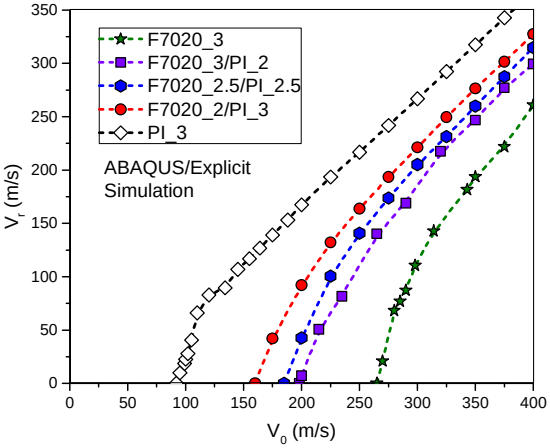

(a)

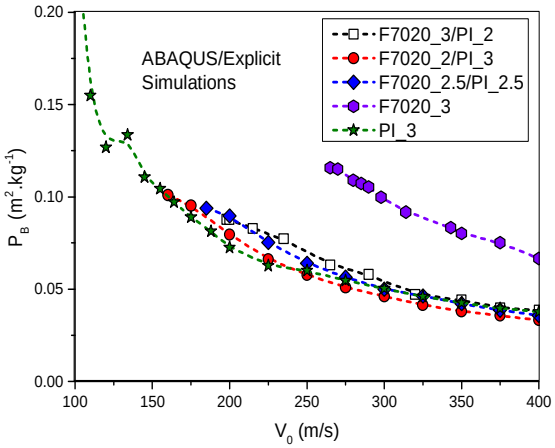

(b)

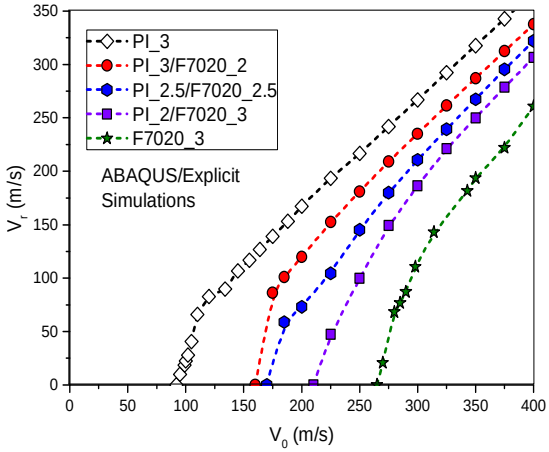

(c)

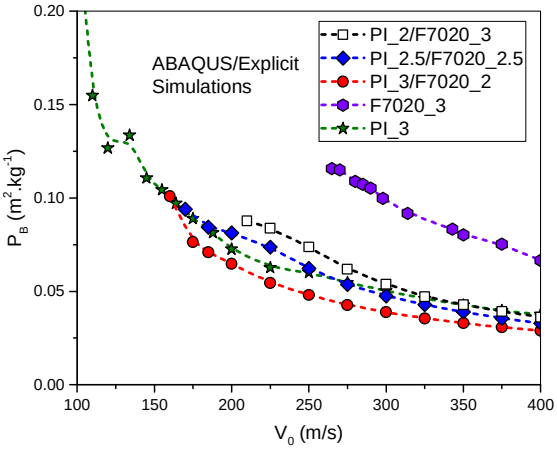

(d)

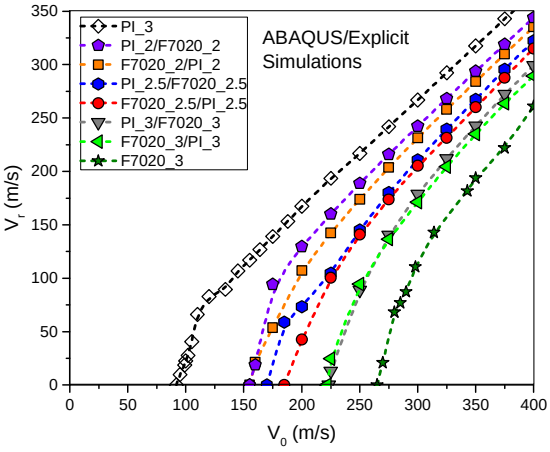

(e)

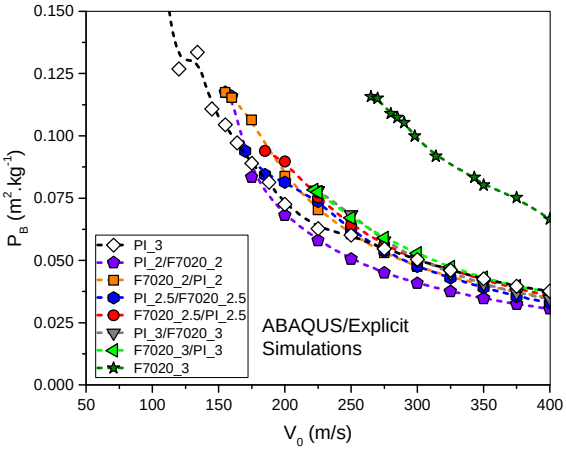

(f)

Figure 179 – Evolution simulée en fonction de la vitesse d'impact du projectile de (a),(c),(d) la vitesse résiduelle du projectile et de (b),(d),(f) la performance balistique pour plusieurs configurations de matériaux bicouches (avec ABAQUS®/Explicit)

CONCLUSION

La caractérisation mécanique des différents matériaux impliqués dans ce travail (alliage d'aluminium F7020, polyimide fritté et résine époxy) a révélé plusieurs comportements différents. Les mécanismes de déformation concernant le métal sont complexes en raison de sa microstructure dépendant non-linéairement de la température. En outre, la matrice d'aluminium présente différentes sensibilités à la vitesse de la déformation (contraintes interne et effective). En ce qui concerne le comportement de la rupture, le comportement observé est très spécifique au matériau fritté. En effet, dans le cas de triaxialités positives, la rupture est causée par la décohésion intergranulaire des grains de poudre. Pour les cas de triaxialité négative, la rupture est causée par le cisaillement intergranulaire des grains de poudre. Dans ce but, les sensibilités à la vitesse de déformation et à la température ont été effectuées à l'aide de tests de compression-cisaillement. En ce qui concerne le polyimide fritté, les mécanismes liés à la déformation sont contrôlés par le déplacement des chaînes. La limite d'élasticité, qui définit le niveau de stress global du polymère, présente des dépendances importantes à la température et à la vitesse de déformation. Le comportement d'hyperélasticité a été étudié dans ce travail avec des dépendances du module caoutchoutique aux conditions thermiques et à la vitesse de déformation. Le comportement e la rupture est très proche de celui observé pour l'alliage d'aluminium F7020. La rupture est donc régie à une échelle différente par rapport aux mécanismes de déformation.

La modélisation du comportement mécanique de l'alliage d'aluminium fritté F7020 a été réalisé à partir d'une nouvelle approche développée au cours de la thèse : l'approche Crystallo-Calorific Hardening (CCH) [3]. Celle-ci permet de prendre en compte des effets de changement de microstructure telle que la dissolution des précipités avec la température contrairement à d'autres. Concernant le polyimide fritté, le comportement mécanique a été modélisé en couplant le modèle coopératif pour la limite d'élasticité avec le modèle de Gent pour l'hyperélasticité. Ces deux modèles ont ensuite été associés dans une expression analytique unifiée prenant en compte également l'adoucissement plastique. Ce modèle a également été utilisé pour la résine epoxy. La modélisation de la rupture a été réalisé suivant la même approche tous les matériaux : une expression multiplicative définissant la déformation à l'initiation de la rupture en fonction de l'état de

contrainte, de la température et de la vitesse de déformation. Pour chaque matériau, une expression spécifique à l'évolution des sensibilités à chacun des paramètres expérimentaux cités a été choisie. Les modèles finaux sont donc différents pour chaque matériau.

Après la détermination de tous les paramètres des modèles, les expressions analytiques ont été implémentées via une subroutine VUMAT en code FORTRAN pour ABAQUS®/Explicit. La validation du modèle numérique a d'abord été réalisée par des comparaisons avec les résultats expérimentaux des impacts à grande vitesse d'une bille en acier sur des matériaux monocouches (alliage d'aluminium F7020 et polyimide fritté). Dans chaque cas, les modèles proposés sont capables de représenter avec précision la vitesse résiduelle du projectile. Le polyimide fritté présente un mode de perforation par fragmentation. Les résultats numériques sur les composites bicouches ont montré que la forte fragilité du polyimide fritté entraîne une perte de performance balistique du matériau quelle que soit l'épaisseur des couches. L'augmentation de la ductilité du polyimide fritté en retardant la rupture intergranulaire entre les grains de poudre serait une manière intéressante d'améliorer ce matériau. La simulation et la validation expérimentale avec un matériau tri-couche ou plus serait également un aspect intéressant de l'étude sur le développement de ces matériaux multicouches.

Pour aller plus loin dans le projet, il est obligatoire de procéder à la validation expérimentale du modèle numérique d'impact sur le matériau multicouche pour plusieurs configurations (plusieurs essais par conditions) et il serait intéressant d'effectuer des tests supplémentaires pour les cibles monocouches. En outre, le travail présenté ne porte que sur les impacts du projectile en acier sphérique sur des cibles minces. Par conséquent, les paramètres à étudier pour une validation plus large pourraient être: l'épaisseur des cibles, la position relative des couches, la forme du projectile, la vitesse du projectile (vitesses plus élevées), le nombre de couches, le type de sollicitation.

Références

1. Queudet, H., et al., *One-step consolidation and precipitation hardening of an ultrafine-grained Al-Zn-Mg alloy powder by Spark Plasma Sintering.* Materials Science and Engineering: A, 2017. **685**: p. 227-234.

2. Schwertz, M., *Technologie Spark Plasma Sintering (SPS) appliquée aux composites polymère/métal pour allègement de structure*, 2014.

3. Francart, C., et al., *Application of the Crystallo-Calorific Hardening approach to the constitutive modeling of the dynamic yield behavior of various metals with different crystalline structures.* International Journal of Impact Engineering, 2017.

4. Richeton, J., et al., *Influence of temperature and strain rate on the mechanical behavior of three amorphous polymers: Characterization and modeling of the compressive yield stress.* International Journal of Solids and Structures, 2006. **43**(7–8): p. 2318-2335.

5. Horgan, C.O., *The remarkable Gent constitutive model for hyperelastic materials.* International Journal of Non-Linear Mechanics, 2015. **68**(0): p. 9-16.

6. Follansbee, P. and U. Kocks, *A constitutive description of the deformation of copper based on the use of the mechanical threshold stress as an internal state variable.* Acta Metallurgica, 1988. **36**(1): p. 81-93.

7. Biswajit Banerjee, A.S.B., *An extended mechanical threshold stress plasticity model: modeling 6061-T6 aluminum alloy.* Journal of Mechanics of Materials and Structures, 2008. **3**(3).

8. Hull, D. and D.J. Bacon, *Introduction to dislocations*. Vol. 257. 1984: Pergamon Press Oxford.

9. Klahn, D., A. Mukherjee, and J. Dorn, *STRAIN-RATE EFFECTS*, 1970, California Univ., Berkeley. Lawrence Radiation Lab.

10. Johnson, G.R. and W.H. Cook. *A constitutive model and data for metals subjected to large strains, high strain rates and high temperatures*. in *Proceedings of the 7th International Symposium on Ballistics*. 1983. The Netherlands.

11. Zerilli, F.J. and R.W. Armstrong. *Constitutive relations for the plastic deformation of metals*. in *High-pressure science and technology—1993*. 1994. AIP Publishing.

12. Rusinek, A. and J.R. Klepaczko, *Shear testing of a sheet steel at wide range of strain rates and a constitutive relation with strain-rate and temperature dependence of the flow stress.* International Journal of Plasticity, 2001. **17**(1): p. 87-115.

13. Bergstrom, J.S., *Mechanics of solid polymers: theory and computational modeling*2015: William Andrew.

14. Eyring, H., *Viscosity, plasticity, and diffusion as examples of absolute reaction rates.* The Journal of Chemical Physics, 1936. **4**(4): p. 283-291.

15. G'sell, C. and J. Jonas, *Determination of the plastic behaviour of solid polymers at constant true strain rate.* Journal of Materials Science, 1979. **14**(3): p. 583-591.

16. Ree, T. and H. Eyring, *Theory of Non-Newtonian Flow. I. Solid Plastic System.* Journal of Applied Physics, 1955. **26**(7): p. 793-800.

17. Manuel J. Garcia R., O.E.R.S., Carlos Lopez, *Hyperelastic Material Modeling*, 2005, Departamento de Ingenieria Mecanica: Medellin.

18. Arruda, E.M. and M.C. Boyce, *A three-dimensional constitutive model for the large stretch behavior of rubber elastic materials.* Journal of the Mechanics and Physics of Solids, 1993. **41**(2): p. 389-412.

19. Bao, Y. and T. Wierzbicki, *A comparative study on various ductile crack formation criteria.* TRANSACTIONS-AMERICAN SOCIETY OF MECHANICAL ENGINEERS JOURNAL OF ENGINEERING MATERIALS AND TECHNOLOGY, 2004. **126**: p. 314-324.

20. Clausen, A.H., et al., *Flow and fracture characteristics of aluminium alloy AA5083–H116 as function of strain rate, temperature and triaxiality.* Materials Science and Engineering: A, 2004. **364**(1): p. 260-272.

21. Wang, J., et al., *Dynamic tensile properties of a single crystal Nickel-base superalloy at high temperatures measured with an improved SHTB technique.* Materials Science and Engineering: A, 2016. **670**: p. 1-8.

22. Rottler, J. and M.O. Robbins, *Growth, microstructure, and failure of crazes in glassy polymers.* Physical Review E, 2003. **68**(1): p. 011801.

23. Ward, I. and J. Sweeney, *An Introduction to the Mechanical Properties of Solid Polymers 2004.* England: John Wiley & Sons, Ltd.

24. Nielsen, L.E., *Cross-linking–effect on physical properties of polymers.* 1969.

25. Karger-Kocsis, J. and T. Czigány, *Strain rate dependence of the work of fracture response of an amorphous poly (ethylene-naphthalate)(PEN) film.* Polymer Engineering & Science, 2000. **40**(8): p. 1809-1815.

26. Johnson, G.R. and W.H. Cook, *Fracture characteristics of three metals subjected to various strains, strain rates, temperatures and pressures.* Engineering fracture mechanics, 1985. **21**(1): p. 31-48.

27. Wierzbicki, T., et al., *Calibration and evaluation of seven fracture models.* International Journal of Mechanical Sciences, 2005. **47**(4): p. 719-743.

28. Tvergaard, V., *Material failure by void growth to coalescence.* Advances in applied Mechanics, 1989. **27**: p. 83-151.

29. Gurson, A.L., *Continuum theory of ductile rupture by void nucleation and growth: Part I—Yield criteria and flow rules for porous ductile media.* Journal of engineering materials and technology, 1977. **99**(1): p. 2-15.

30. CAMPAGNE, L., *Modélisation et simulation de la viscoplasticité et de l'endommagement en grandes vitesses de déformation*, 2003.

31. Belov, N.A., D.G. Eskin, and A.A. Aksenov, *Multicomponent phase diagrams: applications for commercial aluminum alloys*2005: Elsevier.

32. Chinella, J.F. and Z. Guo, *Computational Thermodynamics Characterization of 7075, 7039, and 7020 Aluminum Alloys Using JMatPro*, 2011, DTIC Document.

33. Jankowiak, T., A. Rusinek, and T. Lodygowski, *Validation of the Klepaczko–Malinowski model for friction correction and recommendations on Split Hopkinson Pressure Bar.* Finite Elements in Analysis and Design, 2011. **47**(10): p. 1191-1208.

34. Dorogoy, A., D. Rittel, and A. Godinger, *Modification of the shear-compression specimen for large strain testing.* Experimental mechanics, 2015. **55**(9): p. 1627-1639.

35. Kocks, U. and H. Mecking, *Physics and phenomenology of strain hardening: the FCC case.* Progress in materials science, 2003. **48**(3): p. 171-273.

36. Richeton, J., et al., *Modeling and validation of the large deformation inelastic response of amorphous polymers over a wide range of temperatures and strain rates.* International Journal of Solids and Structures, 2007. **44**(24): p. 7938-7954.

37. Dudrová, E. and M. Kabátová, *Fractography of sintered iron and steels.* Powder Metallurgy Progress, 2008. **8**(2): p. 59-75.

38. Abaqus, *Damage evolution and element removal for ductile metals.* Abaqus Documentation, 2014.